

Unsteady aerodynamics and vortex shedding of a wind turbine blade



Sowmya Srinivasan Iyer

DTU Wind-M-0614

July 2023

M.Sc. Thesis

Unsteady aerodynamics and vortex shedding of a wind turbine blade

European Wind Energy Master
Rotor Design - Aerodynamics

Sowmya Srinivasan Iyer

Technical University of Denmark
and Delft University of Technology,
2023



Unsteady aerodynamics and vortex shedding of a wind turbine blade

Thesis report

by

Sowmya Srinivasan Iyer

to obtain the degree of Master of Science
at Delft University of Technology and
the Technical University of Denmark
to be defended publicly on August 25, 2023 at 13:00

Thesis committee:

Chair:	Professor Carlos Simao Ferreira
Supervisors:	Senior Researcher Franck Bertagnolio Assistant Professor Christian Grinderslev Assistant Professor Wei Yu PhD Candidate Guanqun Xu
External examiner:	Associate Professor Bas van Oudheusden
Place:	DTU Wind and Energy Systems, Lyngby, Denmark
Project Duration:	November, 2022 - August, 2023
Student number:	5150477 / S213852

An electronic version of this thesis is available at <http://repository.tudelft.nl/>.

**Technical University of Denmark
DTU Wind and Energy Systems**

DTU Lyngby Campus
Nils Koppels Alle
Building 403
2800 Kgs. Lyngby, Denmark
Phone +45 45 25 25 25
reception@windenergy.dtu.dk
www.windenergy.dtu.dk

**Delft University of Technology
Faculty of Aerospace Engineering**

TUD Campus
Kluyverweg 1
2629 HS Delft, Netherlands
+31 (0)15 27 85170
DUWIND@tudelft.nl
<https://www.tudelft.nl/duwind/>



Copyright © Sowmya Srinivasan Iyer, 2023
All rights reserved.

Abstract

The thesis presents an analysis of unsteady vortex shedding and vortex induced vibrations (VIV) on wind turbine blades using a combination of Stereoscopic Particle Image Velocimetry (SPIV) and Computational Fluid Dynamics (CFD). A spanwise uniform blade with a symmetric NACA0021 airfoil section, 0.075 m chord, and 0.4 m span was tested experimentally for a static, plunging, and surging blade oscillating at 90 deg angle of attack, 5 Hz, and 2.5 Hz frequency, 1 chord oscillation amplitude. Equivalent CFD simulation cases were run to compare the results and validate the CFD setup, which was used to analyse additional cases of interest. The extent of the three-dimensional flow behaviour due to the tip vortex was described, along with determining the lock-in region for the two motions using additional simulations. The results indicated that the spanwise convection of the tip vortex and the transition to a '2D' flow were only dependent on the blade aspect ratio and independent of the freestream wind speed, the type of motion, and the oscillation frequency. The lock-in region for the plunging and surging blades was presented, noting that all the surging cases were locked in, most likely due to the large oscillation amplitude. However, the surging cases had a positive aerodynamic damping and hence, VIV would not be excited for a freely vibrating blade. It is suggested as future work to test a flexible blade and study the onset and development of VIV.

Executive Summary

The ever-growing demand for clean and sustainable energy requires longer blades to reduce the LCOE. However, the increasing blade length is coupled with increasing flexibility, making them more susceptible to vortex induced vibrations (VIV), especially during standstill conditions due to the high aeroelastic response of the blades Horcas et al. [2020], Skrzypiński [2012], Veers et al. [2023], which could lead to fatigue and failure Heinz et al. [2016], Zou et al. [2015]. An understanding of the exact phenomena that cause the onset and development of VIV on wind turbine blades is still unknown Horcas et al. [2020] and hence, is the focus of this thesis. The edgewise mode is most susceptible to VIV, and the phenomenon is most common during standstill. A combination of experimental techniques using low-speed Stereoscopic Particle Image Velocimetry (SPIV) and Computational Fluid Dynamics (CFD) with an Improved Delayed Detached Eddy Simulation (IDDES) turbulence model was used to analyse a blade undergoing a forced plunging and surging motion. The PIV experiment was performed at the Open Jet Facility at Delft University of Technology. The CFD experiments were run on EllipSys3D Michelsen [1992, 1994], Sørensen [1995].

There are four research questions addressed in this thesis: To what degree do the CFD simulations accurately predict the flow around the blade? For a finite blade, how many chords away from the tip is the transition point where the flow around the blade starts to behave two-dimensional? At what range of frequency and amplitude combinations does lock-in occur? How do the flow around the blade and the loads for a plunging and surging airfoil compare over one cycle? For the PIV experiment, the flow around a static blade at $U_\infty = 5\text{m/s}$ was analysed, followed by a plunging blade and surging blade at 90 deg angle of attack, 5 Hz, and 2.5 Hz frequency, 1 chord oscillation amplitude. The same cases were simulated using CFD, along with many frequency amplitude combinations for both motions so as to obtain a lock-in region.

The CFD results were validated against the PIV flow fields to confirm their accuracy in predicting the flow around the blade. The tip effect was analysed for a static blade for two different aspect ratios and for the plunging and surging blade examining the flow fields around the blade as well as PSDs of the force coefficients, hysteresis loops, the mean, median, and standard deviation of the force coefficients, and power and phase shift over various spanwise positions. The analysis indicated that the spanwise convection of the tip vortex is only dependent on the blade aspect ratio and not on the type of motion or the frequency of oscillation. Next, the lock-in region for a plunging and surging blade was presented, with a comparison of the plunging blade to results from Hu et al. [2021]. It was noted that all the tested cases for the surging blade were locked in, most likely due to the high oscillation amplitude, but they were accompanied by positive aerodynamic damping, and hence, VIV would not occur for a freely vibrating blade for the same condition. Future work should focus on analysing the onset and development of VIV around a flexible blade.

Preface

This thesis was prepared at the Department of Wind Energy at the Technical University of Denmark and the Faculty of Aerospace Engineering from Delft University of Technology in fulfilment of the requirements for acquiring two M.Sc. degrees, M.Sc. in Aerospace Engineering from Delft University of Technology, and M.Sc. in Wind Engineering from the Technical University of Denmark, as part of the European Wind Energy Master (EWEM), within the track of Rotor Design, profile Aerodynamics.

The research described in this thesis is in collaboration with the PhD research of Guanqun Xu, affiliated with Delft University of Technology. This thesis was presented at the Wind Energy Science Conference 2023 in the Unsteady Aerodynamics Session 3.11 by the Author and in the Mini Symposia on Wind Turbine Blade Aerodynamic Measurements Session 3.4b by PhD Candidate Guanqun Xu.

The project was kindly funded by Delft Technical University and The Technical University of Denmark.

Technical University of Denmark and Delft University of Technology, July 31, 2023



Sowmya Srinivasan Iyer

Acknowledgements

I would like to thank my supervisors from both universities for their guidance and support throughout this process. To Assistant Professor Christian Grinderslev, I would like to thank you for your endless patience for my infinite questions and complaints, and for the shared enthusiasm to run more simulations to see the results together. To Assistant Professor Wei Yu and Professor Carlos Simao Ferreira, I would like to thank you for taking time from your extremely busy schedules to spend time in the wind tunnel during the experiment. To Senior Researcher Franck Bertagnolio, I would like to thank you for your suggestions and ideas, leading me to discover new aspects of the results. And to PhD Candidate Guanqun Xu, I would like to thank you for being with me for the late nights in the tunnel, the hundreds of hours post-processing the results, and for being a friend by my side throughout the thesis. I would also like to thank Assistant Professor Andrea Sciacchitano for your help during the wind tunnel experiments, without whom it definitely would not have been possible.

I am grateful to the friends I made during the Master, who kept me sane and healthy with dinners, and sports, and for the company during the long days in the library. To Noor and Amira for treating me like a sister and welcoming me into your home during my time in Delft. To my parents, for their endless support and love, the food they sent to me halfway across the world, and for their unwavering confidence in me, without which I would not have survived. To my sister, for always picking up my late-night calls, for fuelling me with coffee, for all the winter coats, and for being my best friend. And to my partner, without whom I would not have made it through this journey.

I would also like to thank EWEM, DU Wind and the TU Delft Fast Fund for sponsoring my trip to present at the Wind Energy Science Conference.

Nomenclature

This list describes several acronyms and symbols that will be used later in the body of the document

Acronyms

CDS Central Difference Scheme

CFD Computational Fluid Dynamics

DDES Delayed Detached Eddy Simulation

DES Detached Eddy Simulation

DNS Direct Numerical Simulation

FOV Field of View

IDDES Improved Delayed Detached Eddy Simulation

IEC International Electrotechnical Commission

ILES Implicit Large Eddy Simulation

LES Large Eddy Simulation

NACA National Advisory Committee for Aeronautics

PIV Particle Image Velocimetry

POD Proper Orthogonal Decomposition

PSD Power Spectral Density

QUICK Quadratic Upstream Interpolation for Convective Kinematics

RST Reynolds Stress Tensor

SIMPLE Semi-Implicit Method for Pressure-Linked Equations

SPIV Stereoscopic Particle Image Velocimetry

URANS Unsteady Reynolds Averaged Navier-Stokes

VIV Vortex Induced Vibrations

Greek Letters

α Angle of Attack

$\bar{\omega}$	Mean Vorticity
ρ	Density of Fluid
τ	Non-Dimensional Time, tU_∞/c

Latin Symbols

\bar{P}	Mean Aerodynamic Power in One Cycle, $\overline{0.5\rho U_\infty^2 c}$
\bar{u}	Mean Streamwise velocity
\bar{v}	Mean Vertical velocity
\bar{w}	Mean Spanwise velocity
Δf	Frequency Limit = 5% f_{st}
ν_T	Eddy Viscosity
A	Oscillation Amplitude
A^*	Non-Dimensional Amplitude, A/c
AR_{CFD}	CFD Blade Aspect Ratio
AR_{expt}	Experiment Blade Aspect Ratio
c	Chord
cd	Drag Coefficient, $D/0.5\rho U_\infty^2 c$
cl	Lift Coefficient, $L/0.5\rho U_\infty^2 c$
cx	Streamwise Force Coefficient, $Fx/0.5\rho U_\infty^2 c$
cy	Vertical Force Coefficient, $Fy/0.5\rho U_\infty^2 c$
f	Frequency
f^*	Non-Dimensional Frequency, c/TU_∞
f_n	Natural Frequency
f_{st}	Strouhal Frequency
k	Reduced frequency, $\pi fc/U_\infty$
P^*	Non-Dimensional Power, $T/(\rho cAU_\infty^2)\bar{P}$
S_{CFD}	CFD Blade Span
S_{expt}	Experiment Blade Span

T	Oscillation period, $1/f$
T^*	Non-Dimensional Period, TU_∞/c
U^*	Reduced Flow Velocity, U_∞/fc
U_∞	Freestream Velocity
X/c	Normalised Blade Position
2P	2 opposite sign vortex pairs shed per cycle
2S	2 opposite sign vortices shed per cycle
Re	Reynolds Number, $\rho U_\infty c/\mu$
St	Strouhal Number, $f_{st}c/U_\infty$

Contents

Nomenclature	ix
Contents	xiii
List of Figures	xv
List of Tables	xx
1 Introduction and Literature Review	1
1.1 Relevance and Motivation	1
1.2 Report Structure	1
1.3 Unsteady Aerodynamics and Vortex Induced Vibrations	2
1.4 Vortex-Shedding Modes	4
1.5 State of the Art VIV research	5
1.6 Particle Image Velocimetry	8
1.7 Computational Fluid Dynamics	9
1.8 Key Findings	10
1.9 Research Gaps	11
1.10 Research Questions	11
2 Design of Experiment	13
2.1 Methodology	13
2.2 Particle Image Velocimetry	15
2.3 Experimental Setup	16
2.4 Test Cases	21
2.5 Computational Fluid Dynamics	23
3 Results	27
3.1 Validation of CFD Results	27
3.2 Plunging Blade	36
3.3 Surging Blade	60
3.4 Lock-In region	82
4 Conclusion	91
4.1 Summary	91
4.2 CFD Validation	92
4.3 Tip effect	92
4.4 Lock-In	93
4.5 Plunging vs Surging Airfoil	94
4.6 Limitations	95
4.7 Future Work	95

Bibliography	97
A Aerodynamic Loads using the NOCA Method	103
A.1 Steady Case	103
A.2 Plunging 2.5Hz	104
A.3 Plunging 5Hz	107
B CFD Static Cases Implicit Large Eddy Simulation with Aspect Ratio 10	111
C CFD Static Cases Implicit Large Eddy Simulation with Aspect Ratio 20	117
D CFD Static Cases Improved Delayed Detached Eddy Simulation with Aspect Ratio 10	123
E Static Cases for an 81 cm blade, $U_\infty = 5$ m/s	129
F Static Cases for a 40 cm blade, $U_\infty = 5$ m/s	135
G Static Cases for a 40 cm blade, $U_\infty = 3$ m/s	141
H 2.5 Hz Plunging Cases PIV Planes	147
I 5 Hz Plunging Cases PIV Planes	165
J 2.5 Hz Surging Cases PIV Planes	183
K 5 Hz Surging Cases PIV Planes	189
L 2.5 Hz Plunging Cases CFD Planes	195
M 5 Hz Plunging Cases CFD Planes	213
N 2.5 Hz surging Cases CFD Planes	231
O 5 Hz surging Cases CFD Planes	249
P PSD and Time-Series for Plunging Cases	267
Q PSD and Time-Series for Surging Cases	271

List of Figures

1.1	Experimental lock-in region of a NACA0012 airfoil forced to oscillate about quarter-chord. The non-dimensionalized frequency is defined as $f_{enforced} = f_{shed}$. The angle of attack is 40 deg and the Reynolds number is 100,000. The flow is assumed incompressible. The circles are locked-in, the diamonds are unlocked, and the squares have a chaotic behaviour. Reprinted from Besem et al. [2016].	3
1.2	2P-2S Vortex Patterns. Reprinted from Williamson and Roshko [1988]. Curves I and II from Bishop and Hassan [1964].	5
2.1	Velocity Triangle showing Orientation of Blade	14
2.2	Plunging Mechanism Front View	17
2.3	Plunging Mechanism CAD Assembly	17
2.4	Schematic of Slider-Crank Working Mechanism (Not to Scale)	18
2.5	Labelled Diagram of PIV Setup	18
2.6	Calibration Plate Setup. The plate is outlined in red. The laser shoots from the bottom.	19
2.7	PIV Field of View, with positive X in the flow direction, positive Y upwards, and positive Z out of the page. Total overlap length = 58.5 cm.	20
2.8	Front view (left) and side view (right) of the laser sheet illuminating the blade	20
2.9	CFD Mesh	24
2.10	Mesh over the blade with the resolution increasing towards the tip (left) and the blade in the domain mesh (right). The Red dashed line shows the chord section.	24
3.1	Spanwise velocity, \bar{w}/U_∞ around a static blade from 0.5c in front of the tip to 4c inboard from PIV data, freestream velocity coming from the left. The flow is positive into the page. Grey portions of the plot indicate no available data.	28
3.2	Spanwise velocity, \bar{w}/U_∞ around the blade	29
3.3	Spanwise velocity, \bar{w}/U_∞ around a static blade using an Implicit LES on a blade free on both ends with an aspect ratio of 20 (left) and PIV measurements on a cantilevered blade with an aspect ratio of 10 (right). The flow is positive into the page. Freestream velocity coming from the left.	30
3.4	Spanwise velocity, \bar{w}/U_∞ around an 80 cm, 10.7 aspect ratio static blade (left) and 40 cm, 5.3 aspect ratio static blade (right) from PIV data. Far wake data is unavailable for the 40 cm blade. Freestream velocity coming from the left. The flow is positive into the page.	32
3.5	Left to right: Averaged Streamwise Velocity \bar{u}/U_∞ , Spanwise Velocity \bar{w}/U_∞ Field, and Downstream Velocity Deficit from CFD data.. IDDES blade with AR 10 (top), ILES blade with AR 10 (middle), and ILES blade with AR 20 (bottom). Only half of the AR 20 blade from the tip to mid-span is presented.	33

3.6	Vorticity, $\bar{\omega}c/U_\infty$ 3 chords inboard from the tip with the freestream velocity coming from the left. Flow fields from CFD results (left) and PIV results (right).	35
3.7	Vorticity, $\bar{\omega}c/U_\infty$ around a plunging airfoil 3 chords inboard from the tip at 5 Hz (left) and 2.5 Hz (right) with the freestream velocity coming from the left from CFD data.	37
3.8	Flow Around the Tip for a 5 Hz plunging airfoil at 0 deg phase for 1 chord motion amplitude from PIV data. Blade is at $y/c = 0$, $x/c = -2$, $z/c = 0$ to 0.5.	38
3.9	Vorticity, $\bar{\omega}c/U_\infty$ around a plunging airfoil at 5Hz (left), and at 2.5Hz (right) from 3 chords inboard (top) to the tip (bottom) with the freestream velocity coming from the left from CFD data.	39
3.10	Vorticity, $\bar{\omega}c/U_\infty$ around a plunging airfoil at 5Hz, 3 chords inboard from the tip (left) and at the tip (right) with the freestream velocity coming from the left from CFD data.	41
3.11	Velocity Triangles for a Plunging Airfoil	42
3.12	Time series of the cl at various spanwise positions from the tip to mid-span for a plunging airfoil at 5 Hz, 1 chord amplitude for 15 cycles from CFD data.	44
3.13	Time series of the cd at various spanwise positions from the tip to mid-span for a plunging airfoil at 5 Hz, 1 chord amplitude for 15 cycles from CFD data.	45
3.14	PSD of cl (left) and cd (right) for a plunging blade at 5 Hz $\sim 0.78f_{st}$, 1 chord motion amplitude at various spanwise positions from CFD results.	46
3.15	Lissajous figure, A – the amplitude, width – the phase lag. Reprinted from Yu [2018]. Method from Al-Khazali and Askari [2012].	47
3.16	Hysteresis loops of the cl (left) and cd (right) against the angle of attack at different spanwise positions inboard from the tip for a plunging blade at 5 Hz frequency, 1 chord amplitude. Measured in chords away from the tip. The solid line shows the mean load as the blade moves upwards, the dashed line shows the mean load as the blade moves downwards and the surrounding translucent region is the standard deviation over 15 cycles from CFD data. Both loops rotate counter-clockwise.	48
3.17	Plunging airfoil at 5 Hz, 1 chord amplitude. Mean and Median values for cl (a), cd (b), and their phases (c) and (d) respectively at different spanwise positions over 15 cycles from CFD data. Bars represent the standard deviation away from the mean.	50
3.18	Plunging airfoil at 5 Hz, 1 chord amplitude. Mean and Median values for Non-Dimensional Power (a), and its phase (b) respectively at different spanwise positions over 15 cycles from CFD data. Bars represent the standard deviation away from the mean.	51
3.19	Vorticity, $\bar{\omega}c/U_\infty$ around a plunging airfoil at 2.5Hz, 3 chords inboard from the tip (left) and at the tip (right) with the freestream velocity coming from the left from CFD data.	52
3.20	Time series of the cl at various spanwise positions from the tip to mid-span for a plunging airfoil at 2.5 Hz, 1 chord amplitude for 15 cycles from CFD data.	54

3.21	Time series of the cd at various spanwise positions from the tip to mid-span for a plunging airfoil at 2.5 Hz, 1 chord amplitude for 15 cycles from CFD data.	55
3.22	PSD of cl (left) and cd (right) for a plunging blade at 2.5 Hz $\sim 0.39f_{st}$, 1 chord motion amplitude at various spanwise positions from CFD results.	56
3.23	Hysteresis loops of the cl (left) and cd (right) against the angle of attack at different spanwise positions inboard from the tip for a plunging blade at 2.5 Hz frequency, 1 chord amplitude. Measured in chords away from the tip. The solid line shows the mean load as the blade moves upwards, the dashed line shows the mean load as the blade moves downwards and the surrounding translucent region is the standard deviation over 15 cycles from CFD data. Both loops rotate clockwise.	57
3.24	Plunging airfoil at 2.5 Hz, 1 chord amplitude. Mean and Median values for cl (a), cd (b), and their phases (c) and (d) respectively at different spanwise positions over 15 cycles from CFD data. Bars represent the standard deviation away from the mean.	58
3.25	Plunging airfoil at 2.5 Hz, 1 chord amplitude. Mean and Median values for Non-Dimensional Power (a), and its phase (b) respectively at different spanwise positions over 15 cycles from CFD data. Bars represent the standard deviation away from the mean.	59
3.26	Vorticity, $\bar{\omega}c/U_\infty$ around a surging airfoil at 5Hz (left), and at 2.5Hz (right) from 3 chords inboard (top) to the tip (bottom) with the freestream velocity coming from the left from CFD data.	61
3.27	Vorticity, $\bar{\omega}c/U_\infty$ around a surging airfoil 3 chords inboard from the tip at 5 Hz (left) and 2.5 Hz (right) with the freestream velocity coming from the left from CFD data.	63
3.28	Flow on a Surging Blade over one cycle. $U_\infty > V_{m max}$	64
3.29	Vorticity, $\bar{\omega}c/U_\infty$ around a surging airfoil at 5Hz, 3 chords inboard from the tip (left) and at the tip (right) with the freestream velocity coming from the left from CFD data.	65
3.30	Time series of the cy at various spanwise positions from the tip to mid-span for a surging airfoil at 5 Hz, 1 chord amplitude for 10 cycles from CFD data.	67
3.31	Time series of the cx at various spanwise positions from the tip to mid-span for a surging airfoil at 5 Hz, 1 chord amplitude for 10 cycles from CFD data.	68
3.32	Streamwise velocity, \bar{u}/U_∞ around a surging airfoil at 5Hz, 3 chords inboard from the tip with the freestream velocity coming from the left from CFD data.	69
3.33	PSD of cy (left) and cx (right) for a surging blade at 5 Hz $\sim 0.78f_{st}$, 1 chord motion amplitude at various spanwise positions from CFD results.	70
3.34	Hysteresis loops of the cy (left) and cx (right) against the normalised blade position at different spanwise positions inboard from the tip for a surging blade at 5 Hz frequency, 1 chord amplitude. Measured in chords away from the tip. The solid line shows the mean load when the blade moves against the freestream, the dashed line shows the mean load when the blade moves in line with the freestream and the surrounding translucent region is the standard deviation over 10 cycles from CFD data. Both loops rotate clockwise.	71

3.35	Surging airfoil at 5 Hz, 1 chord amplitude. Mean and Median values for cy (a), cx (b), and their phases (c) and (d) respectively at different spanwise positions over 10 cycles from CFD data. Bars represent the standard deviation away from the mean.	73
3.36	Surging blade at 5 Hz, 1 chord amplitude. Mean and Median values for Non-Dimensional Power (a), and its phase (b) respectively at different spanwise positions over 10 cycles from CFD data. Bars represent the standard deviation away from the mean.	74
3.37	Vorticity, $\bar{\omega}c/U_\infty$ around a surging airfoil at 2.5Hz, 3 chords inboard from the tip (left) and at the tip (right) with the freestream velocity coming from the left from CFD data.	75
3.38	Time series of the cy at various spanwise positions from the tip to mid-span for a surging airfoil at 2.5 Hz, 1 chord amplitude for 10 cycles from CFD data.	76
3.39	Time series of the cx at various spanwise positions from the tip to mid-span for a surging airfoil at 2.5 Hz, 1 chord amplitude for 10 cycles from CFD data.	77
3.40	PSD of cy (left) and cx (right) for a surging blade at 2.5 Hz $\sim 0.39f_{st}$, 1 chord motion amplitude at various spanwise positions from CFD results.	78
3.41	Hysteresis loops of the cy (left) and cx (right) against the normalised blade position at different spanwise positions inboard from the tip for a surging blade at 2.5 Hz frequency, 1 chord amplitude. Measured in chords away from the tip. The solid line shows the mean load when the blade moves against the freestream, the dashed line shows the mean load when the blade moves inline with the freestream and the surrounding translucent region is the standard deviation over 10 cycles from CFD data. Both loops rotate clockwise.	79
3.42	Surging airfoil at 2.5 Hz, 1 chord amplitude. Mean and Median values for cy (a), cx (b), and their phases (c) and (d) respectively at different spanwise positions over 10 cycles from CFD data. Bars represent the standard deviation away from the mean.	80
3.43	Surging blade at 2.5 Hz, 1 chord amplitude. Mean and Median values for Non-Dimensional Power (a), and its phase (b) respectively at different spanwise positions over 10 cycles from CFD data. Bars represent the standard deviation away from the mean.	81
3.44	PSDs for a plunging airfoil from CFD data at 6 Hz (top) with amplitudes below 0.4c in the border, at 8 Hz (middle) with all cases locked-in and, at 10 Hz (bottom) with amplitudes below 0.4c unlocked	83
3.45	V-shaped Lock-in region from CFD data for a Plunging Blade.	85
3.46	V-shaped Lock-in region. Amplitude of chordwise oscillations vs the oscillation frequency ratio at 90 angle of attack. Reprinted from Hu et al. [2021]	86
3.47	Dimensionless vortex shedding frequency as a function of the frequency ratio of the forced oscillation of the airfoil. The red line is Reprinted from Hu et al. [2021]	87
3.48	Non-dimensional Power against Non-Dimensional Period for Different Amplitude Ratios for a Plunging Blade from CFD data.	88
3.49	Lock-in region from CFD data for a Surging Blade.	89

3.50 Non-dimensional Power against Non-Dimensional Period for Different Amplitude Ratios for a Surging Blade from CFD data. 90

List of Tables

1.1	Key Values from Literature. References in order from left to right Hu et al. [2021], Besem et al. [2016], Pellegrino and Meskell [2013], Skrzypiński et al. [2014,] *Values are calculated based on values stated in papers. Not all numbers are specified. Different airfoil sections are studied.	10
2.1	Summary of Experimental Design Parameters	14
2.2	Static Cases Test Matrix	21
2.3	Plunging Cases Test Matrix	22
2.4	Surging Cases Test Matrix	22
2.5	Static Blade Test Matrix for CFD Simulations	24
2.6	Plunging Blade Test Matrix for CFD Simulations. $U_\infty = 5m/s$ using an IDDES Solver. $f_{st} = 8.3$ Hz	25
2.7	Surging Blade Test Matrix for CFD Simulations. $U_\infty = 3m/s$ using an IDDES Solver. $f_{st} = 6.4$ Hz	26

CHAPTER 1

Introduction and Literature Review

1.1 Relevance and Motivation

Much of the previous research on vortex induced vibrations (VIV) comes from the field of civil engineering and is for cylinders, which mimic cables, pipelines, and chimneys, with the length and flexibility of the structure aggravating the problem Mottaghi et al. [2020]. Its relevance to the wind industry is becoming much more important as wind turbine blades are getting longer and more flexible because they become more susceptible to VIV, which could lead to failure Veers et al. [2023], Heinz et al. [2016], Zou et al. [2015]. This is especially so when the blades are pitched out of the wind in standstill conditions, due to the high aeroelastic response of the blade Horcas et al. [2020], Skrzypiński [2012]. Wind turbine manufacturers have also begun to indicate vibrations for their larger designs, the causes for which are still not fully known Horcas et al. [2020]. This phenomenon is also expected to affect full-scale Vertical Axis Wind Turbines as they experience high angle of attack variations at velocity regimes around the ‘lock-in’ regime Benner et al. [2019]. Nevertheless, the physics of the flow around a cylinder can be used as a basis to predict the flow around the blade and is a common starting point for much of modern VIV research on wind turbines.

1.2 Report Structure

Chapter 1 provides a literature review that introduces relevant concepts of unsteady aerodynamics, vortex induced vibrations, vortex shedding modes, state-of-the-art research, and, details on the experimental technique used in this thesis. Finally, a summary of key findings and research questions that guide the experimental design is presented. Chapter 2 presents a description of the experimental design, coordinate system, and test cases for the experiment and simulations. Details on the experimental instrumentation and setup as well as a brief description of the numerical simulation are provided. Chapter 3 presents the results and answers the research questions. First, the CFD results are validated and the flow around the static blade is analysed to determine the effect of the tip vortex. Next, the flow and loads around a plunging and surging airfoil are analysed, providing insights into their shedding patterns, the spanwise flow, and the lock-in regions for the motions. Finally, Chapter 4 presents a conclusion that summarises the key results and provides insights on its implications as well as limitations and suggestions for future work.

1.3 Unsteady Aerodynamics and Vortex Induced Vibrations

At high angles of attack, the flow behind an object can become highly separated, shedding vortices that can cause vibrations on the blade itself, similar to the separated flow behind a cylinder Heinz et al. [2016]. Although the vibration itself may not be an issue, in some cases, the shed vortex is similar to a von Karman vortex street which exerts periodic oscillation of aerodynamic forces perpendicular to the flow and structure, which can cause the structure to oscillate, though not all periodic loading will lead to structural vibration. The frequency of the shedding is related to the Strouhal number, $St = f_{st}c/U_\infty$, where f_{st} is the vortex shedding frequency, c is the characteristic length of the object, such as the chord at a certain blade section, and U_∞ is the steady velocity around the flow, usually the freestream flow velocity. Initially, the shedding frequency of the vortex will simply follow the Strouhal number, i.e. the shedding frequency will change with wind speed, but at a certain wind speed, the shedding frequency will approach the natural frequency f_n of the structure, and the vortices will no longer shed at f_{st} , but rather they will ‘lock-in’ to the natural frequency. For cylinders, the Strouhal number is relatively constant around 0.2 over a range of Reynolds numbers from 300 to 2×10^5 Mottaghi et al. [2020], Chen et al. [1984]. Chen and Fang [1996] performed a study on flat plates at different inclination angles and bevel angles and found that at 90 deg angle of attack, the Strouhal number is independent and is also around 0.2 for Reynolds numbers from 1.1×10^4 to 3.2×10^4 . The symmetric airfoil at 90 deg angle of attack behaves very similarly to a flat plate at 90 deg angle of attack and a cylinder, so it is expected that the Strouhal number will also be around 0.2. Bull et al. [2021] shows that for a Reynolds number of 2×10^4 , the modified Strouhal number (modified to use the projected chord for various angles of attack relative to the freestream) is around 0.18 for a static case. When it is plunging, the Strouhal number collapses to a range between 0.1 to 0.17 for a flat plate and between 0.1 to 0.2 for a NACA0021 airfoil. Blevins [1977] presents a relation between the Strouhal number and Reynolds number for a slender cylinder, which is stable around 0.2 for Reynolds numbers between 1×10^3 and 1×10^5 . For a flat plate at 90 degrees angle of attack, the Strouhal number tends to be around 0.15 for a Reynolds number around 1×10^4 Howell and Novak [1980]. The generally higher Strouhal number seen in the blade over the flat plate is due to the sharp trailing edge separation on the flat plate. The NACA0021 airfoil used in this test is expected to behave closer to the NACA0012 airfoil section, though there may be some differences due to the increased thickness.

When the frequency is locked-in, the oscillations become significantly larger, causing much larger and possibly fatal forces on the structure itself. If the force and velocity are in phase during this oscillation, power is injected into the system and if there is negative damping, this can cause failure. Heinz et al. [2016], Grinderslev et al. [2022]. Within the lock-in regime, the structure undergoes near-resonance vibrations Mottaghi et al. [2020]. In extreme cases, the deflections of the blade during ‘lock-in’ could be destructive. A hysteresis behaviour may also be observed based on how ‘lock-in’ is approached - from

low or high wind speeds, and this is associated with different vortex shedding modes Sarpkaya [1979].

There is a threshold where this phenomenon is observed and only outside this region will the vibrations decrease Heinz et al. [2016]. This ‘lock-in’ threshold generally forms a ‘V-shaped’ region Hu et al. [2021], Besem et al. [2016], Pellegrino and Meskell [2013], Hoskoti et al. [2018]. This range where lock-in occurs, i.e. where the vortex shedding frequency locks into the structural frequency is dependent on the amplitude of oscillation such that the larger the amplitude, the larger this frequency range will be Bearman [1984]. This is what leads to it looking like a ‘V-shape’. An example can be seen in Figure 1.1.

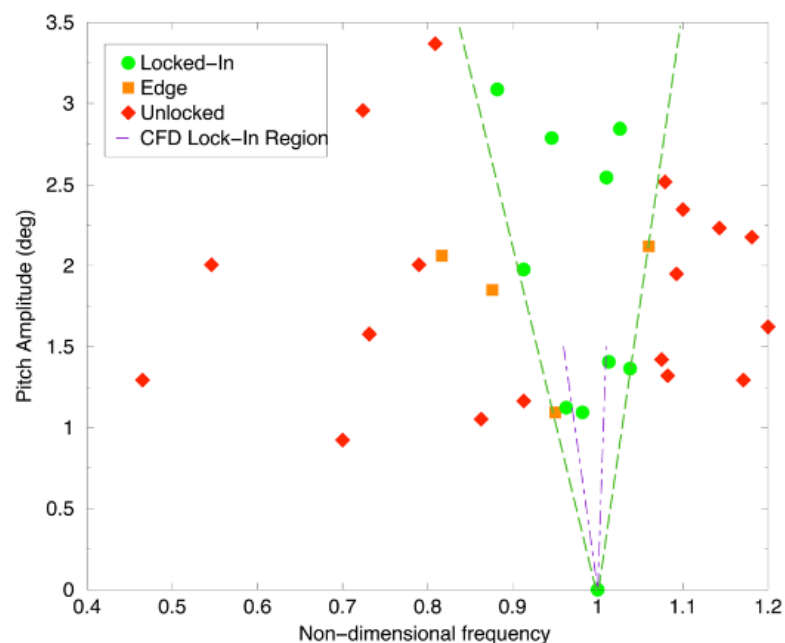


Figure 1.1: Experimental lock-in region of a NACA0012 airfoil forced to oscillate about quarter-chord. The non-dimensionalized frequency is defined as $f_{enforced} = f_{shed}$. The angle of attack is 40 deg and the Reynolds number is 100,000. The flow is assumed incompressible. The circles are locked-in, the diamonds are unlocked, and the squares have a chaotic behaviour. Reprinted from Besem et al. [2016].

The basis of VIV and vortex shedding phenomena goes back to the unsteady aerodynamics of the blade geometry itself. The blade section for this project is the NACA0021 airfoil, which is a symmetrical airfoil with a 21% thickness-chord ratio. Critzos et al. [1955] tested the NACA0021 airfoil at a Re of 1.8×10^6 and 0.5×10^6 from 0 to 180 degrees angle of attack, with Michos et al. [1983] extending the study to 360 degrees, and the 0 to 180 degrees range was also tested for a Re of 0.76×10^6 . The pressure on the airfoil, as well as the lift and drag coefficients, were characterised, showing a maximum drag coefficient around 90 degrees angle of attack. Numerical simulations have also been conducted to study dynamic stall for high angles of attack, to see the effect on the lift coefficient and phase Yu et al. [2010]. Studies on the unsteady aerodynamics of

specifically plunging airfoils have also been conducted. Bull et al. [2021] found that loads exhibited on aircraft wings have a strong dependence on the motion amplitude. Their study was done using a NACA0012 airfoil, which also has a symmetric airfoil section. It was found that the vortex shedding cycle occurs around the structural frequency, which could lead to the lock-in phenomena for VIV. The Strouhal number, $St = f_{st}c/U_\infty$ is used to define the structure based on its shedding frequency.

A lot of modern VIV research, especially on wind turbines is at high Reynolds numbers to match the flow regimes. Unfortunately for this project, the experimental capabilities of the tunnel limit us to low Reynolds numbers. Thus, we can look to early VIV on cylinders, where simulations and experiments were done at very low Reynolds numbers, around 500 Wu and Wang [2018]. For simple shapes such as cylinders, especially in the case of cables, VIV occurs at lower Reynolds numbers, with a transition to galloping, which is also a flow-induced vibration in a single degree of freedom, at higher Reynolds numbers Sourav and Sen [2019].

1.4 Vortex-Shedding Modes

Early VIV work around cylinders showed that there exist vortex shedding modes, showing a resonance regime corresponding to "2S + 2P" mode, generally for elastically mounted cylinders as seen in Figure 1.2 Wu and Wang [2018], Williamson and Govardhan [2008]. Khalak and Williamson [1999], Williamson and Roshko [1988] observed three responses. The first was the "2S" mode, which is when two single vortices are performed in one period, and the second and third referred to the "2P" mode where two vortex pairs were formed each cycle, for transverse motion. Jauvtis and Williamson [2003, 2004] further found another response for a two-degree-of-freedom VIV system. The character of the mode influences the phase of the force and hence whether power is injected into the system or not Mottaghi et al. [2020]. Williamson and Roshko [1988] present the vortex synchronisation regions on the wavelength-amplitude plane as seen in Figure 1.2. The amplitude ratio, A/D is defined as the amplitude of oscillation over the diameter of the cylinder, which is its characteristic length, similar to the chord, c for an airfoil. The wavelength ratio $\lambda/D = UT/D$ where $T = 1/f$ is the period of oscillation, in the direction transverse to the incoming flow. This is often also referred to as the reduced velocity $U^* = 1/St$. Within the lock-in region, the oscillation period $T \approx T_v$ where T_v is the vortex shedding period for a non-oscillating cylinder, i.e. its natural shedding period, which is related to the Strouhal number of the cylinder. In most other literature, this is presented as the frequency ratio, though the results present equivalent conclusions. For a given amplitude ratio, a critical wavelength exists such that below this value, a pair of like-signed vortices coalesce each half-cycle. This results in two vortices with opposite signs fed downstream in the wake per cycle, like the von Karman vortex street. This is referred to as the '2S' shedding mode. Above this wavelength the like-signed vortices convect away from one another and do not coalesce, resulting in them pairing with vortices of the opposite sign. In each cycle, two vortex pairs of opposite signs convect laterally away from the centre line in the transverse direction. This is referred to

as the ‘2P’ shedding mode.

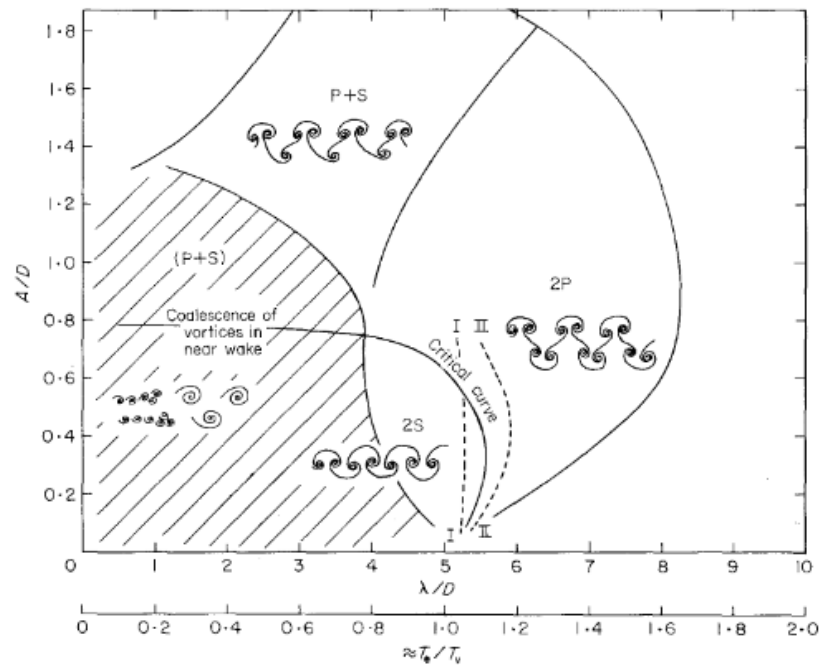


Figure 1.2: 2P-2S Vortex Patterns. Reprinted from Williamson and Roshko [1988]. Curves I and II from Bishop and Hassan [1964].

At the critical wavelength where $T_e = T_v$, only 2 vortices are formed in each cycle that undergo resonant synchronization, where the shed vorticity is more concentrated than at other wavelengths, which is linked to the peaks in the lift curves Mottaghi et al. [2020], Williamson and Roshko [1988]. Curves I and II in Figure 1.2 represent the locations where a sharp change in the loads was observed. Changes in the phase angle of the lift force around the critical wavelength are generally a result of the 2P shedding mode.

1.5 State of the Art VIV research

A lot of research work for full scale is done using Computational Fluid Dynamics (CFD), while experimental work is often parametric and at smaller scales. Besem et al. [2016] noted that the main issue with the available CFD solvers today is their inability to quickly and accurately predict VIV. However, to the knowledge of the author, there is limited work that compared equivalent cases of the two due to sparse experimental data available. Figure 1.1 shows the lock-in region using CFD to be smaller than the experimental region, though this could be due to the solver choice or the range of frequencies and amplitudes tested. The lock-in region seen in the paper by Hu et al. [2021] using modal analysis shows a prediction of the results using modal analysis, but it is limited to a purely two-dimensional analysis.

VIV research for wind turbine blades is still relatively new, with a lot to still be discovered. Most simulation work, such as works by Horcas et al. [2022] and Heinz et al.

[2016] fix the pitch angle around 90 degrees to simulate the blade pitched out of the wind. Young and Lai [2007] perform numerical simulations on a plunging NACA0012 airfoil using a 2D Navier-Stokes solver at a Reynolds number of 20,000. The Reynolds number for this experiment will be around 25,000 for a plunging symmetric airfoil, suggesting that the results should be similar. They also show that the lock-in region may not be symmetrical about the natural shedding frequency due to the sharp trailing edge of the airfoil causing flow separation. However, the results may differ slightly due to the increased thickness of the airfoil from 12% from the NACA0012 to 21% to the NACA0021. Lai and Platzer [1999] experimentally found that for a plunging NACA0012 airfoil at a Reynolds number of 20,000, the wake showed many transitional forms with multiple vortices shed within a single cycle. For higher frequencies, there are more vortices per cycle, leading to an increase in the load frequency and hence, a higher power. This was also in good agreement with the results from Young and Lai [2004]. Unfortunately, these results were only tested at a single Reynolds number and hence, the influence of Reynolds numbers on the shedding for VIV has not been thoroughly studied either. Besem et al. [2016] also states that the Strouhal number should be independent of the Reynolds number, but this is usually for higher Reynolds numbers and may not apply to Reynolds numbers around 25,000. However, most of these studies are for two-dimensional cases, so a large deviation can be expected for the three-dimensional study in this thesis, due to the effect the tip vortices would have on flow separation. Williamson [1988] presents a discussion on the transition to a three-dimensional flow for a cylinder wake. It is concluded that for Reynolds numbers larger than around 180, the flow shows three-dimensional vortex structures in the wake. However, these conclusions were drawn for a cylinder at very low Reynolds numbers and hence, do not necessarily apply to flows in larger Reynolds number regimes. Choi et al. [2015] also notes that at higher Reynolds numbers the viscous effects become more independent of the Reynolds number and hence, two-dimensional simulations may not be realistic enough to account for three-dimensional flow instabilities. Bearman [1984] presents a review of experiments in vortex shedding around bluff bodies and states that the presence of shear layers is the primary reason for vortex shedding and the body merely modifies the shedding through interaction between the wake and circulation at the separation points. It is noted that there is spanwise coupling between the two shear layers is weak, implying that quantities such as the surface pressure are not constant along the span even for a two-dimensional bluff body in the flow.

It should be noted that real wind turbine blades are much more complicated than many of the models used in experimental studies, and they have many vibration modes that can be excited Bearman [1984]. This, however, requires much more complex experimental campaigns or high-fidelity CFD to understand the complexity of the problem.

1.5.1 Free vs Forced Vibrations

For oscillating bluff bodies in the flow, they can generally be classified into free vibration and forced vibration experiments. In free vibrations, the wake from the body due to the incoming wind will excite the body, causing it to oscillate in the flow. Generally,

the maximum amplitude of oscillation will be observed at the ‘resonant point’, which is just $1/St$ Bearman [1984]. In forced vibration experiments, however, the body itself is forced to oscillate in a certain manner, often at a certain fixed frequency and amplitude for each case. For such cases, the extent of the frequency range over which lock-in occurs is dependent on the amplitude of oscillation Bearman [1984]. This range is always expected to encompass the reduced flow velocity $U^* = U_\infty/fc$, i.e. the ‘resonant point’ Bearman [1984]. The shape of the ‘V-region’, i.e. the range of frequencies and amplitudes over which there is lock-in is dependent on the shape of the bluff body in the flow. Unfortunately, most literature on vortex-induced oscillations, and shedding around bluff bodies are for cylinders, which leads to some expected differences in the results and assumptions for blades due to the sharp trailing edge, leading to a different type of separation Bearman [1984]. Unfortunately, no clear pattern for the shape of this region for a forced vibration experiment was determined.

1.5.2 Surging airfoil

To the knowledge of the author, there is little research on vortex-induced vibrations and other flow-induced instabilities on an airfoil undergoing surging motion, i.e. motion in the streamwise direction. Choi et al. [2015] presents an analysis of a surging and plunging airfoil at low Reynolds numbers, $\sim O(10^2)$. The CFD simulation was performed using a 2D assumption, but they note that this assumption may not be adequate to describe the transition around the supercritical Reynolds number. For the experiment presented in this thesis, the Reynolds number will be well above the supercritical Reynolds number so this may not be an issue, though the effect of the leading edge vortex could play a larger role. The results of the simulations from Choi et al. [2015] show that the wake instabilities synchronise with the unsteady airfoil motion leading to a change in the forces, i.e. the shedding locks into the motion frequency, causing peaks in the force coefficient power spectral density plot (PSD) at the motion frequency and its subharmonics. At a 90 deg angle of attack, the critical Reynolds number, Re_{crit} is around 300, with a critical reduced frequency, $k = \pi fc/U_\infty$ of round 0.4. The critical Reynolds number is a threshold value below which a steady separated flow is obtained. A comparison of the plunging and surging results shows that a plunging airfoil shows a higher fluctuating lift amplitude due to the larger added mass and effective angle of attack. It should be noted that this analysis was done with a steady angle of attack at 15 deg. Choi et al. [2015] show that lock-in is obtained, where the wake instability is synchronised to the forcing frequency, similar to how it is seen for a plunging or pitching airfoil section. Lock-in diagrams are presented for a small range of amplitudes and a somewhat ‘V-shaped’ region around the non-dimensional reduced frequency ratio, $k/k_{st} = 1$, along with a secondary peak at $k/k_{st} = 0.5$. This pattern was seen for both the plunging and surging airfoil. The width of the lock-in region was also seen to grow faster for the plunging airfoil. However, it seems that the first region may not be related to the vortex lock-in phenomena, but rather the phase of the leading edge vortex convecting along the airfoil surface. However, this may no longer be valid for airfoils at 90 deg angles of attack since the flow regime is well beyond dynamic stall and it is acting like a bluff body.

1.6 Particle Image Velocimetry

Flow visualisation techniques have developed over the years, allowing us to achieve higher resolution results, higher frequency acquisition as well as resolving flows in all three dimensions and in time. Particle Image Velocimetry (PIV) is one such technique where tracer particles are introduced into the flow to follow the flow field as it deforms around a body. These particles are illuminated by a laser and captured by a camera. The flow field at a specific fixed location, i.e. the field of view (FOV) of the camera is captured at two instances in time that is separated by a small time step, Δt such that the particles have moved only a few pixels. This image pair is processed to track the relative distance travelled by the particles between the images, and, using the known time step, the velocity travelled by the particles, i.e. the flow velocity, is known. Stereoscopic PIV (SPIV) uses a pair of cameras placed at an angle to each other such that together they are able to resolve the velocity in the dimension perpendicular to the laser sheet. High-speed PIV can also be used to capture many images at a very high frequency such that they essentially act as if it was a time-resolved image capture. For rotating or oscillating bodies with fixed amplitudes, the data can also be phase-locked, such that the image is captured at the same phase over each period, and averaged over that single phase. This can then be done over many phases to achieve a phase-locked flow field over the cycle.

These flow fields can be useful visual tools to see the vortex shedding behind the body, but it is also important to be able to calculate the loads. Van Oudheusden [2013] presents a technique to infer the pressure field from the velocity field using the Navier-Stokes equation and the Bernoulli equation. The three steps described to determine the pressure are: 1. acquiring the PIV data, 2. process the velocity field to compute the pressure gradient terms needed for the Poisson equation, and 3. compute the pressure field by spatially integrating the pressure gradient or by using the Poisson equation. To accurately determine the pressure field from this method, however, would require the fully time-resolved three-dimensional flow field. Van Oudheusden [2013] states that this technique is predominantly applied to cases where the flow is considered ‘quasi-2D’ since the resolution of the out-of-plane velocity and pressure gradients would require techniques such as tomographic PIV to get the full 3D FOV.

Noca et al. [1997, 1999] propose a method to measure the instantaneous forces using only the velocity fields and their derivatives for an incompressible flow. This method only requires knowledge of the velocity and vorticity field within a chosen control volume around the body. The equation removed the need to calculate the pressure gradient and the force is the sum of three terms: the volume integral, the surface integral of the flux, and the extra term to describe the unsteady motion, $S_b(t)$. For a steady flow, the force will be equal to the flux across the surface. The force can be expressed as

$$\mathbf{F} = -\frac{1}{N-1} \frac{d}{dt} \int_{V(t)} \mathbf{x} \times \boldsymbol{\omega} dV + \oint_{S(t)} \mathbf{n} \cdot \boldsymbol{\Theta} dS - \frac{1}{N-1} \frac{d}{dt} \oint_{S_s(t)} \mathbf{x} \times (\mathbf{n} \times \mathbf{u}) dS \quad (1.1)$$

where N is the dimension of the space under consideration ($N = 2$ in a two-dimensional space) and $\boldsymbol{\omega}$ the vorticity. The tensor $\boldsymbol{\Theta}$ is given by

$$\Theta = \frac{1}{2}u^2\mathbf{I} - \mathbf{u}\mathbf{u} - \frac{1}{N-1}(\mathbf{u} - \mathbf{u}_s)(\mathbf{x} \times \boldsymbol{\omega}) + \frac{1}{N-1}\boldsymbol{\omega}(\mathbf{x} \times \mathbf{u}) + \frac{1}{N-1}[\mathbf{x} \cdot (\nabla \cdot \mathbf{T})\mathbf{I} - \mathbf{x}(\nabla \cdot \mathbf{T})] + \mathbf{T} \quad (1.2)$$

where T is the viscous stress tensor.

Van Oudheusden et al. [2007], van Oudheusden et al. [2007] evaluates the unsteady load using the NOCA method Noca et al. [1997, 1999] around a chosen control volume using the time mean flow statistics, such that the mean and turbulent momentum terms are used. The work showed that for a predominantly steady flow, an ensemble size of 100 vector fields was sufficient to calculate the forces with sufficient accuracy.

1.7 Computational Fluid Dynamics

The field of computational fluid dynamics has been developing rapidly over the years, with the capability to model complex flows at scales that are not always possible experimentally. For incompressible fluid flows, the Navier-Stokes equations can be solved to obtain the exact solution of the velocity and pressure in time, through Direct Numerical Simulation (DNS), though this is computationally very expensive and currently can only be applied at low Reynolds numbers Ferziger and PeriC [2002]. However, many other turbulence models have been developed to predict and simulate the flow. Lower fidelity models include Reynolds Averaged Navier-Stokes (RANS) and Unsteady Reynolds Averaged Navier-Stokes (URANS) models that decompose the velocity components of the Navier-Stokes equations into their mean and fluctuating quantities and averaging them Pope [2000]. The RANS equation is seen in Equation 1.3.

$$\frac{\partial \bar{u}_i \bar{u}_j}{\partial x_j} = -\frac{1}{\rho} \frac{\partial \bar{p}}{\partial x_i} + \nu \frac{\partial^2 \bar{u}_i}{\partial x_j^2} - \frac{\partial \overline{u'_i u'_j}}{\partial x_j} \quad (1.3)$$

where $\overline{u'_i u'_j}$ is the Reynolds-Stress-Tensor (RST).

This model relies on the use of the Boussinesq hypothesis that relates the RST to the eddy viscosity ν_T and the turbulent kinetic energy in the flow through the eddy viscosity approximation. The model also relies on relating the eddy viscosity to a characteristic length scale, known as Prandtl's mixing length, which is indicative of the size of the eddies in the flow at a given point Pope [2000]. RANS models are modelled using two-equation models such as the $k - \epsilon$, $k - \omega$ and $k - \omega$ Shear-Stress-Transport (SST) models, where k is the turbulent kinetic energy, ϵ is the rate of dissipation of turbulent kinetic energy and, ω is the specific rate of dissipation of turbulent kinetic energy Menter [1992], Mansour et al. [1989], Wilcox [2006].

A higher fidelity model is Large Eddy Simulation (LES), which relies on the Kolmogorov hypothesis that large eddies are geometry dependent and smaller eddies (sub-grid scale) are universal. The velocity components from the Navier-Stokes equations are split into a filtered velocity and the residual velocity at the sub-grid scale. The filtered and sub-grid scale velocity terms are substituted into the Navier-Stokes equation, which leads

to an extra non-linear advection term known as the sub-grid scale tensor. This tensor is modelled using the Boussinesq hypothesis and the turbulent viscosity term resulting in Equation 1.4.

$$\frac{\partial \bar{u}_i}{\partial t} + \bar{u}_j \frac{\partial \bar{u}_i}{\partial x_j} = -\frac{1}{\rho} \frac{\partial \bar{p}}{\partial x_i} + \frac{\partial}{\partial x_j} \left((\nu + \nu_T) \frac{\partial \bar{u}_i}{\partial x_j} \right) \quad (1.4)$$

Here, the incompressibility constraint is exploited to simplify the equation and the pressure is now modified to include the trace term $\frac{1}{3} \delta_{ij} \tau_{kk}$. The viscous dissipation at the sub-grid scale is modelled by the Smagorinsky model which postulates a linear relationship between the sub-grid scale shear stress and the strain rate tensor. A Smagorinsky constant is estimated for different flows at different Reynolds numbers Pope [2000], Katopodes [2019], Germano et al. [1991]. However, the LES model is computationally very expensive.

To achieve the high fidelity results of the LES model with a lower computational cost, the Detached Eddy Simulation (DES) model was developed, which combines the RANS and LES models. This model switches explicitly between an LES or RANS model based on the grid spacing and turbulent length scale. However, this model comes with drawbacks in that a sudden change in grid spacing directly impacts the length scale and can trigger separation, known as grid-induced separation Menter et al. [2003]. A Delayed Detached Eddy Simulation (DDES) model was then developed to eliminate this error by developing a formulation for the shielding function that depends only on the eddy viscosity and wall distance Spalart et al. [2006]. Unfortunately, this resulted in a logarithmic layer mismatch between the inner RANS and outer LES regions for a wall-mounted LES formulation of the original DES model. The model was then further developed into an Improved Delayed Detached Eddy Simulation (IDDES) that fixed this issue Shur et al. [2008], Gritskevich et al. [2012]. The IDDES model features intricate blending and shielding functions that allow it to be used for wall modelling as well as modelling the flow further away Gritskevich et al. [2012].

1.8 Key Findings

Table 1.1: Key Values from Literature. References in order from left to right Hu et al. [2021], Besem et al. [2016], Pellegrino and Meskell [2013], Skrzypiąski et al. [2014]. *Values are calculated based on values stated in papers. Not all numbers are specified. Different airfoil sections are studied.

Motion	Pitching	Plunging	Plunging	Plunging	Pitching
Reynolds Number ($\times 10^6$) [-]	1	12	2	0.7	0.55
Wind Speed [m/s]	14.6	88	29.2	10.2	9
Angle of Attack [deg]	40, 140	24	90	90	90
Chord [m]	1	2	1	1	0.25
Oscillation Frequency [Hz]	2.16	1	4.96	1.30	6
Strouhal Number [-]	0.15	0.23	0.17	0.13	0.165

Figure 1.1 shows the lock-in region from the experimental results range from 0.8 to 1.1 f_{st} . Similarly, Hu et al. [2021] shows the lock-in region for a plunging airfoil between 0.9 to 1.1 f_{st} for a plunging amplitude from 0 to 16% of the chord.

Benner et al. [2019] did experimental work using PIV for a NACA0021 blade section in the cross-flow direction, showing the largest lock-in range at 90 degrees angle of attack. In wind turbine blades at standstill condition, the orientation of the blade leads to the excitation of the edgewise mode in the cross-flow direction Pellegrino and Meskell [2013], Skrzypiński et al. [2014]. This could be simplified to the plunging motion of an airfoil at 90 deg angle of attack. However, it is worth noting that for a real blade, there will be taper, twist, and a change of chord so it will not be a pure plunging motion but a combination of pitching, plunging, and surging motions.

1.8.1 Key Non-Dimensional Parameters

Skrzypiński et al. [2014] presents key parameters involved in defining such vortices and flows that can be used to non-dimensionalise parameters for a more accurate comparison of results. Key non-dimensional parameters include the reduced frequency, $k = \pi fc/U_\infty$, the reduced flow velocity, $U^* = U_\infty/fc$, the Reynolds number, $Re = \rho U_\infty c/\mu$ and the Strouhal Number, $St = f_{st}c/U_\infty$. Skrzypiński et al. [2014] adds key parameters related such as the non-dimensional amplitude, $A^* = A/c$, non-dimensional frequency, $f^* = c/TU_\infty$, non-dimensional power, $P^* = T/(\rho cAU_\infty^2)\bar{P}$, non-dimensional period, $T^* = TU_\infty/c = 1/f^*$ and the non-dimensional time, $\tau = tU_\infty/c$, with f being the frequency, T being the period, c being the chord, U_∞ being the inflow velocity and \bar{P} being the mean aerodynamic power in the cycle.

1.9 Research Gaps

There are still many questions left unanswered, including, 1. the shape of the lock-in region for larger amplitudes and whether or not it is symmetrical about the Strouhal frequency, 2. the difference in loading for a surging versus a plunging airfoil, 3. the effect of 3D aerodynamics and the interaction of the tip vortices with the rest of the wake, and 4. the validation of numerical models against equivalent experimental data. These questions lead to the main research objectives of this project, noting that all of these cannot be answered within the scope of this thesis. Knowledge of the physics behind what conditions cause VIV and what effect that has on the blade could be vital to understanding how to design blades to avoid this, or at least prepare for it. If it is well understood, it could be included in future IEC certifications for large blades to prevent catastrophic failure.

1.10 Research Questions

There are four research questions that will be addressed in this project to address the research gaps.

1. To what degree do the CFD simulations accurately predict the results? Where does it differ and what information is it not able to predict? What extra information are we able to attain from CFD? This is an extremely important research question because it is very difficult to experimentally verify VIV at full scale. However, CFD results are not always reliable, especially if they have not been validated against experimental data. Thus, being able to validate the accuracy of the simulation for the matching cases will allow us to determine the validity of the CFD results and let us expand on those to cases that we cannot test, such as with higher oscillation amplitudes and frequencies that cannot physically be obtained with the available hardware.

2. How many chords away from the tip do we no longer observe the effect of tip vortices in the spanwise direction i.e. what is the transition point where the flow around the blade starts to behave 2D? This would be analysed in several ways, such as plotting a hysteresis loop of $cl - \alpha$ and $cd - \alpha$ for a plunging blade and $cx - X/c$ and $cy - X/c$ for a surging blade from their time series or measuring the spanwise velocity component in the wake. This will help determine if there are different results expected around a tip that is specifically due to the vortices and not the geometry of the blade, since the airfoil section is constant for this study. The effect of the blade aspect ratio on the spanwise convection of the tip vortex would also be studied.

3. At what range of frequencies and amplitudes does lock-in occur for a plunging and surging blade? The goal is to try and find a similar lock-in region that will ideally follow the same 'V-shape' and to determine the lock-in patterns at large oscillation amplitudes. This will be done by analysing hysteresis loops and power spectral density plots based on the time series from CFD results.

4. How do the flow around the blade, and the loads for a plunging and surging airfoil compare over a cycle? This will aid in further research for flexible blades that undergo a combination of motions so that the most probable excitation modes could possibly be pre-determined. Given that the blade tested in this experiment is rigid, the effect of structural damping for the flap and edgewise modes can be eliminated and the pure aerodynamic force comparisons can be analysed. Structural damping does not play a role in this experiment since the tested blade is rigid and the motion is forced, as compared to a rigid body setup with a spring-damper system for a freely vibrating blade such as in Skrzypiński et al. [2014].

CHAPTER 2

Design of Experiment

This chapter presents the details of the experimental design, including the choice of motions, frequencies, and amplitudes to test experimentally using PIV and to simulate using CFD. It details the specifics of the experimental setup used as well as the simulation setup. Lastly, it presents an overview of the test cases chosen for this thesis.

2.1 Methodology

2.1.1 Experimental Design

To answer the research questions, the problem needed to be specifically defined and simplified. Skrzypiński et al. [2014] states that the edgewise mode is excited by VIV under standstill conditions, however, as mentioned earlier, a real blade would be twisted and tapered and undergo a combination of pitching, plunging, and surging. Due to experimental design limitations, the pitching motion was not analysed in this experimental campaign. Many have found large VIV responses occur at 90 degrees angle of attack Hu et al. [2021], Benner et al. [2019], Besem et al. [2016], Pellegrino and Meskell [2013], Skrzypiński et al. [2014], leading it to be the single angle of attack choice for this experiment, especially since it mimics the angle of attack of a blade at standstill. Furthermore, to quantify the aerodynamic loads and the 3D tip effect while removing aeroelastic effects and other unknown complexities, a rigid blade with a constant chord and no taper was chosen. A symmetric NACA0021 airfoil section with a 0.075m chord and 40cm span was chosen to also avoid the additional effect a cambered blade may have on the flow. Figure 2.1 shows the orientation of the blade with respect to the incoming wind at 90 degrees angle of attack, such that the plunging motion excites the edgewise mode. The surging motion, which is perpendicular to the plunging motion, would excite the flapwise mode.

A summary from literature suggests that the fluctuation of the lift coefficient is around the Strouhal frequency and that the ‘lock-in’ region is between 0.8 to 1.2 f_{st} , with the plunging amplitude ranging up to 16% of the chord Hu et al. [2021], Benner et al. [2019], Besem et al. [2016], Pellegrino and Meskell [2013]. Choi et al. [2015] investigates larger amplitudes and lower frequency ranges as well, though the analysis is purely 2D, and hence, the results are expected to differ. The freestream wind speed was set to 3m/s, with a Reynolds number of around 15000 and an expected Strouhal number of around 0.16, suggesting a frequency of around 6.4Hz.

The CFD simulations were set up to mimic the exact experimental tests along with many extra cases for a more in-depth analysis. To the knowledge of the author, there is limited work on larger amplitudes and much larger frequencies, so it was decided to expand the test matrix to analyse these cases as well for the lock-in diagram. The choice of the solver for the CFD simulations is based on the available software. EllipSys3D Michelsen [1992, 1994], Sørensen [1995] was chosen due to its high fidelity and its availability at

the Technical University of Denmark. The details of the solver and set-up are, however, beyond the scope of the thesis. Table 2.1 presents a summary of the design parameters for the experiment.

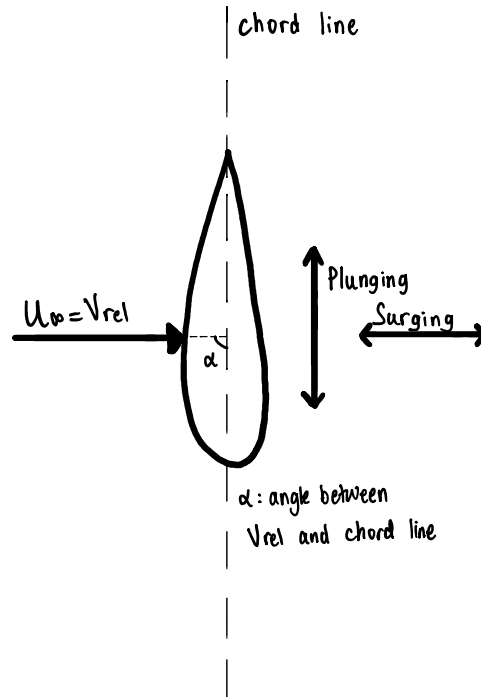


Figure 2.1: Velocity Triangle showing Orientation of Blade

Table 2.1: Summary of Experimental Design Parameters

Variable	Symbol	Value
Freestream Velocity	U_∞	3 m/s
Airfoil Section		NACA0021
Airfoil Chord	c	0.075 m
Reynolds Number	Re	15000
Expected Strouhal Number	St	0.16 (0.1~0.2)
Blade Angle of Attack	α	90 deg
Experiment Blade Span	S_{expt}	0.40 m
Experiment Blade Aspect Ratio	AR_{expt}	5.33
Experiment Boundary Condition		Fixed on one end with flat plate
CFD Experiment Blade	S_{CFD}	0.75 m
CFD Blade Aspect Ratio	AR_{CFD}	10
CFD Boundary Condition		Free on both ends with a symmetric mesh about the midspan
Motions		Crossflow (plunging) and Streamwise (Surging)

2.2 Particle Image Velocimetry

The instrumentation of PIV can be divided into four parts: seeding production, laser, CCD camera, and the PIV acquisition software.

2.2.1 Seeding production:

The *SAFEX fog generator* produces a non-toxic water-glycol droplets. The mean diameter is 1μ m. In order to have stable seeding conditions the knob on the remote control unit should be set at the third tick with the lower button on 10%. Uniform seeding distribution in the flow is achieved by introducing it before the diffusion so that it mixes with the flow and is accelerated with it. The size of the seed is chosen to balance the reflection of the laser light to the camera while maintaining a similar density to air so that it stays well-mixed throughout the flow.

2.2.2 Laser:

The *Quantel Evergreen 200* laser is used as light source. The laser system is a double pulsed Nd:YAG laser, consisting of two cavities producing infrared light of a wavelength of 1064 nm. A second harmonic generator halves the wavelength to $\lambda = 532$ nm (visible green). The pulse duration is 8 ns and the maximum repetition rate is 15 Hz for each pulse. At the laser exit, the beam diameter is 6 mm. At maximum power, the energy in each laser pulse is 200 mJ.

The laser is controlled from the Davis 8 software. With this software, the repetition rate and time separation between two laser pulses can be determined. Based on the number of pixels and the size of the field of view, a pixel displacement criteria of around 10 pixels was set. With a $U_\infty = 3m/s$, the separation time used was $417\mu s$, based on the characteristics of the camera, the test section, and the flow. The information is sent from the computer to the digital delay control unit, producing triggering signals for the laser and CCD camera.

2.2.3 CCD Camera:

The PIV images are recorded with two *Bobcat IMPERX IGV-B1610* CCD camera. It has a resolution of 2560×2160 pixel with 6.5μ m pixel pitch. It can record 10-bit black-and-white images. In double shutter mode, which is used in double frame PIV, the maximum recording rate is 8.3 Hz (120 ms separation time between image pairs). The camera is controlled by the DaVis software.

The first camera exposure (frame A) has a duration of 10μ s and the second exposure (frame B) lasts about 100 ms. This means that, in double shutter mode, frame A collects less light from the ambient with respect to frame B. This leads to more intense background light and noisier particle images. This is used in the post-processing stage, where the brightness of the two images differ, and is used to calculate the difference for the calibration procedure.

To obtain the velocity component perpendicular to the plane captured by a single camera, in this case, the flow perpendicular to the airfoil section at a given span along the blade, a second camera was used, with a different incidence angle to the desired planes, and an angle of 45 deg between the two cameras for the best resolution. When a particle is seen moving in opposite directions by the cameras, then it is resolved as moving in the direction perpendicular to the plane and resolved as the third velocity component.

For the imaging of particles onto the camera sensor, a Nikon $f = 50$ mm lens was used for the camera on top and $f = 80$ mm at the bottom. The optimal $f_{\#}$ was set to 5.6 on both cameras.

2.2.4 PIV Software:

The illumination and acquisition were controlled (with laser and camera settings). Phase-locked PIV was used for this experiment, which was enabled via a trigger in the plunging mechanism. A time delay was set in the DaVis software, which was calculated based on the known frequency, to capture the image at the chosen phase.

2.3 Experimental Setup

Several 60 x 60 cm aluminium profiles were used to construct a frame to mount the plunging mechanism. The large structures would cause perturbations that would affect the flow around the blade and hence, a flat plate was mounted at the fixed end of the blade. This also served as a wall boundary condition, which would mimic the symmetry boundary condition seen in the spanwise flow around the CFD simulated free blade, though there will still be some differences.

2.3.1 Plunging Mechanism

Figure 2.2 shows the front view of the plunging mechanism mounted onto an aluminium profile and Figure 2.3 shows the CAD assembly of the plunging mechanism. The motor is located at the bottom below the rotating disk and is connected to the platform that the blade is mounted to via the slider. The motor is connected to the metal disk via a gear, and the disk is connected to a 3D-printed plate via a hardened plastic rod. The airfoil is mounted onto the plate, which is mounted onto rods such that it can slide laterally. Figure 2.4 shows the working mechanism of the slider-crank system. The plunging mechanism was limited to a maximum oscillation frequency of 6 Hz for an amplitude of 1 chord (0.075 m). Even at this frequency, the motor would shut down after around 16 seconds of use, so the test cases had to be limited by this operational restriction.



Figure 2.2: Plunging Mechanism Front View

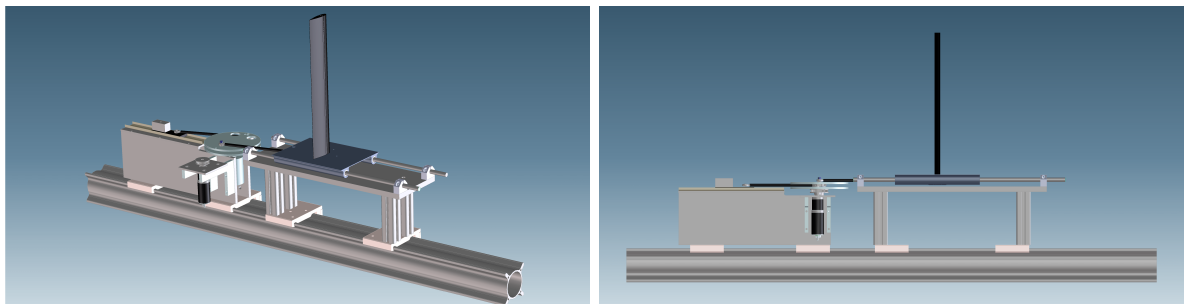


Figure 2.3: Plunging Mechanism CAD Assembly

2.3.2 Wind Tunnel Test Setup

The PIV experiment was performed at the Open Jet Facility at Delft University of Technology, Delft, the Netherlands. Figure 2.5 shows the PIV setup for the plunging configuration. The setup for the surging configuration is nearly identical, with the mechanism rotated 90 degrees such that it is in the direction of the flow, and the flat plate was rotated with it to fit the blade in the hole.

Once the structure was built, the cameras had to be focused and calibrated. A

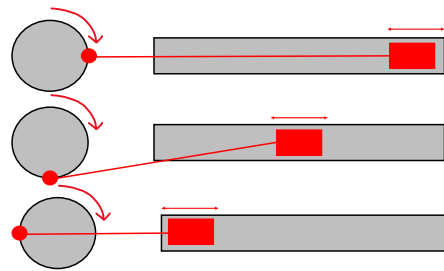


Figure 2.4: Schematic of Slider-Crank Working Mechanism (Not to Scale)

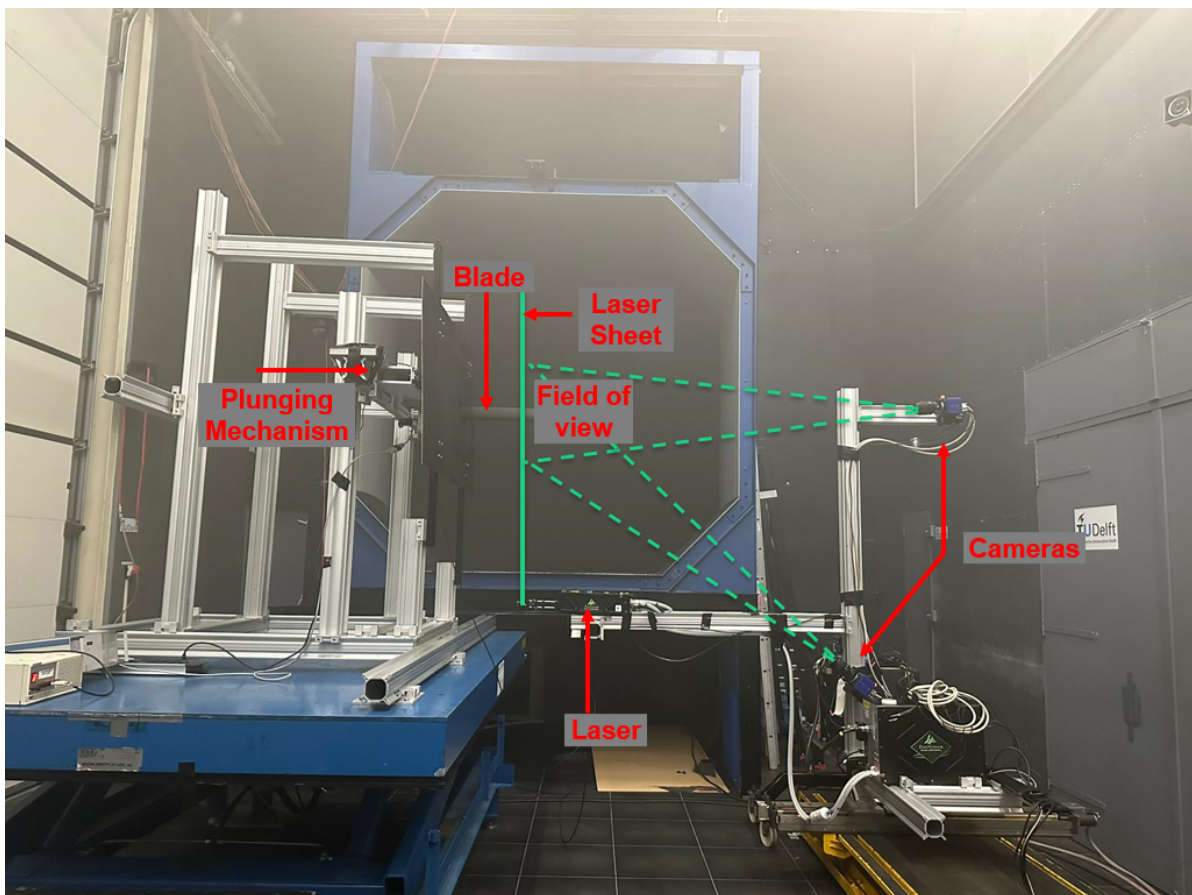


Figure 2.5: Labelled Diagram of PIV Setup

three-dimensional calibration plate was mounted to the structure as seen in Figure 2.6. The laser sheet was then aligned with the plate and the calibration was done to obtain the combined corrected field of view from both cameras.

The cameras and laser were mounted onto a traverse system such that their relative positions would remain unchanged, but they could be moved together to scan different spanwise positions along the blade and to scan different streamwise positions to obtain a

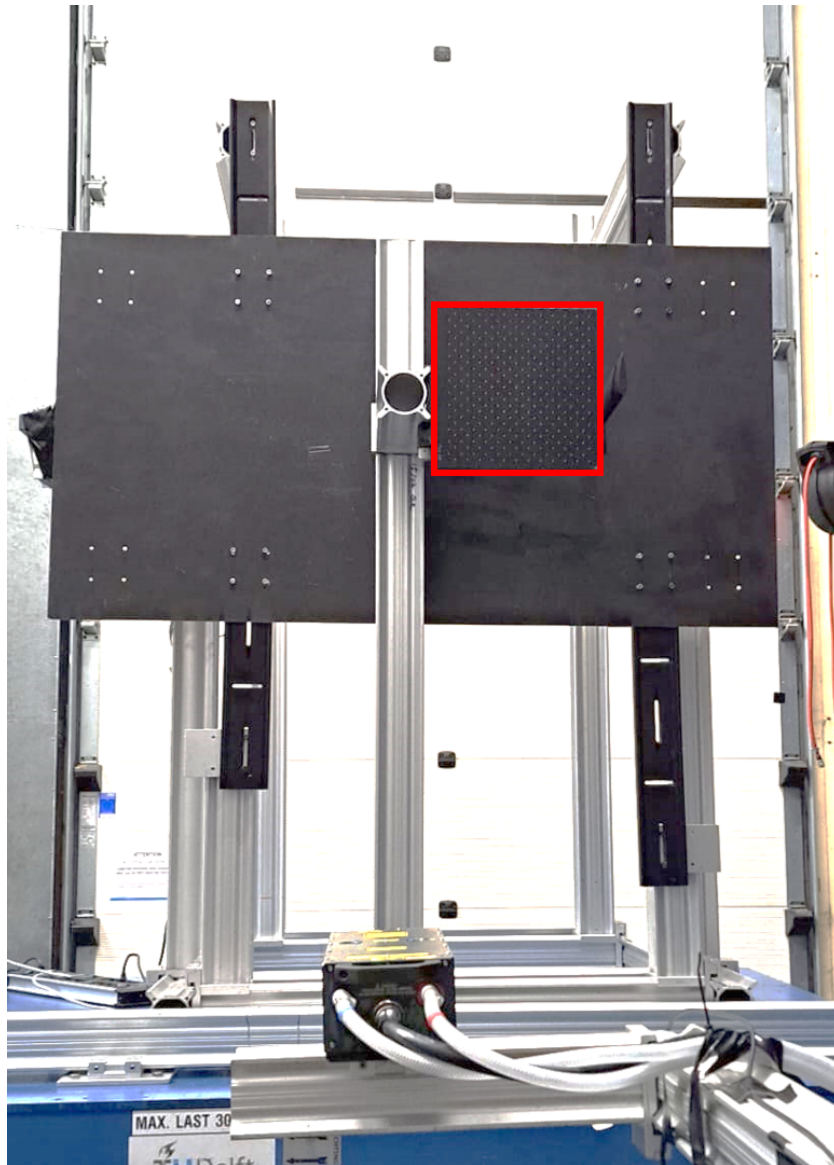


Figure 2.6: Calibration Plate Setup. The plate is outlined in red. The laser shoots from the bottom.

larger total field of view.

The maximum field of view that was possible was 26.6cm x 30.6cm. However, this size was insufficient to get data upwind, in the near wake and in the far wake with this small field of view (FOV). Hence, three streamwise positions were chosen to obtain a larger combined field of view, with a small overlap region for stitching together later. The total field of view was 58.5 cm or 7.8 chords in the x direction and 30.6 cm or 4 chords in the y direction. This is seen in Figure 2.7.

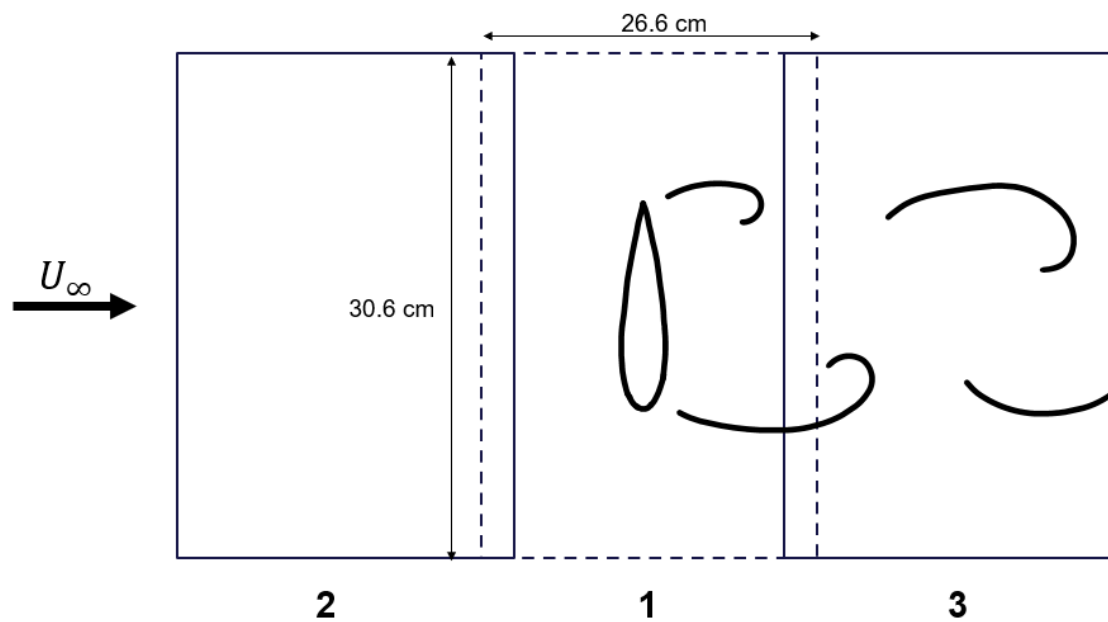


Figure 2.7: PIV Field of View, with positive X in the flow direction, positive Y upwards, and positive Z out of the page. Total overlap length = 58.5 cm.

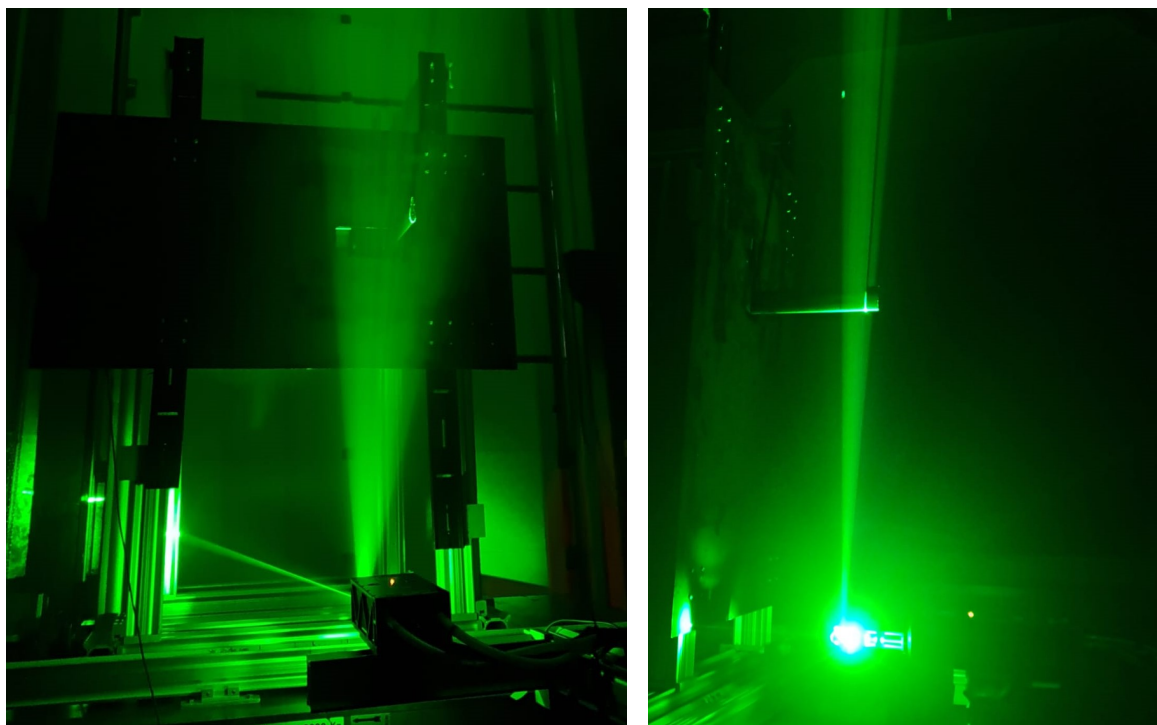


Figure 2.8: Front view (left) and side view (right) of the laser sheet illuminating the blade

2.4 Test Cases

First, a static test was run at this wind speed to capture the flow around the blade at various spanwise positions. A proper orthogonal decomposition (POD) analysis was performed on the wake to determine the shedding frequency though in the future, it will be complemented with a hot wire measurement. Next, a matrix of different frequency and amplitude combinations would need to be done to determine the shape of the lock-in diagram. Due to time limitations for the experiment, a single oscillation amplitude of $1c$ was chosen at two frequency ratios: 0.4 and $0.8 f_{st}$. This was done to ideally capture one frequency that undergoes lock-in and the other that does not, though it is seen later that both undergo lock-in. The same case was chosen for the plunging and surging cases to compare their loads for the same conditions.

Three test case matrices were set up for the static blade test, the plunging test, and the surging test as seen in Table 2.2, Table 2.3 and Table 2.4 respectively. First, a static test was done to measure the Strouhal number of the blade. Originally, an 80 cm blade was used to replicate the CFD blade that has an aspect ratio of 10 . The actual blade used for the plunging and surging tests was only 40 cm due to torque limitations on the motor used, so a static test was also done on the 40 cm blade to compare the effect of the aspect ratio on the results and see if a 40 cm blade was long enough to analyse the spanwise flow and convection of the tip vortex.

The test was originally planned with a freestream velocity of 5 m/s . With an expected Strouhal number of 0.16 , this would lead to a Strouhal frequency of around 10.7 Hz . However, the plunging mechanism was limited to operating at lower frequencies, so it was decided to lower the freestream velocity to 3 m/s such that the Strouhal frequency would be around 6.4 Hz . Hence, tests with the 40 cm blade that was used for the plunging and surging experiments were done at 5 m/s , 4 m/s , and 3 m/s . The static test at 5 m/s for the 80 cm and 40 cm blades can be found in Appendix E and Appendix F respectively.

Table 2.2: Static Cases Test Matrix

Wind Speed	FOV	Blade Length	Spanwise Position	No of Images
5 m/s	1	80 cm	$-0.5\text{ c} - 9\text{ c}$ in steps of 0.5 c	100
5 m/s	2	80 cm	$-0.5\text{ c} - 9\text{ c}$ in steps of 0.5 c	100
5 m/s	3	80 cm	$-0.5\text{ c} - 4\text{ c}$ in steps of 1 c	100
5 m/s	1	40 cm	$-0.5\text{ c} - 4\text{ c}$ in steps of 0.5 c	300
5 m/s	2	40 cm	$-0.5\text{ c} - 3\text{ c}$ in steps of 1 c	100
4 m/s	1	40 cm	$0\text{ c} - 2\text{ c}$ in steps of 1 c	100
4 m/s	2	40 cm	2 c	100
3 m/s	1	40 cm	$0\text{ c} - 4\text{ c}$ in steps of 1 c	200

To get the flow field over one full cycle for the dynamic cases using low-speed PIV, a phase-locked approach was implemented. This was done by calculating the time delay for the data acquisition relative to a fixed phase, in this case, the 0 deg phase. 12 phases were chosen for the data collection: $0, 45, 80, 90, 100, 135, 180, 260, 270, 280$ and 315

deg. For cases where only 4 phases were recorded, 0, 90, 180, and 270 deg were chosen to get a reasonable estimation of the extreme positions. The same procedure was followed for both the plunging and surging experiment, where the same spanwise positions and frequencies were recorded. The spanwise positions were measured inboard, starting from the tip. An extra study was done on the flow field around the tip for a plunging blade at 5 Hz to analyse the spanwise convection of the tip vortex.

Table 2.3: Plunging Cases Test Matrix

FOV	No of Phases	Spanwise Position	No of Images	Frequency of Motion
1, 2, 3	12	Tip, 3c	200	5Hz, 2.5 Hz
1	4	1c, 2c	200	5Hz, 2.5Hz
1	4	-0.5c, -0.25c, 0.25c, 0.5c	200	5Hz

Table 2.4: Surging Cases Test Matrix

FOV	No of Phases	Spanwise Position	No of Images	Frequency of Motion
1, 2, 3	12	Tip, 3c	200	5Hz, 2.5 Hz
1	4	1c, 2c	200	5Hz, 2.5Hz

2.4.1 Results Output and Post Processing

All the results were captured and processed using the DaVis 8 software. First, the time filter was used where the minimum value was subtracted from all the images with a filter length of 5 images. This was done to remove the noise from the images. Next, the PIV image processing was done, where a geometric mask was manually defined for each data set to cover the airfoil and shadow region. A multi-pass decreasing size window was used with the larger window being 128×128 -pixel interrogation window, a round 1:1 Gaussian weight function, and a 50% overlap with a single pass. The smaller window was 64×64 -pixel interrogation window with the same 1:1 round Gaussian weight but with a 75% overlap using 3 passes. Post-processing was also done using a 32×32 -pixel interrogation window for the smaller one, but this led to a larger noise in the final result so 64×64 -pixel interrogation window was chosen. Vector post-processing was also done by setting an allowable vector range to filter outliers in the measured particle velocities. Finally, the average and standard deviation of the velocity fields was calculated.

The average velocity fields were exported and post-processed in a self-written MATLAB code that combined the three fields of view into a single larger flow field. A Gaussian weight function was used to combine the flow fields in the overlapping regions between two fields of view. A POD analysis was performed on some static cases to determine the Strouhal frequency, but it should be noted that this is still just a preliminary estimation. A complementary hot wire experiment was planned to measure the shedding frequencies but due to unforeseen circumstances, it was not completed so POD analysis could not be validated for this thesis.

2.5 Computational Fluid Dynamics

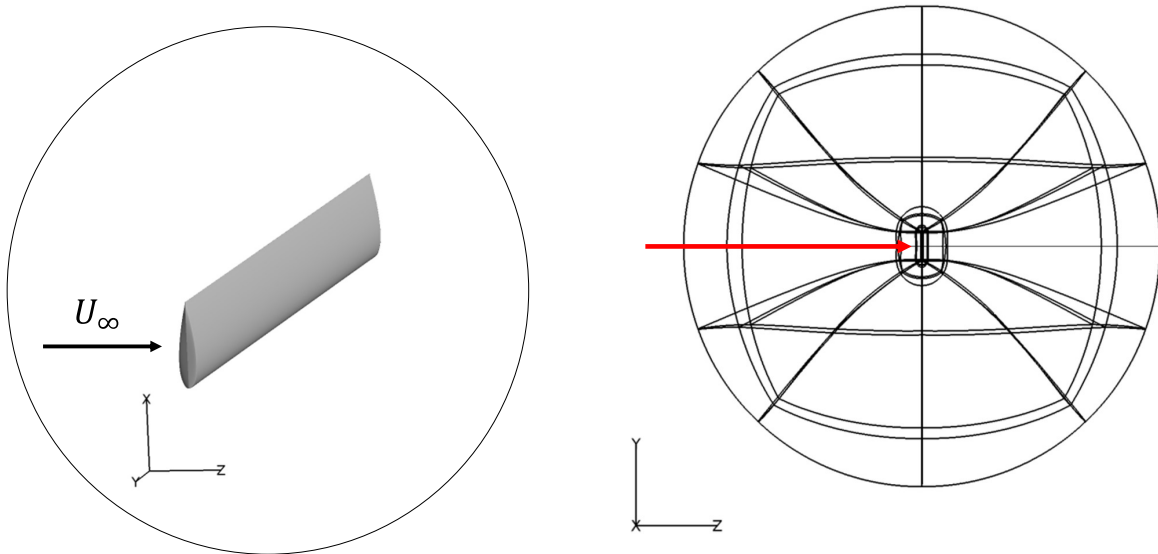
2.5.1 Flow Solver

CFD simulations were run on EllipSys3D Michelsen [1992, 1994], Sørensen [1995] over a range of cases for a static blade as well as a plunging and surging blade. This CFD code solves the incompressible Navier Stokes equations using the finite volume methods in general curvilinear coordinates with a collocated grid arrangement Grinderslev [2020]. An IDDES turbulence model was used Gritskevich et al. [2012], which is a combination of a URANS turbulence model and LES turbulence model. The URANS method used the $k - \omega SST$ model. The decision to use a URANS or LES turbulence model is determined within the EllipSys3D CFD code. A central difference scheme (CDS) was used for the LES portion of the simulation and a quadratic upstream interpolation for convective kinematics (QUICK) scheme was used for the URANS portion of the simulation. The semi-implicit method for pressure linked equations (SIMPLE) algorithm was employed for the pressure correction using Rhie-Chow interpolation to avoid odd/even pressure decoupling. The SIMPLE algorithm solves the momentum equation for the velocity fields within each discrete cell, then uses this velocity to solve for the pressure field within the cell. The pressure correction is used to determine the velocity field again using the momentum equation, and this process is repeated till the momentum and continuity equation are satisfied for the velocity and pressure. A similar setup of the flow solver is seen in Grinderslev et al. [2020].

2.5.2 Simulation Setup

A spherical mesh with a diameter about 150 times the chord containing around 5.25 million cells were generated as seen in Figure 2.9a. The 75mm chord, 750mm span blade was free on both ends with 256 chordwise cells and 128 spanwise cells, being more refined closer to the tips, as seen in Figure 2.10. A laminar inflow condition was set and the outflow is determined by the CFD code within EllipSys3D that determines the outflow in the direction opposing the inflow vector. However, due to the large mesh, the inflow near the blade was only in the z -direction as seen in Figure 2.9a. The time step dt was set to $3e-5$ seconds with a minimum of 6 and a maximum of 20 sub-iterations in each time step and an allowable convergence error of $10e-6$.

Similar to the PIV experiment, a static case was run for the CFD simulations as well. Although an IDDES model was chosen for all the simulations, an Implicit LES (ILES) simulation was also run for the same blade and for a blade with twice the aspect ratio to assess the sensitivity of the chosen turbulence model. The ILES model is simply an LES simulation without a sub-grid-scale dissipation term, i.e. the Smagorinsky constant set to account for viscous dissipation within a cell. This tested the impact of the URANS model for the IDDES simulations because if the ILES and IDDES models provide similar results to the IDDES model, then the added turbulent viscosity in the URANS part of the IDDES simulation is not dominant. The details on the static tests are seen in Table 2.5.



(a) Schematic of the blade in the domain with the freestream wind (not to scale) (b) Spherical Mesh around the Blade. The red arrow points to the blade.

Figure 2.9: CFD Mesh

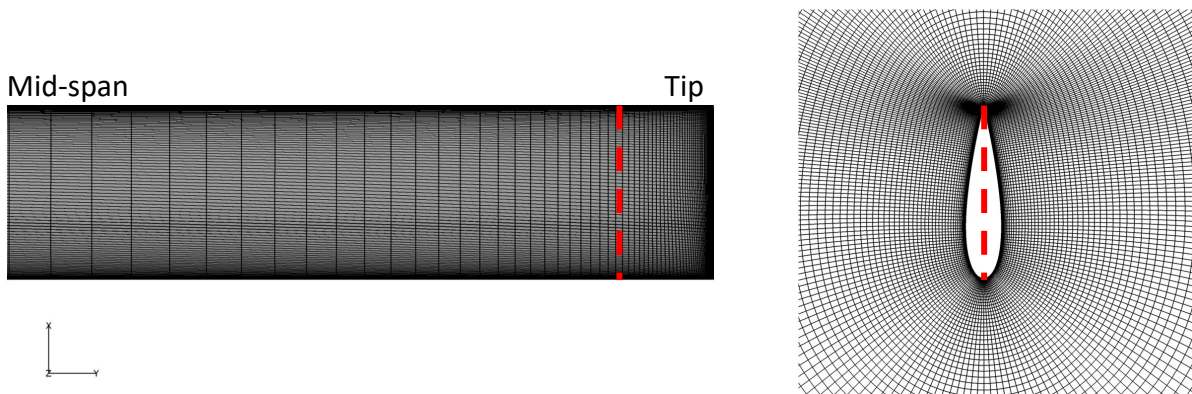


Figure 2.10: Mesh over the blade with the resolution increasing towards the tip (left) and the blade in the domain mesh (right). The Red dashed line shows the chord section.

Table 2.5: Static Blade Test Matrix for CFD Simulations

Test Case	Solver	Freestream Velocity
Static Blade AR 10	Implicit LES	5 m/s
Static Blade AR 20	Implicit LES	5 m/s
Static Blade AR 10	IDDES	5 m/s

Initially, the CFD cases for a static and plunging airfoil were decided and a few cases were run before the experimental campaign to get an idea of the flow to help plan the

experiment. A PSD analysis was performed on the velocity and the shedding frequency was found to be 8.3 Hz at $U_\infty = 5m/s$ leading to a Strouhal number of 0.12. This value was used to determine the frequency ratios seen in the test matrix for the plunging airfoil simulations, seen in Table 2.6. The frequencies chosen were 6 Hz, 8 Hz, 9 Hz, 10 Hz, 11 Hz, 12 Hz, 14 Hz, 16 Hz, 18 Hz, and 20 Hz, and these values were normalised by the f_{st} found from the static CFD case. Due to experimental limitations of the plunging mechanism, the freestream wind speed was reduced to 3 m/s, and hence, additional simulations were run for a 2.5 Hz and 5Hz plunging airfoil at $U_\infty = 3m/s$ and $A/c = 1$ to compare to the PIV results.

Table 2.6: Plunging Blade Test Matrix for CFD Simulations. $U_\infty = 5m/s$ using an IDDES Solver. $f_{st} = 8.3$ Hz

Frequency [Hz]	Frequency Range (f/f_{st})	Amplitude Range (A/c)
6	0.72	0.05, 0.1, 0.2, 0.4, 0.6, 0.8, 1.0
8	0.96	0.05, 0.1, 0.2, 0.4, 0.6, 0.8, 1.0
9	1.08	0.05, 0.1, 0.2, 0.4, 0.6, 0.8, 1.0
10	1.20	0.05, 0.1, 0.2, 0.4, 0.6, 0.8, 1.0
11	1.33	0.05, 0.1, 0.2, 0.4, 0.6, 0.8, 1.0
12	1.45	0.05, 0.1, 0.2, 0.4, 0.6, 0.8, 1.0
14	1.69	0.05, 0.1, 0.2, 0.4, 0.6, 0.8, 1.0
16	1.93	0.05, 0.1, 0.2, 0.4, 0.6, 0.8, 1.0
18	2.17	0.2, 0.4, 0.6, 0.8, 1.0
20	2.41	0.2

The test matrix for the surging airfoil was designed after the PIV experiment had been completed, so U_∞ was changed to $3m/s$. The expected Strouhal frequency was also changed to 6.4 Hz to mimic the value used from the experimental results, however, a static CFD simulation at 3 m/s and a hot wire measurement would be needed to confirm this. The test matrix for the surging airfoil simulations is seen in Table 2.7. Additionally, simulations were run for a 2.5 Hz and 5Hz surging airfoil at $U_\infty = 3m/s$ and $A/c = 1$ to compare to the PIV results.

Table 2.7: Surging Blade Test Matrix for CFD Simulations. $U_\infty = 3m/s$ using an IDDES Solver. $f_{st} = 6.4$ Hz

Frequency [Hz]	Frequency Range (f/f_{st})	Amplitude Range (A/c)
3.32	0.52	0.33, 0.67, 1.0
4.15	0.65	0.33, 0.67, 1.0
4.98	0.78	0.33, 0.67, 1.0
5.81	0.91	0.33, 0.67, 1.0
6.64	1.03	0.33, 0.67, 1.0
7.47	1.17	0.33, 0.67, 1.0
8.30	1.28	0.33, 0.67, 1.0
9.13	1.43	0.33, 0.67, 1.0
9.96	1.56	0.33, 0.67, 1.0
10.79	1.69	0.33, 0.67, 1.0

2.5.3 Personal Involvement

All simulations were set up and performed by Assistant Professor Christian Grinderslev from the Technical University of Denmark, Lyngby. The CFD was used as a black box tool and making the mesh and running the simulations was not within the scope of the thesis. The test matrix of cases to run was decided by the author, with suggestions from the supervisors. The output files containing the forces and flow fields at various planes were provided to the author and all the further post-processing of the data was done by the author. The planes containing the velocities and pressure values as well as the load file was provided as an output to the author. Further post-processing of the planes to attain the velocity and pressure fields to compare to the PIV flow fields. Codes to post-process the loads and time series were also written by the author.

This section presents the results of the experiments and simulations performed. It attempts to answer the research questions and give an insight into the vortex shedding around the blade undergoing different motions. First, a validation of the CFD results is done, so that the simulation results could be further used for analysis to answer other research questions. Then, an analysis of the different motions at different frequencies is performed, analysing the spanwise convection of the tip vortex, the time series of the loads, hysteresis loops, and aerodynamic power, followed by an overall analysis of lock-in.

3.1 Validation of CFD Results

In order to draw conclusions from the CFD results, they must first be validated against the experimental data to ensure that the simulations accurately predicted the flow. This is done for a static blade as well as the plunging and surging blade.

3.1.1 Static Cases

For the static blade, two aspect ratios were run for both the PIV experiments and the CFD simulations, as seen in Table 2.2 and Table 2.5 respectively. The flat plate boundary for the experimental results was supposed to act as a reflection boundary condition such that a free blade with twice the aspect ratio would behave the same in the CFD simulations. In all the cases, we see the common trend that the streamwise wake deficit and vorticity increase from the tip and are at a maximum at the root for the fixed blade and at the mid-span for the free blade and that the spanwise velocity increases from the tip till around 2.5 chords inboard.

3.1.1.1 3D Flow Around a Finite Blade

To analyse the flow pattern around the blade and quantify the tip effect, the spanwise velocity component was used to determine the convection of the tip vortex inboard. A qualitative comparison of the spanwise flow and the vorticity in the wake at different spanwise positions will be presented. For the dynamic CFD results, the time series of the cl and cd will also be analysed to see if there is a phase shift in the loads and how they travel across the span from the tip to the mid-chord.

For the static 80 cm blade in the experiment, the flow field was measured at 19 different chordwise positions from 0.5 chords in front of the tip to 9 chords inboard for an 81 cm (aspect ratio of 10.80). All three velocity fields and the vorticity field can be seen in Appendix E. Figure 3.1, which shows the spanwise velocity field for chosen spanwise locations is presented below. The spanwise velocity at all the available fields of view can be found in Figure E.4.

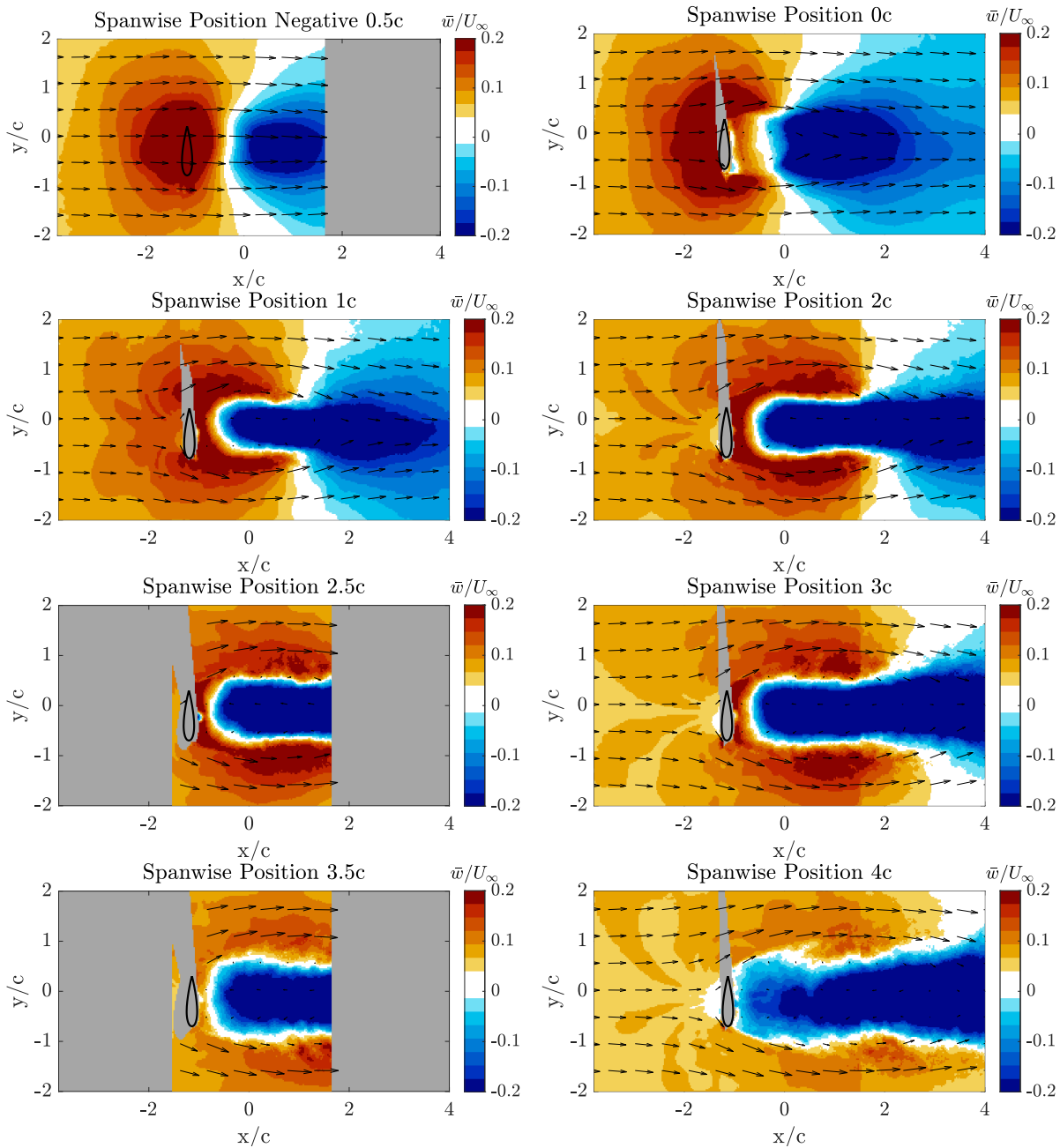


Figure 3.1: Spanwise velocity, \bar{w}/U_∞ around a static blade from 0.5c in front of the tip to 4c inboard from PIV data, freestream velocity coming from the left. The flow is positive into the page. Grey portions of the plot indicate no available data.

As can be seen from the figures, the positive spanwise velocity (seen in red) immediately behind the airfoil as well as the large negative velocity (in blue) increases in magnitude from negative 0.5 chords up to around 3 chords inboard but then begins to decelerate as we move further inboard and is 0 at the wall. This suggests a suction of the flow around the blade, which pulls in flow from upwind of the airfoil and sucks it downwind in the spanwise direction. The flow is visualised in Figure 3.2.

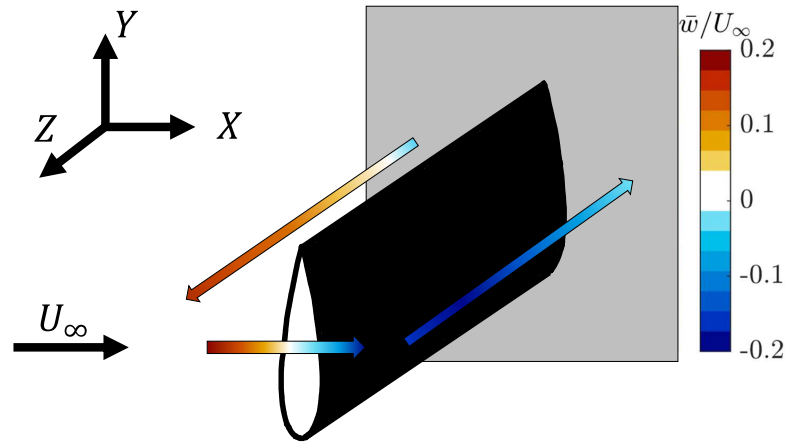


Figure 3.2: Spanwise velocity, \bar{w}/U_∞ around the blade

To validate that a blade with twice the aspect ratio that is free on both ends would produce similar results, we can qualitatively compare it with the ILES case with an aspect ratio of 20, seen in Figure 3.3. Here we see that the flow follows the same pattern of accelerating till around 2.5 chords in the wake and then decelerating to 0 at mid-span. This resembles the flow pattern visualised in Figure 3.2, confirming that a free blade with twice the aspect ratio accurately predicts the flow around a blade with a fixed end and flat plate boundary condition while being geometrically less complicated to save meshing and computational effort. It is worth noting that with a limited number of planes that are spread far apart, it is difficult to judge if the maximum flow acceleration is further inboard at around 3 chords like in the experimental results. Furthermore, the planes available from CFD and PIV data differ, so only a general qualitative comparison is possible. It should also be noted that the ILES simulation was used as a comparison because of the blade aspect ratio, but the IDDES simulations will be more accurate. For a static blade, the model sufficiently predicts the flow, so the comparison is still valid.

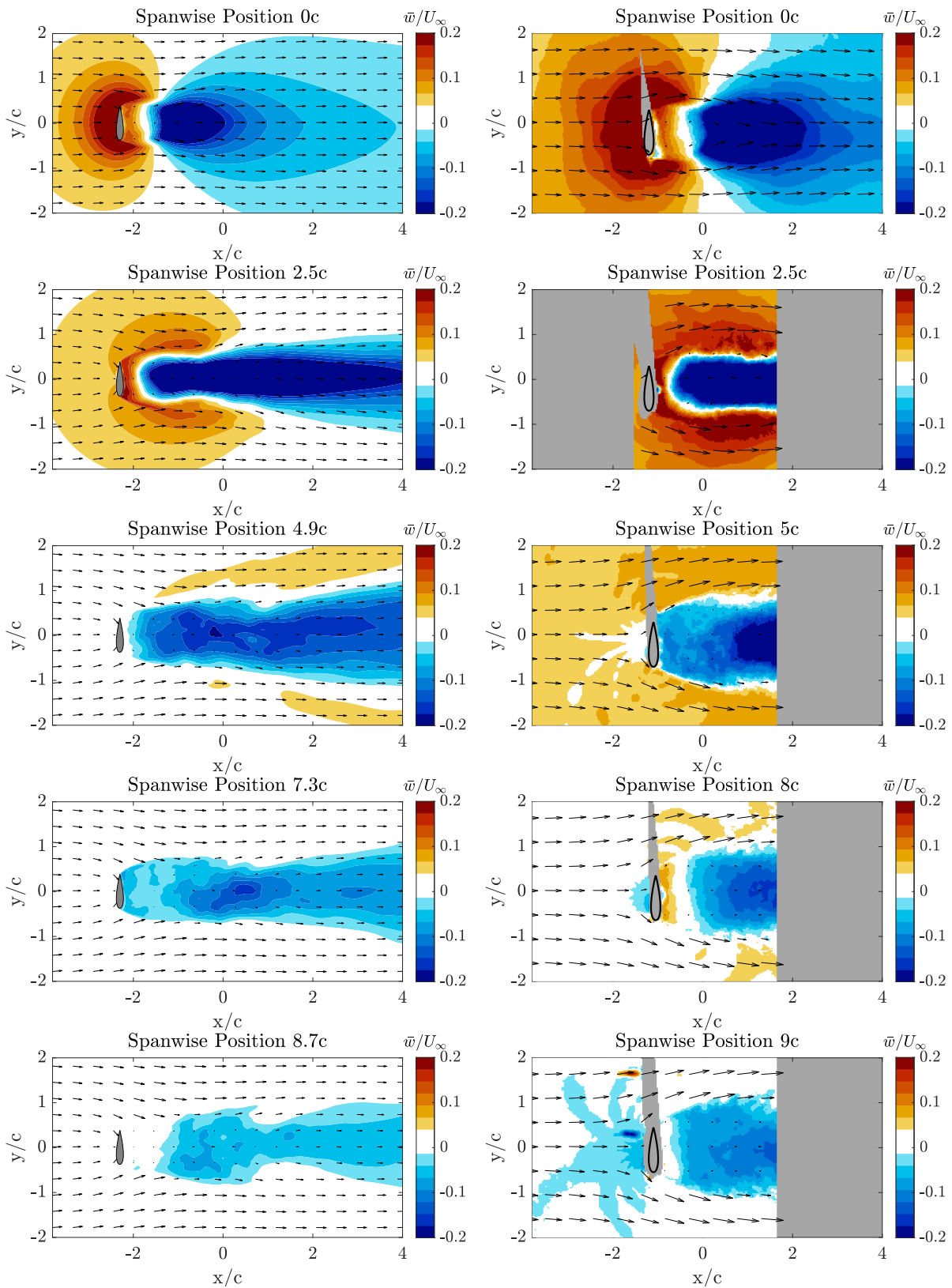


Figure 3.3: Spanwise velocity, \bar{w}/U_∞ around a static blade using an Implicit LES on a blade free on both ends with an aspect ratio of 20 (left) and PIV measurements on a cantilevered blade with an aspect ratio of 10 (right). The flow is positive into the page. Freestream velocity coming from the left.

3.1.1.2 Effect of Blade Aspect Ratio

To see the effect of the blade aspect ratio and further evaluate the spanwise acceleration of the flow, the spanwise flow for PIV measurements on the 80 cm and 40 cm blades were compared for the same spanwise position inboard of the tip, seen in Figure 3.4. The spanwise velocity fields for all the available fields of view from the PIV experiments for the static blade can be found in Figure E.4 for the 80 cm blade and in Figure F.4 for the 40 cm blade.

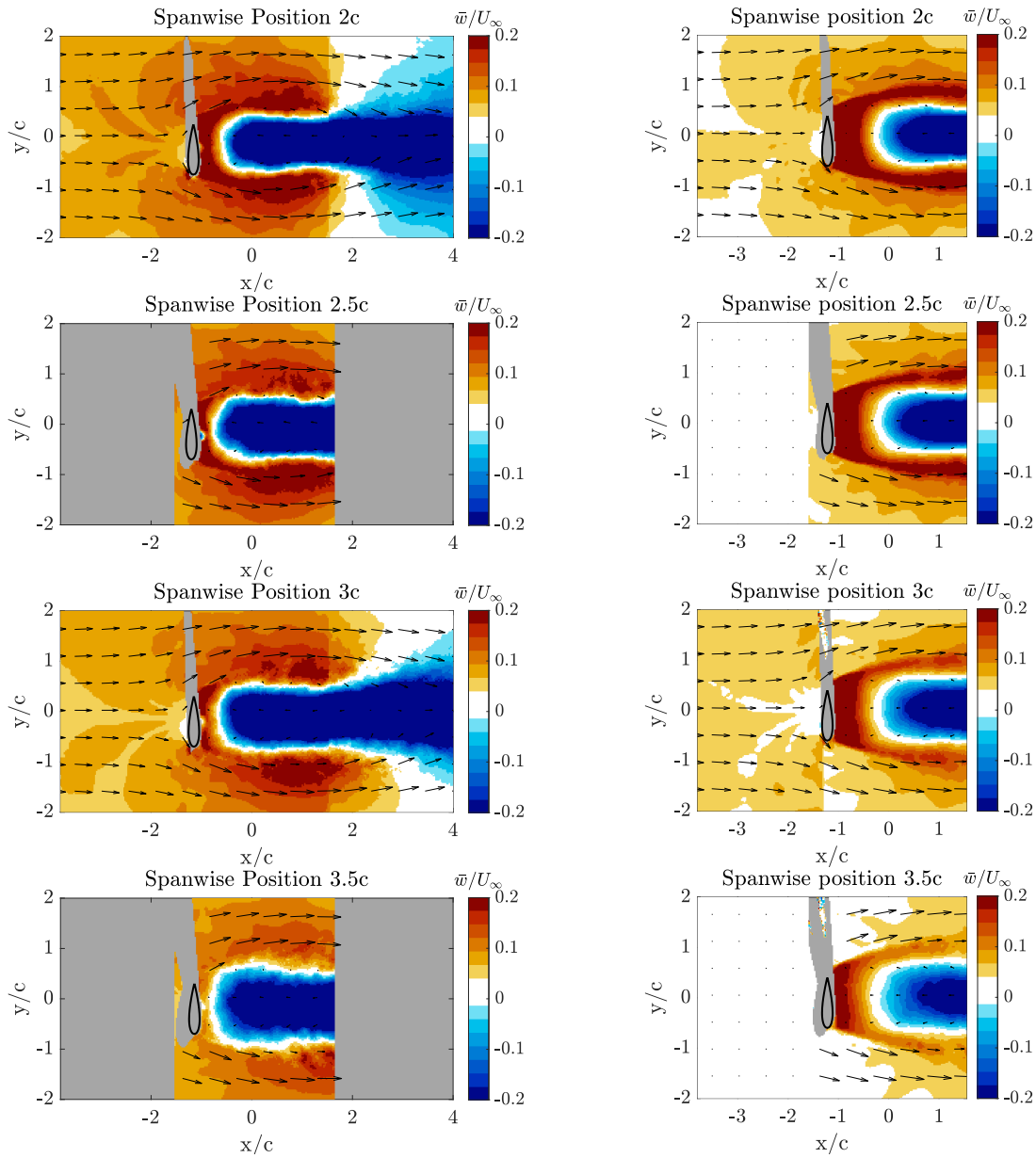


Figure 3.4: Spanwise velocity, \bar{w}/U_∞ around an 80 cm, 10.7 aspect ratio static blade (left) and 40 cm, 5.3 aspect ratio static blade (right) from PIV data. Far wake data is unavailable for the 40 cm blade. Freestream velocity coming from the left. The flow is positive into the page.

Figure 3.4 shows that the spanwise flow accelerates and peaks around 3 chords for the 80 cm blade but at around 2.5 chords for the 40 cm blade. Both cases were measured with a freestream wind speed of 5 m/s. However, the far wake region was also measured for a freestream wind speed of 3 m/s and the development of the wake showed the same pattern, seen in Figure G.4, suggesting that the spanwise convection of the tip vortex is independent of the freestream wind speed. This hypothesis needs to be further studied since the tested wind speeds are very close and only the far wake data was

available at limited spanwise positions. All the flow fields for the 40 cm static blade at 3 m/s freestream can be found in Appendix G. However, this conclusion is once again a qualitative analysis of the flow field. To support the visual analysis and quantify the flow, the top view of the blade and the wake velocity was plotted for the CFD results as seen in Figure 3.5.

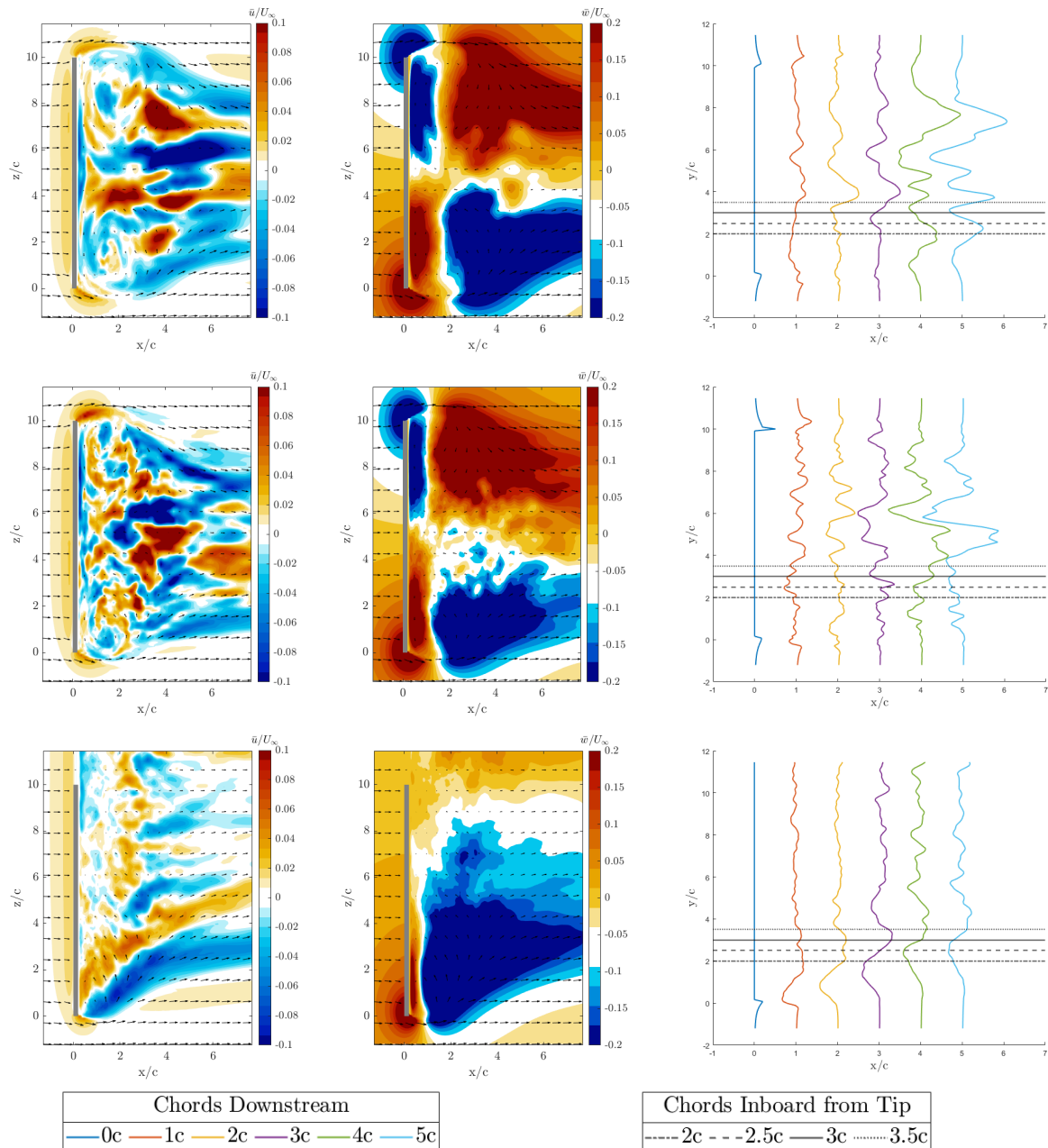


Figure 3.5: Left to right: Averaged Streamwise Velocity \bar{u}/U_∞ , Spanwise Velocity \bar{w}/U_∞ Field, and Downstream Velocity Deficit from CFD data.. IDDES blade with AR 10 (top), ILES blade with AR 10 (middle), and ILES blade with AR 20 (bottom). Only half of the AR 20 blade from the tip to mid-span is presented.

The largest fluctuations in the velocity deficits are in line with the largest spanwise acceleration at 2.5 chords for the AR 10 blade and 3 chords for the AR 20 blade, as seen by the portion that is the darkest blue in the spanwise flow field (middle). This point also matches the region where the tip vortex recirculates in the wake, as seen in the streamwise flow components (left). It is also seen that the effect of the tip vortex circulation is not as pronounced for the longer blade, which is an expected result, since as the blade tends to infinity and becomes ‘2D’, the effect of the tip vortex can be ignored. It is important to characterise when the flow around the blade becomes somewhat 2D so that the shedding at different spanwise locations can also be characterised. Since the blade is symmetric with a constant cross-section, data taken at around 3 chords inboard from the tip can be considered ‘2D’ while spanwise positions between the tip and 3 chords can be considered ‘3D’, with increased complexity in the flow.

The PIV and CFD flow fields show an excellent agreement, and it was concluded that for the shorter blades with an aspect ratio of around 10, the spanwise flow is largest between 2 to 2.5c chords inboard, and for the longer blades with an aspect ratio of around 20, the spanwise flow was largest around 3 to 3.5 chords inboard. It was also concluded that the ILES model showed excellent agreement with the IDDES model and hence, the earlier analysis using the ILES results to compare with the PIV results from the 80 cm blade are reasonable. However, the IDDES model was used for all the dynamic cases because the effect of the smaller eddies and viscous dissipation will be larger for a moving blade.

All the flow fields around the static blades for the PIV and CFD results can be found in the Appendix.

3.1.2 Plunging and Surging Blade

Next, a comparison of the flow fields for the plunging and surging blade was performed to validate the CFD simulation. This also allowed further conclusions on the loads and lock-in phenomena which were done using CFD data only, since time series data was not available from the experiment. The PIV flow fields were phase-locked and the phase average flow field over the 12 phases was plotted. To have a fair comparison, a similar analysis was performed on the CFD results. The same 12 phase angles were defined and the time series was processed such that the flow field was extracted at the given phase over all the cycles, averaged, and then plotted. A comparison of some flow fields is presented in Figure 3.6. All flow fields for the dynamic cases can be found in the Appendix.

The vorticity field at 0 deg phase, at 3 chords inboard for a plunging and surging blade at 2.5 Hz and 5 Hz are plotted for all the dynamic cases.

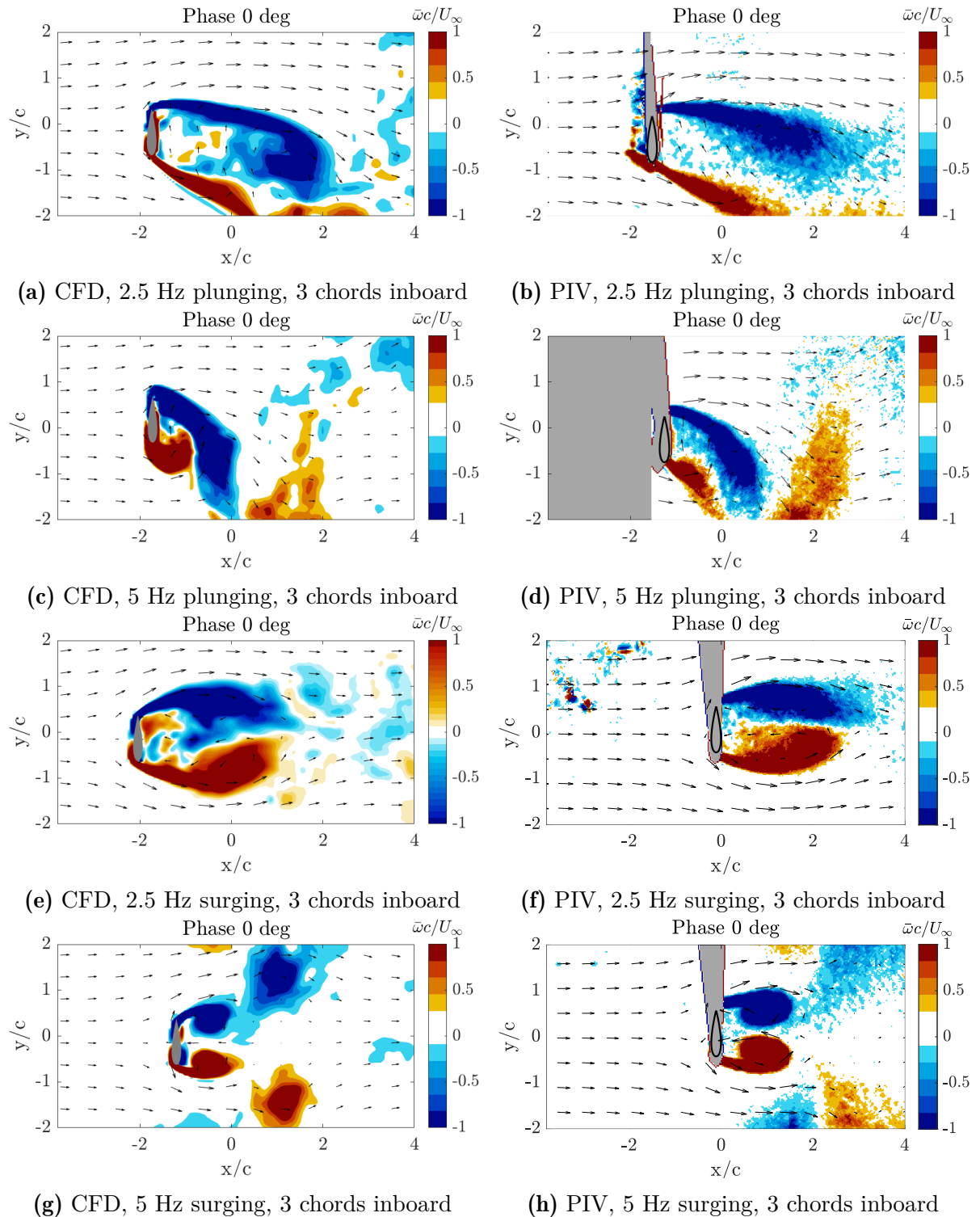


Figure 3.6: Vorticity, $\bar{\omega}c/U_\infty$ 3 chords inboard from the tip with the freestream velocity coming from the left. Flow fields from CFD results (left) and PIV results (right).

Once again, the flow fields show excellent agreement between the CFD and PIV

results, though the vorticity is slightly over-predicted by the CFD simulation. The vortex structures in the flow are also less noisy in the CFD simulations since the PIV results are limited by the number of samples, and with a highly unsteady flow, a larger sample size would be needed for a higher resolution of the smaller structures in the wake. The CFD results also tend to under-predict the vertical velocity component very close to the airfoil, but it could also be due to the fact that the PIV result has a shadow region around the blade that cannot be resolved. The benefit of the CFD result is that there is no data lost to a shadow region and that the flow fields are resolved in time, so time series analysis on the frequencies and unsteady loads can be performed. It can also provide valuable information for parts of the flow that are missing from PIV, such as in Figure 3.6d where the upstream data was not captured during the experiment but can be inferred from the CFD results. It was concluded that the CFD simulations for the static and dynamic cases were visually similar enough to consider accurate and therefore, the results from simulations at other frequencies and amplitudes as well as the integrated forces over the blade could be considered accurate and used for further analysis.

3.2 Plunging Blade

Figure 2.1 shows the orientation of the plunging airfoil with respect to the incoming wind. Figure 3.11 shows the velocity triangles at four phases during the plunging cycle.

3.2.1 Effect of Motion Frequency on the Shed Vortex

In the experiment, two frequencies, 2.5 Hz and 5 Hz were tested at the same oscillation amplitude of 1 chord. With an expected Strouhal frequency of 6.4 Hz based on a POD analysis of the experimental results, it was predicted that the 5 Hz case would be locked in and the 2.5 Hz case would not. Figure 3.7 shows a comparison of the vorticity over four phases at the two frequencies 3 chords inboard from the tip so as to analyse the ‘2D’ flow characteristics.

However, due to the extremely large oscillation amplitude, both frequencies showed von Karman-like vortex shedding, with the vortices shed twice per cycle at the motion frequency, suggesting lock-in. Unfortunately, without a time series or hot wire analysis, a frequency analysis cannot be performed to confirm the shedding frequency of the flow from experimental data. A notable difference between the flow fields is the convection of the vortices downwind, which is largely affected by the motion frequency, due to its influence on the relative velocity experienced by the vortices leaving the body. The shedding of the von Karman-like vortex structures begins around 2 chords inboard for both frequencies and is significant at 3 chords inboards. This suggests that the frequency of motion does not influence the convection of the tip vortex inboard and when the blade starts to behave 2D, and that it is only dependent on the aspect ratio of the blade.

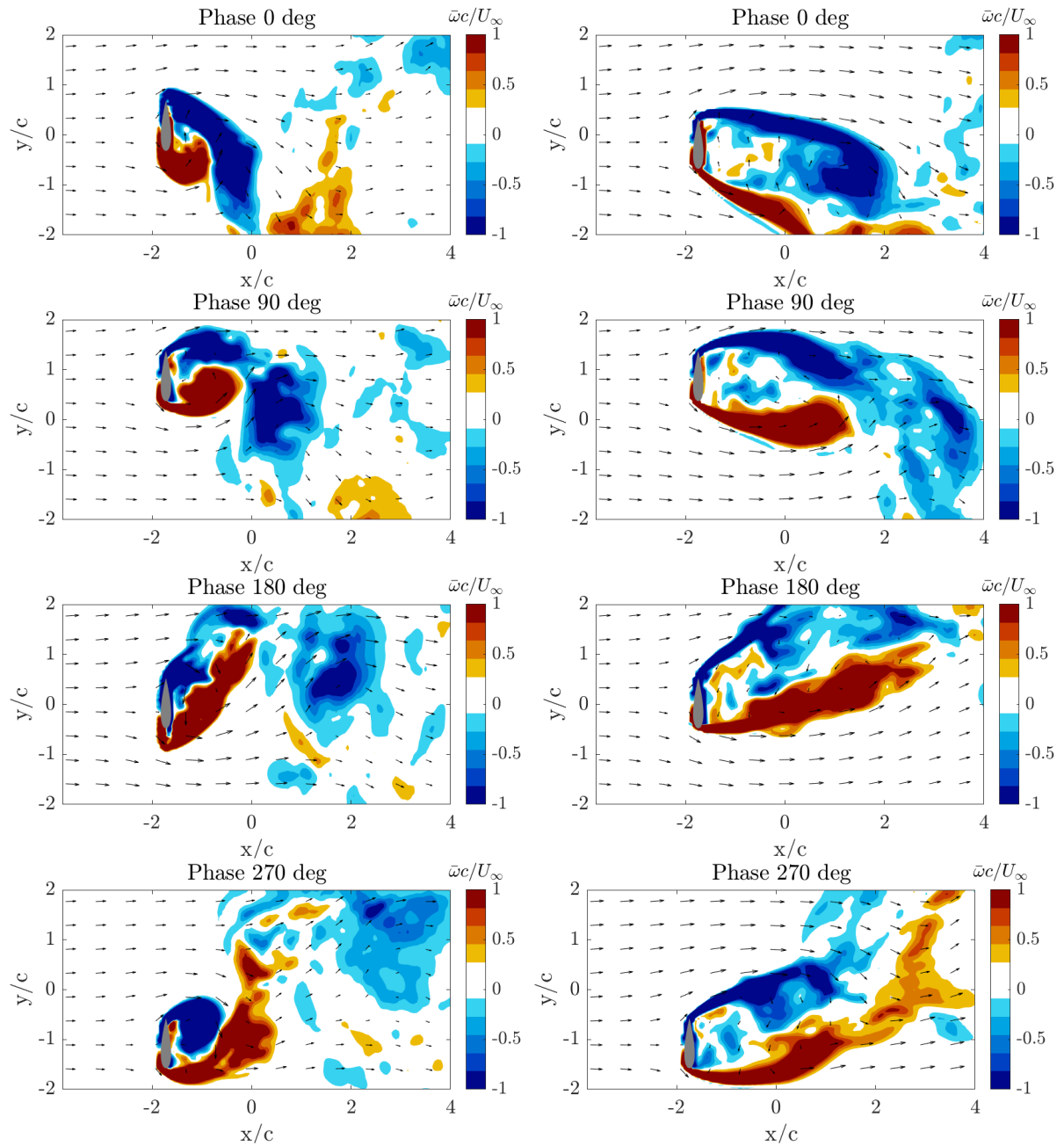


Figure 3.7: Vorticity, $\bar{\omega}c/U_\infty$ around a plunging airfoil 3 chords inboard from the tip at 5 Hz (left) and 2.5 Hz (right) with the freestream velocity coming from the left from CFD data.

Vorticity and other flow fields at all 12 phases for the plunging blade at all available spanwise positions can be found in Appendix L for 2.5 Hz and in Appendix M for 5 Hz for the CFD simulations and in Appendix H and Appendix I for the 2.5 Hz and 5 Hz PIV measurements respectively. At both frequencies, two counter-rotating von Karman-like vortices are once per cycle at each extreme position. The shedding is clearer at 5 Hz and not very obvious at 2.5 Hz, initially suggesting that it may not be locked in. However,

this could be due to the increased effect of the freestream velocity on convecting the vortices further downstream and out of the available field of view.

3.2.2 Spanwise Vortex Shedding and 3D Flow Around the Tip of a Finite Blade

To characterise the spanwise convection around a blade in motion, first, the spanwise velocity and vorticity were captured around the tip, seen in Figure 3.8.

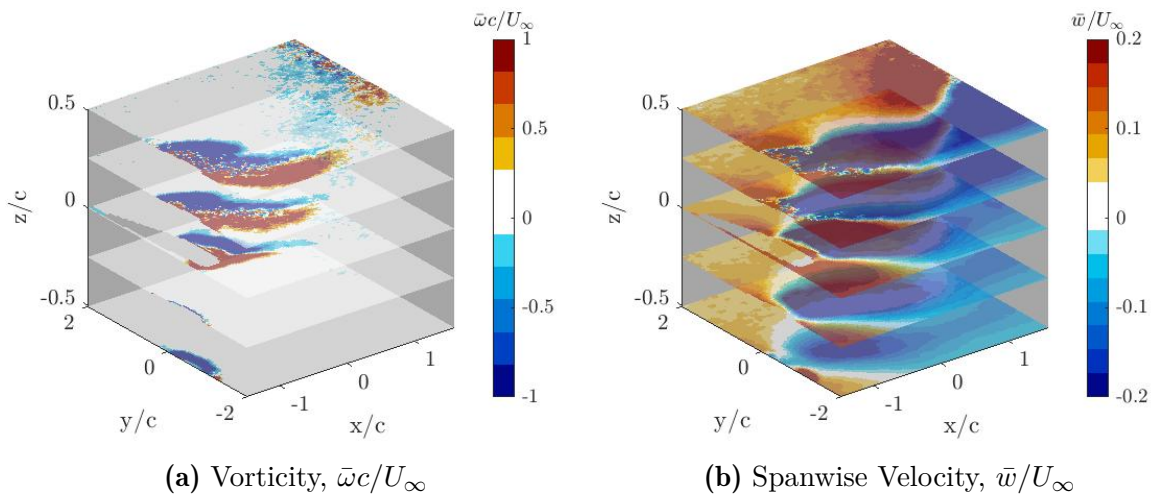


Figure 3.8: Flow Around the Tip for a 5 Hz plunging airfoil at 0 deg phase for 1 chord motion amplitude from PIV data. Blade is at $y/c = 0$, $x/c = -2$, $z/c = 0$ to 0.5.

Figure 3.8 shows the flow field from half a chord in front of the tip to half a chord inboard to visualise the flow just around the tip. The figure shows that although the spanwise flow begins accelerating in front of the blade, there is no vorticity present in that region. The flow gets sucked from the tip towards the root immediately downstream of the blade, and this also convects the tip vortex towards the root of the blade. However, no clear von Karman vortex is shed so close to the tip.

Next, the development of the flow from the tip to 3 chords inboard is analysed. Figure 3.9 presents a comparison of the vorticity around the airfoil at 0 deg phase for 2 frequencies, 5 Hz and 2.5 Hz, at four spanwise positions: 3 chords inboard, 2 chords inboard, 1 chord inboard and at the tip. Other phases and spanwise positions are seen in Appendix M and Appendix L. CFD data is presented instead of the PIV data because some fields of view are missing from the PIV measurements at 1 chord and 2 chords inboard. The equivalent PIV flow fields are available in Appendix I and Appendix H respectively.

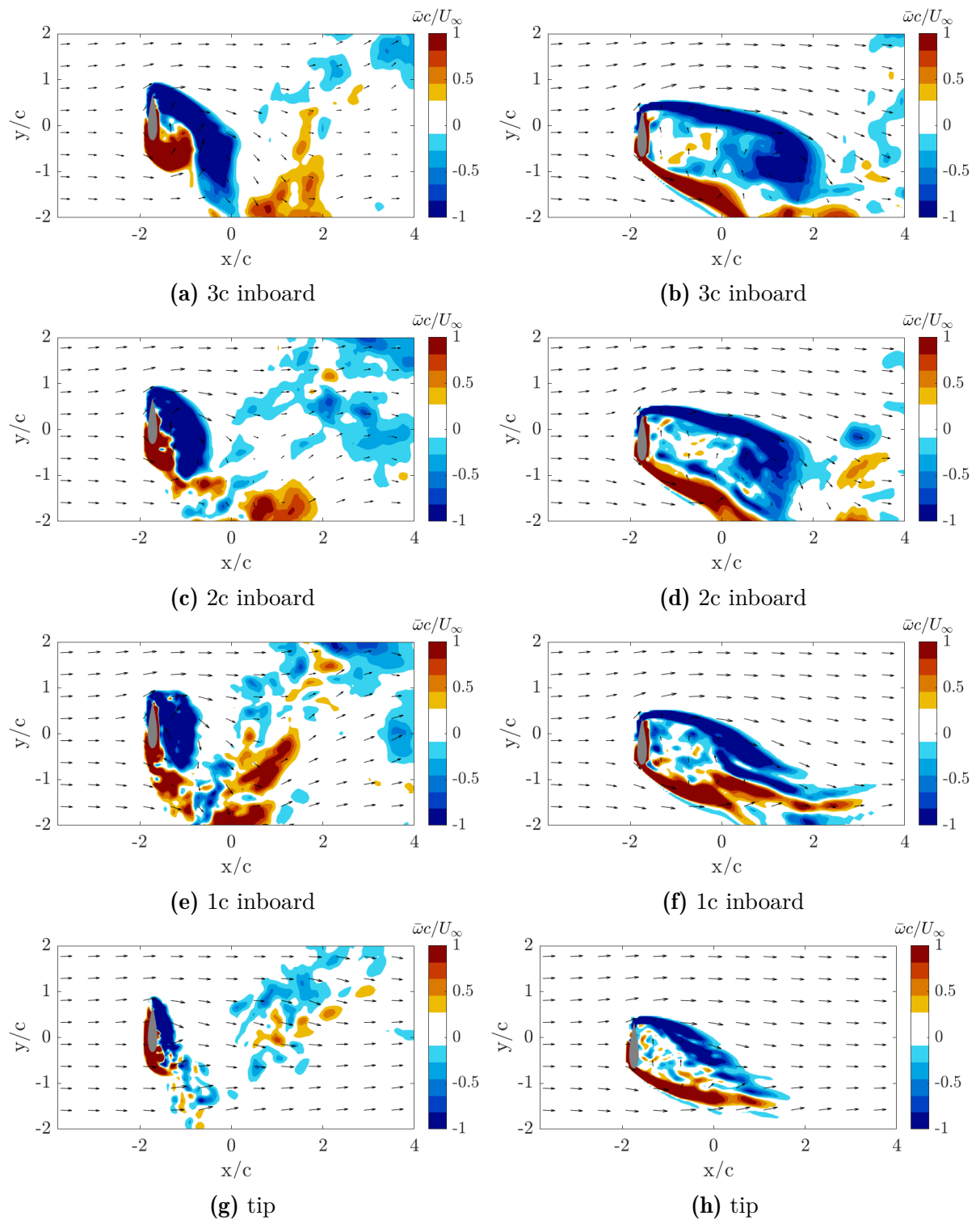


Figure 3.9: Vorticity, $\bar{\omega}c/U_\infty$ around a plunging airfoil at 5Hz (left), and at 2.5Hz (right) from 3 chords inboard (top) to the tip (bottom) with the freestream velocity coming from the left from CFD data.

Figure 3.9 shows that as we move from 3 chords inboard towards the tip, the strength and size of the shed vortex becomes smaller, with no clear ‘vortex blob’ being shed at the tip. At 5 Hz, the shed vortex at the tip is smaller and is only convected around 2 chords downstream. The vortex shed 3 chords inboard and is much larger in both its width as well as its convection 4 chords downstream. The flow fields at 2.5 Hz on the right show that the shed vorticity extends longer in the wake. This is because at a lower frequency, the period is longer and hence, there is more time for the wake to be convected downstream within one cycle before the same motion phase occurs again. The freestream wind speed is the same in both cases, but its effect in convecting the vorticity downstream is larger for the lower frequency case since it has a higher influence on the relative velocity experienced at the airfoil. Already 1 chord inboard from the tip we see the ‘vortex blob’ leaving the airfoil and this phenomenon becomes stronger further inboard. The difference in the shedding pattern is clearer with a visualisation of the whole cycle. A comparison is presented 3 chords inboard and at the tip for four phases: 0 deg, 90 deg, 180 deg, and 270 deg seen in Figure 3.10 at 5 Hz and in Figure 3.19 at 2.5 Hz.

3.2.3 Spanwise Development at 5 Hz

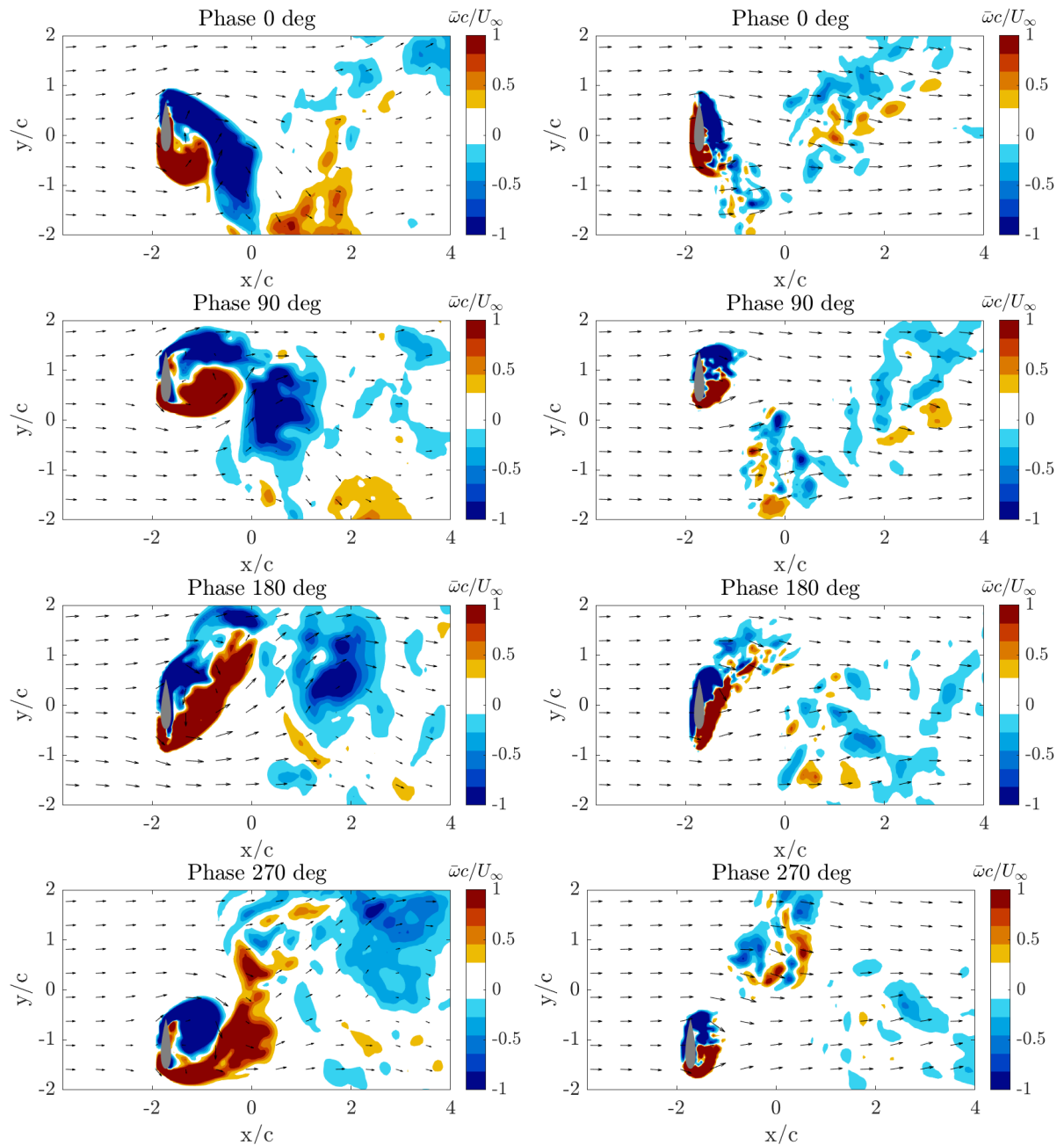


Figure 3.10: Vorticity, $\bar{\omega}c/U_\infty$ around a plunging airfoil at 5Hz, 3 chords inboard from the tip (left) and at the tip (right) with the freestream velocity coming from the left from CFD data.

Over the four phases, it is clear that at 3 chords inboard, there are two counter-rotating vortices shed per cycle, which resembles a von Karman vortex, which is not seen at the tip. This is also reflected in the flow around the static blade, where the spanwise flow

stopped accelerating around 2 chords inboard, and beyond that point, the 3D effects no longer dominate the flow. This suggests that VIV may be more likely further inboard, though VIV is not really experienced for a forced motion since the blade itself cannot naturally lock-in to the shedding frequency.

It is also important to note that the vortex shed at 90 deg when the airfoil is at the top, is more pronounced than the vortex shed at 270 deg, and this is most likely due to the sharp trailing edge at the top, leading to a less attached and more unsteady flow. Figure 3.11 shows a diagram showing the airfoil at four phases over one cycle, with the direction of the relative flow and angle of attack over the cycle. It is clear that as the airfoil moves upwards and has an angle of attack greater than 90 deg with the relative incoming flow, the sharp trailing edge experiences the velocity due to the motion. Compared to the part of the cycle between 90 deg and 270 deg phase when the airfoil moves downwards and the smooth leading edge is facing the flow against the motion, the forces on the blade and the shed vortex are less steady when the flow separates from the sharp trailing edge. This is also reflected in the time series plots presented in Figure 3.12 and Figure 3.13, where the time series data does not present as a smooth sinusoid due to the high unsteadiness from such a high frequency.

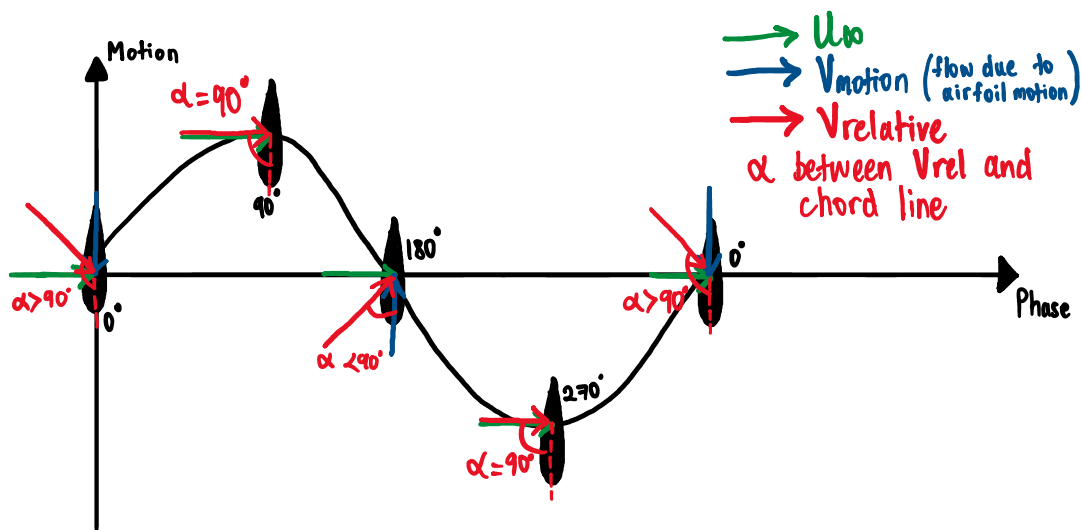


Figure 3.11: Velocity Triangles for a Plunging Airfoil

Figure 3.12 shows the time series of the lift coefficient of a plunging airfoil at 5 Hz, 1 chord amplitude at various spanwise positions from the tip to mid-span for 5 cycles. At the tip, the value is in the order of $e-5$ and hence, can be taken as 0, i.e. there is no lift produced at the tip. The cl follows a sinusoidal pattern at all the positions but has a large variation in the magnitude which peaks around 2.6 chords inboard and then stabilises.

The cl and cd were found using the relative flow velocity and resolving the normal and tangential force components with the angle of attack defined in Figure 3.11.

$$cl = cx \cdot \cos(\alpha) - cy \cdot \sin(\alpha) \quad (3.1)$$

$$cd = cx \cdot \sin(\alpha) + cy \cdot \cos(\alpha) \quad (3.2)$$

with cx as the force coefficient in the streamwise direction and cy as the force component in the vertical direction.

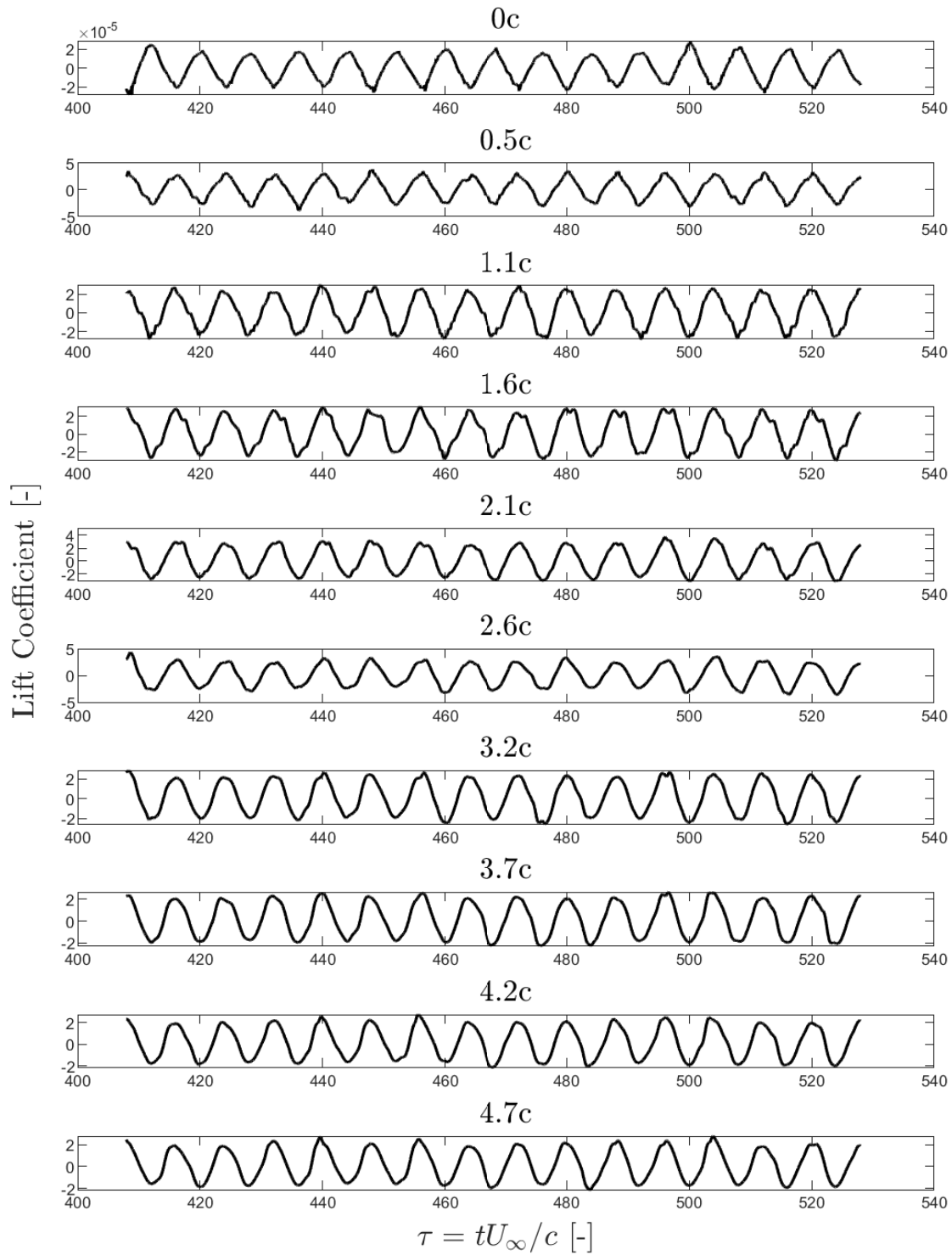


Figure 3.12: Time series of the cl at various spanwise positions from the tip to mid-span for a plunging airfoil at 5 Hz, 1 chord amplitude for 15 cycles from CFD data.

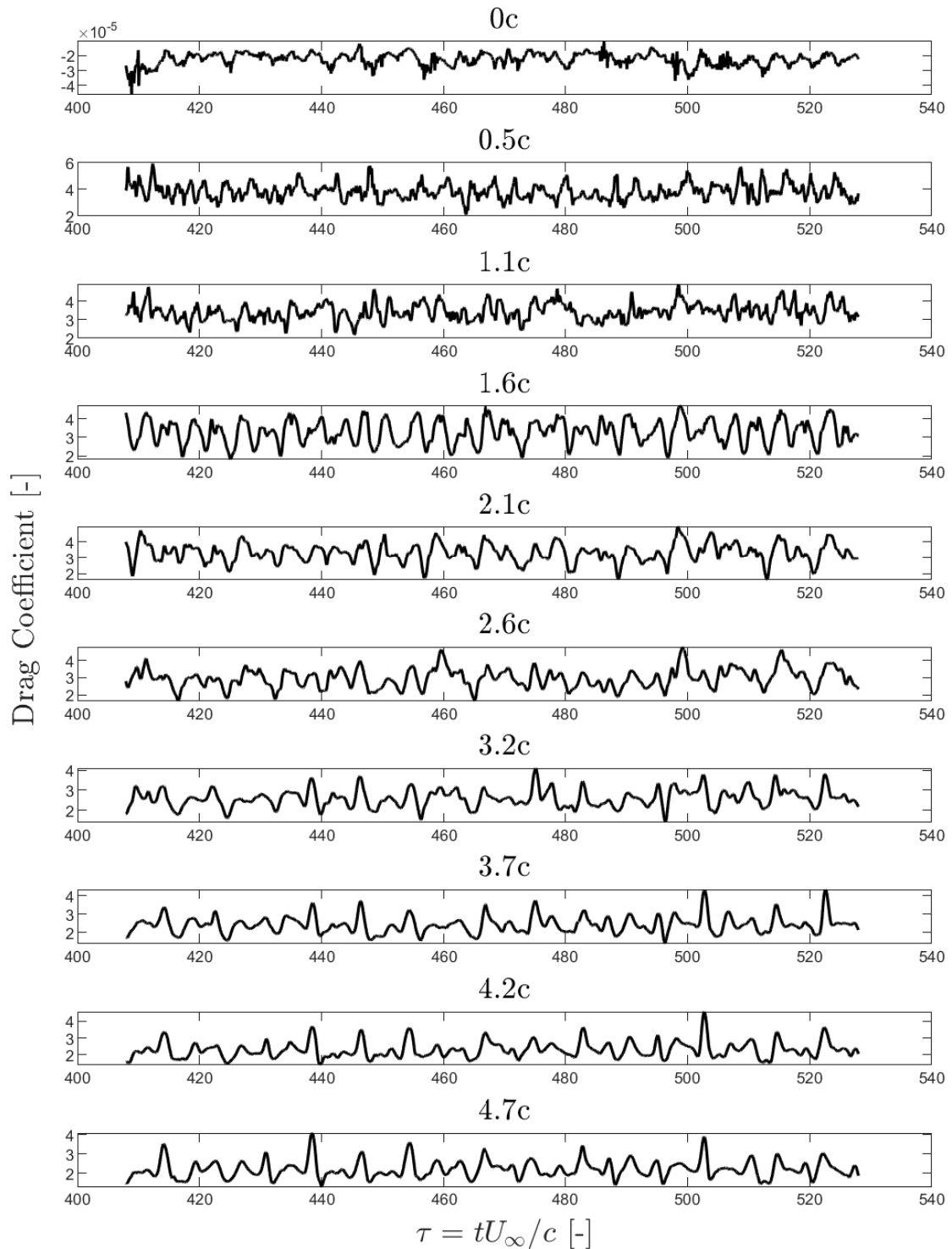


Figure 3.13: Time series of the cd at various spanwise positions from the tip to mid-span for a plunging airfoil at 5 Hz, 1 chord amplitude for 15 cycles from CFD data.

Figure 3.14 presents a PSD analysis of the lift coefficient and drag coefficient at five

different spanwise positions, 1 chord, 2 chords, 3 chords, 4 chords, and 5 chords inboard from the tip, and confirms that both 5 Hz plunging blade are locked in, with a peak at the motion frequency and its harmonic, as defined by Hu et al. [2021], Choi et al. [2015]. The PSD is normalised by the maximum value.

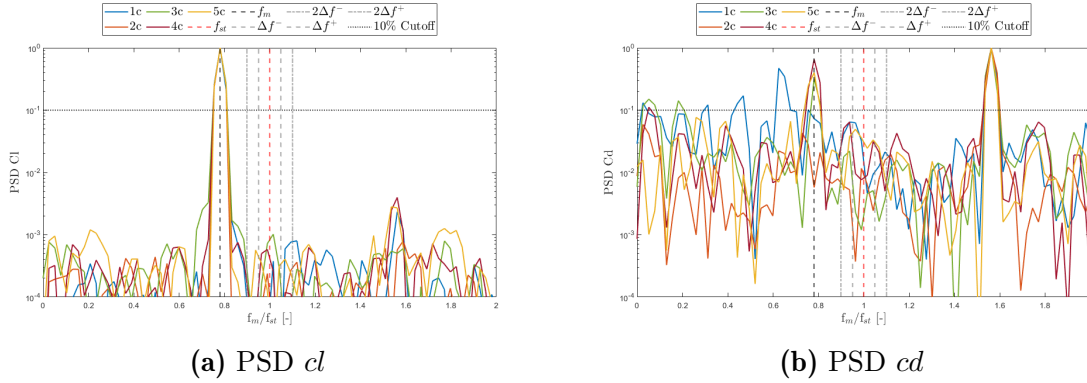


Figure 3.14: PSD of cl (left) and cd (right) for a plunging blade at 5 Hz $\sim 0.78f_{st}$, 1 chord motion amplitude at various spanwise positions from CFD results.

The PSD in Figure 3.14a shows that at all the spanwise positions, the blade appears to be locked in, though some peaks are seen at f_{st} , though their energy is 0.001% of the maximum peak and hence, negligible in comparison. It is interesting to see that all the spanwise positions show lock-in despite the flow fields in Figure 3.9 showing a large difference in the shed vorticity pattern between 1 chord and 3 chords inboard from the tip. This is likely because the cl is a periodic force as seen in Figure 3.12 and is dependent on the shed vorticity over one cycle. Figure 3.14b shows a dominant peak at twice the motion frequency, which is expected since the cd has a peak each time a vortex is shed, which is twice in one cycle. It is also interesting to note that the peak at the motion frequency generally tends to increase further inboard, with the exception of the peak at 2 chords that is lower than at 1 chord. To further analyse the load and investigate the effect of the tip vortex being convected in the spanwise direction on the loads experienced by the blade, hysteresis loops of the lift and drag coefficient were plotted over the angle of attack, seen in Figure 3.16. The mean and standard deviation of the cl and cd over 15 cycles are plotted from 1 chord inboard to 5 chord inboard (mid-span).

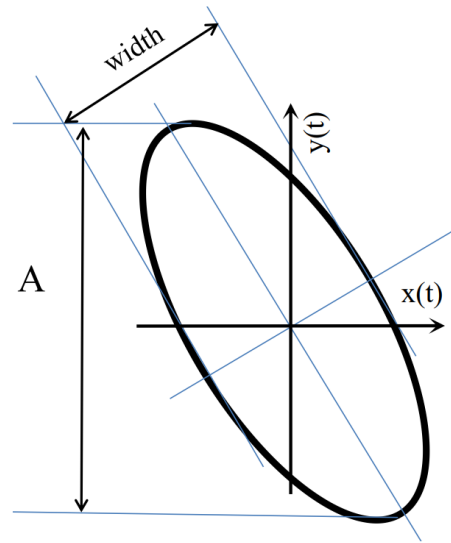


Figure 3.15: Lissajous figure, A – the amplitude, width – the phase lag. Reprinted from Yu [2018]. Method from Al-Khazali and Askari [2012].

Figure 3.15 presents a method developed by Al-Khazali and Askari [2012] that analyses the shape and direction of the hysteresis loop and gives an idea about the phase lag and amplitude. The direction of rotation and positive or negative slope of the loop influence whether the phase lag is positive or negative.

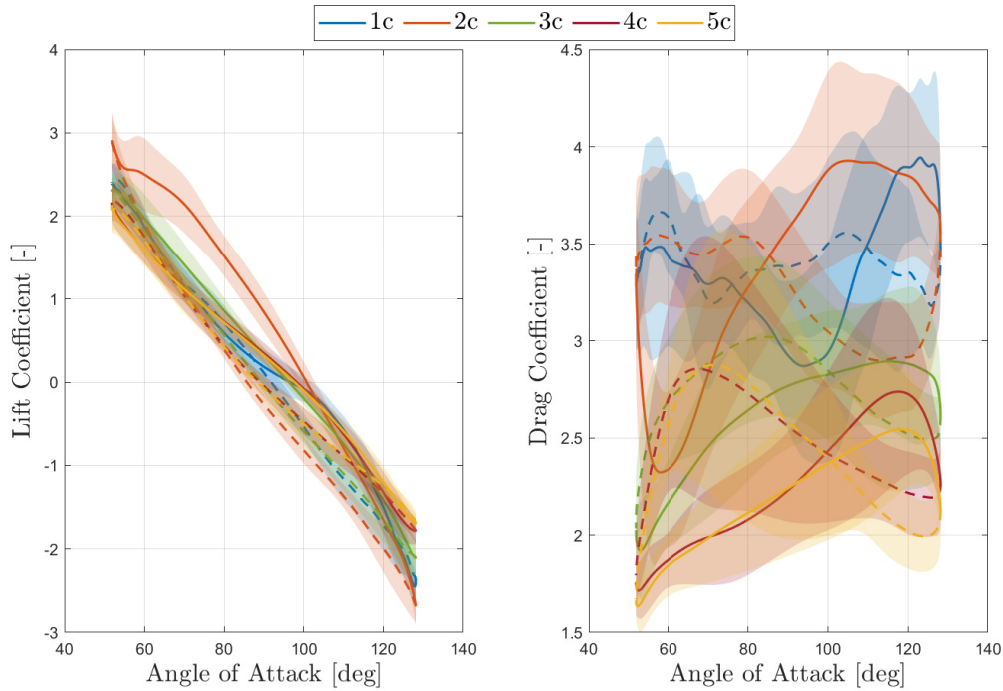


Figure 3.16: Hysteresis loops of the cl (left) and cd (right) against the angle of attack at different spanwise positions inboard from the tip for a plunging blade at 5 Hz frequency, 1 chord amplitude. Measured in chords away from the tip. The solid line shows the mean load as the blade moves upwards, the dashed line shows the mean load as the blade moves downwards and the surrounding translucent region is the standard deviation over 15 cycles from CFD data. Both loops rotate counter-clockwise.

The solid lines represent the motion from phase 270 deg to phase 90 deg in Figure 3.11 where the blade moves up and the trailing edge faces the flow from the blade motion. The dashed lines represent the motion from 90 deg to 270 deg phase where the blade moves down and the leading edge faces the flow from the blade motion.

Hu et al. [2021], Hoskoti et al. [2018], Choi et al. [2015], Skrzypiński and Gaunaa [2015], Meskell and Pellegrino [2019] and many others suggest that when lock-in occurs, the $cl - \alpha$ hysteresis loop will be smooth. In Figure 3.16 the $cl - \alpha$ hysteresis loop is relatively smooth at all the plotted spanwise positions, suggesting that lock-in has occurred, with a slight deviation at 2 chords inboard. This deviation occurs during the solid line portion of the loop when the blade moves upwards, which is expected to be less smooth due to the sharp trailing edge facing the flow. The standard deviation is relatively small and gets smaller further inboard, suggesting that the load becomes more stable and the oscillation becomes more quasi-steady and more ‘2D’. Figure 3.9 shows the spanwise development of the shed vorticity and the shed vortex becomes less chaotic and has clearer vortex structures further inboard, leading to a lower standard deviation in the load. The counter-clockwise rotation and negative slope angle indicate a phase lag, though the width of the loops is very small, so the lag over the cycle is minimal. The $cd - \alpha$ hysteresis loop on the other hand is chaotic and crosses over itself. The cd time

series plot is much more chaotic, with sharper peaks, and it does not follow a smooth sinusoidal pattern. With large variations in the angle of attack and relative flow faced by the airfoil section, the drag force variation is also large. This is especially so since the angles of attack experienced are well above the stall regime of the airfoil and hence, the drag forces are much more pronounced and the stall contributes to the high drag on the blade. The horizontal figure 8 shape is because the cd is at twice the frequency of the cl because there are two vortices shed each cycle, which cause a peak in the load, and this is in line with the definition for the loops by Al-Khazali and Askari [2012], and seen in Figure 3.14. It is also interesting to note that the loops move further downward as we move further inboard from the tip with the exception of the loop at 2 chords which is higher than at 1 chord, i.e. the drag coefficient is lower, and the loops are also smoother, which agrees with what was observed in Figure 3.14b. The smooth hysteresis loops suggest that the effect of the tip vortex may not be dominant further inboard, as seen in Figure 3.9 where the shed vortices are smoother further inboard and from Figure 3.5 where it was concluded that the spanwise convection of the tip vortex is no longer as dominant beyond 2.5 chords inboard. This is why there is such a large difference between the cd loops at 1 and 2 chords inboard which are similar to one another but with a larger magnitude than the loops at 3, 4, and 5 chords inboard, that has a similar shape and magnitude to one another, but a lower drag force at 1 and 2 chords. $cd - \alpha$ hysteresis loops also show a slight positive slope, suggesting a small phase lag.

To quantify the phase shift seen in the loads as the tip vortex moves inboard from the tip towards the mid-span, the mean, median, and standard deviation about the mean are calculated for the cl , cd , and the phase angle for the cl and cd at different spanwise positions over 15 cycles, as seen in Figure 3.17. The phase angle plot shows the phase angle in the cycle between -180 and 180 deg where the maximum or minimum cl or cd occurs at that given spanwise position. The maximum and minimum points are taken as discrete points from the time series, and a Gaussian interpolation may have resulted in higher accuracy. However, there was a high resolution of points in the time series so the error is minimal.

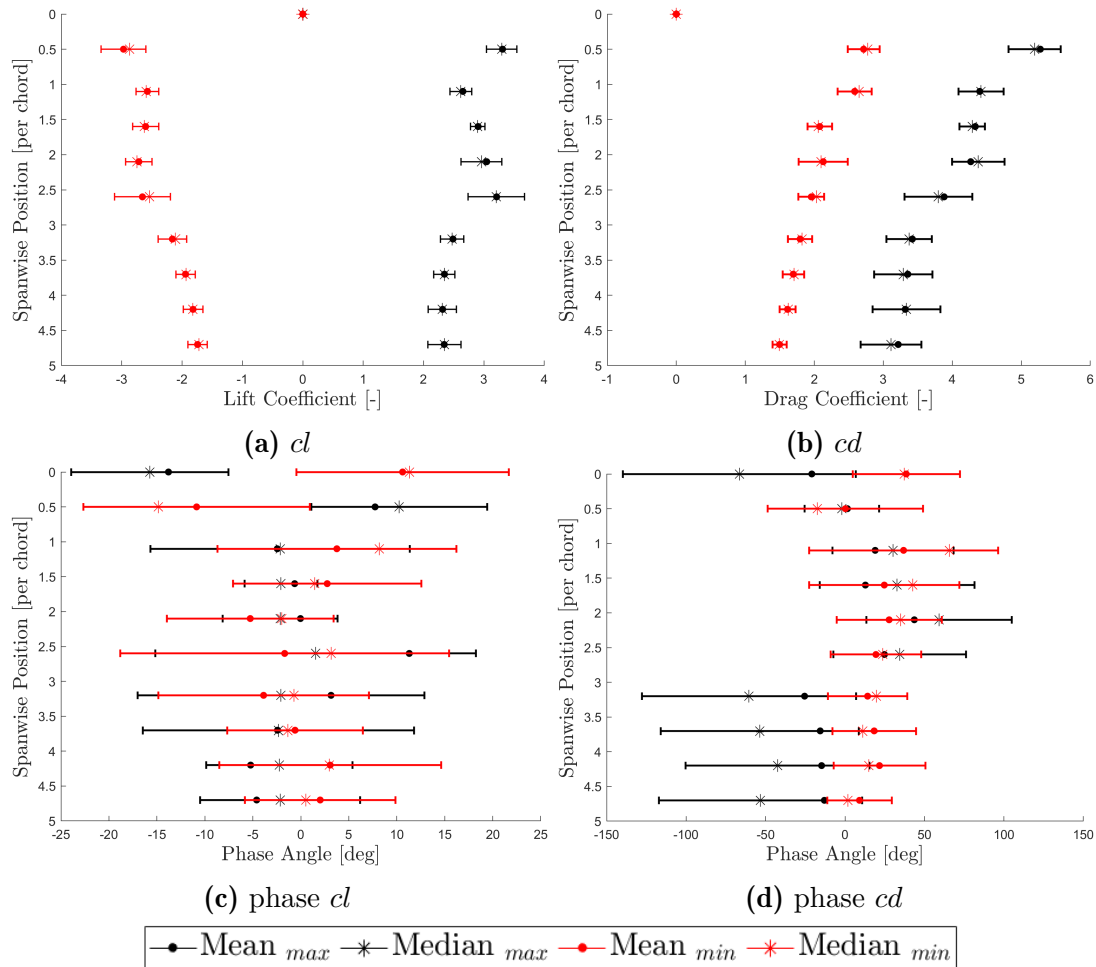


Figure 3.17: Plunging airfoil at 5 Hz, 1 chord amplitude. Mean and Median values for cl (a), cd (b), and their phases (c) and (d) respectively at different spanwise positions over 15 cycles from CFD data. Bars represent the standard deviation away from the mean.

The legend shows the mean value of the peak in the time series, denoted by the dot, and the median value of the peak denoted by the star, both in black with the subscript ‘max’. The mean value of the trough, denoted by the dot, and the median value of the trough, denoted by the star are in red, with the subscript ‘min’. The phase angle corresponds to the phase at which the maximum or minimum force coefficient occurs in a cycle. The bars represent one standard deviation from the mean on either side.

From these plots, there is a very clear pattern in the loads that stabilises around 3 chords inboard, which once again agrees with the earlier conclusion that the spanwise vortex convection travels to around 2.5 chords inboard and then the flow becomes ‘2D’, and this seems to hold for a plunging blade as well. The largest standard deviation in the loads is seen at around 2.5 c inboard. The standard deviation for the phase angle is relatively large for both the cl and the cd though the mean phase angle does not vary much from 3 chords inboard. The large variation in the cd is also because of the double peak occurring per cycle.

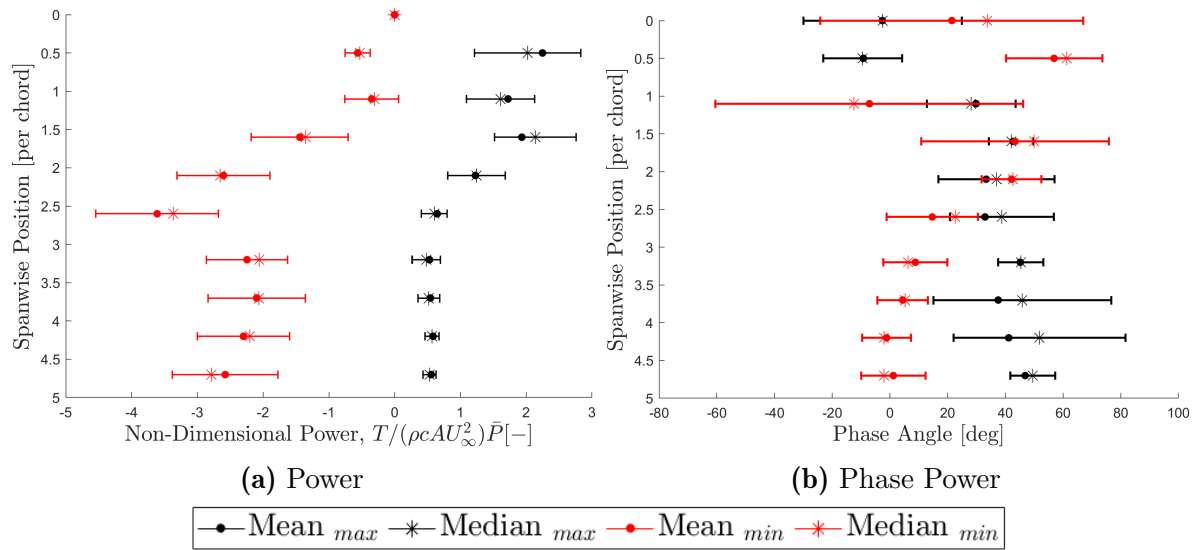


Figure 3.18: Plunging airfoil at 5 Hz, 1 chord amplitude. Mean and Median values for Non-Dimensional Power (a), and its phase (b) respectively at different spanwise positions over 15 cycles from CFD data. Bars represent the standard deviation away from the mean.

The non-dimensional power was also calculated over 15 cycles as seen in Figure 3.18, with the non-dimensional power $P^* = T/(\rho c A U_\infty^2) \bar{P}$ where \bar{P} is the mean aerodynamic power. The power stabilises around 3 chords inboard but sees an increase in the magnitude of the negative power from the tip to 2.5 chords in. The minimum power dominates over the positive power because the velocity and load are not in phase, leading to positive damping in this case. The integrated power over the blade is negative for this case, and for a free vibration case, the blade would probably be damped out. There is a phase shift in both the minimum and maximum power values over the cycle, which is likely due to the phase lag in the loads as seen from Figure 3.16, with the standard deviation in the phase becoming smaller further inboard as the hysteresis loops also become less wide.

3.2.4 Spanwise Development at 2.5 Hz

Figure 3.19 shows the vorticity field at 3 chords inboard and at the tip for a plunging airfoil at 2.5 Hz. Similar to what was seen at 5 Hz, von Karman-like vortices are shed at the 3 chord position but not at the tip. As mentioned earlier, the vortex is convected further in the wake due to the lower motion velocity and hence the higher effect of the freestream velocity. The flow also seems less chaotic and with a lower frequency, the flow is also much less unsteady.

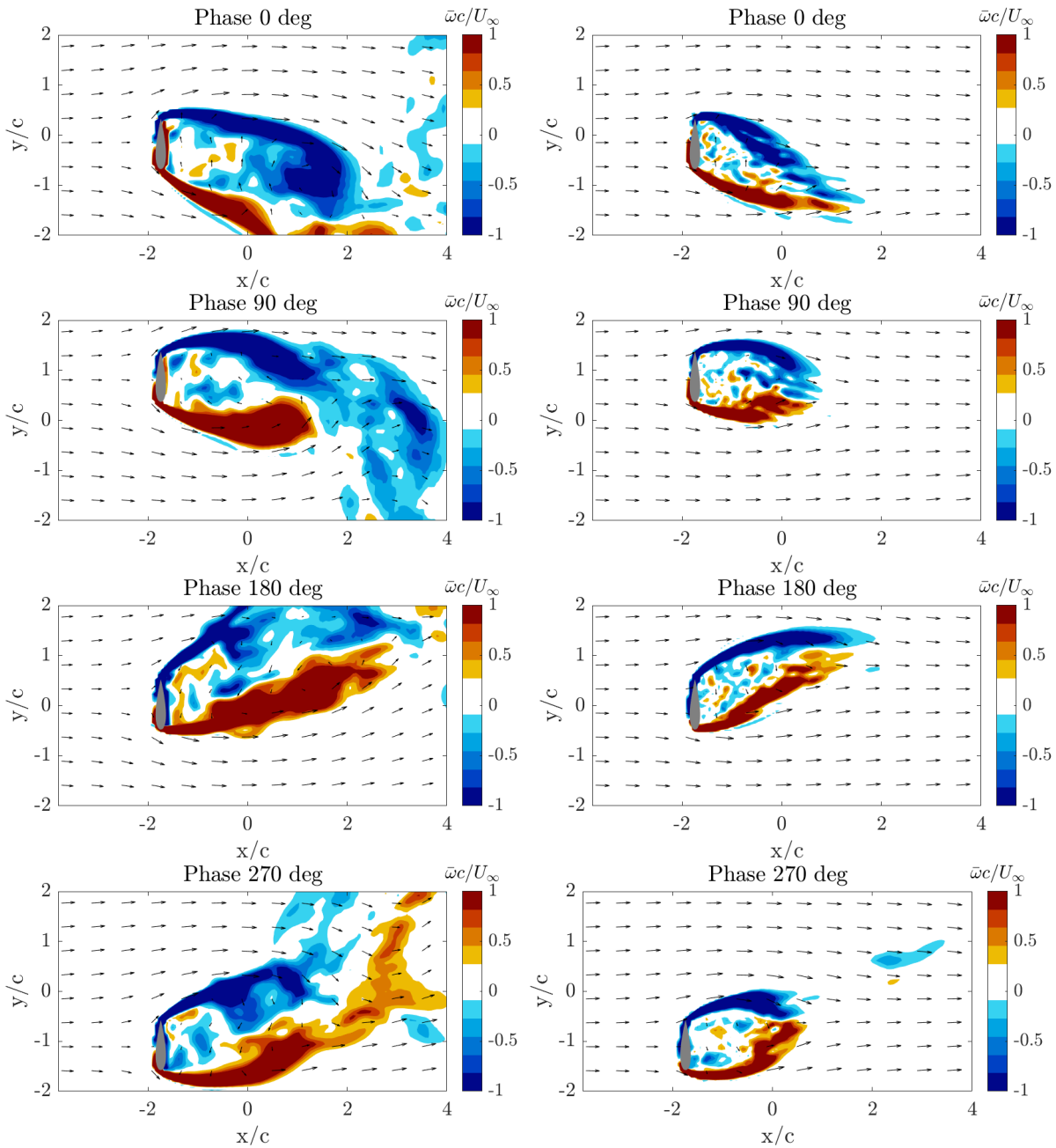


Figure 3.19: Vorticity, $\bar{\omega}c/U_\infty$ around a plunging airfoil at 2.5Hz, 3 chords inboard from the tip (left) and at the tip (right) with the freestream velocity coming from the left from CFD data.

Similar to the previous analysis, a time series plot of the cl and cd were plotted, as seen in Figure 3.20 and Figure 3.21 respectively. Similar to the case at 5 Hz, the cl presents as a smooth sinusoidal plot. The cd time series plot is much more chaotic than the cl , but a more regular pattern compared to the 5 Hz case is visible. The flow fields in Figure 3.19 already indicate this because the shed vortices are somewhat smoother and there is less difference between the vortex leaving the leading and trailing edge. In all

cases, the values of the forces at the very tip do not show any pattern, and the magnitude is negligible.

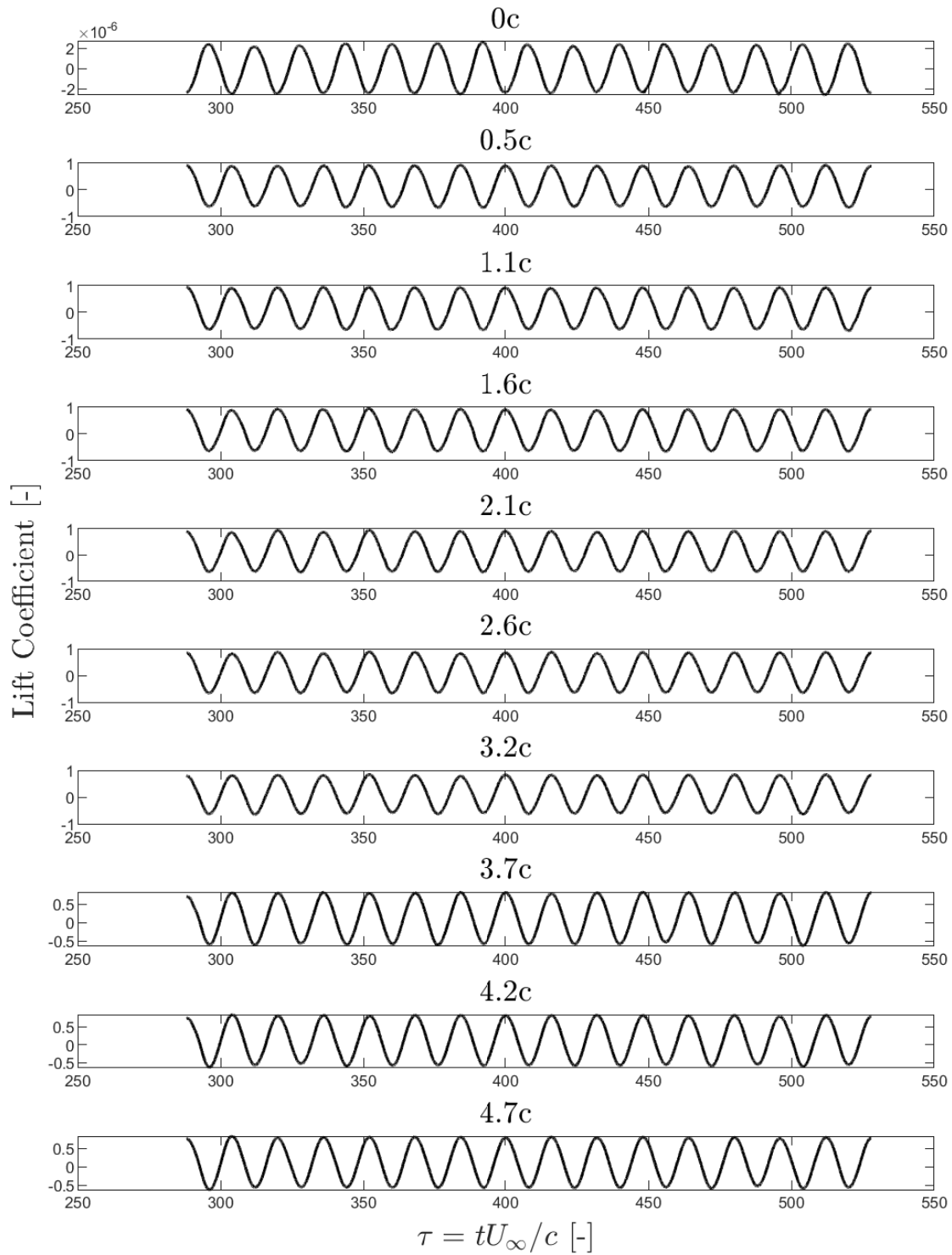


Figure 3.20: Time series of the cl at various spanwise positions from the tip to mid-span for a plunging airfoil at 2.5 Hz, 1 chord amplitude for 15 cycles from CFD data.

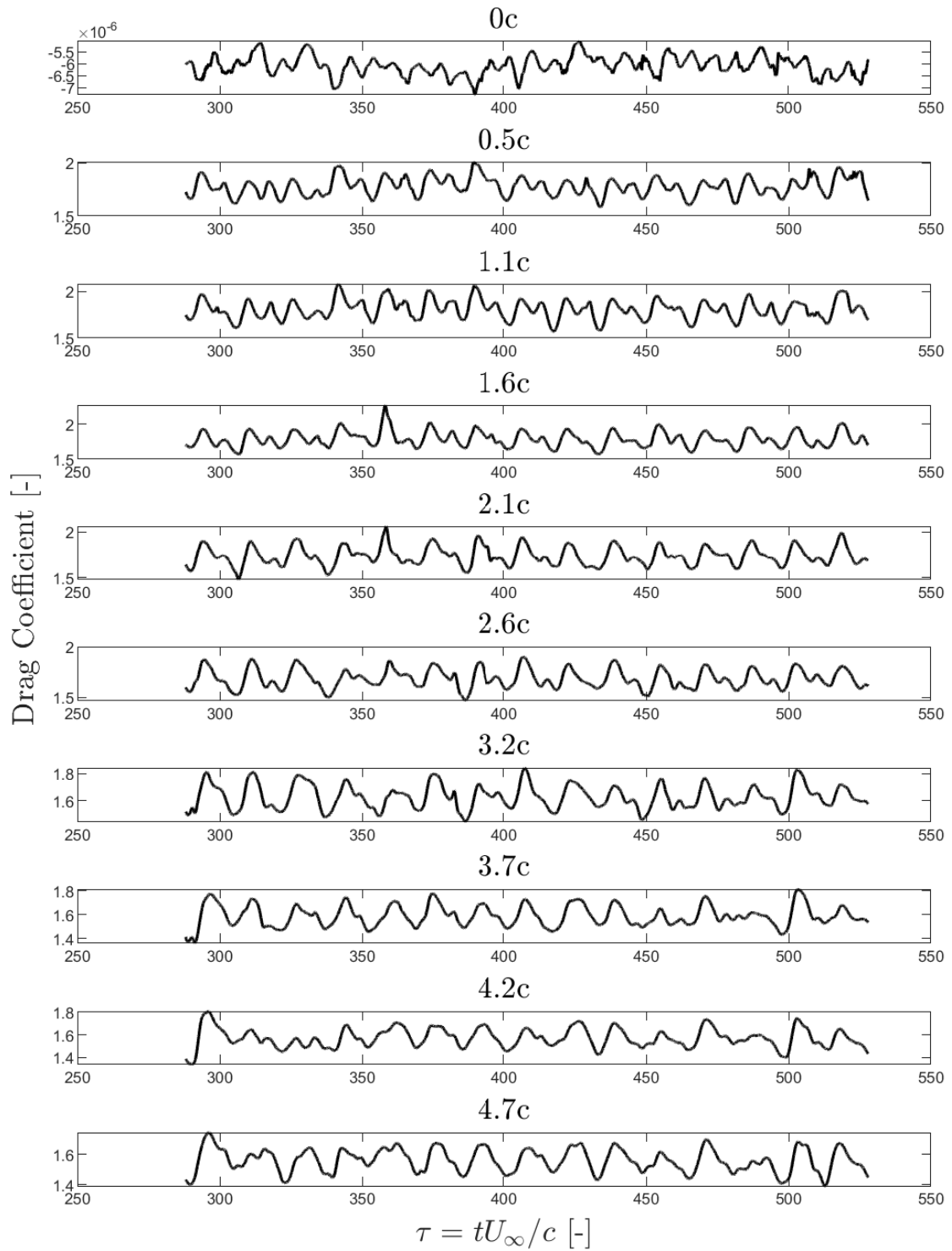


Figure 3.21: Time series of the cd at various spanwise positions from the tip to mid-span for a plunging airfoil at 2.5 Hz, 1 chord amplitude for 15 cycles from CFD data.

From the time series plots, a PSD analysis was performed on the cd at various spanwise

positions and is presented in Figure 3.22. The analysis shows that at all the measured spanwise positions, the blade appears to be locked in with a peak at the motion frequency and its harmonics. There seems to be very little variation between the different spanwise positions.

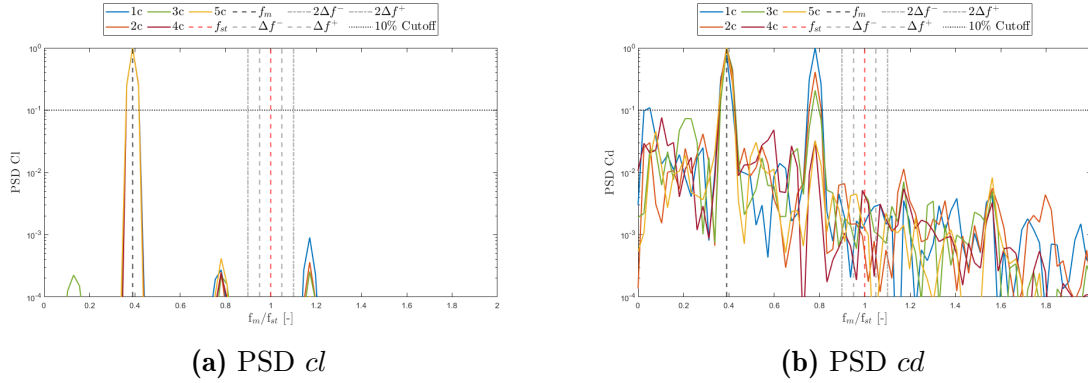


Figure 3.22: PSD of cl (left) and cd (right) for a plunging blade at $2.5 \text{ Hz} \sim 0.39 f_{st}$, 1 chord motion amplitude at various spanwise positions from CFD results.

Figure 3.22a shows a clean PSD of the cl which shows all the spanwise positions in lock-in. This was seen earlier for 5 Hz as well, which is once again surprising since the flow fields show less strong vortices shed close to the tip. The PSD of the cd in Figure 3.22b on the other hand is very chaotic, with many smaller peaks, though at much lower energy levels. A clear dominant peak occurs at twice the motion frequency which is due to the shedding of two vortices per cycle. It is interesting to see that the magnitude of the energy in the peak decreases further inboard from the tip. To further analyse the loads and the spanwise convection of the tip vortex, a hysteresis loop of the cl and cd was plotted.

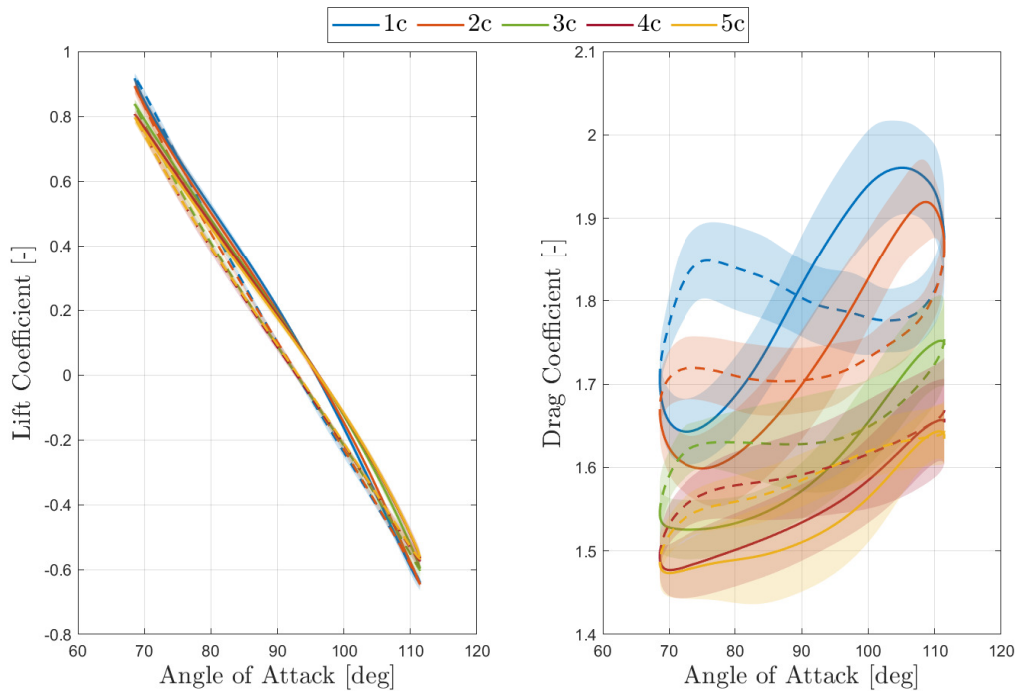


Figure 3.23: Hysteresis loops of the cl (left) and cd (right) against the angle of attack at different spanwise positions inboard from the tip for a plunging blade at 2.5 Hz frequency, 1 chord amplitude. Measured in chords away from the tip. The solid line shows the mean load as the blade moves upwards, the dashed line shows the mean load as the blade moves downwards and the surrounding translucent region is the standard deviation over 15 cycles from CFD data. Both loops rotate clockwise.

Hysteresis loops of the mean cl and cd and their standard deviation over 15 cycles were plotted against the angle of attack, and they are much smoother than those at 5 Hz, as seen in Figure 3.23. The $cl - \alpha$ curve is extremely smooth across all spanwise positions, suggesting that once again, this case resembles lock-in. The negligible standard deviation suggests that the flow is quasi-steady. This is also seen from Figure 3.20 where the time series is extremely smooth with little to no visual difference across the spanwise positions, leading to smooth $cl - \alpha$ loops that overlap one another. It can also be seen that as we move further inboard from the tip, the $cl - \alpha$ loop becomes slightly less steep, indicative of a smaller amplitude as seen in Figure 3.15, though the difference is marginal. The clockwise rotation indicates a phase lead, though the width of the loop is smaller than that at 5 Hz, suggesting an almost negligible phase difference.

The $cd - \alpha$ hysteresis loop once again forms a figure 8 as it crosses over itself. As previously mentioned, this is because the two vortices shed per cycle causing two peaks in the cd per cycle. The curves also shift further downward, i.e. have a lower cd further inboard from the tip which was seen in the peak at twice the motion frequency in Figure 3.22b, and the loops as well as their standard deviations become smaller. The difference in how much each loop shifts downwards decreases further inboard, with the 4c and 5c loops almost overlapping. This was also seen in Figure 3.22b where the peak at

twice the motion frequency reduced further inboard, and the peaks at 4c and 5c inboard almost overlapped. Once again referring to Figure 3.9 and Figure 3.5, the spanwise convection of the tip vortex lasts till around 2.5 chords inboard, which is seen by how the drag force becomes smaller further inboard since the effect of the tip vortex decreases. This analysis further confirms the earlier hypothesis that the spanwise convection of the tip vortex is not dependent on the oscillation frequency, since the same pattern was seen at both 5 Hz and 2.5 Hz for the plunging blade. The $cd - \alpha$ slope angle is more pronounced than at 5 Hz, and with a clockwise rotating loop, there is a phase lead. The width of the loops gets smaller further inboard, suggesting that the phase difference over the loop decreases further inboard.

To further validate the earlier hypothesis that the spanwise vortex convection is independent of the motion frequency, the forces, and their phase were analysed.

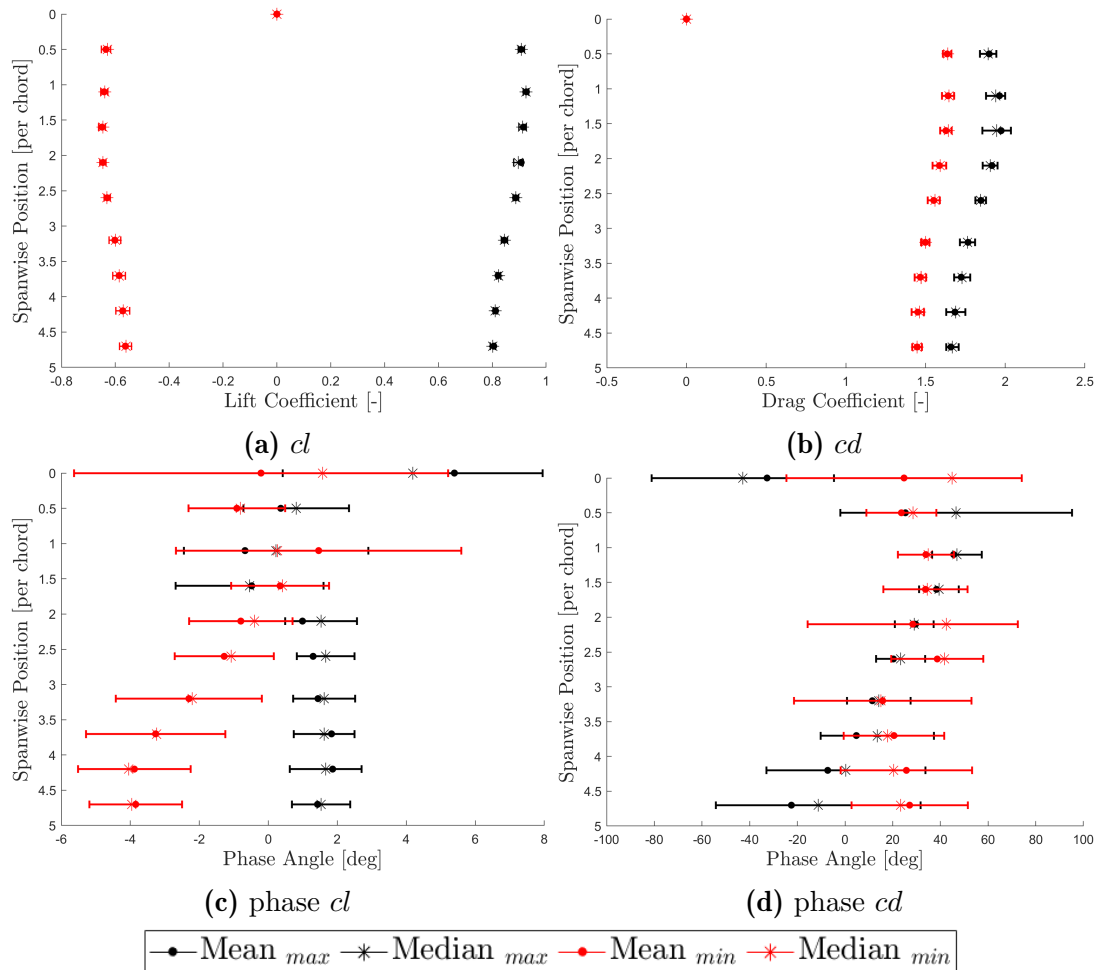


Figure 3.24: Plunging airfoil at 2.5 Hz, 1 chord amplitude. Mean and Median values for cl (a), cd (b), and their phases (c) and (d) respectively at different spanwise positions over 15 cycles from CFD data. Bars represent the standard deviation away from the mean.

The mean, median, and standard deviation plots of the cl , cd and their phase over the blade span were plotted, as seen in Figure 3.24. As seen in the hysteresis loops earlier, major unsteadiness is not observed, however, the plot does show minor fluctuations in the phase, which seem to stabilise by 3 chords inboard, as the standard deviation decreases and the mean phase angle varies less. This is in line with all the results seen earlier, confirming that the spanwise tip vortex convection is indeed independent of the motion frequency, and constant for a given blade aspect ratio. This would of course need to be further investigated over a range of blade aspect ratios to validate the theory. Once again, the same plots were also made for the power, and the power and phase resembled the cl plots almost exactly, once again suggesting that the velocity and force are in phase.

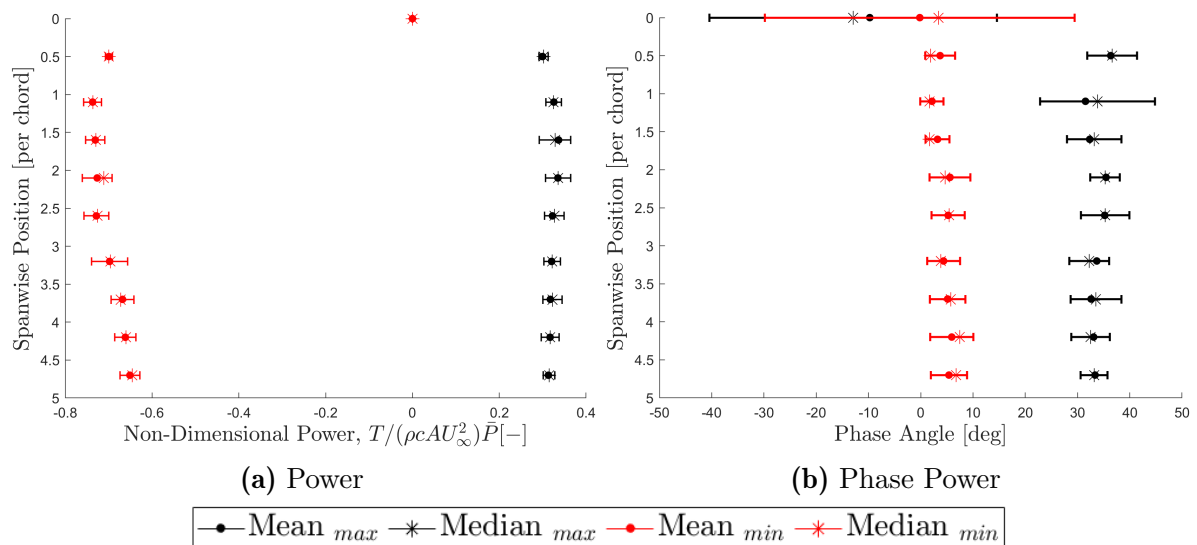


Figure 3.25: Plunging airfoil at 2.5 Hz, 1 chord amplitude. Mean and Median values for Non-Dimensional Power (a), and its phase (b) respectively at different spanwise positions over 15 cycles from CFD data. Bars represent the standard deviation away from the mean.

The variation in the magnitude of the power and phase is minimal overall spanwise positions seen in Figure 3.25. The magnitude of the cl and cd for the 2.5 Hz plunging blade are around half the magnitude of the loads at 5 Hz, but the power at 2.5 Hz is about four times smaller. Once again, the magnitude of the negative power is larger than the positive power, indicating that the integrated blade power will be negative for this frequency-amplitude combination and would probably damp out in the case of a free vibrating blade. The standard deviation in the phase is much smaller than what was seen at 5 Hz, and this is likely because of the smaller phase difference in the loads in Figure 3.23 with the loops having a smaller width. The phase at which the minimum power occurs for the 2.5 Hz plunging blade is around 5 deg and the phase at which the maximum power occurs is around 35 deg as compared to around 0 deg and 50 deg respectively at 5 Hz from 3 chords inboard. This phase difference at which the minimum and maximum powers are observed could be because of the rotation of the loop, where the

clockwise rotation for the 2.5Hz plunging blade leads to a phase lead, causing the phases between the minimum and maximum to be closer together and the counter-clockwise rotation at 5 Hz results in a phase lag causing the phases at which the minimum and maximum power occur to be further away.

Compared to the plunging blade at 5 Hz, the loads are much smoother at 2.5 Hz since the flow is less unsteady. This is reflected in a smoother sinusoidal pattern in the time series, cleaner peaks in the PSD, and a smoother hysteresis loop with a lower standard deviation. There is also less variation in the magnitude of the load coefficient, normalised power, and their phases across the spanwise positions.

3.3 Surging Blade

The same two frequencies of 2.5 Hz and 5 Hz were tested for a surging airfoil as well, so as to compare the flow and load for the ‘edgewise’ and ‘flapwise’ motions. A similar analysis of the motion frequency on the spanwise convection of the tip vortex and the growth of the shed vortex over the blade at these two frequencies was also performed.

3.3.1 Effect of Motion Frequency on the Shed Vortex

Figure 3.26 presents a comparison of the vorticity around a surging blade at 0 deg phase at two frequencies, 5 Hz and 2.5 Hz, for four spanwise positions: 3 chords inboard, 2 chords inboard 1 chord inboard, and the tip.

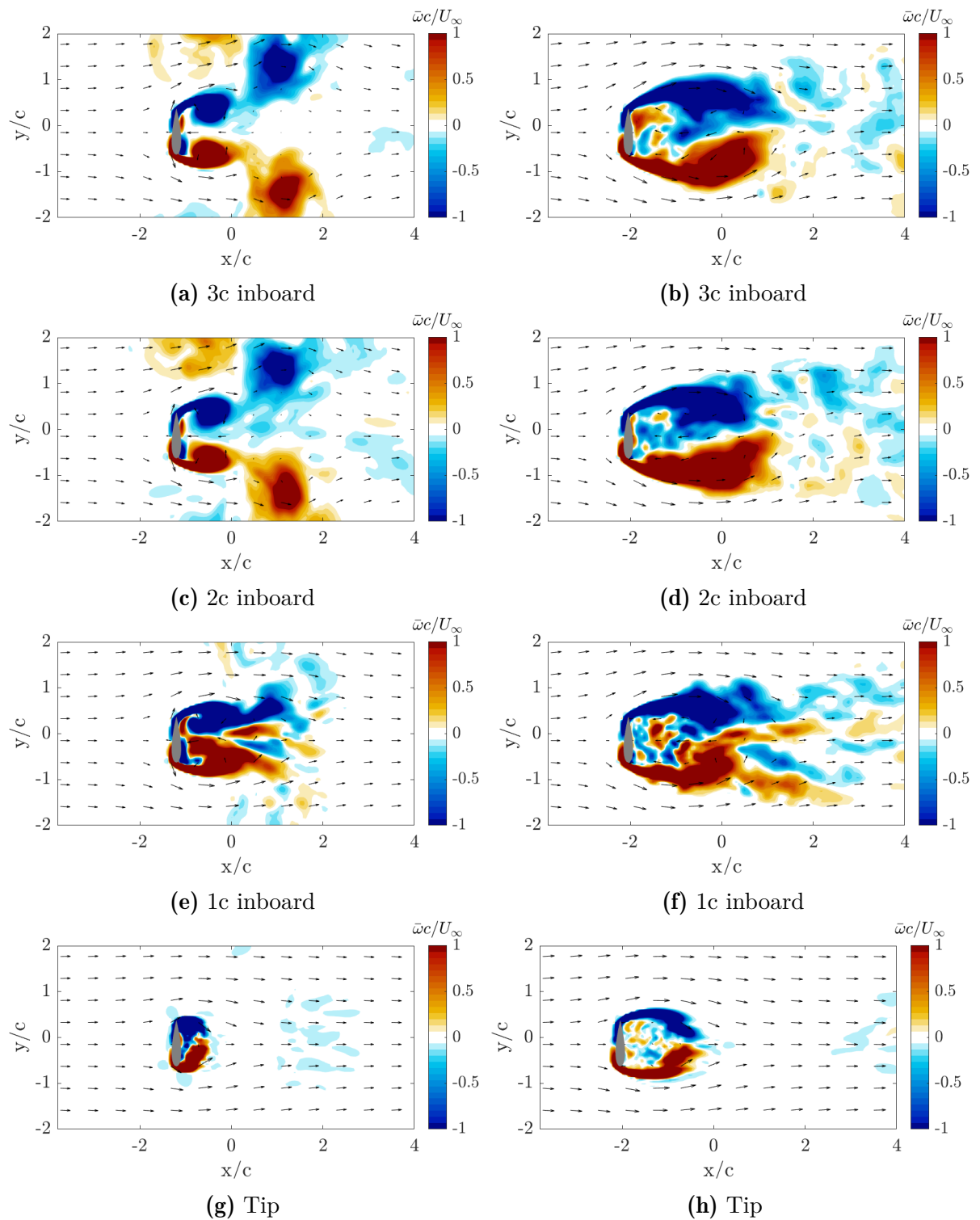


Figure 3.26: Vorticity, $\bar{\omega}c/U_\infty$ around a surging airfoil at 5Hz (left), and at 2.5Hz (right) from 3 chords inboard (top) to the tip (bottom) with the freestream velocity coming from the left from CFD data.

As seen earlier, at 2.5 Hz, the motion velocity is not large enough to force the shedding of von Karman-like vortex structures, and this is for all spanwise positions visualised in Figure 3.26. However, the strength of the shed vortex does increase further inboard from the tip and begins to look somewhat stable around 2 chords inboard, with minimal visual difference between the shedding 2 chords inboard and 3 chords inboard positions. This comparison also holds at 5 Hz, where the flow fields look very similar. These distinct shed vortices are not present at the tip or 1 chord inboard, but it becomes very clear 2 chords inboard. This suggests that around 2 chords inboard from the tip, the flow becomes relatively ‘2D’, which is in agreement with what was observed from the static blade as well as from the plunging blade.

Figure 3.27 shows the shed vortices at four phases: 0 deg, 90 deg, 180 deg, and 270 deg for two frequencies, 5 Hz and 2.5 Hz. Vorticity and other flow fields at all 12 phases for the surging blade at all available spanwise positions can be found in Appendix N for 2.5 Hz and in Appendix O for 5Hz for the CFD simulations and in Appendix J and Appendix K for the 2.5 Hz and 5 Hz PIV measurements respectively.

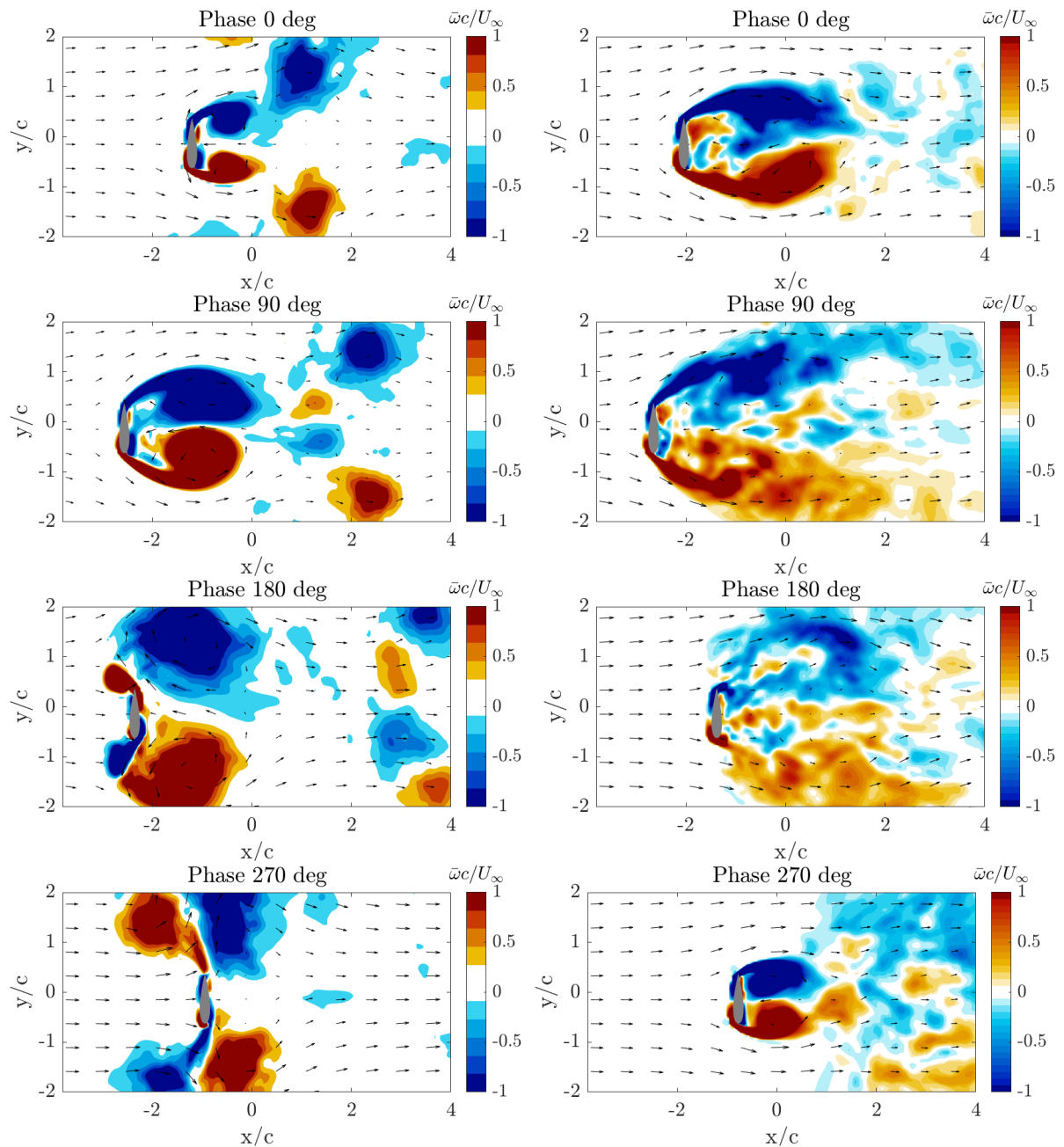


Figure 3.27: Vorticity, $\bar{\omega}c/U_\infty$ around a surging airfoil 3 chords inboard from the tip at 5 Hz (left) and 2.5 Hz (right) with the freestream velocity coming from the left from CFD data.

The flow around the airfoil in surging motion is significantly different than that of a plunging airfoil since it is moving in the direction of the freestream wind and hence the forcing on the flow is much larger. Figure 3.28 shows the flow experienced on the blade due to the surging motion. As can be seen, the maximum and minimum relative velocities are at 0 and 180 deg phase, where the airfoil is either at its maximum motion velocity pushing against the incoming wind at 0 deg or at its maximum velocity in the

direction of the wind at 180 deg and hence faces the lowest relative flow. The flow fields show that at 5 Hz, larger vortices are shed at 90 deg as compared to 270 deg because of the larger relative building up to 90 deg, which leads to a larger convection speed to carry the vortices away. Two vortex pairs are shed per cycle, one pair at 90 deg and the other at 270 deg when the blade is experiencing a change in the direction of its acceleration. This is also similar to the shed vortices seen for the plunging blade that released a vortex each half cycle during the change in acceleration, but since there is no change in the angle of attack and the blade motion is symmetric with respect to the freestream at all points during its cycle, it sheds a vortex from both the leading and trailing edge each half cycle. Clear vortices are shed because $V_{m|max} \approx U_\infty$ at 5 Hz, with $V_{m|max} = 2.36\text{m/s}$, versus at 2.5 Hz where $V_{m|max} = 1.18\text{m/s}$ for 1 chord oscillation amplitude. With $U_\infty = 3\text{m/s}$, the freestream velocity dominates over the motion frequency at 2.5 Hz, and hence no distinct von Karman-like vortex structures are shed. The vorticity is still the strongest and most concentrated at 0 deg phase where V_{rel} is maximum, and smallest at 180 deg where V_{rel} is minimum, but the motion frequency is not high enough to shed distinct vortex structures. Since there is no real angle of attack with respect to the incoming flow, the streamwise and vertical force coefficients were analysed.

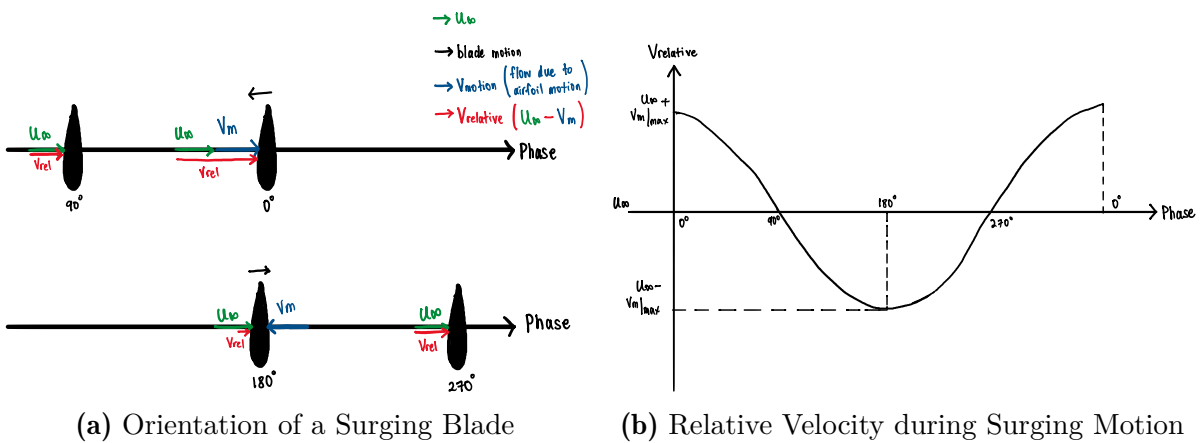


Figure 3.28: Flow on a Surging Blade over one cycle. $U_\infty > V_{m|max}$

3.3.2 Spanwise Development at 5 Hz

Figure 3.29 shows the shed vortices at four phases: 0 deg, 90 deg, 180 deg, and 270 deg for two spanwise positions, 3 chords inboard and the tip at 5 Hz.

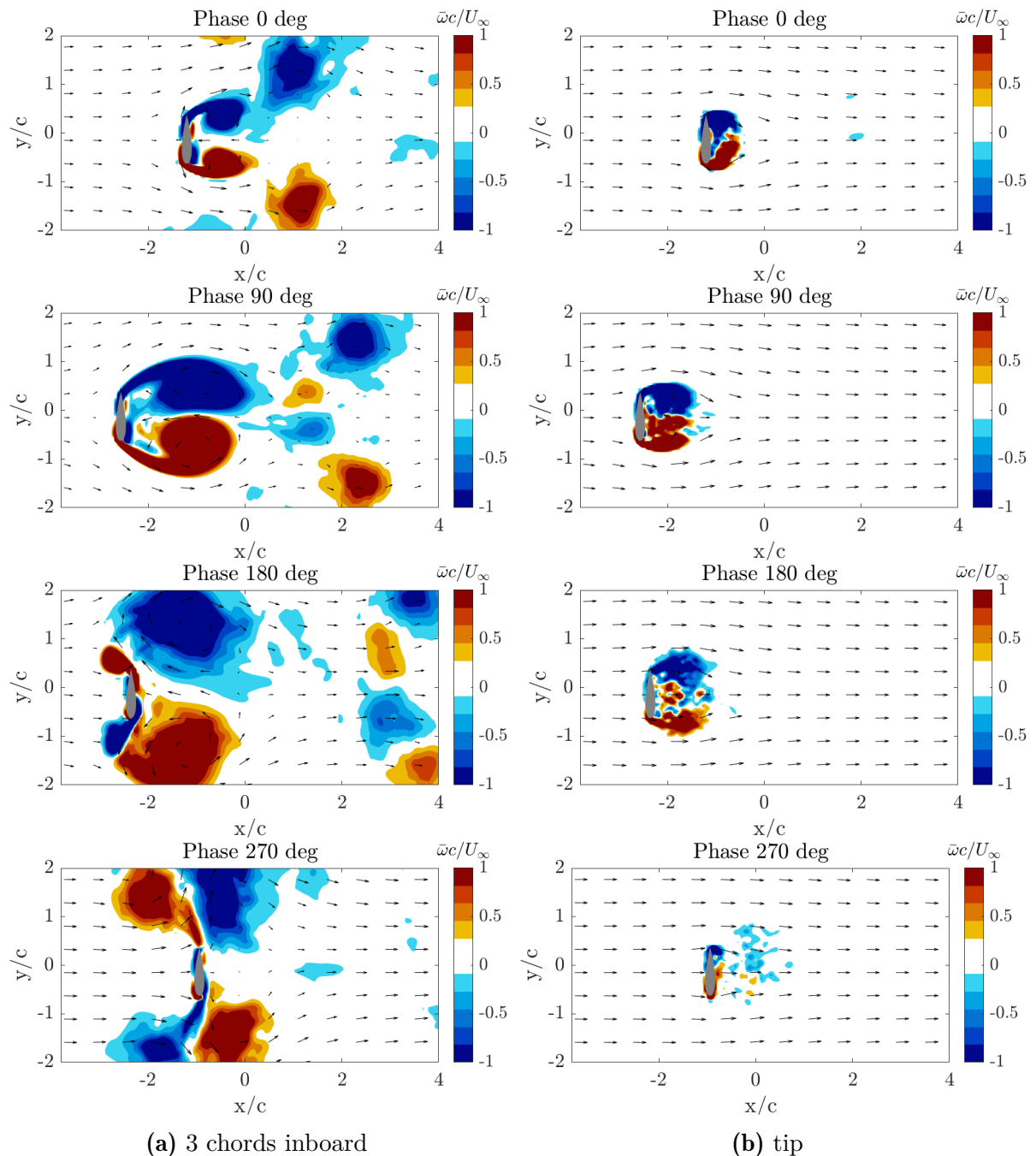


Figure 3.29: Vorticity, $\bar{\omega}c/U_\infty$ around a surging airfoil at 5Hz, 3 chords inboard from the tip (left) and at the tip (right) with the freestream velocity coming from the left from CFD data.

Similar to the static blade and plunging blade, the vorticity shed 3 chords inboard of the tip is much stronger than the vorticity shed at the tip. 3 chords inboard, von Karman-like vortices are observed, with a pair of counter-rotating vortices shed every half cycle, whereas, at the tip, there is no distinct vortex structure. As seen earlier, the

distinct vortex structures were visible 2 chords inboard, but to quantify the spanwise convection of the tip vortex, the time series of the streamwise force coefficient c_x and vertical force coefficient c_y were analysed.

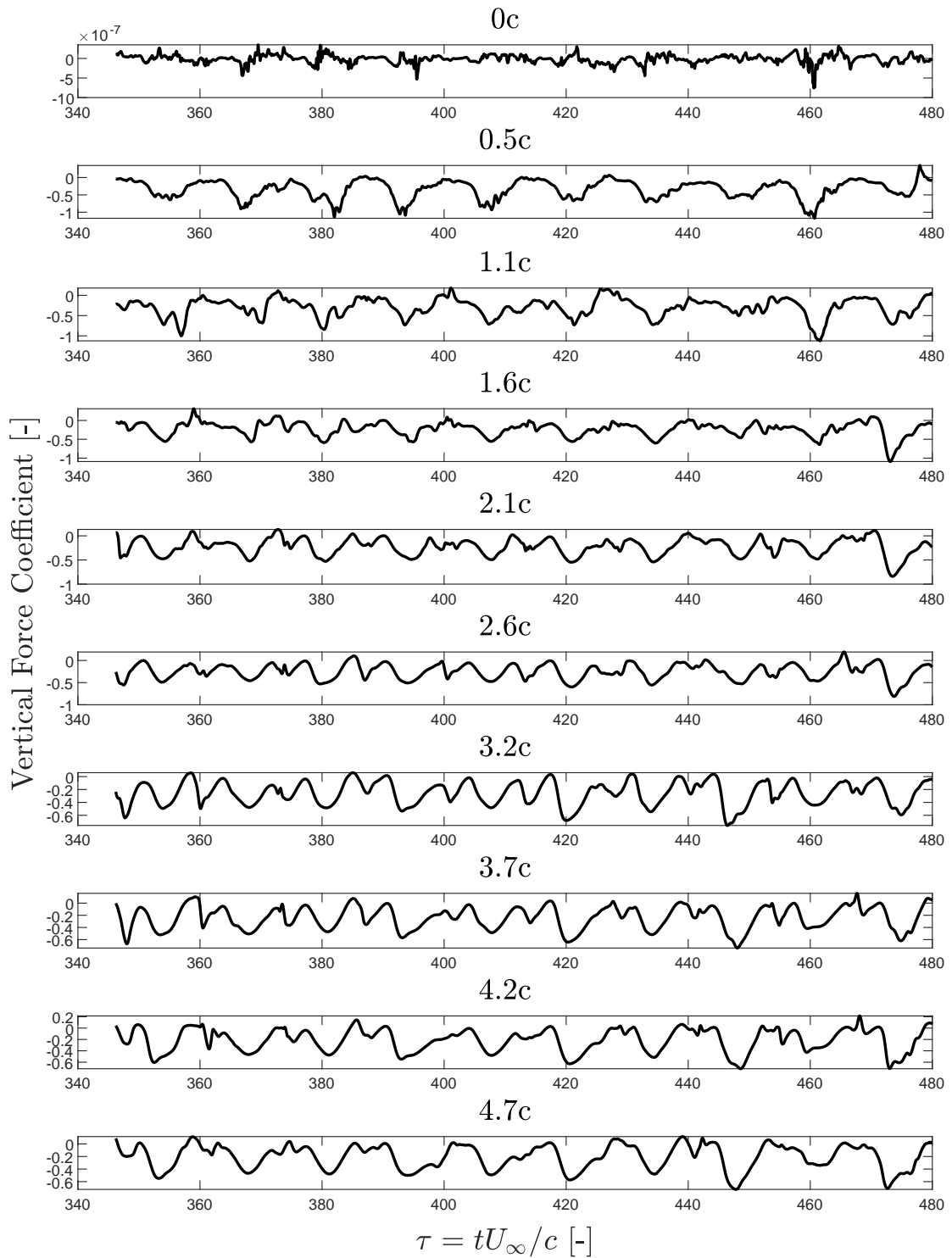


Figure 3.30: Time series of the c_y at various spanwise positions from the tip to mid-span for a surging airfoil at 5 Hz, 1 chord amplitude for 10 cycles from CFD data.

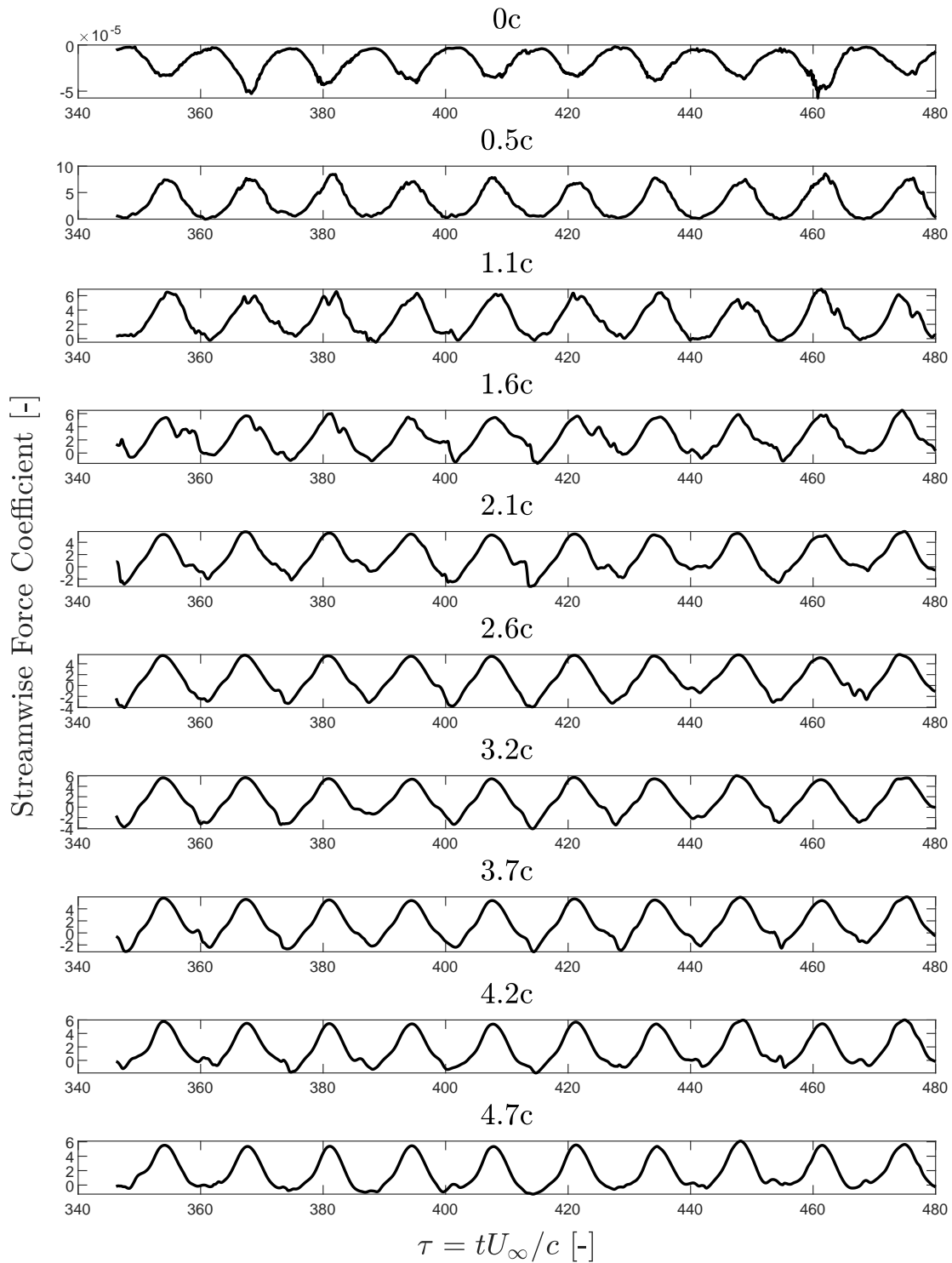


Figure 3.31: Time series of the c_x at various spanwise positions from the tip to mid-span for a surging airfoil at 5 Hz, 1 chord amplitude for 10 cycles from CFD data.

Looking at the flow around the blade in Figure 3.28, the maximum streamwise

force occurs at 0 deg phase, where the blade experiences the largest relative inflow. Furthermore, at this point in the cycle, the blade also has the largest added mass effect since it is pushing directly against the incoming flow. The cx time series plot shows distinct peaks and troughs, with the maximum occurring at 0 deg phase and the minimum occurring at 180 deg phase. Figure 3.32 shows the streamwise flow around the blade at the four phases. At 180 deg, it is clear that there is a large flow in the direction opposite the freestream just downwind of the blade and an almost equal magnitude component upwind of the blade as well. The cx calculated on the blade is the integrated force at that spanwise blade element and hence, the effect of the relative flow results in the smallest force at this point. The cy time series does not show much of a pattern and is chaotic even further inboard, since there is no actual angle of attack relative to the incoming flow, the airfoil remains as a bluff body against at 90 deg throughout the cycle.

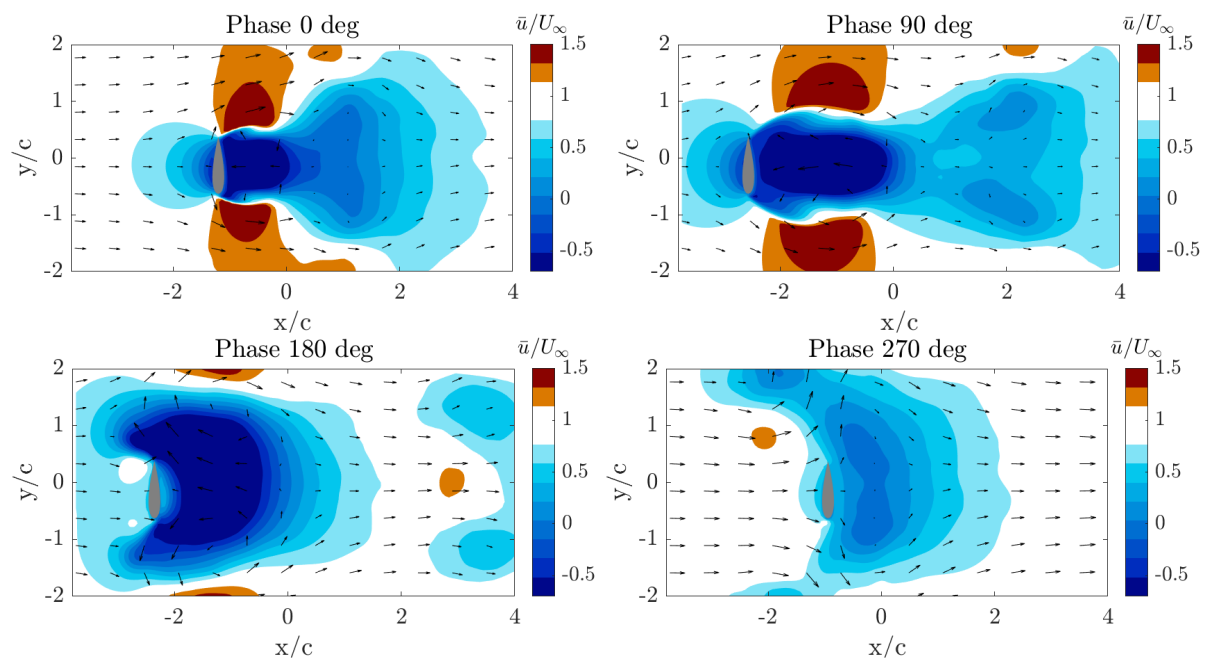


Figure 3.32: Streamwise velocity, \bar{u}/U_∞ around a surging airfoil at 5Hz, 3 chords inboard from the tip with the freestream velocity coming from the left from CFD data.

Figure 3.33 presents a PSD analysis of the streamwise force coefficient cx and vertical force coefficient cy at four different spanwise positions, 1 chord, 2 chords, 3 chords, 4 chords, and 5 chords inboard from the tip, and confirms that both 5 Hz surging blade is locked in, with a peak at the motion frequency and its harmonics, as defined by Hu et al. [2021], Choi et al. [2015].

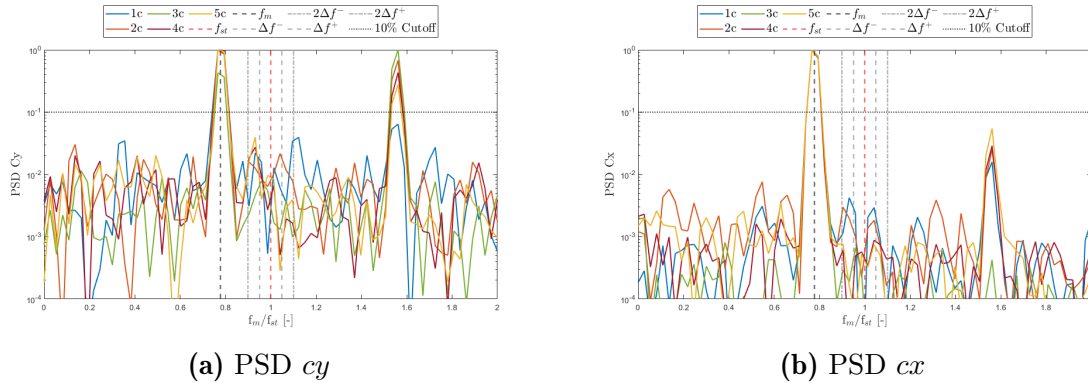


Figure 3.33: PSD of c_y (left) and c_x (right) for a surging blade at 5 Hz $\sim 0.78f_{st}$, 1 chord motion amplitude at various spanwise positions from CFD results.

Figure 3.33b clearly shows that the 5 Hz surging blade is locked in across all the spanwise positions plotted. It also shows peaks at harmonics of the motion frequency, and is somewhat chaotic with peaks around f_{st} , though their energy is less than 1% of the dominant peak and hence, they are not significant. The peak at the second harmonic seems to increase in energy as the spanwise position moves further inboard from the tip. Figure 3.33a on the other hand is much more chaotic and shows a large secondary peak at twice the shedding frequency. This is most likely because there are two vortex pairs shed per cycle as seen in Figure 3.29 and the blade passes through these large vortices, causing a large peak only in c_y that is not just a peak due to the harmonic. It is interesting to note that at 3 chords inboard, the energy of the first peak is the lowest, but the energy of the second peak is the highest. The energy of the second peak at 1 chord inboard is significantly lower than the other spanwise positions.

To further analyse the loads, hysteresis loops of the streamwise and vertical force coefficient were plotted as seen in Figure 3.34.

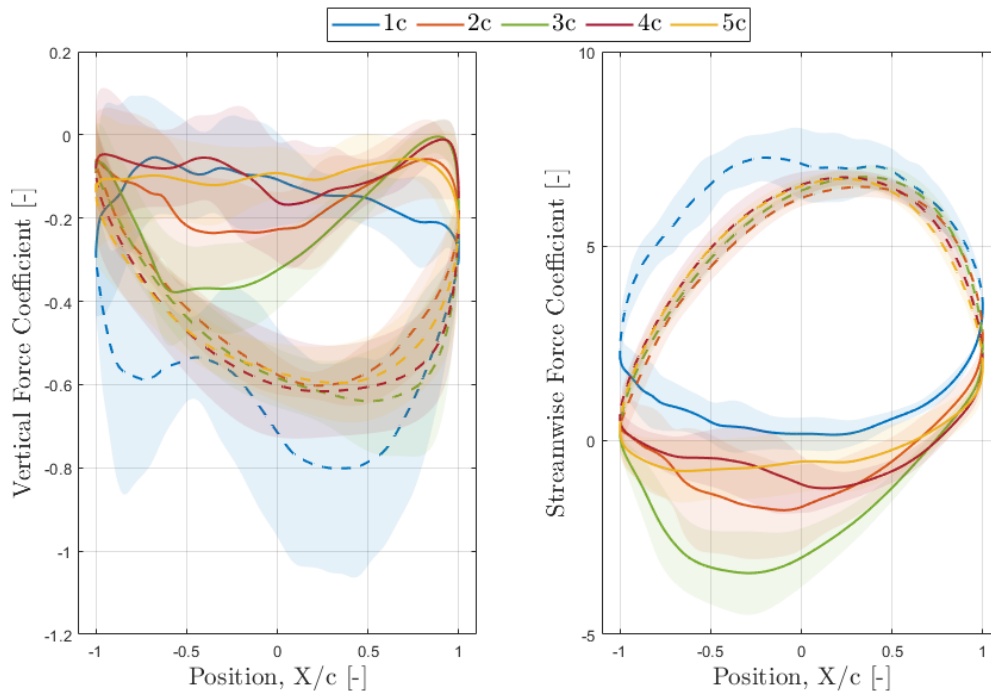


Figure 3.34: Hysteresis loops of the c_y (left) and c_x (right) against the normalised blade position at different spanwise positions inboard from the tip for a surging blade at 5 Hz frequency, 1 chord amplitude. Measured in chords away from the tip. The solid line shows the mean load when the blade moves against the freestream, the dashed line shows the mean load when the blade moves in line with the freestream and the surrounding translucent region is the standard deviation over 10 cycles from CFD data. Both loops rotate clockwise.

The solid lines represent the motion from phase 270 deg to phase 90 deg in Figure 3.28 where the blade moves against the freestream. The dashed lines represent the motion from 90 deg to 270 deg phase where the blade moves in the direction of the freestream.

Hysteresis loops of the mean c_x and c_y and their standard deviation over 10 cycles were plotted against the normalised blade position X/c as seen in Figure 3.34. Choi et al. [2015] presents a definition for lock-in for a surging blade having a smooth hysteresis loop for the force against the motion rather than the angle of attack, which is analysed here. Both the $c_x - X/c$ and $c_y - X/c$ curves form large hysteresis loops, though the c_x loop is much smoother. In both plots, the loop at the 1 chord inboard position does not follow the same pattern as the rest and is not as smooth. From 2 chords inwards, the loops seem to follow a similar shape suggesting that the flow around the blade behaves ‘2D’. In the $c_y - X/c$ curve, the loop seems to get larger and with less variation further inboard, and the extremely low value at 1 chord is reflected in Figure 3.33a, whereas, in the $c_x - X/c$ curve, the loops get smaller further inboard, not counting the loop at 1 chord. The solid line portion of both plots is less smooth than the dashed lines, which is expected since the blade motion is opposing the freestream wind, causing larger unsteadiness. At 1 chord inboard, the c_x loop is always positive, as compared to the

other spanwise positions where the solid line portion as the blade moves against the freestream is negative and the dashed line portion where the blade moves in the direction of the wind is positive. This is also seen from the vortex shedding pattern presented in Figure 3.27 that compares the spanwise shedding from the tip to 3 chords inboard. At 1 chord inboard in Figure 3.26e, the vorticity behind the blade is spread out and there is no distinct vortex blob being shed behind the blade. At 2 and 3 chords inboard, however, there are distinct vortices shed from both the leading and trailing edge of the blade, which causes the induced velocity on the blade to change, resulting in a negative streamwise force. Both loops rotate clockwise indicating a phase lead, but with a very positive slope in the cx and a negative slope in the cy . The width of the loop is large, especially for cx , indicating a large phase difference over the loop. Figure 3.29 shows the vorticity around the surging blade, and at 3 chords inboard, the shed vortex blobs are significant. Over the cycle, it is clear that the shed vortices from the previous half cycle still remain within about 6 chords downwind and thus, may still have some effect on the induced velocity seen at the blade. Especially in the dashed line portion of the hysteresis loop where the blade moves from 90 deg back to 270 deg in the direction of the freestream wind, the blade interacts with the vortices shed from the previous half cycle, seen clearly at 180 deg phase when the blade moves into two very large vortex structures. It is around this portion in the hysteresis loop where the normalised position is 0 where the largest width is seen, and the largest deviation from the centre line, i.e. the largest phase difference is observed.

To analyse the effect of the tip vortex, the mean, median, and standard deviation of the force coefficients and their phases were plotted.

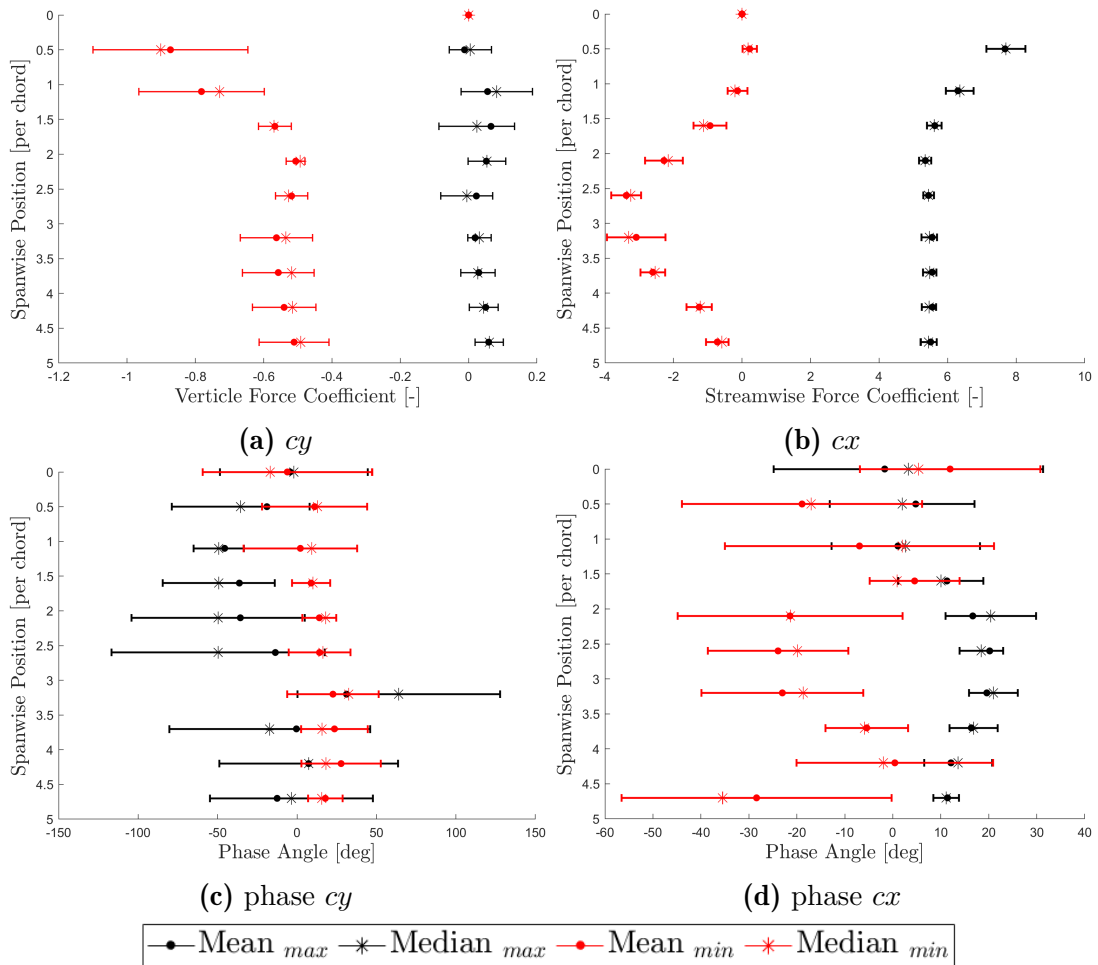


Figure 3.35: Surging airfoil at 5 Hz, 1 chord amplitude. Mean and Median values for c_y (a), c_x (b), and their phases (c) and (d) respectively at different spanwise positions over 10 cycles from CFD data. Bars represent the standard deviation away from the mean.

The mean, median, and standard deviation of the c_y (left) and c_x (right) as well as their phase for the time series data is presented in Figure 3.35. The minimum values in the c_x plot follow an interesting pattern that shows the largest force magnitude around 2.5 chords inboard. The standard deviation in the force coefficients is the largest near the tip, and the magnitude of c_y stays constant from around 2.5 chords inboard, but no other significant pattern is visible from the plots. The mean of the phase angles for c_y is relatively constant, though there is the exception of the phase for the max c_y at 3 chords. The standard deviation in the phase is rather large for c_y , which is in line with the rather chaotic time series. The large standard deviation in phase for the minimum c_x could be due to the small double peaks occurring at the troughs of the c_x time series, and this pattern was also seen in Figure 3.34 where the solid lines for the $c_x - X/c$ curve have a much larger variation than the dashed lines.

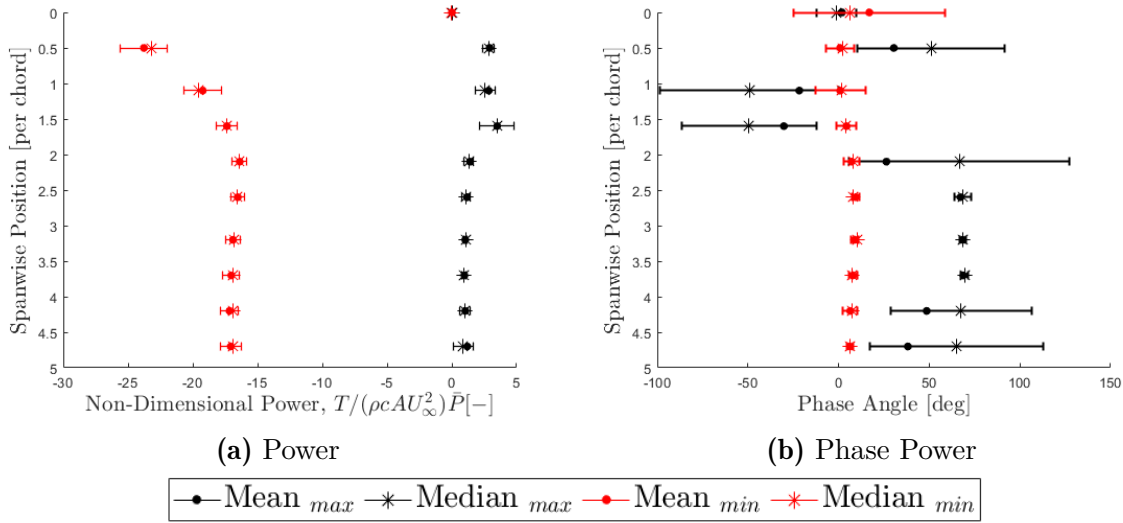


Figure 3.36: Surging blade at 5 Hz, 1 chord amplitude. Mean and Median values for Non-Dimensional Power (a), and its phase (b) respectively at different spanwise positions over 10 cycles from CFD data. Bars represent the standard deviation away from the mean.

Figure 3.36 shows the non-dimensional power for a surging blade at 5 Hz, 1 chord amplitude. The power values become constant with a low standard deviation around 2 chords inboard for the minimum power, and it is nearly constant at all spanwise positions for the maximum power, which is close to 1. The negative power is over 15 times larger than the positive power, and the integrated power is always negative for all the tested surging blades as seen later in Figure 3.49. This is due to the positive damping during the surging motion, which is also seen in wind turbine blades where the flapwise mode has high aerodynamic damping, which is why it is less prone to VIV. The largest (negative) power occurs at around 10 deg phase at all the spanwise positions. This could be a combination of the highest relative velocity faced at phase 0 deg as seen in Figure 3.28b combined with the largest negative streamwise force around that position in the cycle seen in Figure 3.34 and the phase lead from the loop rotation and slope. The phase angle where the highest positive power occurs would be when the velocity and load are in phase, which seems to vary greatly over the spanwise positions, and with a large standard deviation and hence, should be disregarded.

3.3.3 Spanwise Development at 2.5 Hz

At 2.5 Hz, the force exerted by the blade on the flow is not significant enough to cause the shedding of a von Karman-like vortex. However, as mentioned earlier, the shedding is stronger 3 chords inboard than at the tip.

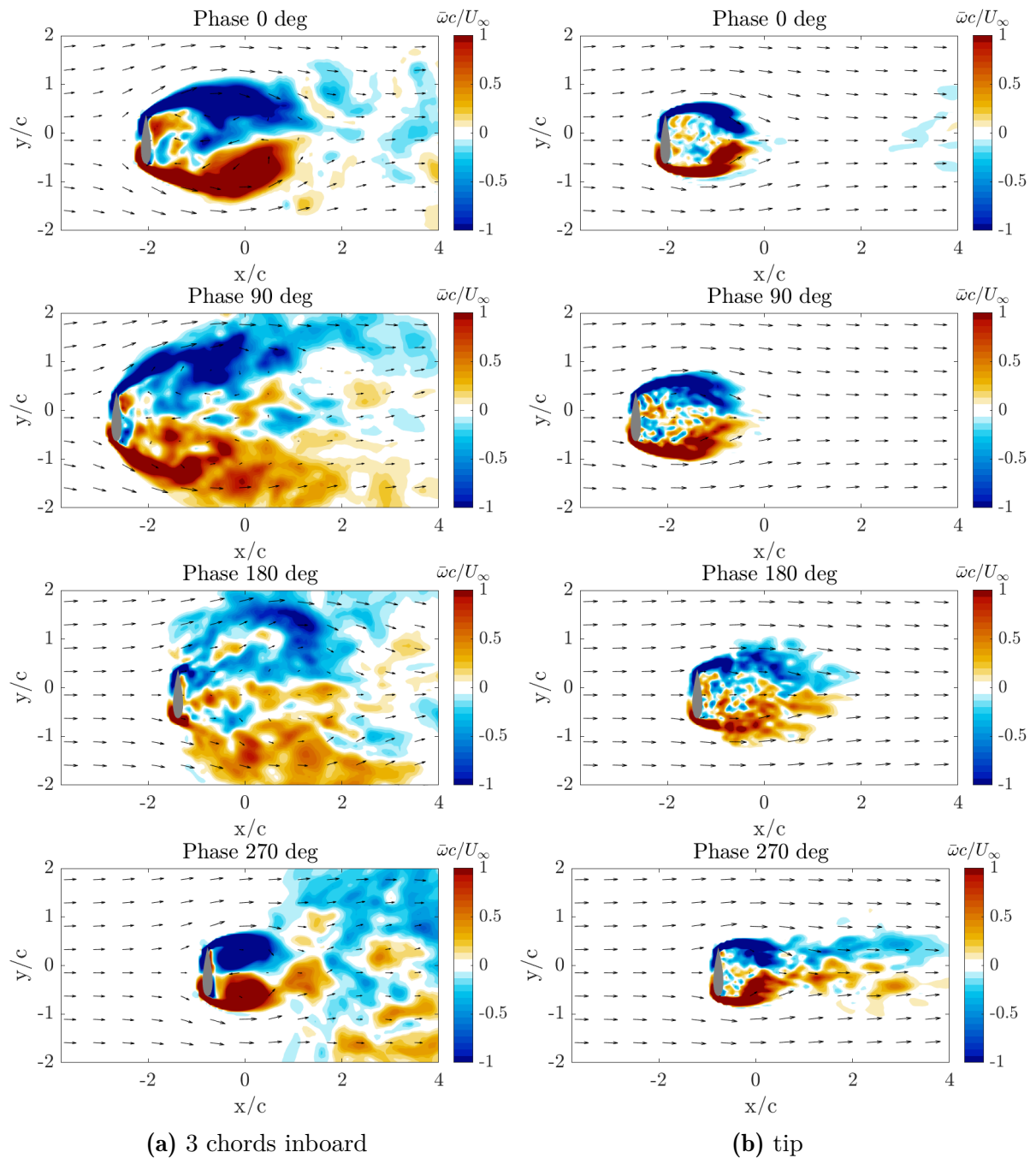


Figure 3.37: Vorticity, $\bar{\omega}c/U_\infty$ around a surging airfoil at 2.5Hz, 3 chords inboard from the tip (left) and at the tip (right) with the freestream velocity coming from the left from CFD data.

Figure 3.26 showed that the vorticity pattern stabilised around 2 chords inboard, but to quantify it, the time series and hysteresis loops were once again analysed.

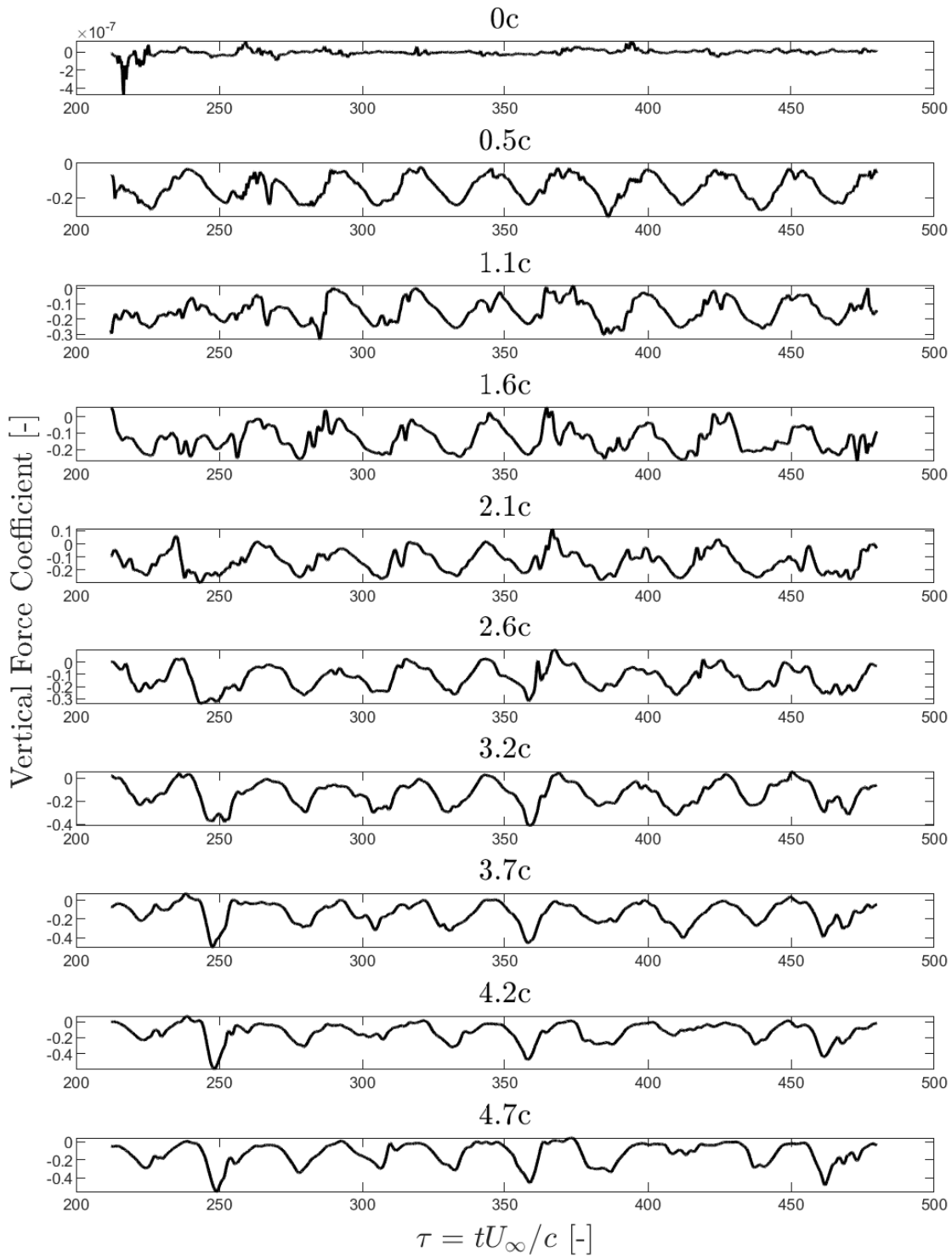


Figure 3.38: Time series of the c_y at various spanwise positions from the tip to mid-span for a surging airfoil at 2.5 Hz, 1 chord amplitude for 10 cycles from CFD data.

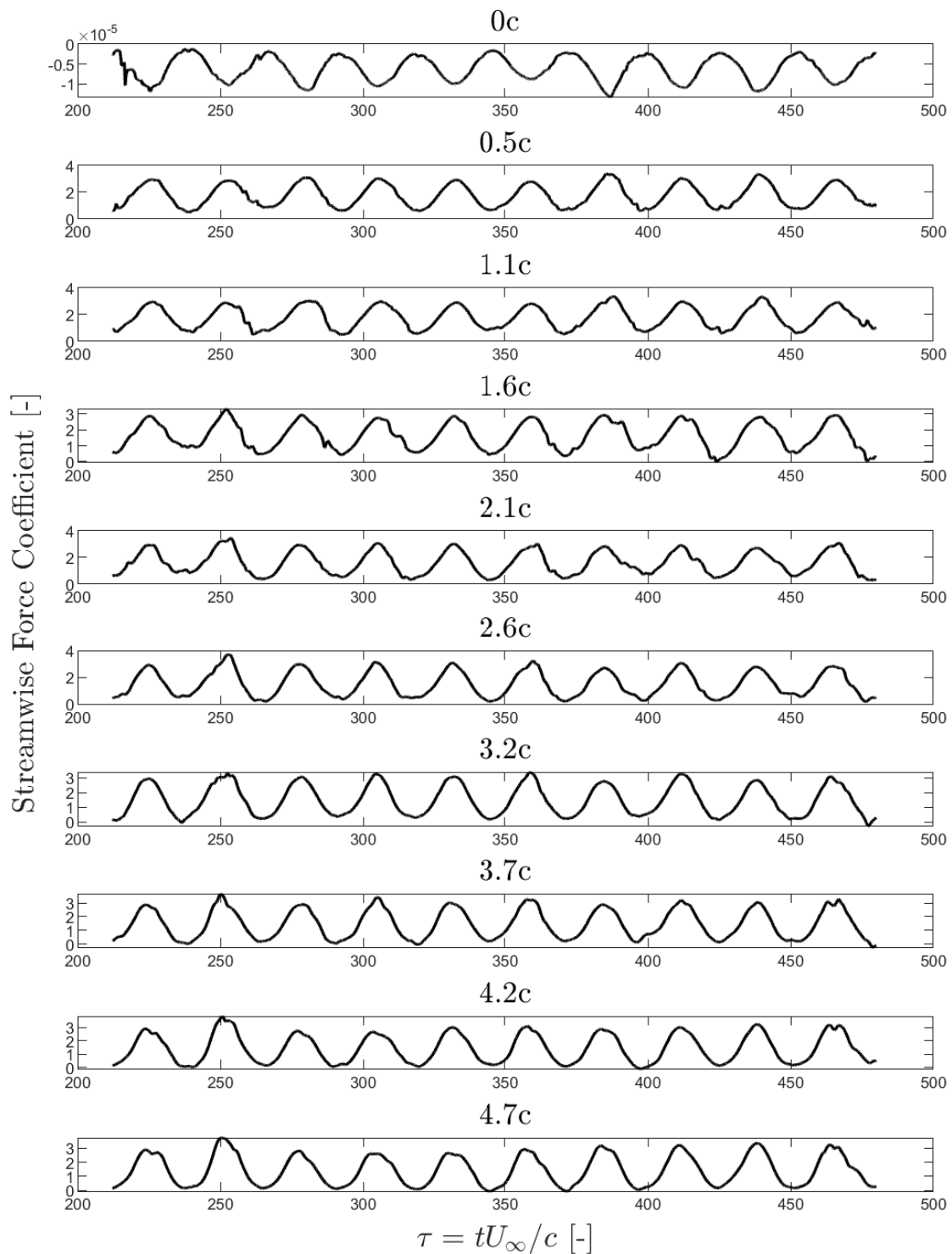


Figure 3.39: Time series of the c_x at various spanwise positions from the tip to mid-span for a surging airfoil at 2.5 Hz, 1 chord amplitude for 10 cycles from CFD data.

Unlike for the 5 Hz surging airfoil, there seems to be a stronger sinusoidal pattern for

the vertical force cy , though the peaks seem to plateau from around 3 chords inboard as compared to sharper peaks from 0.5 chords to 2 chords. The cx time series plot shows a similar pattern to the one seen for the 5 Hz surging blade, with sharp peaks but slightly more rounded troughs. A PSD analysis was performed on cx and cy over various spanwise positions, presented in Figure 3.40.

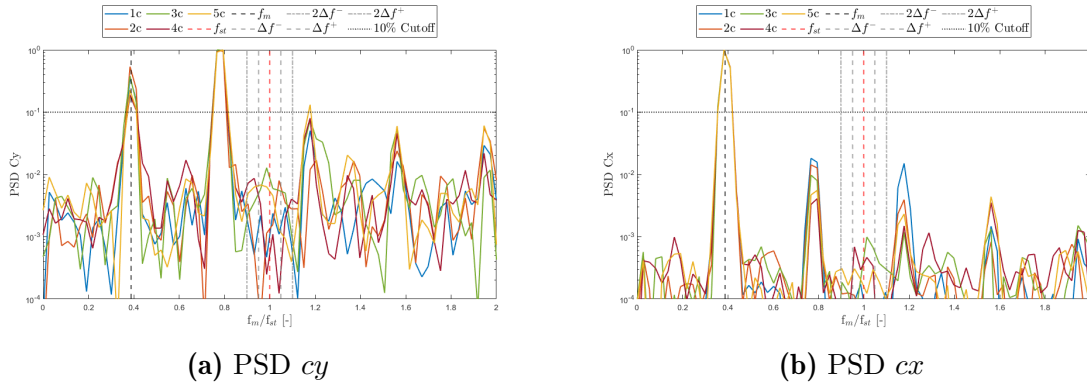


Figure 3.40: PSD of cy (left) and cx (right) for a surging blade at 2.5 Hz $\sim 0.39f_{st}$, 1 chord motion amplitude at various spanwise positions from CFD results.

The PSD seen in Figure 3.40b clearly shows that the surging blade at 2.5 Hz is locked in over all the spanwise positions. It also shows peaks at the motion frequency harmonics that slowly become less energetic as the harmonics get higher. There are once again some chaotic peaks near the shedding frequency, but similar to the previous cases, they are around 1% the energy of the dominating peak and hence, are not significant. The peak at the first harmonic shows that the energy decreases further inboard from the tip with the exception of the load at 5 chords being slightly larger than at 4 chords, though the difference is marginal. This pattern is also seen for the peak at the second harmonic. The PSD of cy in Figure 3.40a is once again much more chaotic, with the peak at twice the motion frequency being larger than the peak at the motion frequency. As seen in Figure 3.37 where the shed vorticity is not as strong as at 5 Hz, but the blade still sheds two vortex pairs per cycle. This could also be why the peak at the motion frequency is lower because the load from the shed vorticity is more dominant than from the motion since the motion frequency is lower than at 5 Hz. In the peak at the motion frequency, we see that the magnitude of the peak decreases further inboard whereas at the second harmonic, the energy increases further inboard.

Hysteresis loops of the forces against the normalised blade position are seen in Figure 3.41.

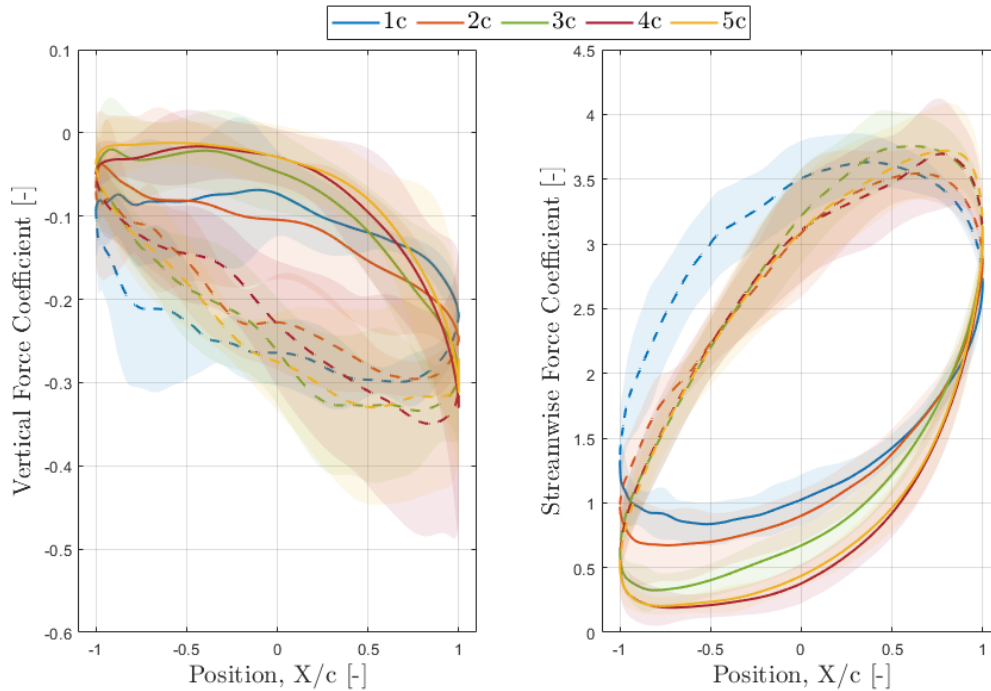


Figure 3.41: Hysteresis loops of the c_y (left) and c_x (right) against the normalised blade position at different spanwise positions inboard from the tip for a surging blade at 2.5 Hz frequency, 1 chord amplitude. Measured in chords away from the tip. The solid line shows the mean load when the blade moves against the freestream, the dashed line shows the mean load when the blade moves inline with the freestream and the surrounding translucent region is the standard deviation over 10 cycles from CFD data. Both loops rotate clockwise.

Both hysteresis loops in Figure 3.41 have a more oblong shape and are at an angle. With a clockwise rotation, both hysteresis loops have a small phase lead, though, with a smaller width than at 5 Hz, the phase difference across the cycles is smaller. Significant slope angles were not observed for the 5 Hz surging blade. The c_y loop moves upwards further inboard, but the loops at 3 chords, 4 chords, and 5 chords almost overlap each other, which was also seen in Figure 3.40a where the same pattern was observed from the peak at the second harmonic. The c_x loop at 1 chord inboard differs greatly from the others, which is seen in the second harmonic in Figure 3.40b, but in general, the loops tend to move downwards further inboard, which is observed in the first harmonic in Figure 3.40b, where the peaks decreased in energy further inboard. This difference can be explained using Figure 3.26 where the vorticity shed at 1 chord inboard is not as strong and large as the vorticity shed at 2 and 3 chords inboard. The difference at 2 and 3 chords is also minimal, with the shedding being marginally stronger at 3 chords, which is seen from the solid line portion of the loop moving further down further inboard. The solid line portion when the airfoil moves from 270 deg to 90 deg against the wind seen in Figure 3.27 shows the vorticity from the leading and trailing edge growing stronger and larger, thus having a greater effect on the induced velocity and hence a

larger difference in the load and phase, hence the larger width of the cx loop. Unlike at 5 Hz, the dashed line portion where the blade moves from 90 deg to 270 deg in line with the freestream wind, the shed vorticity from the previous half cycle is not very strong to the interaction of the blade with the shed vorticity is minimal, resulting in a smaller load and a smoother dashed portion of the cx loop. The dissipation of the vorticity seen at 180 deg in Figure 3.27 results in a larger unsteadiness in the vertical force, which is visible in the unsteady dashed portion of the cy loop. The magnitude of the forces at 2.5 Hz is also around half the magnitude of those observed at 5 Hz for the same oscillation amplitude of 1 chord. This is expected since the lower motion frequency results in a lower relative velocity and thus, a lower force. cx is always positive and cy is always negative suggesting that the motion velocity is not strong enough against the freestream to exert an opposing force. This was seen in the 5 Hz surging blade where the streamwise force in the portion of the cycle opposing the freestream became negative.

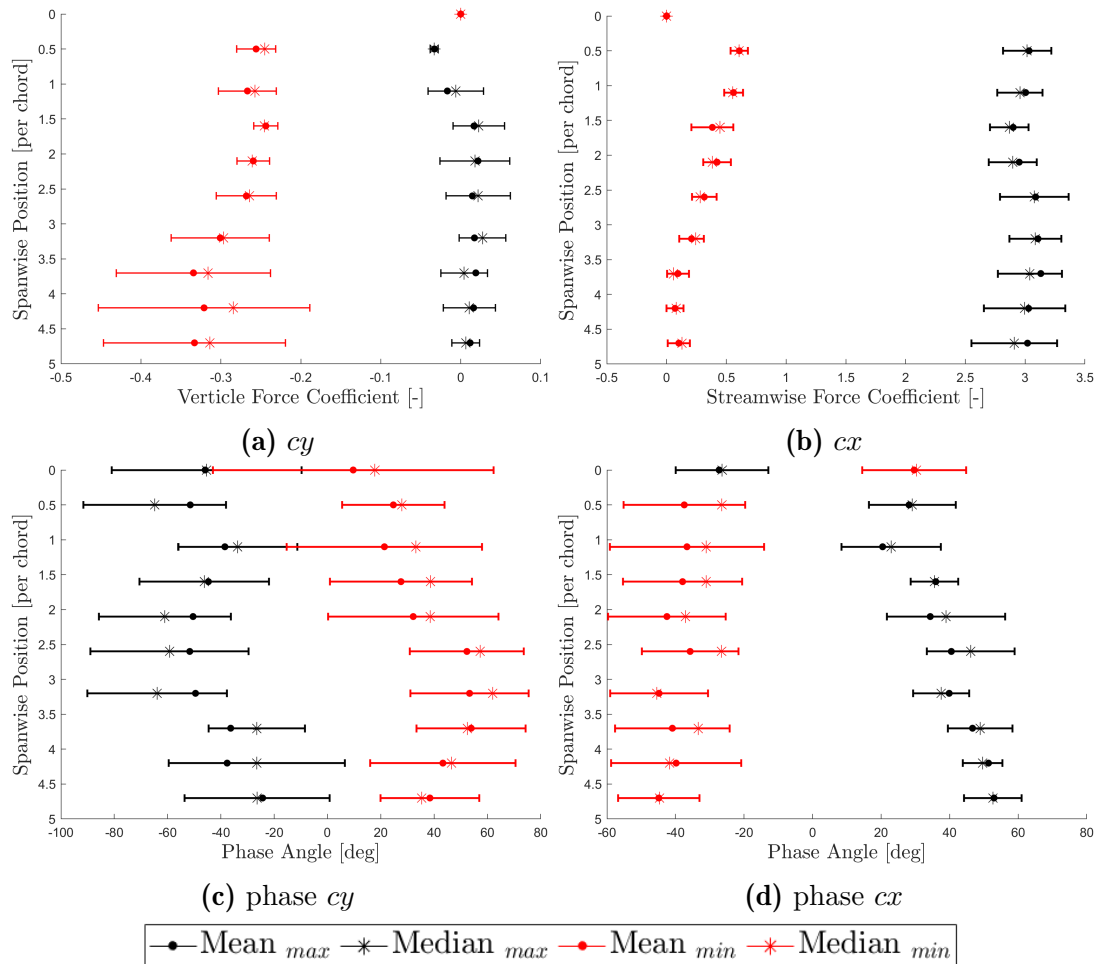


Figure 3.42: Surging airfoil at 2.5 Hz, 1 chord amplitude. Mean and Median values for cy (a), cx (b), and their phases (c) and (d) respectively at different spanwise positions over 10 cycles from CFD data. Bars represent the standard deviation away from the mean.

Figure 3.42 presents the mean, median and standard deviation of the c_y and c_x and their phase shifts. Interestingly, the standard deviation for the minimum c_y increases further inboard, and though the magnitude of the force coefficient becomes relatively constant about 3 chords from the tip, the standard deviation varies greatly, which is seen from the greater irregularity in the time series. The standard deviation of the maximum c_x is also larger further inboard, but this was observed earlier by the plateaus in the troughs in the time series. The phase angle becomes more or less stable from around 3.5 chords inboard for all the cases, though a large standard deviation is observed at all spanwise positions. The mean value, however, remains relatively constant.

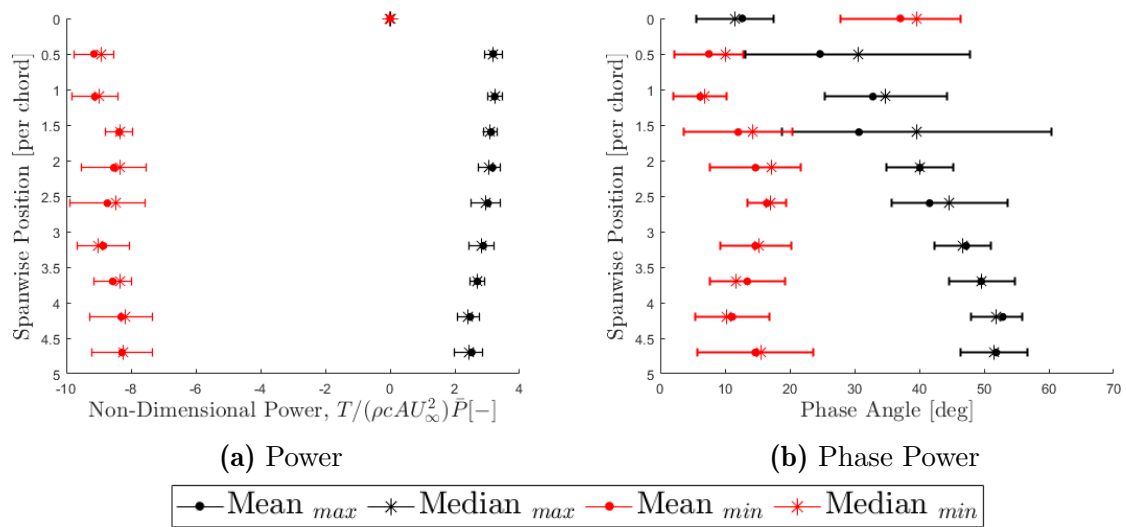


Figure 3.43: Surging blade at 2.5 Hz, 1 chord amplitude. Mean and Median values for Non-Dimensional Power (a), and its phase (b) respectively at different spanwise positions over 10 cycles from CFD data. Bars represent the standard deviation away from the mean.

Figure 3.43 shows the non-dimensional power for a surging blade at 2.5 Hz. The dominant power values are once again negative as stated earlier, but the magnitude of the negative non-dimensional power is about half of what was observed at 5 Hz, but the positive power is around twice the value, though the difference is still small since it is now around 2. Since the blade is moving at a lower frequency, the relative flow velocity experienced by the blade is lower, and combined with a lower force, the power is smaller. Interestingly, the phase angle where the maximum negative power occurs seems to be around 15 deg, possibly due to the increase in the slope of the streamwise hysteresis loop at 2.5 Hz in Figure 3.41 as compared to at 5 Hz Figure 3.34, causing a larger phase lead between the load and velocity to cause the phase shift in the power.

The 2.5 Hz surging blade is less chaotic than the 5 Hz surging blade, as was also seen for the plunging blade. This is because the motion frequency is lower and hence, the relative flow faced by the blade and therefore the loads it experiences from the induced velocity and vorticity is lower. It should be noted that the 2.5 Hz surging blade PSD

and hysteresis loops are significantly more chaotic than those seen on the plunging blade at 2.5 Hz, which is most likely due to the larger unsteadiness experienced by the surging blade as it is forced directly against the freestream.

3.4 Lock-In region

CFD simulations were run over a range of frequencies and amplitudes to determine the lock-in region for both a plunging and surging blade. A detailed analysis of the cases that match the PIV experiment was done in order to analyse the shedding, loads, and phases over the blade.

Hu et al. [2021], Hoskoti et al. [2018], Choi et al. [2015], Skrzypiński and Gaunaa [2015], Meskell and Pellegrino [2019] and many others suggest that when lock-in occurs, the $cl - \alpha$ or $cx - X/c$ hysteresis loop will be smooth and that a PSD of the time series would show a peak only at the motion frequency (or its harmonics) since the shedding has locked onto that frequency instead of shedding at the Strouhal frequency. Choi et al. [2015] further defines the vortex lock-in region as when the dominant peaks in the lift spectrum occur at the motion frequency and its harmonics. This is also seen in the results of a 2D plunging blade by Hu et al. [2021], where the dominant peak is at the motion frequency and secondary peaks at the harmonics are observed, and smooth hysteresis loops were observed for locked in cases. However, this analysis has mostly been performed on a 2D blade, which as stated earlier in chapter 1 will have some notable differences in the 3D analysis, with less clear peaks or shifted peaks due to interactions of vortices travelling in a spanwise direction, and also due to phase differences along the spanwise shedding. Thus, to determine whether a certain case was locked in, a Δf threshold of the energy of secondary peaks near f_{st} was set to allow for these effects. Additionally, the cl and cd time series will be analysed to see if smooth sinusoidal patterns are seen. All PSDs presented are taken at the mid-span position to try and mimic the ‘2D’ results as much as possible. This analysis was only done on the CFD results due to the unavailability of a fully resolved time series for the experimental data.

A PSD analysis was performed on the time series data for each combination of frequency and amplitude and the location and magnitude of the peak was used to determine whether that combination was locked-in, was on the border, or was not locked-in. the time series was taken at the mid-span position to try and eliminate any spanwise tip effects and have a ‘2D’ analysis. Example PSDs for the three cases are seen in Figure 3.44. The Δf threshold was set to 5% f_{st} about f_{st} , with a maximum allowable difference of $2\Delta f$, or 10% f_{st} . The PSD was normalised with the maximum value at each amplitude, and the threshold of 10% of the maximum peak for lock-in and 1% of the maximum peak for the border, i.e. a peak magnitude of 10^{-1} or 10^{-2} was set to determine if the peak in the spectrum would be considered as locked-in or on the border respectively. It is worth noting that the motion frequency peak will always be seen and will generally be the largest one since the blade is being forced at that frequency, so the loads will show it. The other frequencies present in the flow are due to the shedding frequency and its harmonics.

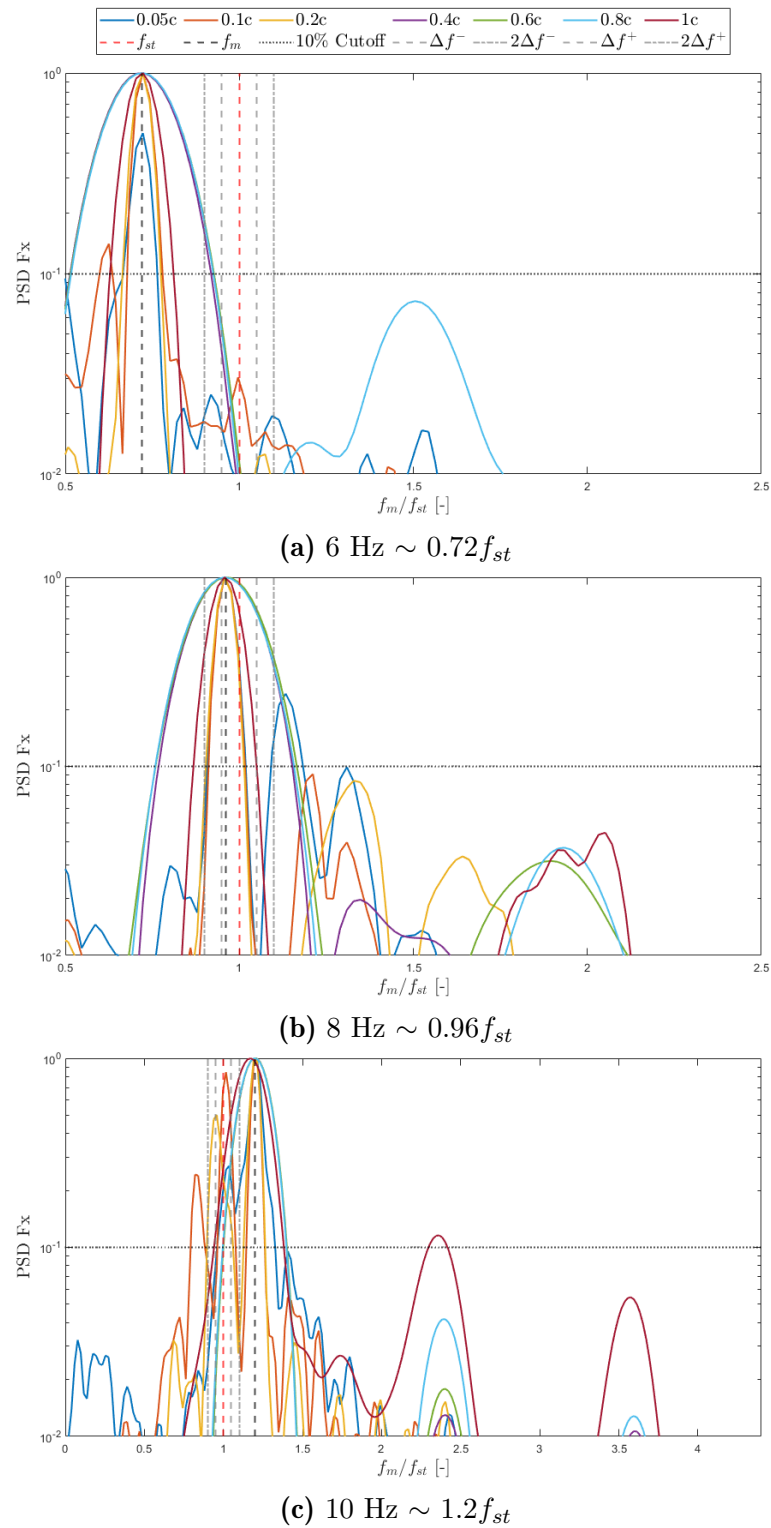


Figure 3.44: PSDs for a plunging airfoil from CFD data at 6 Hz (top) with amplitudes below 0.4c in the border, at 8 Hz (middle) with all cases locked-in and, at 10 Hz (bottom) with amplitudes below 0.4c unlocked

In Figure 3.44b, all the peaks occur at the motion frequency for all amplitudes and there are no secondary peaks within the threshold regions. It is worth noting that for the three lowest amplitudes, $0.05c$, $0.1c$, and $0.2c$, secondary peaks begin to occur just beyond the threshold region. This could be further investigated since there is no specific literature on how such a lock-in region is defined for a 3D blade, or for when a 2D assumption can be applied to a finite blade. The secondary peaks may also show a shift in frequency even if they are locked in due to the spanwise convection of the tip vortex. At 10 Hz in Figure 3.44c, the peaks at the three lowest amplitudes, $0.05c$, $0.1c$, and $0.2c$ are large around f_{st} , clearly suggesting that these cases are shedding the vortices at the Strouhal frequency and not at the motion frequency despite them having peaks at the motion frequency as well. Lastly, at 6 Hz in Figure 3.44a, the peaks at the three lowest amplitudes, $0.05c$, $0.1c$, and $0.2c$ are within the Δf threshold, but the magnitude of the energy is between 10% and 1% of the maximum peak energy, so it was considered to be a case on the border. It is interesting to note that the peaks are wider between $0.4c$ and $0.8c$, though the specific reason is unknown.

The non-dimensional power was also calculated for all the cases using the definition by Skrzypiński et al. [2014].

3.4.1 Plunging Blade

The PSD analysis was performed on all the simulations and the lock-in diagram of the non-dimensional amplitude against the non-dimensional frequency was plotted. Additionally, the non-dimensional power was also presented in the same plot, seen in Figure 3.45.

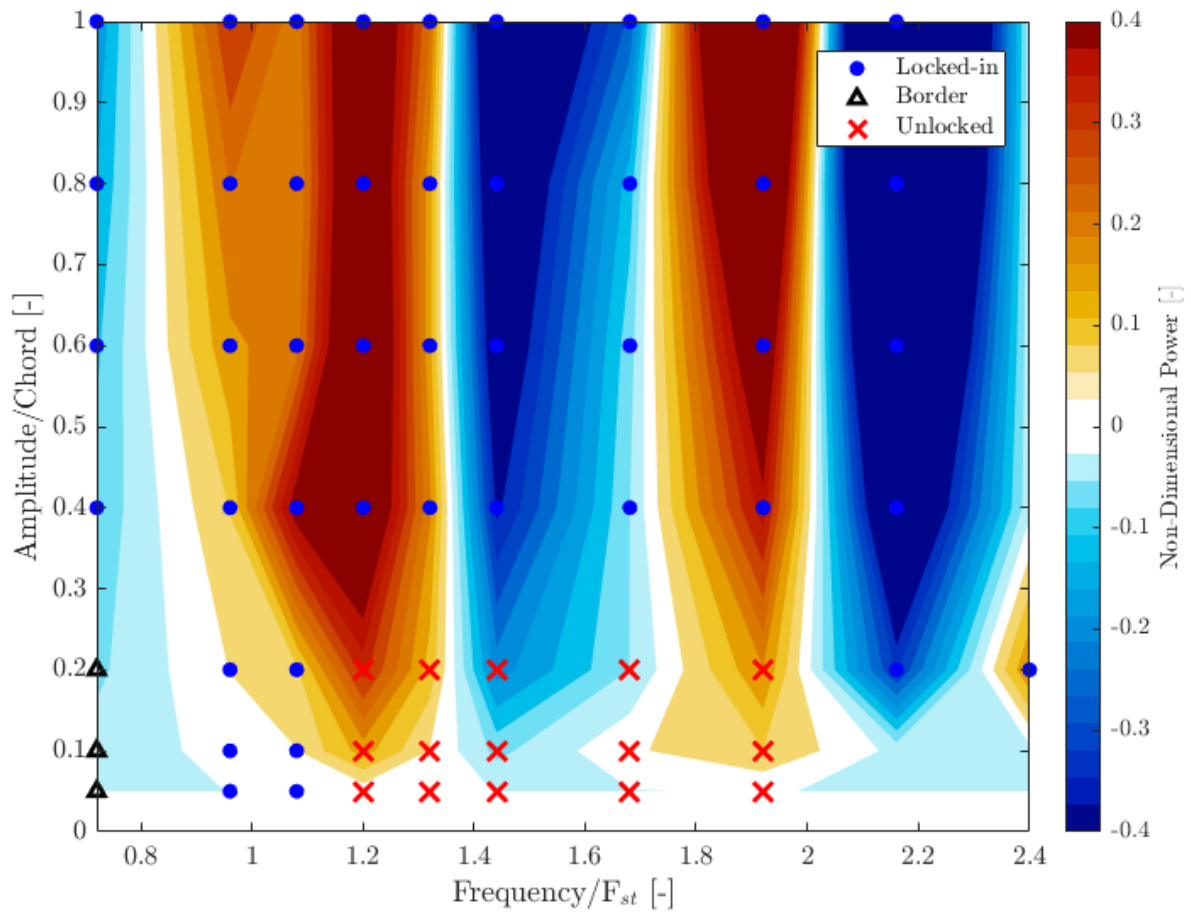


Figure 3.45: V-shaped Lock-in region from CFD data for a Plunging Blade.

For free vibration experiments, lock-in usually occurs in the positive power region where power is injected from the flow to the blade. This happens when the load and velocity are in phase, causing a positive power, which is with negative aerodynamic damping. However, for a forced vibration analysis like in this case, there can still be lock-in even with negative power when the load and velocity are not in phase since the motion is being forced on the blade. At amplitudes of $0.4c$ and larger, lock-in occurs at all the simulated frequencies. This was also seen in an analysis performed by Choi et al. [2015] which presented similar lock-in for very high amplitudes. Hu et al. [2021] presents a lock-in diagram for a similar plunging blade and some of the frequency-amplitude combinations were chosen for the CFD simulations presented here.

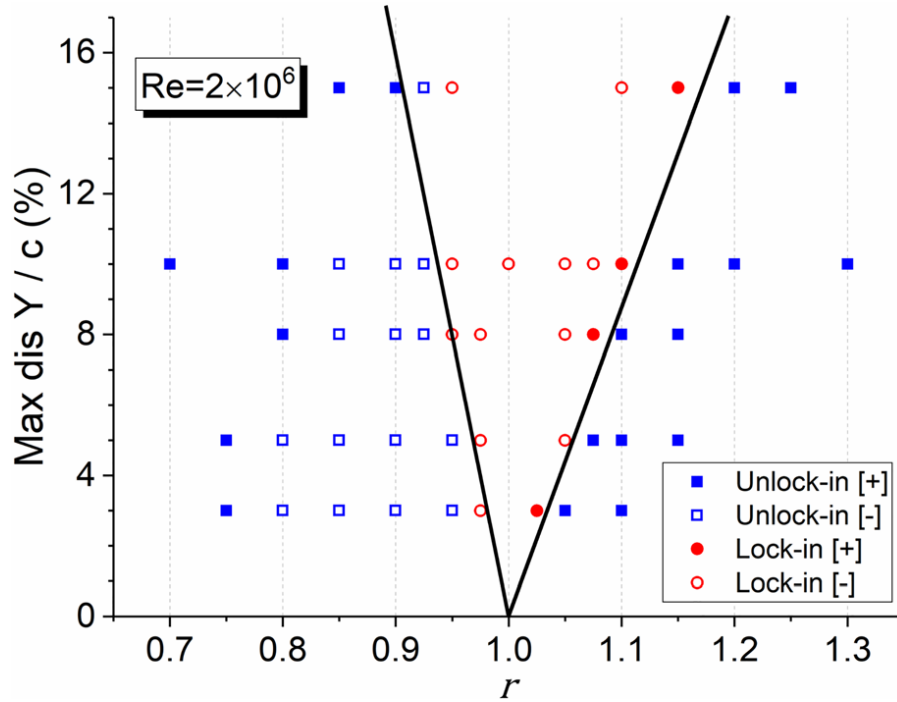


Figure 3.46: V-shaped Lock-in region. Amplitude of chordwise oscillations vs the oscillation frequency ratio at 90 angle of attack. Reprinted from Hu et al. [2021]

Referring to Figure 3.46 from Hu et al. [2021], it is expected that frequencies lower than $0.95 f_{st}$ or larger than $1.05 f_{st}$ would be unlocked at $0.05c$ (5% Y/c) amplitude and that frequencies lower than $0.93 f_{st}$ or larger than $1.15 f_{st}$ would be unlocked at $0.1c$ (10% Y/c) amplitude. A similar asymmetric region is observed, though the V-shape is not distinct from the results in this thesis. Furthermore, at the equivalent frequency and amplitude combinations presented in Hu et al. [2021], the lock-in region at $0.05c$ amplitude is wider, especially at the lower frequency analysed, where they are on the border at $0.72 f_{st}$. Projecting the lock-in region to $0.2c$ amplitude, it would be expected that $1.2 f_{st}$ would be locked in, but this is not the case. This could be because Hu et al. [2021] performed a purely 2D study using modal analysis whereas a 3D blade is simulated in this work. Differences may also be due to the difference in Reynolds numbers, where the simulations from Hu et al. [2021] are at $Re = 2 \times 10^6$ and the operating Reynolds number for the CFD simulations presented in Figure 3.45 are $Re = 2.4 \times 10^4$. A detailed analysis at a motion amplitude of $0.1c$ (10% Y/c) is seen in Figure 3.47.

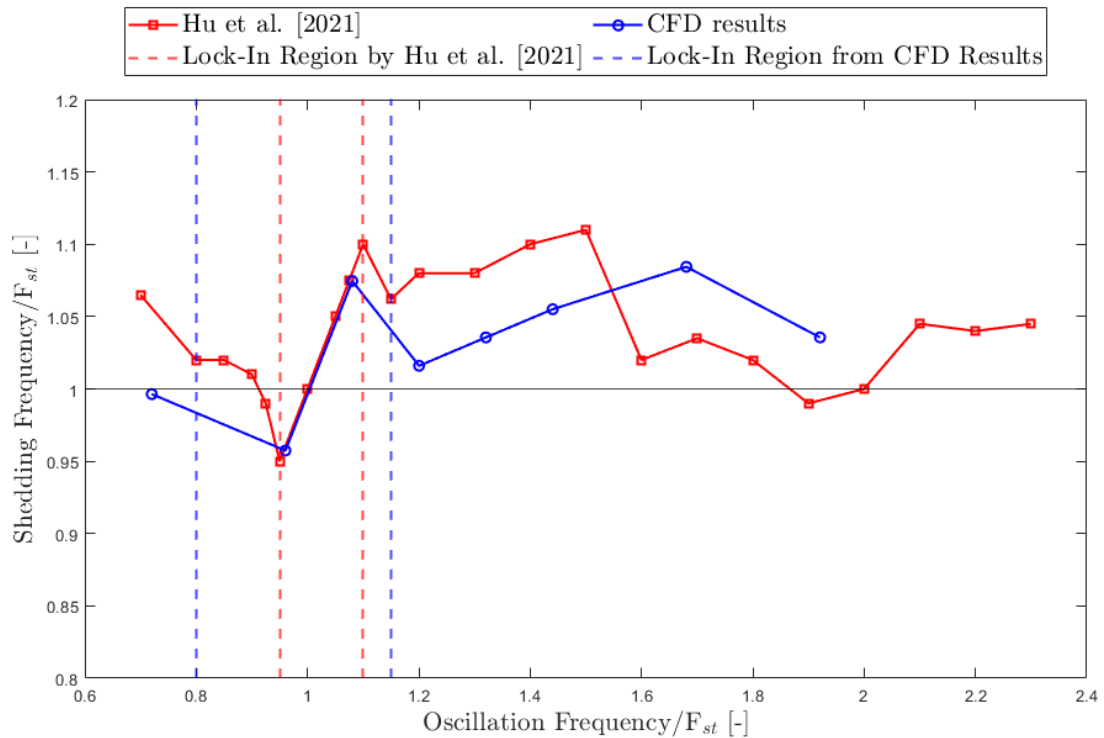


Figure 3.47: Dimensionless vortex shedding frequency as a function of the frequency ratio of the forced oscillation of the airfoil. The red line is Reprinted from Hu et al. [2021]

Figure 3.47 presents a comparison of the non-dimensional shedding frequency f_{shed}/f_{st} over against the non-dimensional motion frequency f_{motion}/f_{st} that is compared to the results at the oscillation amplitude of 0.1 c from Hu et al. [2021]. The red line shows the reprinted data with the lock-in region from $0.95 < f_{motion}/f_{st} \leq 1.1$. A straight line with a linear relationship between the two frequency ratios is observed in the lock-in region. The blue line presents the CFD result. The limits of the lock-in region from the CFD results are not definite since a higher resolution of frequencies is needed to determine the exact point where lock-in is not observed. However, the upper limit was set to $f_{motion}/f_{st} = 1.15$, which is in between $f_{motion}/f_{st} = 1.1$ where lock-in is observed and $f_{motion}/f_{st} = 1.2$ where the blade is no longer locked in. The lower limit, on the other hand, is much more arbitrary. Below $f_{motion}/f_{st} = 1$, there are only two points at 0.96 and 0.72. The limit was set to 0.8 because the PSD at $0.72 f_{st}$, 6 Hz oscillation frequency with 1 chord amplitude was considered to be a border case since there is a large peak at the motion frequency and a peak of about 3% of its energy at f_{st} . The point at f_{st} is plotted in Figure 3.47, but if the point was instead plotted at the motion frequency, the straight line region where lock-in occurs would extend to include that frequency as well. In general, there is surprisingly good agreement between the two lines over the lock-in region and the general shape of the plot in the unlocked regions. Differences between the plots are most likely due to the 2D versus 3D analysis of the blade. What is interesting to note is the plot crossing over the point $f_{shed}/f_{st} = 1$ at $f_{motion}/f_{st} = 2$. This could either be because the frequency of motion is so large that it dominates the flow, or because it is a

harmonic.

The non-dimensional power $P^* = T/(\rho c A U_\infty^2) \bar{P}$ where \bar{P} is the mean aerodynamic power was also plotted against the non-dimensional period $T^* = T U_\infty / c$ for all the amplitudes as seen in Figure 3.48. The non-dimensional period is $1/St$. The mean aerodynamic power is integrated across the spanwise sections and is the total power over the blade.

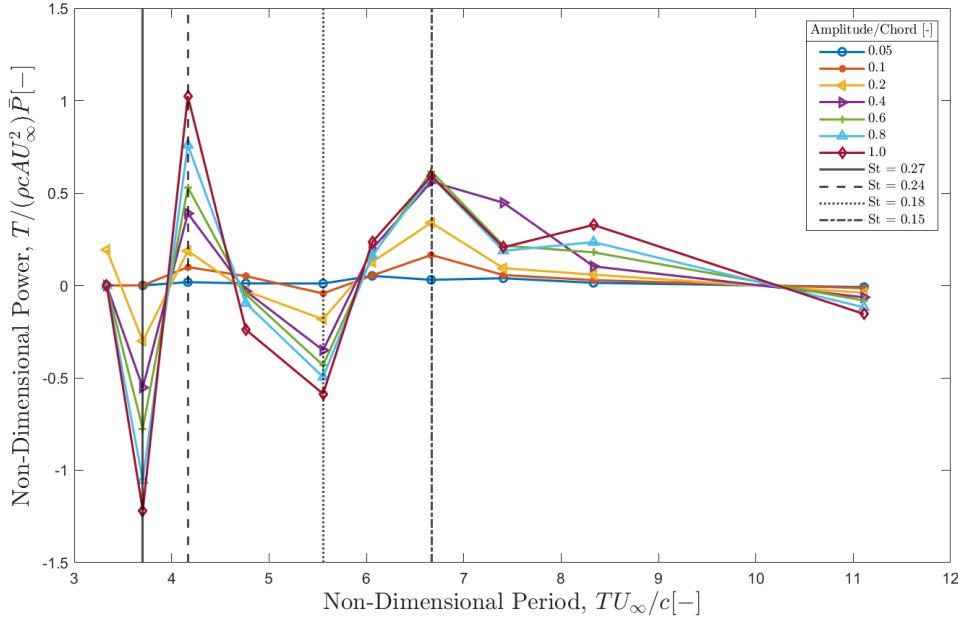


Figure 3.48: Non-dimensional Power against Non-Dimensional Period for Different Amplitude Ratios for a Plunging Blade from CFD data.

Zou et al. [2015] presents a similar analysis for a forced edgewise motion where the non-dimensional power P^* is plotted against the non-dimensional period T^* for a combination of non-dimensional amplitude A^*/T^* ratios where $*$ = A/c , and found that a peak occurs at the Strouhal number, $St = 1/T^*$. Figure 3.48 plots the non-dimensional power against the non-dimensional period for certain non-dimensional amplitude ratios, but they are not non-dimensionalised by the period. The plot shows four peaks in the plot. The peaks at $St = 0.27$ and $St = 0.18$ may not be as relevant since they occur at negative power values, which would be damped out in a free vibration case. The peak at $St = 0.24$ occurs at very high frequencies, with a predicted shedding frequency of 16 Hz. The expected St is around 0.16, but with large 3D effects, a St of 0.15 could be considered a decent representation. The peak at 0.24 could be a harmonic, but it is more likely that the flow is simply dominated by the motion frequency since a very large peak also occurs at 18Hz. This also agrees with Figure 3.45, where the blade is once again locked in at 18 Hz at $0.2c$ amplitude after being unlocked earlier, which is most likely because the forcing frequency is so high that it completely dominated the relative flow seen by the airfoil and the resultant wake. However, it should be noted the drawn conclusion may not be equivalent to the one presented in Zou et al. [2015] since the lines

only represent a certain amplitude ratio which is not non-dimensionalised by T^* for that value.

3.4.2 Surging Blade

Using the same methodology for a surging airfoil, the lock-in diagram is presented in Figure 3.49. Unlike in the plunging case, there is no V-shaped region for the surging airfoil, with all the simulations showing a peak at the motion frequency. This is because the motion of the airfoil is forcing the flow so much that the shedding is forced to follow the motion. This was already seen at 5 Hz, which is only $0.8 f_{st}$. At much higher frequencies, the forcing becomes even stronger. The power is always negative because the force experienced by the blade is always out of phase with the velocity, as seen in the time series analysis earlier.

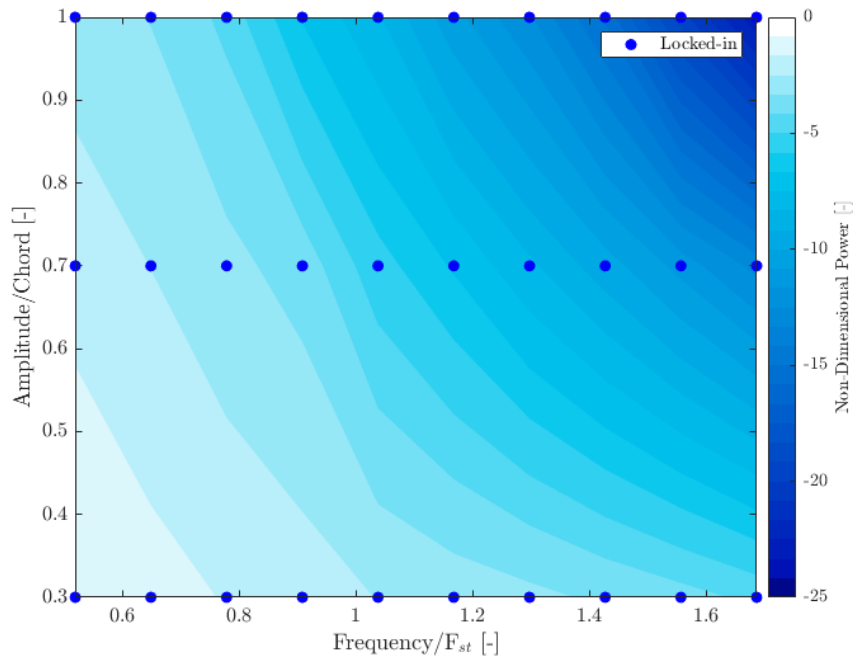


Figure 3.49: Lock-in region from CFD data for a Surging Blade.

Figure 3.50 presents the non-dimensional power against the non-dimensional period for the surging airfoil. At $T^* = 8$ and above, i.e. at frequencies of 5 Hz and below, P^* seems to stabilise and tend towards a plateau close to 0. At frequencies higher than this, the power starts to diverge greatly, with the difference in the power at larger amplitudes growing. This is because of the effect of the larger frequency of motion on the relative velocity experienced by the blade as it forces the flow. The clear vortices visible at 5 Hz already showed the large effect the flow had on the shedding. Furthermore, the amplitude of motion also affects the relative flow seen by the blade, since a larger amplitude at the same frequency requires a larger relative motion by the blade to complete the cycle.

This effect grows as the frequency increases, as seen in the growing power at higher amplitudes.

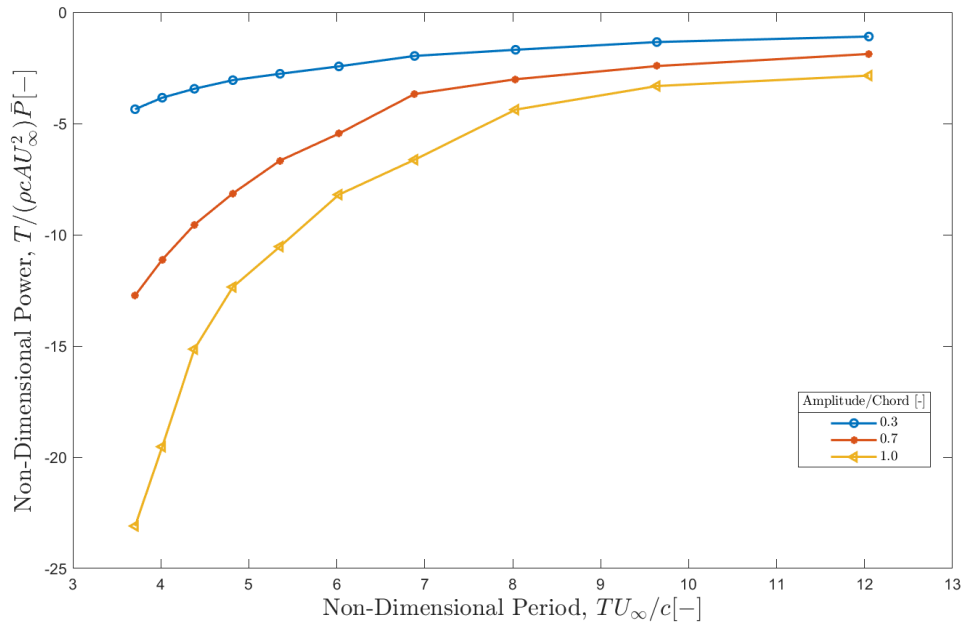


Figure 3.50: Non-dimensional Power against Non-Dimensional Period for Different Amplitude Ratios for a Surging Blade from CFD data.

This chapter presents an overview of the thesis and summarises the key points addressed along with discussions about the results as well as future work.

The experimental design was limited by the motor and the type of PIV equipment, so the extra numerical simulation was an excellent addition to the data. The experiment was used to validate the CFD results, and with more available data regarding the loads and time series from the simulation, it was possible to conduct a much deeper analysis of the results.

4.1 Summary

A brief introduction on the relevance of VIV in the wind industry is presented, followed by a literature review on the relevant research related to the topic. The key findings and research gaps are summarised and the research questions to address these gaps are established. Next, the design of the experiment is presented, introducing the experimental technique PIV, the details on the specifications for the experiment, and the experimental setup of both the wind tunnel and plunging mechanism. A summary of the test cases is presented, followed by a brief overview of the CFD setup including details on the flow solver and simulation conditions, noting that the simulations were run by Assistant Professor Christian Grinderslev from the Technical University of Denmark. Then, the results of the thesis, which aim to answer the research questions are presented. First, the CFD results are validated against the experimental PIV results so that they can be further used for analysis. This is done by analysing the flow around a static blade to validate the 3D flow around the tip of a finite blade and the effect of chosen blade aspect ratio, and by comparing equivalent flow fields for a plunging and surging blade to ensure the CFD simulation is able to accurately predict the flow around both a static and dynamic blade. Next, the flow around a plunging blade is analysed, first determining the effect of the motion frequency on the blade by comparing the results for a blade oscillating at 5 Hz and 2.5 Hz with the same oscillation amplitude of 1 chord. A brief discussion of the spanwise flow and vorticity around the tip of a plunging blade at 5 Hz is presented, followed by a detailed analysis of the flow field and loads around the blade at 5 Hz and 2.5 Hz to analyse the spanwise convection of the tip vortex and the development of the flow. The same analysis on the effect of the motion frequency and the spanwise convection of the tip vortex is performed for a surging blade at 5 Hz and 2.5 Hz frequency, 1 chord oscillation amplitude. Finally, the lock-in region for the plunging and surging blade is presented, followed by a conclusion of the results is provided along with limitations of the research and suggestions for future work.

4.2 CFD Validation

Flow fields were captured during the PIV experiment and reproduced using CFD simulations. The cases considered were a static blade with an aspect ratio of around 5 and around 10 for the PIV experiment with a flat plate boundary condition at the fixed end, which was replicated with twice the aspect ratio for the CFD simulations to ensure the same boundary condition since the blade was free on both ends. Next, dynamic cases for a plunging and surging blade for $U_\infty = 3m/s$ were simulated at 2.5 Hz and 5 Hz oscillation frequency, 1 chord oscillation amplitude. All the flow fields showed excellent agreement between the CFD simulations and the PIV flow fields, with some minor over prediction of the vertical velocity components near the airfoil section from the CFD simulations. This was attributed to possibly be due to a better resolution around the airfoil from the CFD simulations that were unavailable from the PIV results due to the shadow region in the flow. The flow fields were compared at various spanwise positions from the tip and the development of the flow around the airfoil was nearly identical for the equivalent test case. It was concluded that the CFD simulations were accurate and hence the additional data such as the spanwise field of view for the static blade as well as the time series and blade loads could be used for further analysis.

4.3 Tip effect

The study on the flow around a finite static blade and the effect of the blade aspect ratio showed that the flow field around a cantilevered blade with a flat plate boundary condition on the fixed end is equivalent to the flow around a blade that is free at both ends and has twice the aspect ratio. The study also indicates that the maximum velocity of the spanwise flow behind the blade is only dependent on the blade aspect ratio and independent of the freestream wind speed, the type of motion (plunging or surging), or the frequency of motion. This affects the spanwise convection of the tip vortex which convects to a similar point inboard and thus, determines the transition point at which the flow around the blade behaves ‘2D’.

The differences between the flow patterns at different oscillation amplitudes were evaluated for a plunging and surging blade. For a plunging blade, von Karman-like vortex structures were shed at 5 Hz, but these were less evident at 2.5 Hz. This could be due to the lower relative flow speed experienced by the blade that causes the wake to be convected further downstream and out of the available field of view from the PIV results. Unfortunately, the output plane for the CFD result was chosen to reproduce the available PIV field of view and hence, further analysis on the far wake is needed to confirm this. Nevertheless, a PSD analysis of the cl and cd showed a peak in the motion frequency for both cases over spanwise positions from 1 chord inboard to 5 chords inboard suggesting that they were locked in. An analysis of the $cl - \alpha$ and $cd - \alpha$ hysteresis loops, as well as the mean and standard deviation of the cl and cd and their phases over many spanwise positions, showed a clear phase shift up till around 2.5 chords inboard, after which the standard deviations about the mean became smaller and the phase was

consistent, confirming that the effect of the tip vortex is no longer present. The $cd - \alpha$ hysteresis loops formed a horizontal figure-8 because the frequency is twice that of cl . The cl PSD showed a clean peak at the motion frequency despite the spanwise convection of the tip vortex, though patterns of changing energy further inboard were observed in the harmonics, and were reflected in the hysteresis loops, suggesting that the tip vortex may not affect the onset of lock-in, but may affect the magnitude of load experienced by the blade and hence, the amplitude of oscillation for a freely vibrating blade.

The flow around a surging blade was shown to be much more complicated, with forcing in the streamwise direction opposing the incoming wind and causing two vortex pairs to be shed each cycle. It was also seen that at 2.5 Hz, the motion velocity was not large enough to force the flow against the incoming freestream, and von Karman-like vortex structures were not observed. Upon analysing the $cx - X/c$ and $cy - X/c$ hysteresis loops and the mean, median, and standard deviation plots, the same stability 2.5 chords inboard from the tip was observed, and a PSD of the cx and cy were analysed to confirm that both frequencies were locked in over spanwise positions from 1 chord inboard to 5 chords inboard. More prominent effects on the portions of the hysteresis loops moving with and against the freestream were visible at 5 Hz where the blade velocity was large enough to shed large vortex structures that interacted with the blade during the second half of its cycle, thereby causing much more unsteady loading. Once again, the cx and cy PSDs showed peaks at the motion frequency for all the spanwise positions, suggesting that lock-in may not be spanwise dependent for a symmetric rigid blade, but as mentioned earlier, the tip vortex may affect the magnitude of the load. The PSD of cy also showed a stronger peak at twice the motion frequency, indicating that it is more influenced by the two vortex pairs shed per cycle rather than the motion frequency.

For both the plunging and surging blade, the PSD plots of the force coefficients showed peaks at the motion frequency across all the spanwise positions, but the hysteresis loops, mean, median, and standard deviation plots, and spanwise power plots confirmed the change in the loads and their phase, which was observed in the vorticity fields.

It was concluded that for a 40 cm blade fixed on one end with an aspect ratio of around 5, the tip vortex was convected till around 2.5 chords inboard, and beyond that point, the flow was considered to be ‘2D’ as the effect of the tip vortex was no longer dominant. The results were independent of the freestream velocity for the static case and the motion frequency for the dynamic cases. The static analysis of the 80 cm blade fixed on one end with an aspect ratio of around 10 saw the tip vortex convected till around 3 chords inboard, though further analysis on this longer blade undergoing oscillatory motion would be needed to confirm that the length that the tip vortex is convected inboard is only dependent on the blade aspect ratio.

4.4 Lock-In

For the plunging blade, the V-shaped lock-in region seen in Hu et al. [2021], Besem et al. [2016], Hoskoti et al. [2018], Meskell and Pellegrino [2019] and other literature is not clearly observed. This was not an expected result, but it is most likely because the

chosen oscillation amplitudes are too large. A comparison with the results from Hu et al. [2021] showed reasonable agreement at 0.1 chords oscillation amplitude, though there were differences which are most likely attributed to the 3D analysis of a finite blade compared to the 2D analysis from literature. From the P^* vs T^* plot, two shedding frequencies or Strouhal numbers were identified for the plunging blade. The value at $St = 0.15$ is very close to the expected value of 0.16, and the second value at 0.24 could be a harmonic that has shifted due to the 3D effect. Heinz et al. [2016], Grinderslev et al. [2022], Skrzypiński et al. [2014] and others show that for free vibrations, once the lock-in instability occurs, there is a positive energy transfer that will result in large oscillation amplitudes since there is negative aerodynamic damping, which may lead to large fatigue loading and catastrophic results. Since the motion in this thesis is forced, lock-in also occurs when negative power is observed because the force and velocity are out of phase, with positive aerodynamic damping. For a freely vibrating blade such as an actual wind turbine blade, the oscillation would either damp out to an equilibrium where the power injected into the blade is in equilibrium with the power extracted, causing a limit cycle oscillation, or the vibration would damp out completely. What is most important to note is that the initiation of lock-in and other aerodynamic instabilities should be investigated more, to avoid the onset of large vibrations.

The surging blade always shows positive aerodynamic damping, with a negative power. Though a V-shaped lock-in region may occur at lower amplitudes as seen in Choi et al. [2015], at such large amplitudes, the oscillation in a freely vibrating blade will damp out and such large deflections are unlikely to occur. This is also an expected result since the surging blade was meant to resemble the flapwise motion which has a high aerodynamic damping. Furthermore, previous research by Zou et al. [2015], Pellegrino and Meskell [2013], Skrzypiński et al. [2014] indicated that lock-in is most prevalent in the edge-wise motion for wind turbine blades at standstill, so future work should focus on this mode. From the P^* vs T^* plot, no clear shedding frequency or Strouhal number was identified for the surging blade.

4.5 Plunging vs Surging Airfoil

A comparison of a plunging versus a surging airfoil was not done because the magnitude of the loads, as well as the motion of the vortex structures around the blade, were significantly different. The surging blade experienced streamwise loads around an order of magnitude larger than the cl and cd for the plunging blade, but it was along with a much larger damping leading to a larger negative non-dimensional power. The lock-in diagrams for the plunging and surging blade greatly differed, with all the surging cases being locked in. However, this could be because the minimum tested amplitude was 0.3 chords, and at the same amplitude, all the plunging cases were locked in as well, though some cases experienced positive power while others experienced negative power. At lower amplitudes, the V-shaped region may occur. The most notable difference, however, is that the non-dimensional power for the surging blade was negative for all cases. This is because the load experienced on the blade is always out of phase with the motion velocity

and accompanied by a large positive damping, which was confirmed by analysing the blade motion and hysteresis loops. There would need to be a vortex street that induces a force at twice the shedding frequency to have negative aerodynamic damping in this direction.

4.6 Limitations

The largest limitation in the results is the inability to accurately confirm the shedding frequency. A POD analysis on low-speed PIV data is not an accurate method for obtaining the frequency of shedding and a hot wire measurement must be taken to confirm the real shedding frequency. The shedding frequency from the CFD simulation was also limited in accuracy as it was only tested for a single wind speed of 5 m/s, which resulted in $St = 0.13$ for $Re = 25000$ as compared to the shedding frequency at 3 m/s from the PIV data that gave $St = 0.16$ for $Re = 15000$.

Another limitation was the large spacing between the measured phase for the PIV experiment. This limited the ability to calculate the unsteady load using the NOCA method Noca et al. [1997, 1999], and hence, forces our results to rely on the loads from the CFD simulations.

4.7 Future Work

This work sets a foundation for further development in many aspects, including an expansion of the test cases for the experiment and simulation presented here as well as modifications to better analyse the VIV phenomenon.

4.7.1 Expanding the Test Campaign

Future work would involve testing the static blade and oscillating blade for different blade aspect ratios to better quantify the convection of the tip vortex inboard, and find a relation between the blade aspect ratio and the point where the flow around the blade becomes ‘2D’. The experimental campaign should be complemented with a hot wire measurement to obtain the shedding frequency in the wake and compare it to those obtained from the CFD results. Ideally, high-speed PIV is used such that the experimental data is also time-resolved and a better comparison of the hysteresis loops and phase shift can be done. The aerodynamic load from the flow field could also be calculated using the Navier-Stokes equation in methods described by Van Oudheusden [2013] to compare to those obtained using the NOCA method. Lower amplitude and frequency combinations should also be simulated for both a plunging and surging blade to better resolve the V-shape in the lock-in diagram. If the same blade could be mounted to a free spring system such that it is free to vibrate, a comparison of the lock-in and the loads for a free vibration case could be compared to the forced vibration results to analyse which forced motions are realistic. This would also most likely result in either a mix of the streamwise and crossflow motions being excited with the crossflow excitation

being dominant. More focus should be devoted to a plunging blade, with the possible inclusion of a pitching motion to better excite the edgewise mode and study the onset of the instability.

4.7.2 Loads

The NOCA method was attempted to evaluate the loads on the blade using CFD flow fields as an initial estimate. Though analysis of the static loads showed somewhat promising results with a 7% error between the force coefficients measured from the NOCA method compared to the integrated blade loads output from the CFD results, the unsteady loads showed unreasonable results and need further improvement to be accurate. The initial results are found in Appendix A, though the dynamic cases are very inaccurate and will be considered as future work.

4.7.3 Beyond the Thesis

This thesis does an analysis of a rigid, symmetric blade with a constant cross-section and no taper. The same setup could be used to test wind coming at different inclination angles to the blade, but further work should be done using a flexible blade to include aeroelastic phenomena. This will also allow for a more reasonable comparison between loads in the streamwise and crossflow direction. Future tests should also use a dynamically scaled wind turbine blade to understand the effect of twist, taper, and cambered airfoils on VIV and the spanwise convection of the tip vortex. With different sections of the blade experiencing different flow patterns and different Reynolds numbers, there may also be spanwise lock-in at certain wind speeds.

The research on VIV in wind turbine blades is a young field with a long road ahead of it and many things to discover. These results are just a start to characterise certain aspects of the flow to help develop an understanding of the phenomenon so that it can be prevented.

Bibliography

- [1] S. G. Horcas, T. Barlas, F. Zahle, and N. N. Sørensen. Vortex induced vibrations of wind turbine blades: Influence of the tip geometry. *Physics of Fluids*, 32(6), 6 2020. ISSN 10897666. doi: 10.1063/5.0004005.
- [2] Witold Robert Skrzypiński. *Analysis and modeling of unsteady aerodynamics with application to wind turbine blade vibration at standstill conditions*. PhD thesis, Technical University of Denmark (DTU), Risø, 2 2012. URL <http://orbit.dtu.dk/en/projects/analysis-and-modeling->.
- [3] Paul Veers, Carlo L. Bottasso, Lance Manuel, Jonathan Naughton, Lucy Pao, Joshua Paquette, Amy Robertson, Michael Robinson, Shreyas Ananthan, Thanasis Barlas, Alessandro Bianchini, Henrik Bredmose, Sergio González Horcas, Jonathan Keller, Helge Aagaard Madsen, James Manwell, Patrick Moriarty, Stephen Nolet, and Jennifer Rinker. Grand challenges in the design, manufacture, and operation of future wind turbine systems. *Wind Energy Science*, 8(7):1071–1131, 7 2023. ISSN 2366-7451. doi: 10.5194/wes-8-1071-2023. URL <https://wes.copernicus.org/articles/8/1071/2023/>.
- [4] Joachim C. Heinz, Niels N. Sørensen, Frederik Zahle, and Witold Skrzypiński. Vortex-induced vibrations on a modern wind turbine blade. *Wind Energy*, 19(11): 2041–2051, 11 2016. ISSN 10991824. doi: 10.1002/we.1967.
- [5] F. Zou, V. A. Riziotis, S. G. Voutsinas, and J. Wang. Analysis of vortex-induced and stall-induced vibrations at standstill conditions using a free wake aerodynamic code. *Wind Energy*, 18(12):2145–2169, 12 2015. ISSN 10991824. doi: 10.1002/we.1811.
- [6] Jess A Michelsen. General rights Basis3D-a Platform for Development of Multiblock PDE Solvers-release. Technical report, Technical University of Denmark, 1992.
- [7] J Michelsen. Block Structured Multigrid Solution of 2D and 3D Elliptic PDE's. Technical report, Technical University of Denmark, 1994.
- [8] Niels N. Sørensen. General purpose flow solver applied to flow over hills. Technical report, Risø National Laboratory, 1995.
- [9] Ping Hu, Chong Sun, Xiaocheng Zhu, and Zhaohui Du. Investigations on vortex-induced vibration of a wind turbine airfoil at a high angle of attack via modal analysis. *Journal of Renewable and Sustainable Energy*, 13(3), 5 2021. ISSN 19417012. doi: 10.1063/5.0040509.
- [10] Sohrob Mottaghi, Rene Gabbai, and Haym Benaroya. Literature in Vortex-Induced Oscillations. In *Solid Mechanics and its Applications*, volume 260, pages 7–56. Springer Verlag, 2020. doi: 10.1007/978-3-030-26133-7{_}2.

- [11] Bridget M. Benner, Daniel W. Carlson, Banafsheh Seyed-Aghazadeh, and Yahya Modarres-Sadeghi. Vortex-Induced Vibration of symmetric airfoils used in Vertical-Axis Wind Turbines. *Journal of Fluids and Structures*, 91, 11 2019. ISSN 10958622. doi: 10.1016/j.jfluidstructs.2019.01.018.
- [12] S. S. Chen, M. P. Paidoussis, M. K. Au-Yang, and H. Saunders. Flow-Induced Vibration of Circular Cylindrical Structures by S.S. Chen, M.P. Paidoussis, and M.K. Au-Yang . *The Journal of the Acoustical Society of America*, 75(1):299–299, 1 1984. ISSN 0001-4966. doi: 10.1121/1.390308.
- [13] Jerry M Chen and Yuan-Cheng Fang. Strouhal numbers of inclined flat plates. Technical report, National Chung-Hsing University, Taichung, 2 1996.
- [14] S. Bull, N. Chiereghin, I. Gursul, and D. J. Cleaver. Unsteady aerodynamics of a plunging airfoil in transient motion. *Journal of Fluids and Structures*, 103, 5 2021. ISSN 10958622. doi: 10.1016/j.jfluidstructs.2021.103288.
- [15] Robert D Blevins. *Flow-induced vibration*. New York, 1977.
- [16] J F Howell and M Novak. Vortex shedding from circular cylinders in turbulent flow. In *Wind engineering*, pages 619–629. Elsevier, 1980.
- [17] Christian Grinderslev, Niels Nørmark Sørensen, Georg Raimund Pirrung, and Sergio González Horcas. Multiple limit cycle amplitudes in high fidelity predictions of standstill wind turbine blade vibrations. *Wind Energy Science*, 7(6):2201–2213, 2022. doi: 10.5194/wes-2022-61. URL <https://doi.org/10.5194/wes-2022-61>.
- [18] T Sarpkaya. Vortex-Induced Oscillations A Selective Review. Technical report, Naval Postgraduate School, 1979. URL http://asmedigitalcollection.asme.org/appliedmechanics/article-pdf/46/2/241/5877132/241_1.pdf.
- [19] Fanny M. Besem, Joshua D. Kamrass, Jeffrey P. Thomas, Deman Tang, and Robert E. Kielb. Vortex-Induced Vibration and Frequency Lock-In of an Airfoil at High Angles of Attack. *Journal of Fluids Engineering, Transactions of the ASME*, 138(1), 1 2016. ISSN 1528901X. doi: 10.1115/1.4031134.
- [20] Alberto Pellegrino and Craig Meskell. Vortex shedding from a wind turbine blade section at high angles of attack. *Journal of Wind Engineering and Industrial Aerodynamics*, 121:131–137, 2013. ISSN 01676105. doi: 10.1016/j.jweia.2013.08.002.
- [21] Lokanna Hoskoti, Ajay Misra, and Mahesh M. Sucheendran. Frequency lock-in during vortex induced vibration of a rotating blade. *Journal of Fluids and Structures*, 80:145–164, 7 2018. ISSN 10958622. doi: 10.1016/j.jfluidstructs.2018.03.011.
- [22] P W Bearman. VORTEX SHEDDING FROM OSCILLATING BLUFF BODIES. Technical report, Imperial College, London, 1984. URL www.annualreviews.org.

- [23] Chris C Critzos, Harry H Heyson, and Robert W Boswinkle. NATIONAL ADVISORY COMMITTEE FOR AERONAUTICS TECHNICAL NOTE 3361 AERODYNAMIC CHARACTERISTICS OF NACA 0012 AIRFOIL SECTION AT ANGLES OF ATTACK FROM 0° TO 180°. Technical report, National Advisory Committee for Aeronautics, Langley Field, 1 1955.
- [24] A Michos, G Bergeles, and N Athanassiadis. Aerodynamic Characteristics of NACA 0012 Airfoil in Relation to Wind Generators. Technical Report 4, National Technical University, Athens, 1983.
- [25] G. H. Yu, X. C. Zhu, and Z. H. Du. Numerical simulation of a wind turbine airfoil: Dynamic stall and comparison with experiments. *Proceedings of the Institution of Mechanical Engineers, Part A: Journal of Power and Energy*, 224(5):657–677, 1 2010. ISSN 09576509. doi: 10.1243/09576509JPE942.
- [26] Wenbo Wu and Jiasong Wang. Numerical simulation of VIV for a circular cylinder with a downstream control rod at low Reynolds number. *European Journal of Mechanics, B/Fluids*, 68:153–166, 3 2018. ISSN 09977546. doi: 10.1016/j.euromechflu.2017.12.005.
- [27] K. Sourav and Subhankar Sen. Transition of VIV-only motion of a square cylinder to combined VIV and galloping at low Reynolds numbers. *Ocean Engineering*, 187, 9 2019. ISSN 00298018. doi: 10.1016/j.oceaneng.2019.106208.
- [28] C. H.K. Williamson and R. Govardhan. A brief review of recent results in vortex-induced vibrations. *Journal of Wind Engineering and Industrial Aerodynamics*, 96 (6-7):713–735, 6 2008. ISSN 01676105. doi: 10.1016/j.jweia.2007.06.019.
- [29] A Khalak and C H K Williamson. MOTIONS, FORCES AND MODE TRANSITIONS IN VORTEX-INDUCED VIBRATIONS AT LOW MASS-DAMPING. Technical report, Cornell University, Ithaca, 7 1999. URL <http://www.idealibrary.comon>.
- [30] C H K Williamson and A Roshko. VORTEX FORMATION IN THE WAKE OF AN OSCILLATING CYLINDER. Technical report, California Institute of Technology, Pasadena, 1 1988.
- [31] N. Jauvtis and C. H.K. Williamson. Vortex-induced vibration of a cylinder with two degrees of freedom. *Journal of Fluids and Structures*, 17(7):1035–1042, 2003. ISSN 08899746. doi: 10.1016/S0889-9746(03)00051-3.
- [32] N. Jauvtis and C. H.K. Williamson. The effect of two degrees of freedom on vortex-induced vibration at low mass and damping. *Journal of Fluid Mechanics*, 509:23–62, 6 2004. ISSN 00221120. doi: 10.1017/S0022112004008778.
- [33] R E D Bishop and A Y Hassan. The Lift and Drag Forces on a Circular Cylinder Oscillating in a Flowing Fluid. Technical Report 1368, University College London, London, 1964. URL <https://about.jstor.org/terms>.

- [34] S. G. Horcas, N. N. Sørensen, F. Zahle, G. R. Pirrung, and T. Barlas. Vibrations of wind turbine blades in standstill: Mapping the influence of the inflow angles. *Physics of Fluids*, 34(5), 5 2022. ISSN 10897666. doi: 10.1063/5.0088036.
- [35] John Young and Joseph C.S. Lai. Vortex lock-in phenomenon in the wake of a plunging airfoil. *AIAA Journal*, 45(2):485–490, 2 2007. ISSN 00011452. doi: 10.2514/1.23594.
- [36] J. C.S. Lai and M. F. Platzer. Jet characteristics of a plunging airfoil. *AIAA journal*, 37(12):1529–1537, 1999. ISSN 00011452. doi: 10.2514/2.641.
- [37] J. Young and J. C.S. Lai. Oscillation frequency and amplitude effects on the wake of a plunging airfoil. *AIAA Journal*, 42(10):2042–2052, 2004. ISSN 00011452. doi: 10.2514/1.5070.
- [38] C. H. K. Williamson. The existence of two stages in the transition to three-dimensionality of a cylinder wake. *Physics of Fluids*, 31(11):3165, 1988. ISSN 00319171. doi: 10.1063/1.866925.
- [39] Jesoon Choi, Tim Colonius, and David R. Williams. Surging and plunging oscillations of an airfoil at low Reynolds number. *Journal of Fluid Mechanics*, 763:237–253, 1 2015. ISSN 14697645. doi: 10.1017/jfm.2014.674.
- [40] B. W. Van Oudheusden. PIV-based pressure measurement. *Measurement Science and Technology*, 24(3), 2013. ISSN 13616501. doi: 10.1088/0957-0233/24/3/032001.
- [41] F Noca, D Shiels, and D Jeon. Measuring Instantaneous Fluid Dynamic Forces on Bodies, using Only Velocity Fields and Their Derivatives. Technical report, California Institute of Technology, Pasadena, 1 1997.
- [42] F Noca, D Shiels, and D Jeon. A COMPARISON OF METHODS FOR EVALUATING TIME-DEPENDENT FLUID DYNAMIC FORCES ON BODIES, USING ONLY VELOCITY FIELDS AND THEIR DERIVATIVES. Technical report, California Institute of Technology, Pasadena, 3 1999. URL <http://www.idealibrary.com>.
- [43] B. W. Van Oudheusden, F. Scarano, E. W.M. Roosenboom, E. W.F. Casimiri, and L. J. Souverein. Evaluation of integral forces and pressure fields from planar velocimetry data for incompressible and compressible flows. *Experiments in Fluids*, 43(2-3):153–162, 1 2007. ISSN 07234864. doi: 10.1007/s00348-007-0261-y.
- [44] Bas W van Oudheusden, Eric WF Casimiri, and Fulvio Scarano. Aerodynamic Load Measurement of a Low Speed Airfoil using Particle Image Velocimetry. Technical report, Delft University of Technology, Delft, 1 2007.
- [45] Joel H Ferziger and Milovan Perić. Computational methods for fluid dynamics, 2002.

- [46] Stephen B Pope. *Turbulent flows*. Cambridge university press, 2000. ISBN 0521598869.
- [47] Florian R Menter. Improved two-equation k-omega turbulence models for aerodynamic flows. Technical report, National Aeronautics and Space Administration, 10 1992.
- [48] N N Mansour, J Kim, and P Moin. Near-wall k-epsilon turbulence modeling. *AIAA journal*, 27(8):1068–1073, 1989. ISSN 0001-1452.
- [49] D C Wilcox. Turbulence Modelling For CFD 3rd ed (La Canada Flintridge, CA: DCW Industries Inc.). *The Aeronautical Journal*, 2006.
- [50] N Katopodes. Chapter 8—Turbulent Flow. *Free-Surface Flow; Environmental Fluid Mechanics; Butterworth: Oxford, UK*, pages 540–615, 2019.
- [51] Massimo Germano, Ugo Piomelli, Parviz Moin, and William H Cabot. A dynamic subgrid-scale eddy viscosity model. *Physics of Fluids A: Fluid Dynamics*, 3(7): 1760–1765, 1991. ISSN 0899-8213.
- [52] Florian R Menter, Martin Kuntz, and Robin Langtry. Ten years of industrial experience with the SST turbulence model. *Turbulence, heat and mass transfer*, 4 (1):625–632, 2003.
- [53] Philippe R Spalart, Shur Deck, Michael L Shur, Kyle D Squires, M Kh Strelets, and Andrei Travin. A new version of detached-eddy simulation, resistant to ambiguous grid densities. *Theoretical and computational fluid dynamics*, 20:181–195, 2006. ISSN 0935-4964.
- [54] Mikhail L Shur, Philippe R Spalart, Mikhail Kh Strelets, and Andrey K Travin. A hybrid RANS-LES approach with delayed-DES and wall-modelled LES capabilities. *International journal of heat and fluid flow*, 29(6):1638–1649, 2008. ISSN 0142-727X.
- [55] Mikhail S. Gritskevich, Andrey V. Garbaruk, Jochen Schütze, and Florian R. Menter. Development of DDES and IDDES formulations for the k- ω shear stress transport model. *Flow, Turbulence and Combustion*, 88(3):431–449, 4 2012. ISSN 13866184. doi: 10.1007/s10494-011-9378-4.
- [56] Witold Robert Skrzypiński, Mac Gaunaa, Niels Sørensen, Frederik Zahle, and Joachim Heinz. Self-induced vibrations of a DU96-W-180 airfoil in stall. *Wind Energy*, 17(4):641–655, 2014. ISSN 10991824. doi: 10.1002/we.1596.
- [57] Witold Skrzypiński, Mac Gaunaa, Niels Sørensen, Frederik Zahle, and Joachim Heinz. Vortex-induced vibrations of a DU96-W-180 airfoil at 90° angle of attack. *Wind Energy*, 17(10):1495–1514, 2014. ISSN 10991824. doi: 10.1002/we.1647.
- [58] Christian Grinderslev. *General rights Fluid-Structure Interaction for Wind Turbines in Atmospheric Flow*. PhD thesis, Technical University of Denmark, DTU Risø Campus, Roskilde, 12 2020. URL <https://doi.org/10.11581/dtu:00000104>.

-
- [59] Christian Grinderslev, Niels Nørmark Sørensen, Sergio González Horcas, Niels Troldborg, and Frederik Zahle. Wind turbines in atmospheric flow-FSI simulations with hybrid LES-IDDES turbulence modelling. *Wind Energy Science*, 12 2020. doi: 10.5194/wes-2020-122. URL <https://doi.org/10.5194/wes-2020-122>.
- [60] Wei Yu. *The wake of an unsteady actuator disc*. PhD thesis, Delft University of Technology, 2018. URL <https://doi.org/10.4233/uuid:0e3a2402-585c-41b1->.
- [61] Hisham A H Al-Khazali and Mohamad R Askari. Geometrical and Graphical Representations Analysis of Lissajous Figures in Rotor Dynamic System. 2(5): 971–978, 2012. ISSN 2250-3021. URL www.iosrjen.org.
- [62] Witold Skrzypiński and Mac Gaunaa. Wind turbine blade vibration at standstill conditions - The effect of imposing lag on the aerodynamic response of an elastically mounted airfoil. *Wind Energy*, 18(3):515–527, 3 2015. ISSN 10991824. doi: 10.1002/we.1712.
- [63] Craig Meskell and Alberto Pellegrino. Vortex shedding lock-in due to pitching oscillation of a wind turbine blade section at high angles of attack. *International Journal of Aerospace Engineering*, 2019, 2019. ISSN 16875974. doi: 10.1155/2019/6919505.

APPENDIX A

Aerodynamic Loads using the NOCA Method

The CFD simulations provided loads at 20 blade sections in the three directions. To attain the aerodynamic loads from the experimental PIV data, the NOCA method was used to determine the loads on the blade due to the flow around the blade within a pre-defined control volume.

A.1 Steady Case

As an initial validation, the NOCA method was used to validate the steady case. The chosen control volume was the maximum available flow field for the PIV results. The analysis was only done on the CFD data and the streamwise load is presented in Figure A.1 and the crossflow load is presented in Figure A.2.

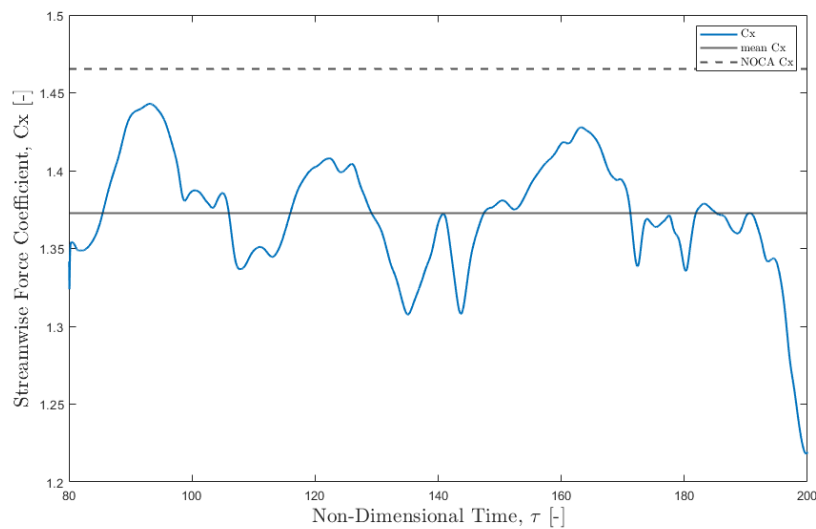


Figure A.1: Streamwise load calculation for a steady flow at $U_\infty = 5\text{m/s}$

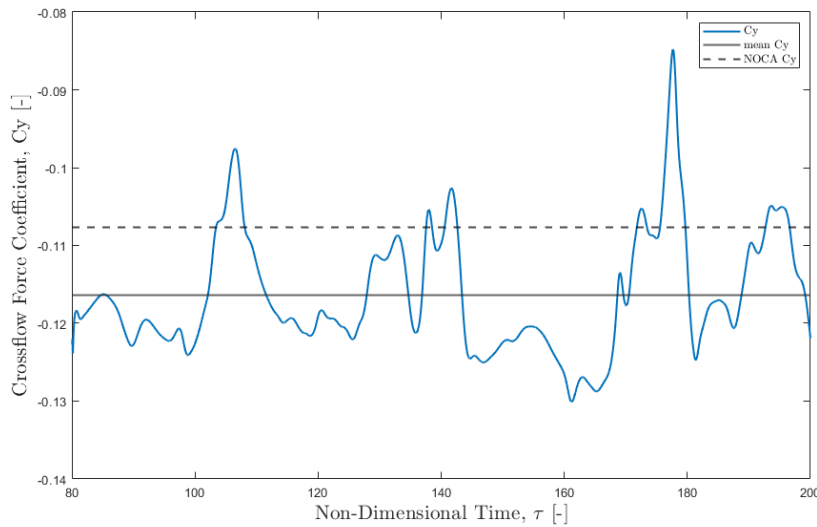


Figure A.2: Crossflow load calculation for a steady flow at $U_\infty = 5\text{m/s}$

The blue lines show the varying load against the non-dimensional time, with peaks and troughs seen in the load due to the von Karman like vortices shed behind the blade. The average load is calculated from the CFD time series and is presented as the solid line. The velocity fields are then averaged over the entire time series and the NOCA method is applied to it to calculate the load. The error in the streamwise load, C_x was -6.77% , and the error in the crossflow direction, C_y was 7.53% . The streamwise force was over-predicted and the crossflow force was under-predicted using the NOCA method, however, with a relatively small error.

A.2 Plunging 2.5Hz

The analysis was then done on the CFD data for the 2.5 Hz plunging airfoil. Various control volumes were defined, as seen in Figure A.5, and a sensitivity analysis was performed on the control volume size.

First, however, the average force in the streamwise and crossflow direction was calculated over the cycle. The phase average load was calculated as seen in Figure A.3.

The solid lines show the average load over all the cycles and the thinner lines show the load experienced over one specific cycle.

Next, seven different control volumes were defined, as seen in Figure A.5, and the relative error with respect to the average load from Figure A.3 was calculated. This was normalised against the error from control volume 1 since this is the largest possible control volume to calculate the load over. Relative to the average load, the streamwise force coefficients were within $\pm 10\%$, whereas the crossflow force coefficient ranged from 50 to 180% away from the average for the largest control volume seen in Figure A.4. The NOCA method only integrates the momentum due to the aerodynamic forces and hence, only calculates the aerodynamic force on the blade. During the plunging motion,

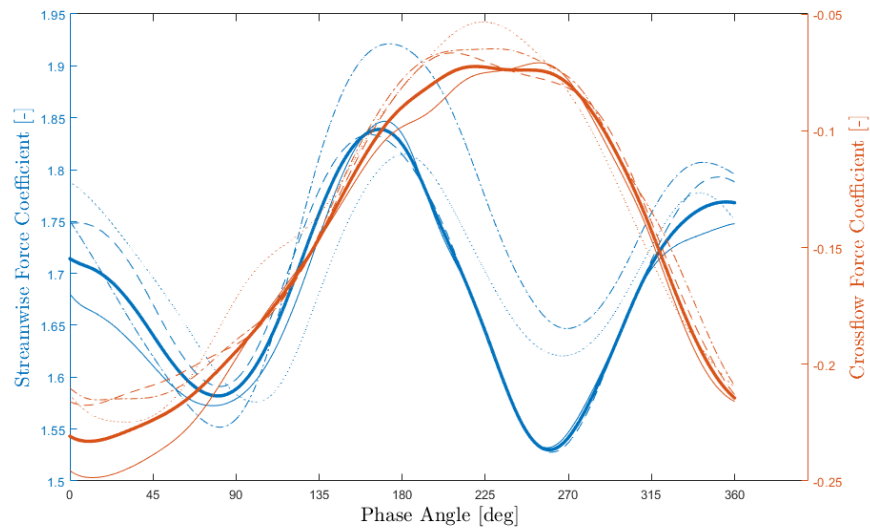


Figure A.3: Average Streamwise and Crossflow force coefficients (solid line)

however, the blade experiences high crossflow forces that are not due to aerodynamics and hence, are not captured by the NOCA analysis. This leads to a larger discrepancy in the crossflow load coefficients.

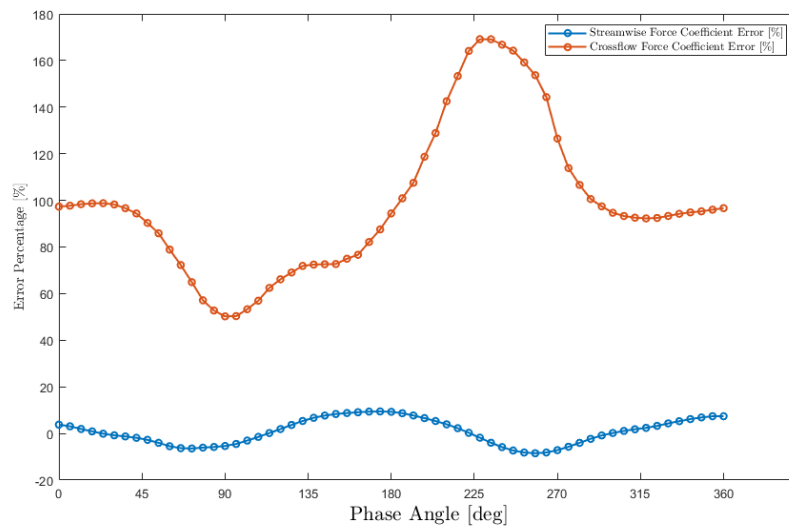


Figure A.4: Error between the largest Control Volume and CFD loads

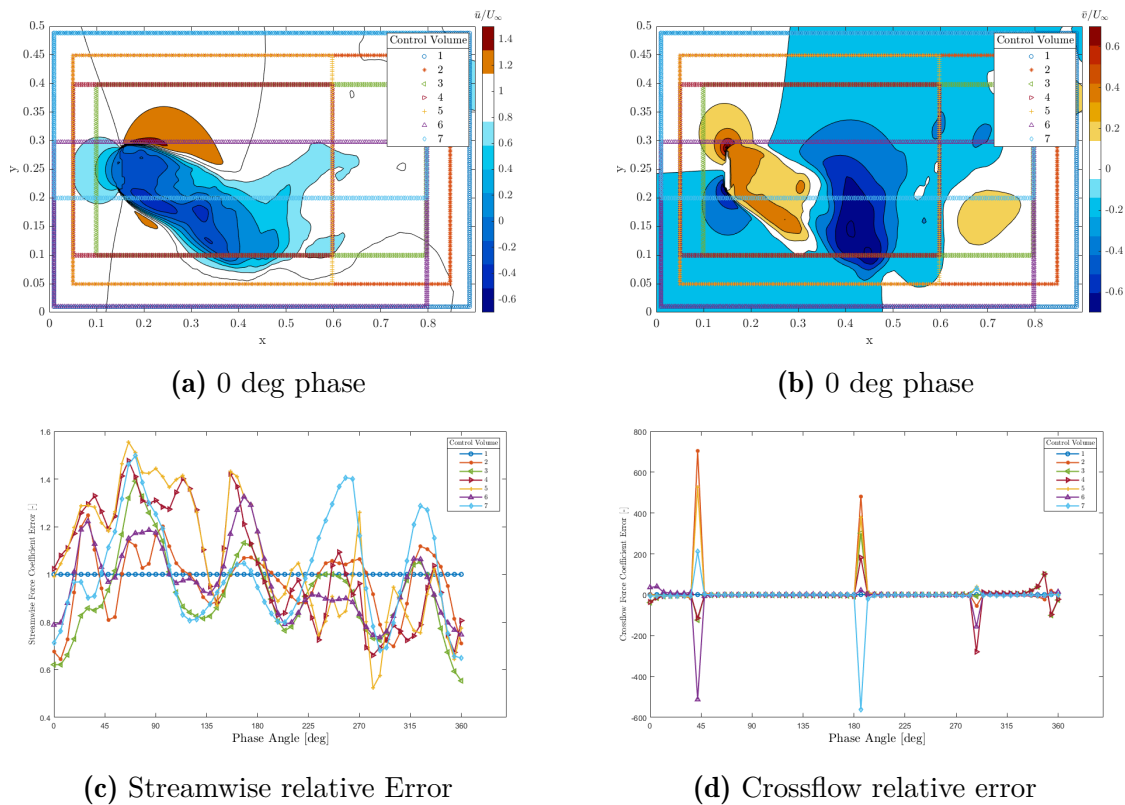


Figure A.5: Control Volumes around plunging airfoil at 2.5 Hz 3 chords inboard from the tip. Streamwise velocity field (left) and Crossflow/Vertical velocity field (right) and the relative error with respect to integrated blade loads 3 chords inboard from the tip.

The streamwise error is relatively low for all the defined control volumes, without significant differences between control volumes 4 and 5 with a shorter wake capture than the rest. This suggests that capturing most of the wake in the streamwise position, like in control volumes 4 and 5, is sufficient for the streamwise load. For the crossflow force coefficient, however, there are a few points with significant differences in the load. These occur at around 45 deg, 180 deg, 270 deg, and close to 0 deg phase. Control volume 6, in purple, shows a high negative error around 45 deg. This control volume only captures the lower half of the flow and does not capture data between around 45 deg phase and 135 deg phase. This could be why there is such a large error at 45 deg because a large portion of the shed flow is missing from the control volume. However, this is still the opposite of what is expected, because at 45 deg, the wake should be captured by the control volume, and there should be a large deviation from 45 to 135 deg which is not seen. Similarly, control volume 7 shows a large negative error around 180 deg, though it misses information between 135 and 225 deg. Strangely, the largest error is seen in control volume 2, which is the second largest control volume and hence, it captures most of the flow instabilities. The sensitivity study is limited and requires much deeper analysis to have a more reasonable conclusion. However, this analysis does show that even the largest control volume is not sufficiently large enough to capture the loads in

such an unsteady motion.

A.3 Plunging 5Hz

Figure A.6 presents the averaged force coefficients for a plunging airfoil at 5 Hz. Already the loads calculated from the CFD simulations are not smooth and sinusoidal like for 2.5 Hz. This was already seen earlier in Figure 3.12 and Figure 3.13, where the time series plots were much more chaotic at 5 Hz than at 2.5 Hz.

The streamwise force coefficient error was between 180 and 450 % and the crossflow force coefficient error was between -170 and 700% seen in Figure A.7.

Even the largest control volume presents an extremely large error compared to CFD blade loads. Nevertheless, the same seven control volumes were tested for the 5 Hz plunging blade to see if any trends could be identified.

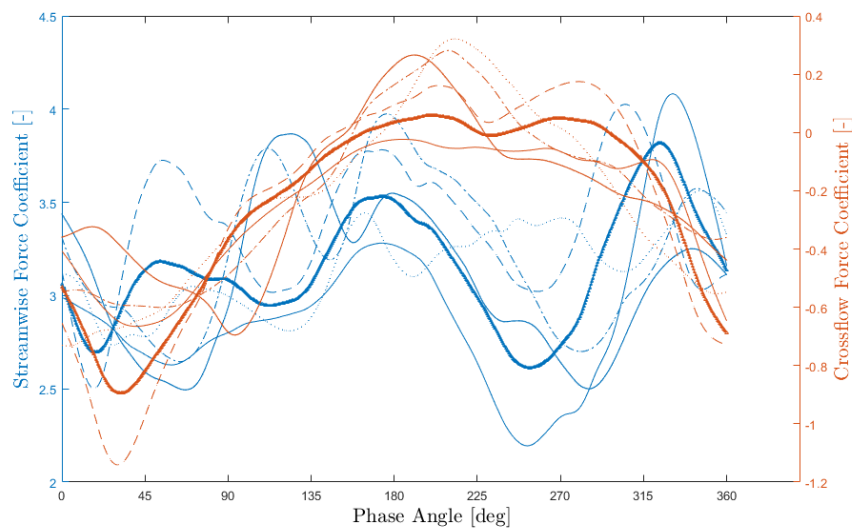


Figure A.6: Average Streamwise and Crossflow force coefficients (solid line)

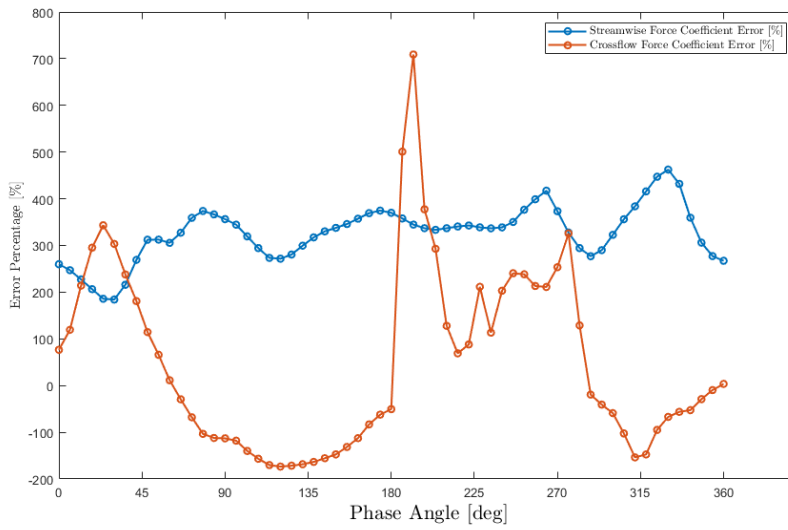


Figure A.7: Error between the largest Control Volume and CFD loads

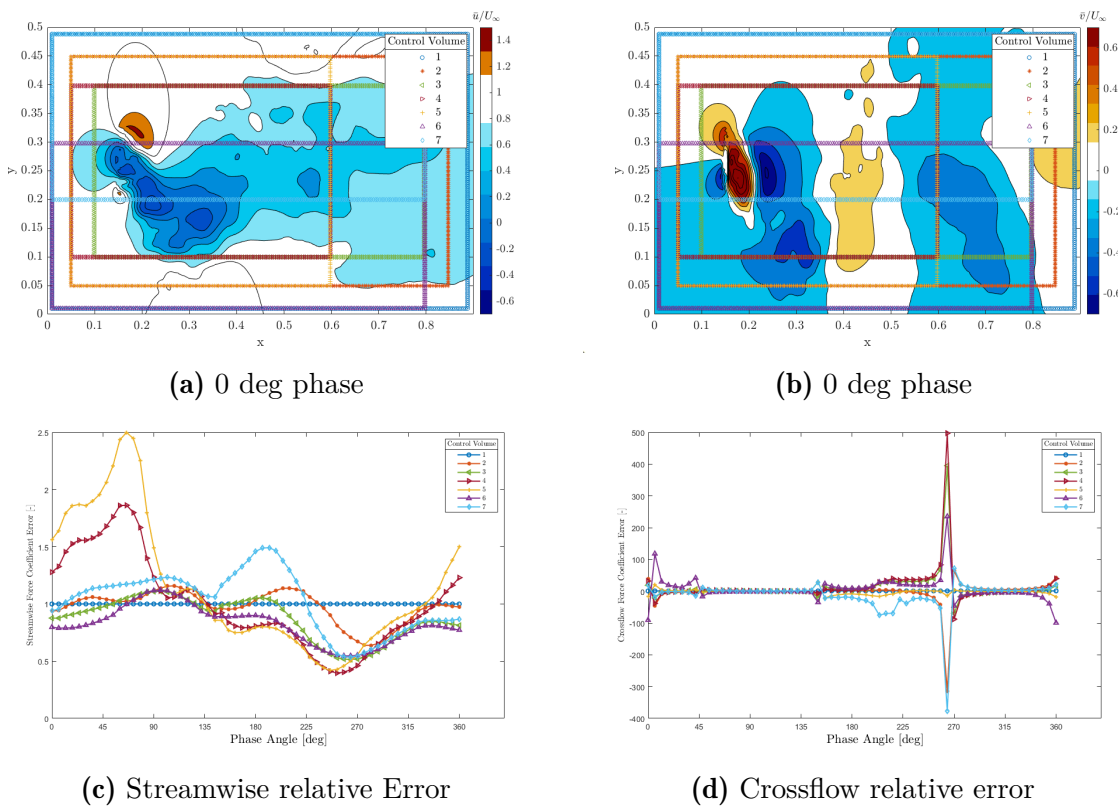


Figure A.8: Control Volumes around plunging airfoil at 5 Hz 3 chords inboard from the tip. Streamwise velocity field (left) and Crossflow/Vertical velocity field (right) and the relative error with respect to integrated blade loads 3 chords inboard from the tip.

Figure A.8 presents the control volumes as well as the streamwise and crossflow errors relative to the largest control volume. For the streamwise error, a significantly larger error is seen for control volumes 4 and 5 which do not capture the full wake, which is expected. In general, the streamwise errors are higher around 45 deg and 225 deg, suggesting that the inertia of the flow may have some effect on the load since it is 45 deg after the maximum velocity at each point in the cycle at 0 and 180 deg. The crossflow error is particularly high at 270 deg for all the control volumes, with negative errors for control volumes 2 and 7, that capture a short wake and only the top half of the flow respectively. The result for control volume 7 makes sense since it is not able to capture the flow at 270 deg at all and hence, greatly under-predicts the load. The rest of the control volumes show an over-prediction of the load at 270 deg, which could be due to the large unsteady effects of the sharp trailing edge. However, in general, the errors between the load calculated using the NOCA method and the CFD data are too large to consider the method accurate. A larger control volume is needed to have a more accurate load estimation. These discrepancies are expected between the NOCA method and the CFD loads since the NOCA method only integrates the momentum from the aerodynamic forces and does not take into account the crossflow forcing for the plunging blade. This is also why the errors are significantly larger in the crossflow direction.

The NOCA method was not used to analyse the surging cases since the streamwise forcing on the blade is much larger than the crossflow forcing experienced by the plunging blade. This would result in an even larger discrepancy in the calculated loads.

The NOCA method was used to evaluate the loads on a static blade and for a plunging blade. An analysis of the force coefficients of a static blade showed an error of around 7% for both the streamwise and crossflow directions. Large discrepancies were seen even for the largest control volume for the plunging blade, with a much higher error in the crossflow direction. The errors were also larger for a 5 Hz blade compared to a 2.5 Hz blade.

APPENDIX B

CFD Static Cases Implicit Large Eddy Simulation with Aspect Ratio 10

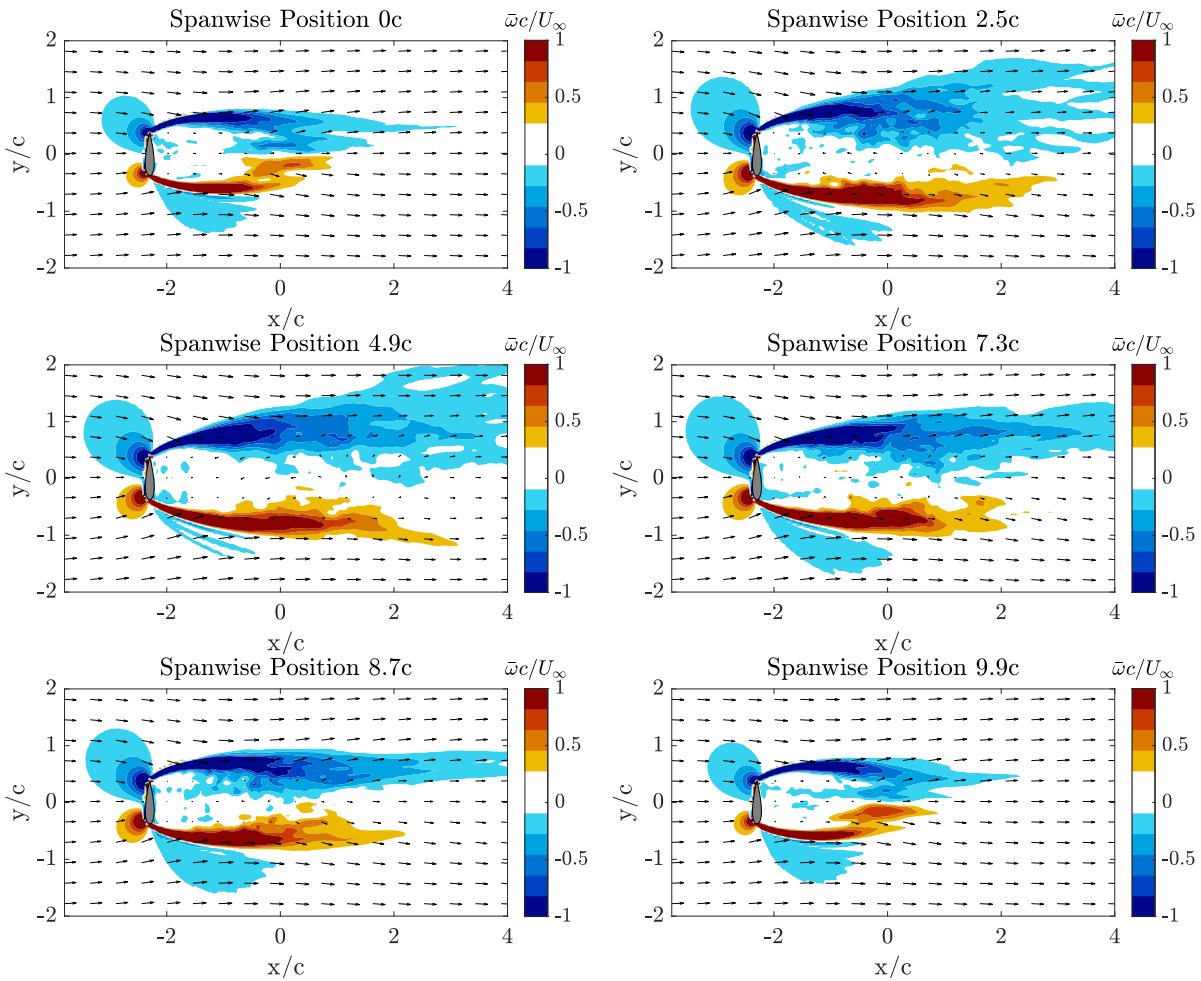


Figure B.1: Vorticity, $\bar{\omega}c/U_\infty$ around a static blade using an Implicit LES, with a blade aspect ratio of 10. The blade is free on both ends, with a symmetry boundary condition at the mid-plane. Freestream velocity coming from the left.

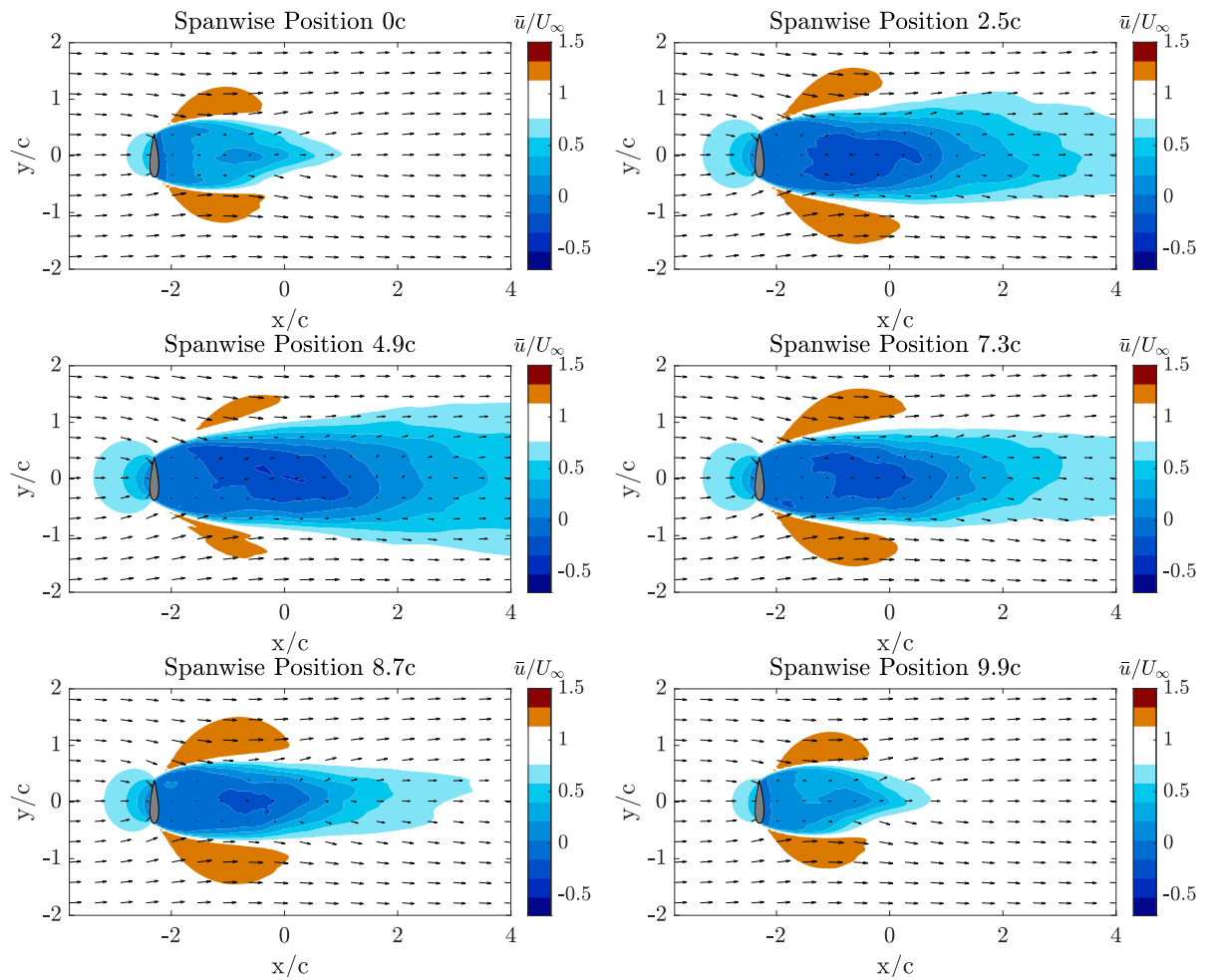


Figure B.2: Streamwise velocity, \bar{u}/U_∞ around a static blade using an Implicit LES, with a blade aspect ratio of 10. The blade is free on both ends, with a symmetry boundary condition at the mid-plane. Freestream velocity coming from the left.

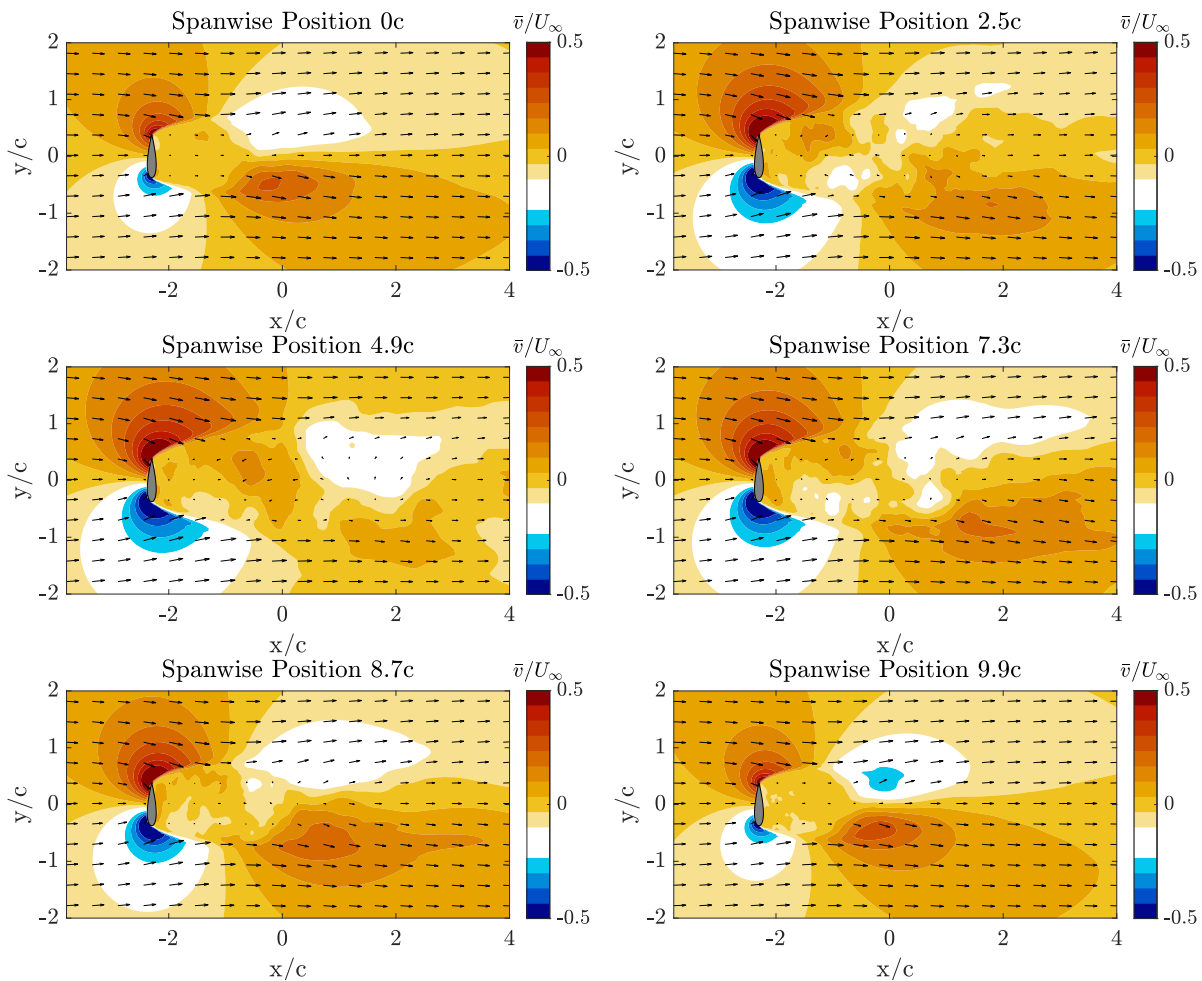


Figure B.3: Vertical velocity, \bar{v}/U_∞ around a static blade using an Implicit LES, with a blade aspect ratio of 10. The blade is free on both ends, with a symmetry boundary condition at the mid-plane. Freestream velocity coming from the left.

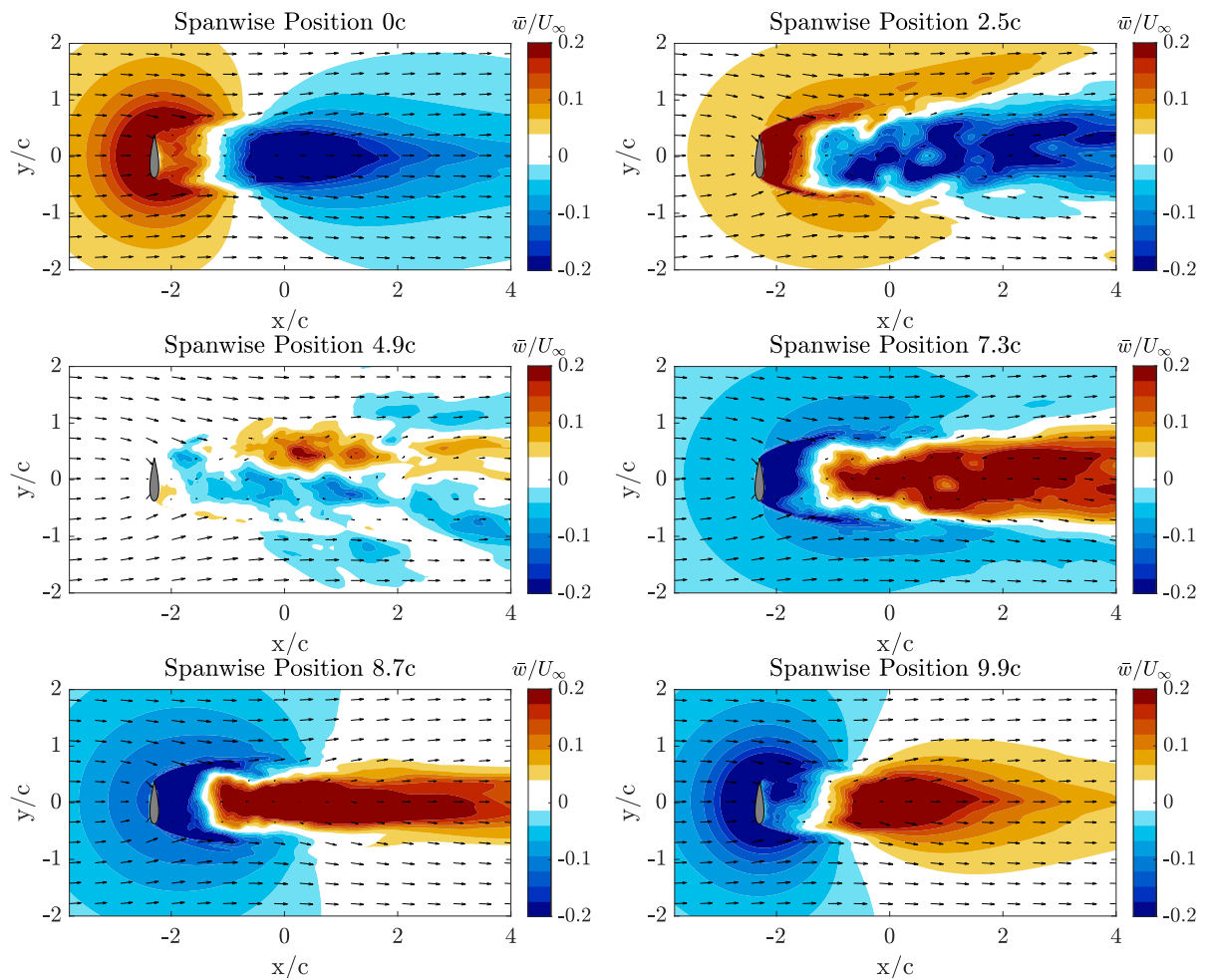


Figure B.4: Spanwise velocity, \bar{w}/U_∞ around a static blade using an Implicit LES, with a blade aspect ratio of 10. The blade is free on both ends, with a symmetry boundary condition at the mid-plane. The flow is positive into the page. Freestream velocity coming from the left.

APPENDIX C

CFD Static Cases Implicit Large Eddy Simulation with Aspect Ratio 20

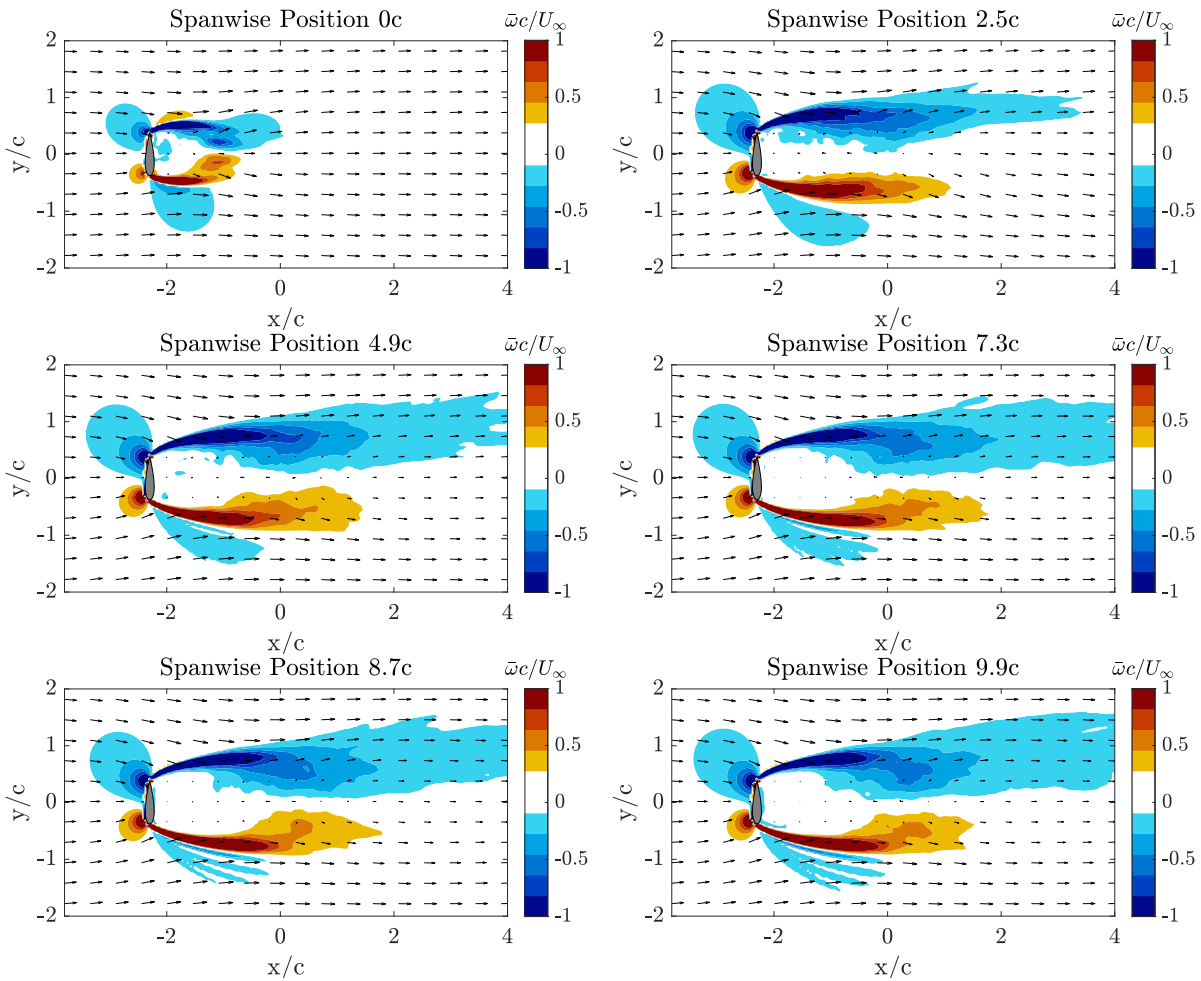


Figure C.1: Vorticity, $\bar{\omega}c/U_\infty$ around a static blade using an Implicit LES, with a blade aspect ratio of 20. The blade is free on both ends, with a symmetry boundary condition at the mid-plane. Freestream velocity coming from the left.

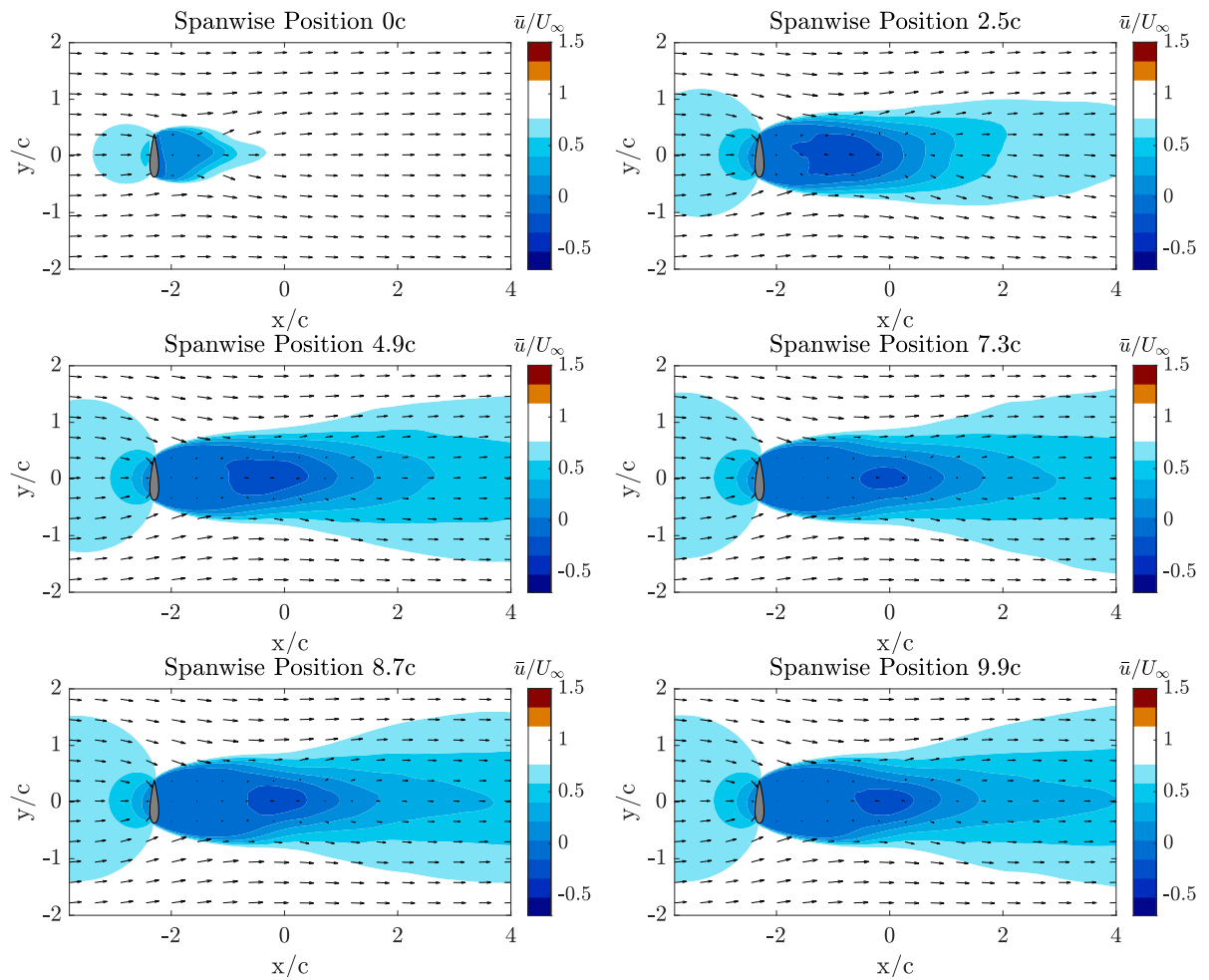


Figure C.2: Streamwise velocity, \bar{u}/U_∞ around a static blade using an Implicit LES, with a blade aspect ratio of 20. The blade is free on both ends, with a symmetry boundary condition at the mid-plane. Freestream velocity coming from the left.

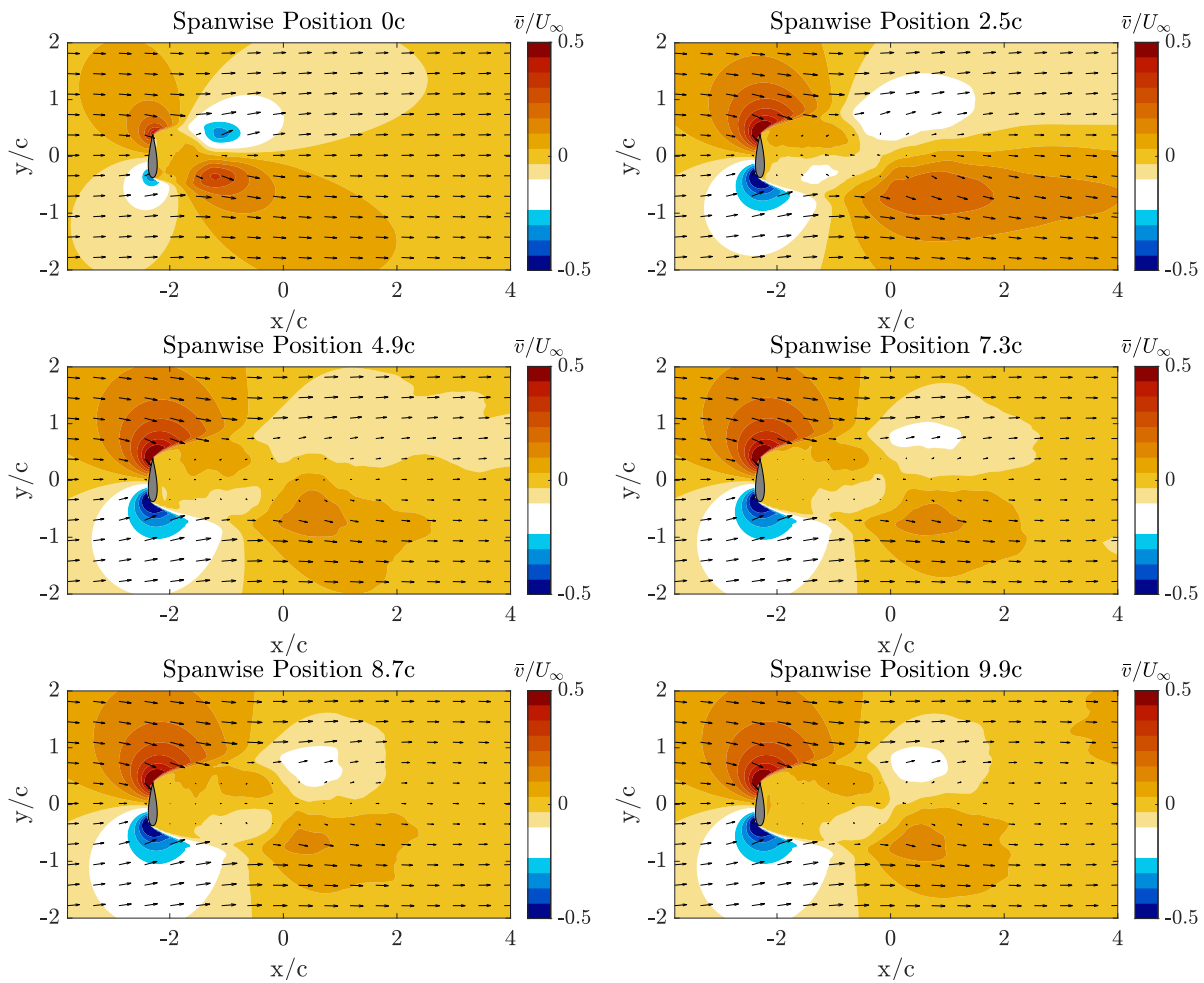


Figure C.3: Vertical velocity, \bar{v}/U_∞ around a static blade using an Implicit LES, with a blade aspect ratio of 20. The blade is free on both ends, with a symmetry boundary condition at the mid-plane. Freestream velocity coming from the left.

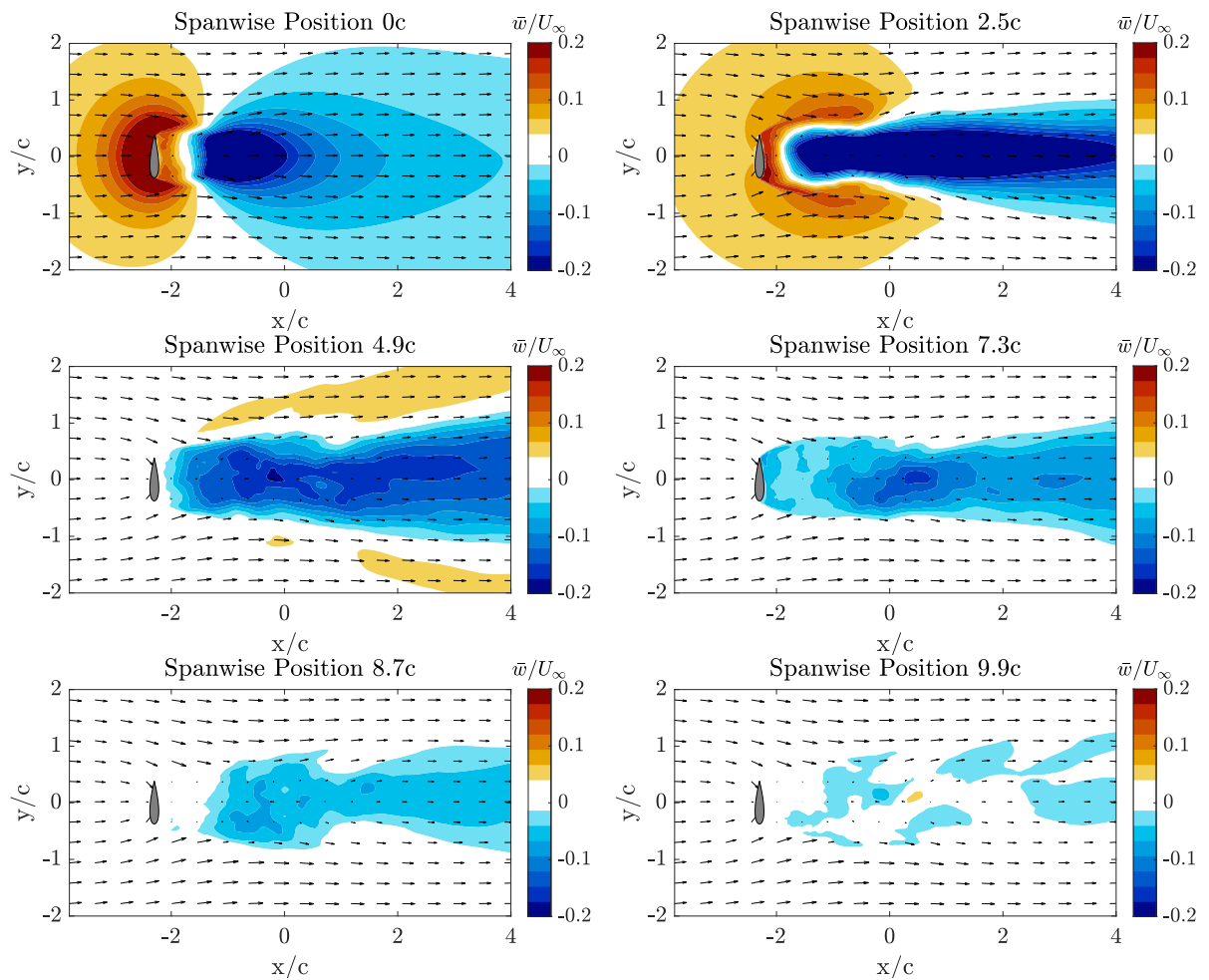


Figure C.4: Spanwise velocity, \bar{w}/U_∞ around a static blade using an Implicit LES, with a blade aspect ratio of 20. The blade is free on both ends, with a symmetry boundary condition at the mid-plane. The flow is positive into the page. Freestream velocity coming from the left.

APPENDIX D

CFD Static Cases Improved Delayed Detached Eddy Simulation with Aspect Ratio 10

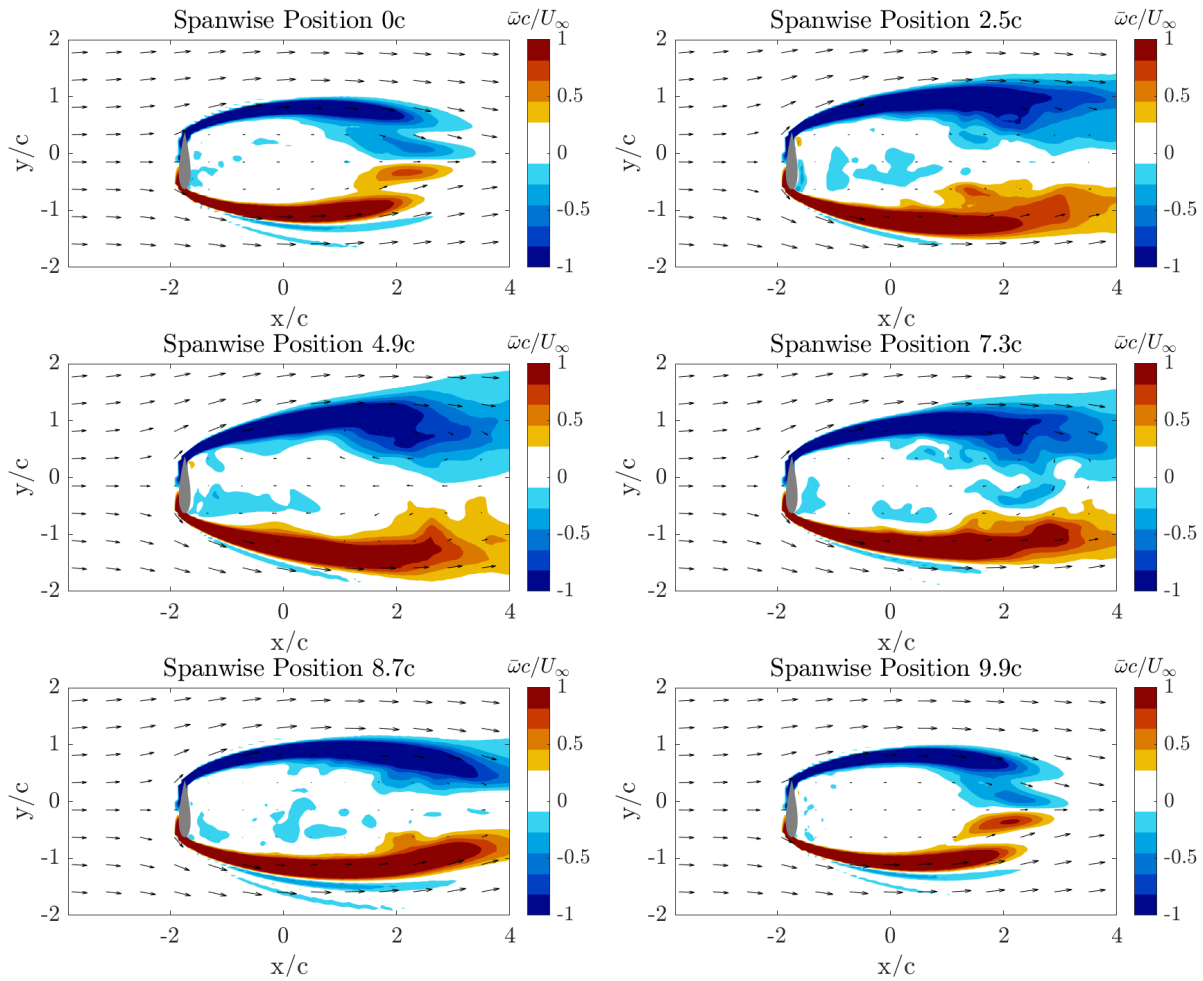


Figure D.1: Vorticity, $\bar{\omega}c/U_\infty$ around a static blade using an IDDES simulation, with a blade aspect ratio of 10. The blade is free on both ends, with a symmetry boundary condition at the mid-plane. Freestream velocity coming from the left.

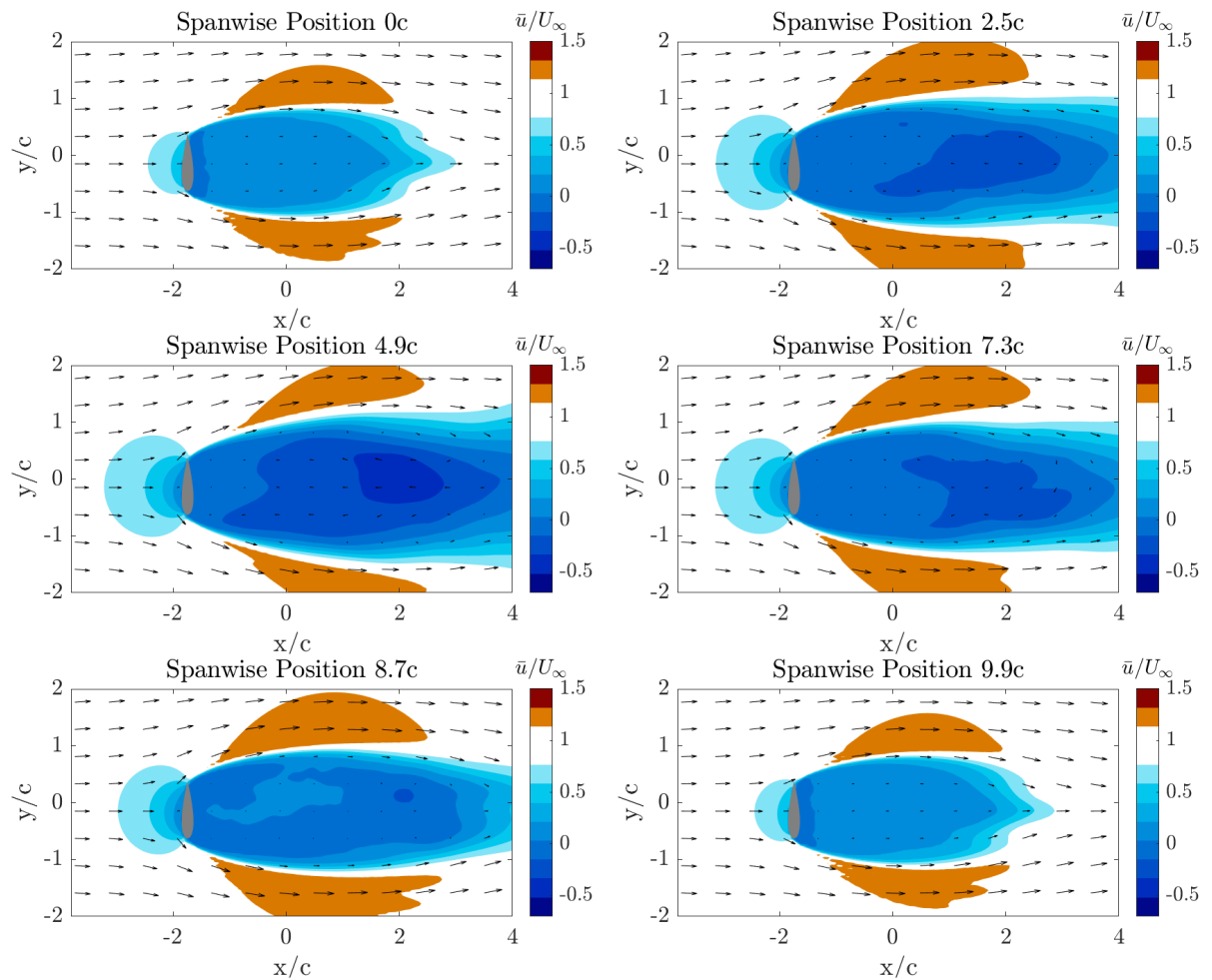


Figure D.2: Streamwise velocity, \bar{u}/U_∞ around a static blade using an IDDES simulation, with a blade aspect ratio of 10. The blade is free on both ends, with a symmetry boundary condition at the mid-plane. Freestream velocity coming from the left.

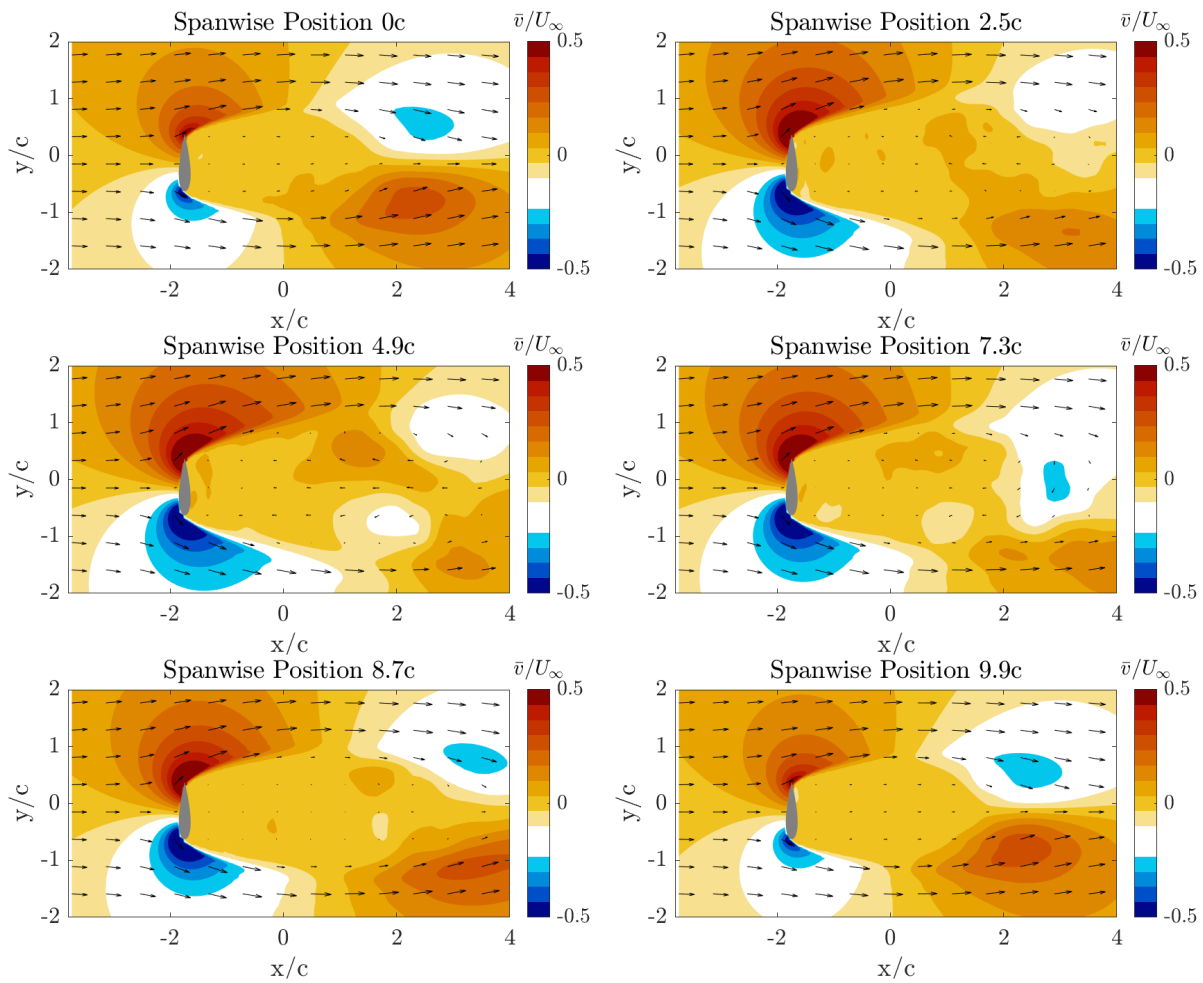


Figure D.3: Vertical velocity, \bar{v}/U_∞ around a static blade using an IDDES simulation, with a blade aspect ratio of 10. The blade is free on both ends, with a symmetry boundary condition at the mid-plane. Freestream velocity coming from the left.

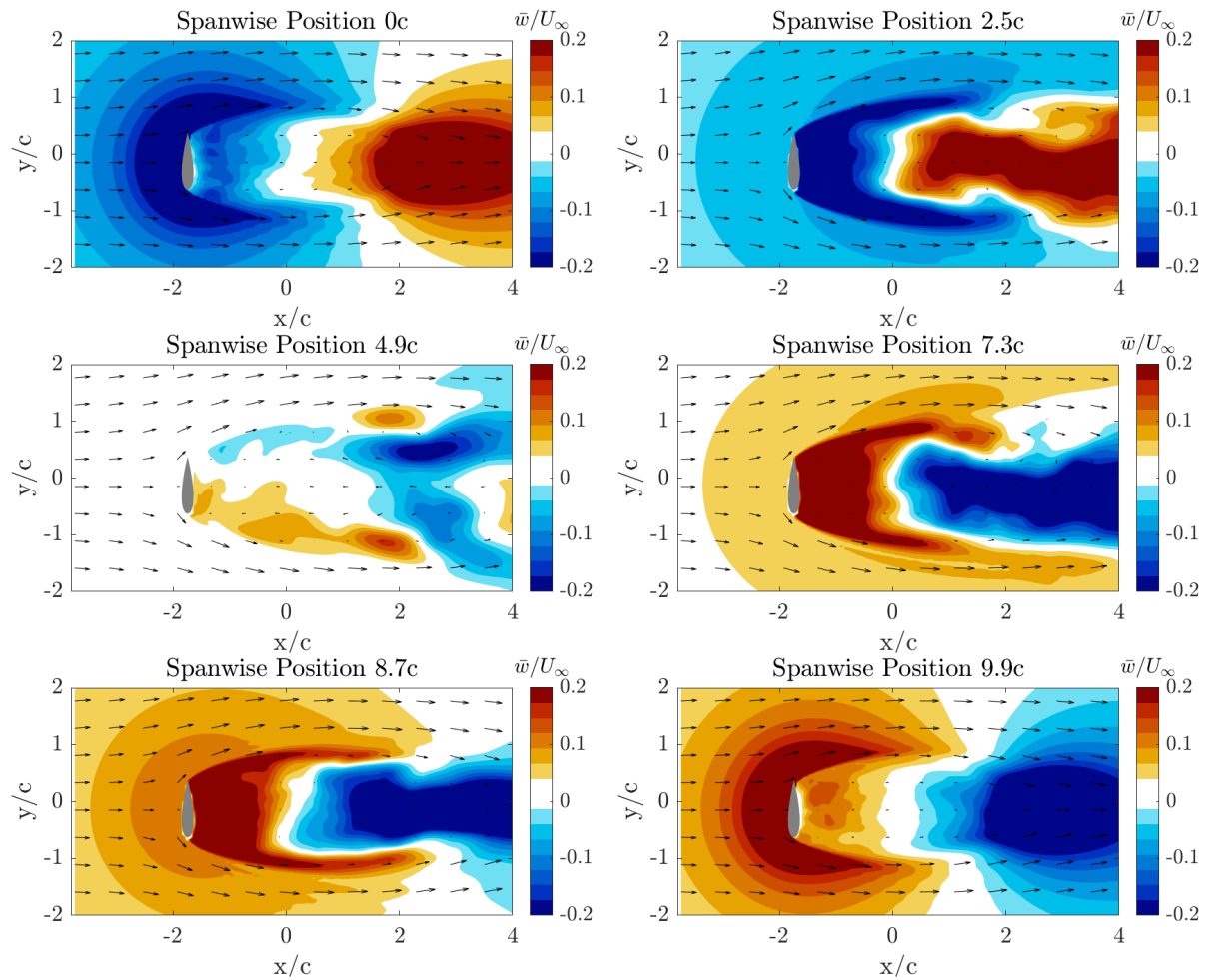


Figure D.4: Spanwise velocity, \bar{w}/U_∞ around a static blade using an IDDES simulation, with a blade aspect ratio of 10. The blade is free on both ends, with a symmetry boundary condition at the mid-plane. The flow is positive into the page. Freestream velocity coming from the left.

APPENDIX E

Static Cases for an 81 cm
blade, $U_{\infty} = 5 \text{ m/s}$

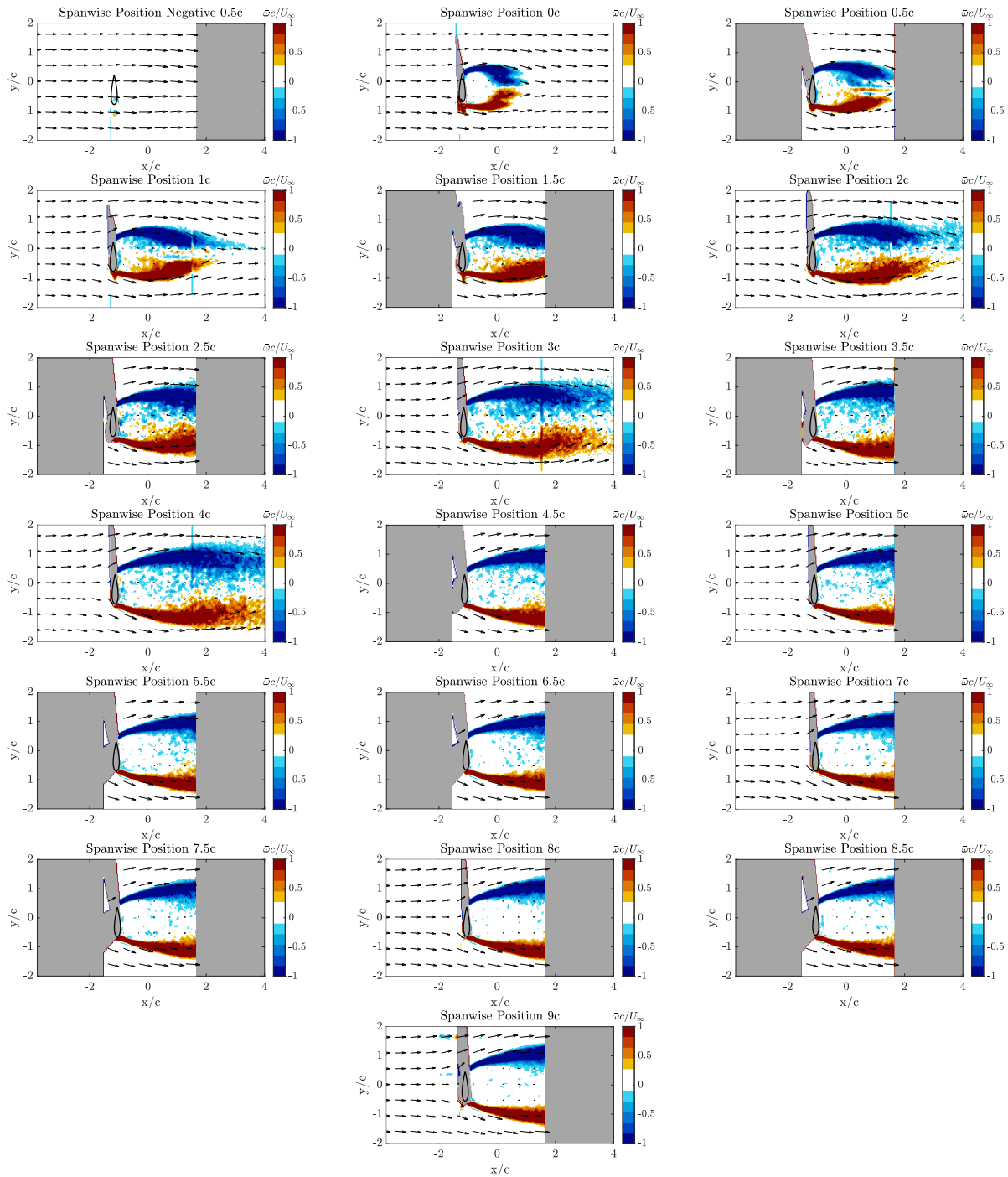


Figure E.1: Vorticity, $\bar{\omega}c/U_\infty$ around a static blade from 0.5c in front of the tip to 9c inboard, freestream velocity coming from the left. Grey portions of the plot indicate no available data.

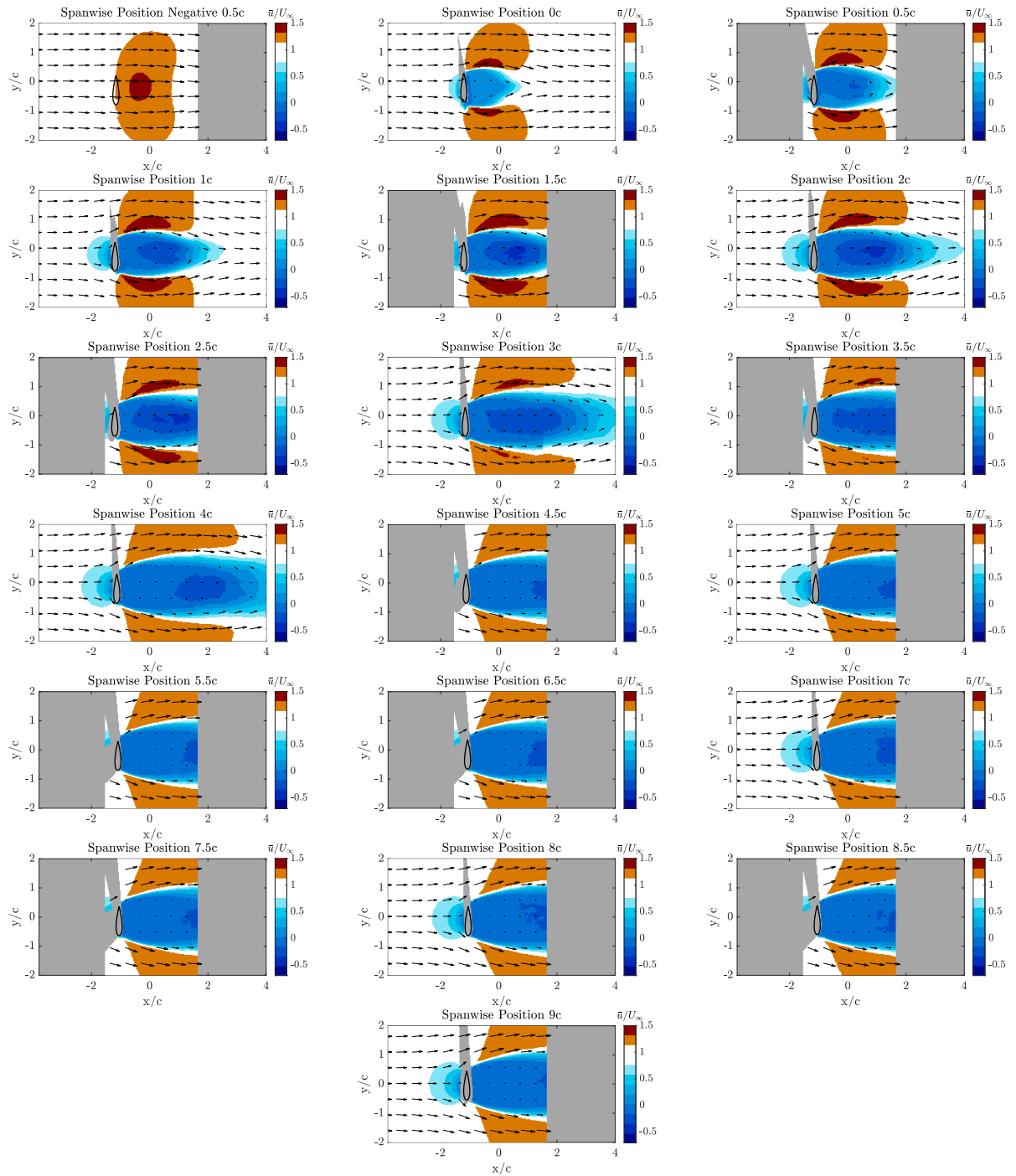


Figure E.2: Streamwise velocity, \bar{u}/U_∞ around a static blade from 0.5c in front of the tip to 9c inboard, freestream velocity coming from the left. Grey portions of the plot indicate no available data.

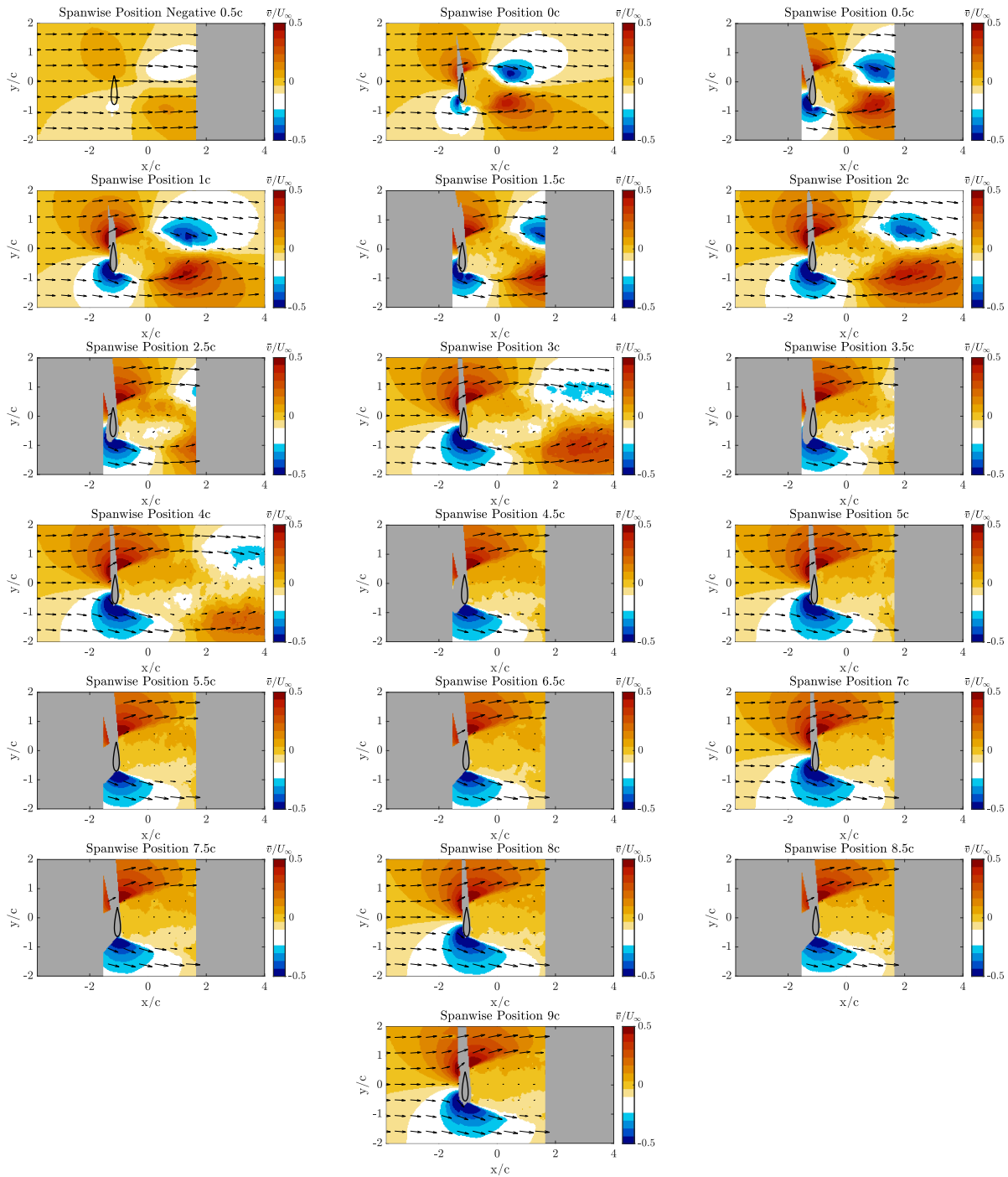


Figure E.3: Vertical velocity, \bar{v}/U_∞ around a static blade from 0.5c in front of the tip to 9c inboard, freestream velocity coming from the left. Grey portions of the plot indicate no available data.

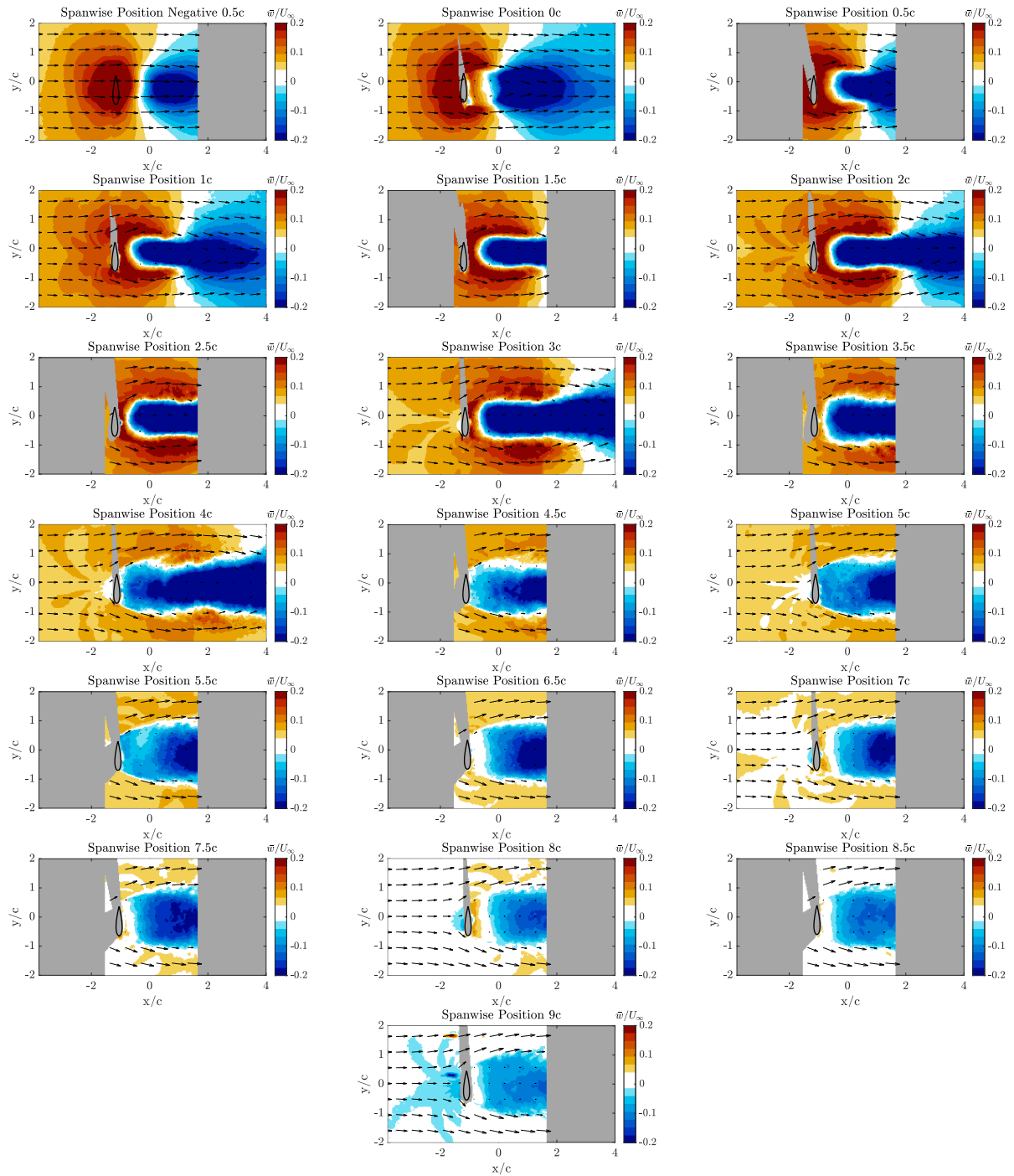


Figure E.4: Spanwise velocity, \bar{w}/U_∞ around a static blade from 0.5c in front of the tip to 9c inboard, freestream velocity coming from the left. The flow is positive into the page. Grey portions of the plot indicate no available data.

APPENDIX F

Static Cases for a 40 cm blade,

$$U_{\infty} = 5 \text{ m/s}$$

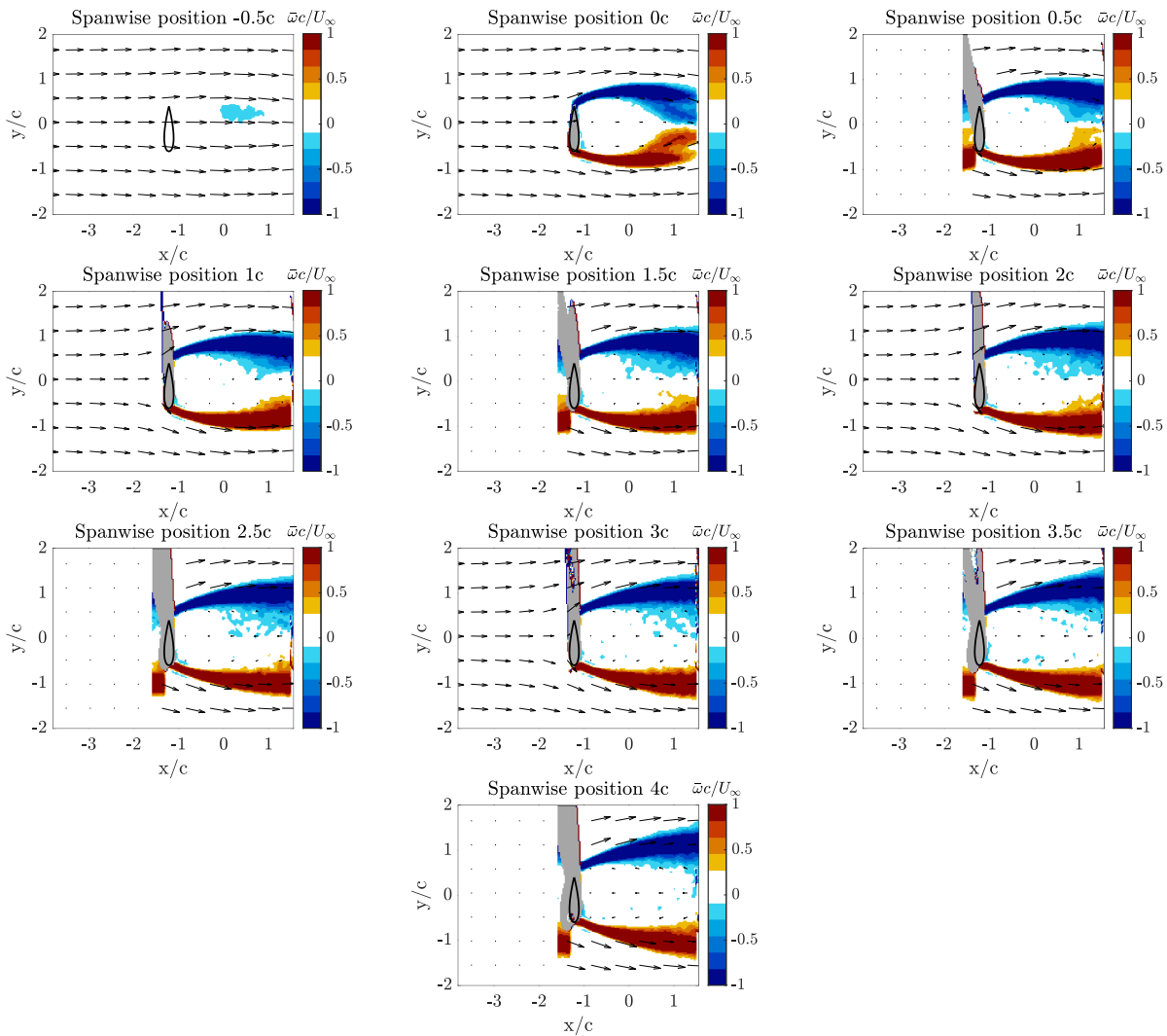


Figure F.1: Vorticity, $\bar{\omega}c/U_\infty$ around a static blade from 0.5c in front of the tip to 4c inboard, freestream velocity coming from the left. White portions of the plot without velocity vectors indicate no available data.

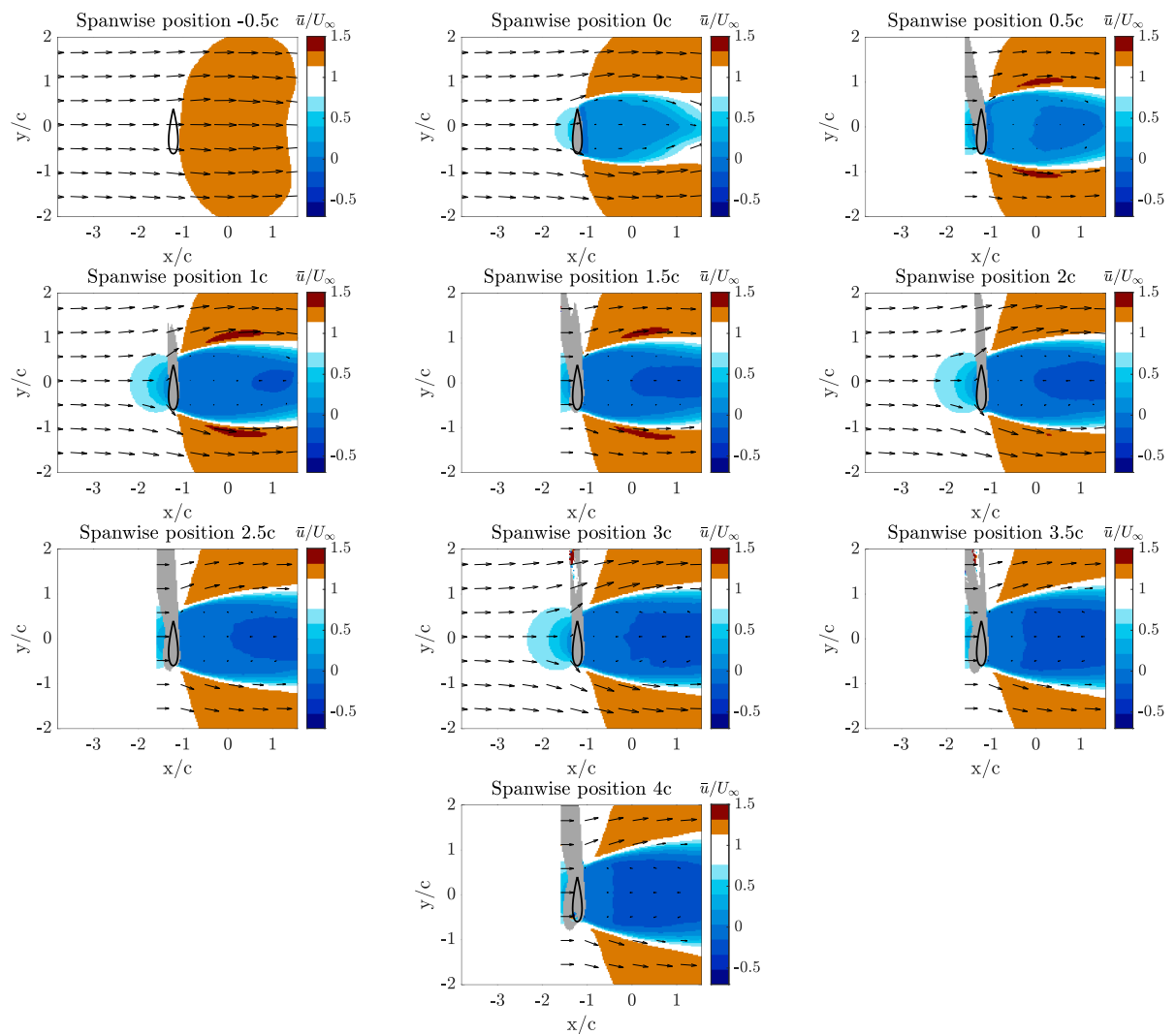


Figure F.2: Streamwise velocity, \bar{u}/U_∞ around a static blade from $0.5c$ in front of the tip to $4c$ inboard, freestream velocity coming from the left. White portions of the plot without velocity vectors indicate no available data.

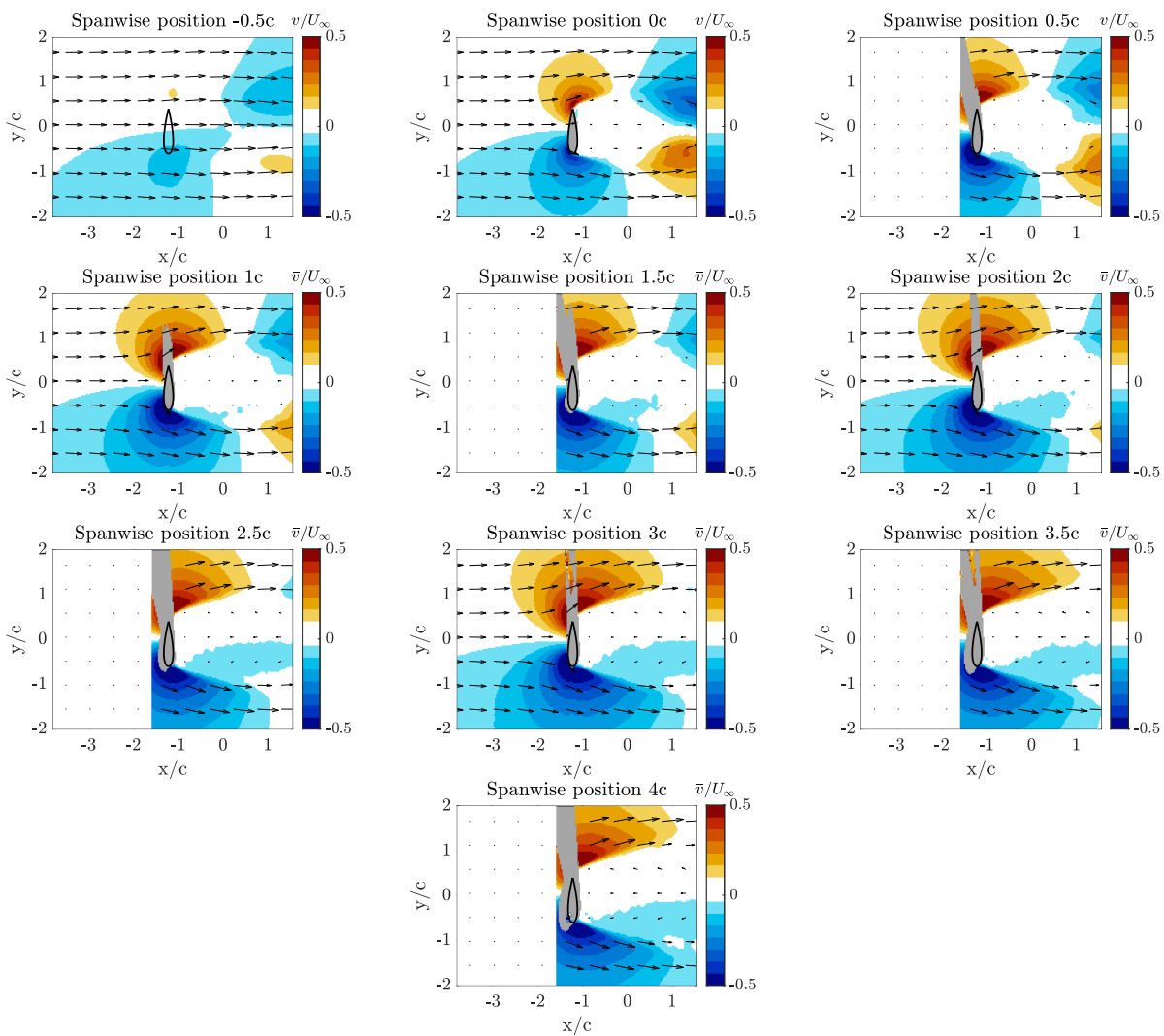


Figure F.3: Vertical velocity, \bar{v}/U_∞ around a static blade from $0.5c$ in front of the tip to $4c$ inboard, freestream velocity coming from the left. White portions of the plot without velocity vectors indicate no available data.

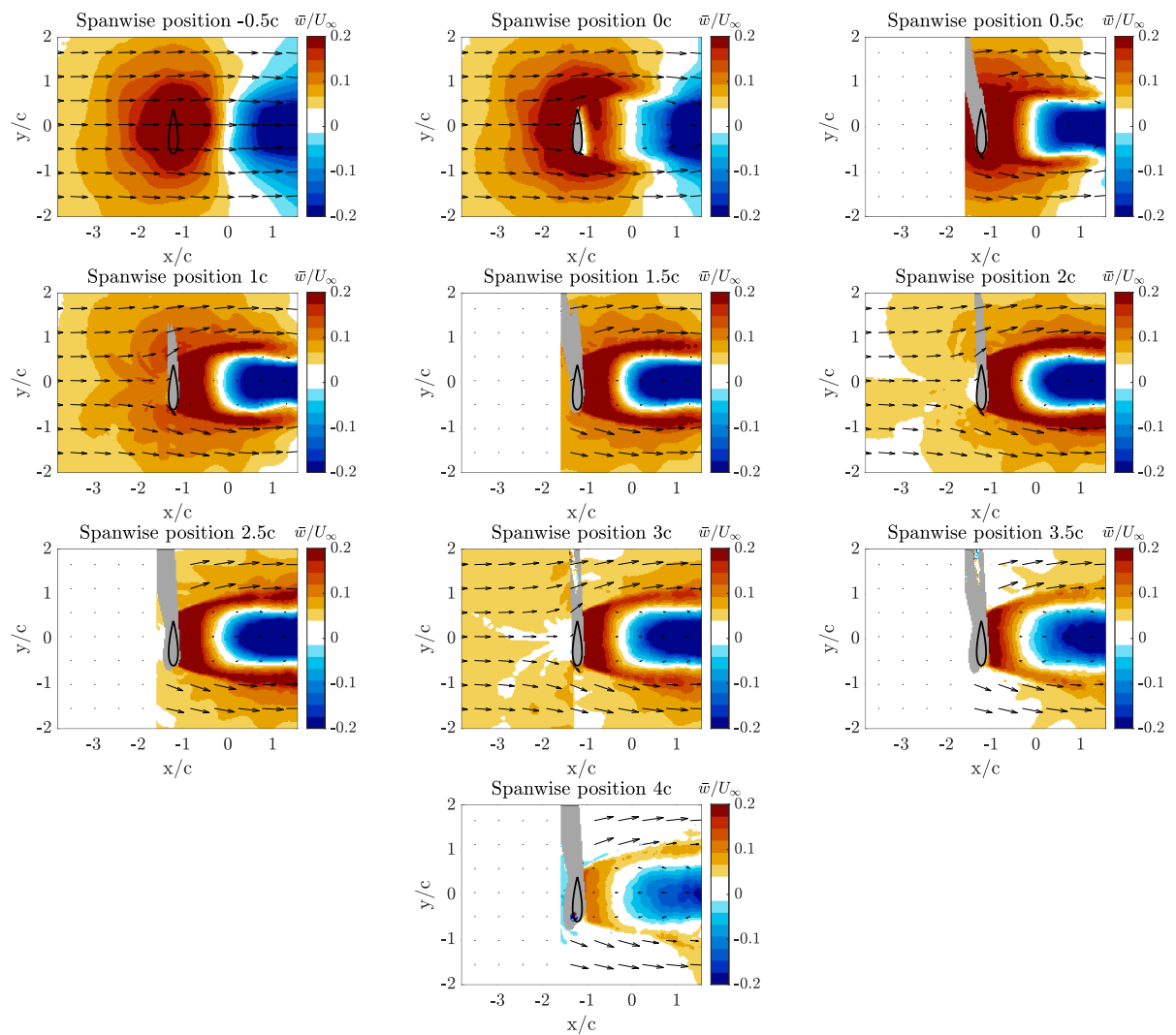


Figure F.4: Spanwise velocity, \bar{w}/U_∞ around a static blade from $0.5c$ in front of the tip to $4c$ inboard, freestream velocity coming from the left. The flow is positive into the page. White portions of the plot without velocity vectors indicate no available data.

APPENDIX G

Static Cases for a 40 cm blade,

$$U_{\infty} = 3 \text{ m/s}$$

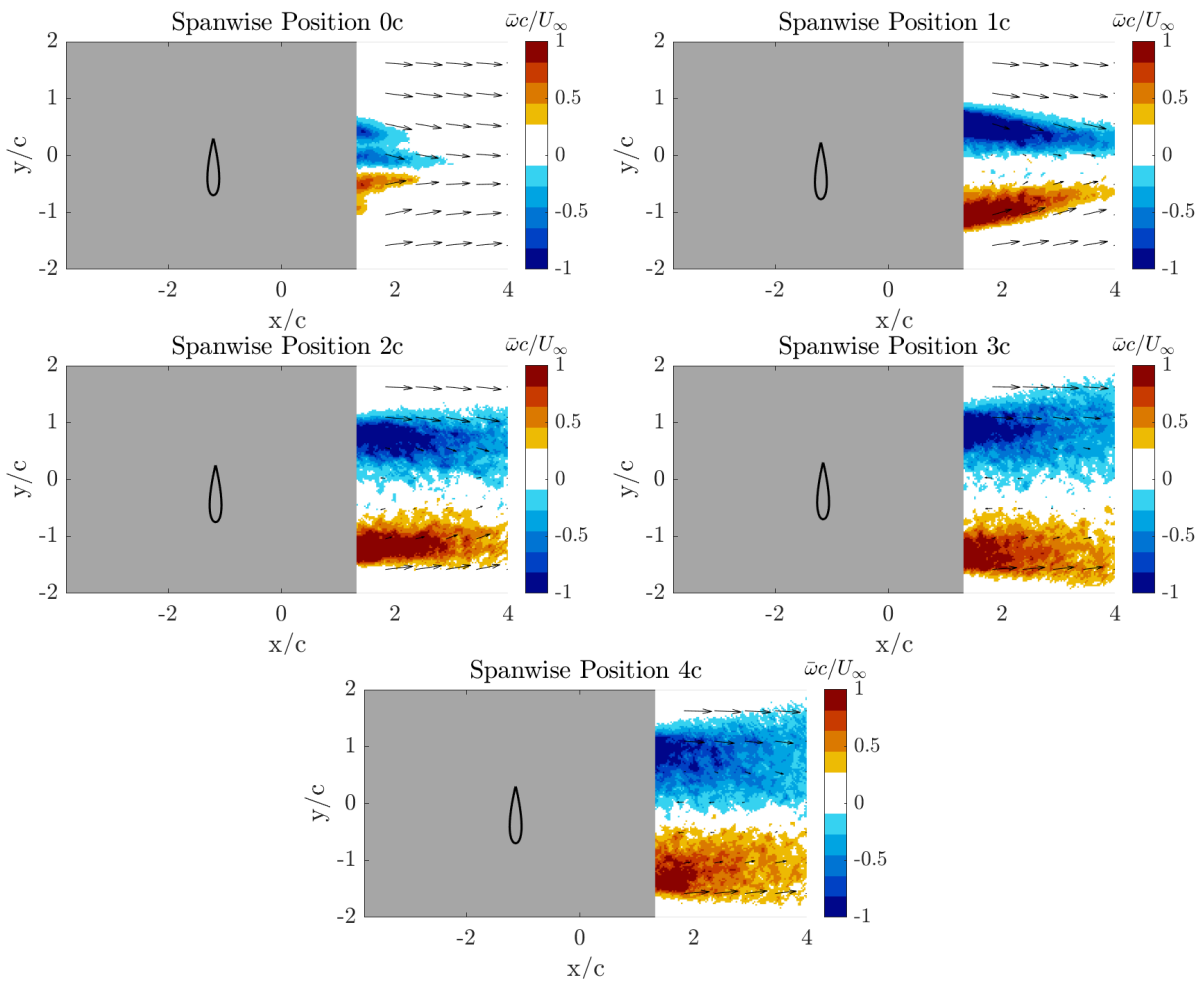


Figure G.1: Vorticity, $\bar{\omega}c/U_\infty$ around a 40 cm static blade from the tip to 4c inboard, freestream velocity coming from the left. Grey portions of the plot indicate no available data.

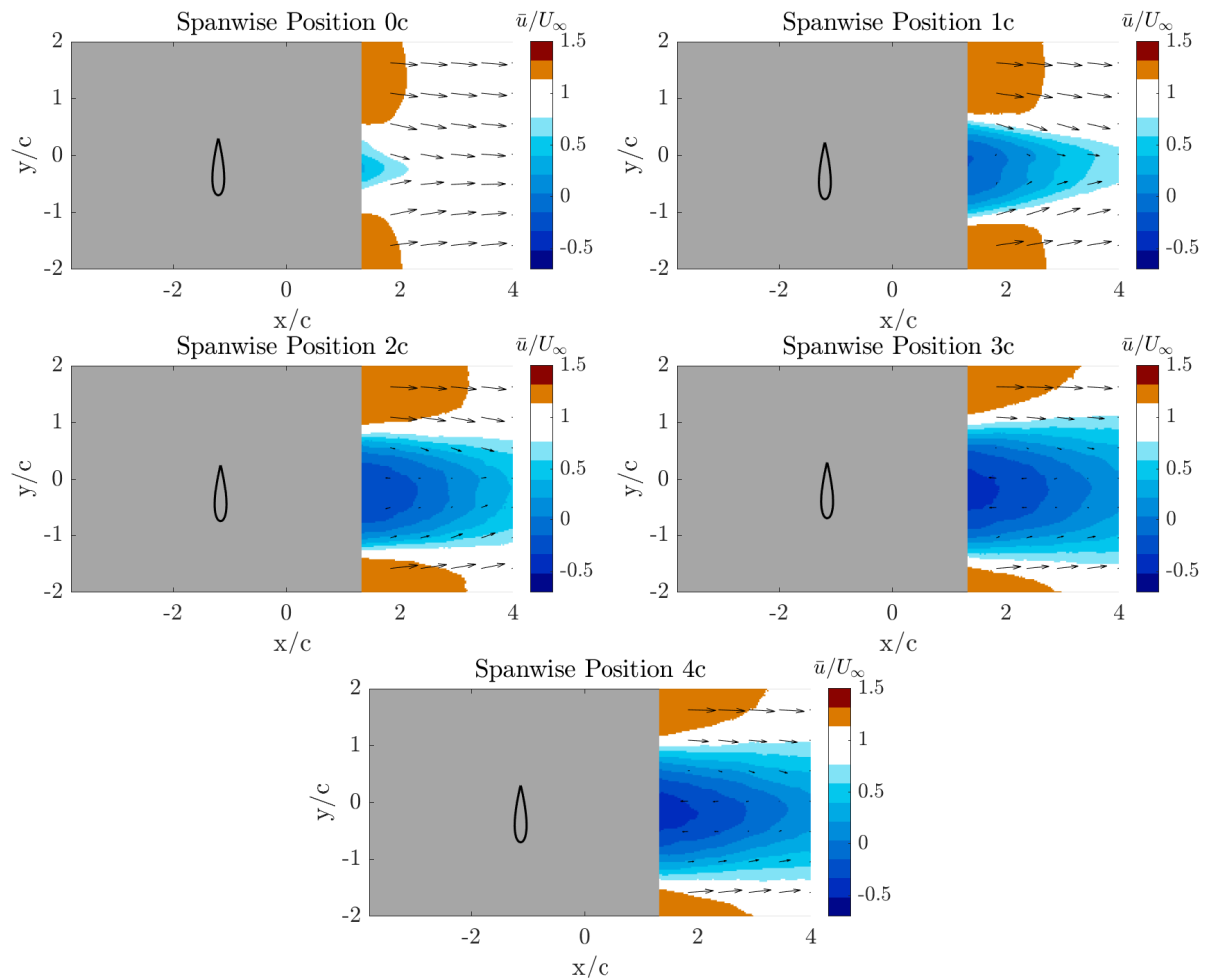


Figure G.2: Streamwise velocity, \bar{u}/U_∞ around a 40 cm static blade from the tip to 4c inboard, freestream velocity coming from the left. Grey portions of the plot indicate no available data.

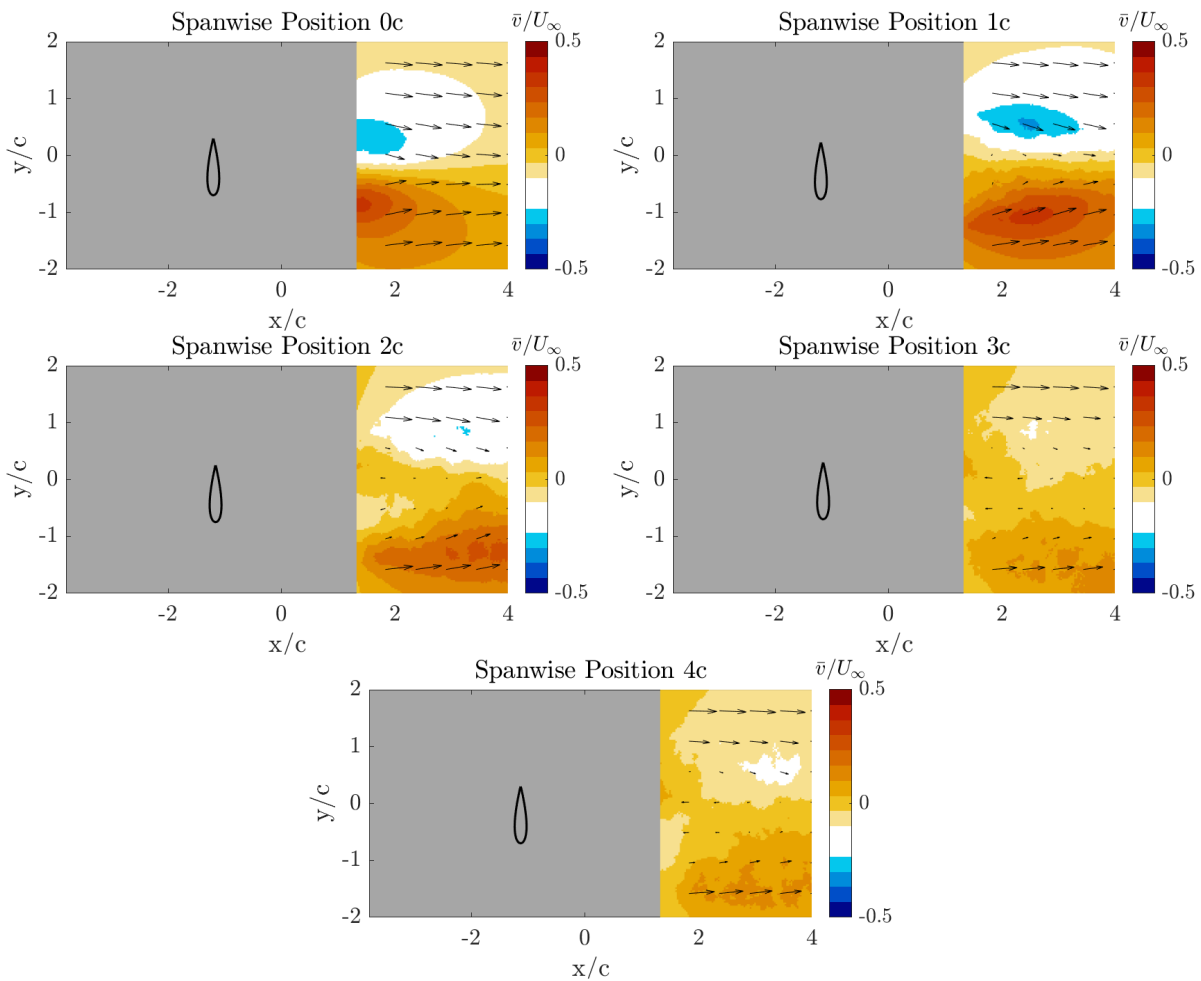


Figure G.3: Vertical velocity, \bar{v}/U_∞ around a 40 cm static blade from the tip to 4c inboard, freestream velocity coming from the left. Grey portions of the plot indicate no available data.

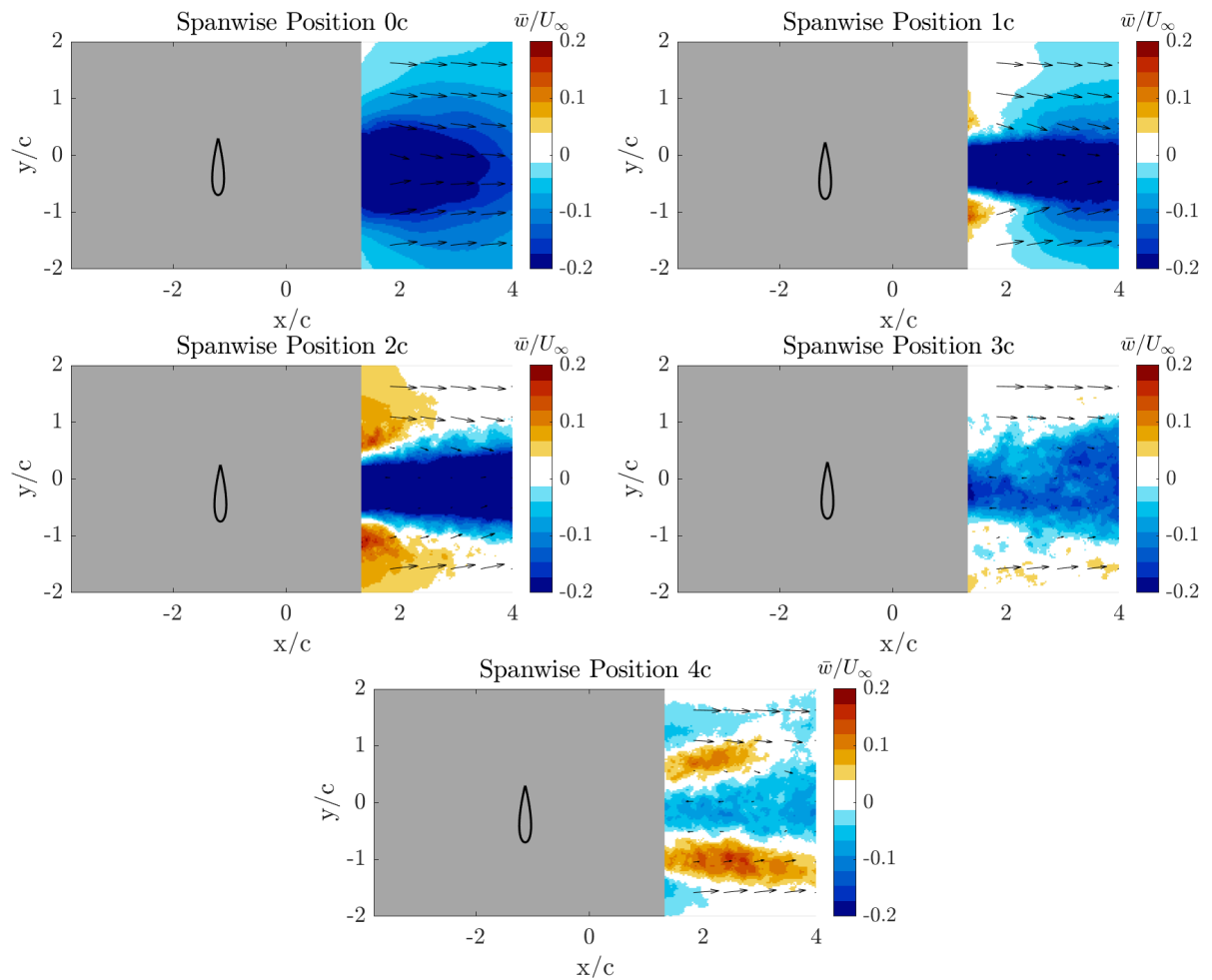


Figure G.4: Spanwise velocity, \bar{w}/U_∞ around a 40 cm static blade from the tip to 4c inboard, freestream velocity coming from the left. The flow is positive into the page. Grey portions of the plot indicate no available data.

APPENDIX H

2.5 Hz Plunging Cases PIV Planes

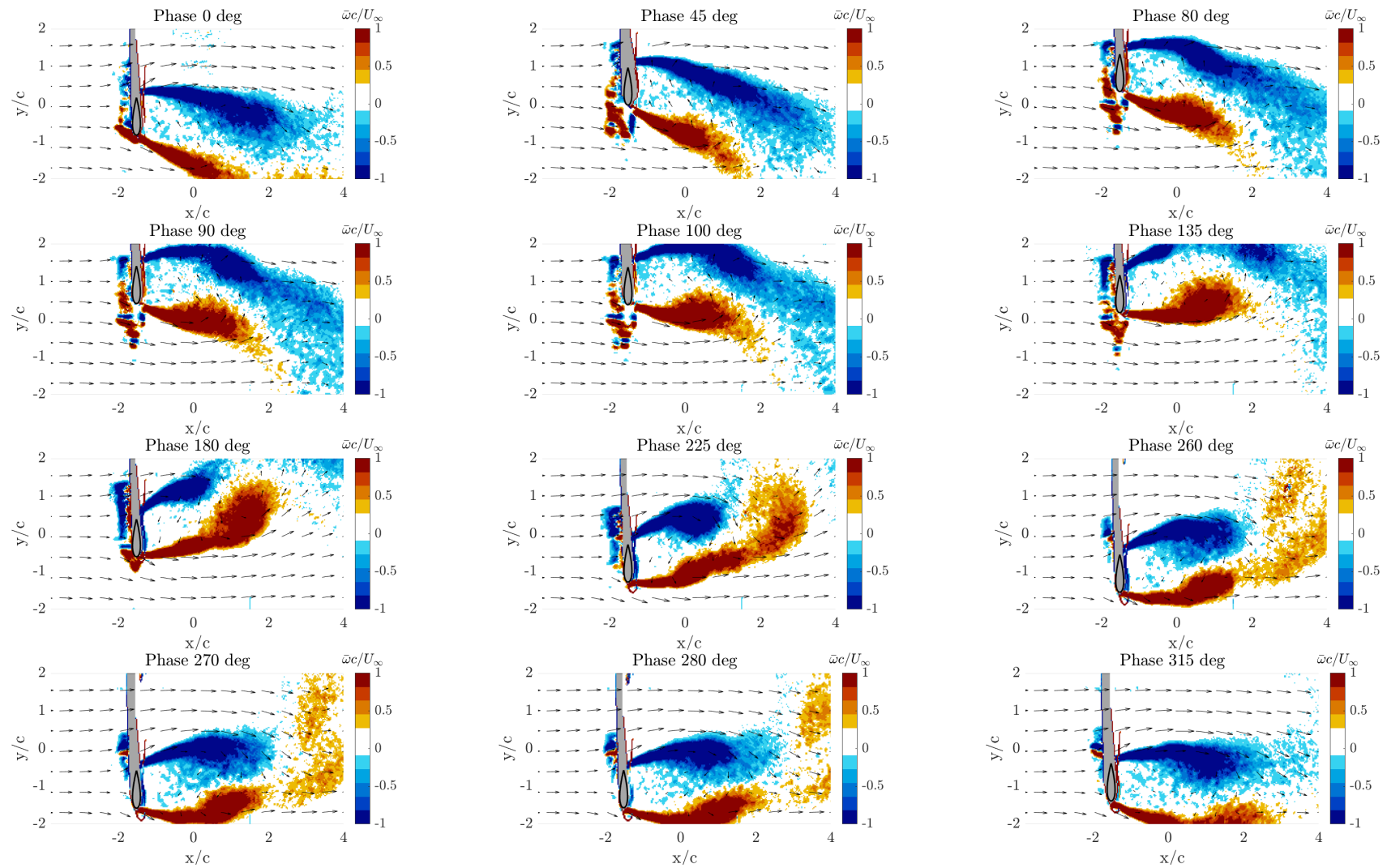


Figure H.1: Vorticity, $\bar{\omega}c/U_\infty$ around a plunging airfoil at 2.5hz, 3 chords inboard from the tip with the freestream velocity coming from the left.

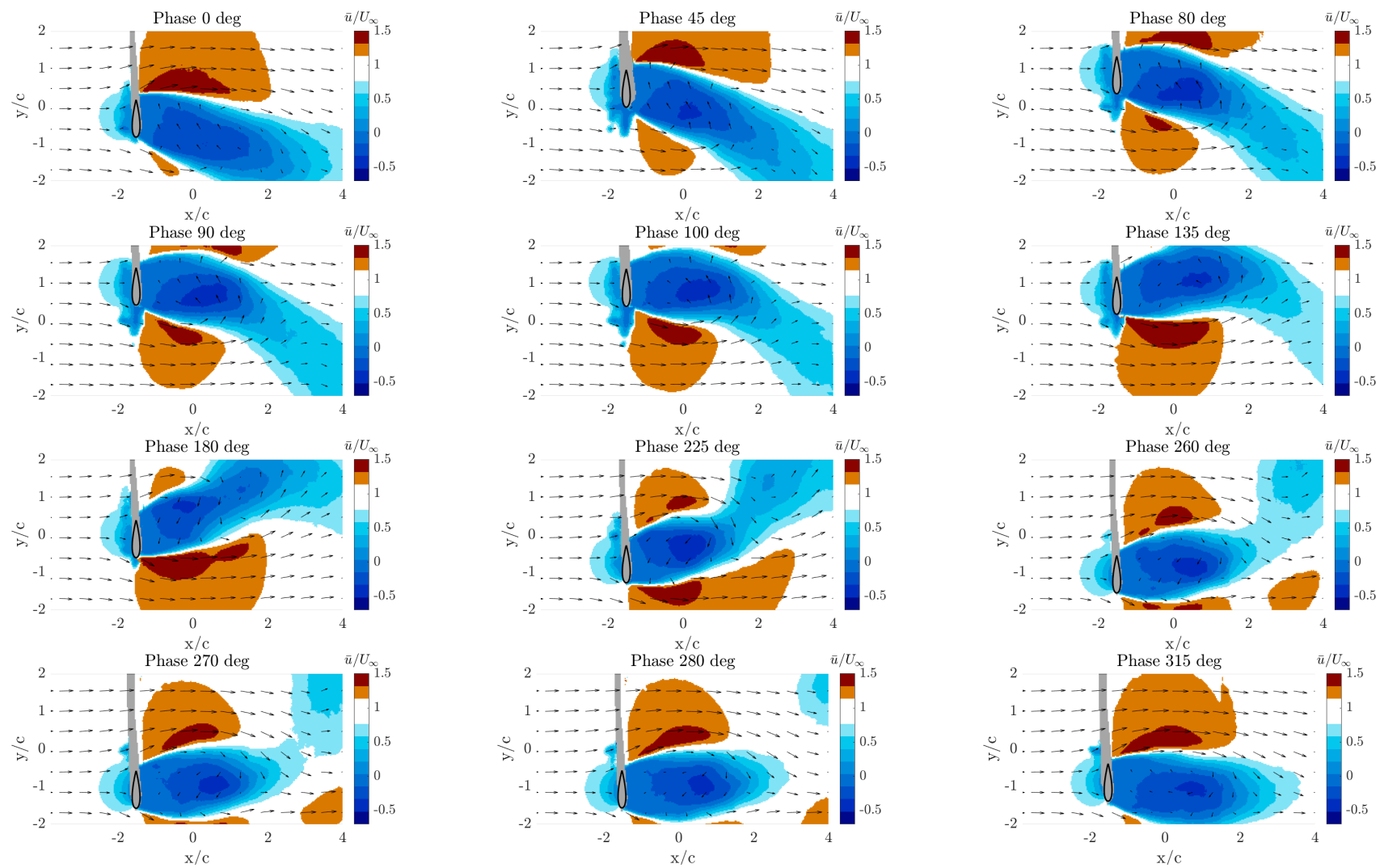


Figure H.2: Streamwise velocity, \bar{u}/U_∞ around a plunging airfoil at 2.5 Hz, 3 chords inboard from the tip with the freestream velocity coming from the left.

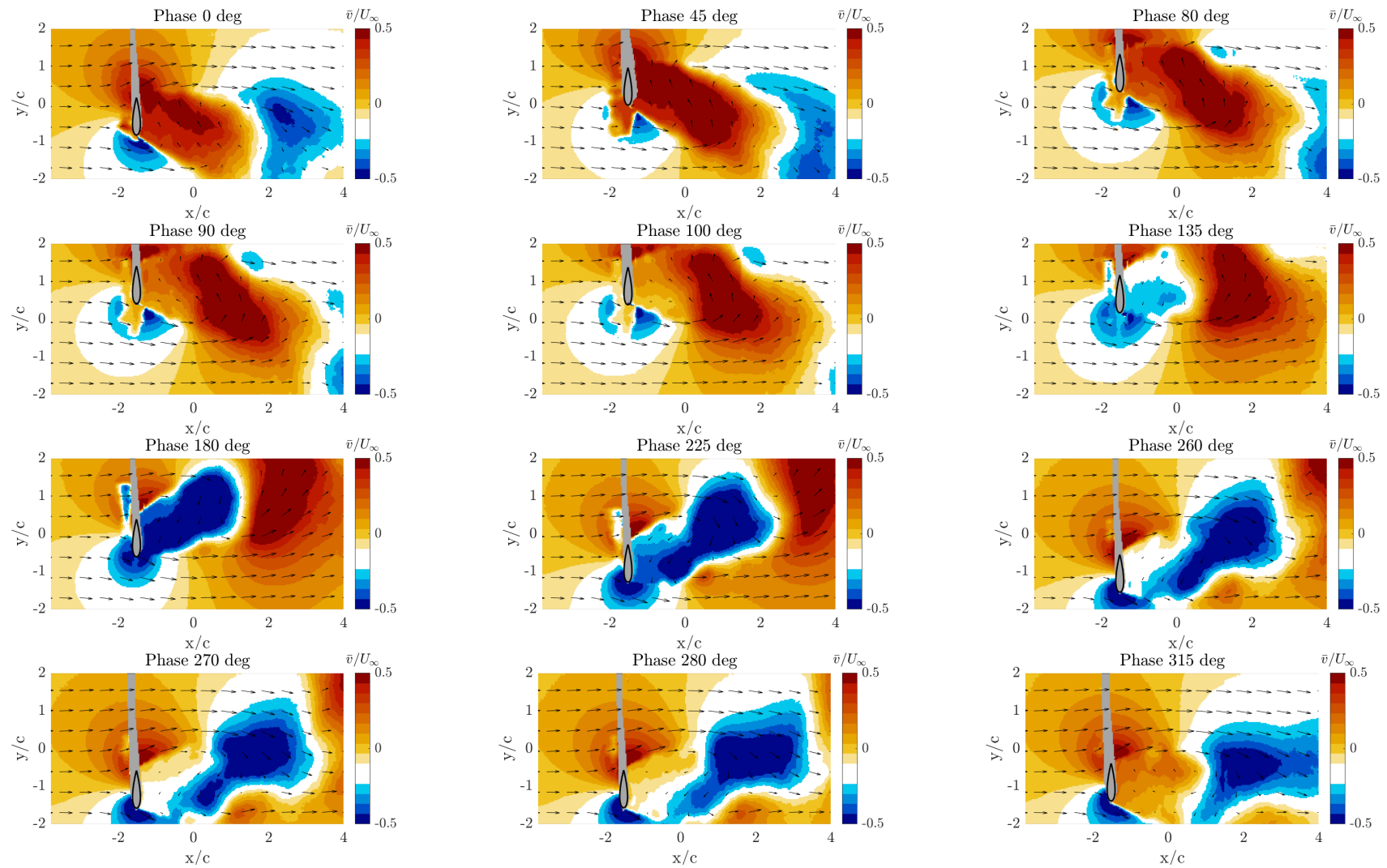


Figure H.3: Vertical velocity, \bar{v}/U_∞ around a plunging airfoil at 2.5Hz, 3 chords inboard from the tip with the freestream velocity coming from the left.

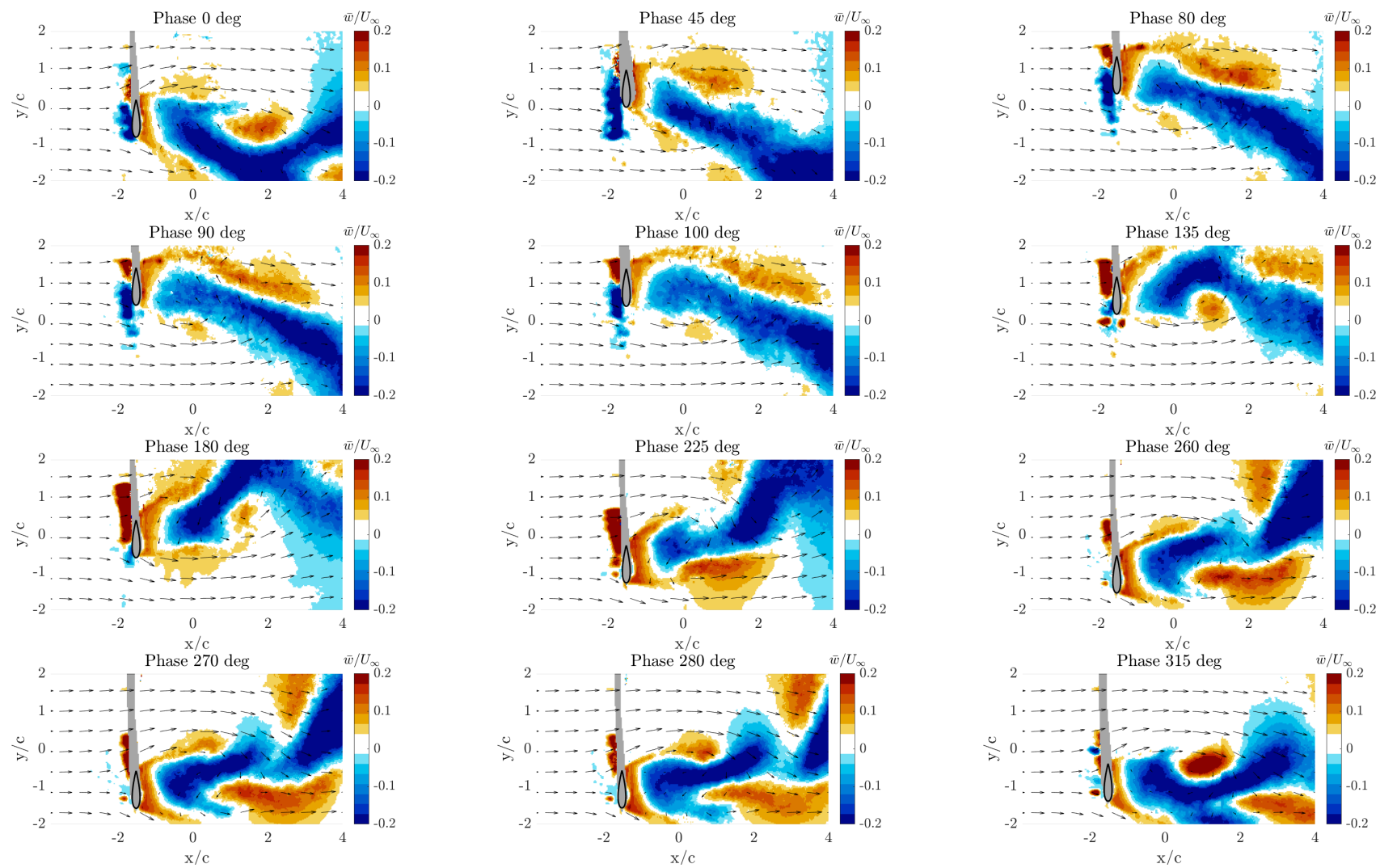


Figure H.4: Spanwise velocity, \bar{w}/U_∞ around a plunging airfoil at 2.5 Hz, 3 chords inboard from the tip with the freestream velocity coming from the left. The flow is positive into the page.

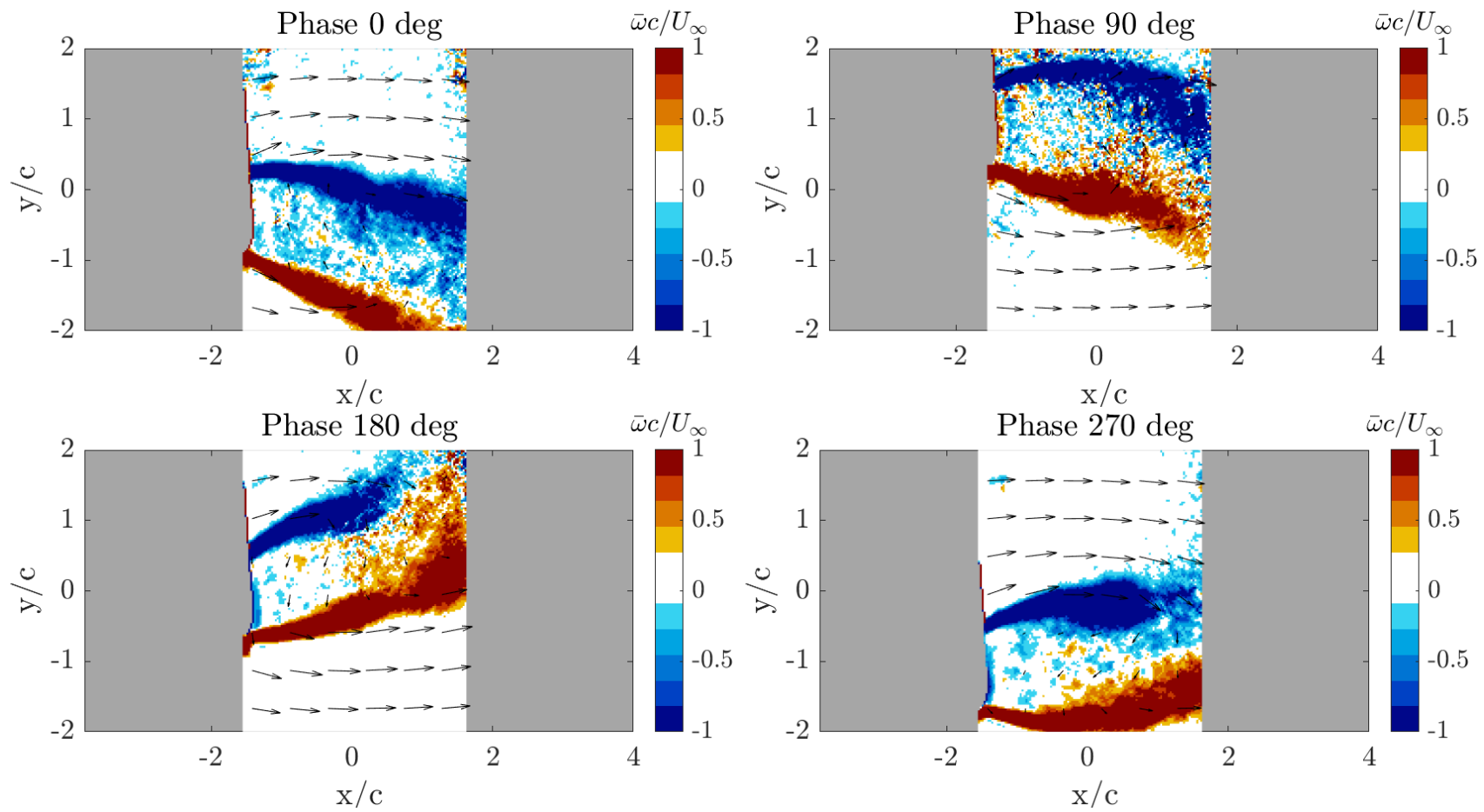


Figure H.5: Vorticity, $\bar{\omega}c/U_\infty$ around a plunging airfoil at 2.5hz, 2 chords inboard from the tip with the freestream velocity coming from the left.

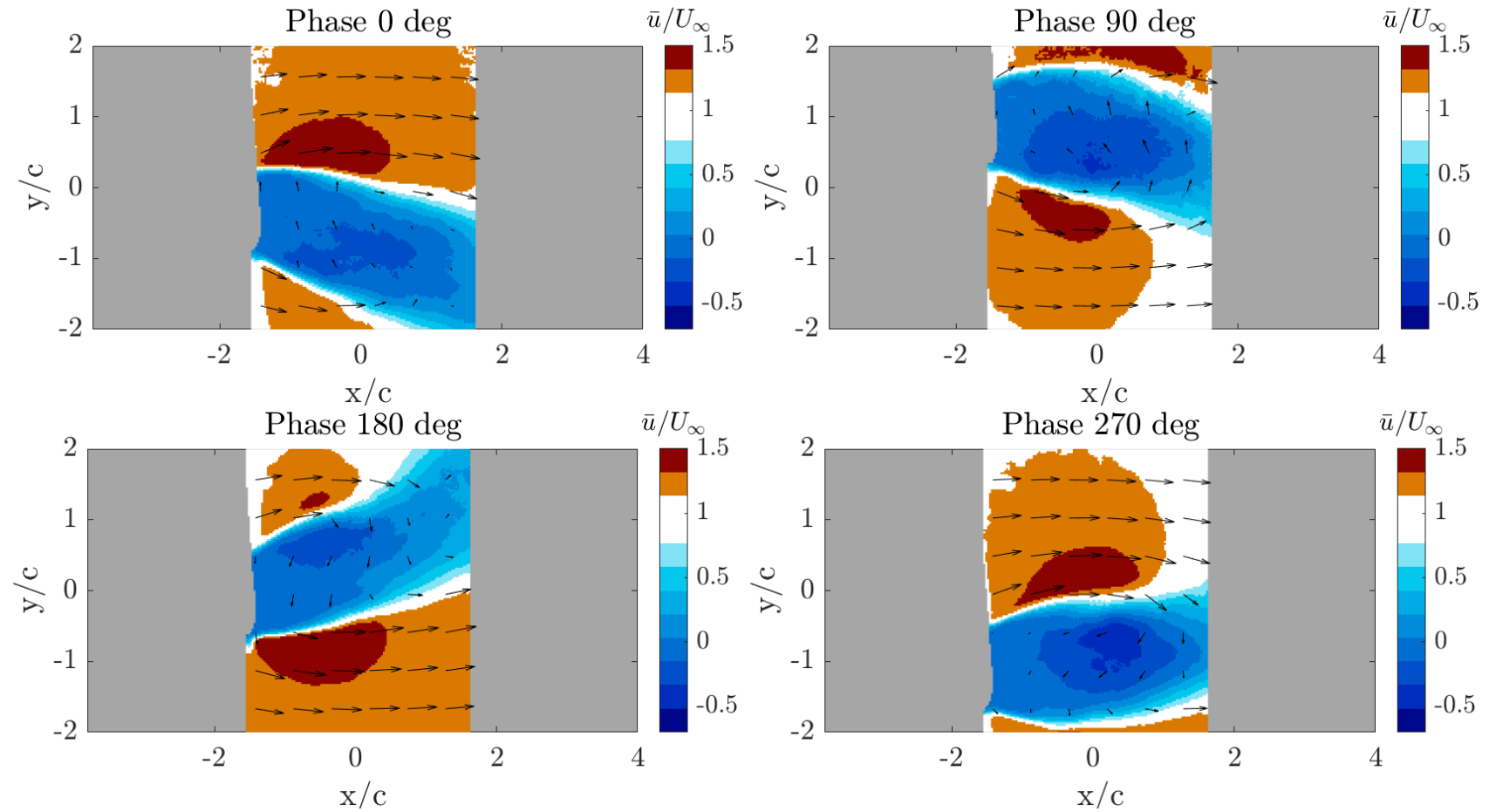


Figure H.6: Streamwise velocity, \bar{u}/U_∞ around a plunging airfoil at 2.5hz, 2 chords inboard from the tip with the freestream velocity coming from the left.

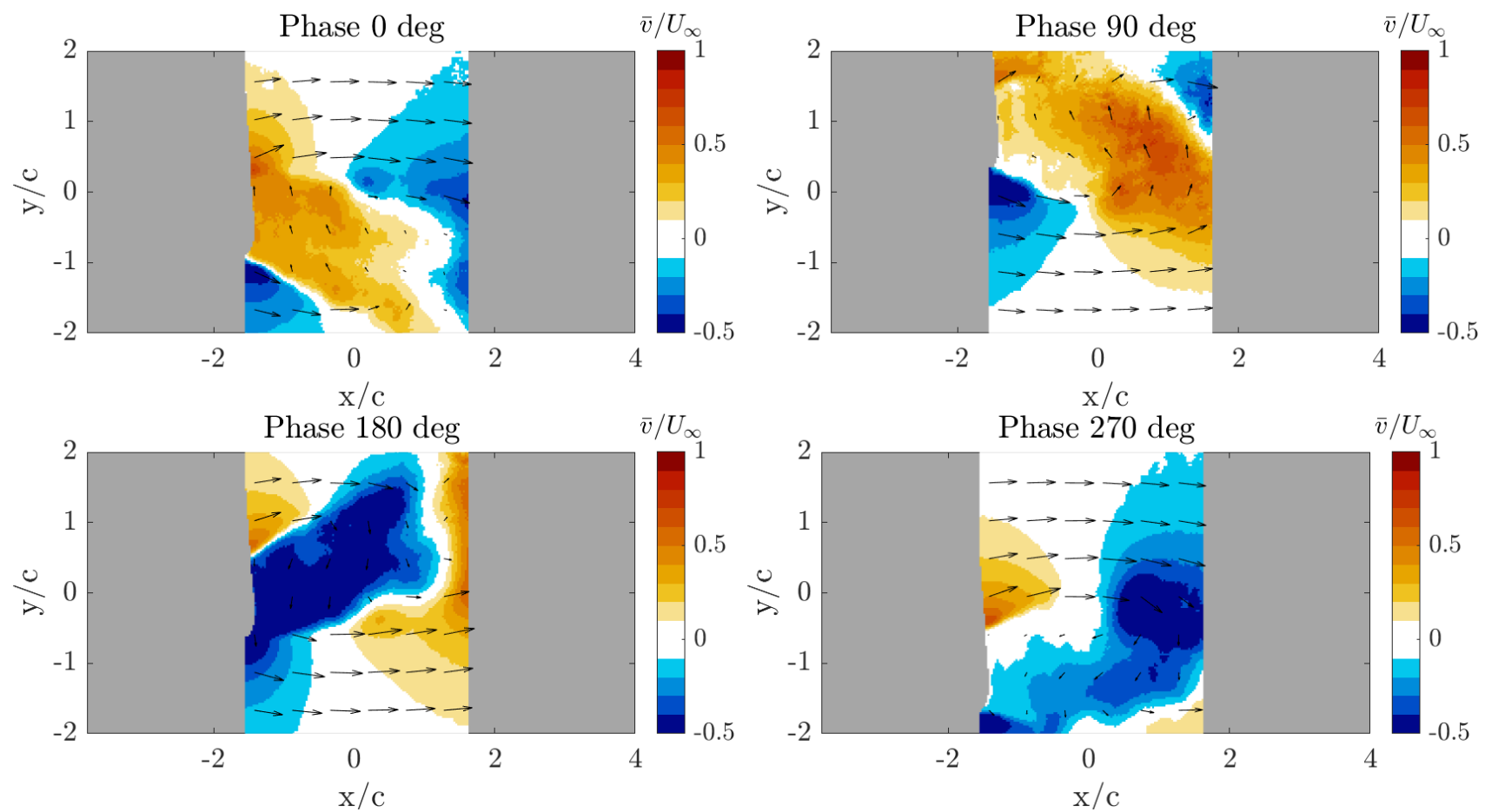


Figure H.7: Vertical velocity, \bar{v}/U_∞ around a plunging airfoil at 2.5hz, 2 chords inboard from the tip with the freestream velocity coming from the left.

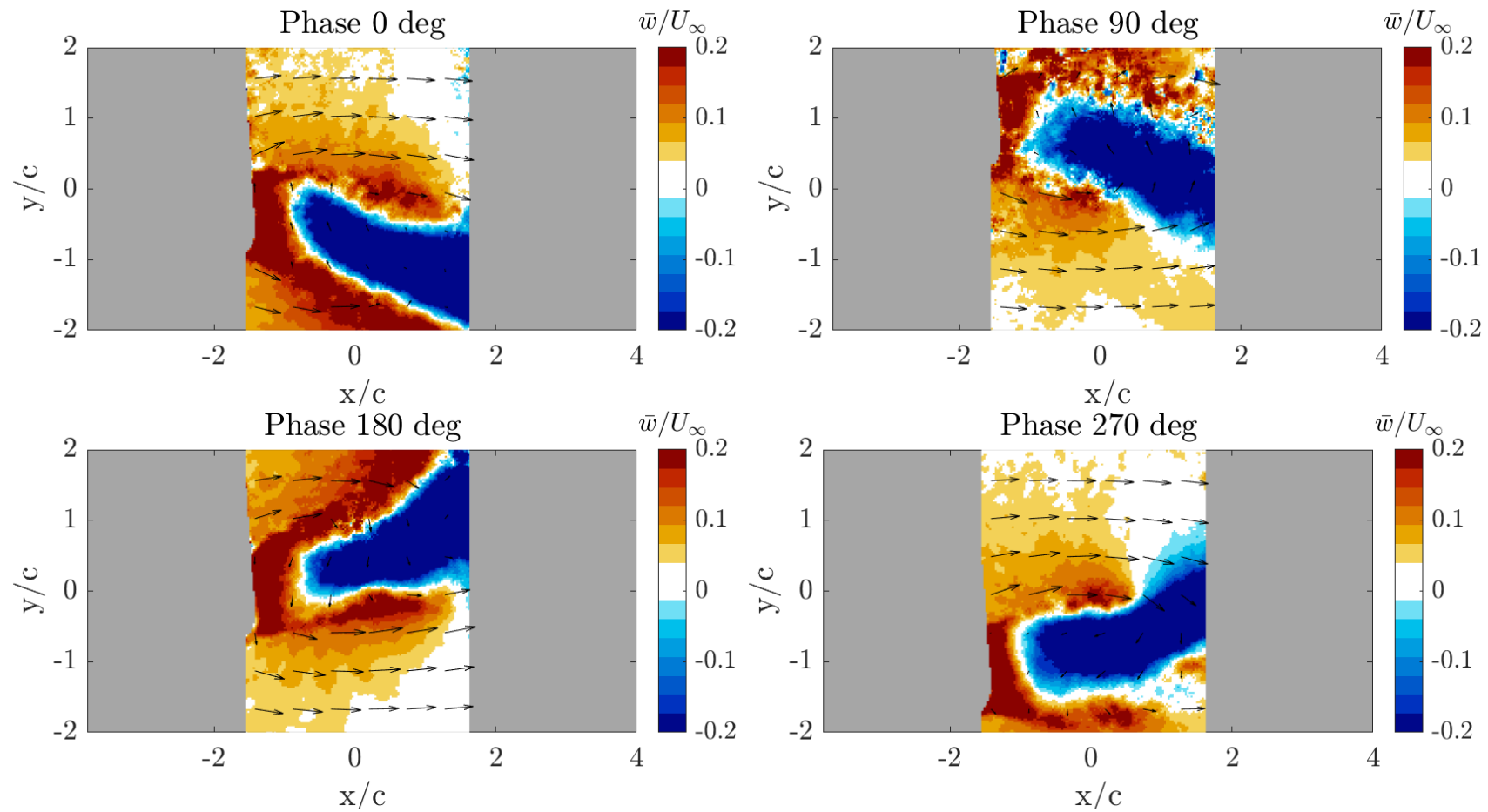


Figure H.8: Spanwise velocity, \bar{w}/U_∞ around a plunging airfoil at 2.5hz, 2 chords inboard from the tip with the freestream velocity coming from the left. The flow is positive into the page.

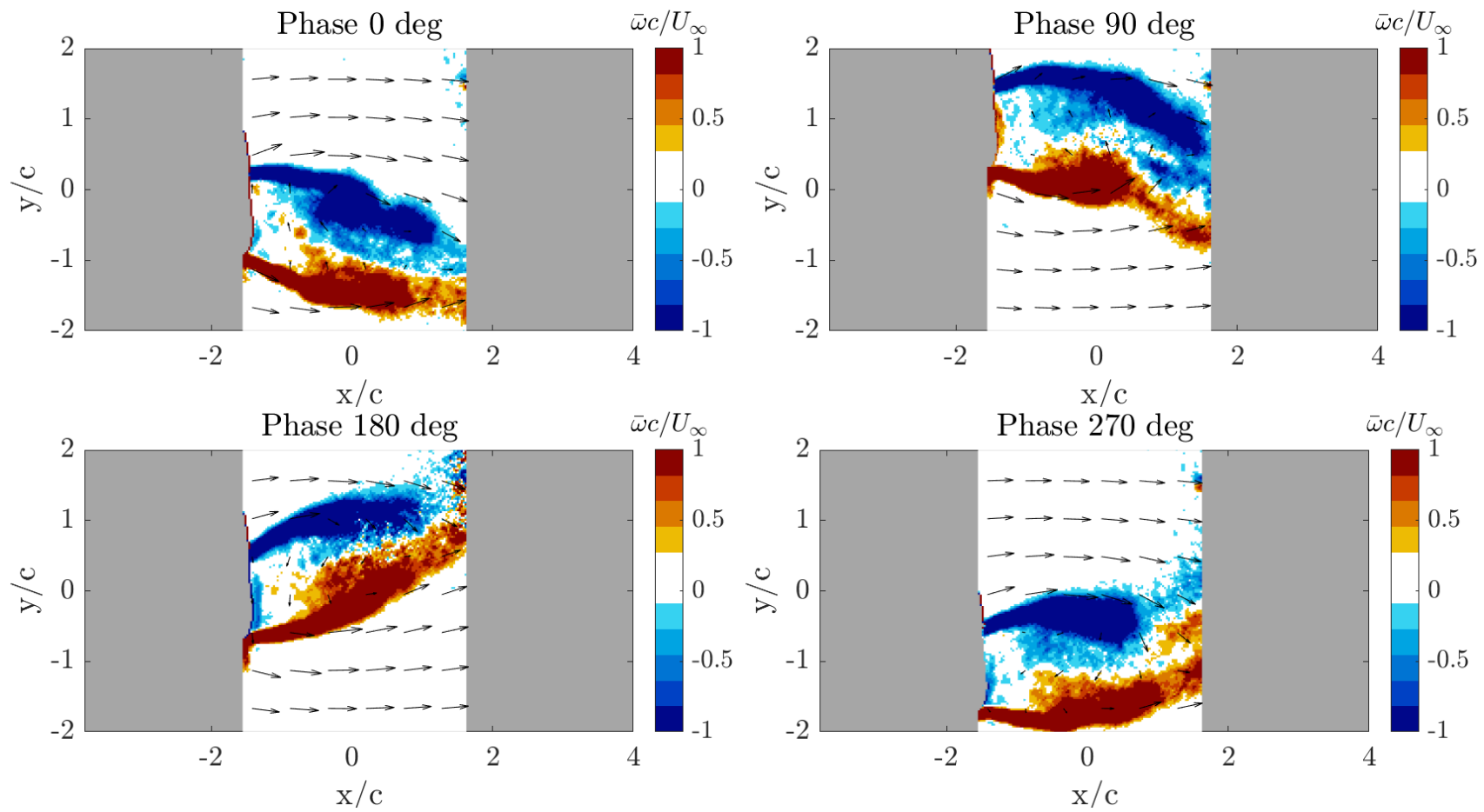


Figure H.9: Vorticity, $\bar{\omega}c/U_\infty$ around a plunging airfoil at 2.5hz, 1 chord inboard from the tip with the freestream velocity coming from the left.

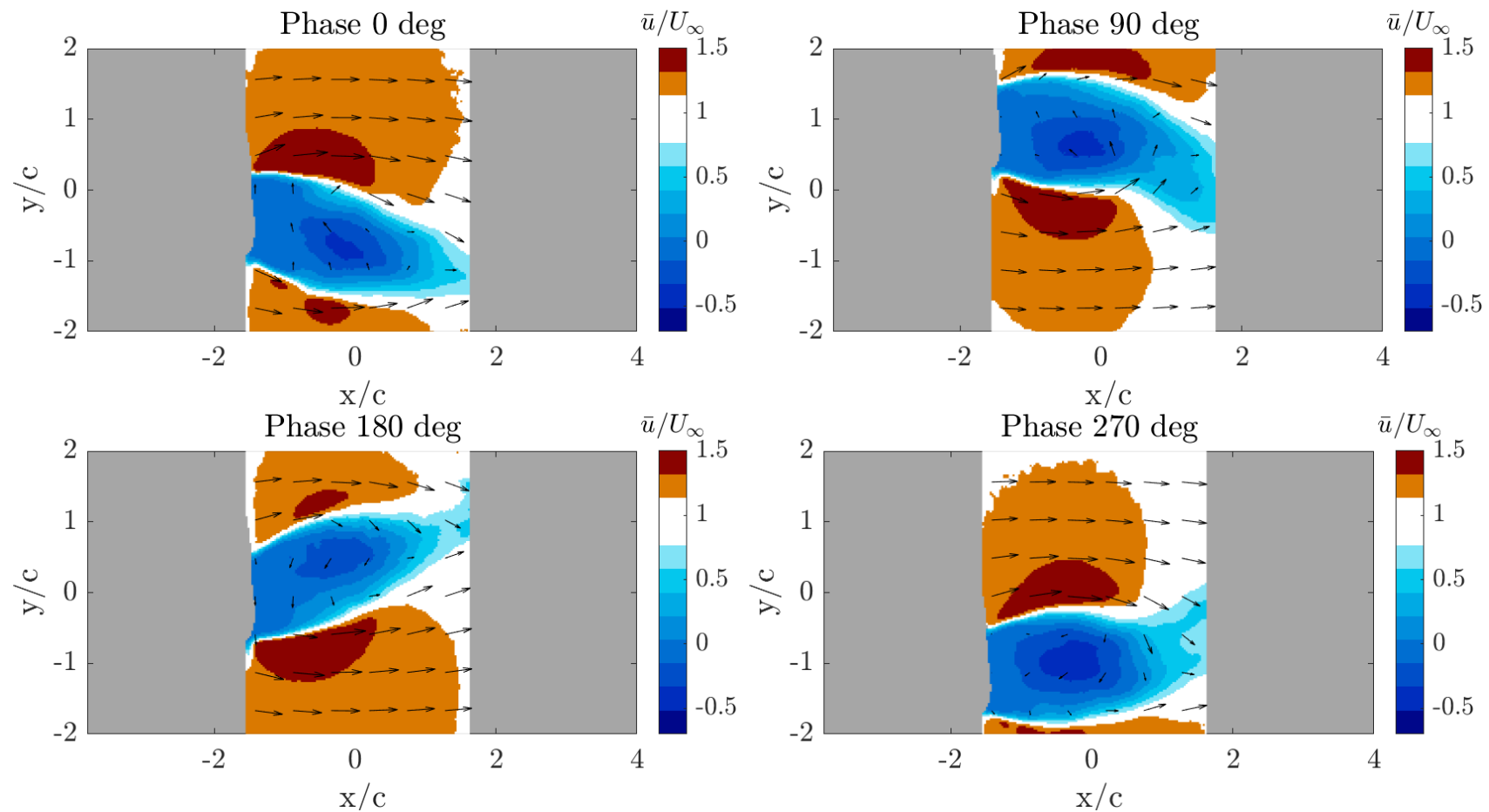


Figure H.10: Streamwise velocity, \bar{u}/U_∞ around a plunging airfoil at 2.5hz, 1 chord inboard from the tip with the freestream velocity coming from the left.

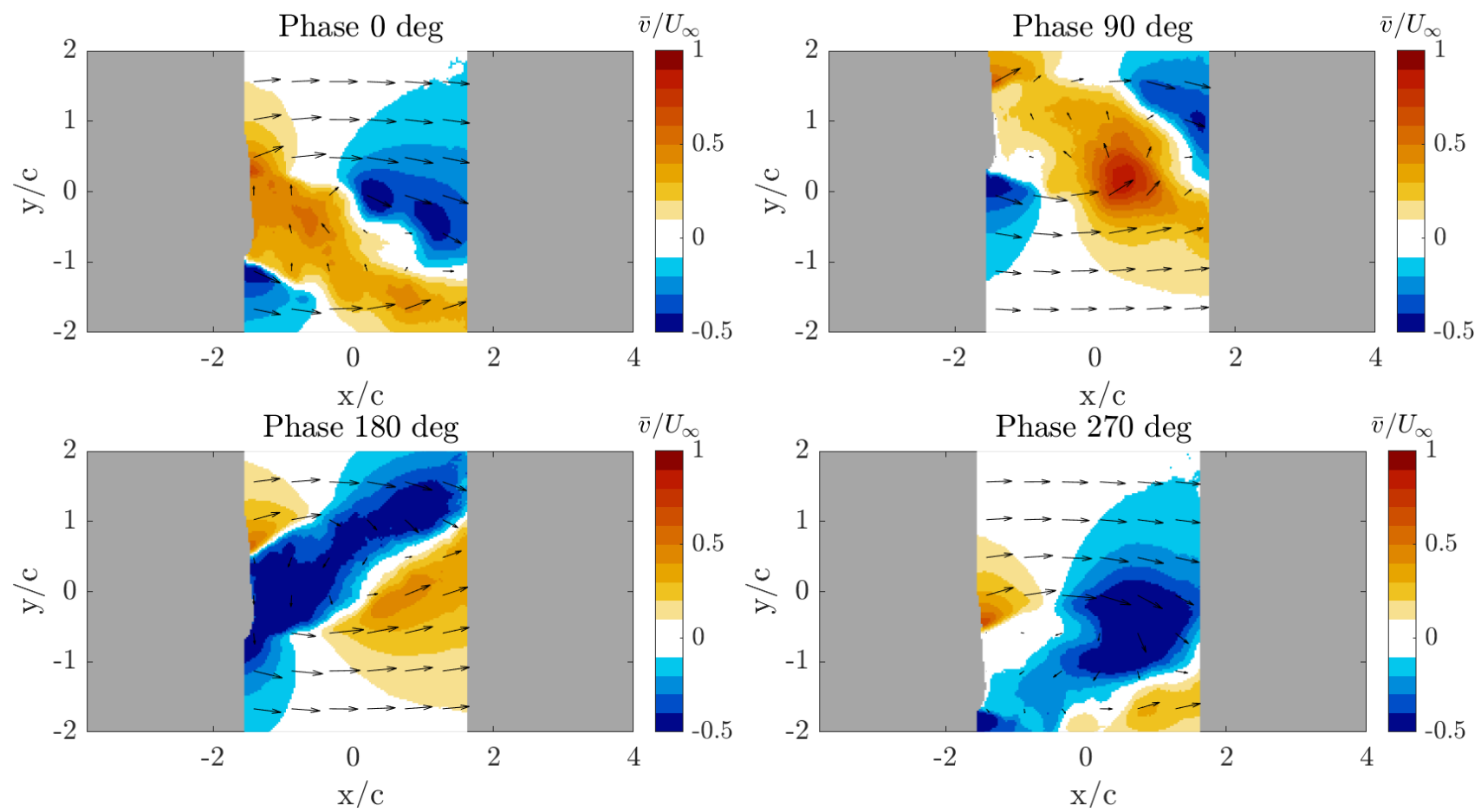


Figure H.11: Vertical velocity, \bar{v}/U_∞ around a plunging airfoil at 2.5hz, 1 chord inboard from the tip with the freestream velocity coming from the left.

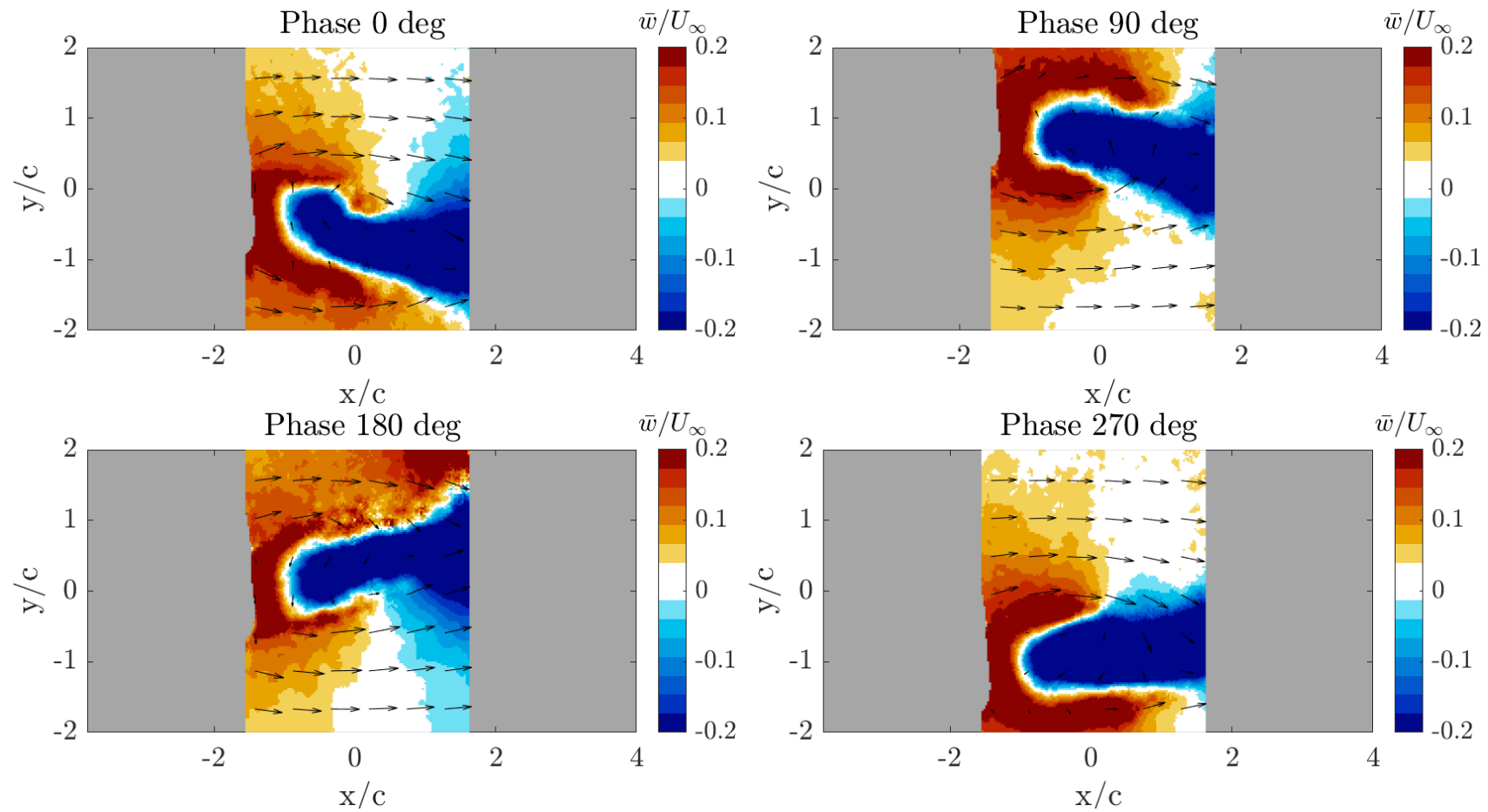


Figure H.12: Spanwise velocity, \bar{w}/U_∞ around a plunging airfoil at 2.5hz, 1 chord inboard from the tip with the freestream velocity coming from the left. The flow is positive into the page.

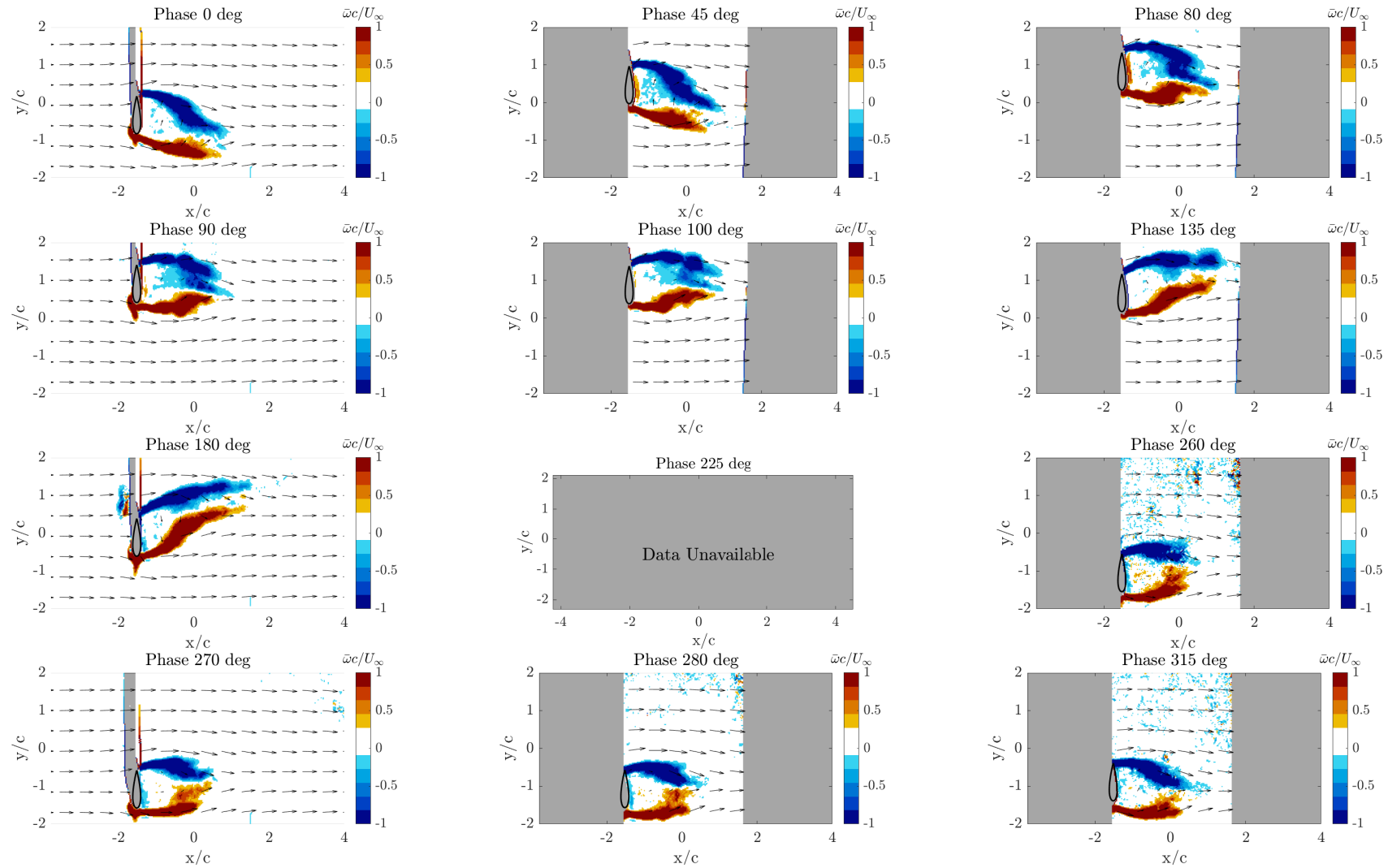


Figure H.13: Vorticity, $\bar{\omega}c/U_\infty$ around a plunging airfoil at 2.5Hz, at from the tip with the freestream velocity coming from the left.

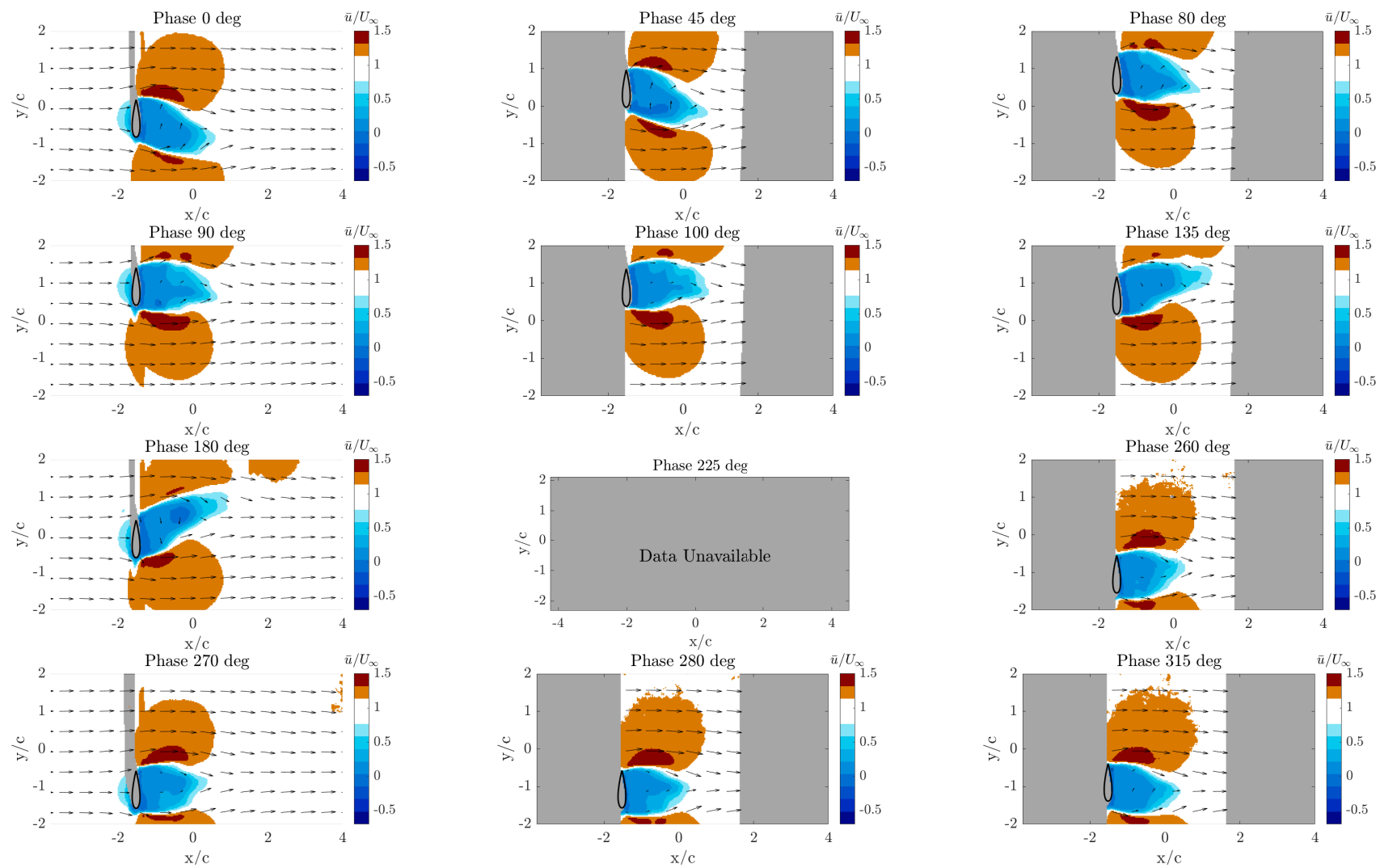


Figure H.14: Streamwise velocity, \bar{u}/U_∞ around a plunging airfoil at 2.5 Hz, at the tip with the freestream velocity coming from the left.

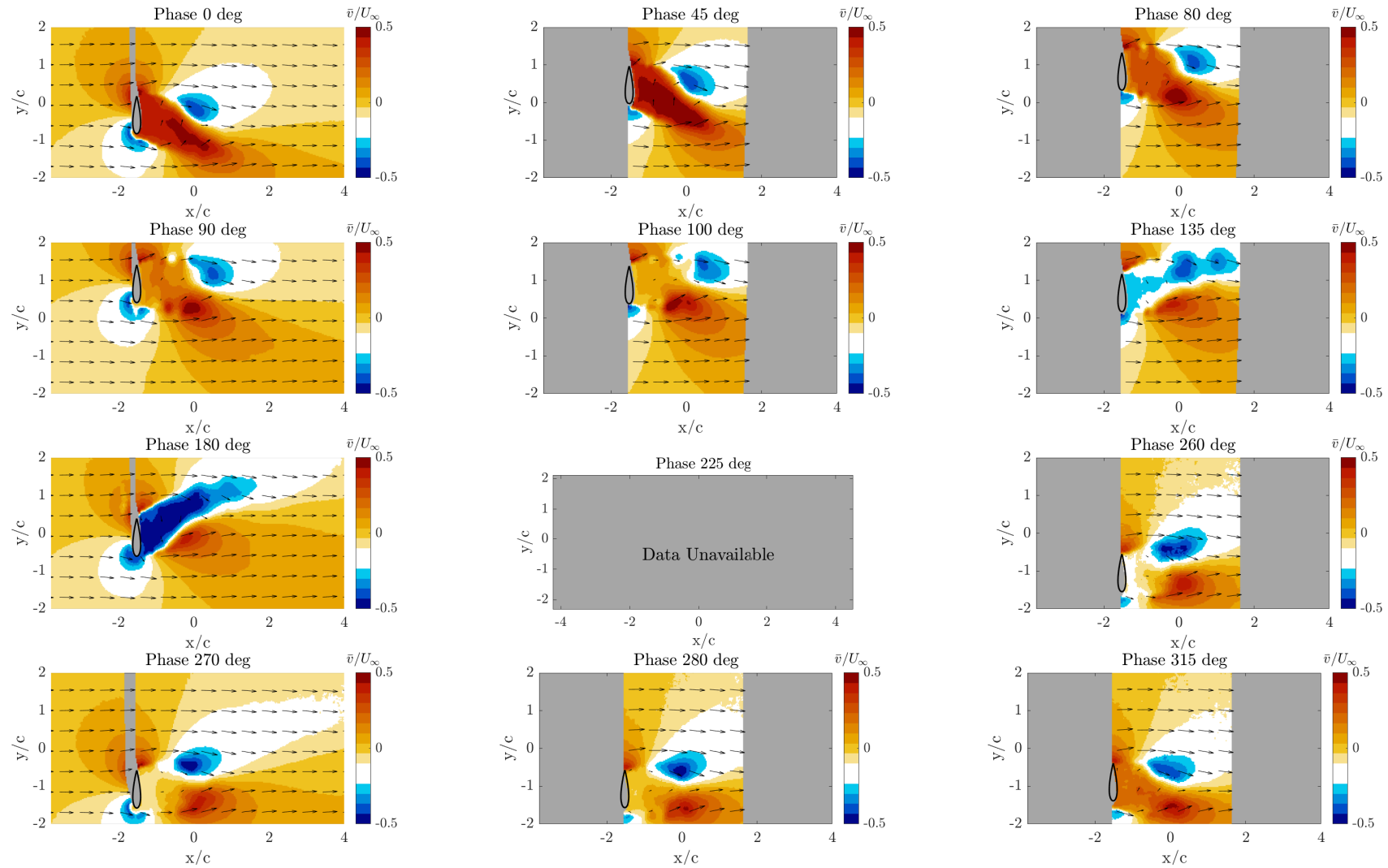


Figure H.15: Vertical velocity, \bar{v}/U_∞ around a plunging airfoil at 2.5hz, at the tip with the freestream velocity coming from the left.

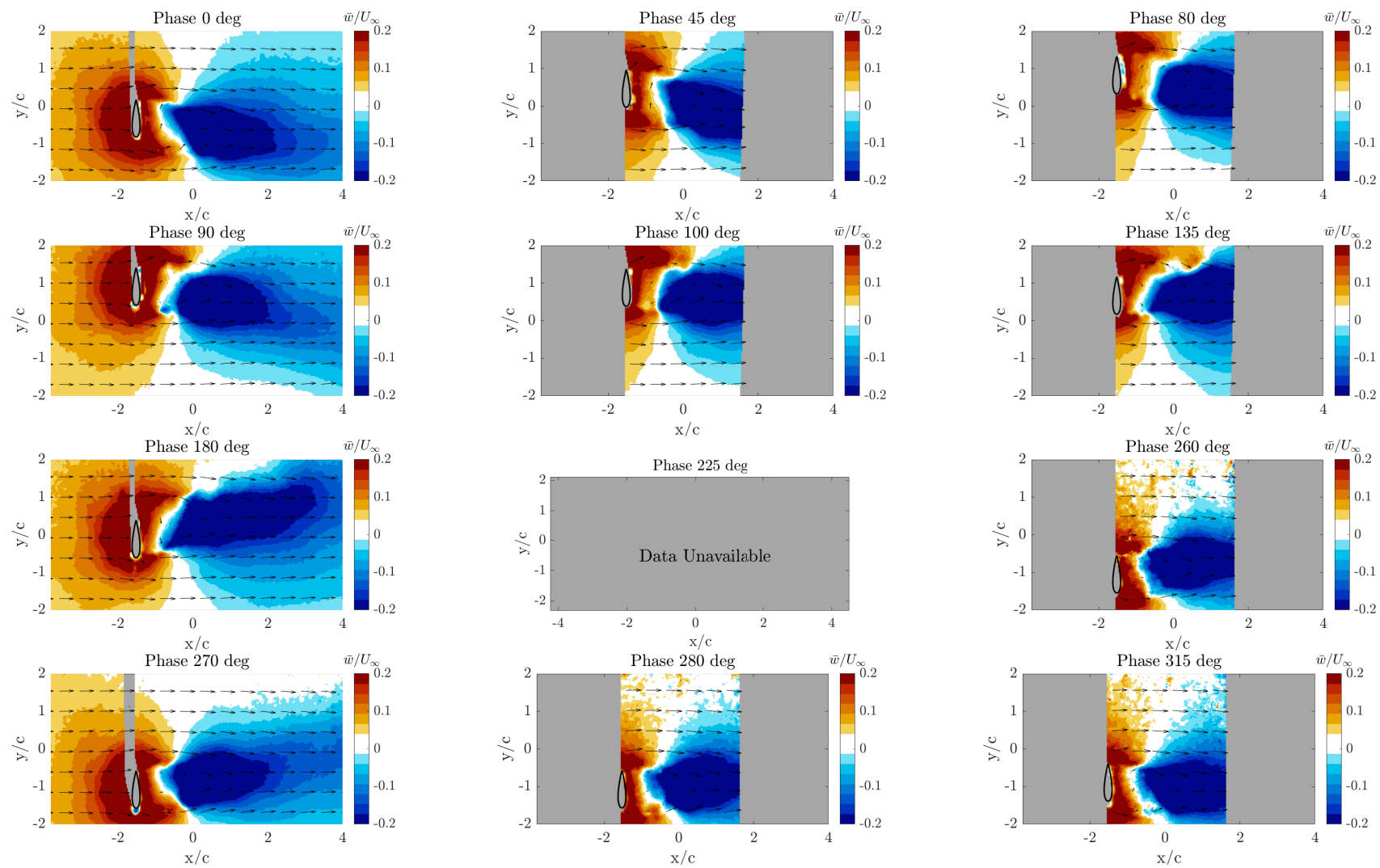


Figure H.16: Spanwise velocity, \bar{w}/U_∞ around a plunging airfoil at 2.5 Hz, at the tip with the freestream velocity coming from the left. The flow is positive into the page.

APPENDIX I

5 Hz Plunging Cases PIV Planes

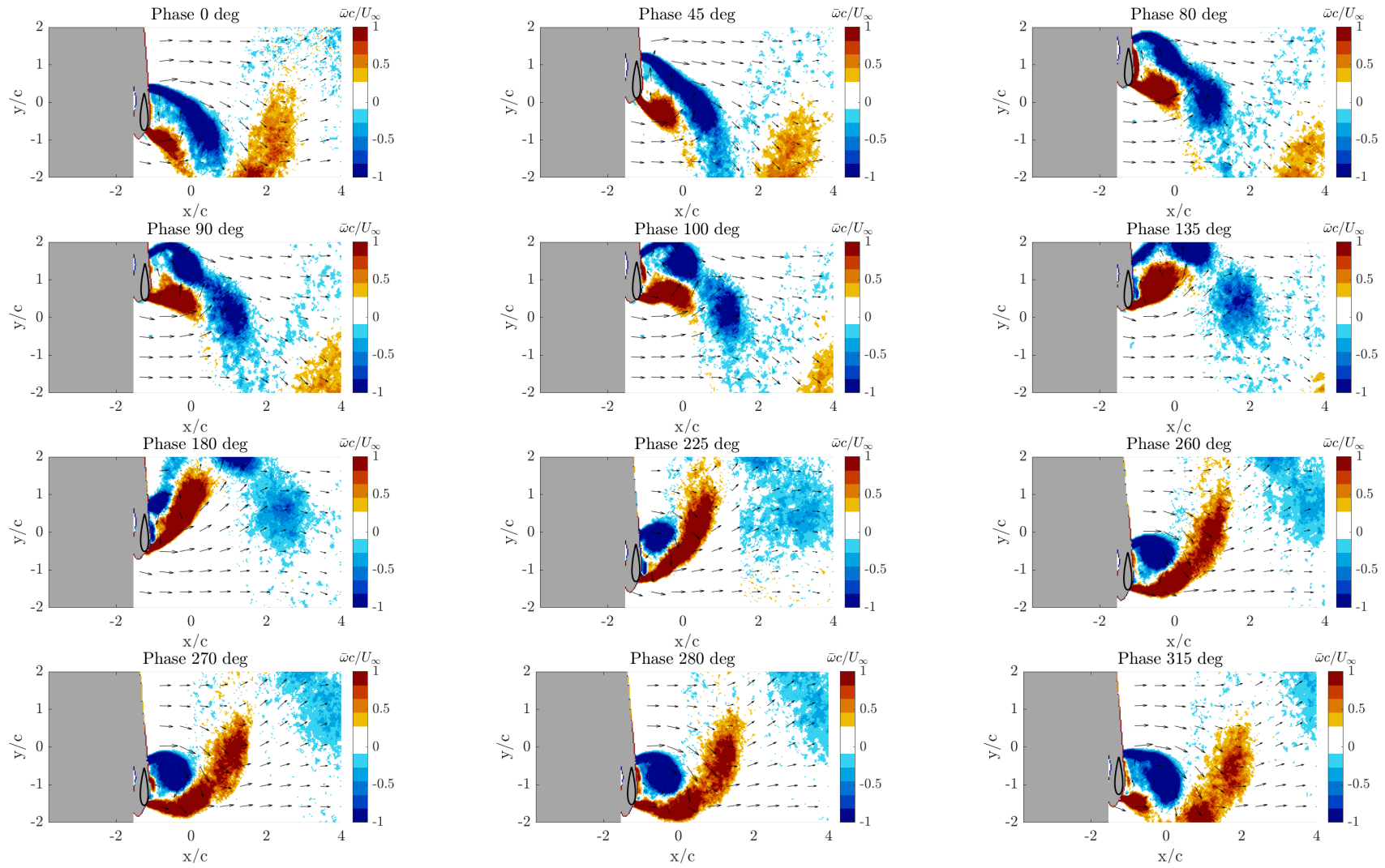


Figure I.1: Vorticity, $\bar{\omega}c/U_\infty$ around a plunging airfoil at 5Hz, 3 chords inboard from the tip with the freestream velocity coming from the left.

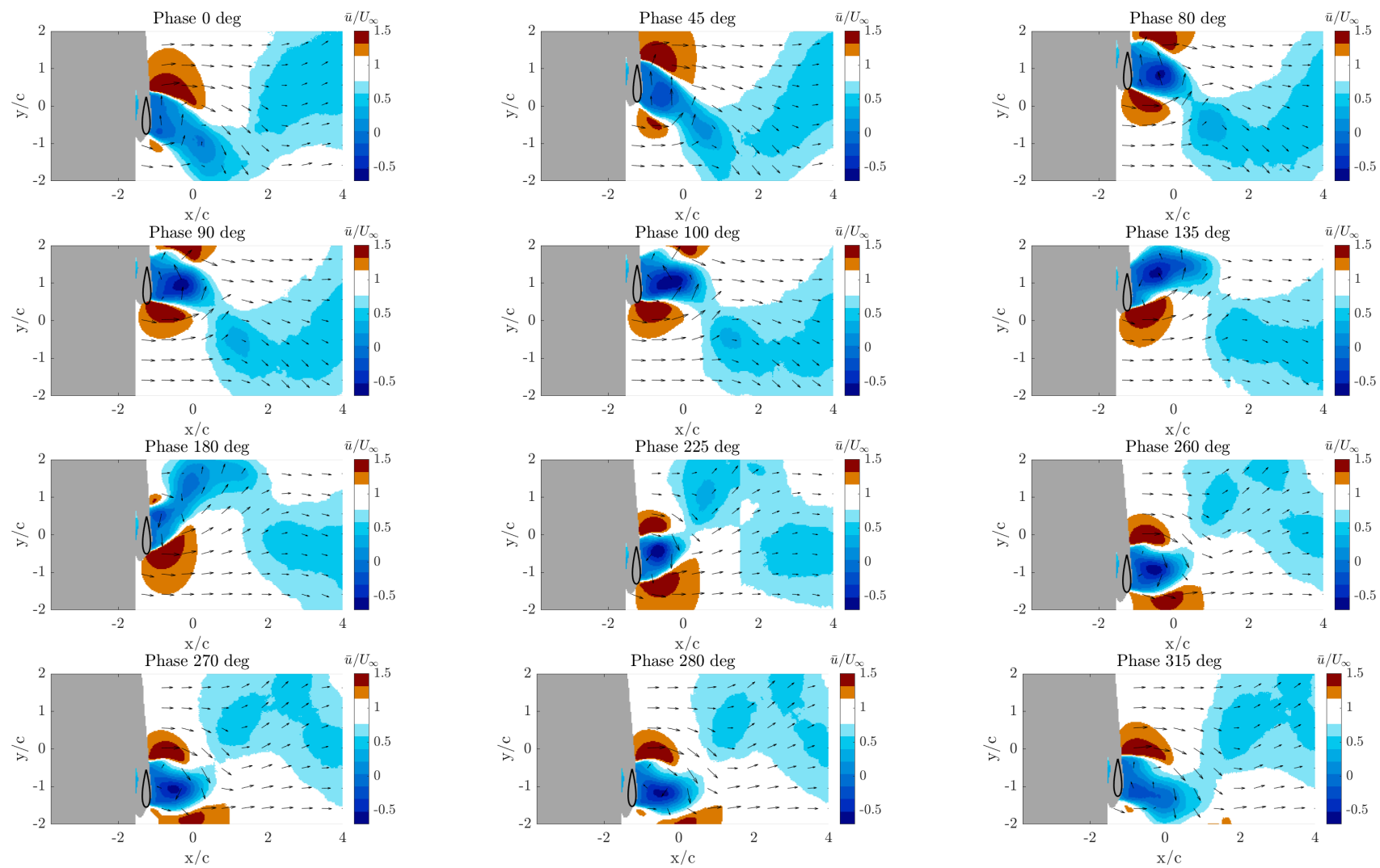


Figure I.2: Streamwise velocity, \bar{u}/U_∞ around a plunging airfoil at 5Hz, 3 chords inboard from the tip with the freestream velocity coming from the left.

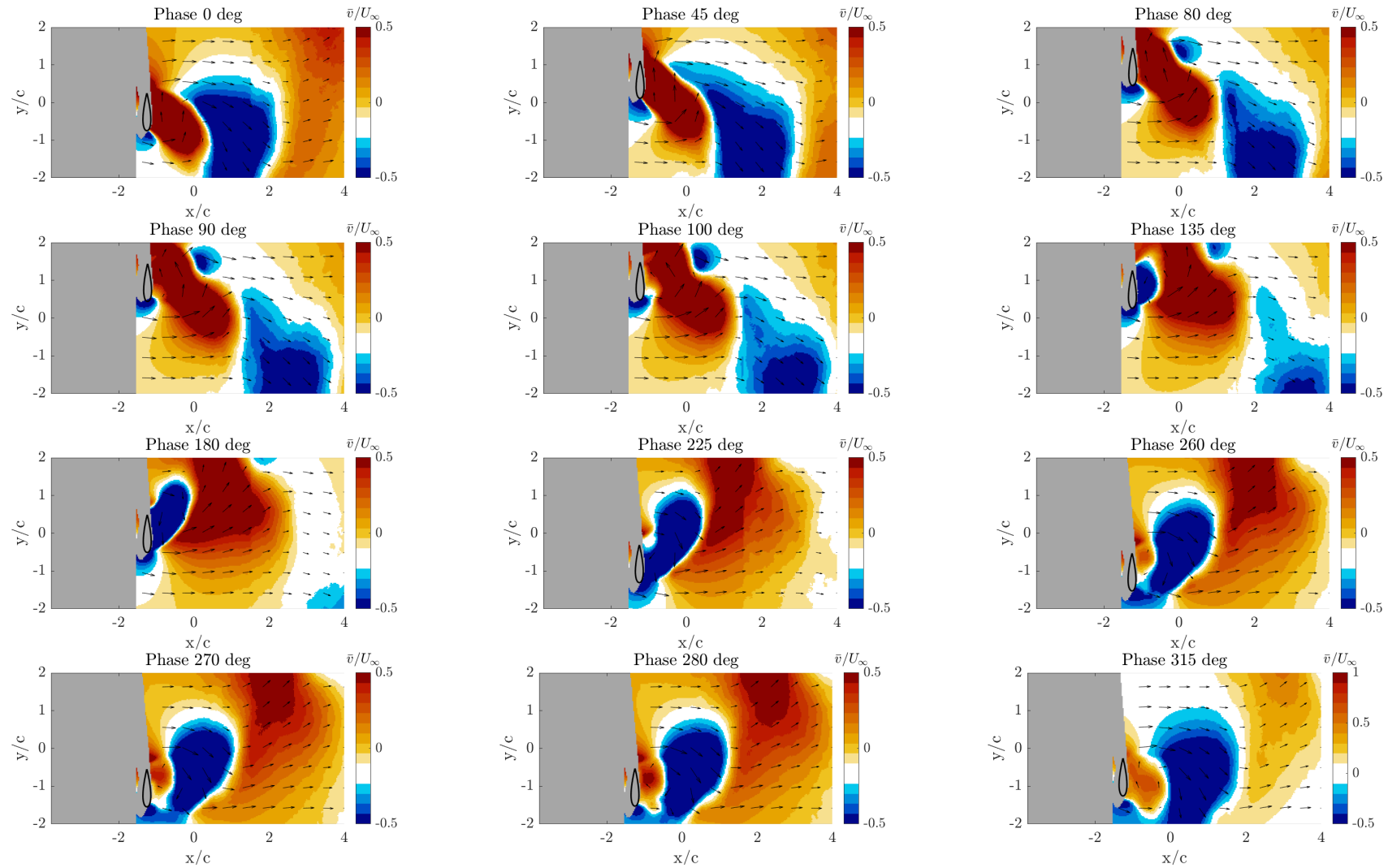


Figure I.3: Vertical velocity, \bar{v}/U_∞ around a plunging airfoil at 5Hz, 3 chords inboard from the tip with the freestream velocity coming from the left.

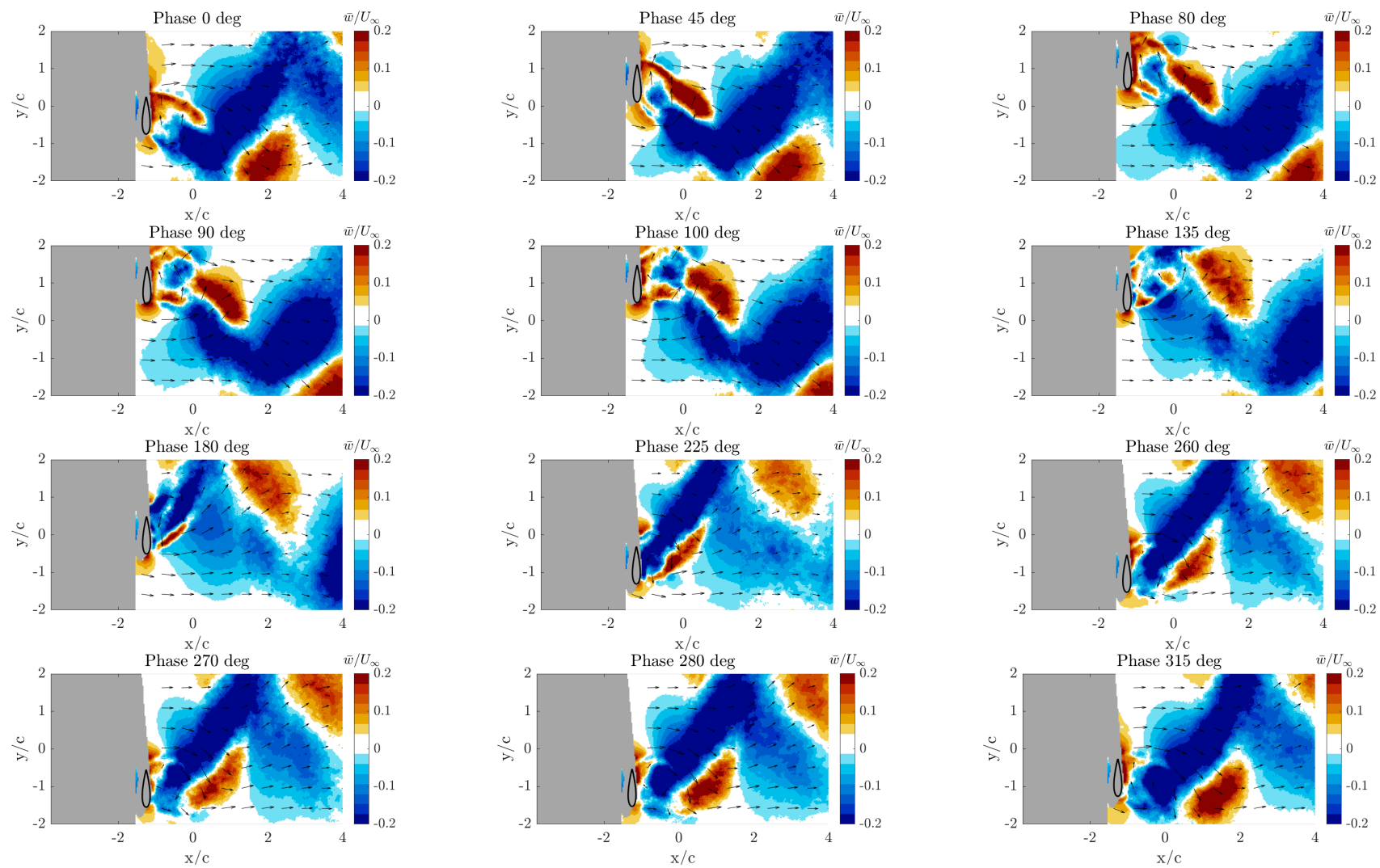


Figure I.4: Spanwise velocity, \bar{w}/U_∞ around a plunging airfoil at 5Hz, 3 chords inboard from the tip with the freestream velocity coming from the left. The flow is positive into the page.

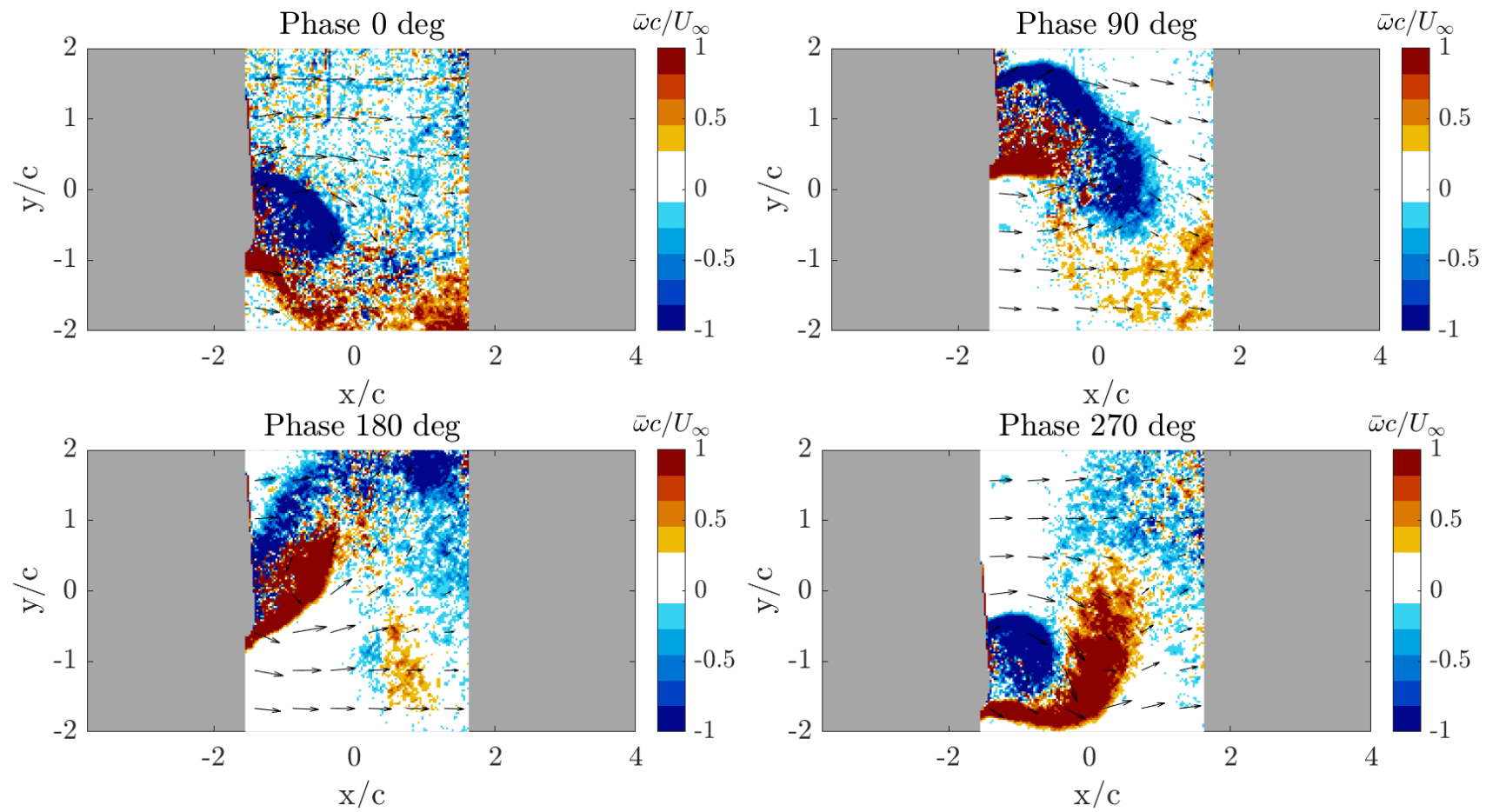


Figure I.5: Vorticity, $\bar{\omega}c/U_\infty$ around a plunging airfoil at 5Hz, 2 chords inboard from the tip with the freestream velocity coming from the left.

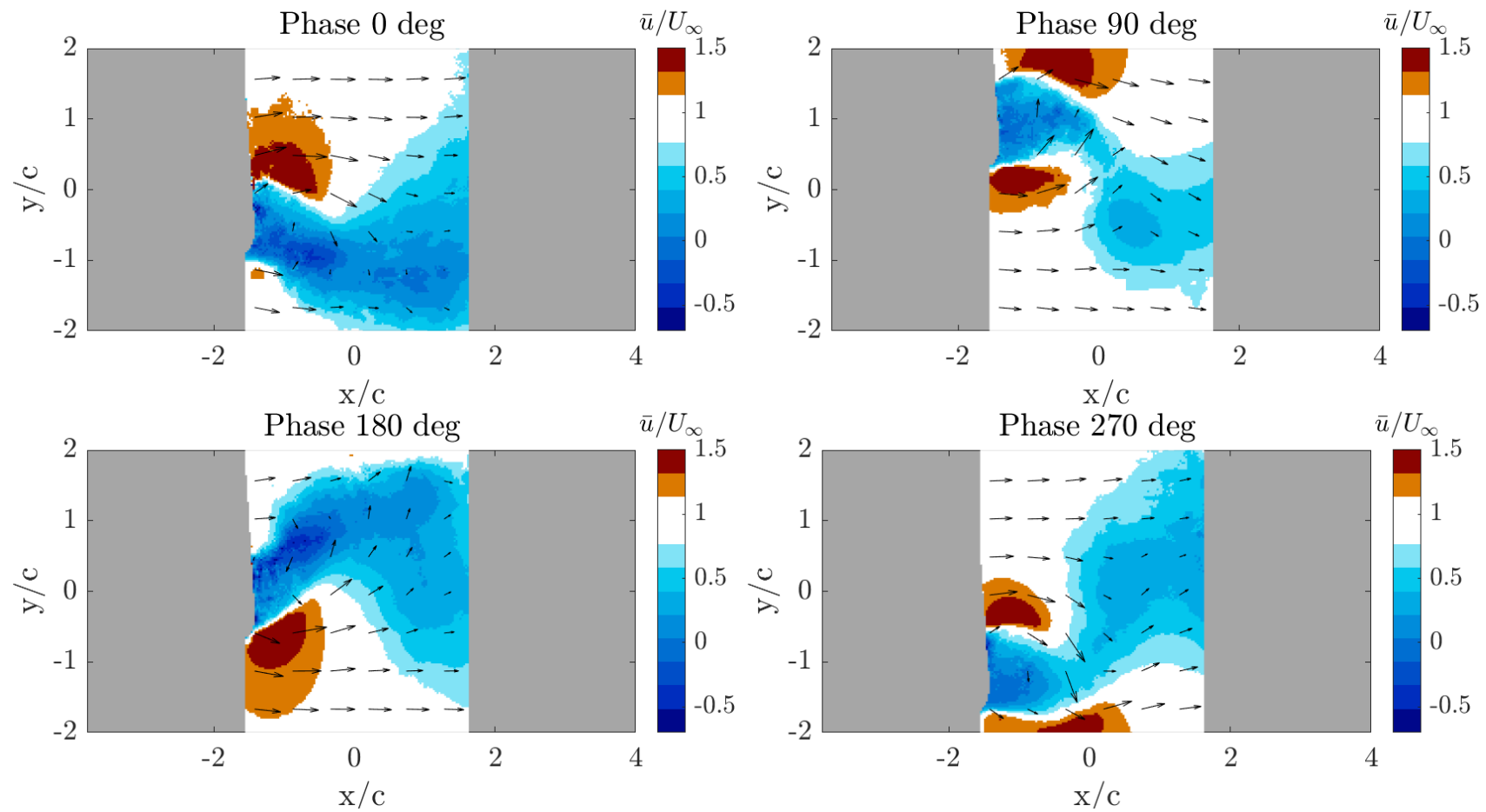


Figure I.6: Streamwise velocity, \bar{u}/U_∞ around a plunging airfoil at 5Hz, 2 chords inboard from the tip with the freestream velocity coming from the left.

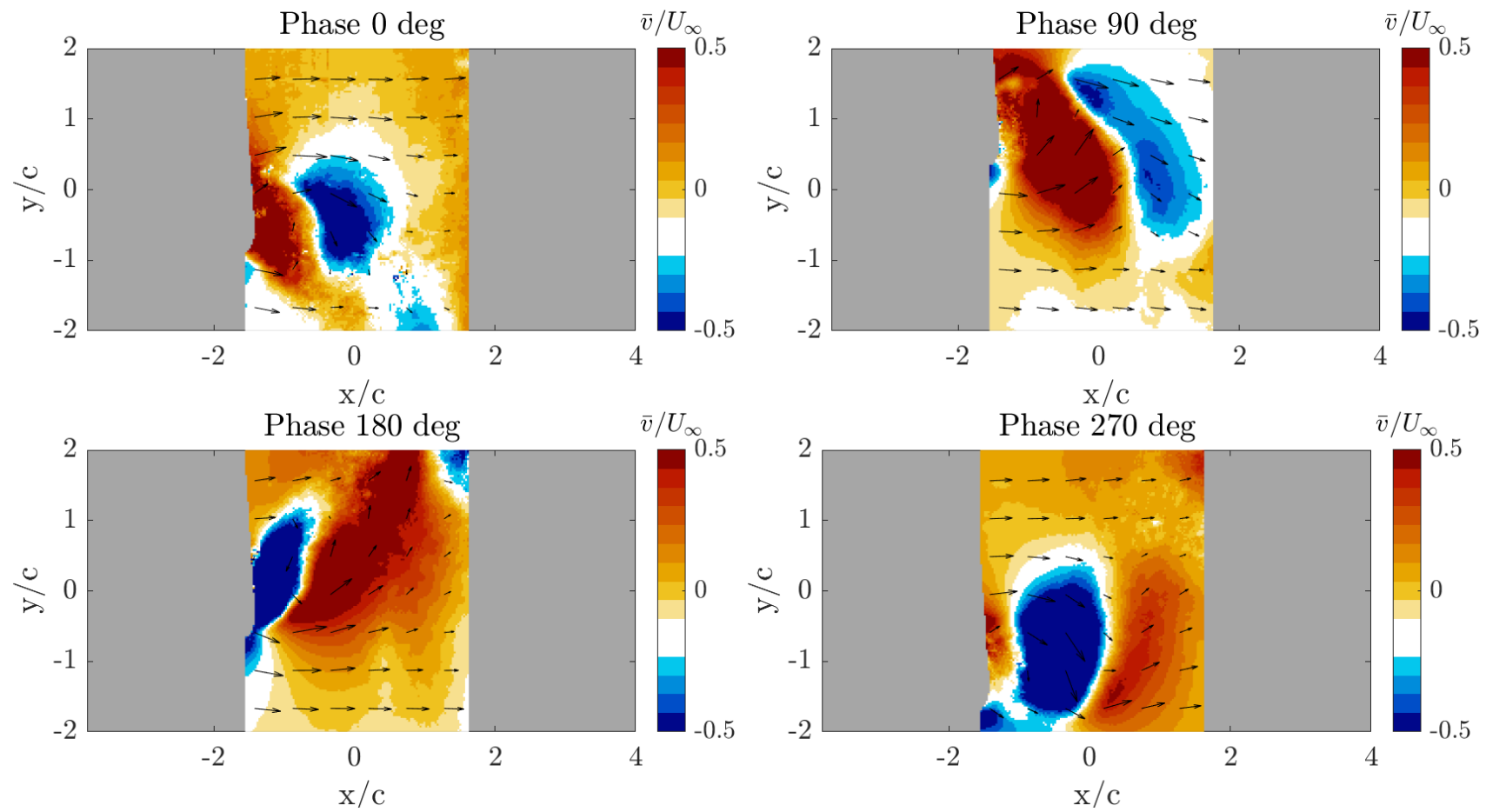


Figure I.7: Vertical velocity, \bar{v}/U_∞ around a plunging airfoil at 5Hz, 2 chords inboard from the tip with the freestream velocity coming from the left.

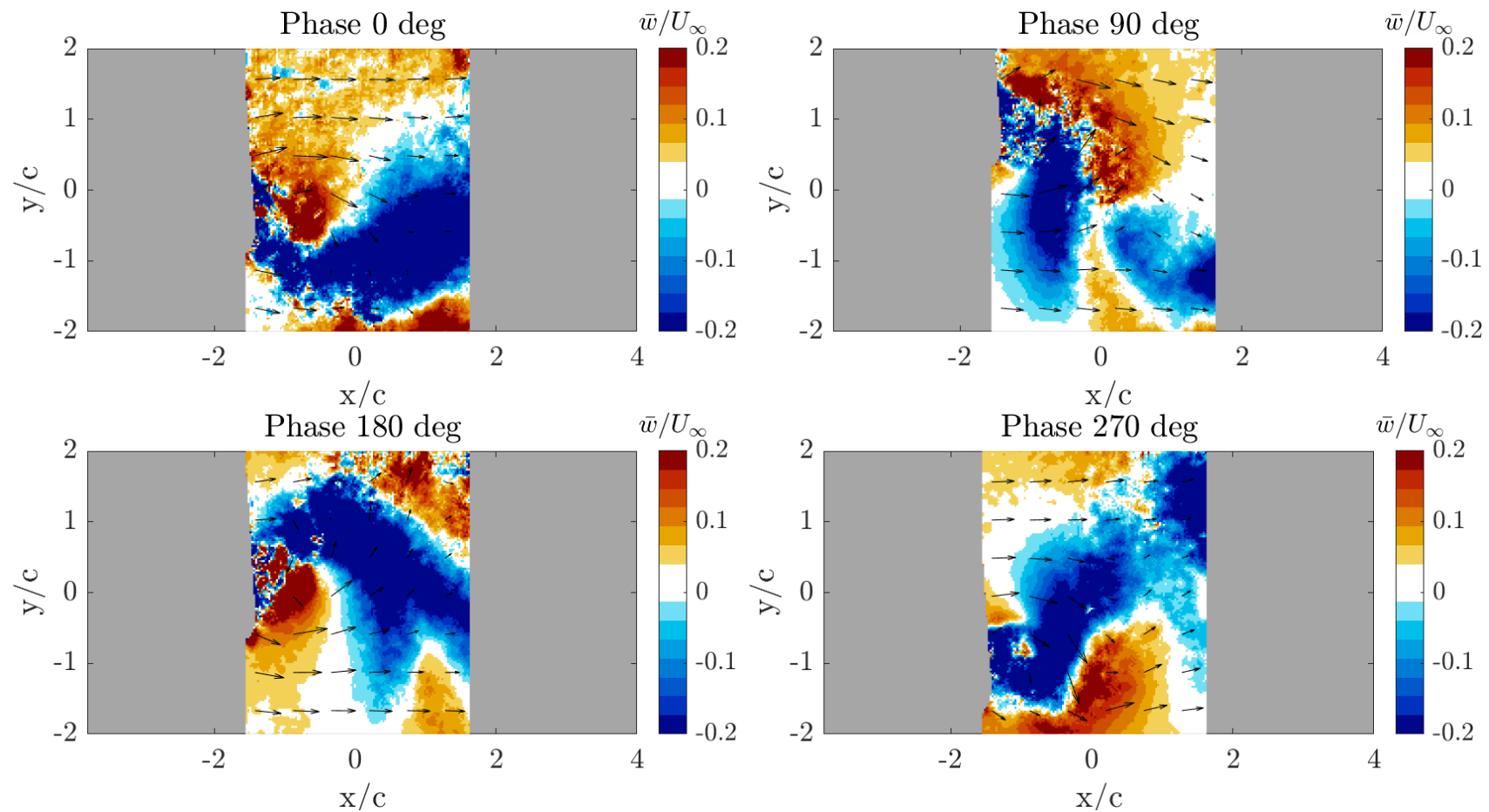


Figure I.8: Spanwise velocity, \bar{w}/U_∞ around a plunging airfoil at 5Hz, 2 chords inboard from the tip with the freestream velocity coming from the left. The flow is positive into the page.

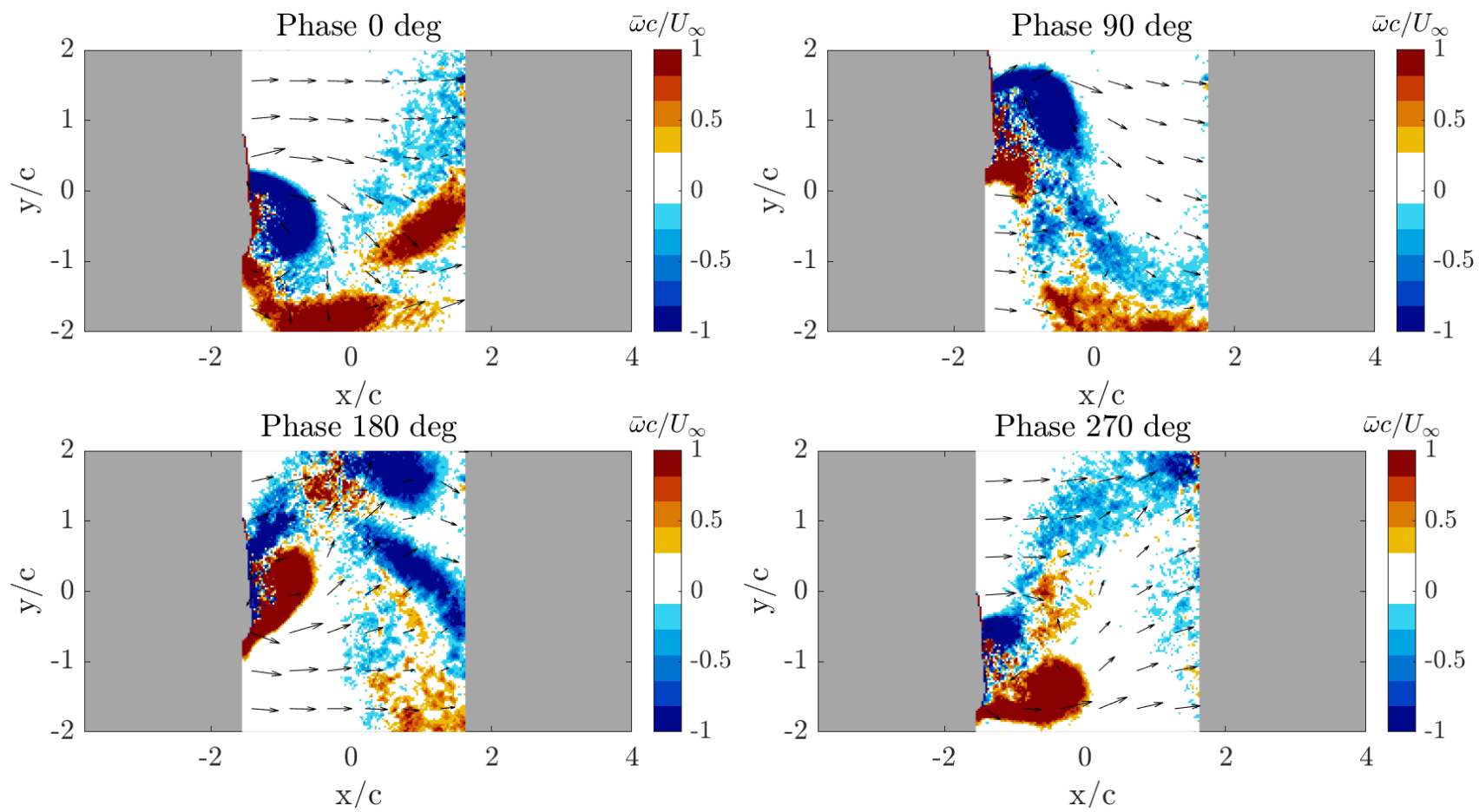


Figure I.9: Vorticity, $\bar{\omega}c/U_\infty$ around a plunging airfoil at 5Hz, 1 chord inboard from the tip with the freestream velocity coming from the left.

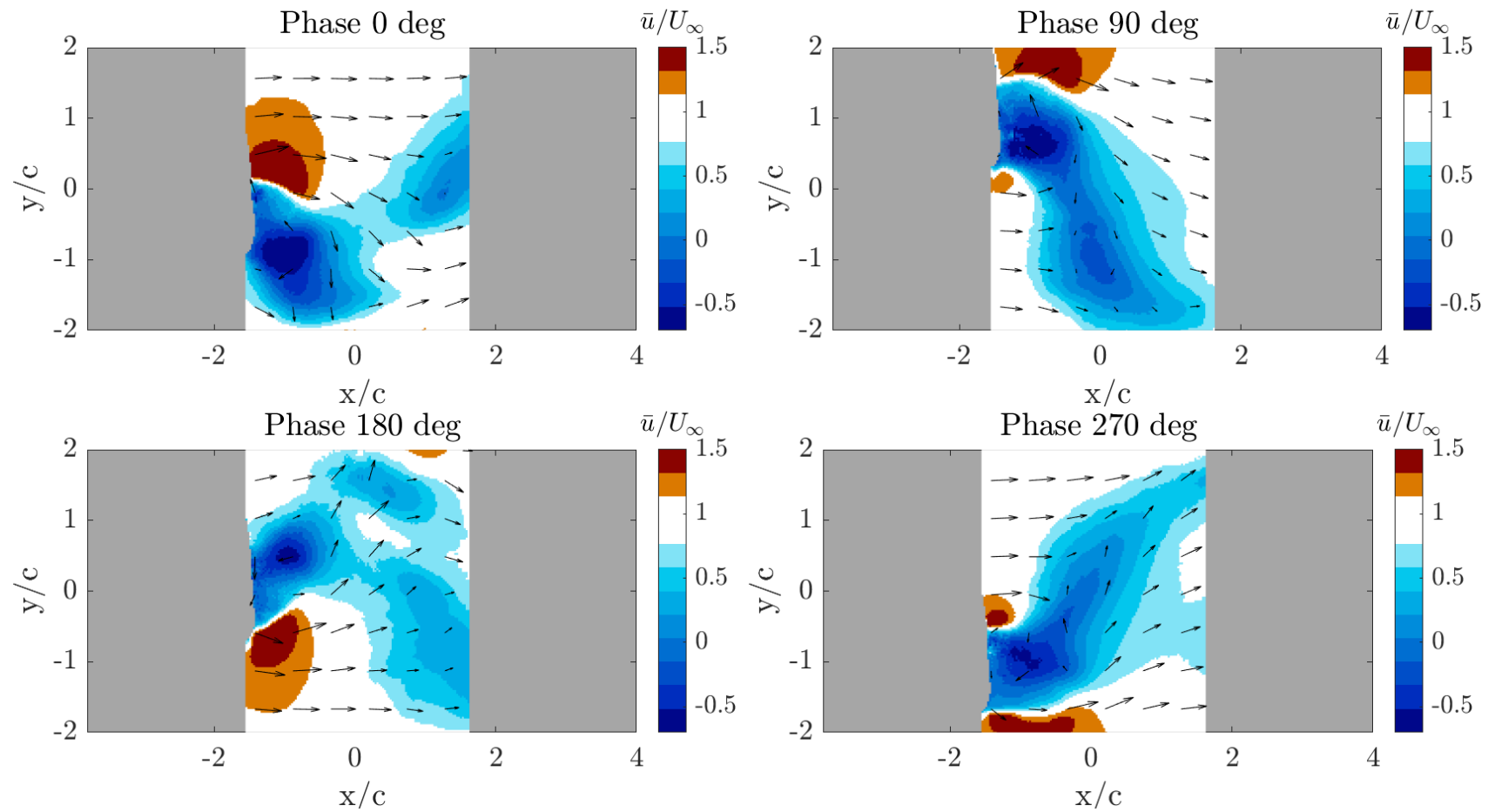


Figure I.10: Streamwise velocity, \bar{u}/U_∞ around a plunging airfoil at 5Hz, 1 chord inboard from the tip with the freestream velocity coming from the left.

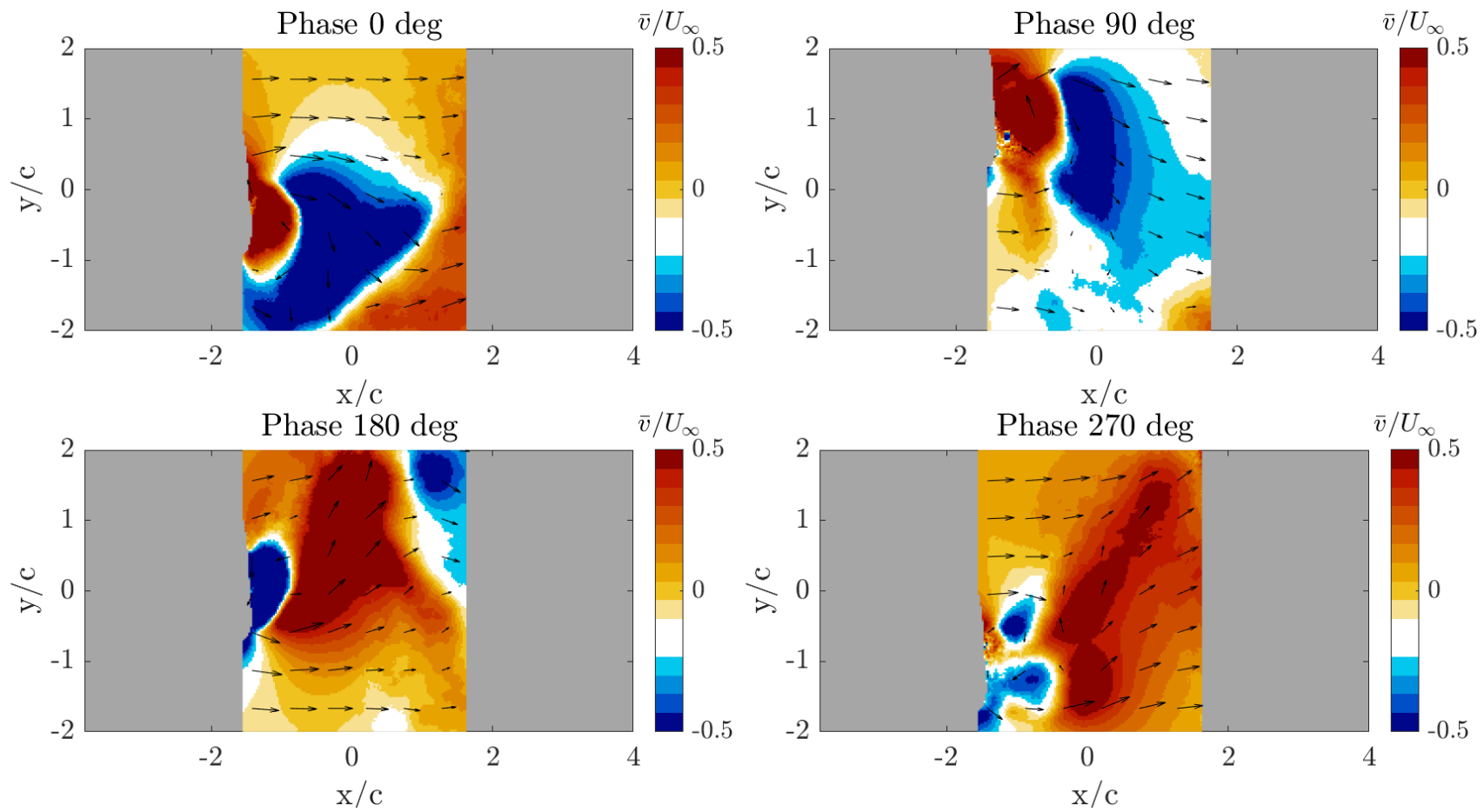


Figure I.11: Vertical velocity, \bar{v}/U_∞ around a plunging airfoil at 5Hz, 1 chord inboard from the tip with the freestream velocity coming from the left.

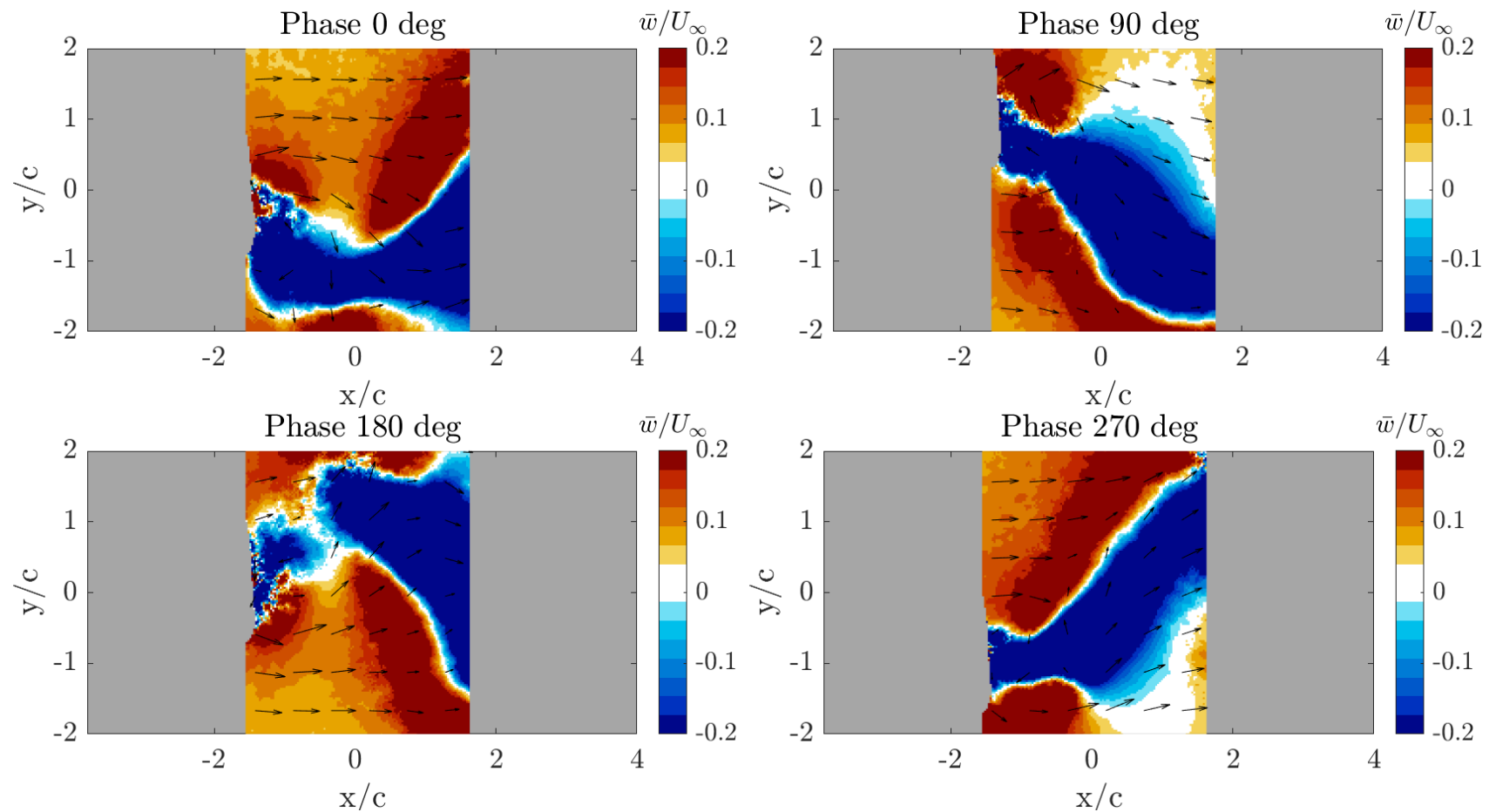


Figure I.12: Spanwise velocity, \bar{w}/U_∞ around a plunging airfoil at 5Hz, 1 chord inboard from the tip with the freestream velocity coming from the left. The flow is positive into the page.

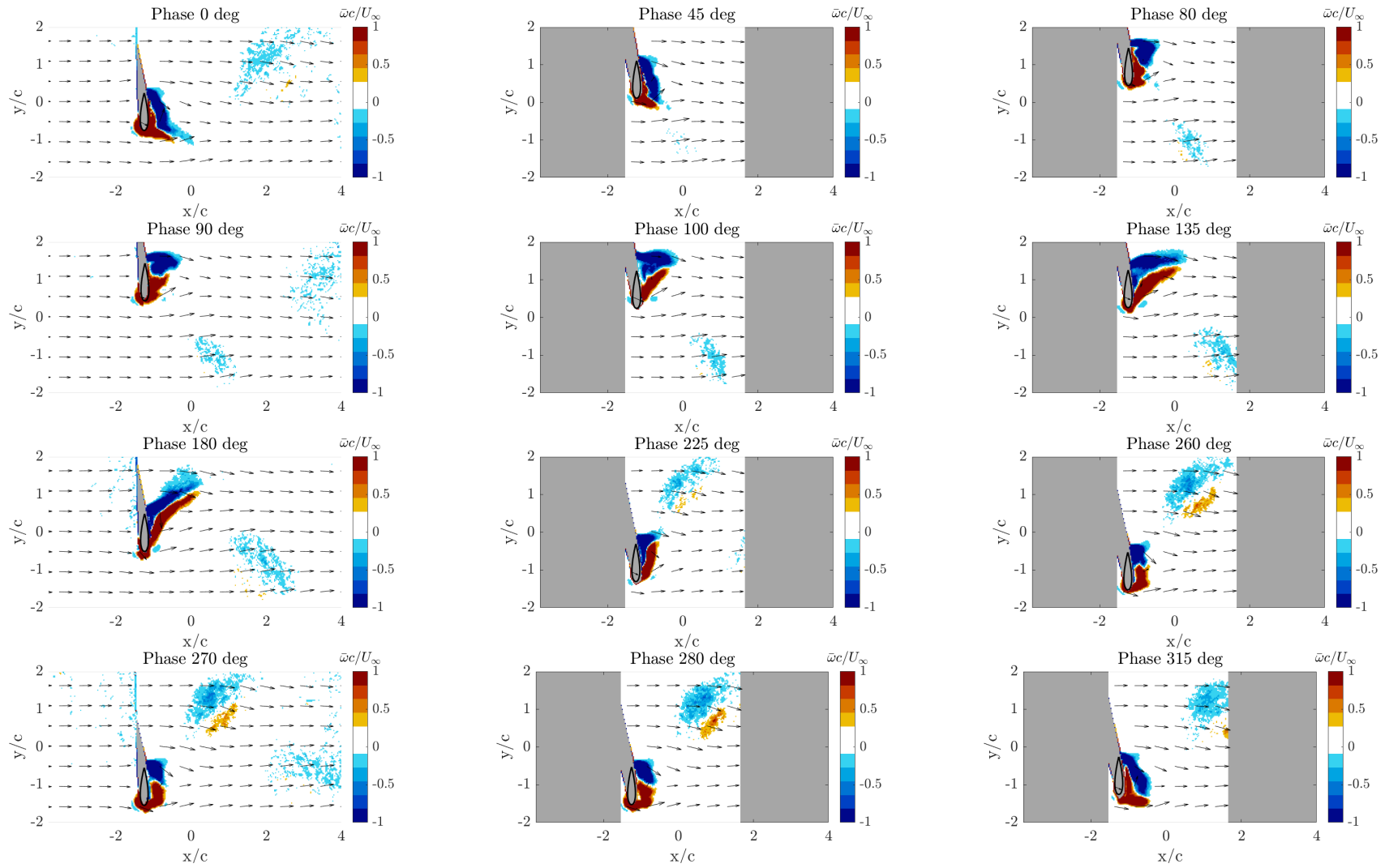


Figure I.13: Vorticity, $\bar{\omega}c/U_\infty$ around a plunging airfoil at 5Hz, at from the tip with the freestream velocity coming from the left.

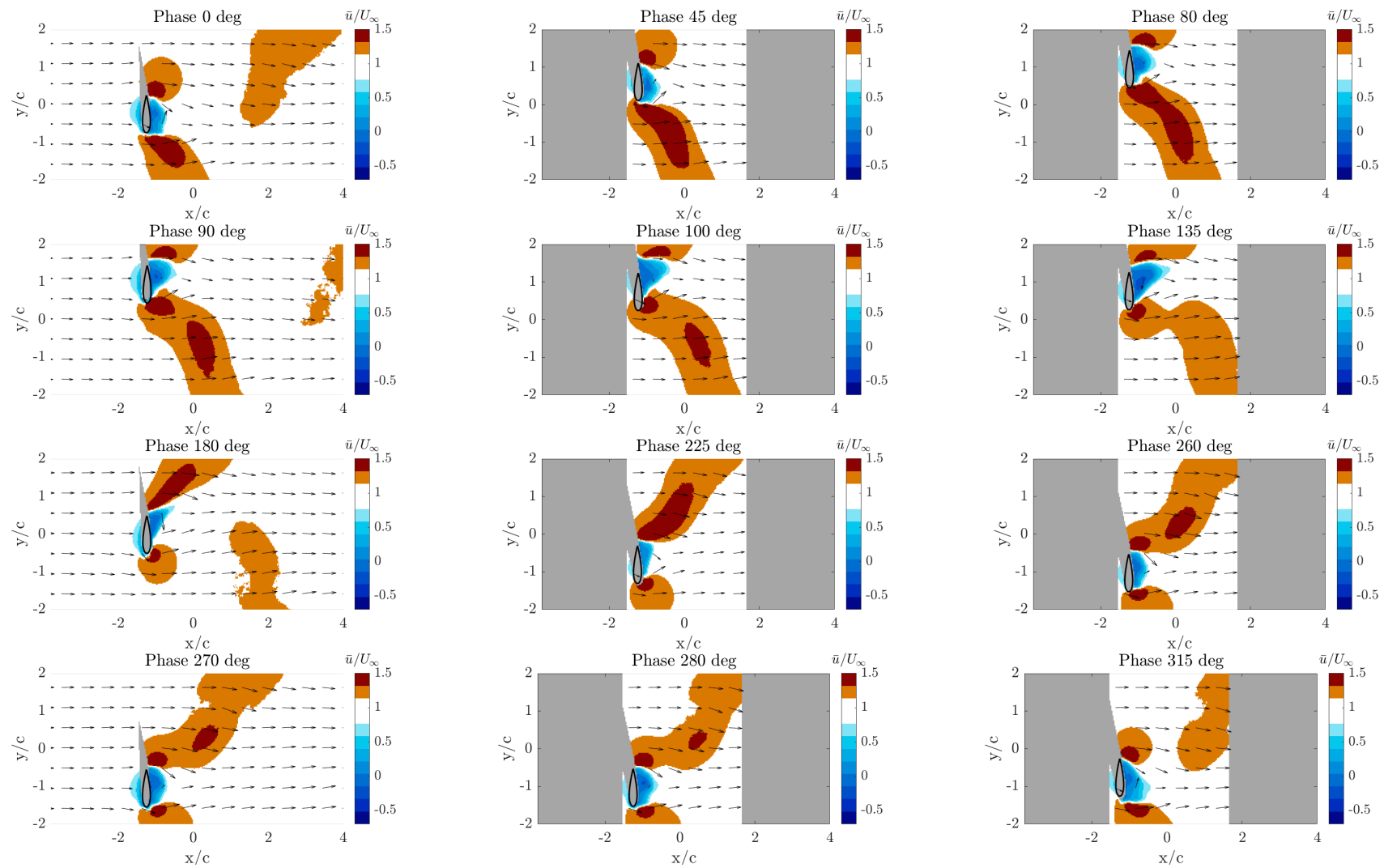


Figure I.14: Streamwise velocity, \bar{u}/U_∞ around a plunging airfoil at 5Hz, at the tip with the freestream velocity coming from the left.

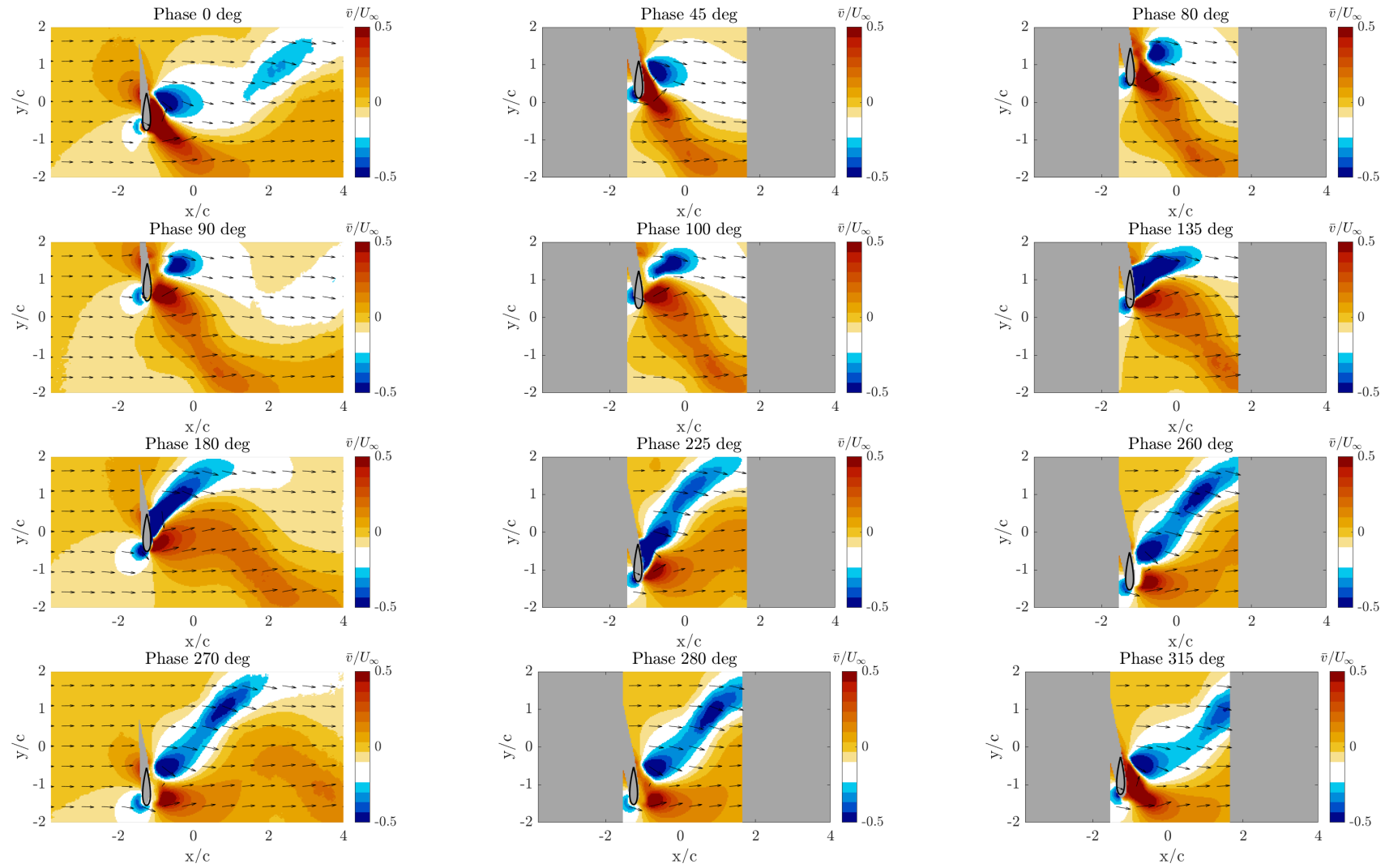


Figure I.15: Vertical velocity, \bar{v}/U_∞ around a plunging airfoil at 5Hz, at the tip with the freestream velocity coming from the left.

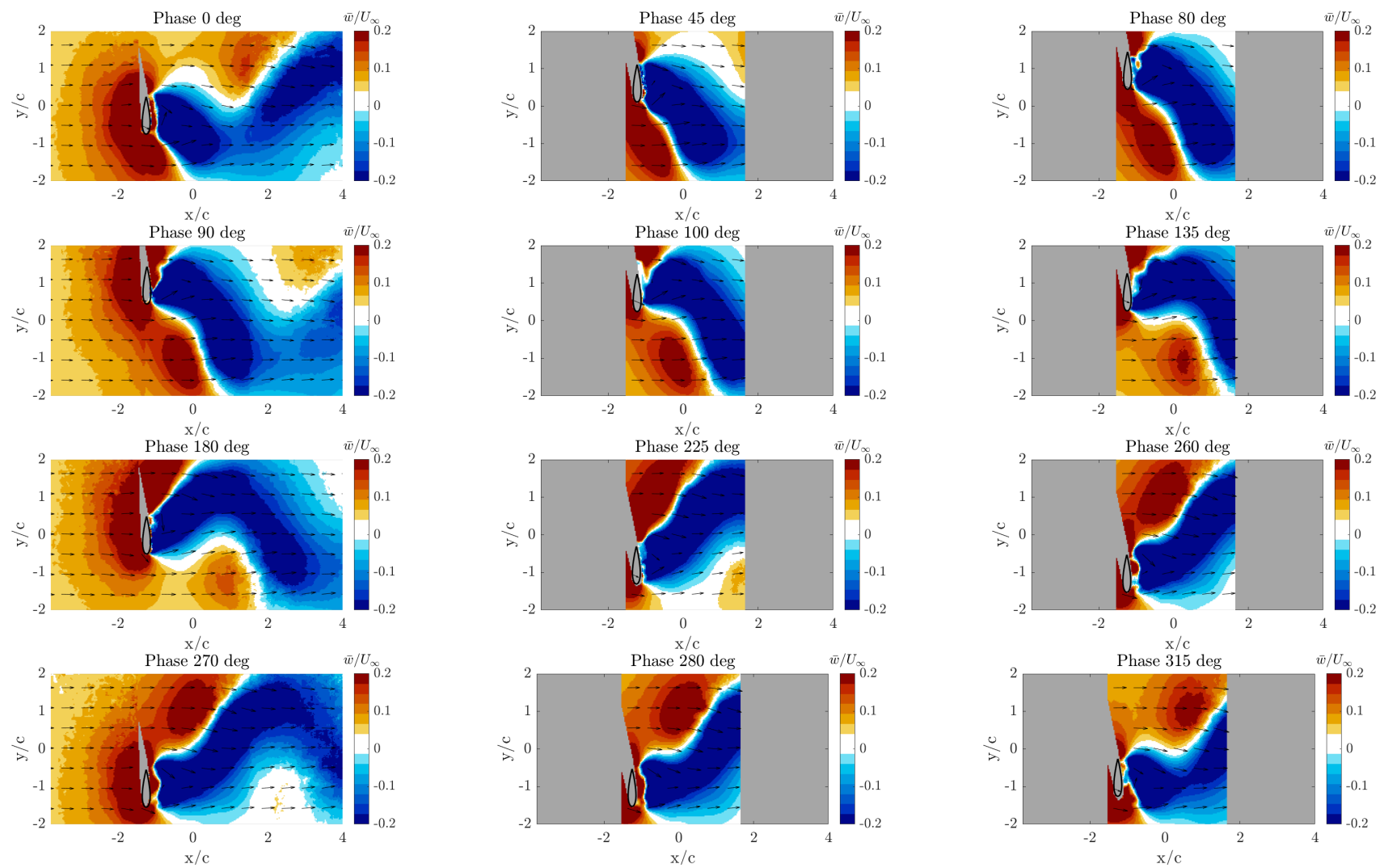


Figure I.16: Spanwise velocity, \bar{w}/U_∞ around a plunging airfoil at 5Hz, at the tip with the freestream velocity coming from the left. The flow is positive into the page.

APPENDIX J

2.5 Hz Surging Cases PIV Planes

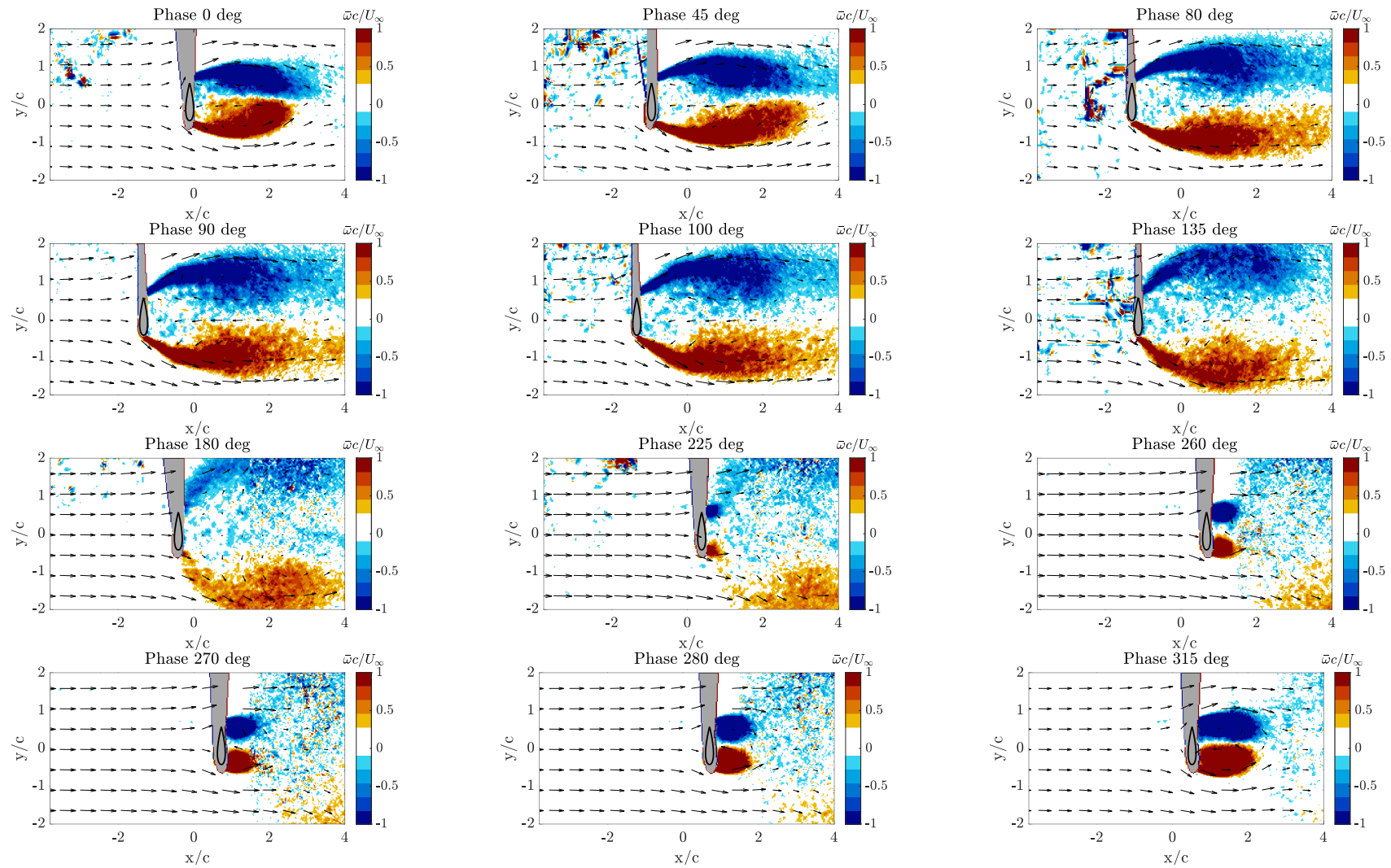


Figure J.1: Vorticity, $\bar{\omega}c/U_\infty$ around a surging airfoil at 2.5Hz, 3 chords inboard from the tip with the freestream velocity coming from the left.

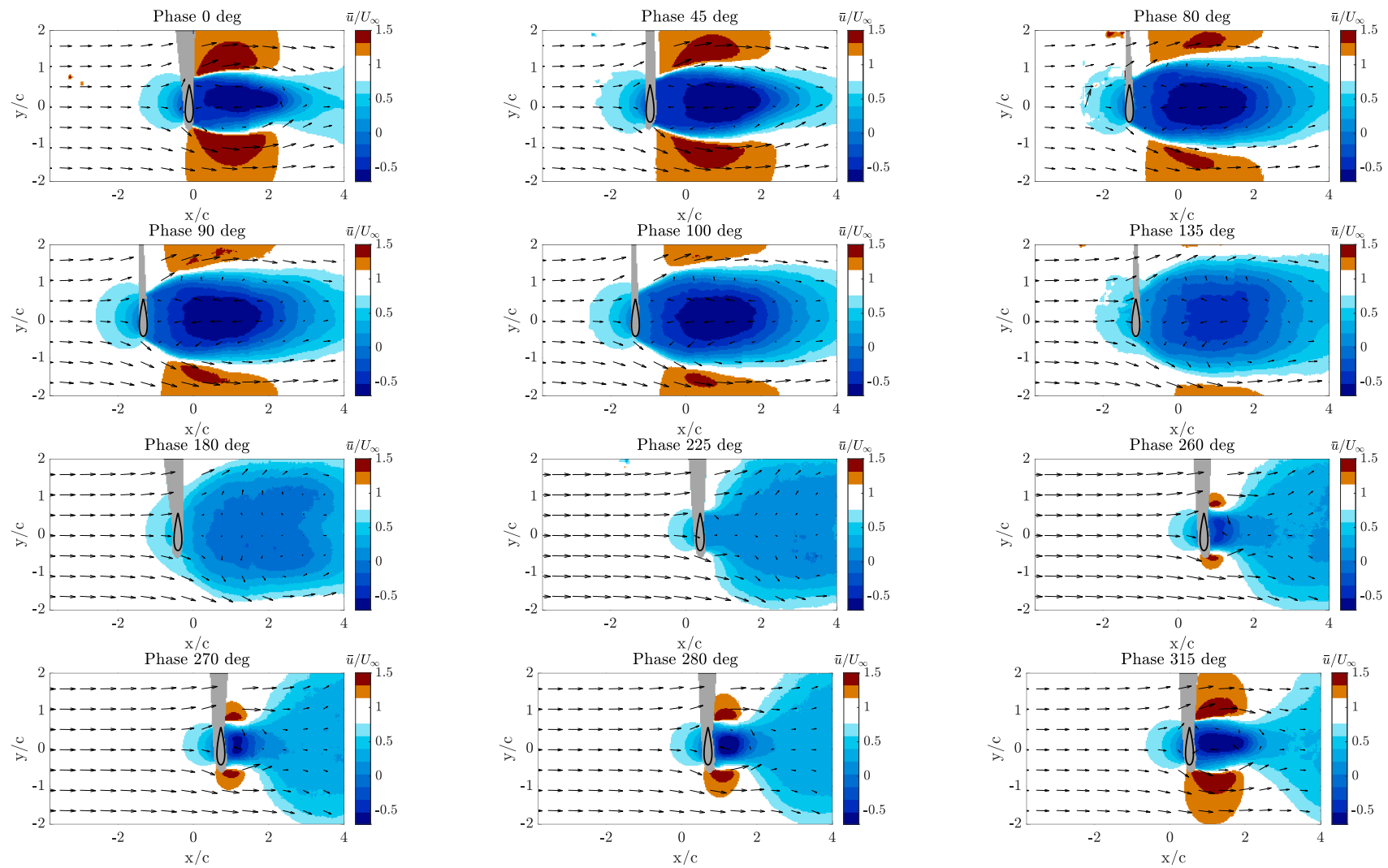


Figure J.2: Streamwise velocity, \bar{u}/U_∞ around a surging airfoil at 2.5Hz, 3 chords inboard from the tip with the freestream velocity coming from the left.

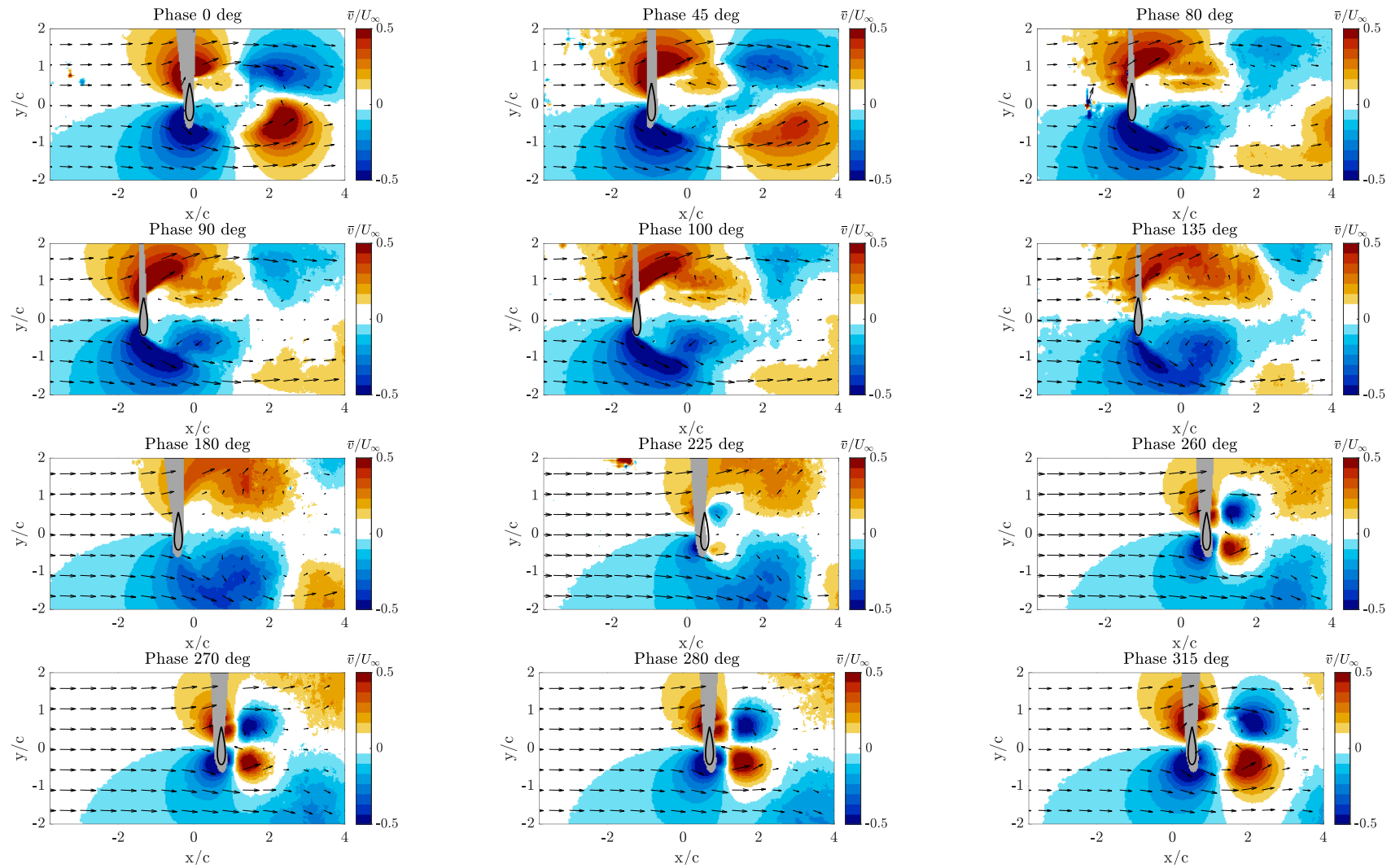


Figure J.3: Vertical velocity, \bar{v}/U_∞ around a surging airfoil at 2.5Hz, 3 chords inboard from the tip with the freestream velocity coming from the left.

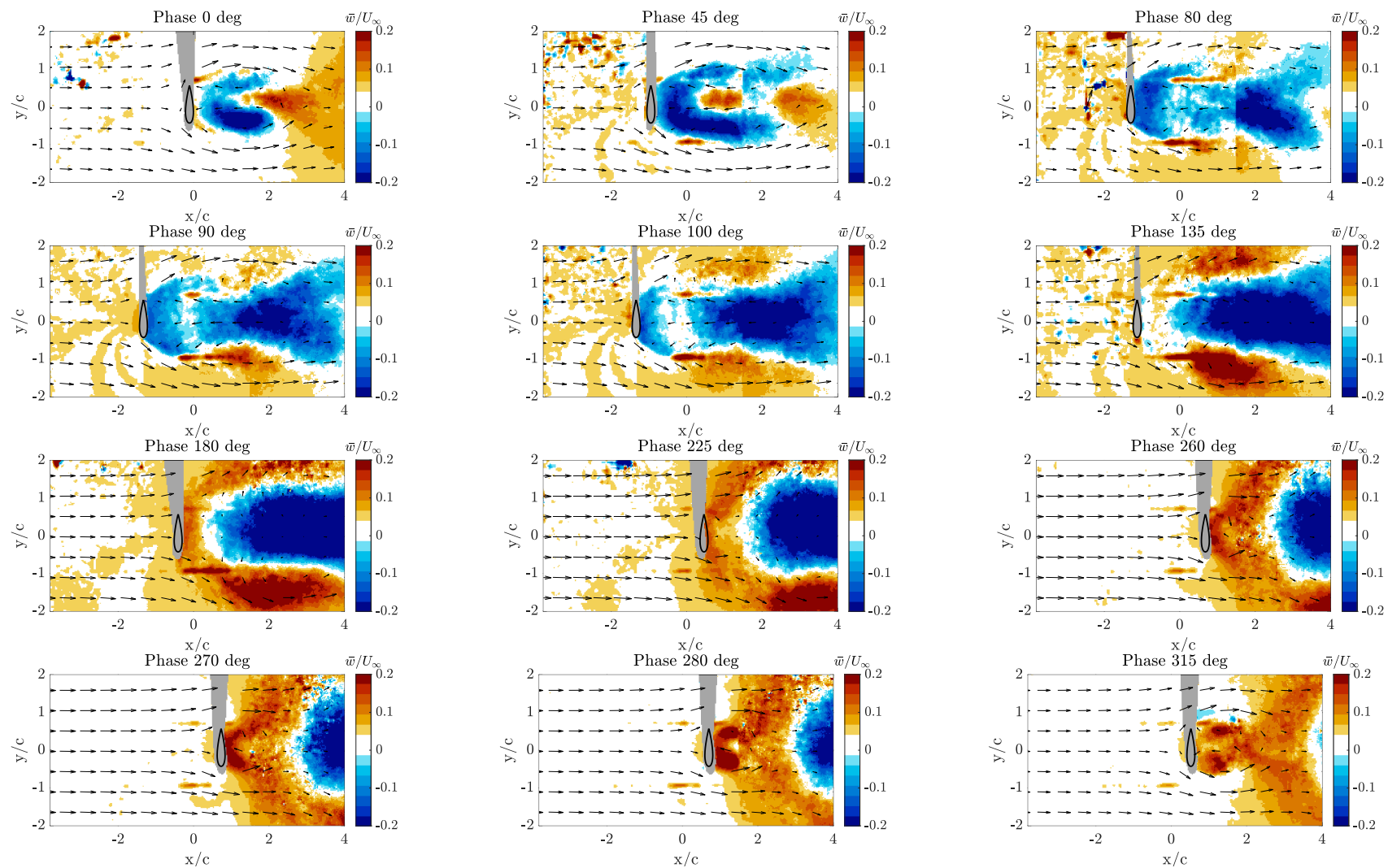


Figure J.4: Spanwise velocity, \bar{w}/U_∞ around a surging airfoil at 2.5Hz, 3 chords inboard from the tip with the freestream velocity coming from the left. The flow is positive into the page.

APPENDIX **K**

5 Hz Surging Cases PIV Planes

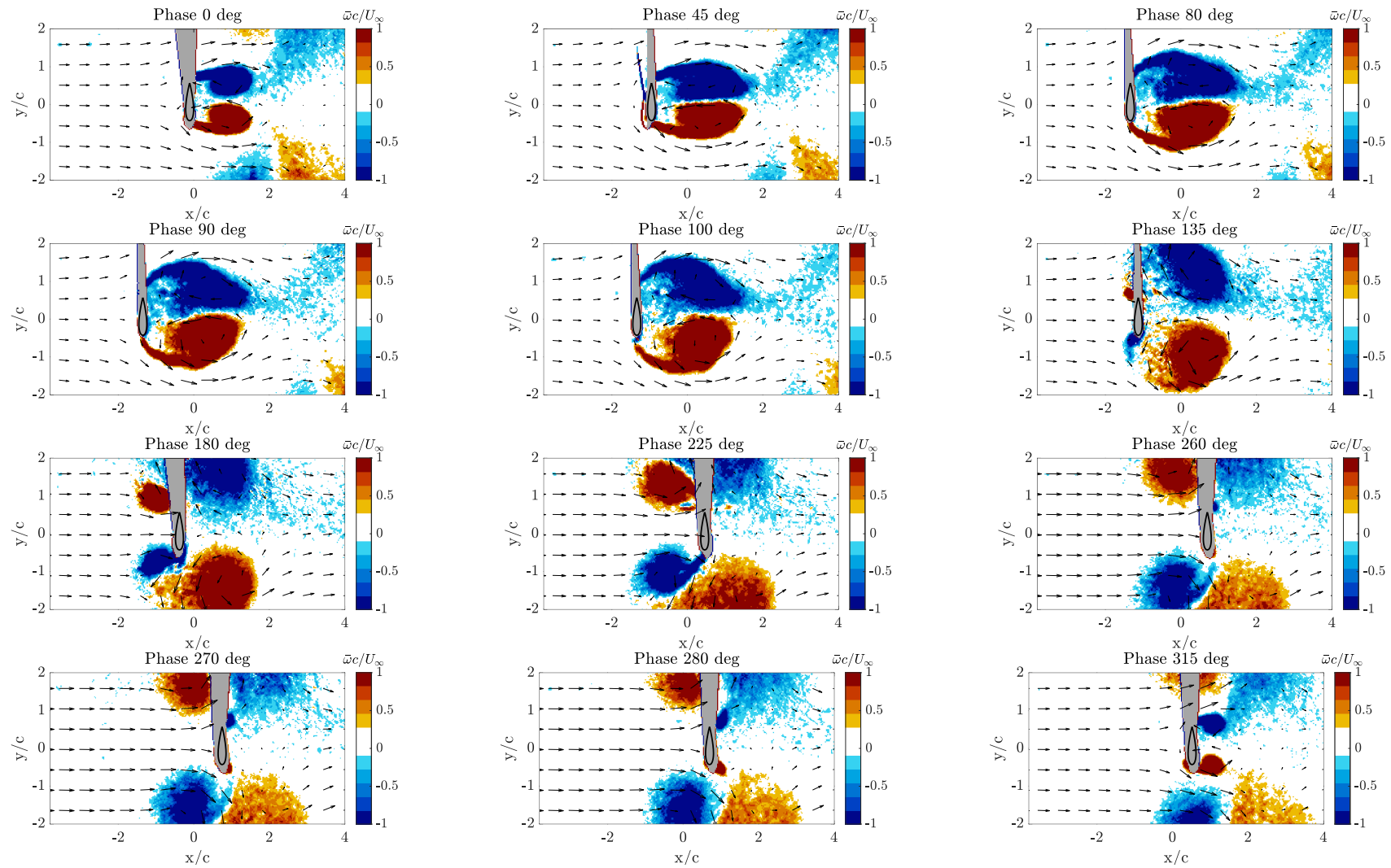


Figure K.1: Vorticity, $\bar{\omega}c/U_\infty$ around a surging airfoil at 5Hz, 3 chords inboard from the tip with the freestream velocity coming from the left.

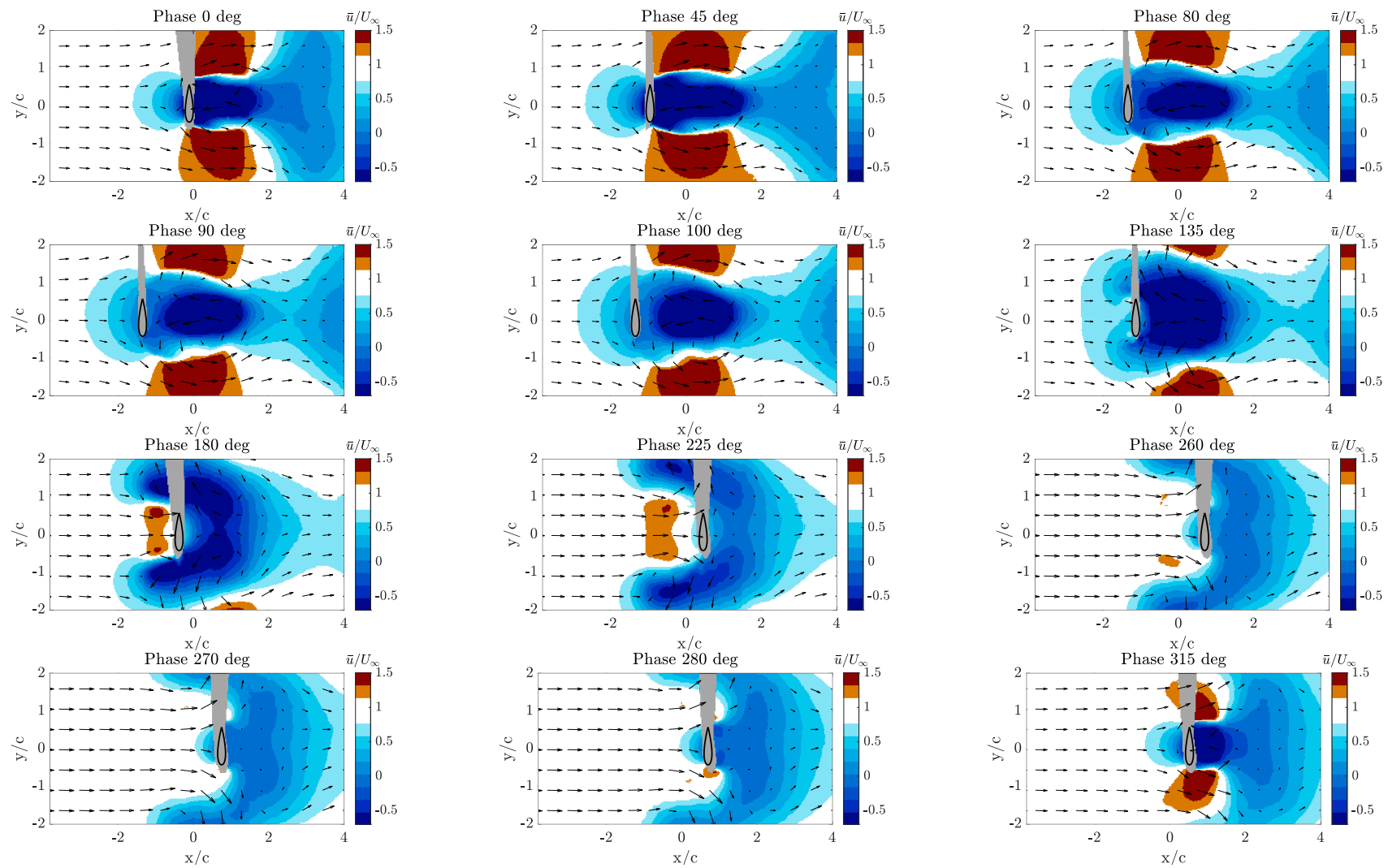


Figure K.2: Streamwise velocity, \bar{u}/U_∞ around a surging airfoil at 5Hz, 3 chords inboard from the tip with the freestream velocity coming from the left.

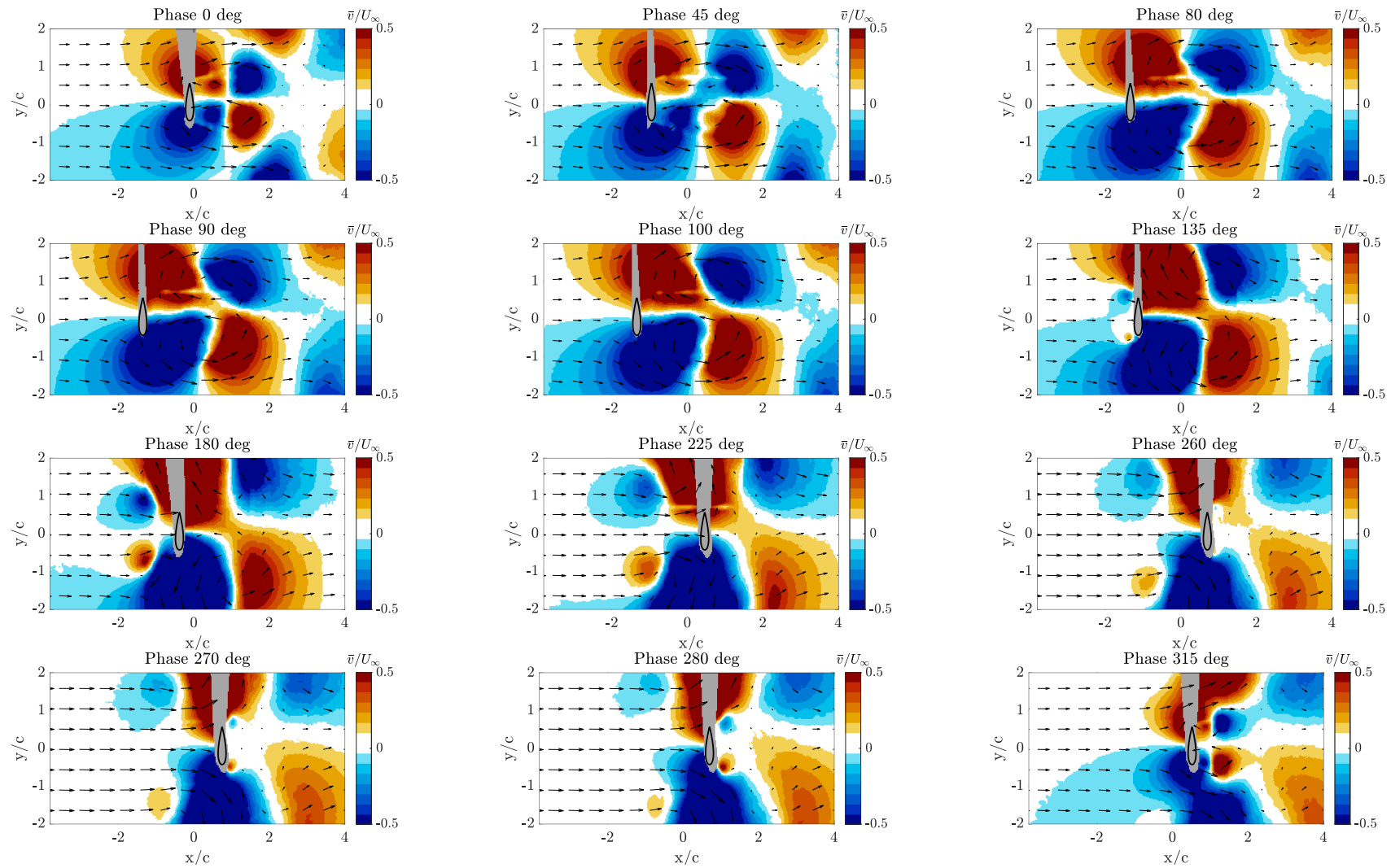


Figure K.3: Vertical velocity, \bar{v}/U_∞ around a surging airfoil at 5Hz, 3 chords inboard from the tip with the freestream velocity coming from the left.

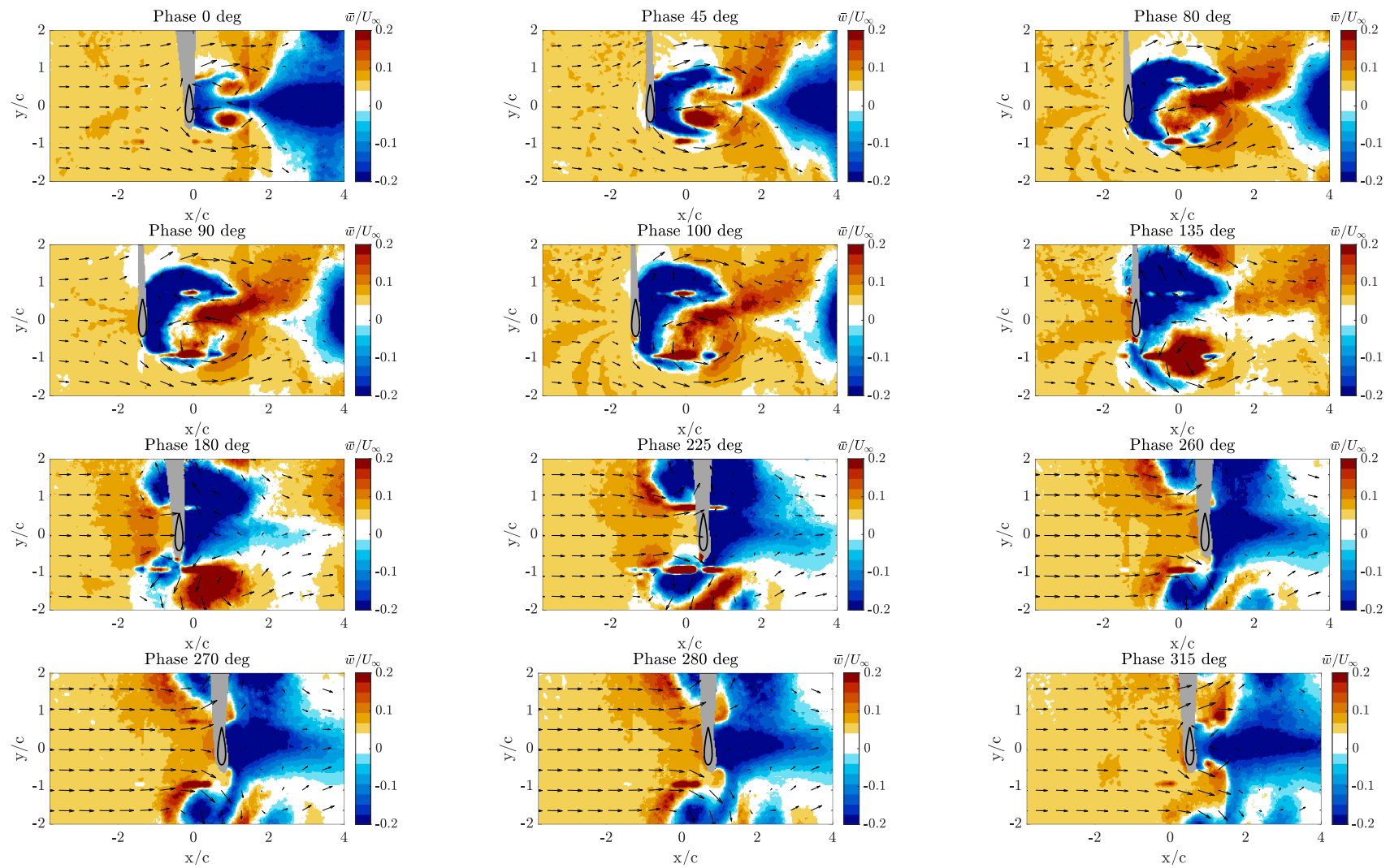


Figure K.4: Spanwise velocity, \bar{w}/U_∞ around a surging airfoil at 5Hz, 3 chords inboard from the tip with the freestream velocity coming from the left. The flow is positive into the page.

APPENDIX L

2.5 Hz Plunging Cases CFD Planes

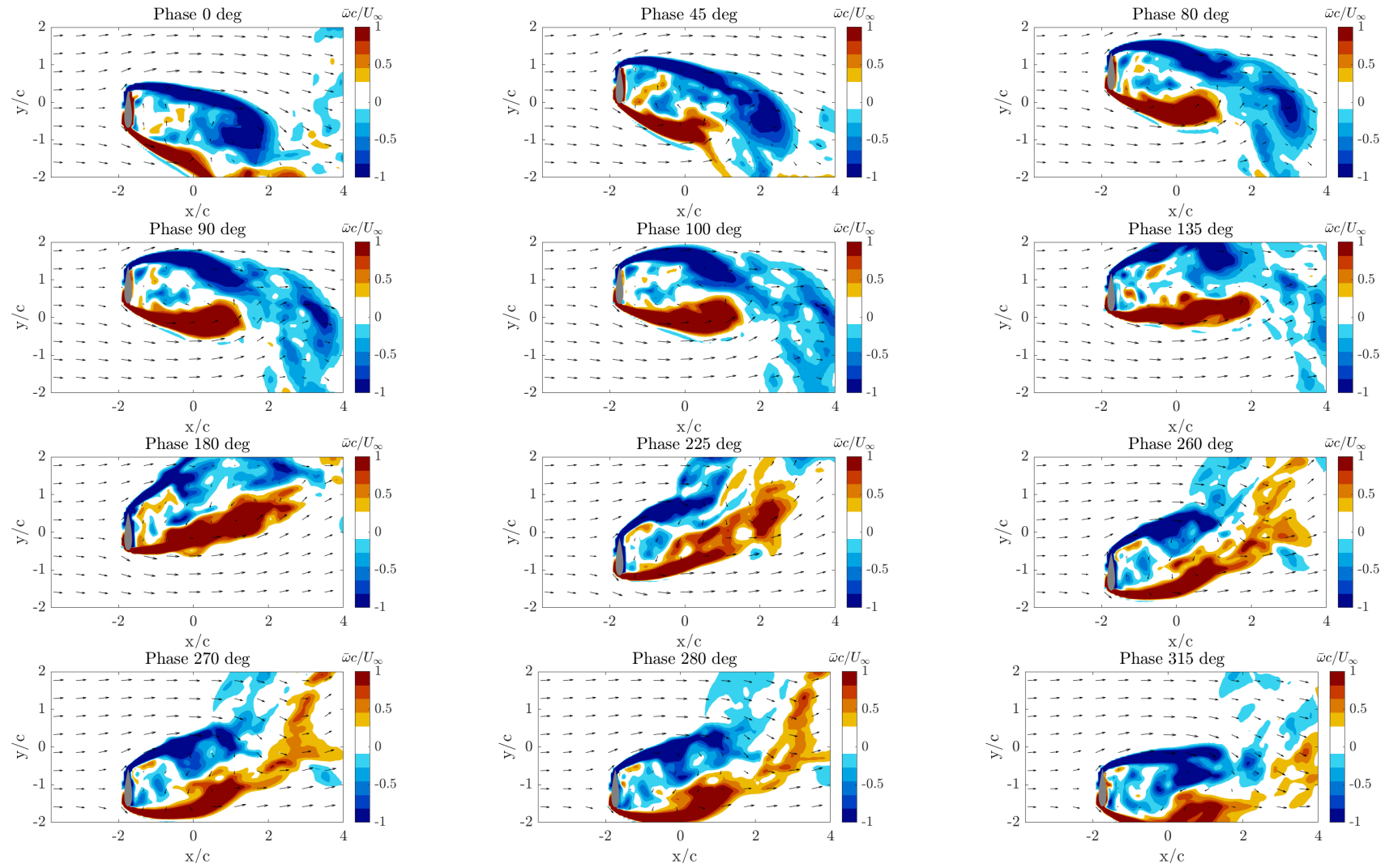


Figure L.1: Vorticity, $\bar{\omega}c/U_\infty$ around a plunging airfoil at 2.5Hz, 3 chords inboard from the tip with the freestream velocity coming from the left.

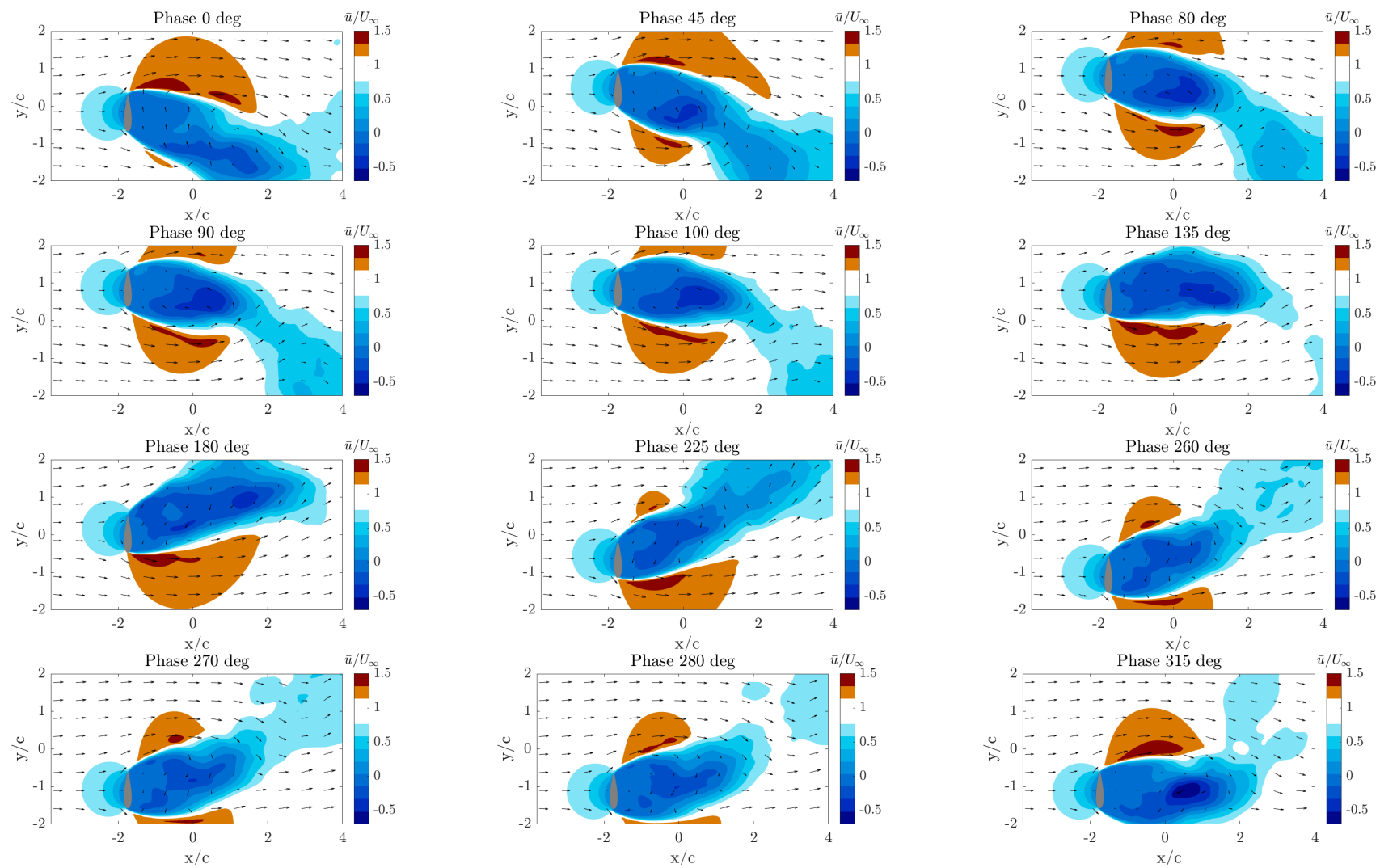


Figure L.2: Streamwise velocity, \bar{u}/U_∞ around a plunging airfoil at 2.5Hz, 3 chords inboard from the tip with the freestream velocity coming from the left.

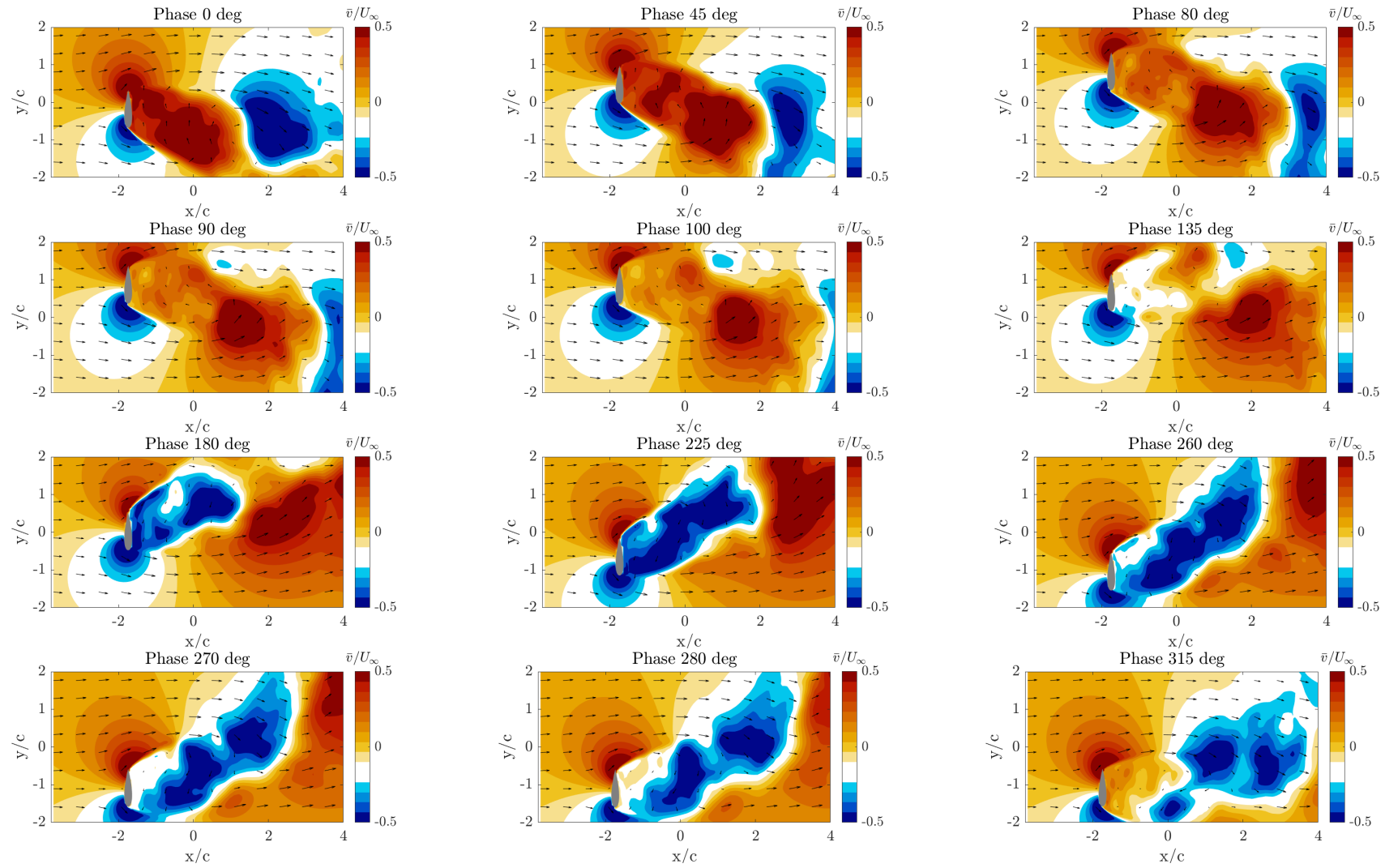


Figure L.3: Vertical velocity, \bar{v}/U_∞ around a plunging airfoil at 2.5Hz, 3 chords inboard from the tip with the freestream velocity coming from the left.

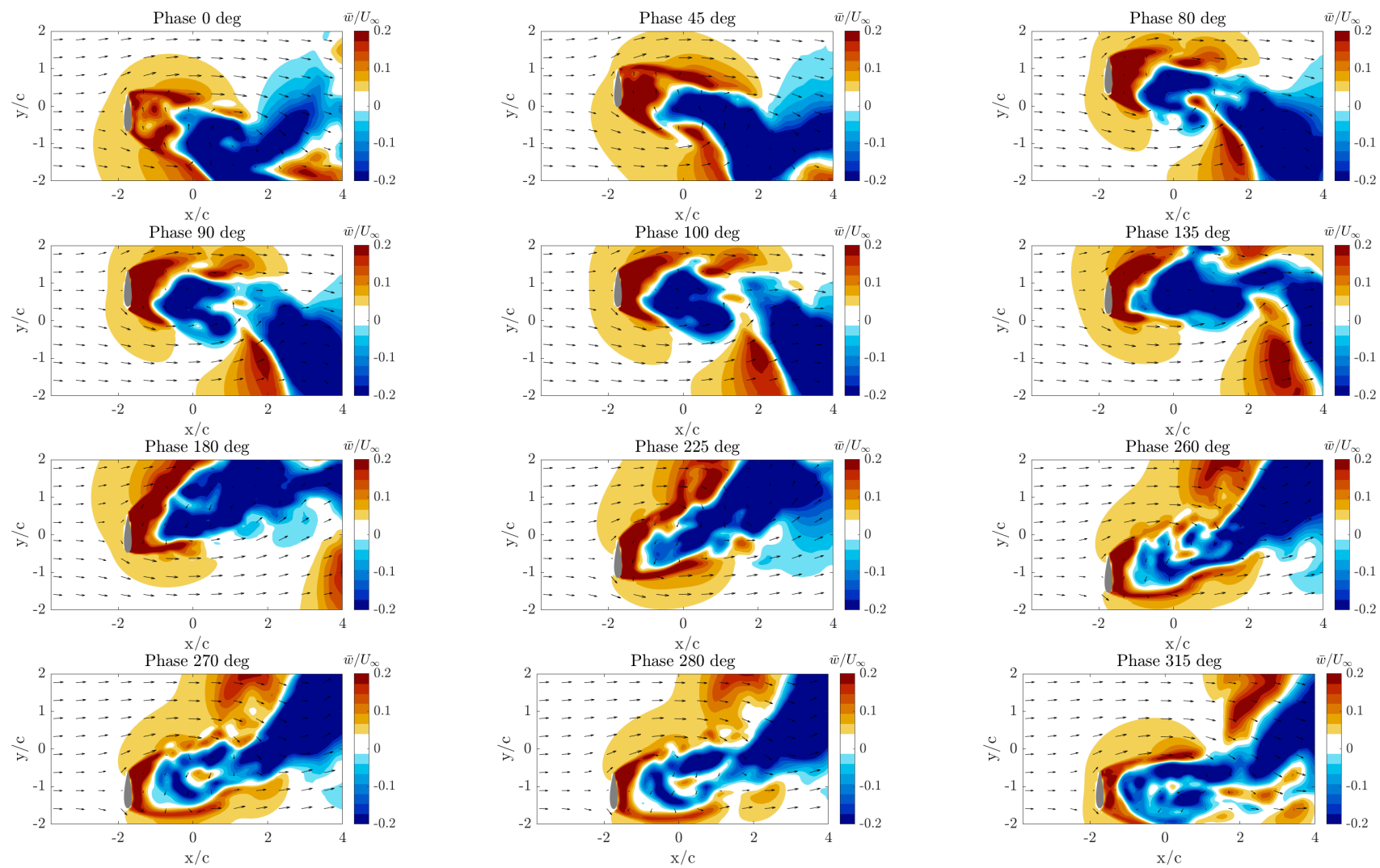


Figure L.4: Spanwise velocity, \bar{w}/U_∞ around a plunging airfoil at 2.5Hz, 3 chords inboard from the tip with the freestream velocity coming from the left. The flow is positive into the page.

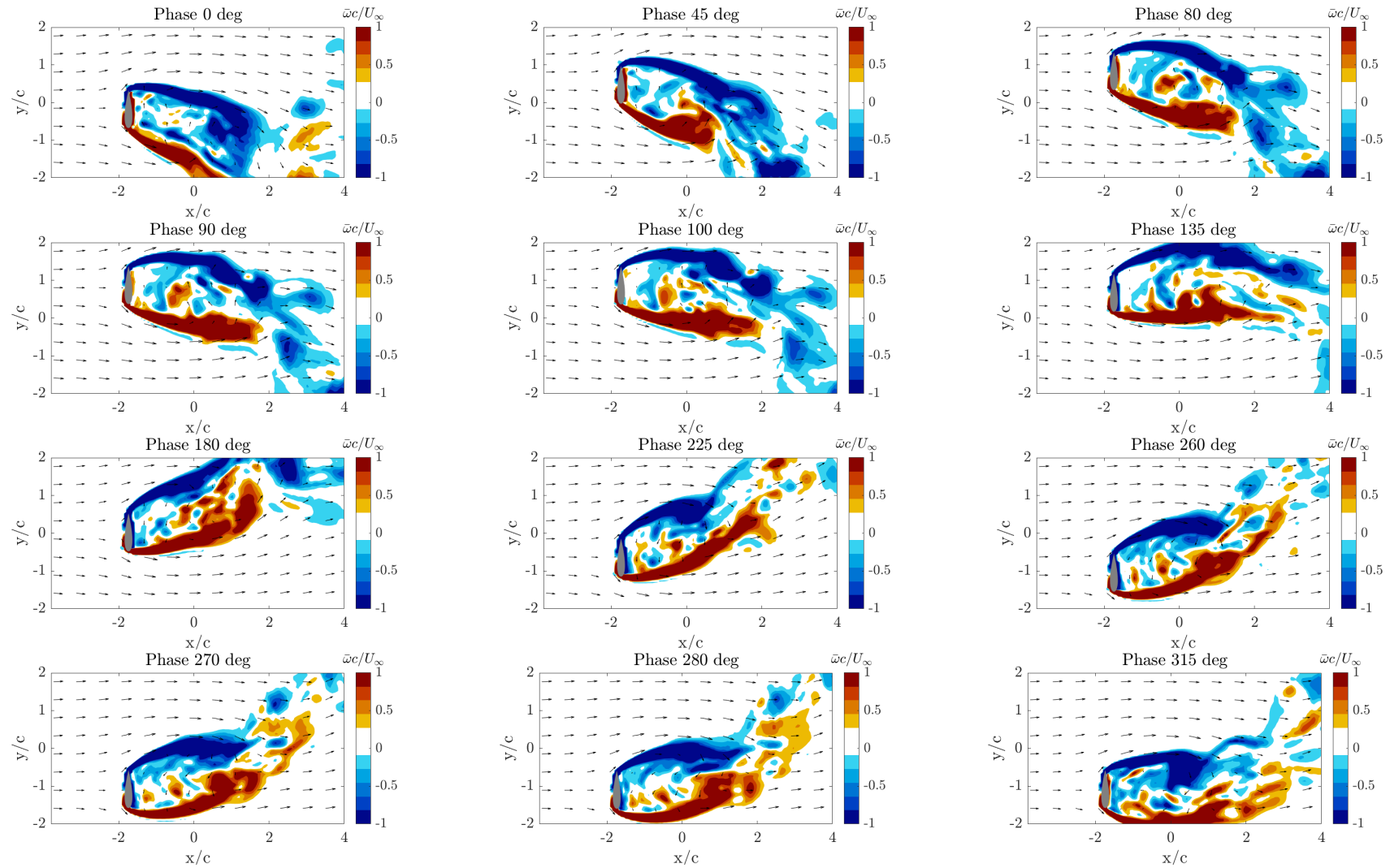


Figure L.5: Vorticity, $\bar{\omega}c/U_\infty$ around a plunging airfoil at 2.5Hz, 2 chords inboard from the tip with the freestream velocity coming from the left.

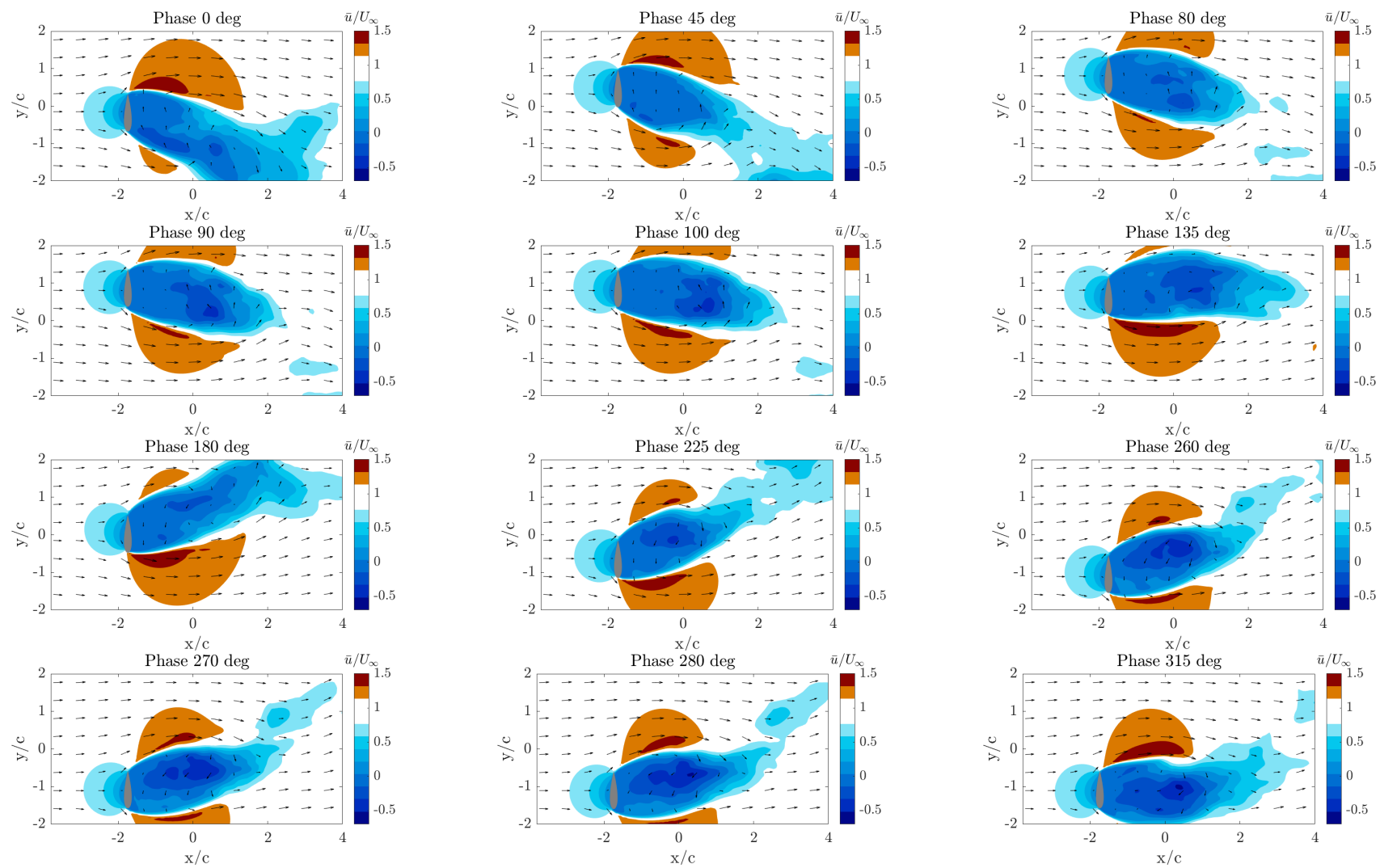


Figure L.6: Streamwise velocity, \bar{u}/U_∞ around a plunging airfoil at 2.5Hz, 2 chords inboard from the tip with the freestream velocity coming from the left.

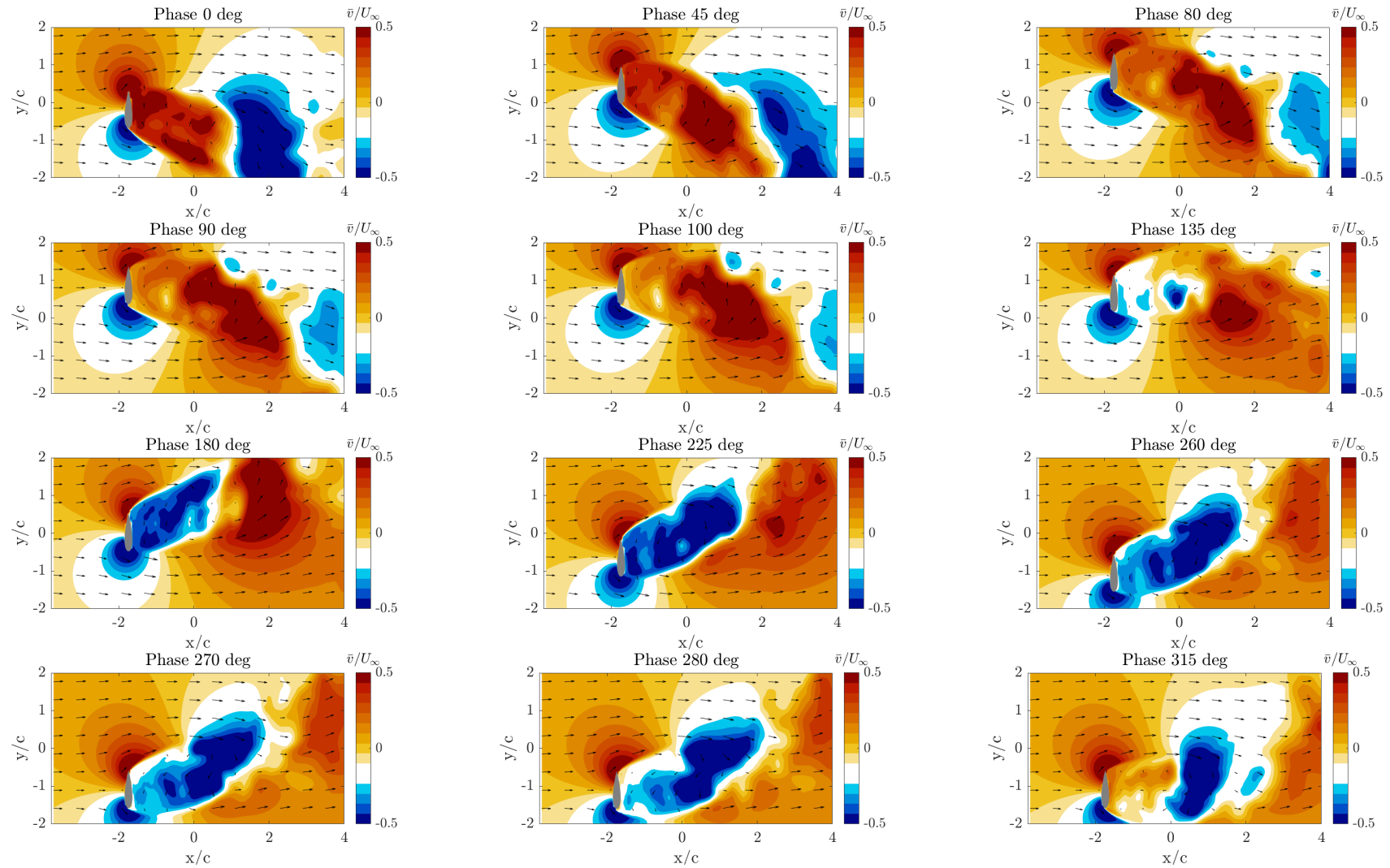


Figure L.7: Vertical velocity, \bar{v}/U_∞ around a plunging airfoil at 2.5Hz, 2 chords inboard from the tip with the freestream velocity coming from the left.

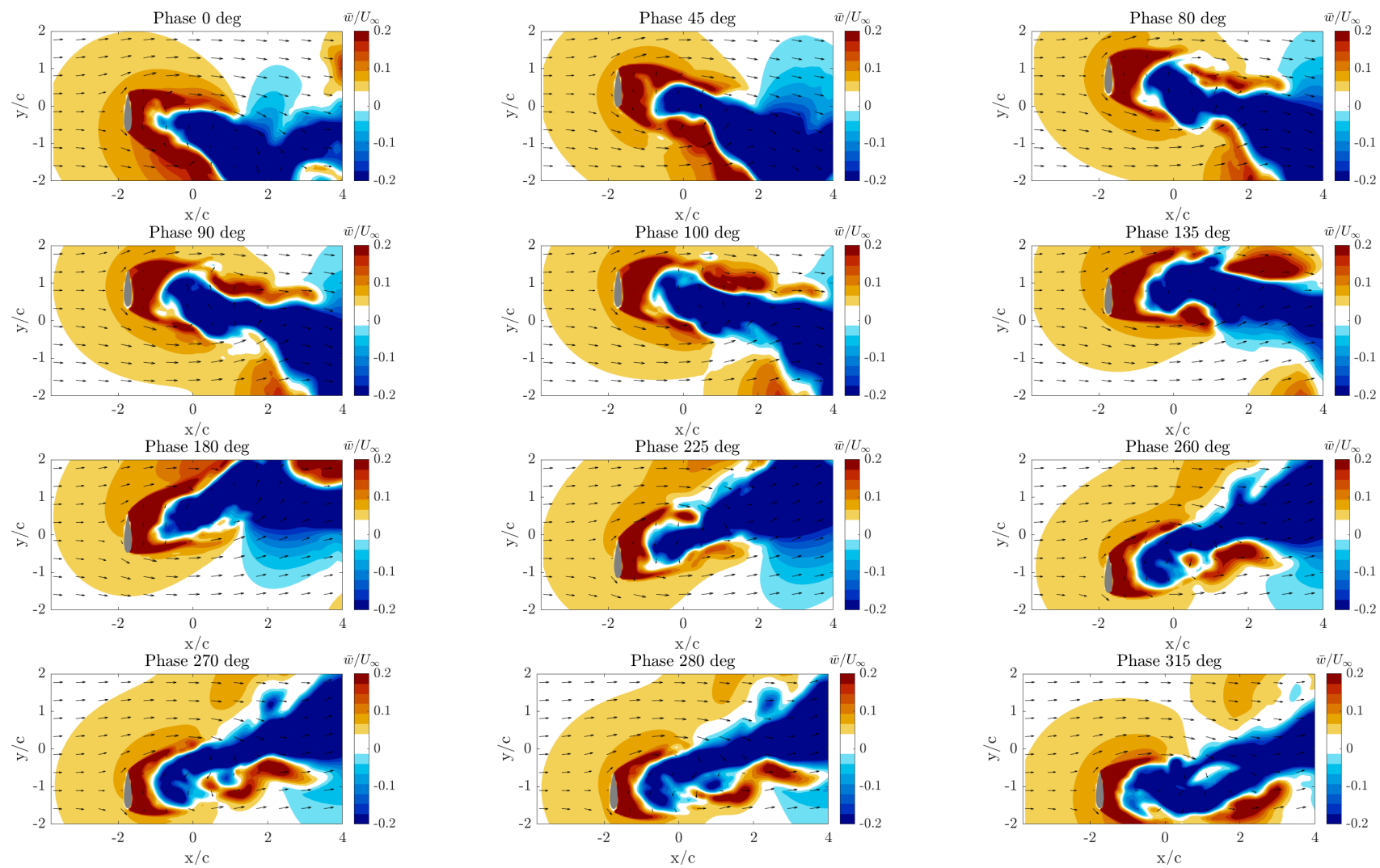


Figure L.8: Spanwise velocity, \bar{w}/U_∞ around a plunging airfoil at 2.5Hz, 2 chords inboard from the tip with the freestream velocity coming from the left. The flow is positive into the page.

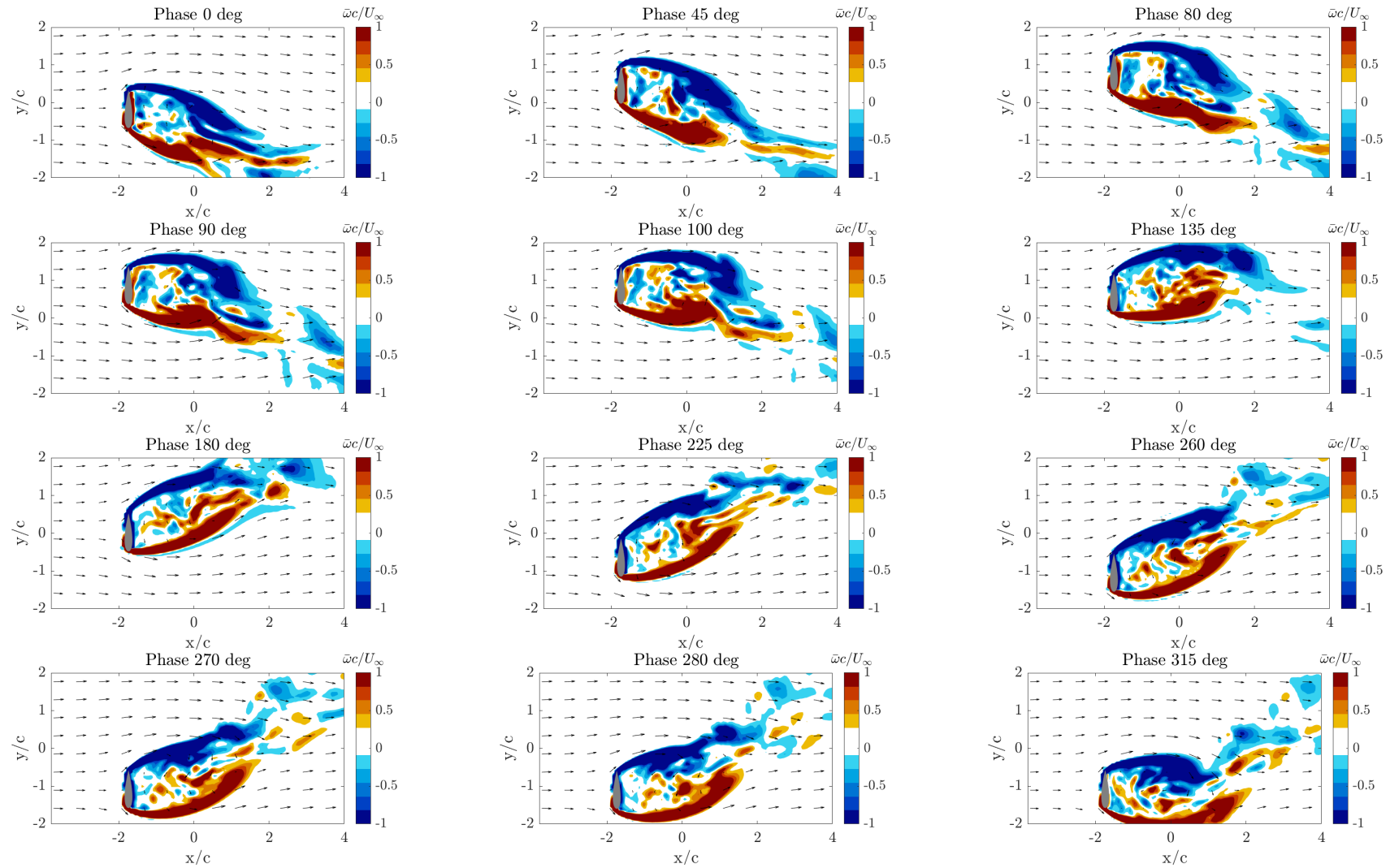


Figure L.9: Vorticity, $\bar{\omega}c/U_\infty$ around a plunging airfoil at 2.5Hz, 1 chord inboard from the tip with the freestream velocity coming from the left.

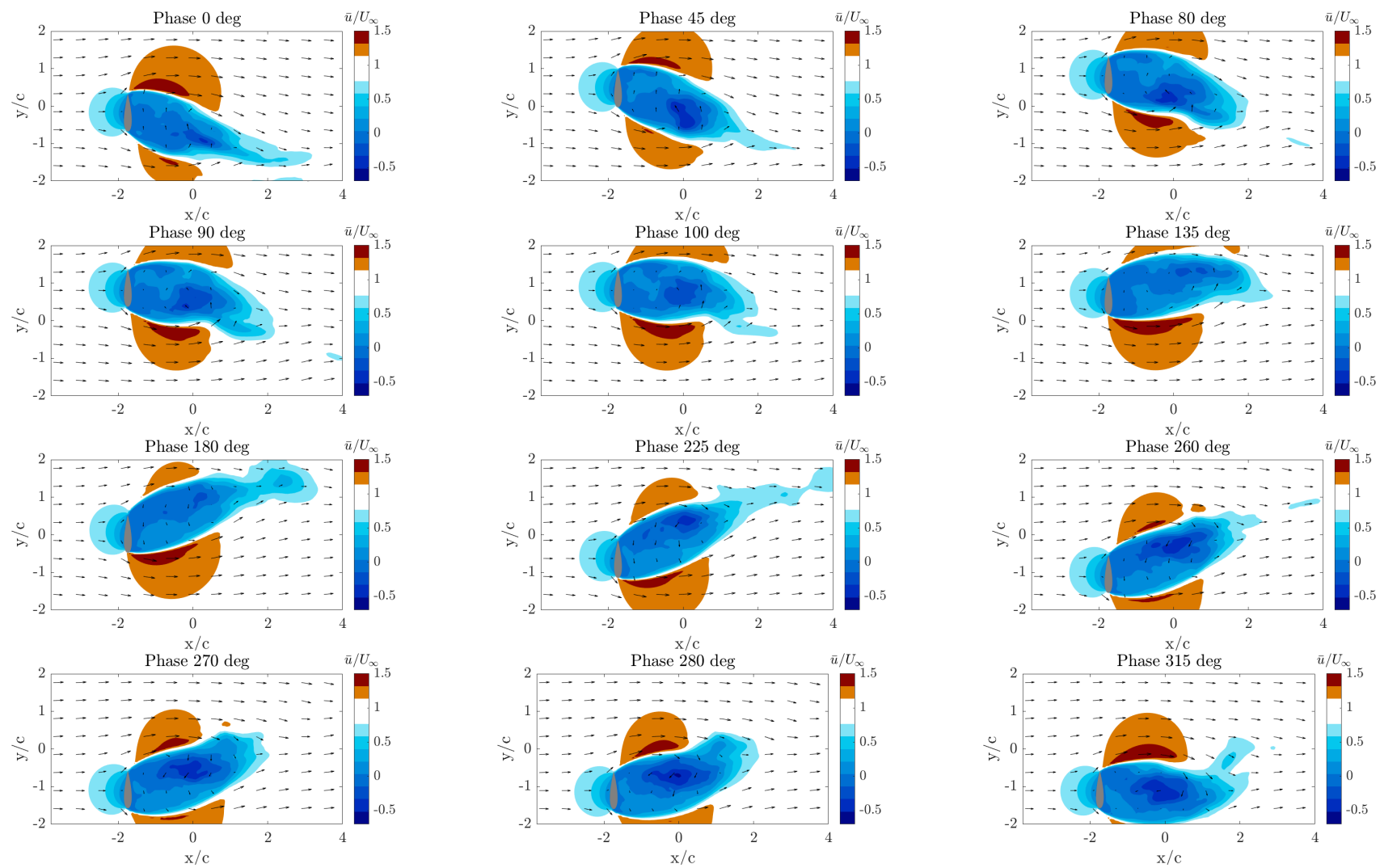


Figure L.10: Streamwise velocity, \bar{u}/U_∞ around a plunging airfoil at 2.5Hz, 1 chord inboard from the tip with the freestream velocity coming from the left.

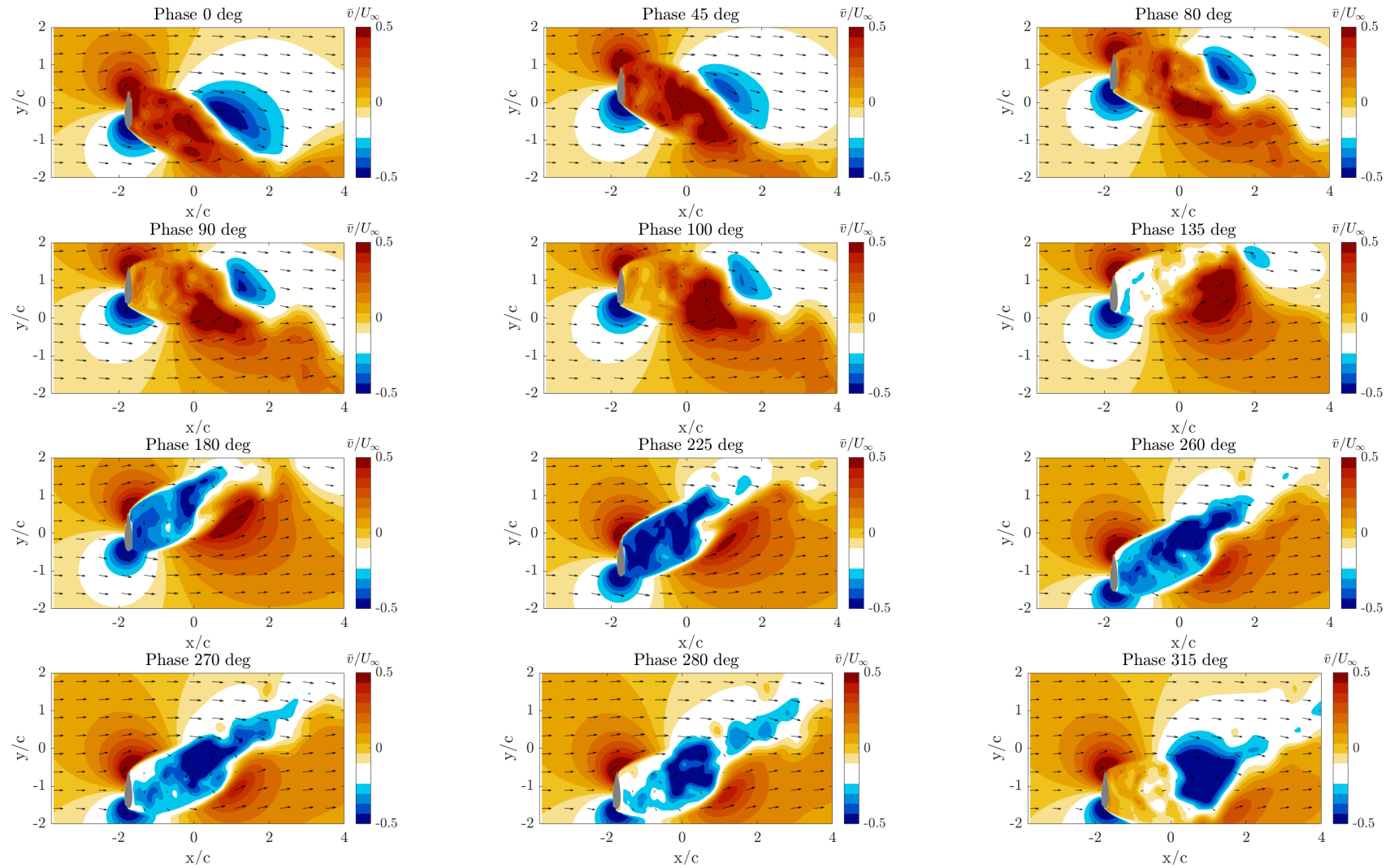


Figure L.11: Vertical velocity, \bar{v}/U_∞ around a plunging airfoil at 2.5Hz, 1 chord inboard from the tip with the freestream velocity coming from the left.

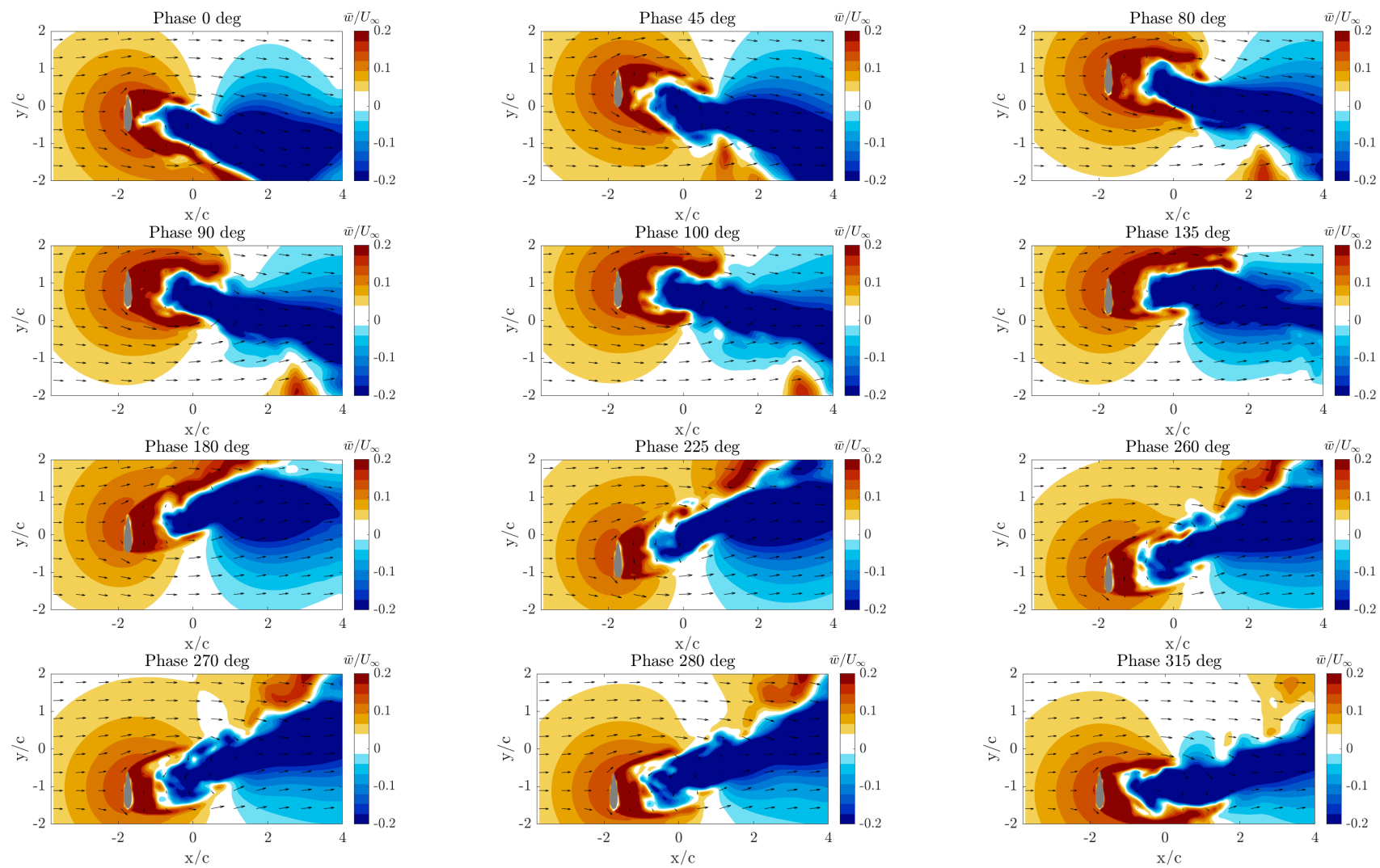


Figure L.12: Spanwise velocity, \bar{w}/U_∞ around a plunging airfoil at 2.5Hz, 1 chord inboard from the tip with the freestream velocity coming from the left. The flow is positive into the page.

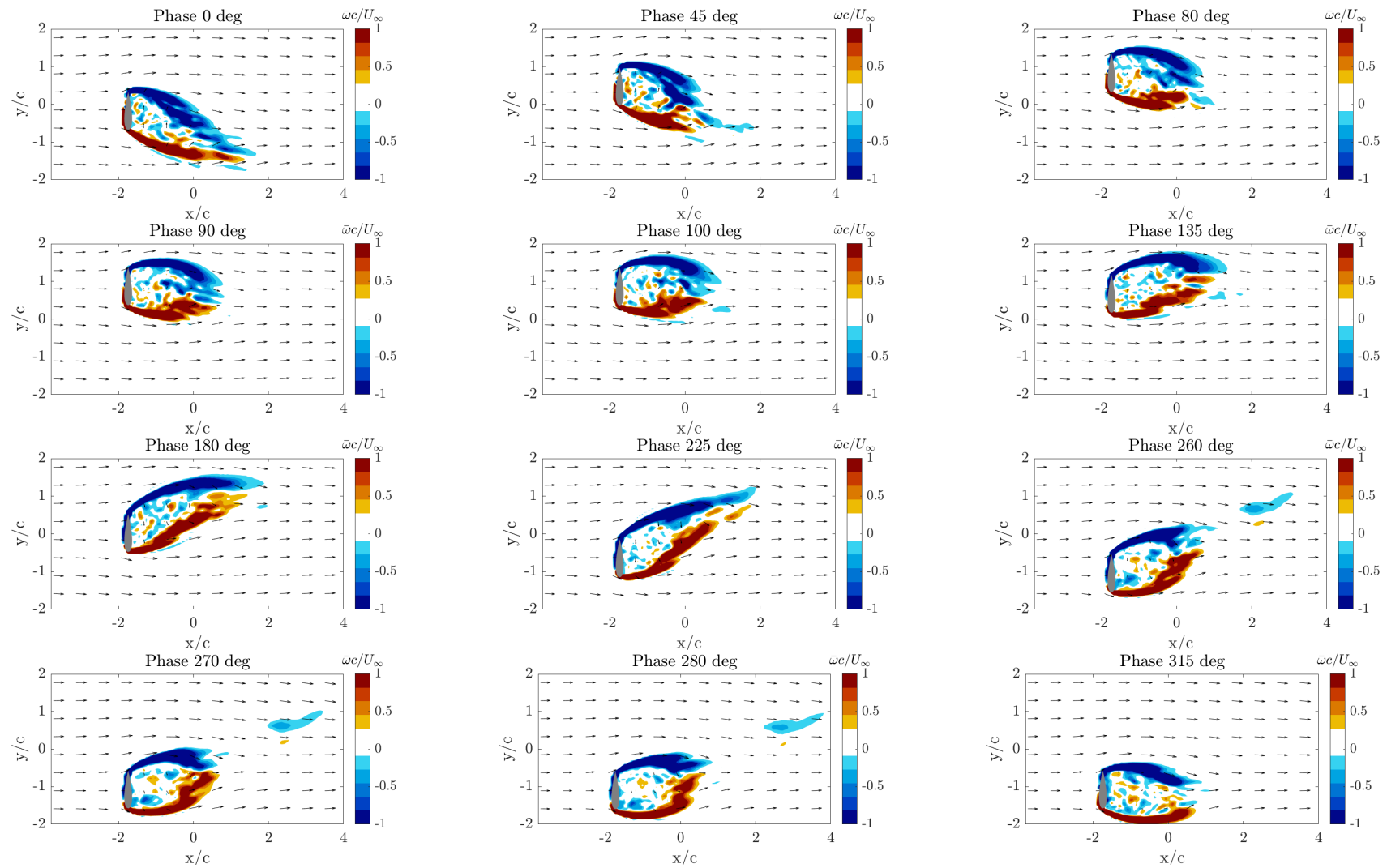


Figure L.13: Vorticity, $\bar{\omega}c/U_\infty$ around a plunging airfoil at 2.5Hz, at the tip with the freestream velocity coming from the left.

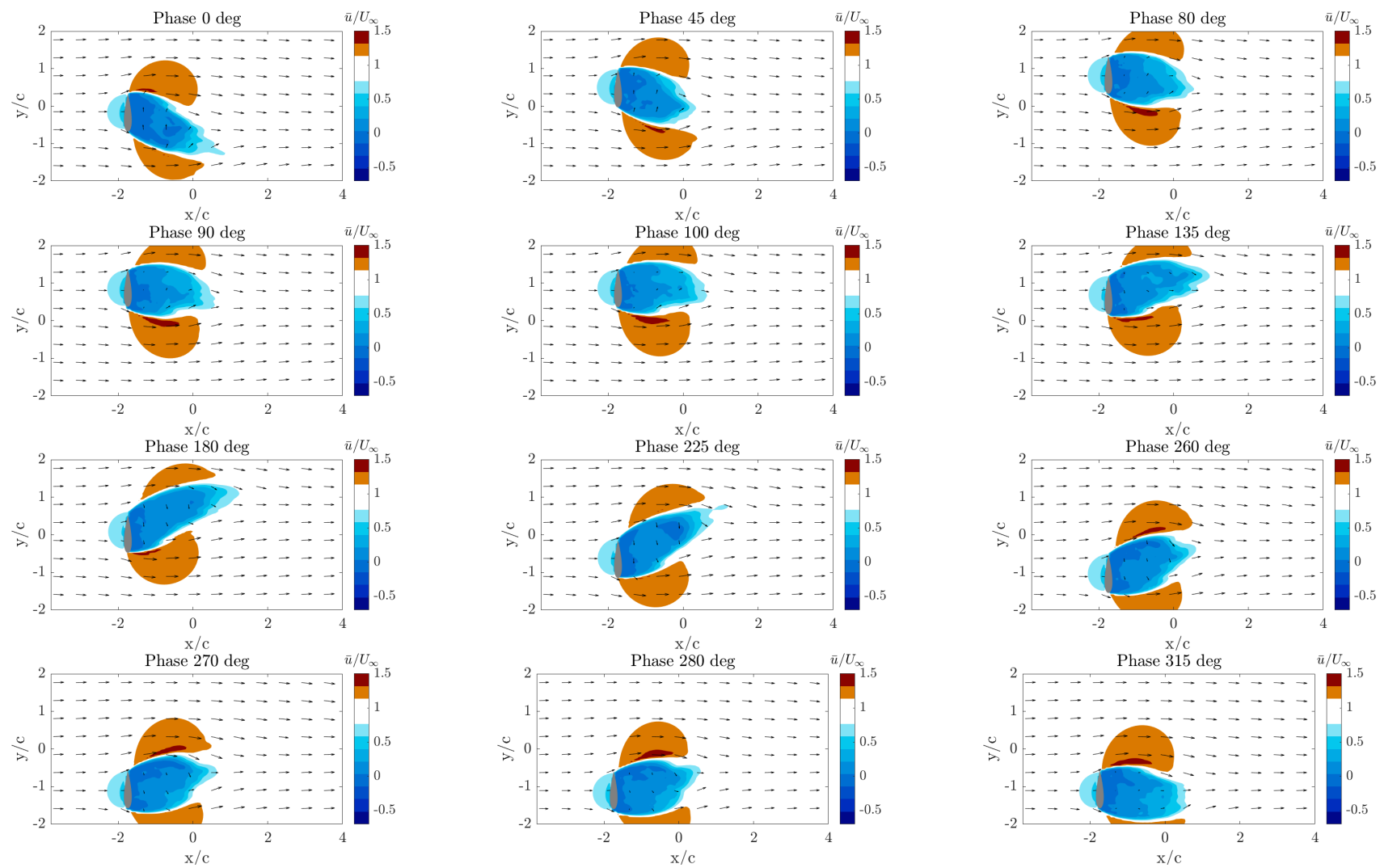


Figure L.14: Streamwise velocity, \bar{u}/U_∞ around a plunging airfoil at 2.5Hz, at the tip with the freestream velocity coming from the left.

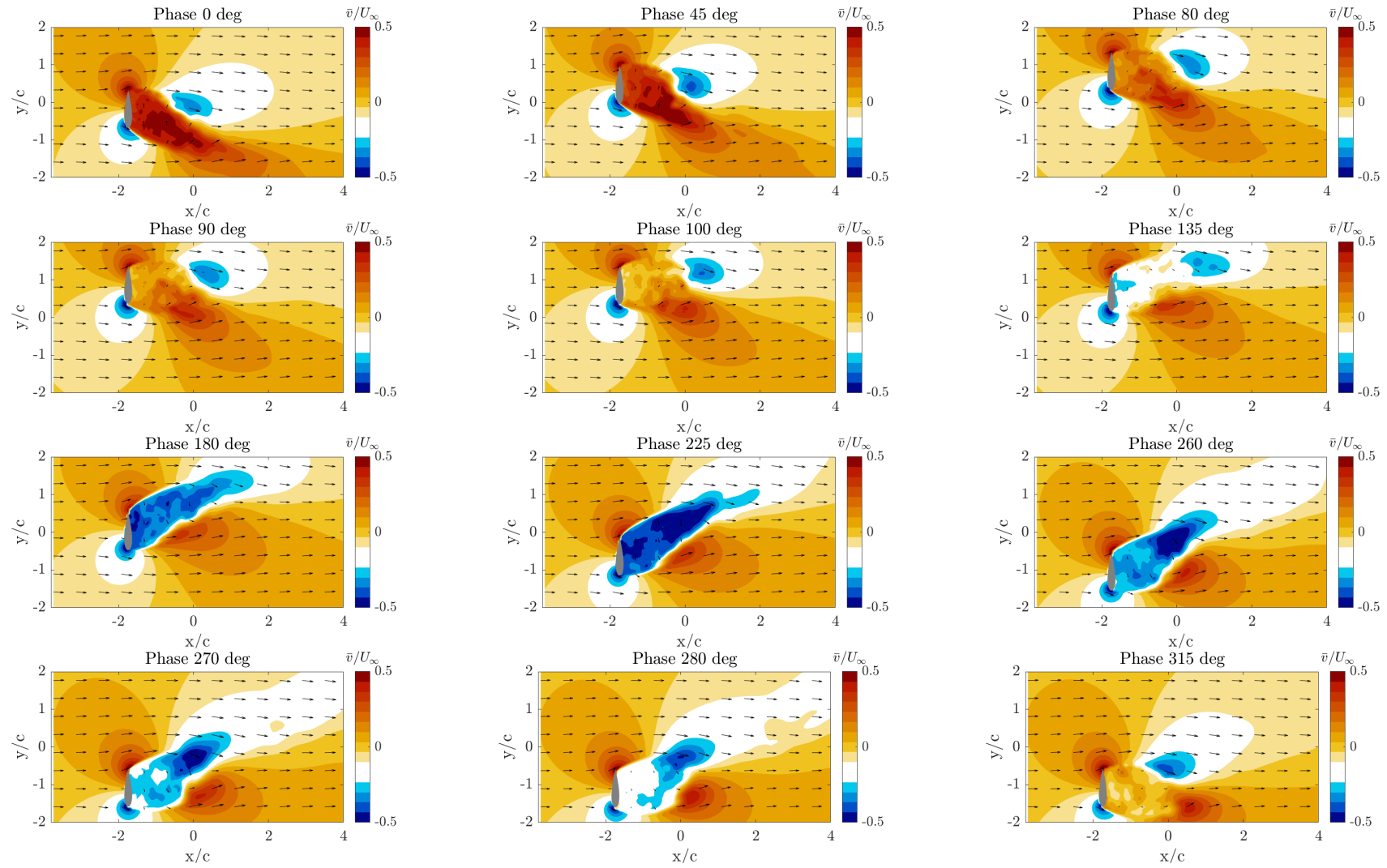


Figure L.15: Vertical velocity, \bar{v}/U_∞ around a plunging airfoil at 2.5Hz, at the tip with the freestream velocity coming from the left.

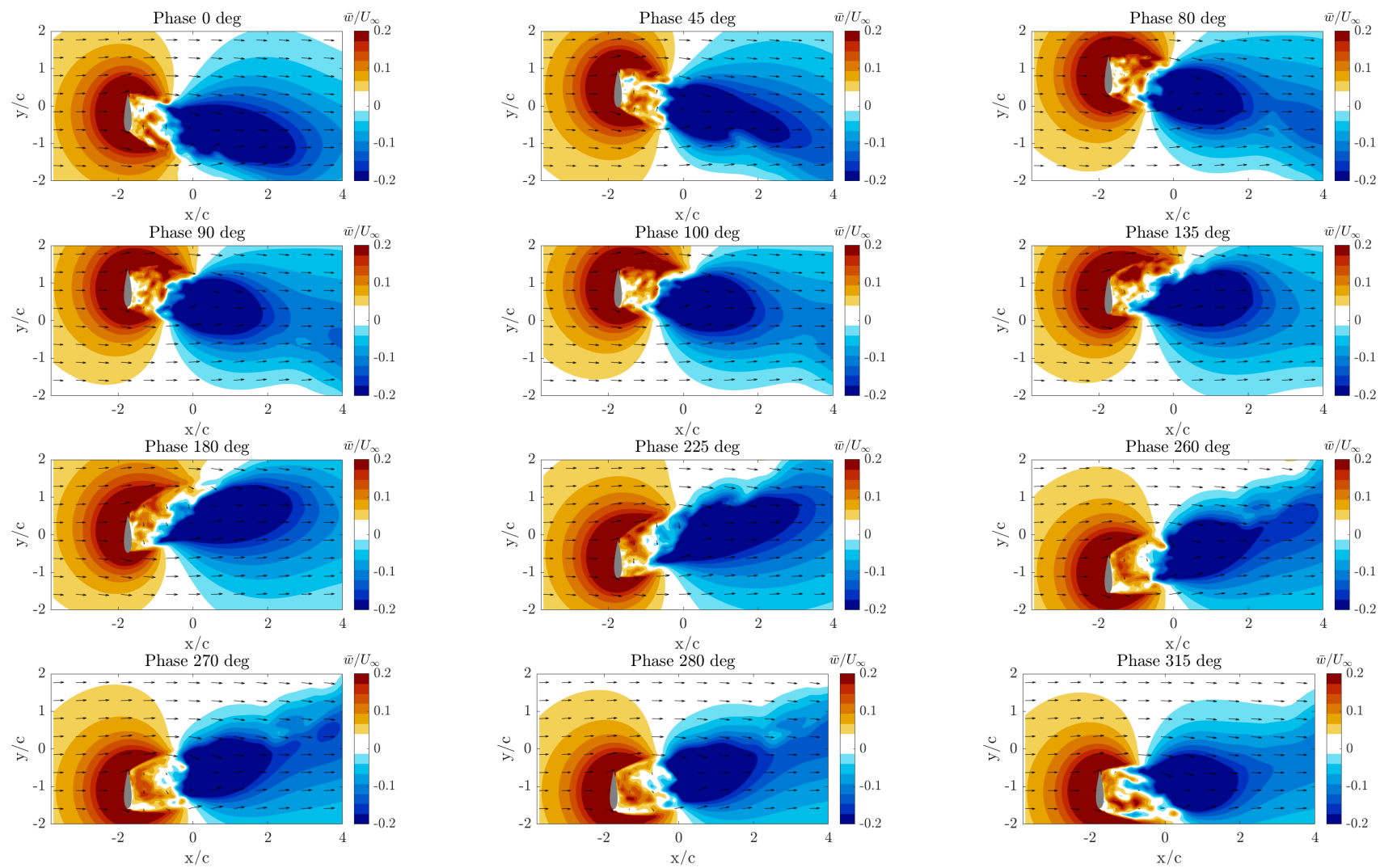


Figure L.16: Spanwise velocity, \bar{w}/U_∞ around a plunging airfoil at 2.5Hz, at the tip with the freestream velocity coming from the left. The flow is positive into the page.

APPENDIX **M**

5 Hz Plunging Cases CFD Planes

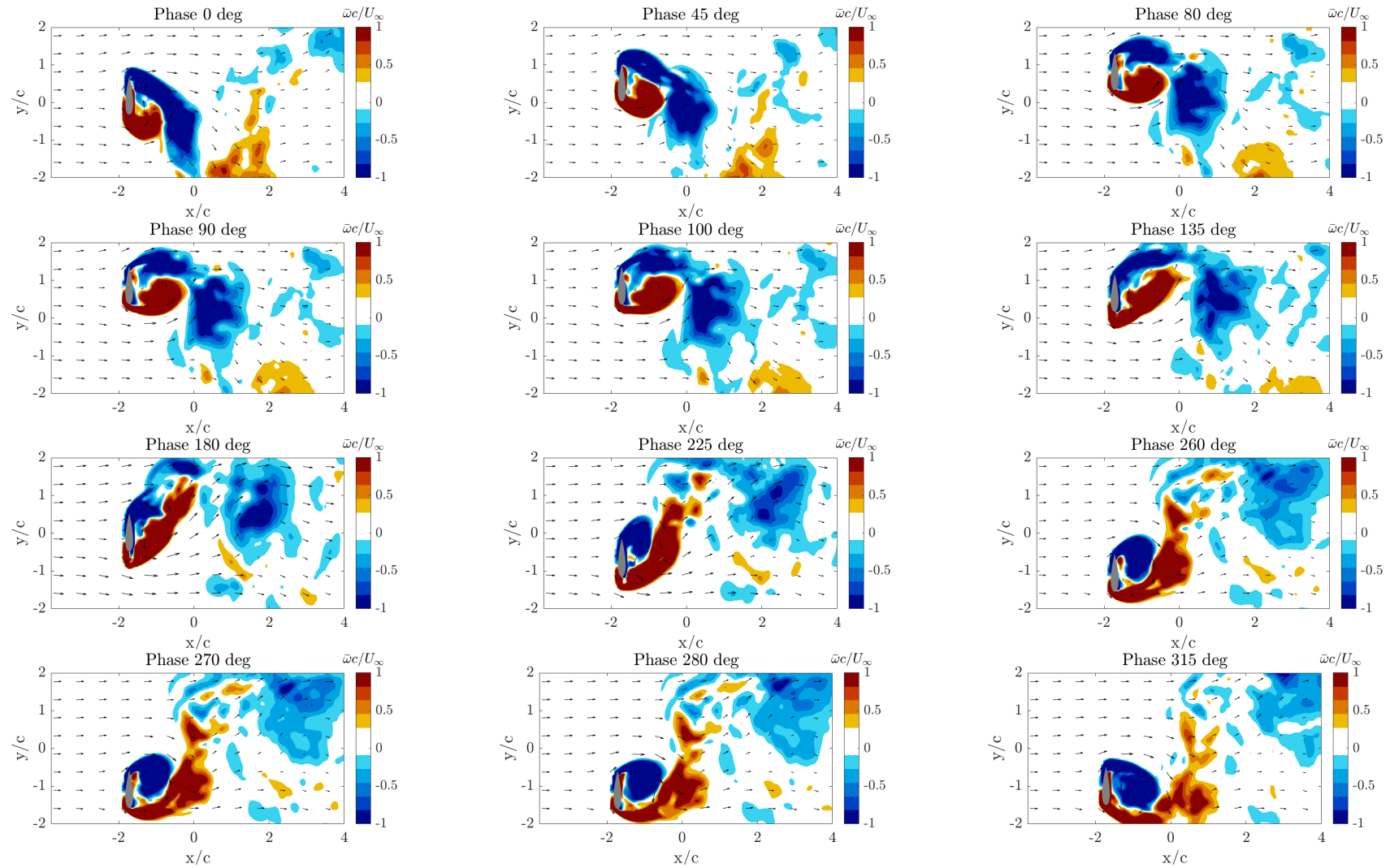


Figure M.1: Vorticity, $\bar{\omega}c/U_\infty$ around a plunging airfoil at 5Hz, 3 chords inboard from the tip with the freestream velocity coming from the left.

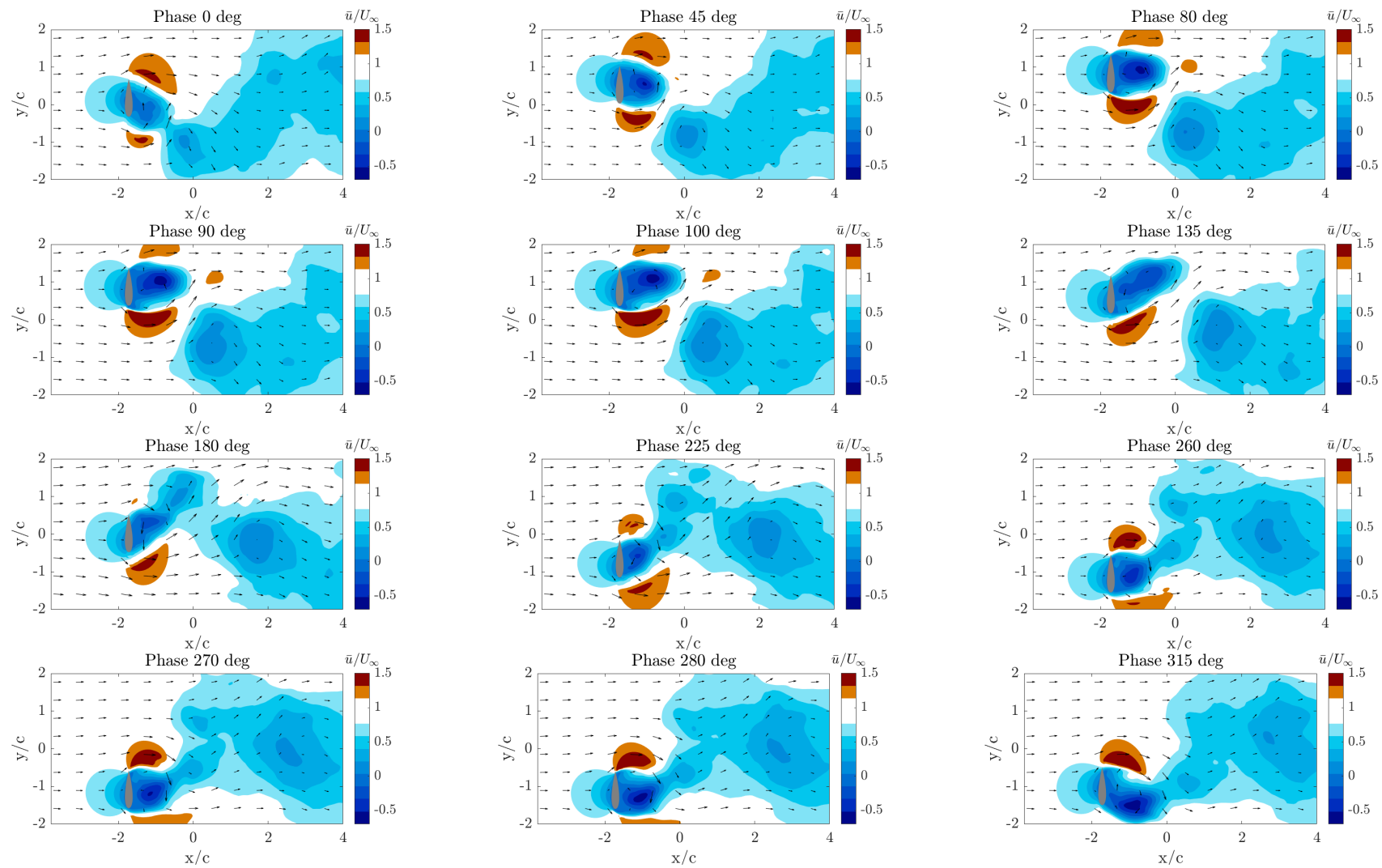


Figure M.2: Streamwise velocity, \bar{u}/U_∞ around a plunging airfoil at 5Hz, 3 chords inboard from the tip with the freestream velocity coming from the left.

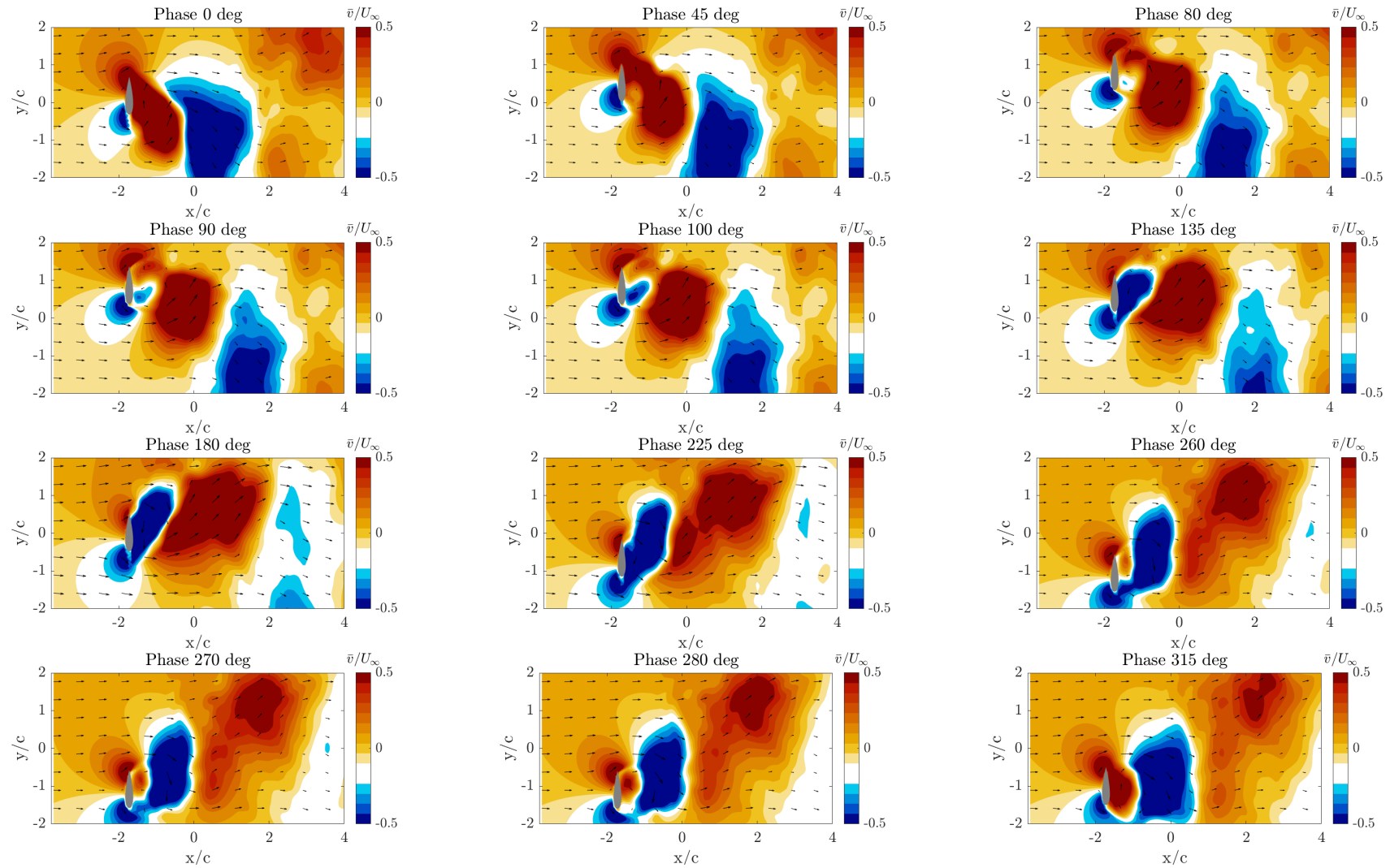


Figure M.3: Vertical velocity, \bar{v}/U_∞ around a plunging airfoil at 5Hz, 3 chords inboard from the tip with the freestream velocity coming from the left.

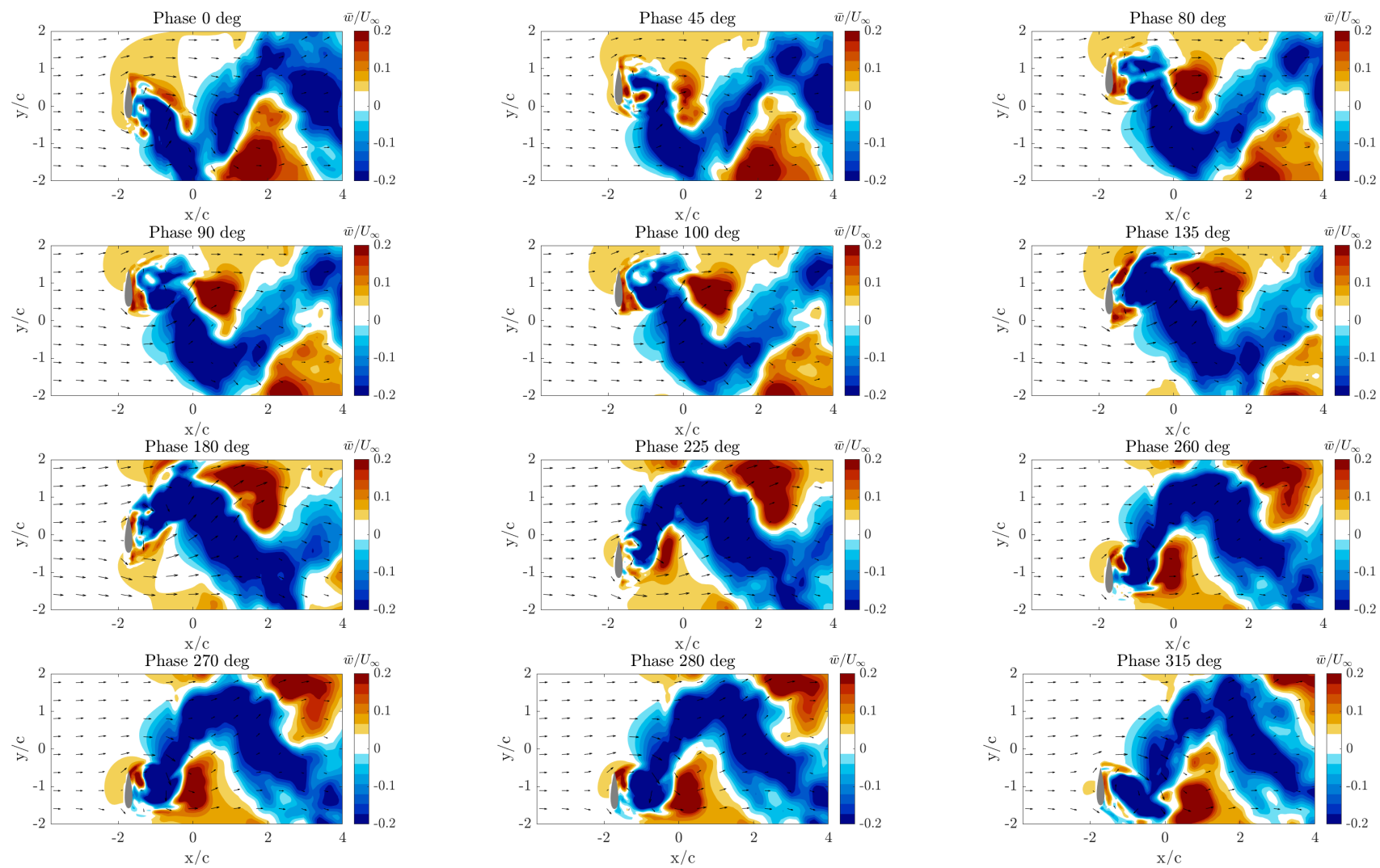


Figure M.4: Spanwise velocity, \bar{w}/U_∞ around a plunging airfoil at 5 Hz, 3 chords inboard from the tip with the freestream velocity coming from the left. The flow is positive into the page.

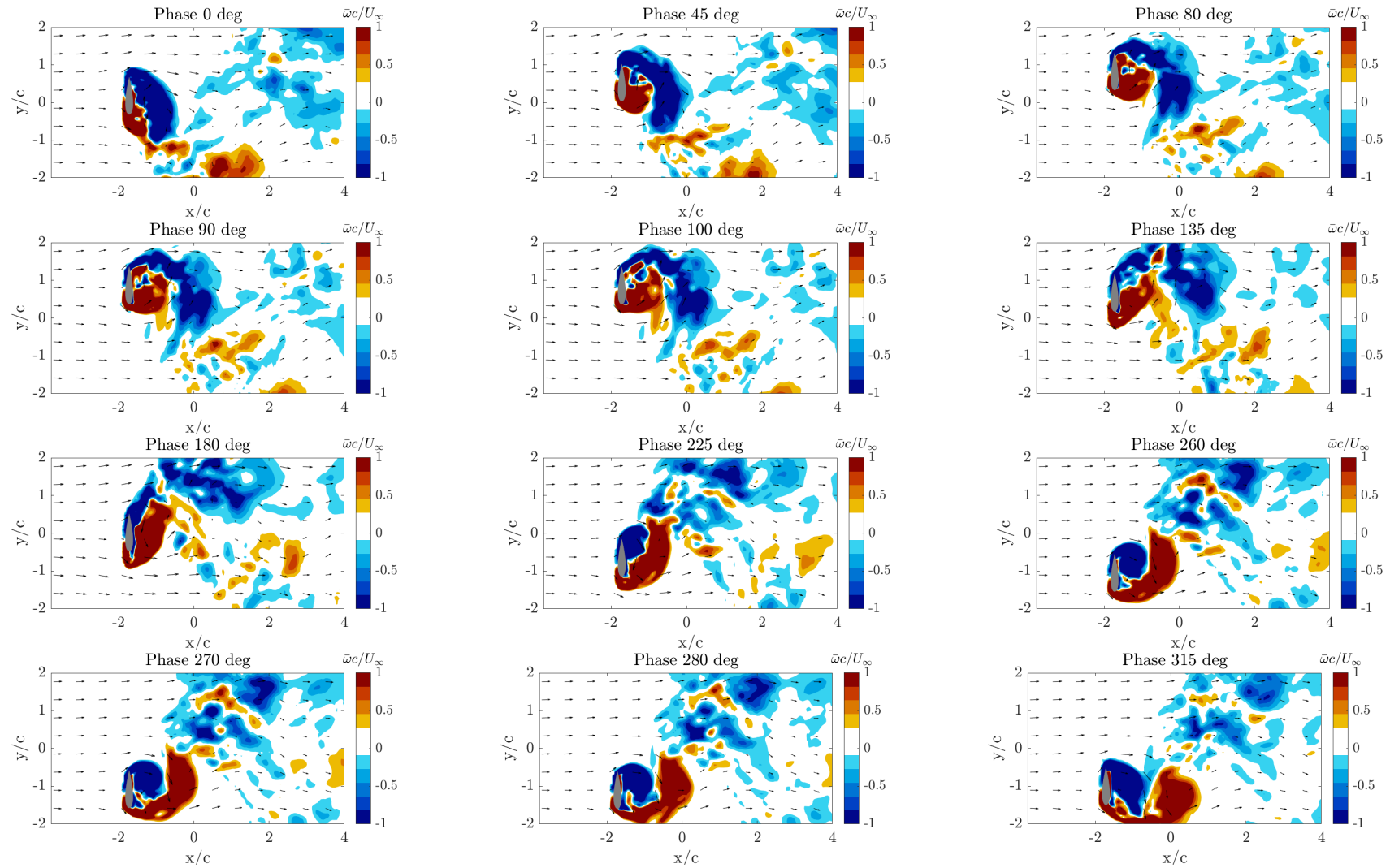


Figure M.5: Vorticity, $\bar{\omega}c/U_\infty$ around a plunging airfoil at 5Hz, 2 chords inboard from the tip with the freestream velocity coming from the left.

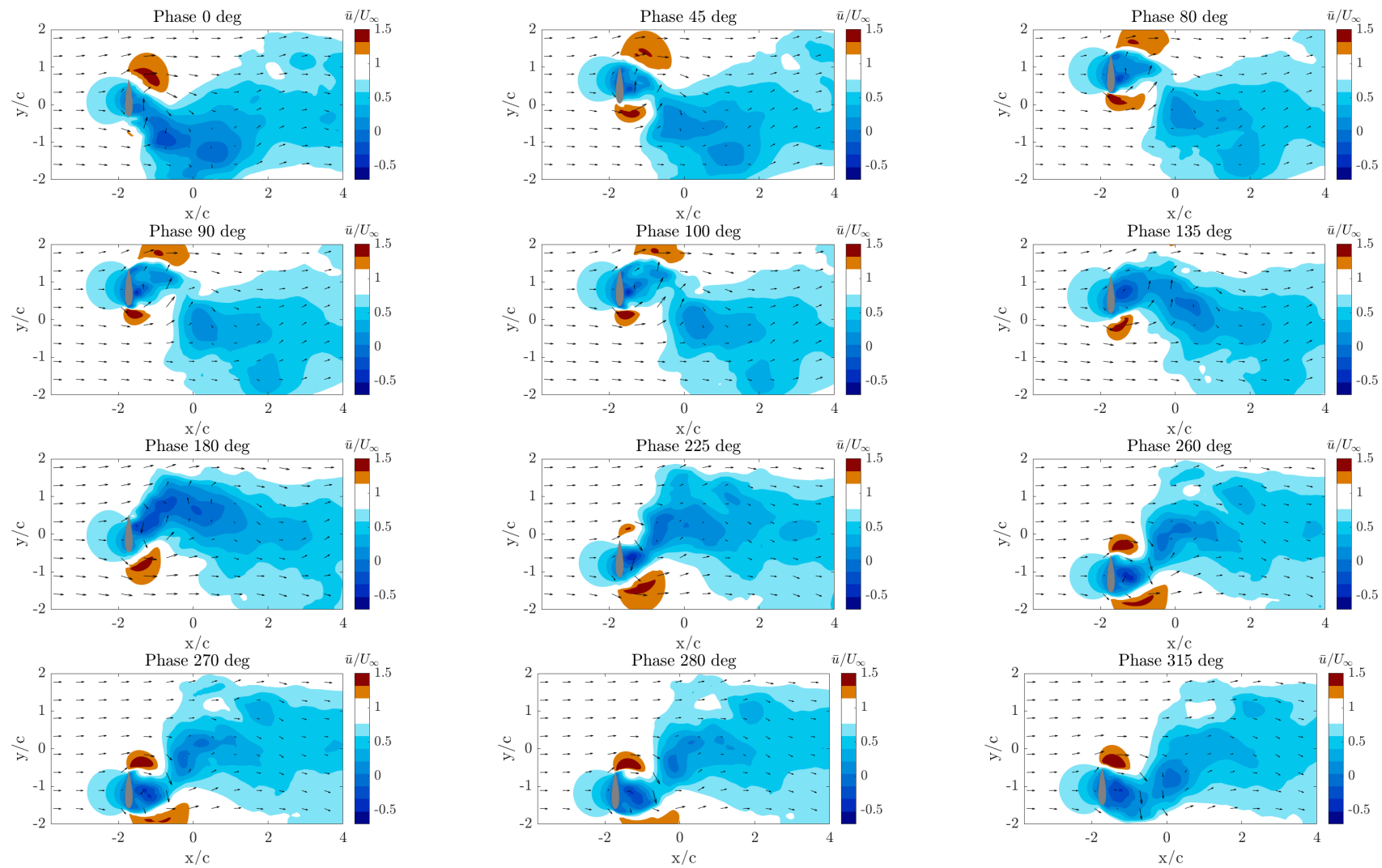


Figure M.6: Streamwise velocity, \bar{u}/U_∞ around a plunging airfoil at 5Hz, 2 chords inboard from the tip with the freestream velocity coming from the left.

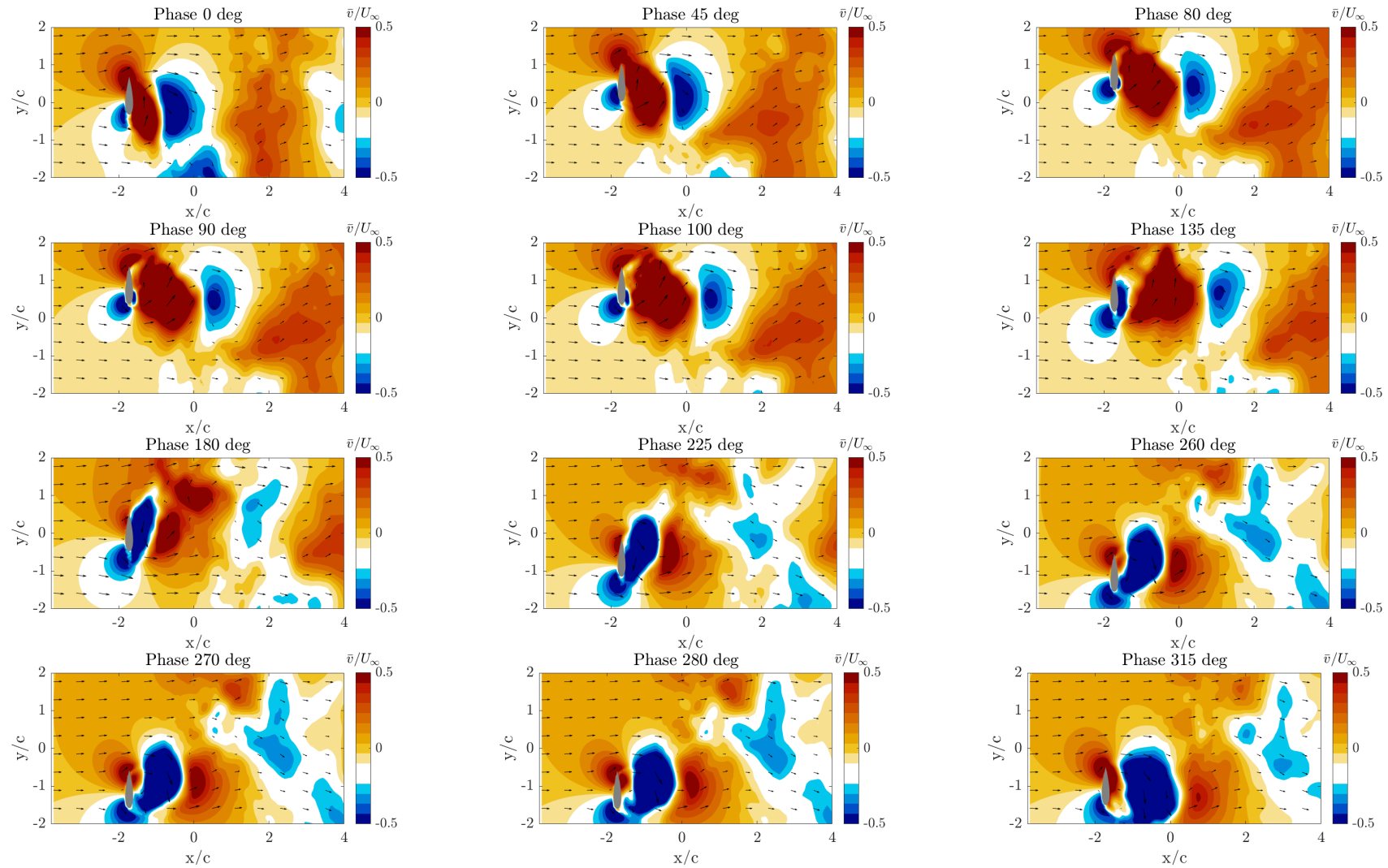


Figure M.7: Vertical velocity, \bar{v}/U_∞ around a plunging airfoil at 5Hz, 2 chords inboard from the tip with the freestream velocity coming from the left.

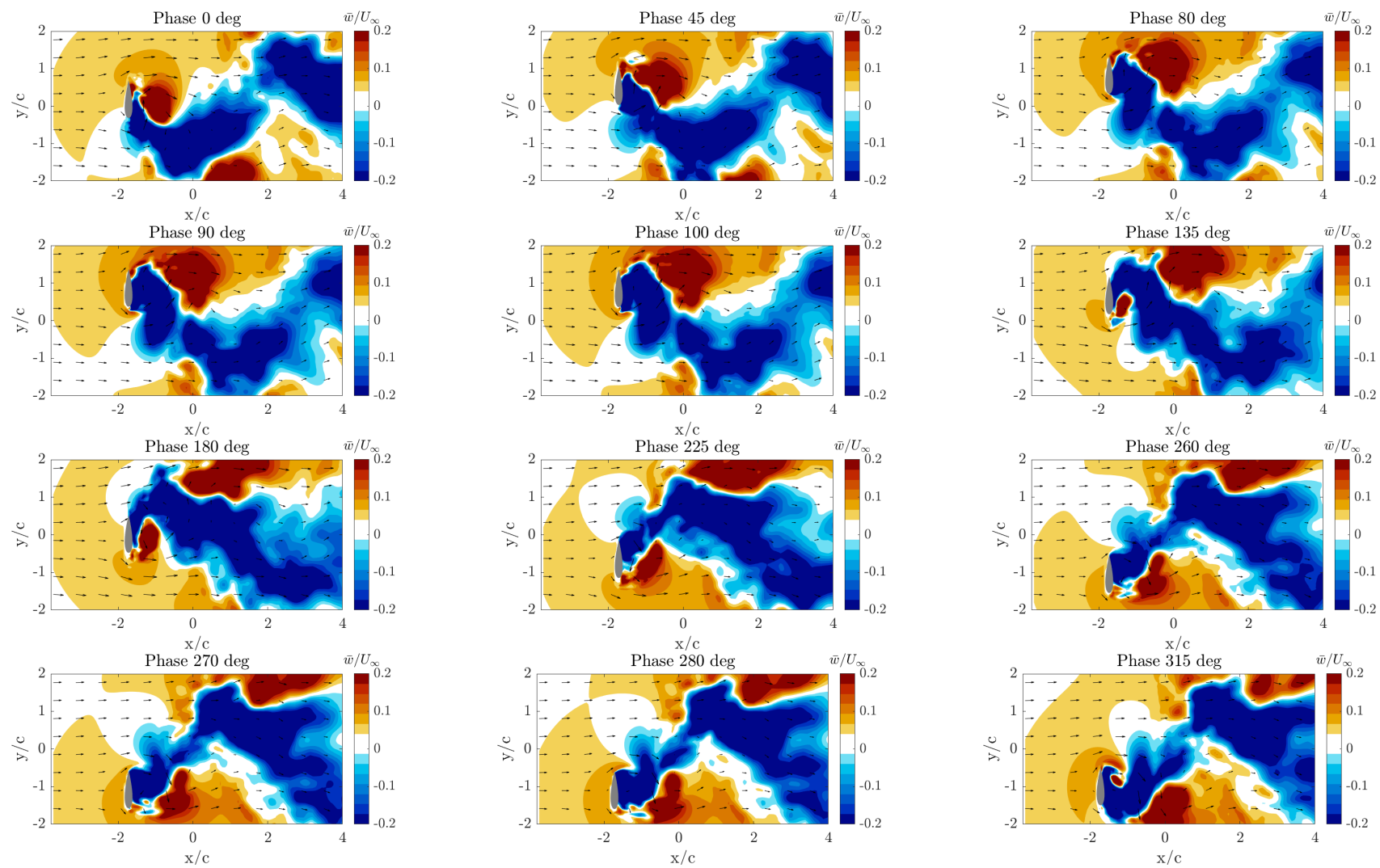


Figure M.8: Spanwise velocity, \bar{w}/U_∞ around a plunging airfoil at 5Hz, 2 chords inboard from the tip with the freestream velocity coming from the left. The flow is positive into the page.

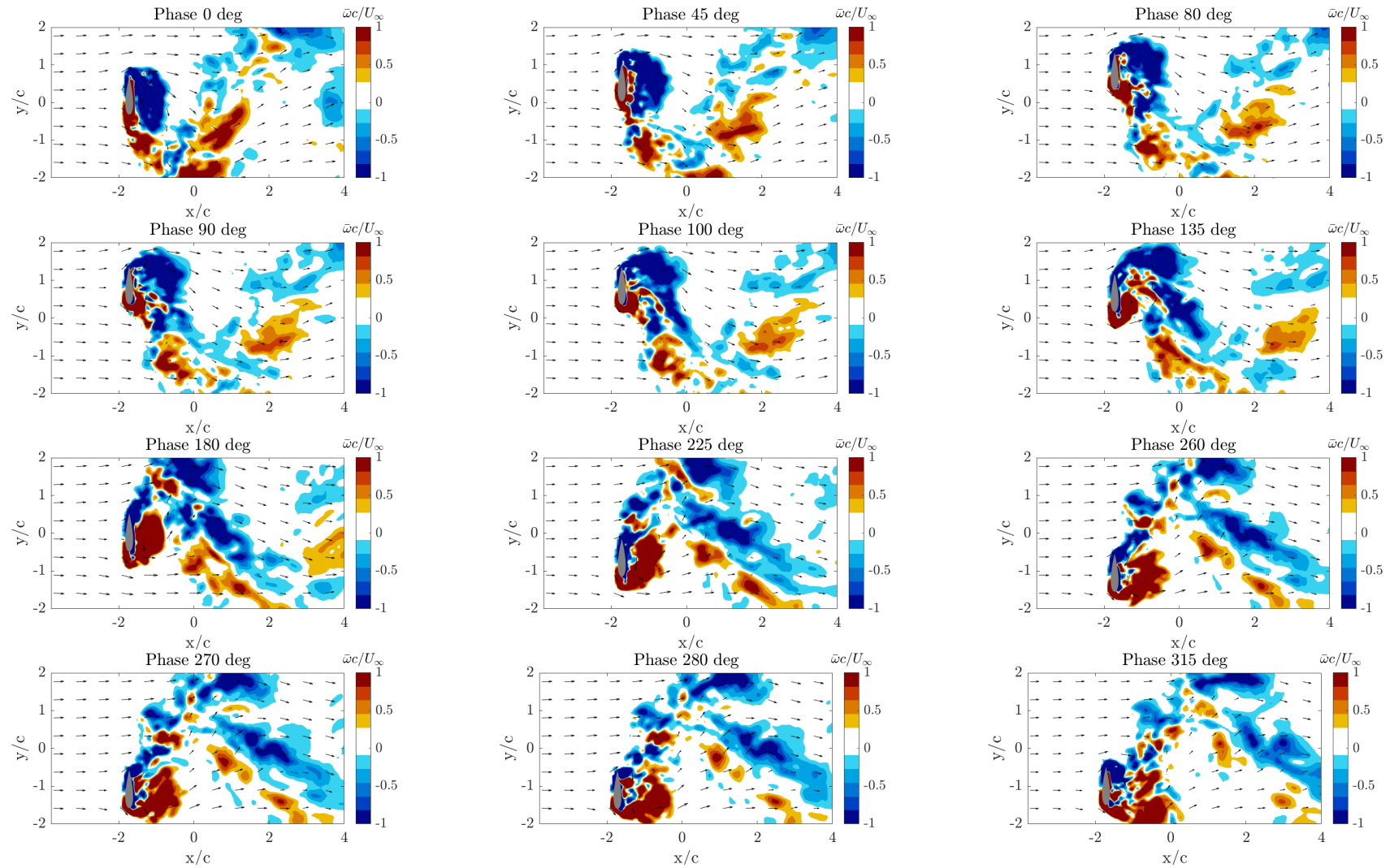


Figure M.9: Vorticity, $\bar{\omega}c/U_\infty$ around a plunging airfoil at 5Hz, 1 chord inboard from the tip with the freestream velocity coming from the left.

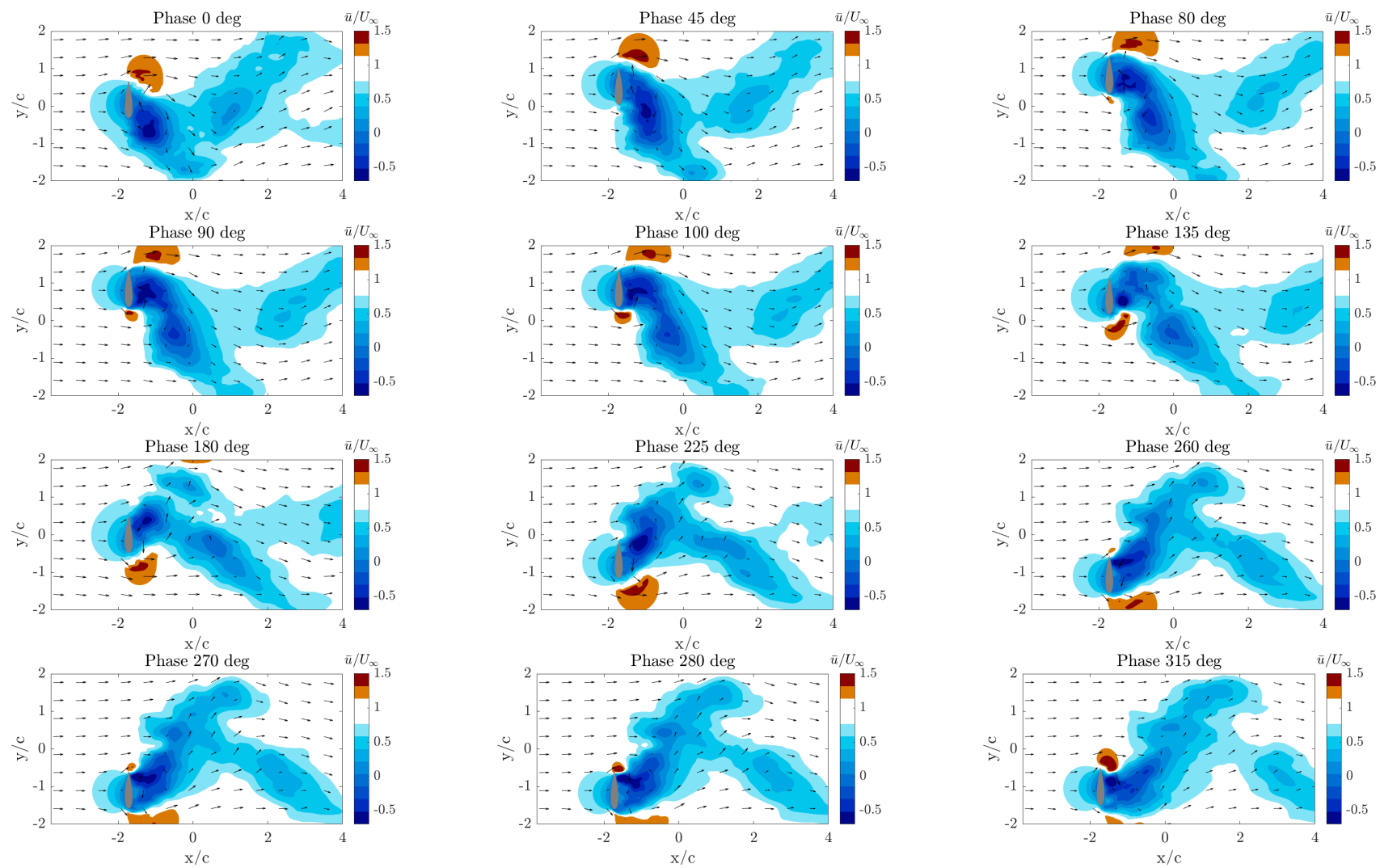


Figure M.10: Streamwise velocity, \bar{u}/U_∞ around a plunging airfoil at 5Hz, 1 chord inboard from the tip with the freestream velocity coming from the left.

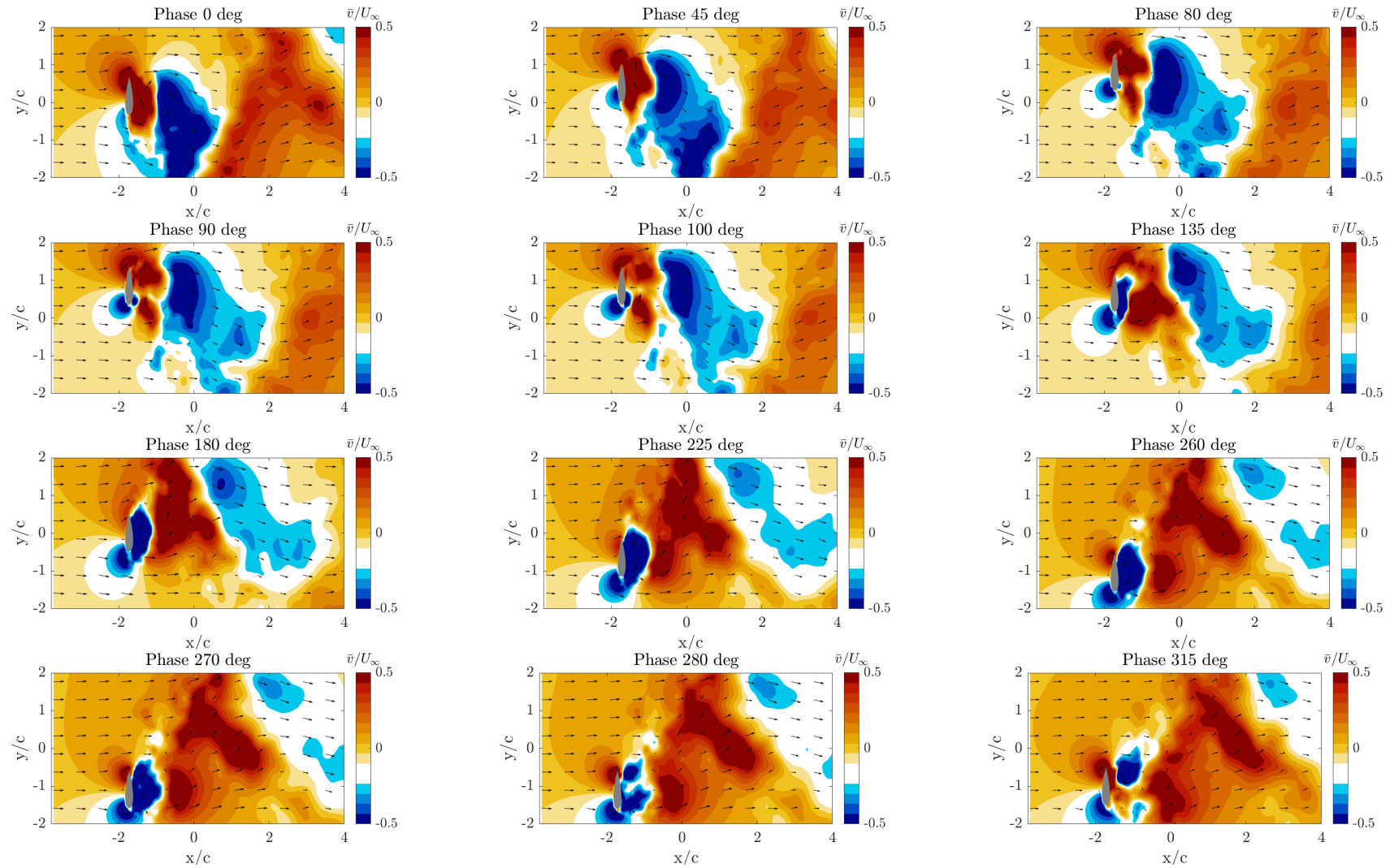


Figure M.11: Vertical velocity, \bar{v}/U_∞ around a plunging airfoil at 5Hz, 1 chord inboard from the tip with the freestream velocity coming from the left.

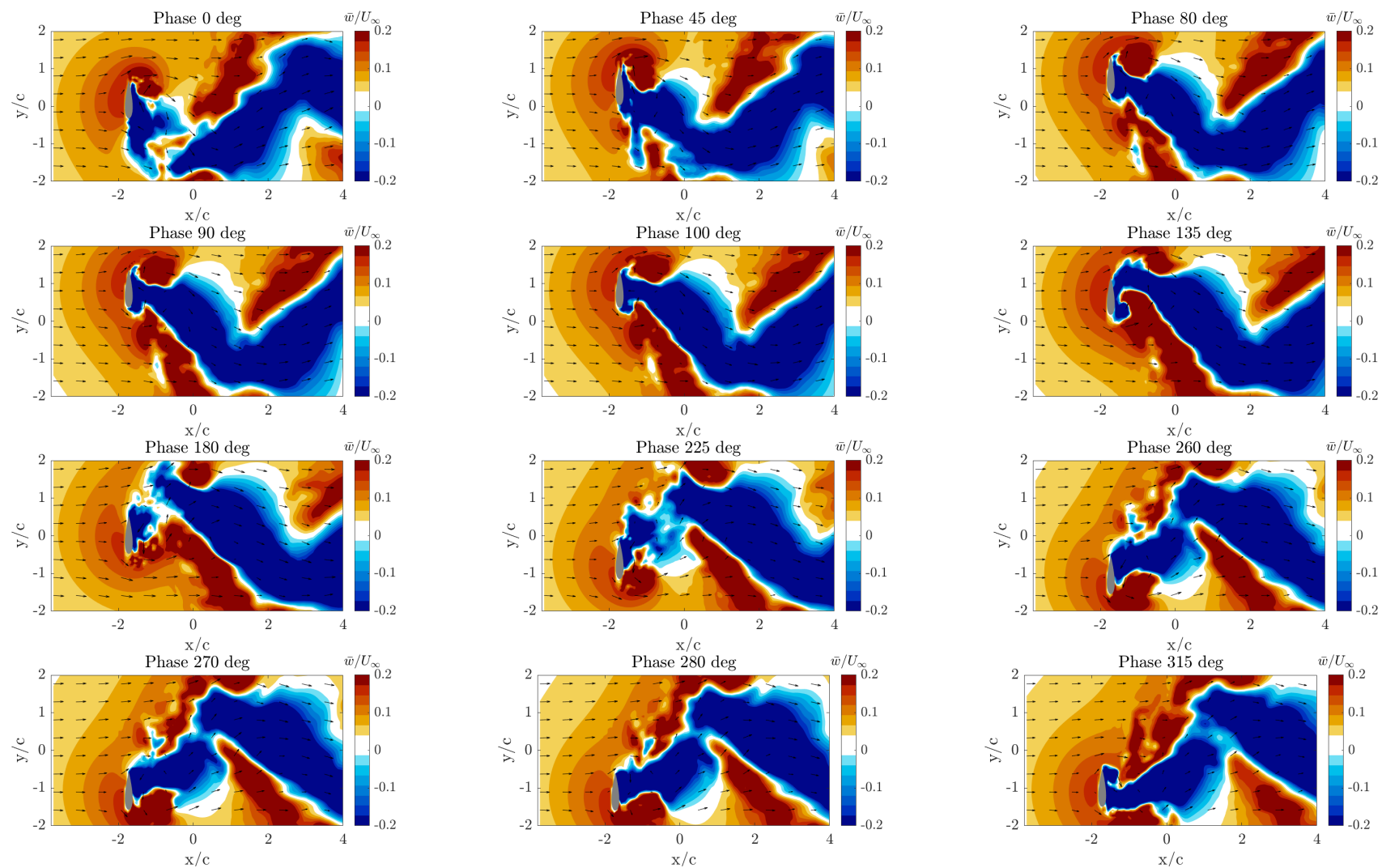


Figure M.12: Spanwise velocity, \bar{w}/U_∞ around a plunging airfoil at 5Hz, 1 chord inboard from the tip with the freestream velocity coming from the left. The flow is positive into the page.

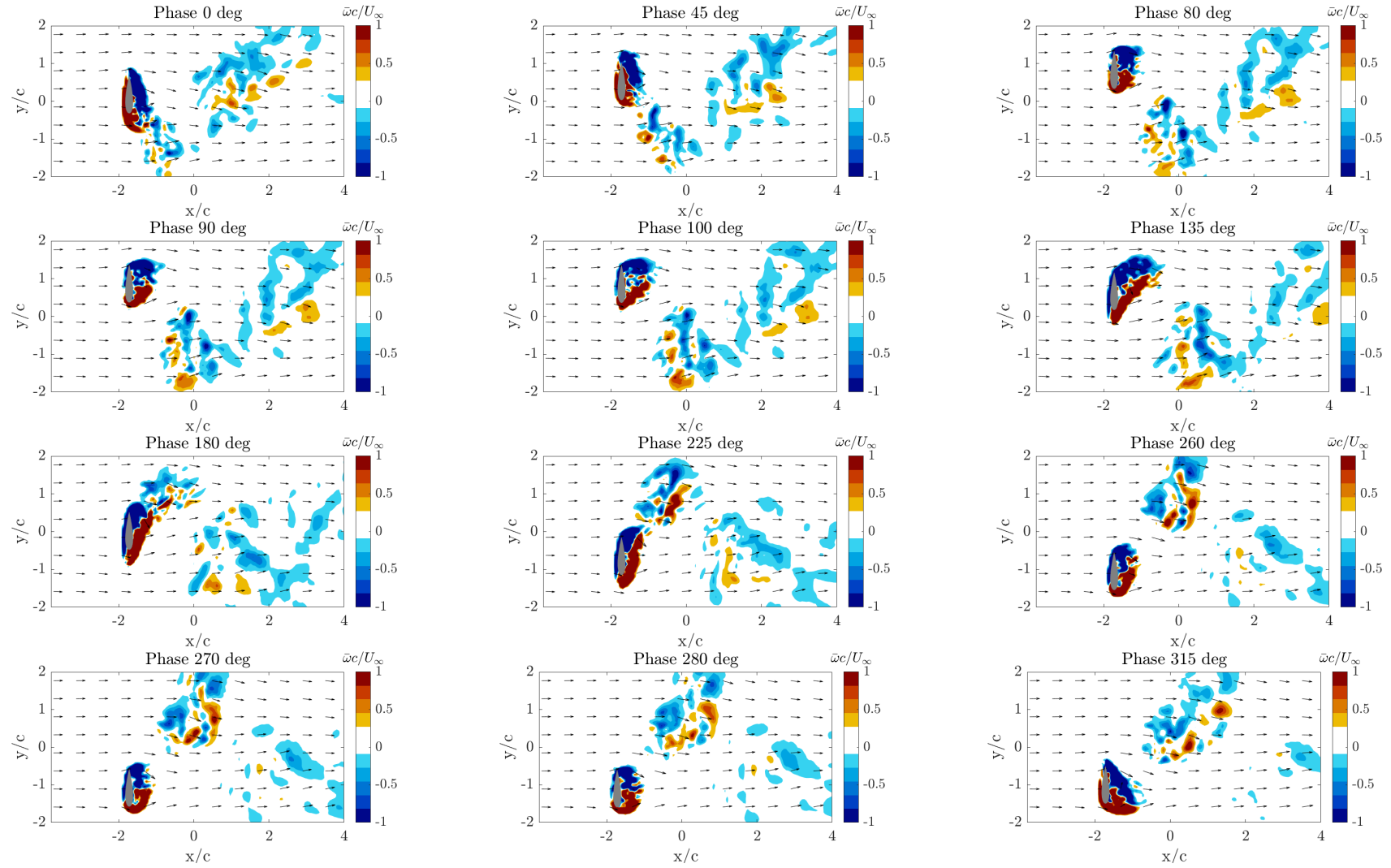


Figure M.13: Vorticity, $\bar{\omega}c/U_\infty$ around a plunging airfoil at 5Hz, at the tip with the freestream velocity coming from the left.

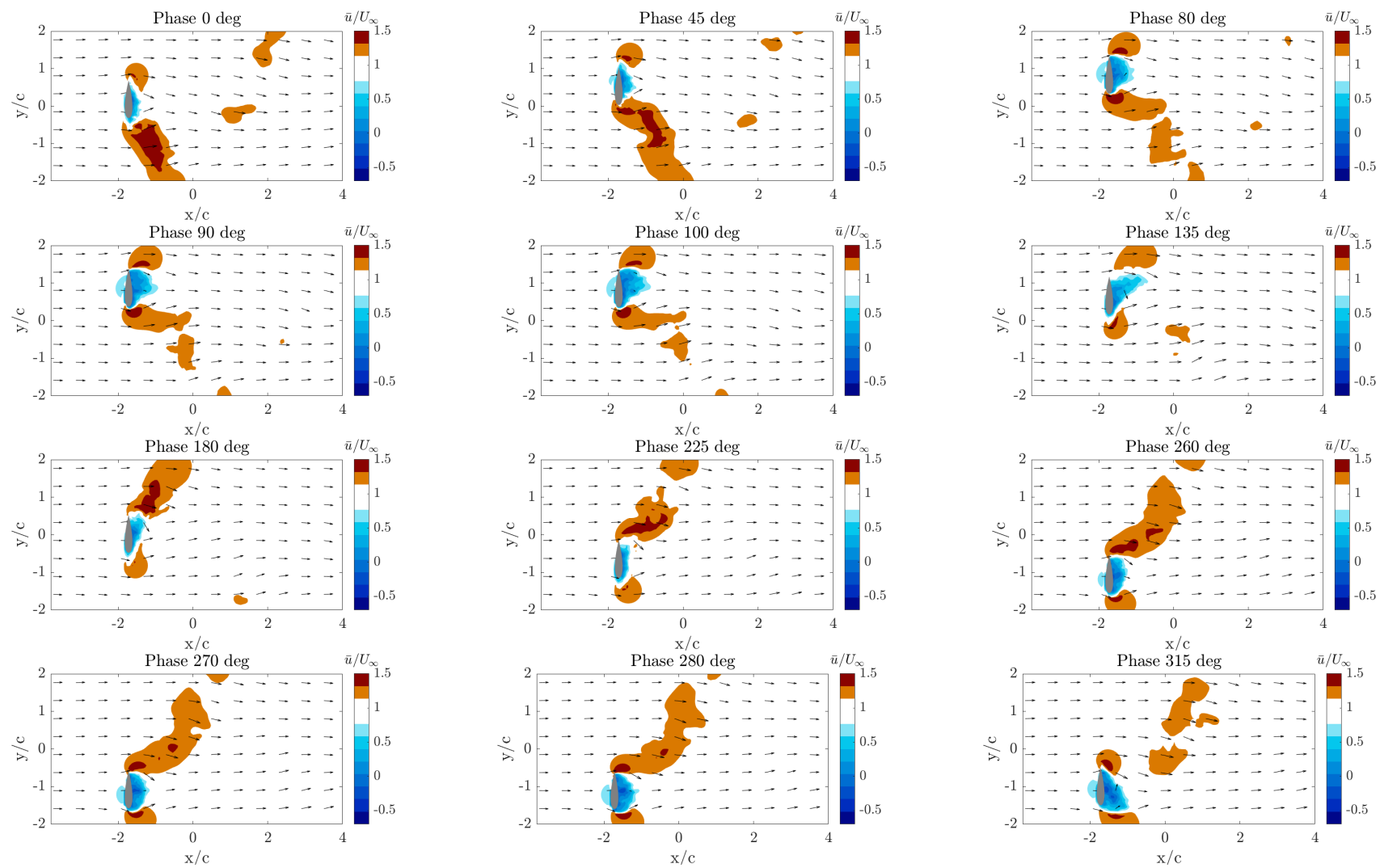


Figure M.14: Streamwise velocity, \bar{u}/U_∞ around a plunging airfoil at 5Hz, at the tip with the freestream velocity coming from the left.

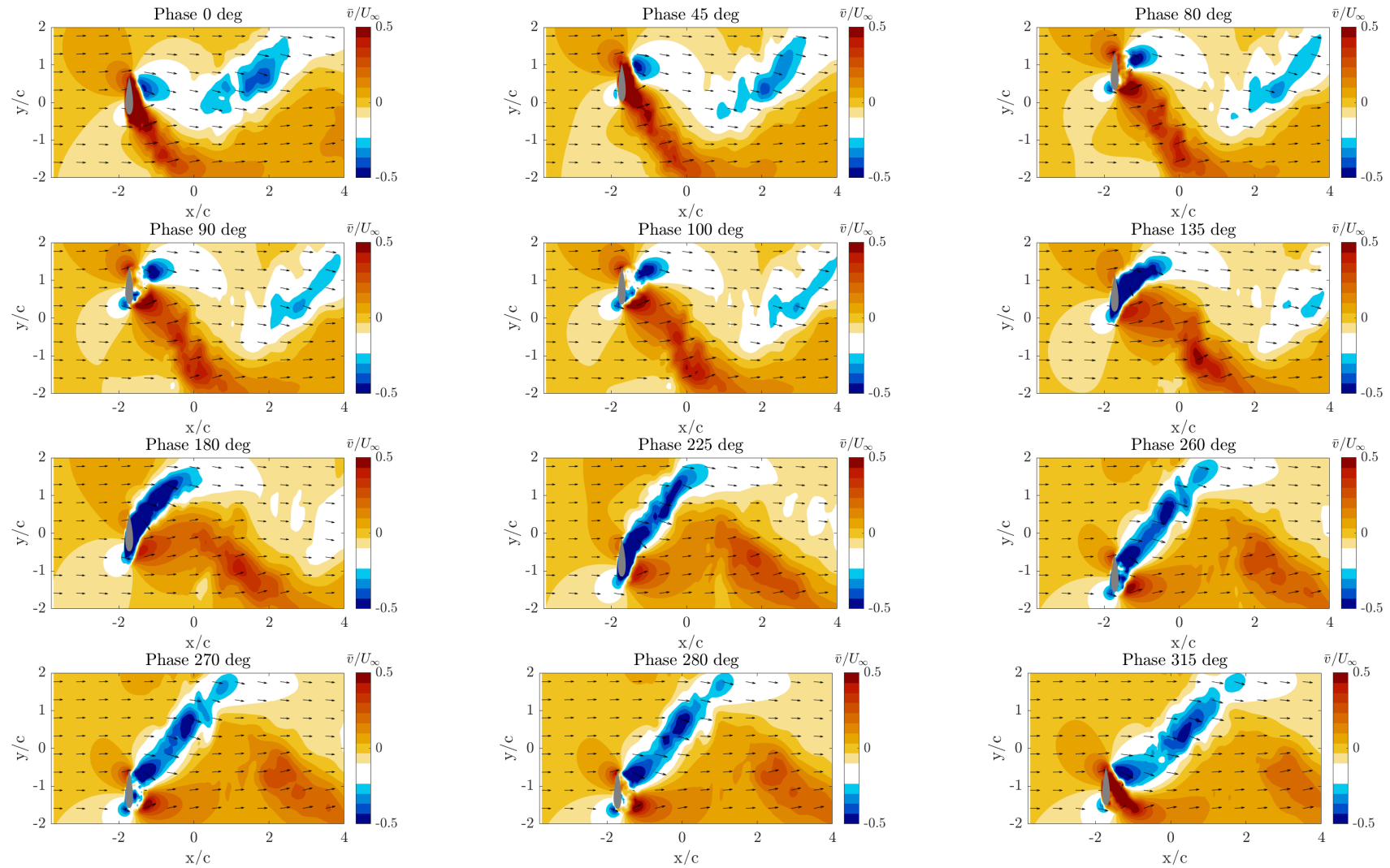


Figure M.15: Vertical velocity, \bar{v}/U_∞ around a plunging airfoil at 5Hz, at the tip with the freestream velocity coming from the left.

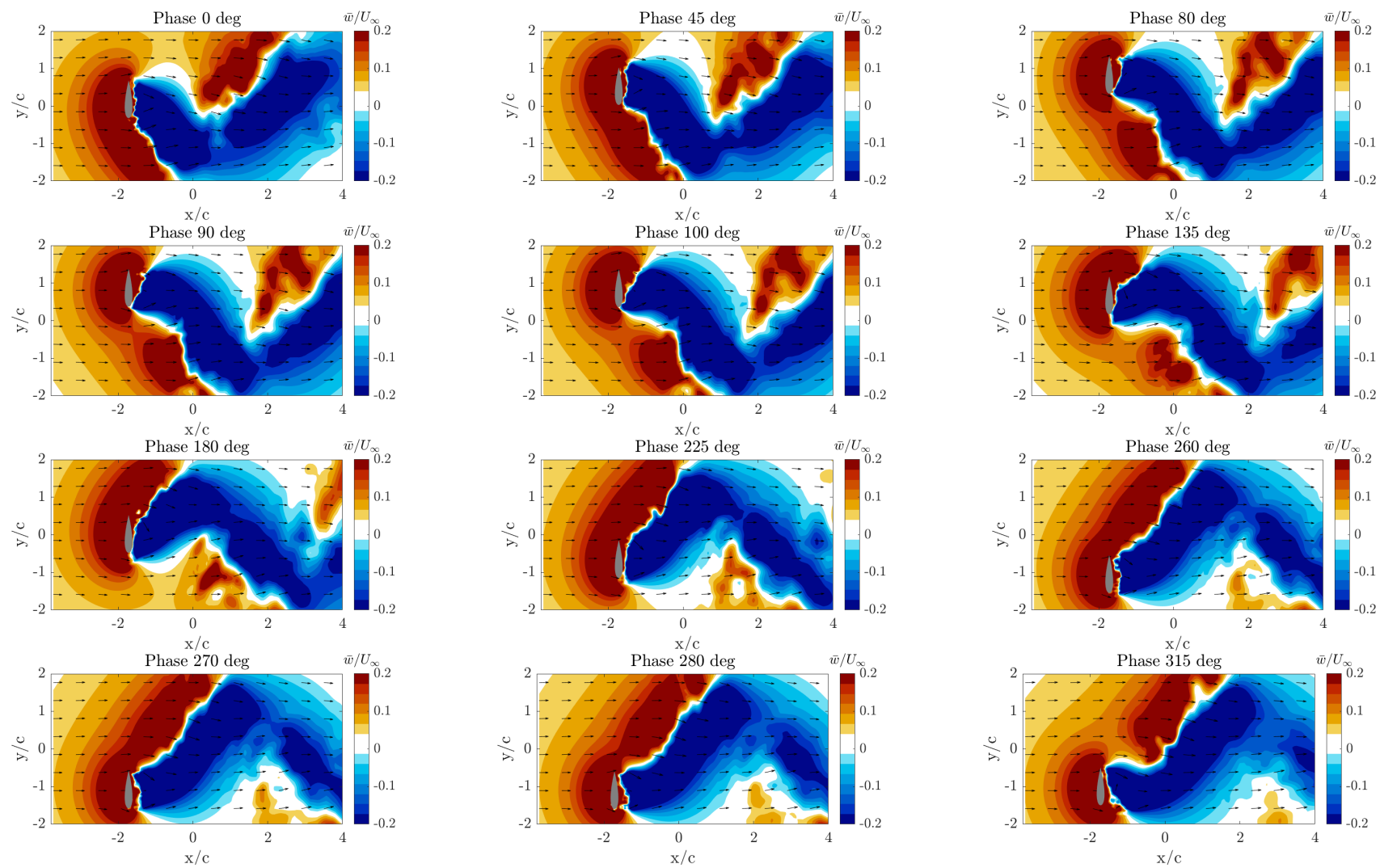


Figure M.16: Spanwise velocity, \bar{w}/U_∞ around a plunging airfoil at 5Hz, at the tip with the freestream velocity coming from the left. The flow is positive into the page.

APPENDIX N

2.5 Hz surging Cases CFD Planes

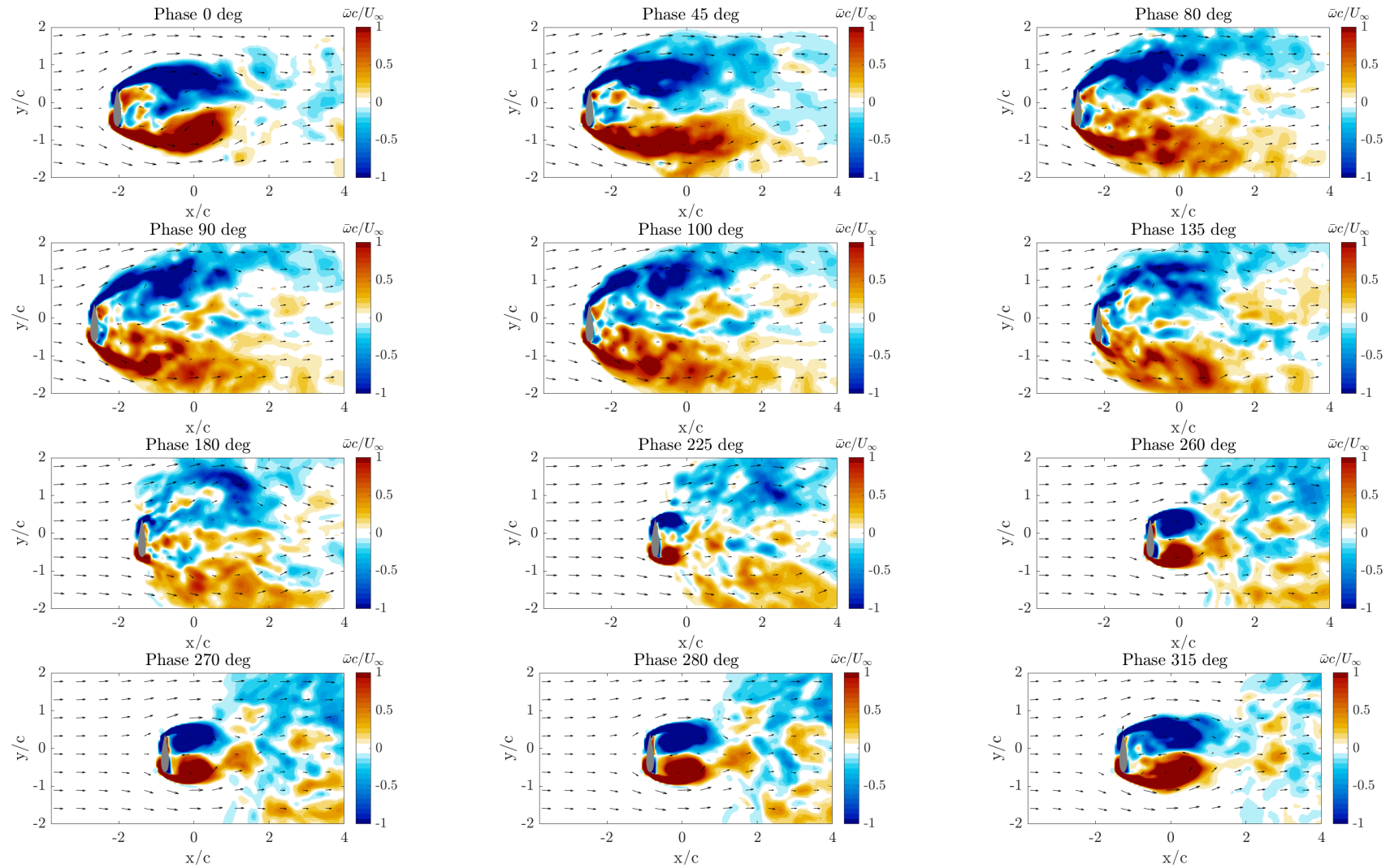


Figure N.1: Vorticity, $\bar{\omega}c/U_\infty$ around a surging airfoil at 2.5Hz, 3 chords inboard from the tip with the freestream velocity coming from the left.

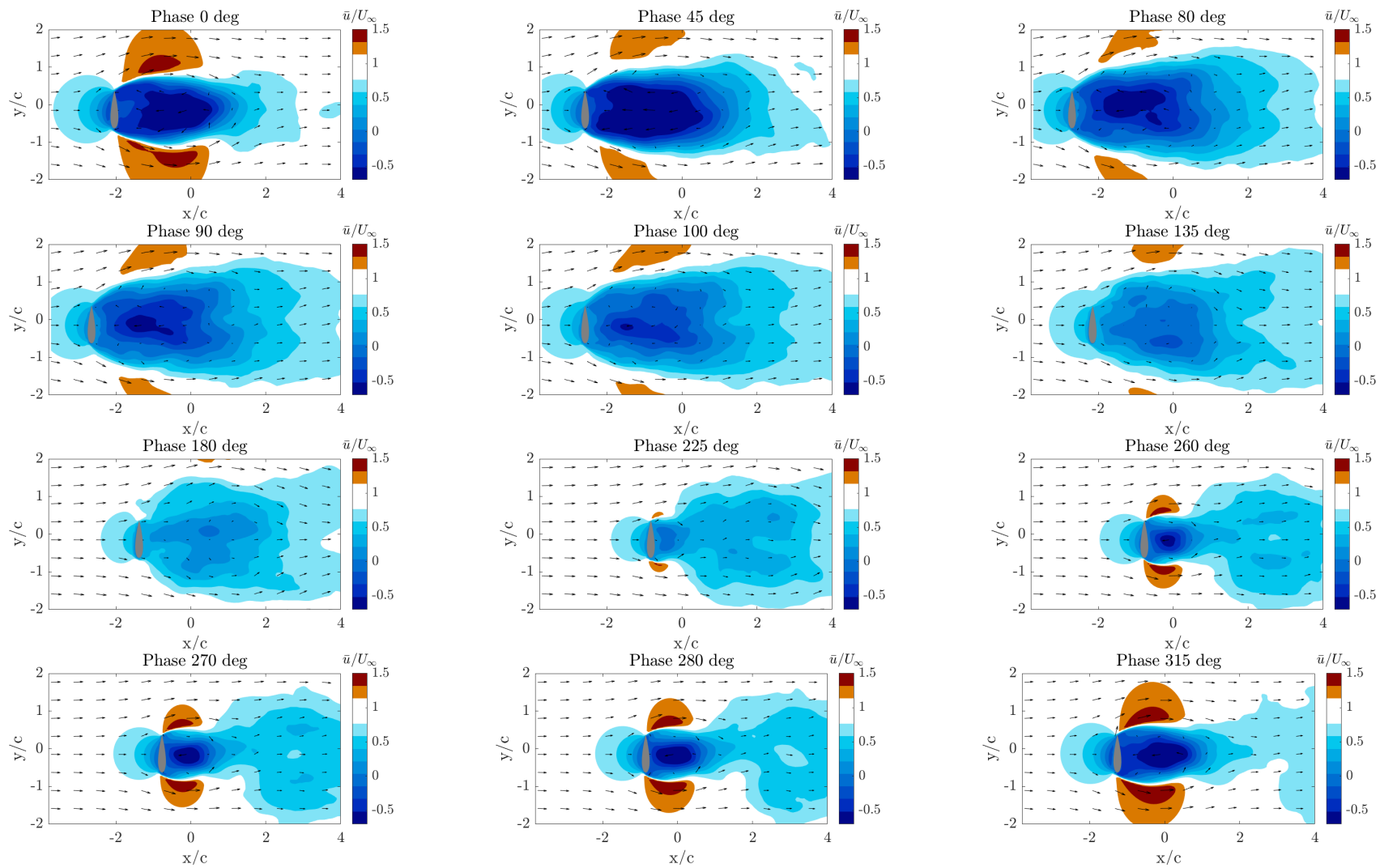


Figure N.2: Streamwise velocity, \bar{u}/U_∞ around a surging airfoil at 2.5Hz, 3 chords inboard from the tip with the freestream velocity coming from the left.

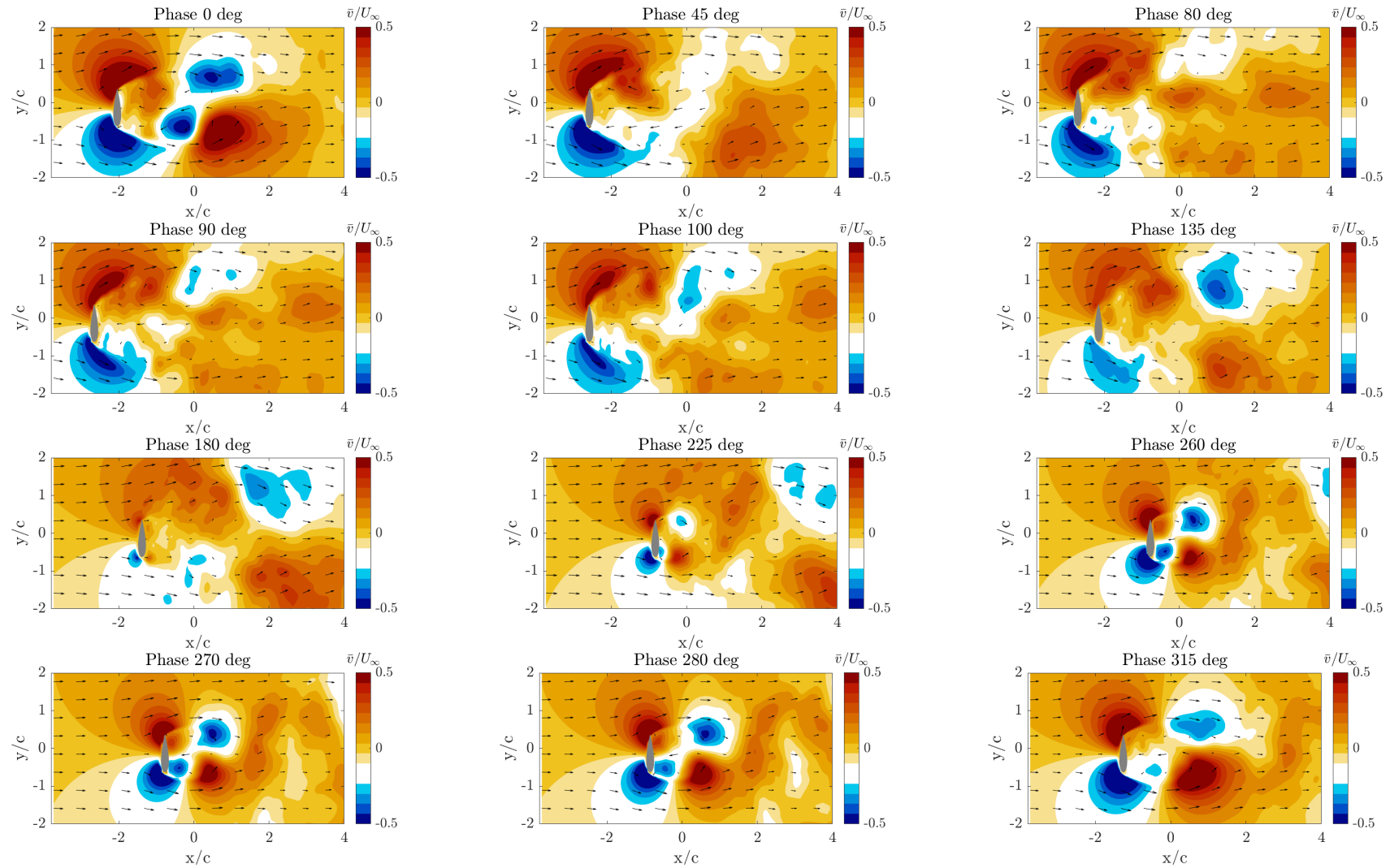


Figure N.3: Vertical velocity, \bar{v}/U_∞ around a surging airfoil at 2.5Hz, 3 chords inboard from the tip with the freestream velocity coming from the left.

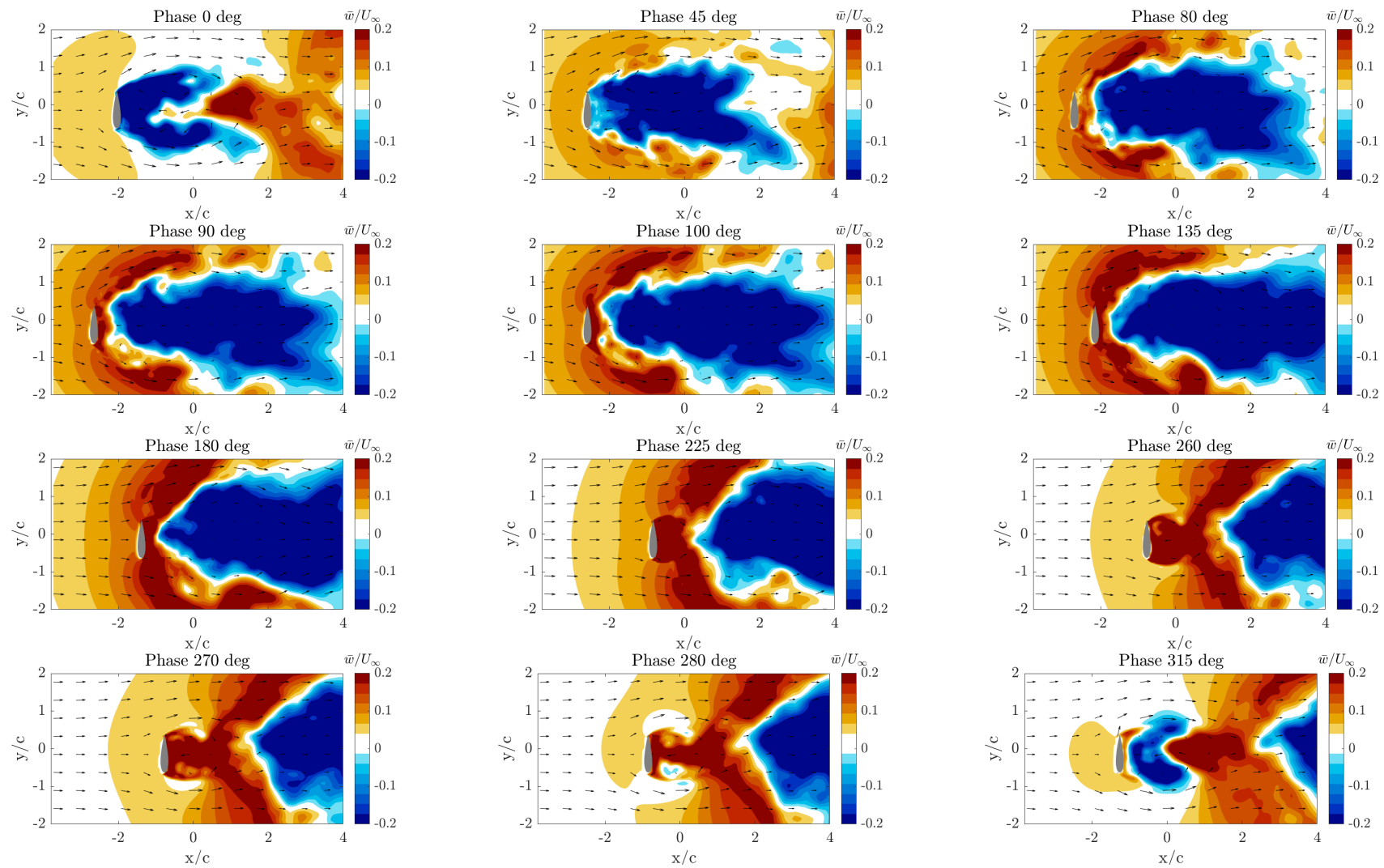


Figure N.4: Spanwise velocity, \bar{w}/U_∞ around a surging airfoil at 2.5Hz, 3 chords inboard from the tip with the freestream velocity coming from the left. The flow is positive into the page.

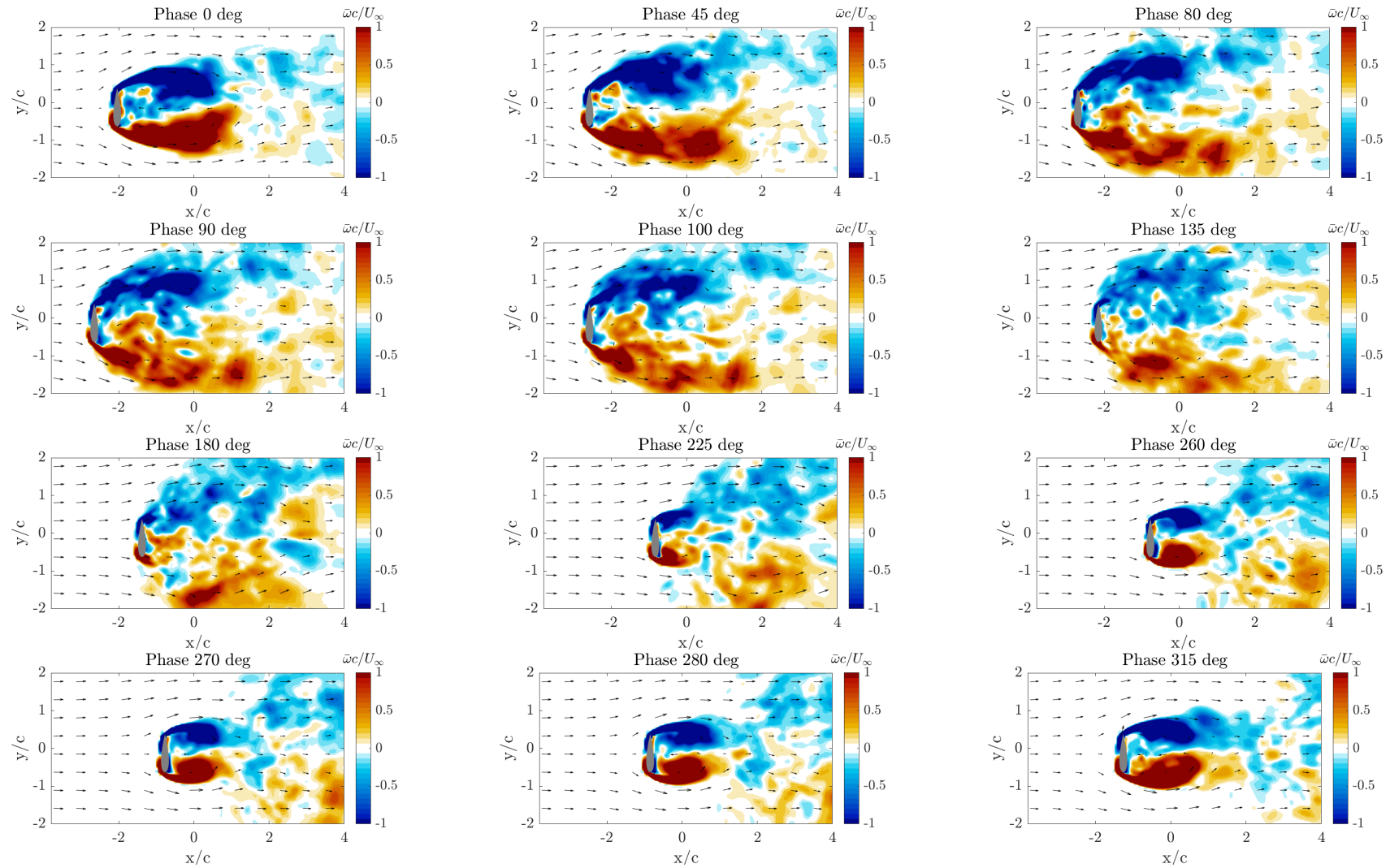


Figure N.5: Vorticity, $\bar{\omega}c/U_\infty$ around a surging airfoil at 2.5Hz, 2 chords inboard from the tip with the freestream velocity coming from the left.

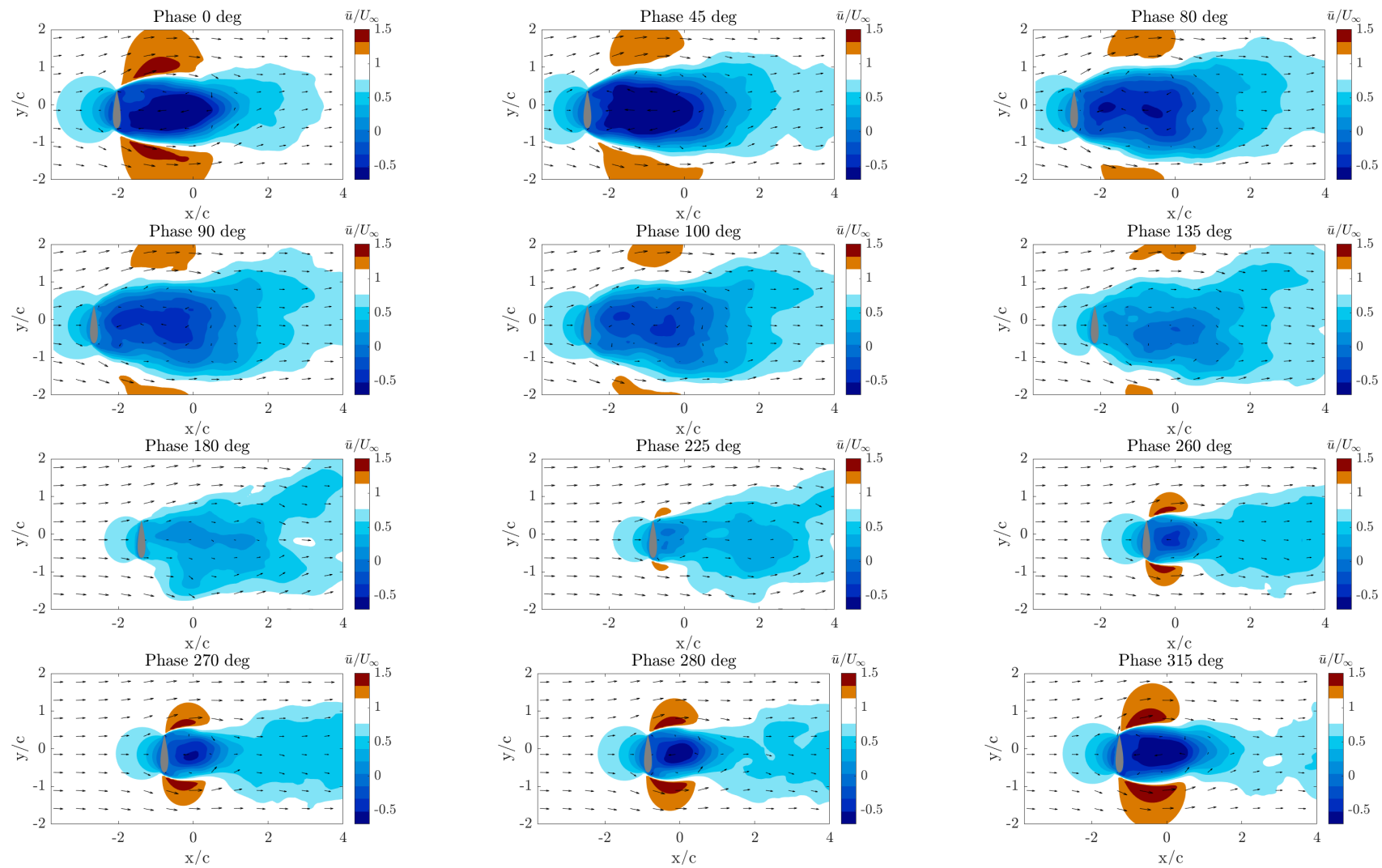


Figure N.6: Streamwise velocity, \bar{u}/U_∞ around a surging airfoil at 2.5Hz, 2 chords inboard from the tip with the freestream velocity coming from the left.

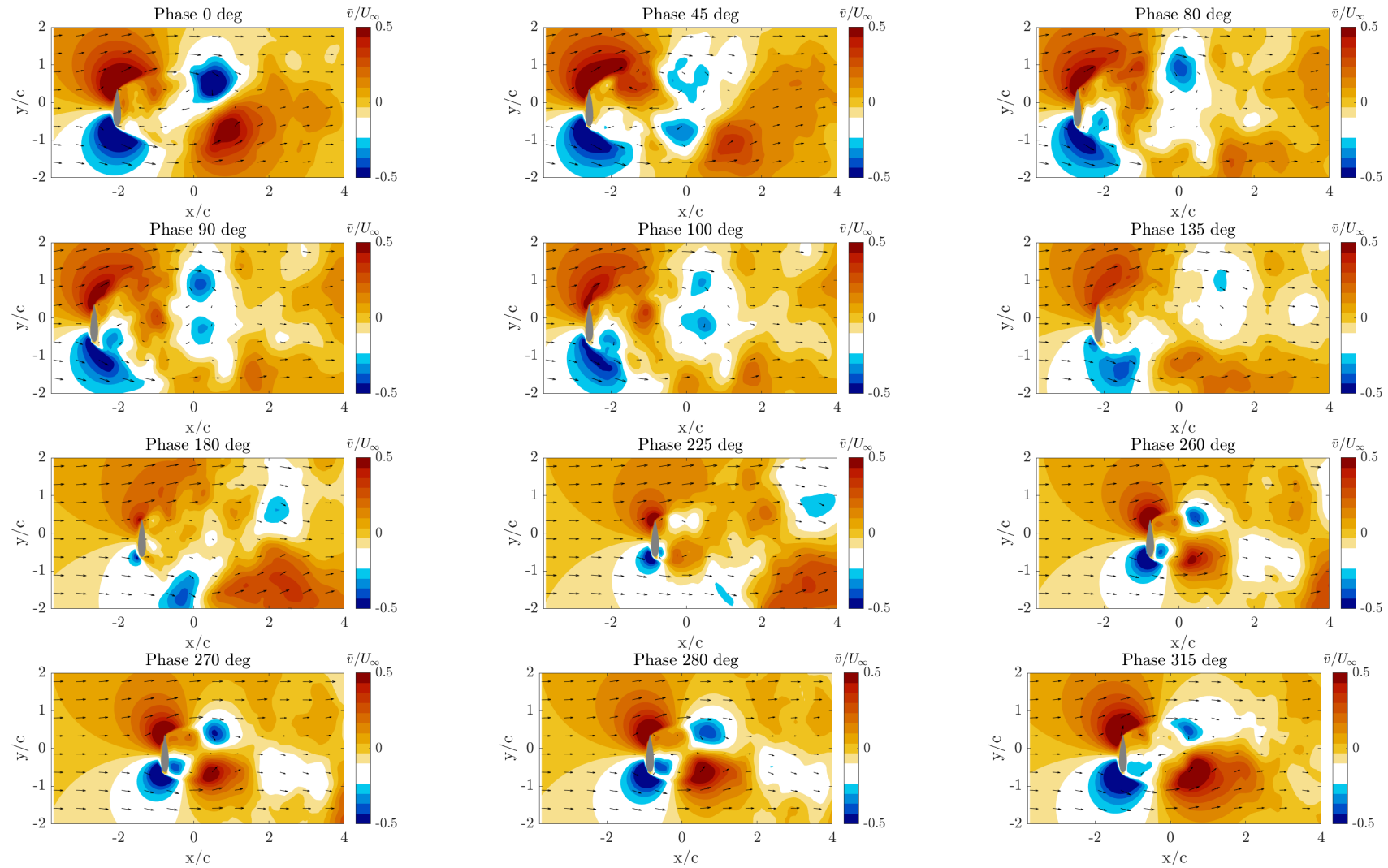


Figure N.7: Vertical velocity, \bar{v}/U_∞ around a surging airfoil at 2.5Hz, 2 chords inboard from the tip with the freestream velocity coming from the left.

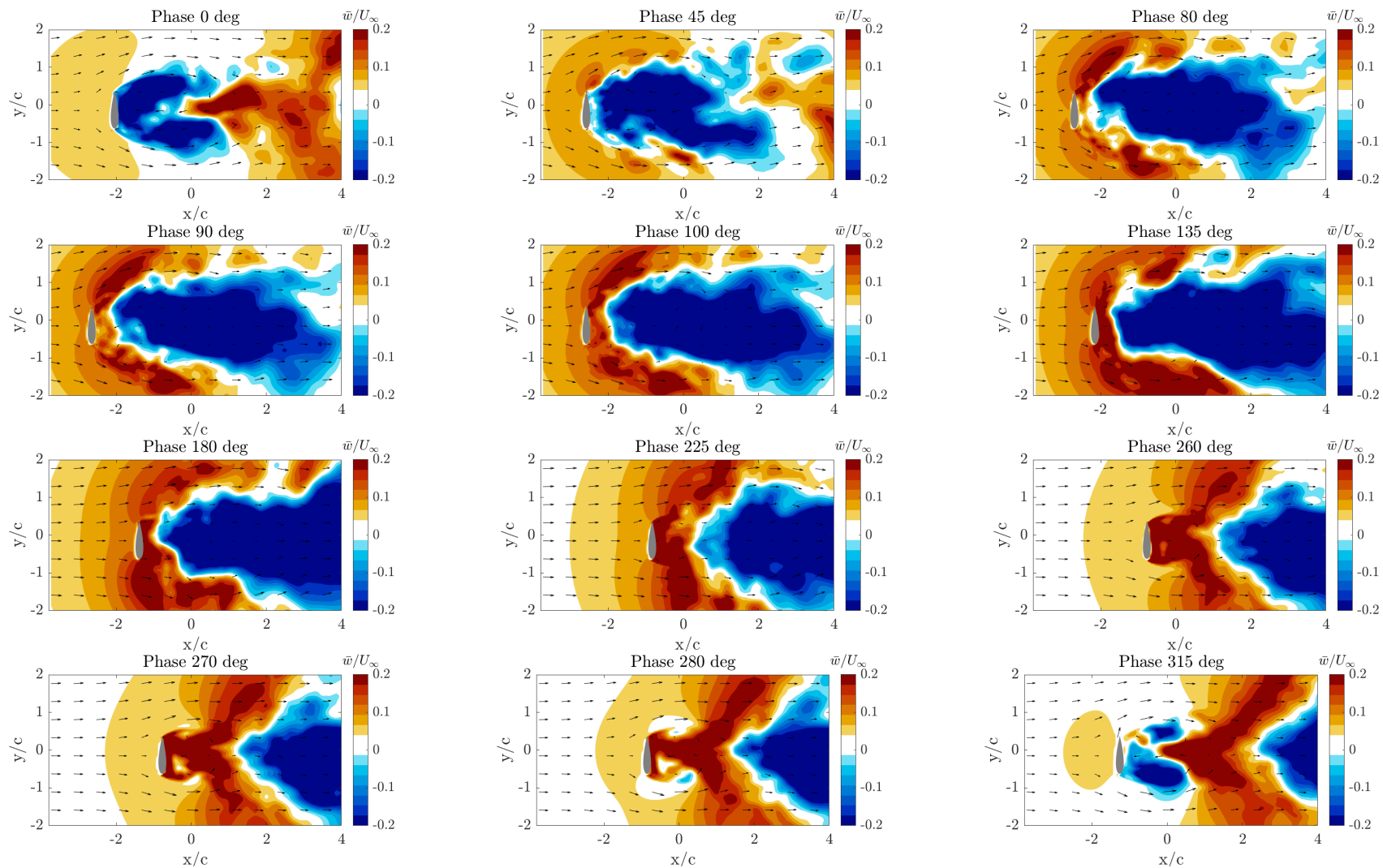


Figure N.8: Spanwise velocity, \bar{w}/U_∞ around a surging airfoil at 2.5Hz, 2 chords inboard from the tip with the freestream velocity coming from the left. The flow is positive into the page.

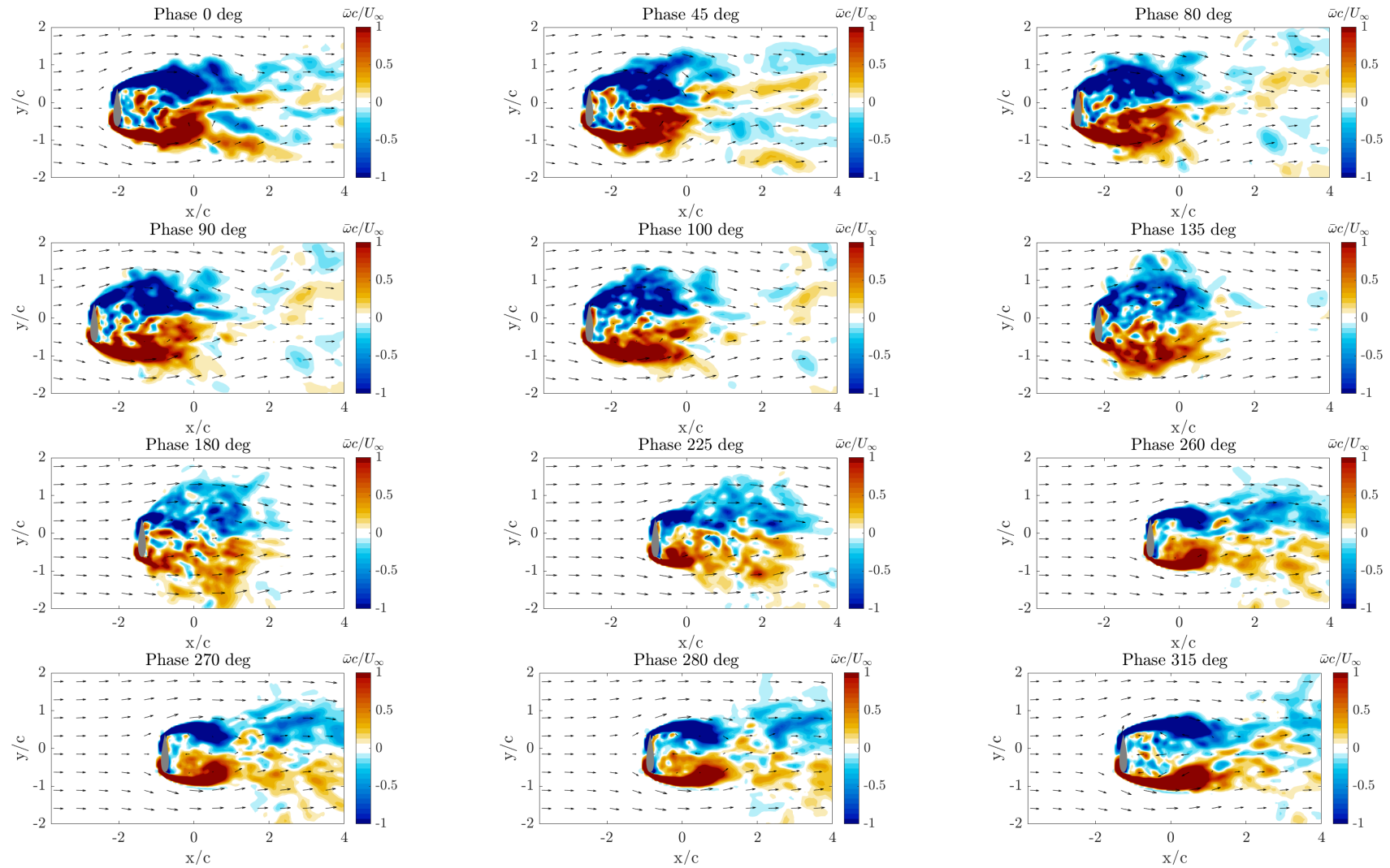


Figure N.9: Vorticity, $\bar{\omega}c/U_\infty$ around a surging airfoil at 2.5Hz, 1 chord inboard from the tip with the freestream velocity coming from the left.

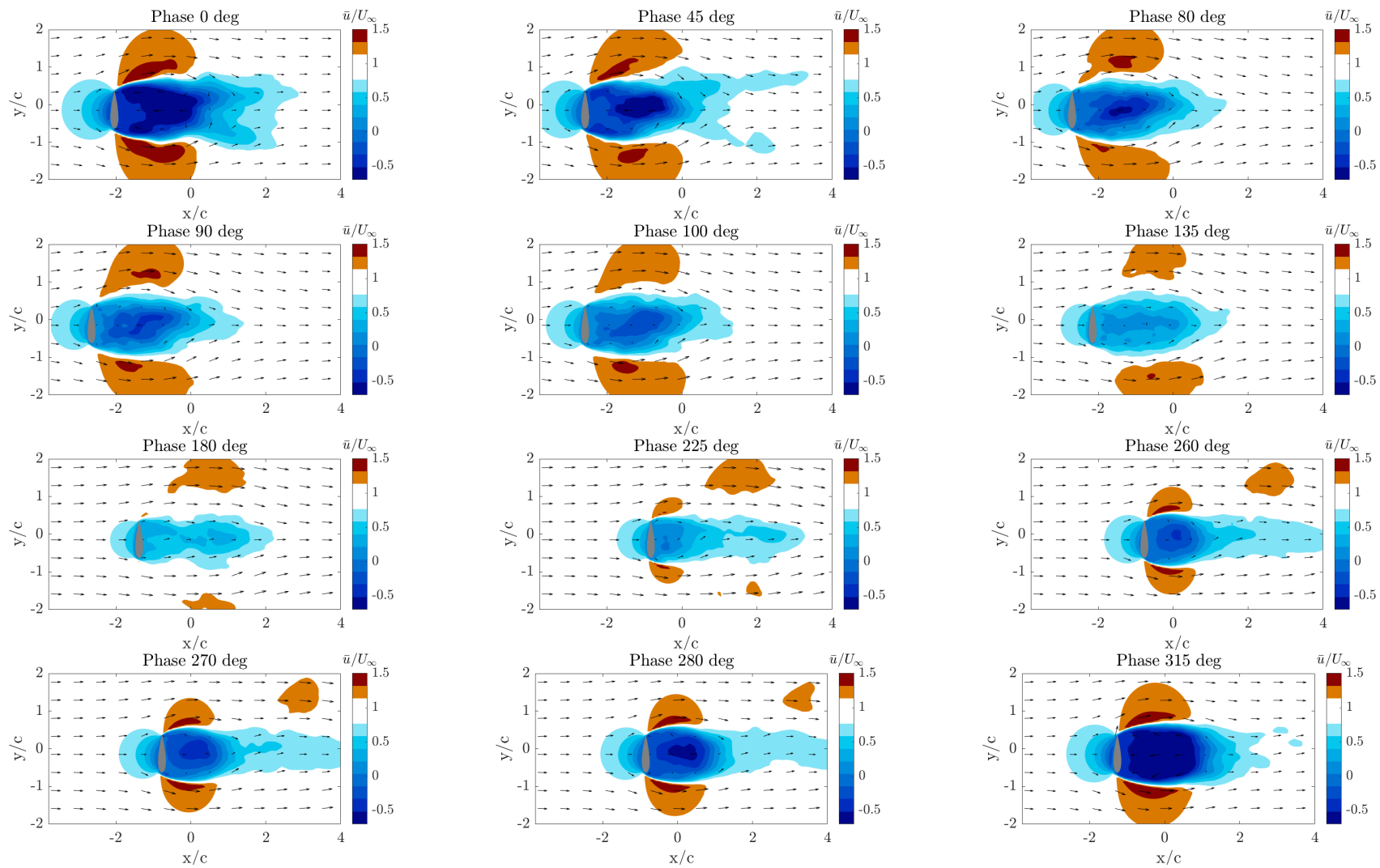


Figure N.10: Streamwise velocity, \bar{u}/U_∞ around a surging airfoil at 2.5Hz, 1 chord inboard from the tip with the freestream velocity coming from the left.

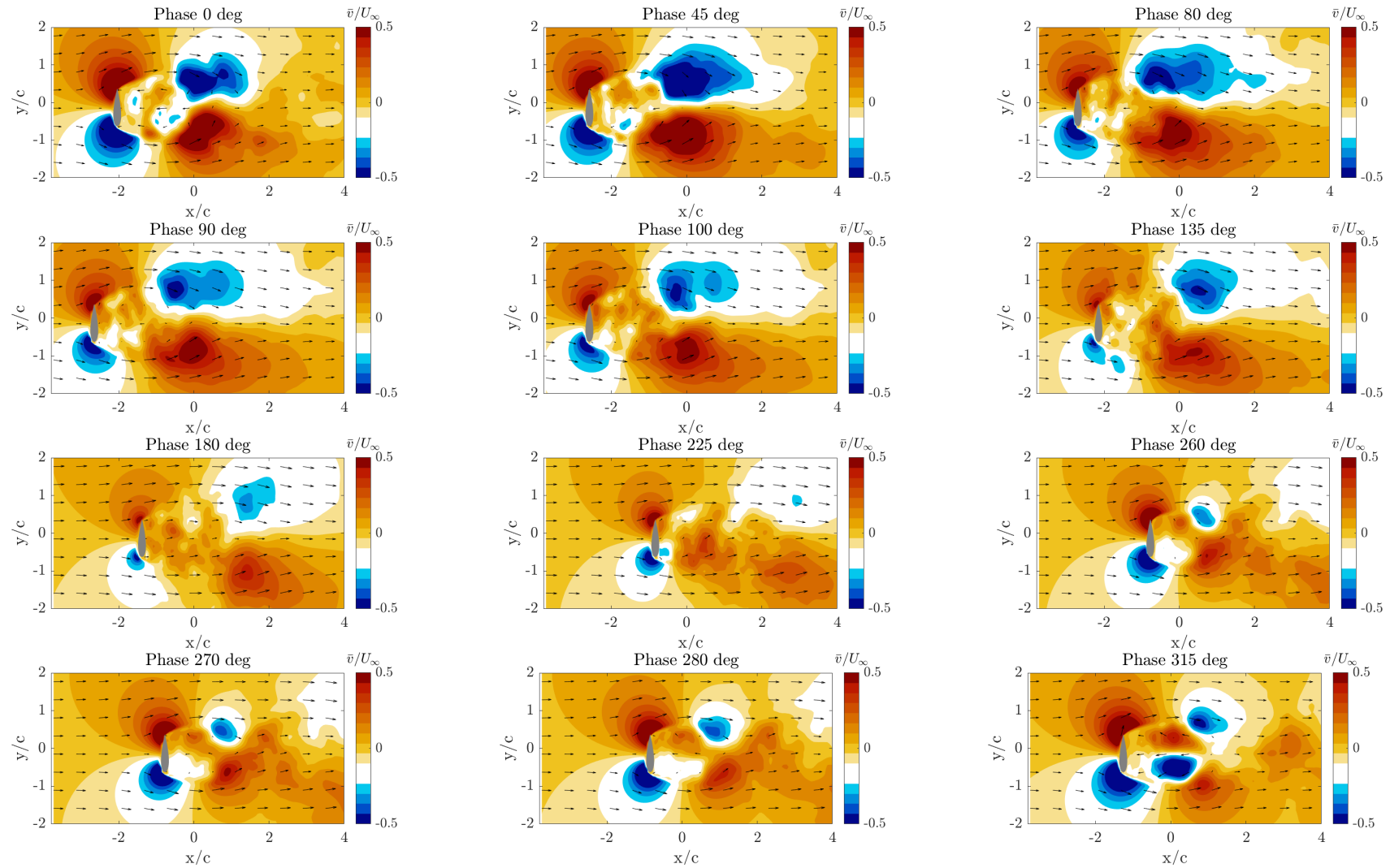


Figure N.11: Vertical velocity, \bar{v}/U_∞ around a surging airfoil at 2.5Hz, 1 chord inboard from the tip with the freestream velocity coming from the left.

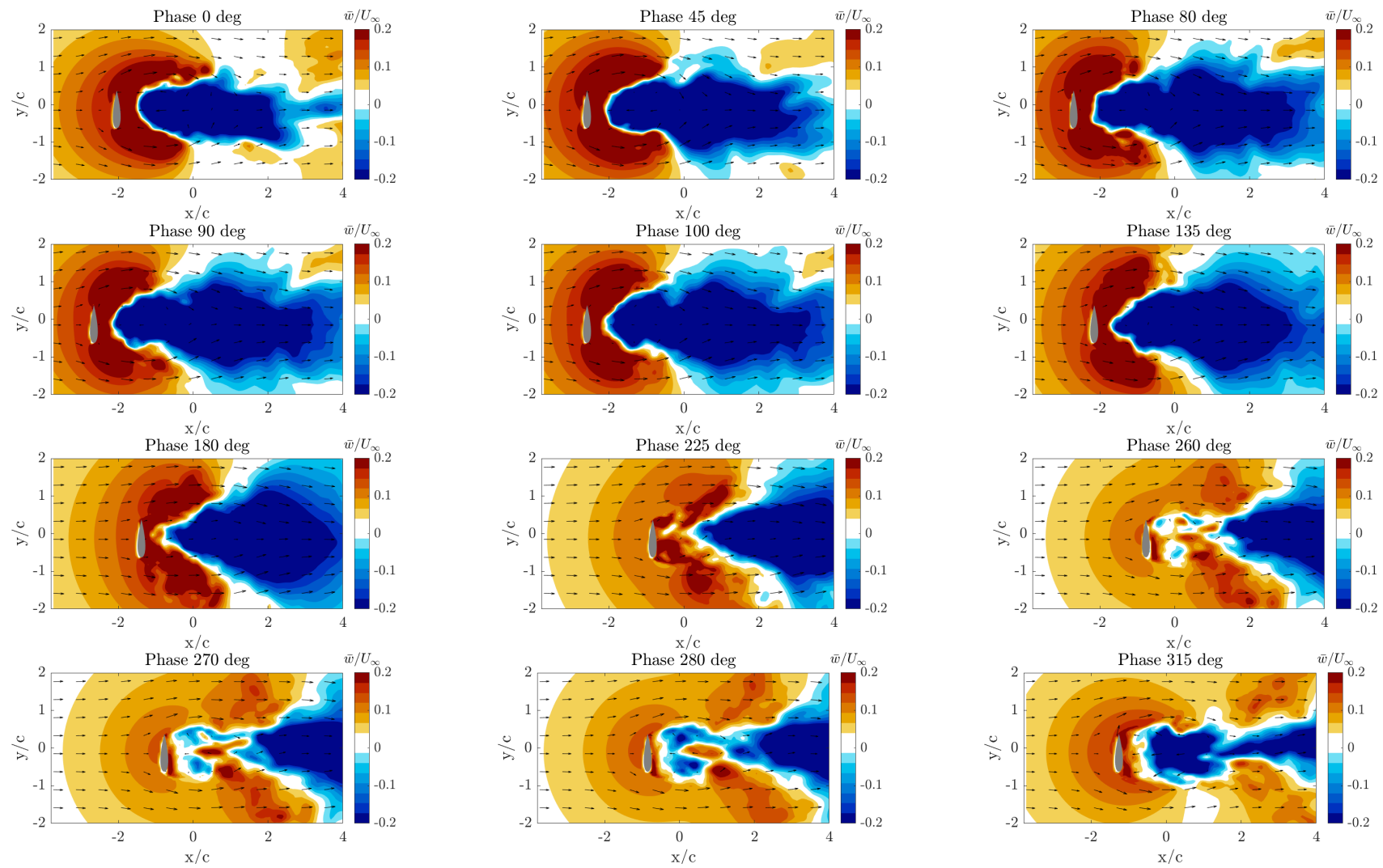


Figure N.12: Spanwise velocity, \bar{w}/U_∞ around a surging airfoil at 2.5Hz, 1 chord inboard from the tip with the freestream velocity coming from the left. The flow is positive into the page.

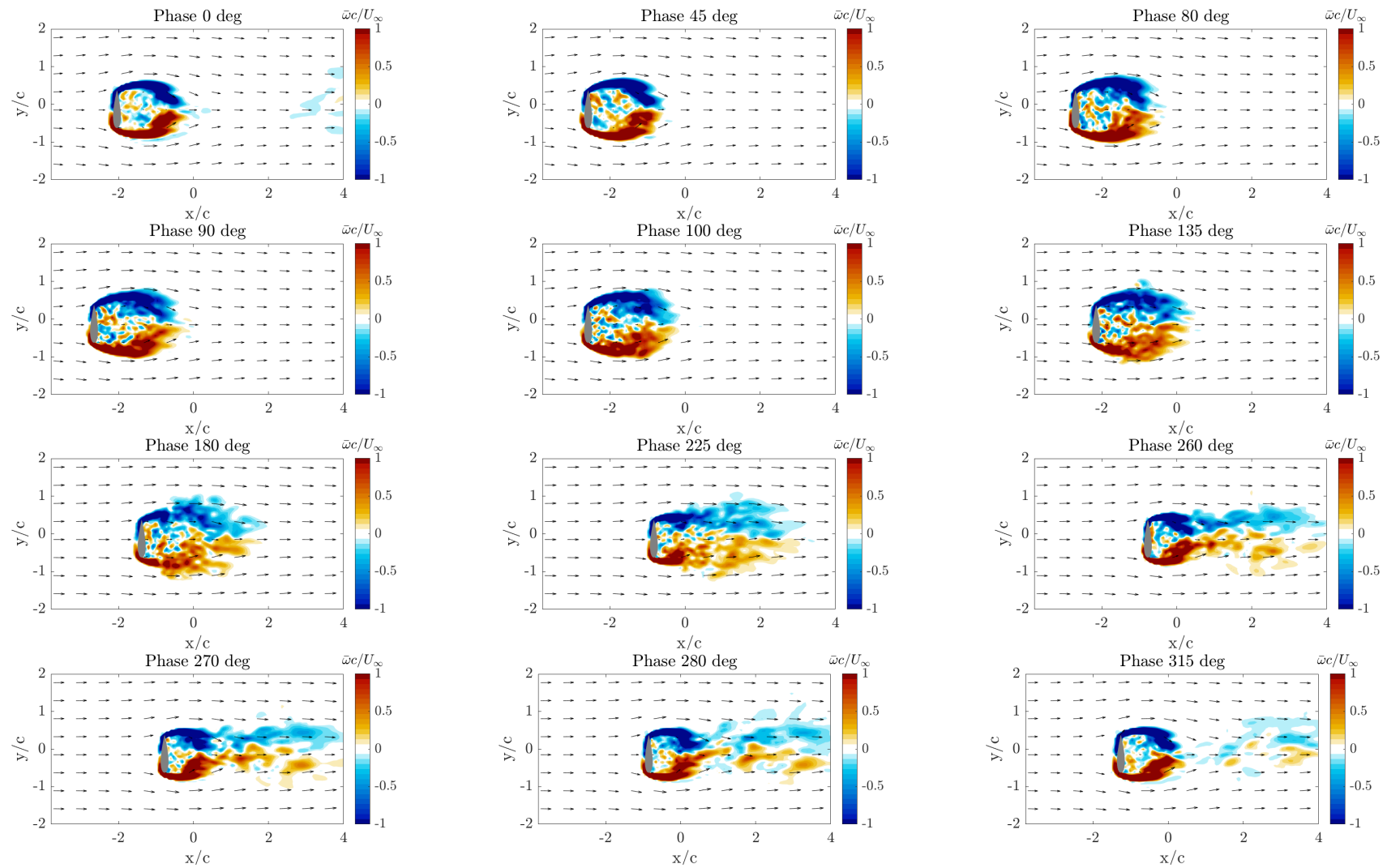


Figure N.13: Vorticity, $\bar{\omega}c/U_\infty$ around a surging airfoil at 2.5Hz, at the tip with the freestream velocity coming from the left.

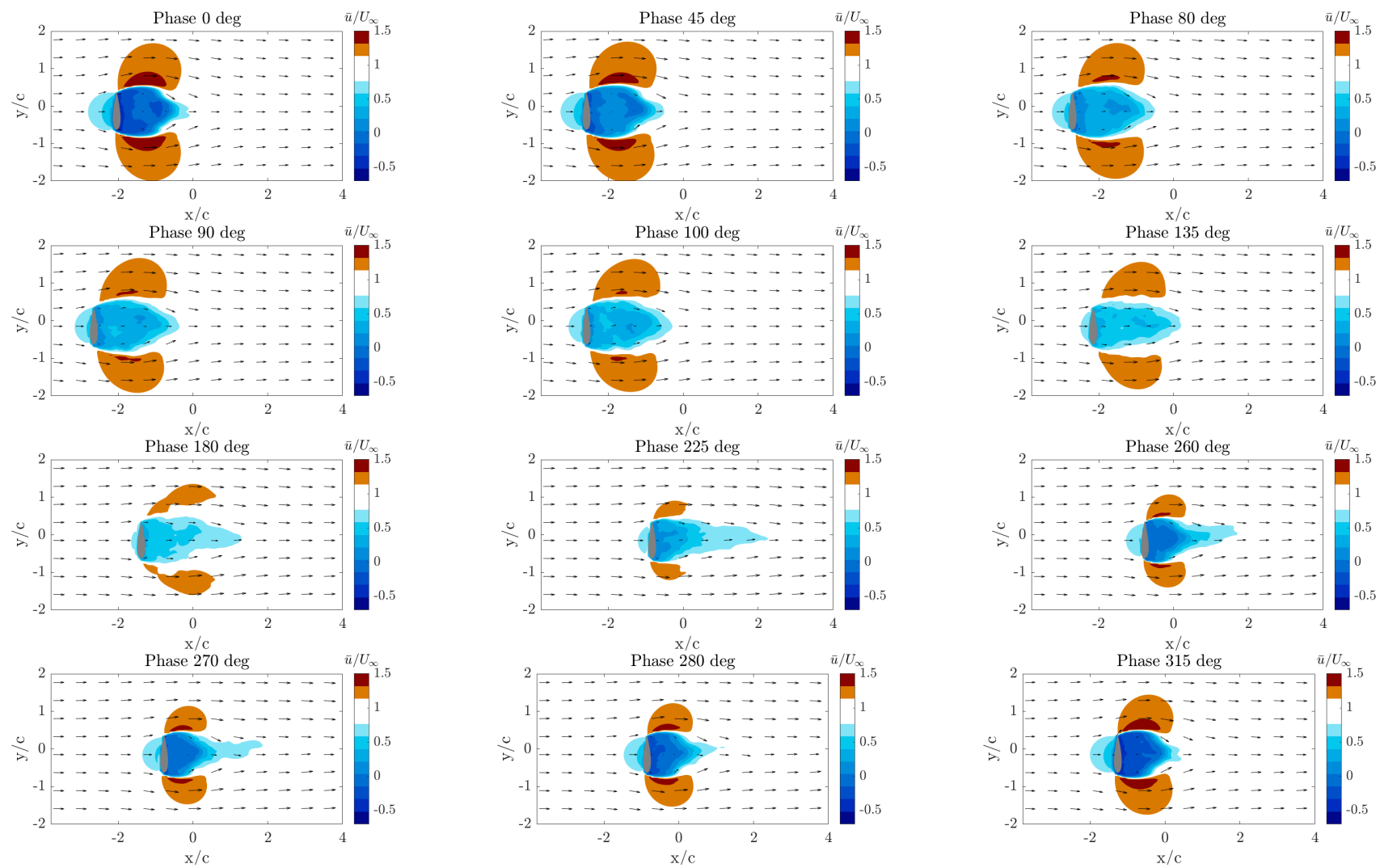


Figure N.14: Streamwise velocity, \bar{u}/U_∞ around a surging airfoil at 2.5Hz, at the tip with the freestream velocity coming from the left.

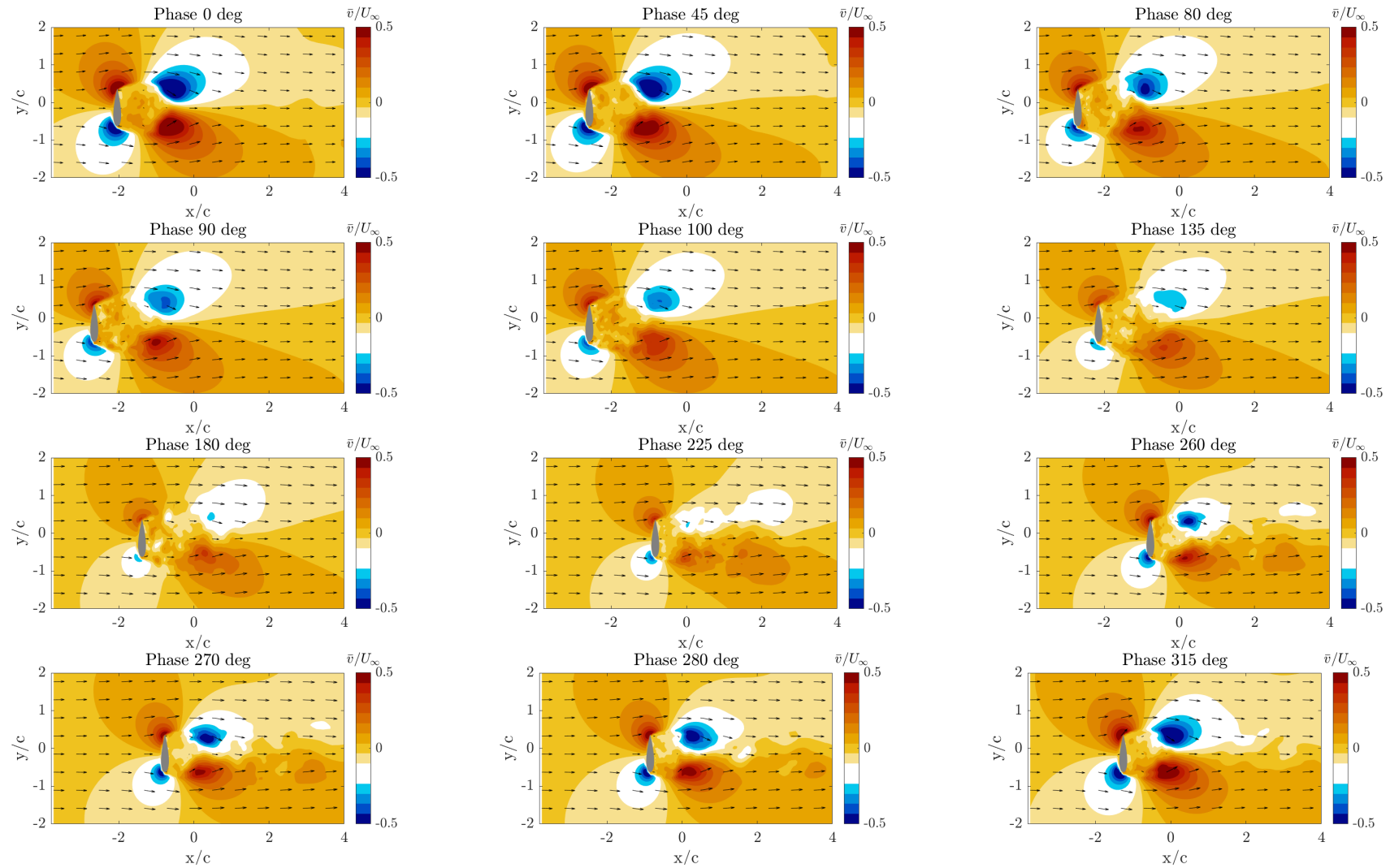


Figure N.15: Vertical velocity, \bar{v}/U_∞ around a surging airfoil at 2.5Hz, at the tip with the freestream velocity coming from the left.

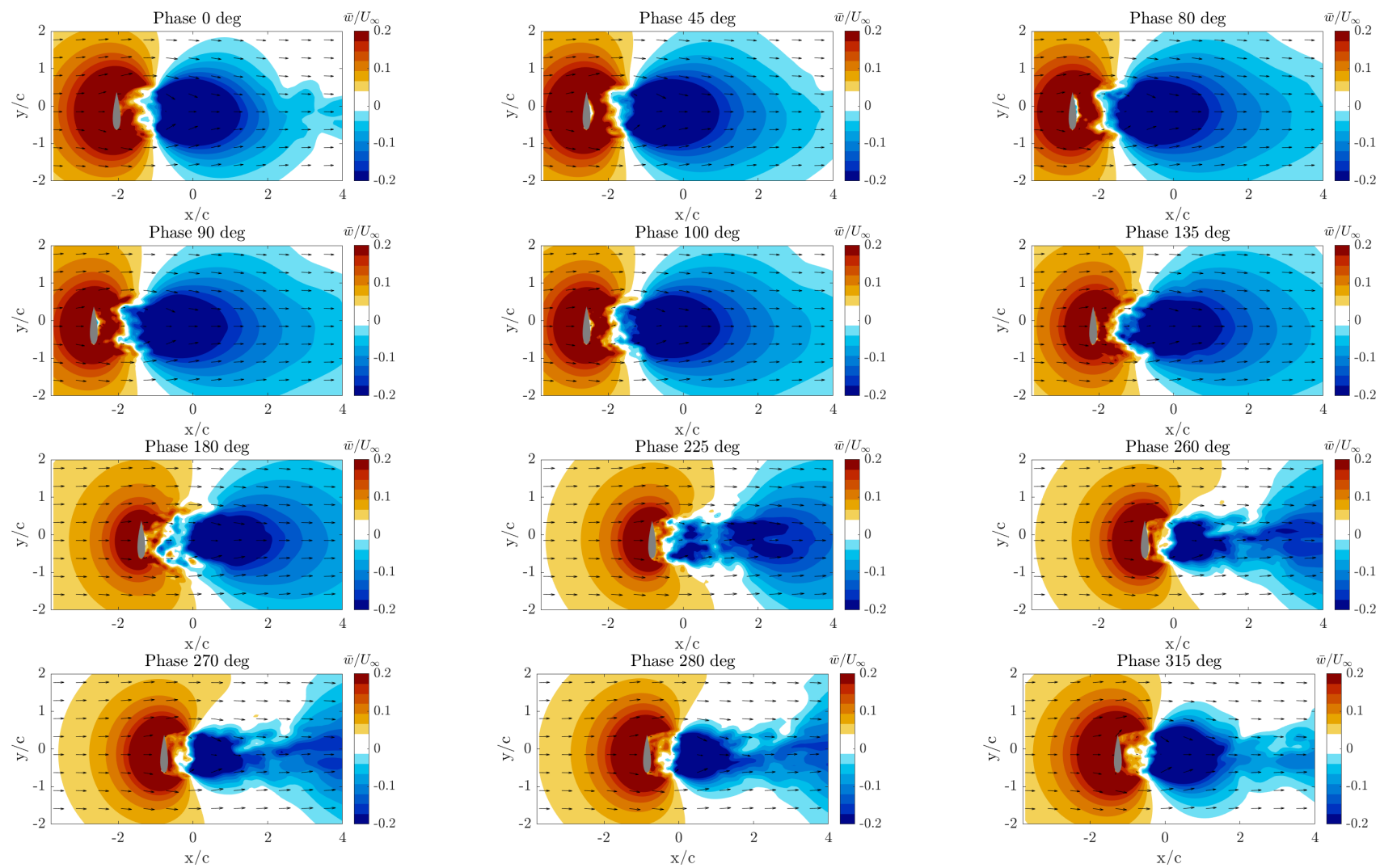


Figure N.16: Spanwise velocity, \bar{w}/U_∞ around a surging airfoil at 2.5Hz, at the tip with the freestream velocity coming from the left. The flow is positive into the page.

APPENDIX ○

5 Hz surging Cases CFD Planes

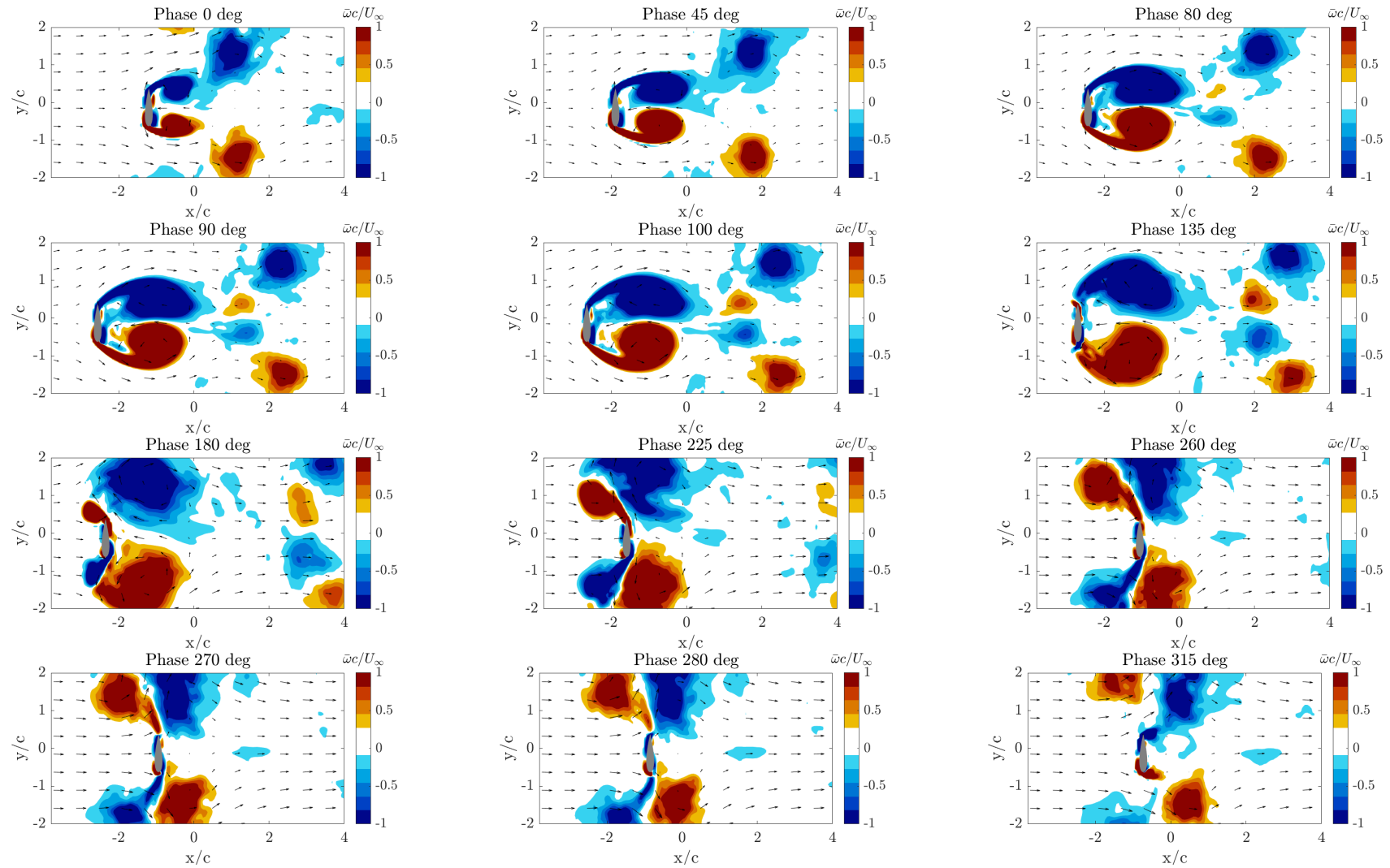


Figure O.1: Vorticity, $\bar{\omega}c/U_\infty$ around a surging airfoil at 5Hz, 3 chords inboard from the tip with the freestream velocity coming from the left.

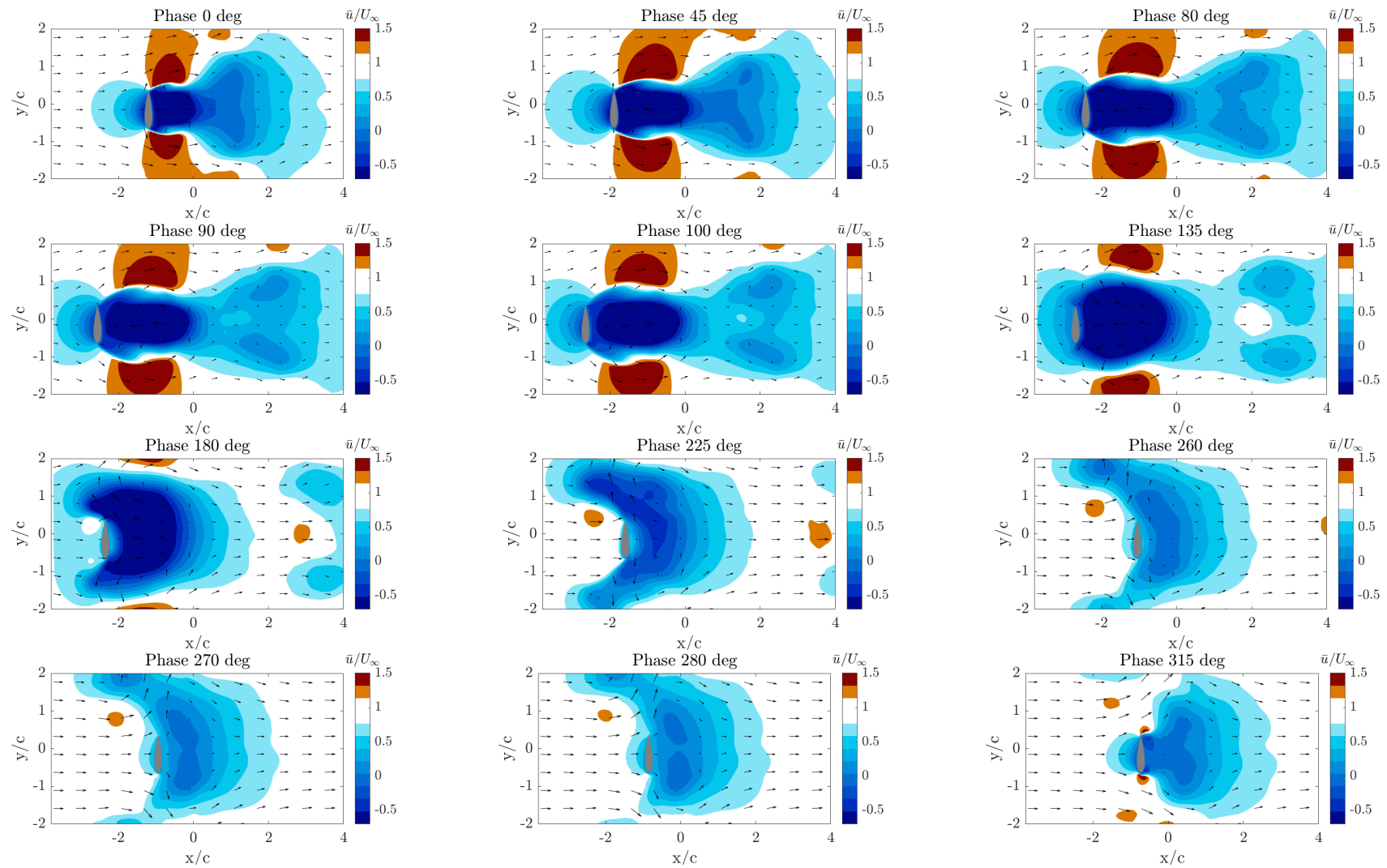


Figure O.2: Streamwise velocity, \bar{u}/U_∞ around a surging airfoil at 5Hz, 3 chords inboard from the tip with the freestream velocity coming from the left.

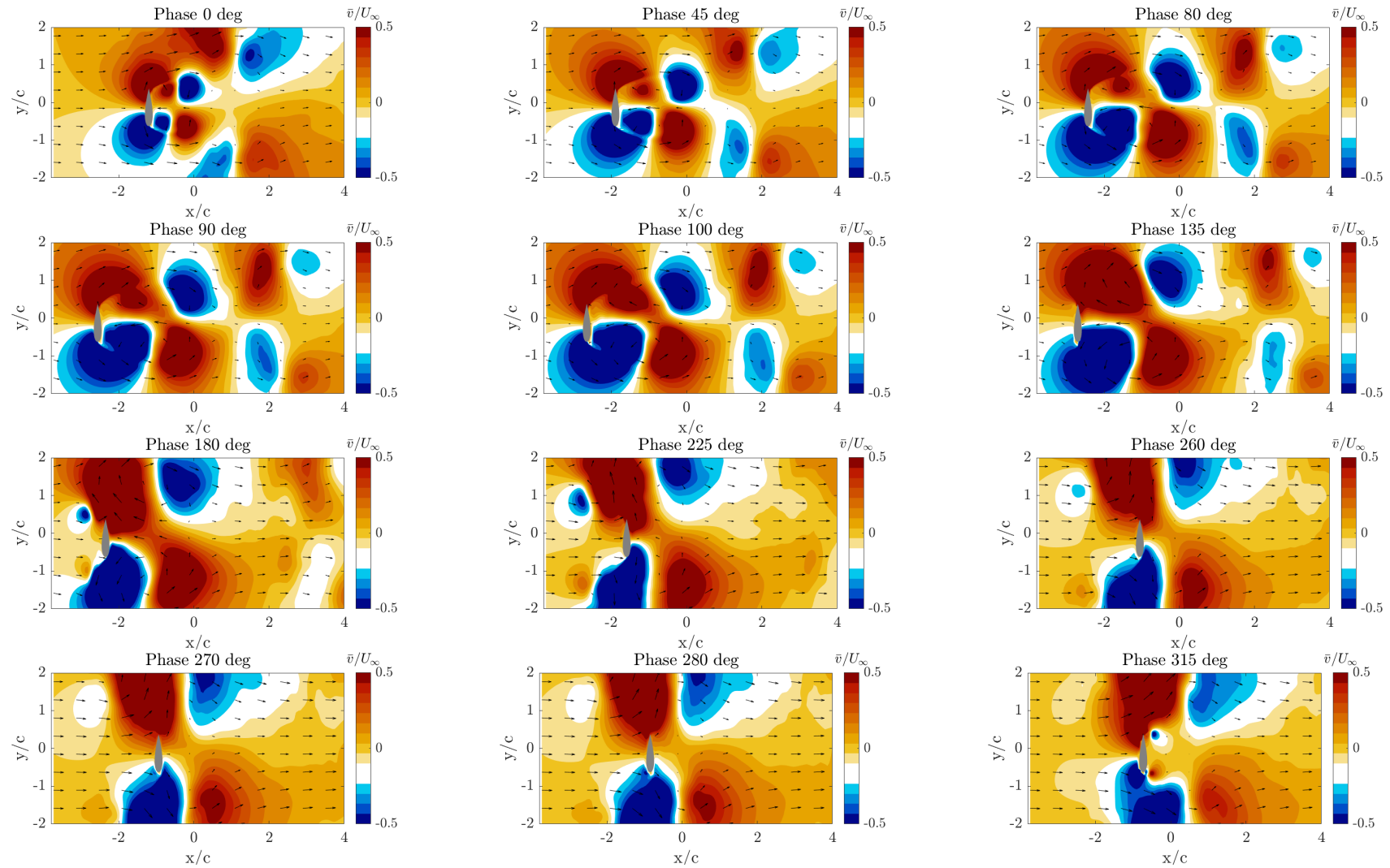


Figure O.3: Vertical velocity, \bar{v}/U_∞ around a surging airfoil at 5Hz, 3 chords inboard from the tip with the freestream velocity coming from the left.

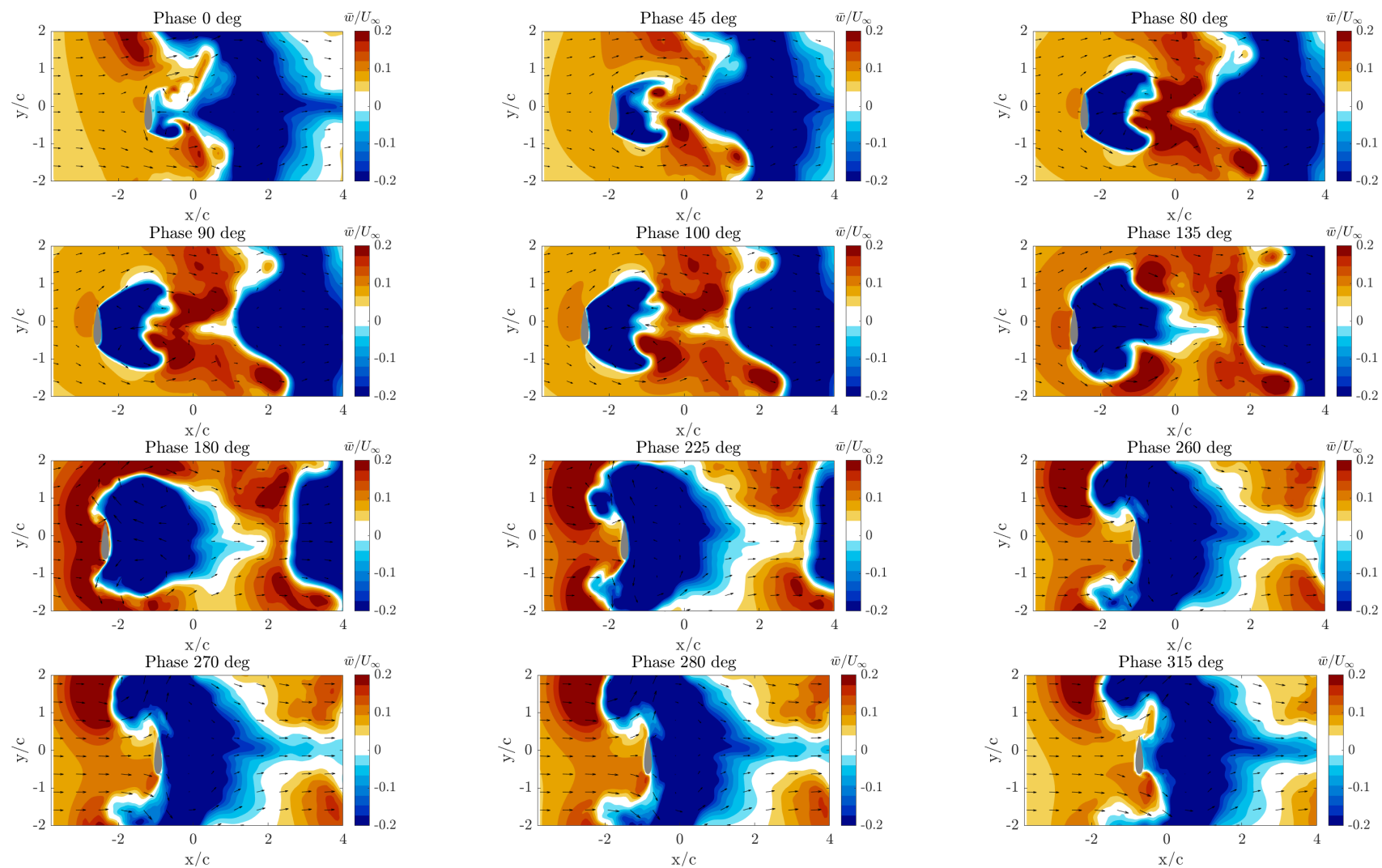


Figure O.4: Spanwise velocity, \bar{w}/U_∞ around a surging airfoil at 5Hz, 3 chords inboard from the tip with the freestream velocity coming from the left. The flow is positive into the page.

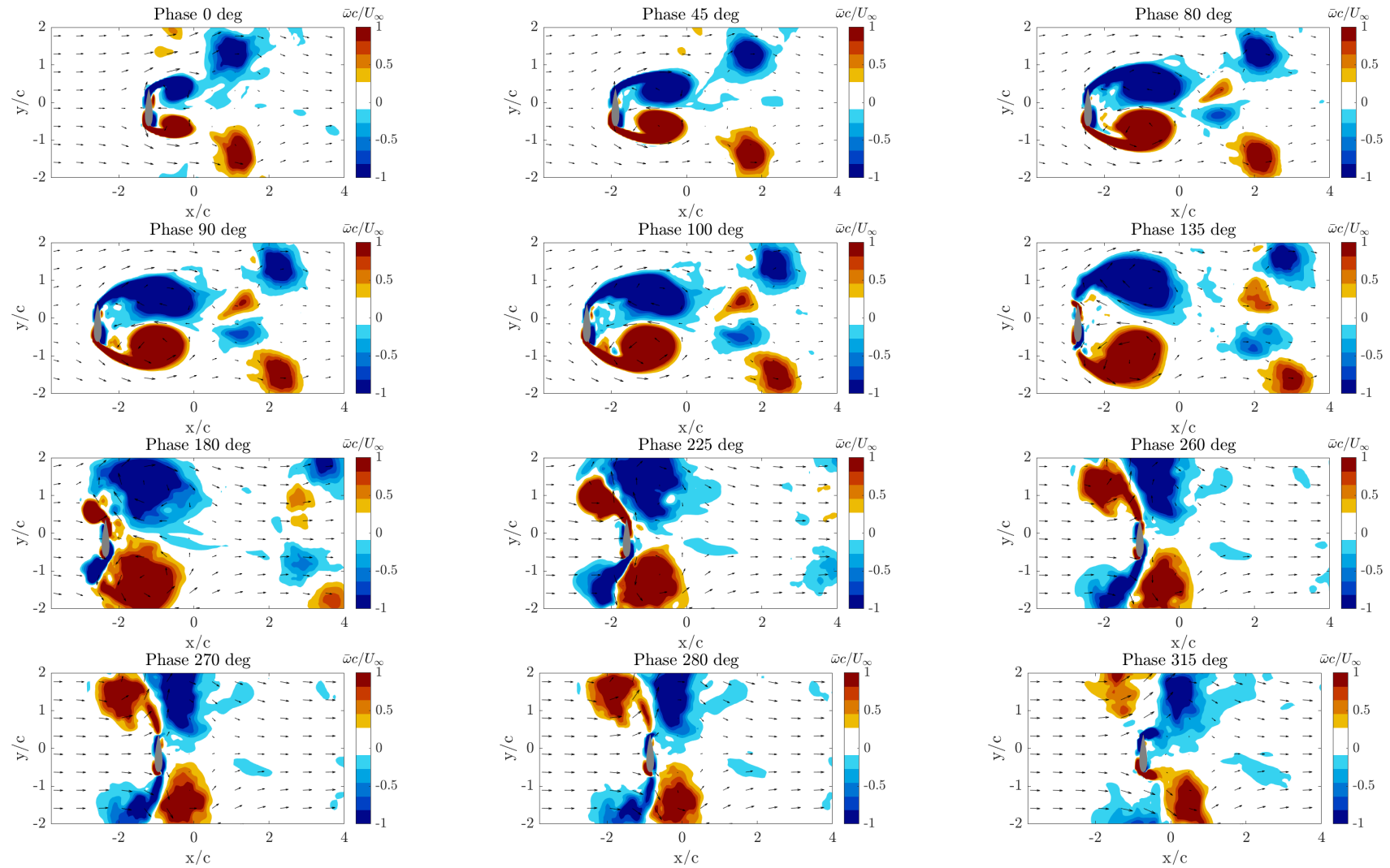


Figure O.5: Vorticity, $\bar{\omega}c/U_\infty$ around a surging airfoil at 5Hz, 2 chords inboard from the tip with the freestream velocity coming from the left.

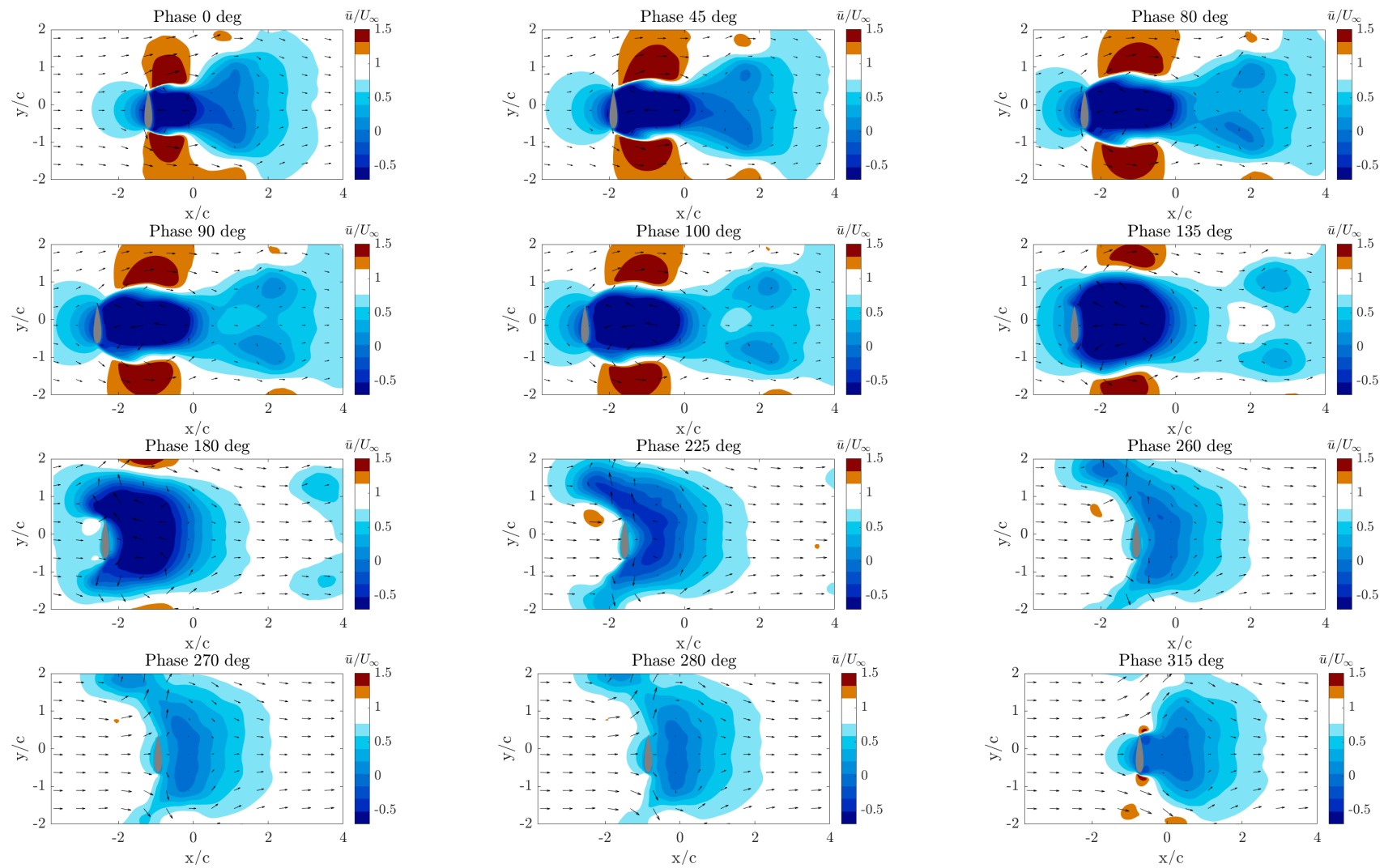


Figure 0.6: Streamwise velocity, \bar{u}/U_∞ around a surging airfoil at 5Hz, 2 chords inboard from the tip with the freestream velocity coming from the left.

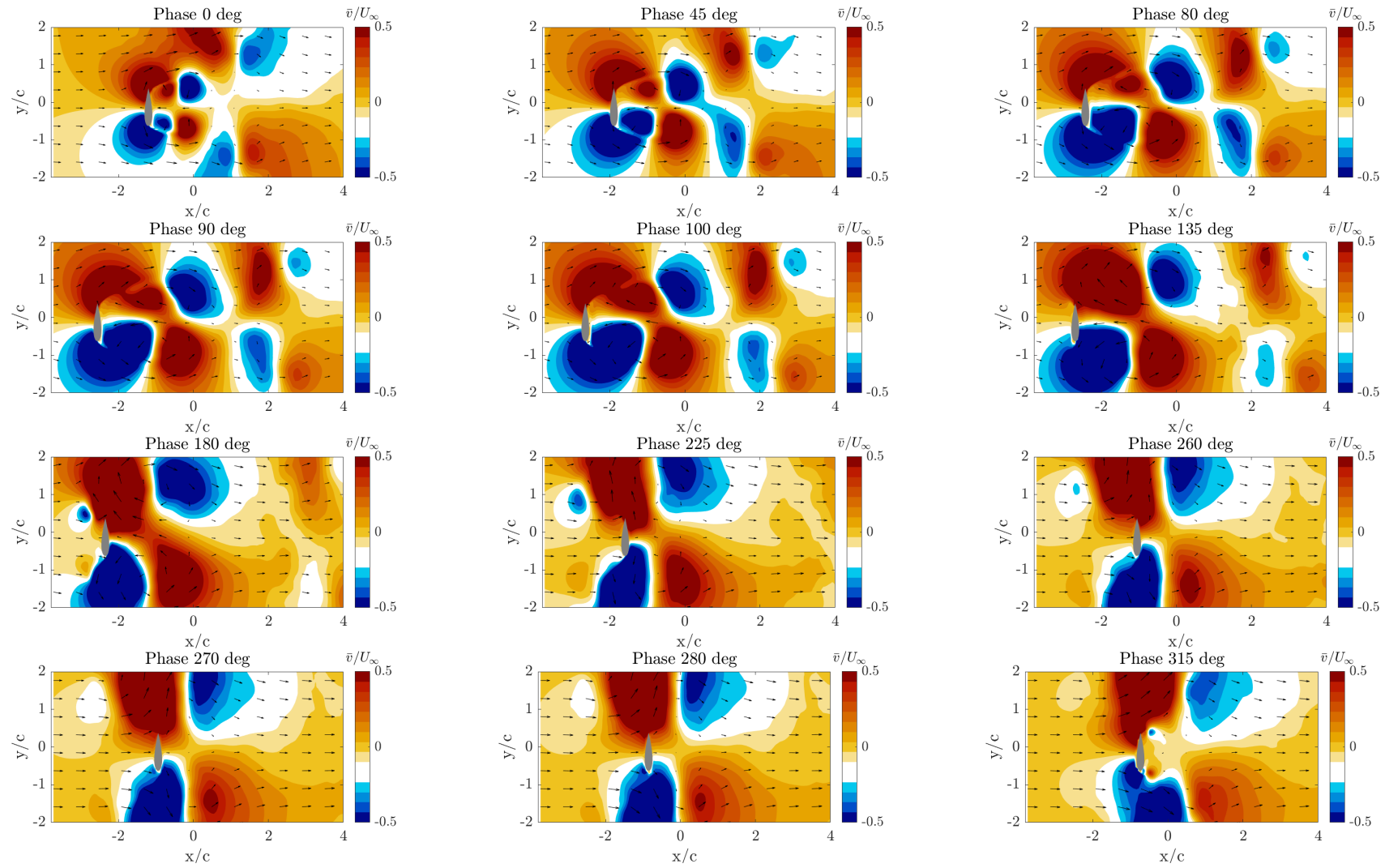


Figure O.7: Vertical velocity, \bar{v}/U_∞ around a surging airfoil at 5Hz, 2 chords inboard from the tip with the freestream velocity coming from the left.

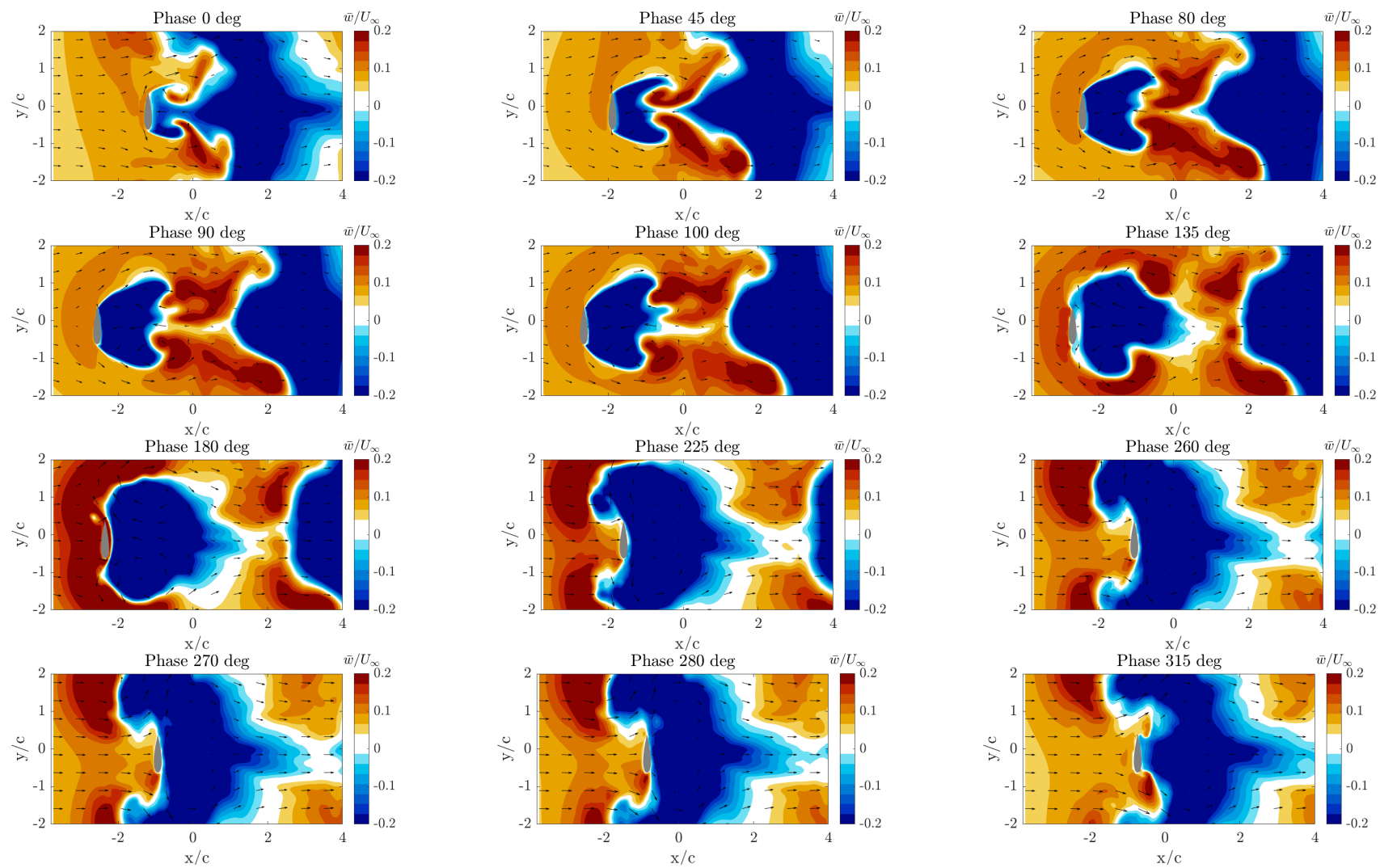


Figure O.8: Spanwise velocity, \bar{w}/U_∞ around a surging airfoil at 5Hz, 2 chords inboard from the tip with the freestream velocity coming from the left. The flow is positive into the page.

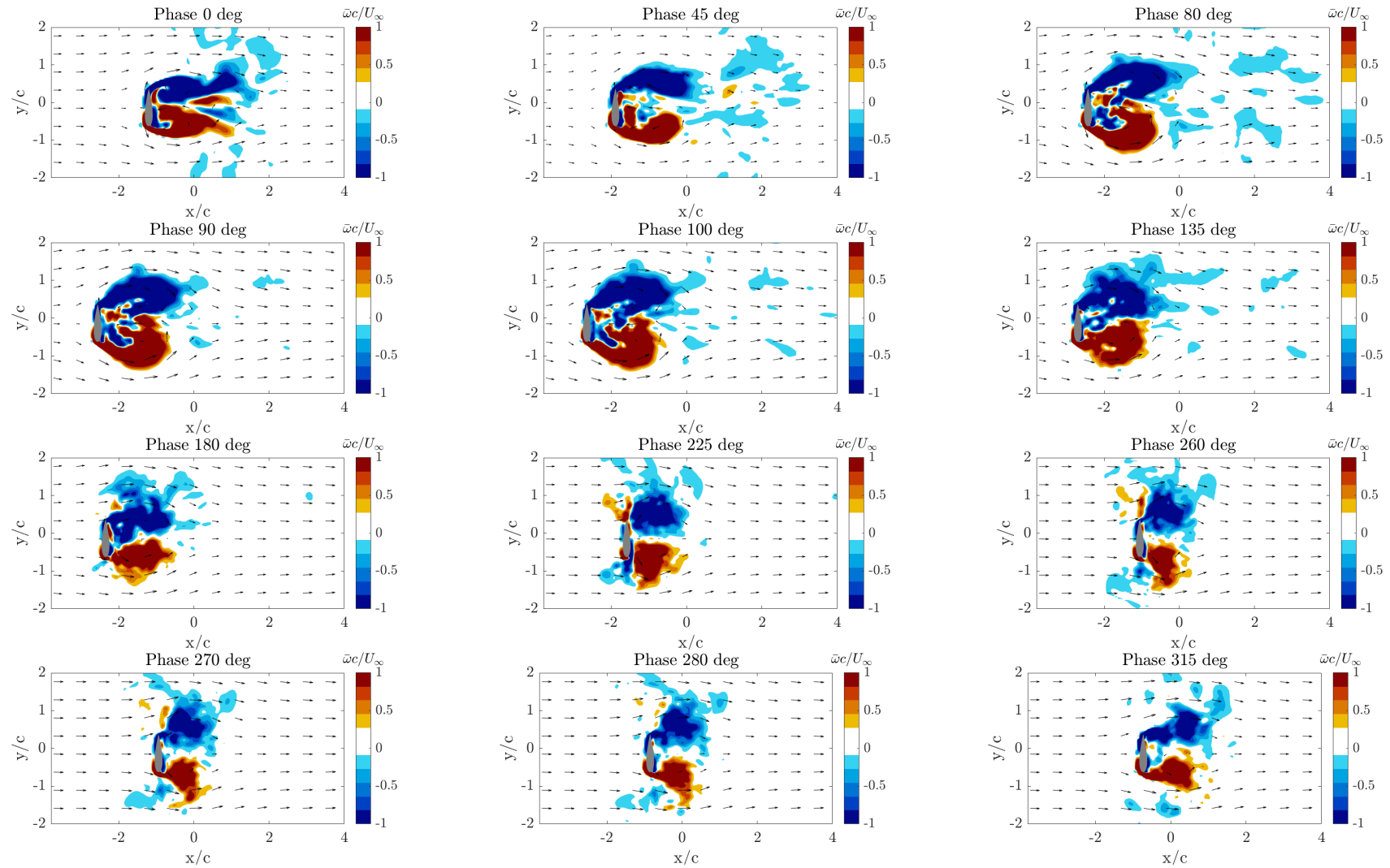


Figure O.9: Vorticity, $\bar{\omega}c/U_\infty$ around a surging airfoil at 5Hz, 1 chord inboard from the tip with the freestream velocity coming from the left.

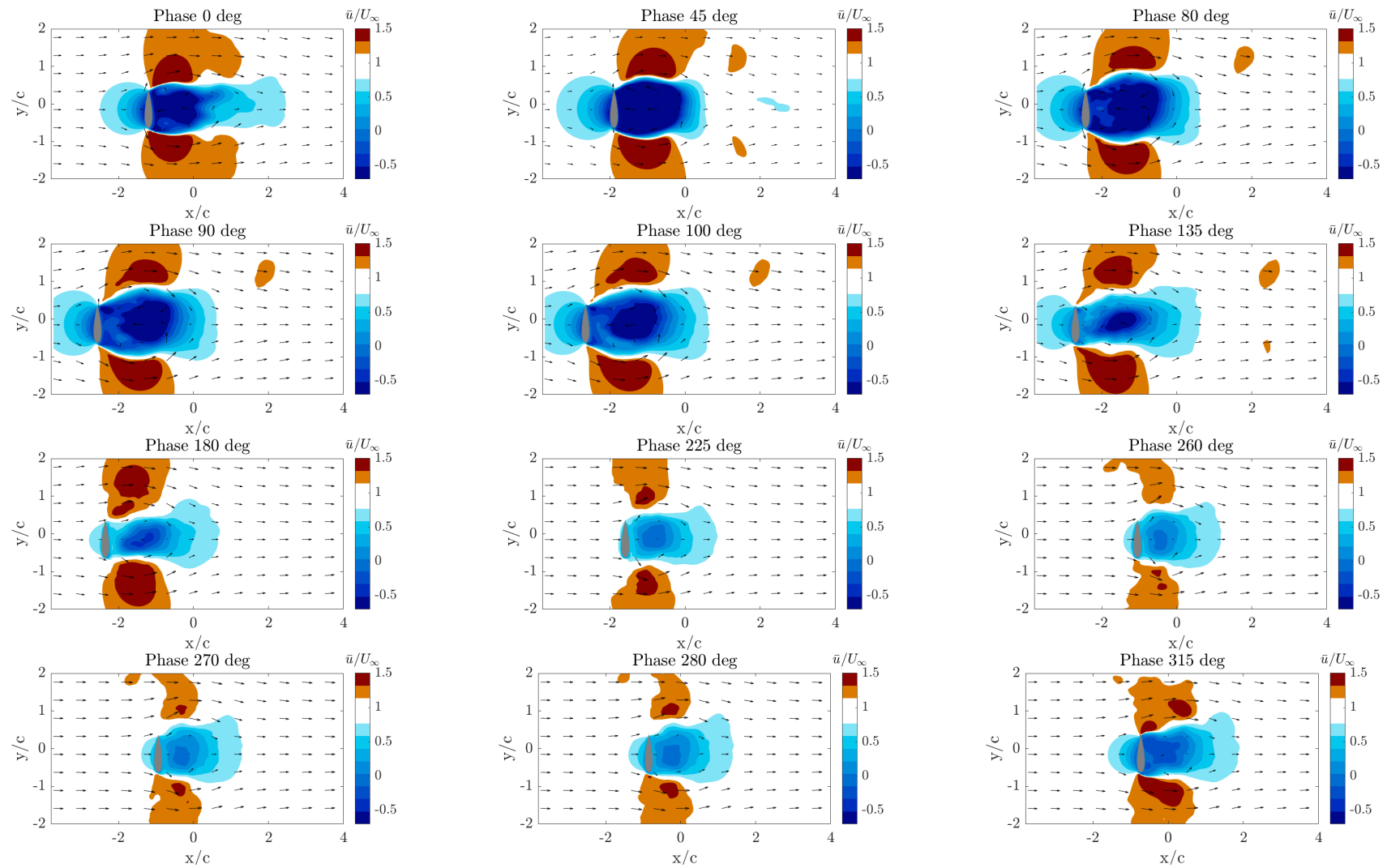


Figure O.10: Streamwise velocity, \bar{u}/U_∞ around a surging airfoil at 5Hz, 1 chord inboard from the tip with the freestream velocity coming from the left.

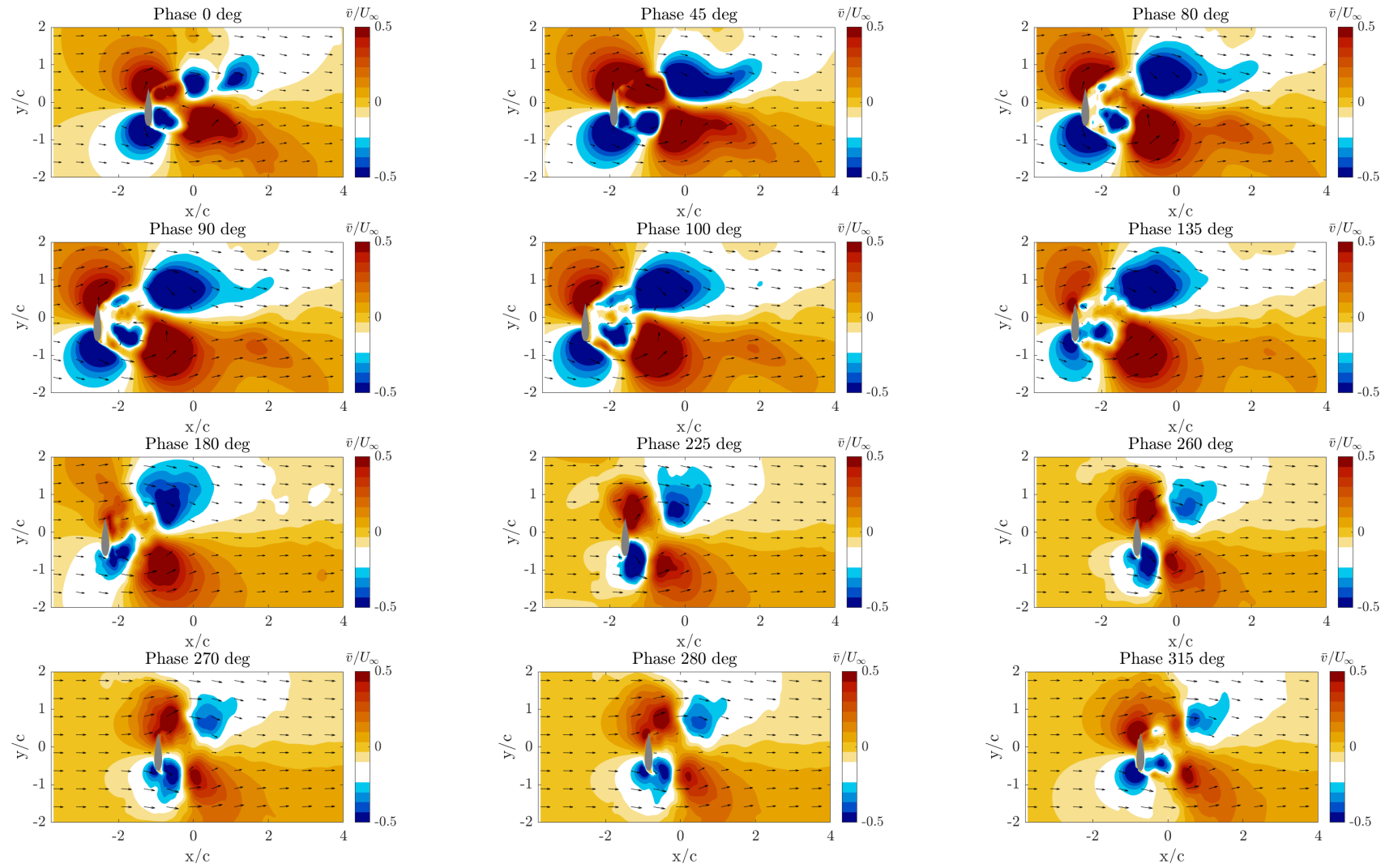


Figure O.11: Vertical velocity, \bar{v}/U_∞ around a surging airfoil at 5Hz, 1 chord inboard from the tip with the freestream velocity coming from the left.

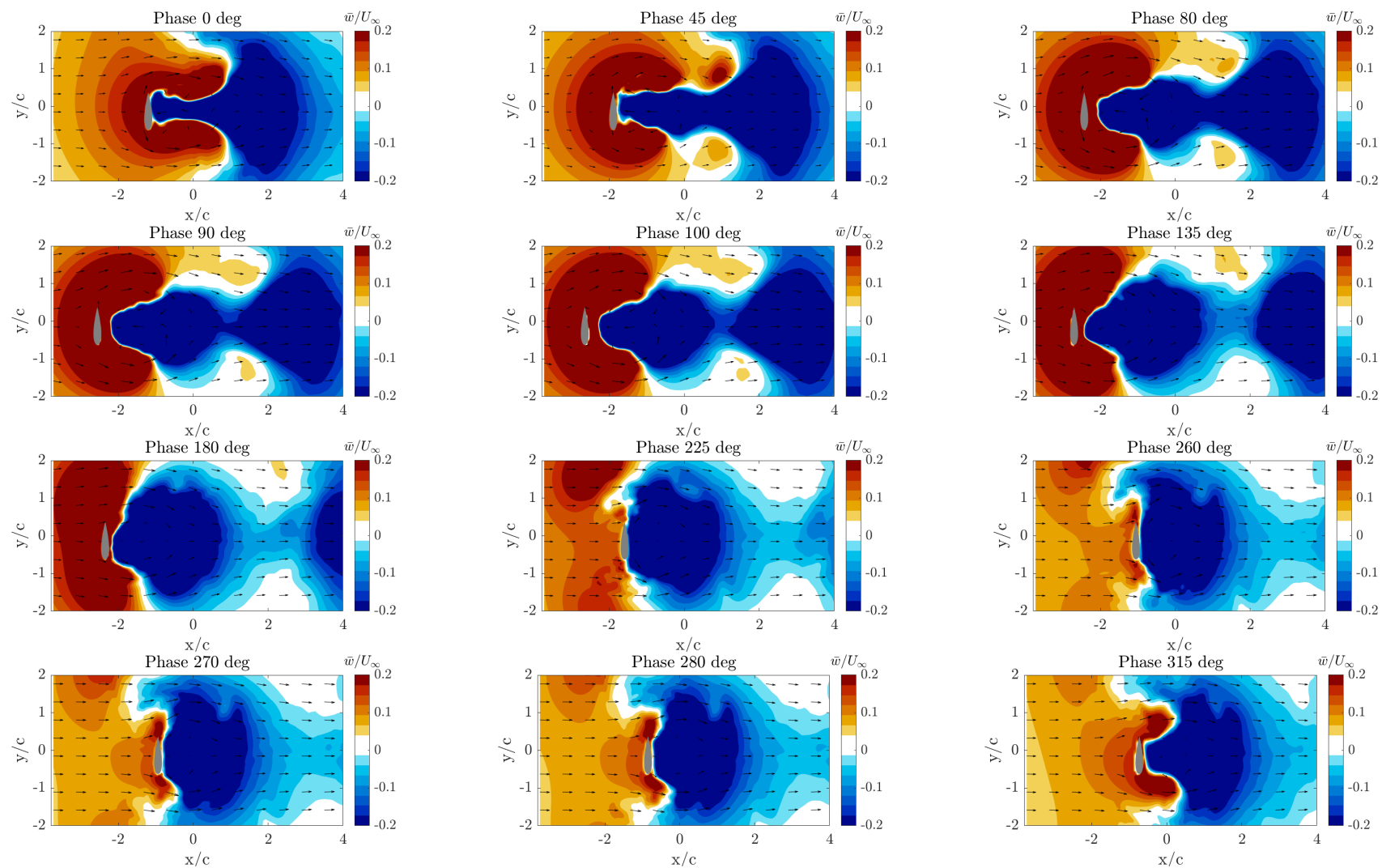


Figure O.12: Spanwise velocity, \bar{w}/U_∞ around a surging airfoil at 5Hz, 1 chord inboard from the tip with the freestream velocity coming from the left. The flow is positive into the page.

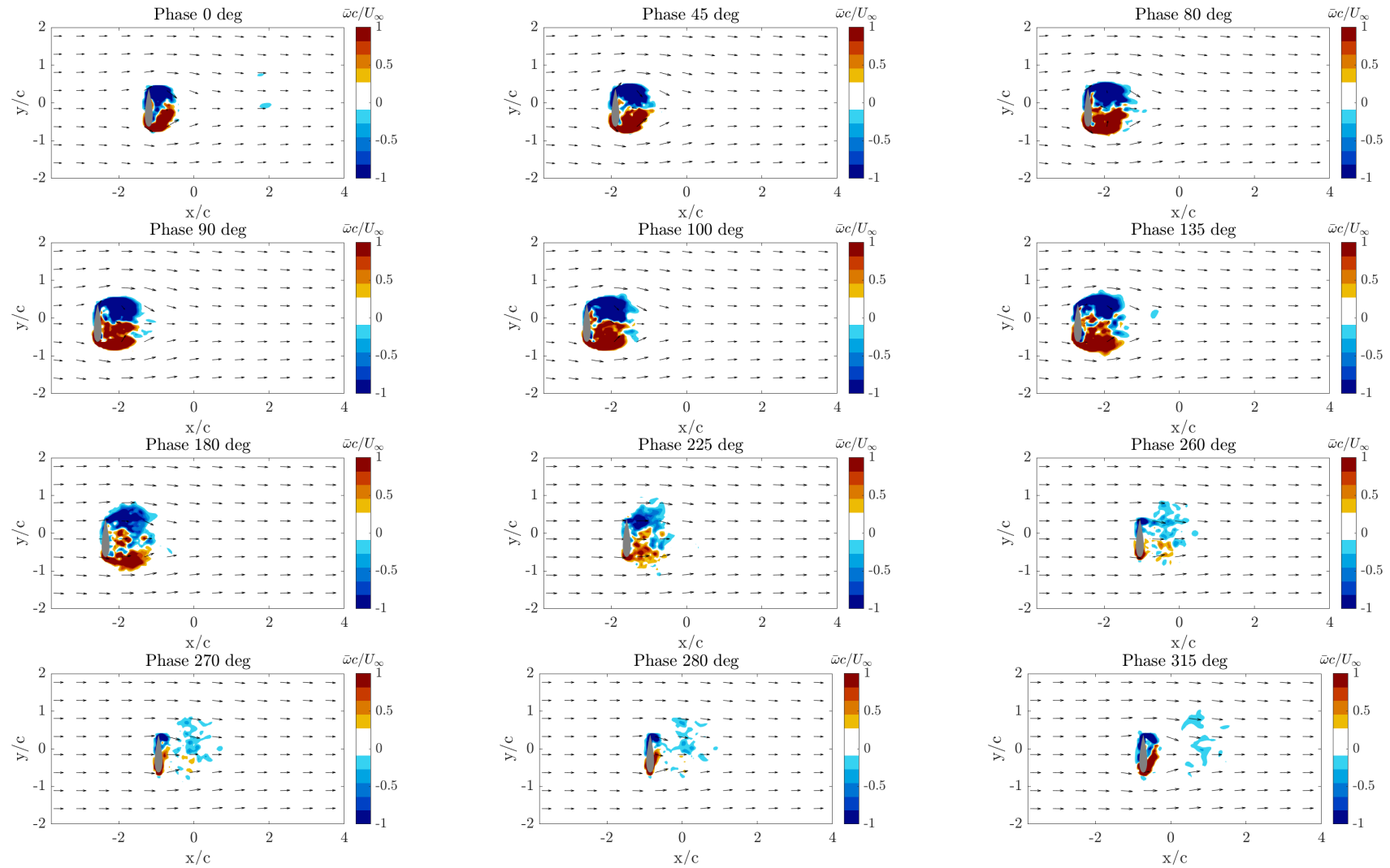


Figure O.13: Vorticity, $\bar{\omega}c/U_\infty$ around a surging airfoil at 5Hz, at the tip with the freestream velocity coming from the left.

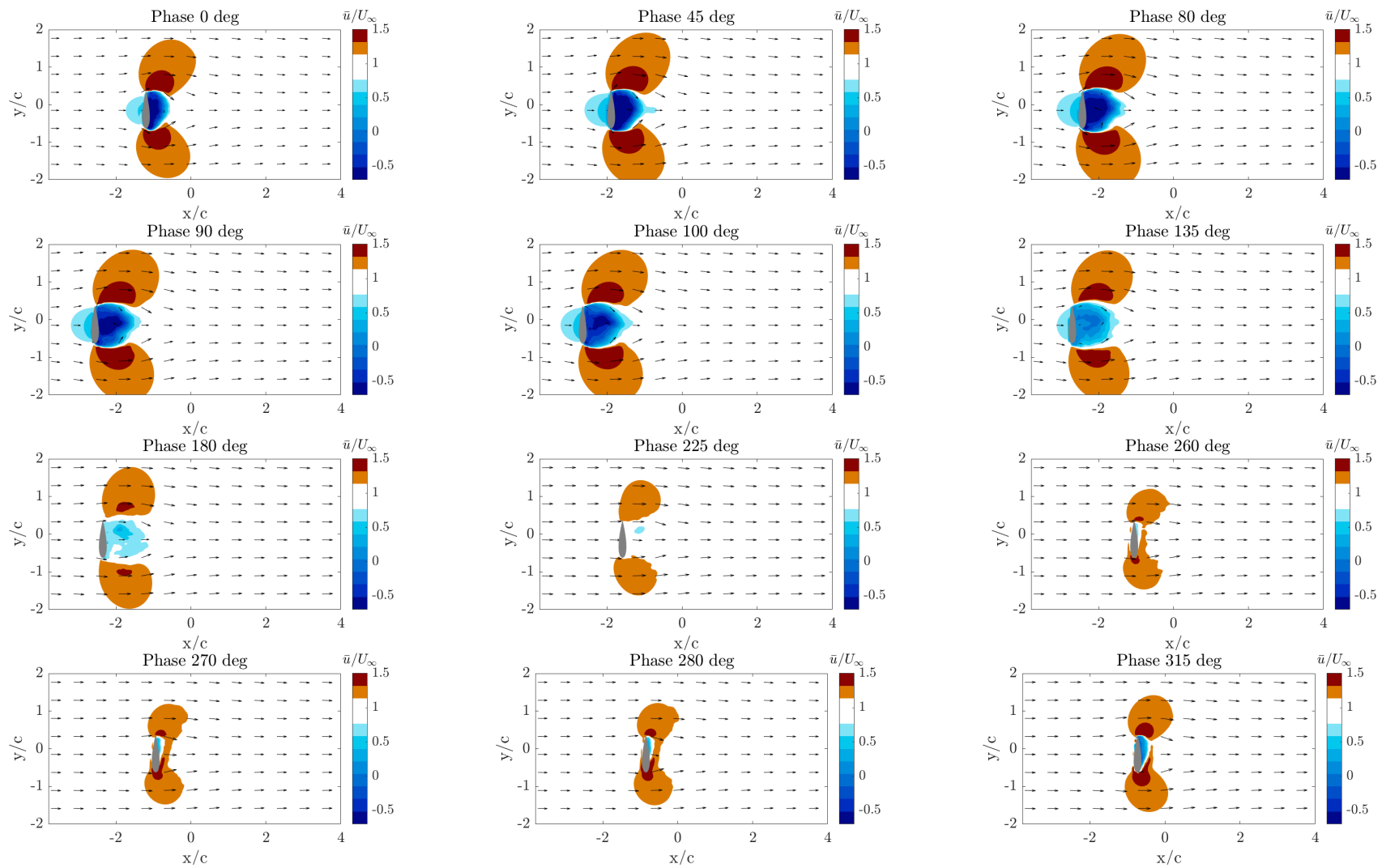


Figure O.14: Streamwise velocity, \bar{u}/U_∞ around a surging airfoil at 5Hz, at the tip with the freestream velocity coming from the left.

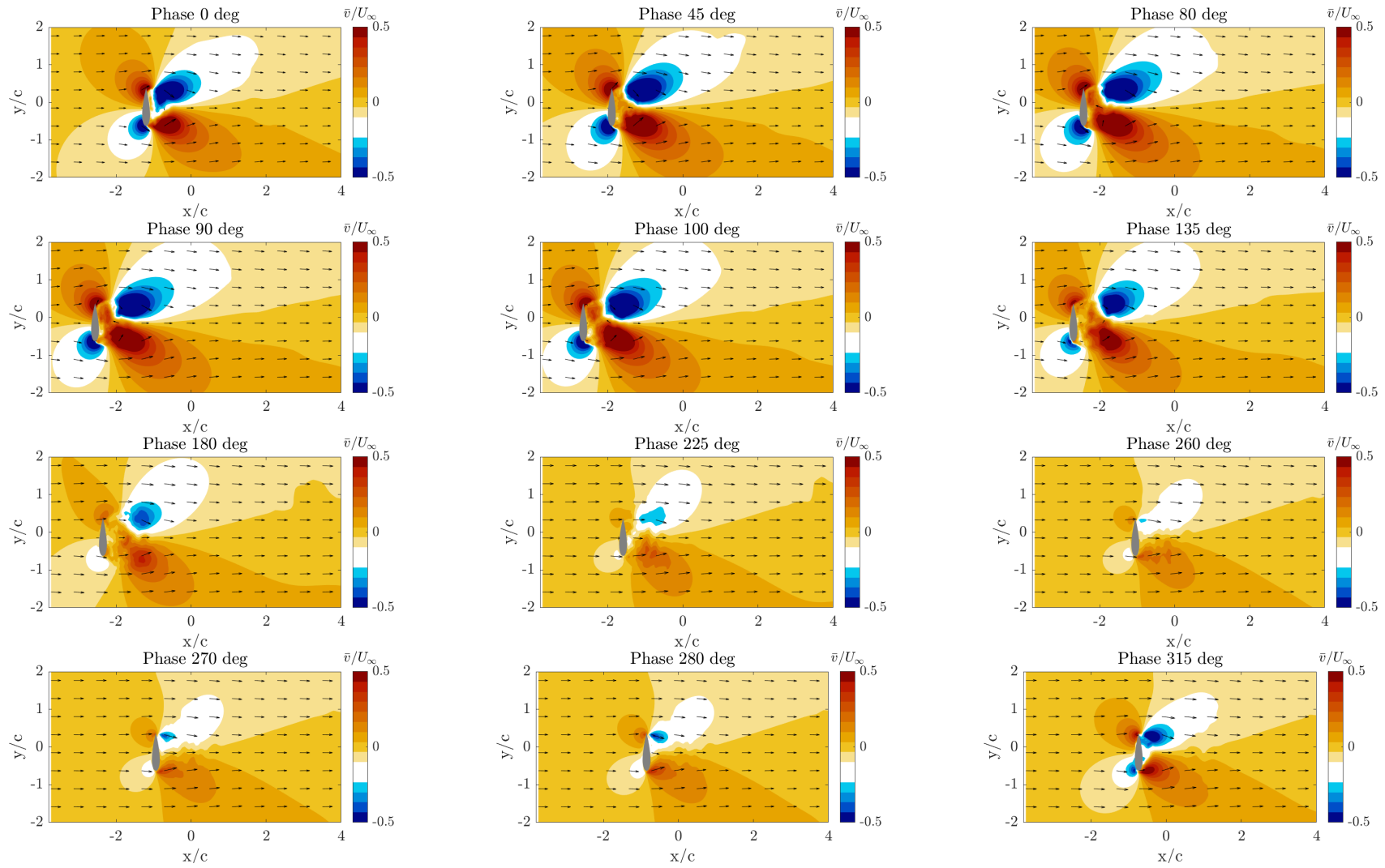


Figure O.15: Vertical velocity, \bar{v}/U_∞ around a surging airfoil at 5Hz, at the tip with the freestream velocity coming from the left.

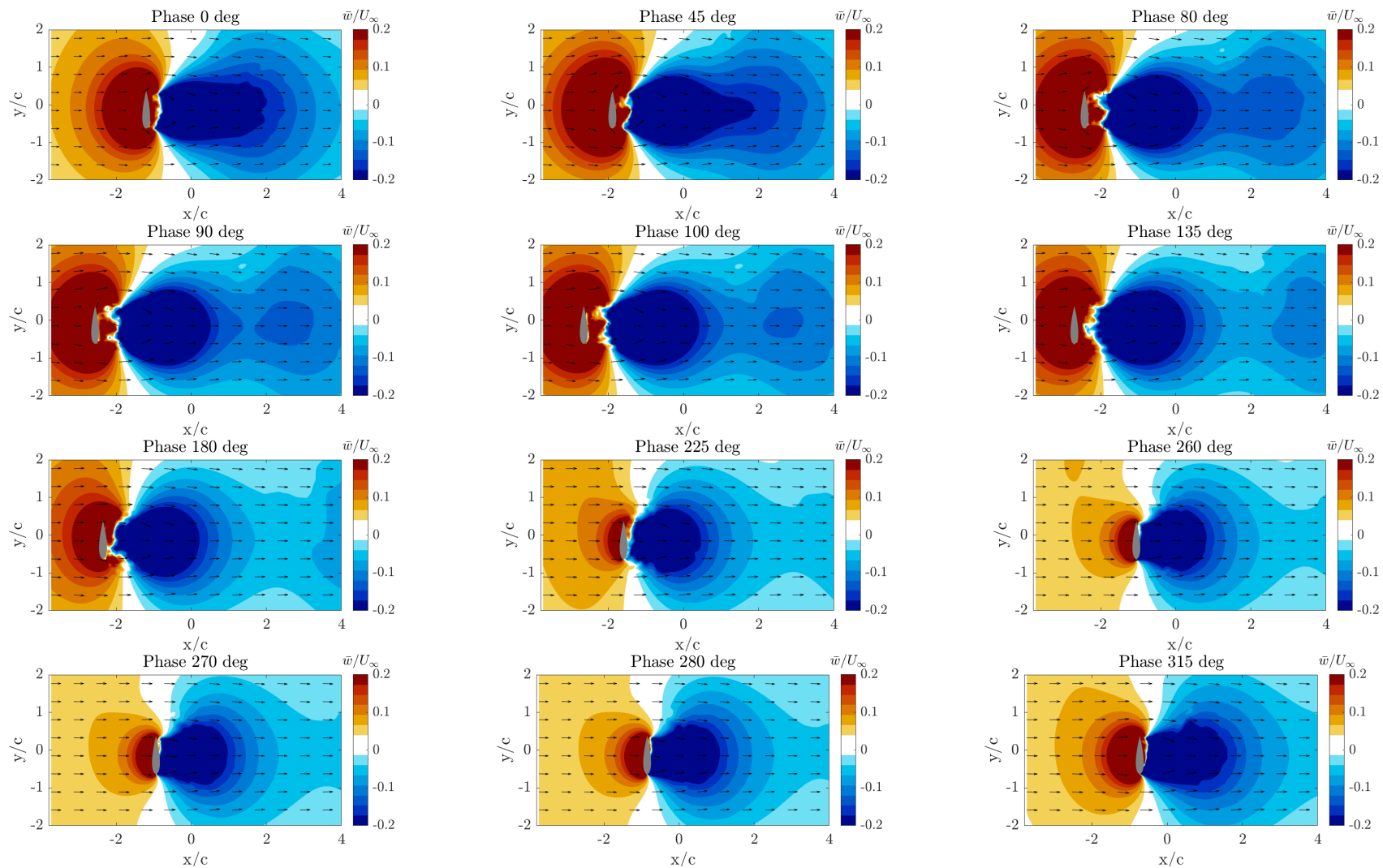


Figure O.16: Spanwise velocity, \bar{w}/U_∞ around a surging airfoil at 5Hz, at the tip with the freestream velocity coming from the left. The flow is positive into the page.

APPENDIX P

PSD and Time-Series for Plunging Cases

Criteria to determine lock-in:

- Single peak at motion frequency f_m : Lock-in, marked with a circle
- Secondary peak at the Strouhal frequency f_{st} with a PSD energy within 10% of the largest peak: Unlocked, marked with an X
- Secondary peak at the Strouhal frequency f_{st} with a PSD energy less 10% but larger than 1% of the largest peak: Border, marked with a triangle

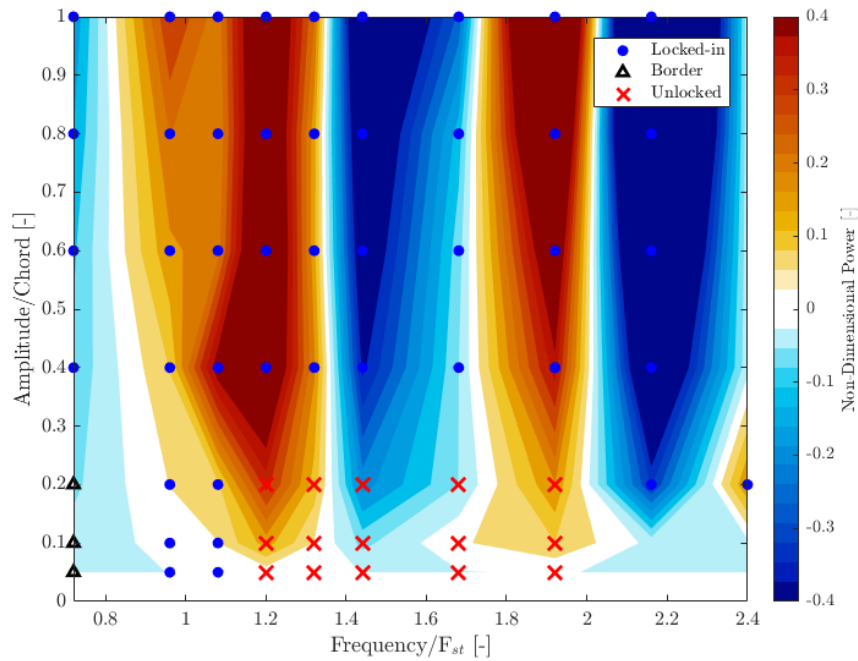
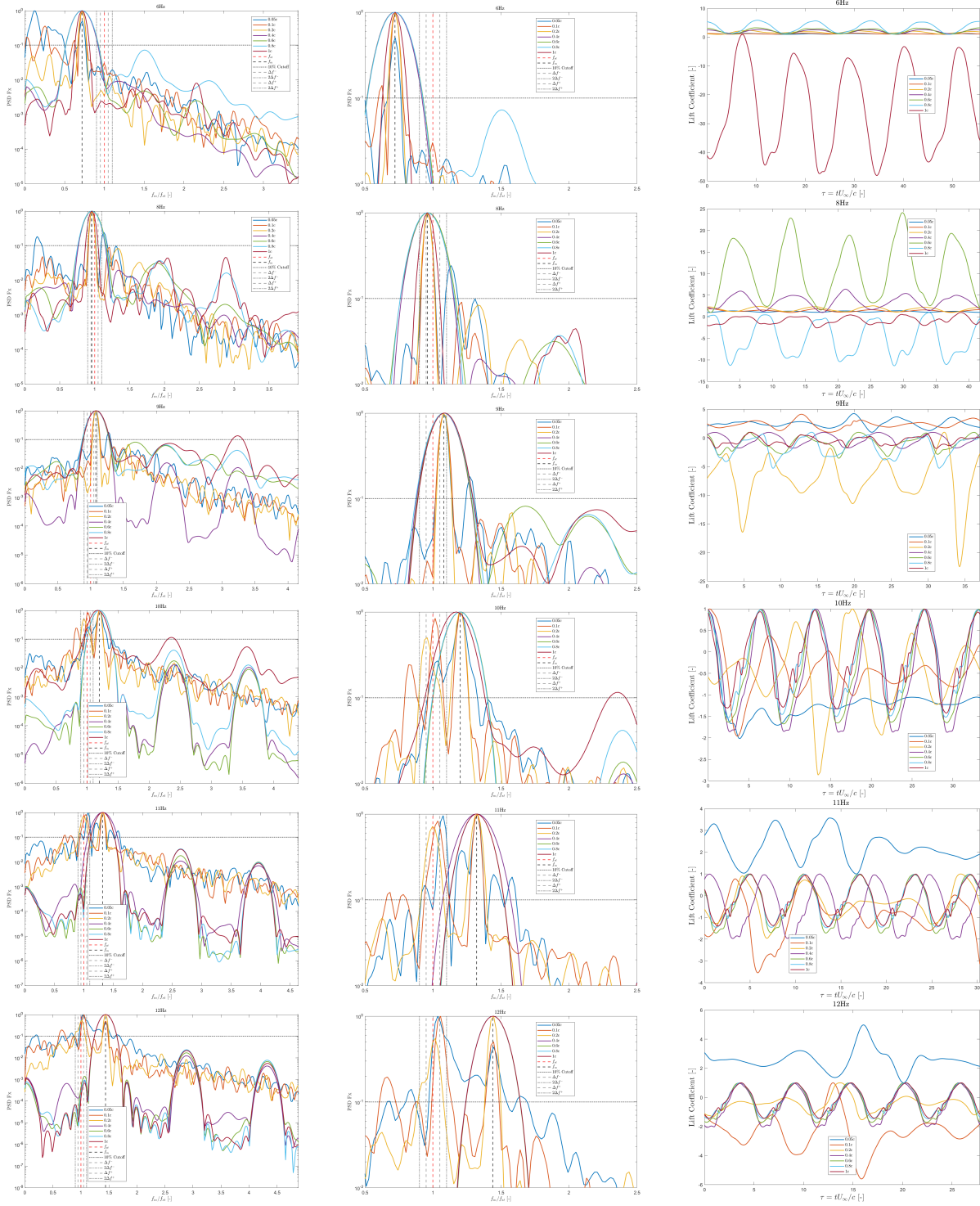


Figure P.1: Lock-in diagram, with non-dimensional power plotted on the non-dimensional amplitude (a/c) against the non-dimensional frequency (f_m/f_{st})



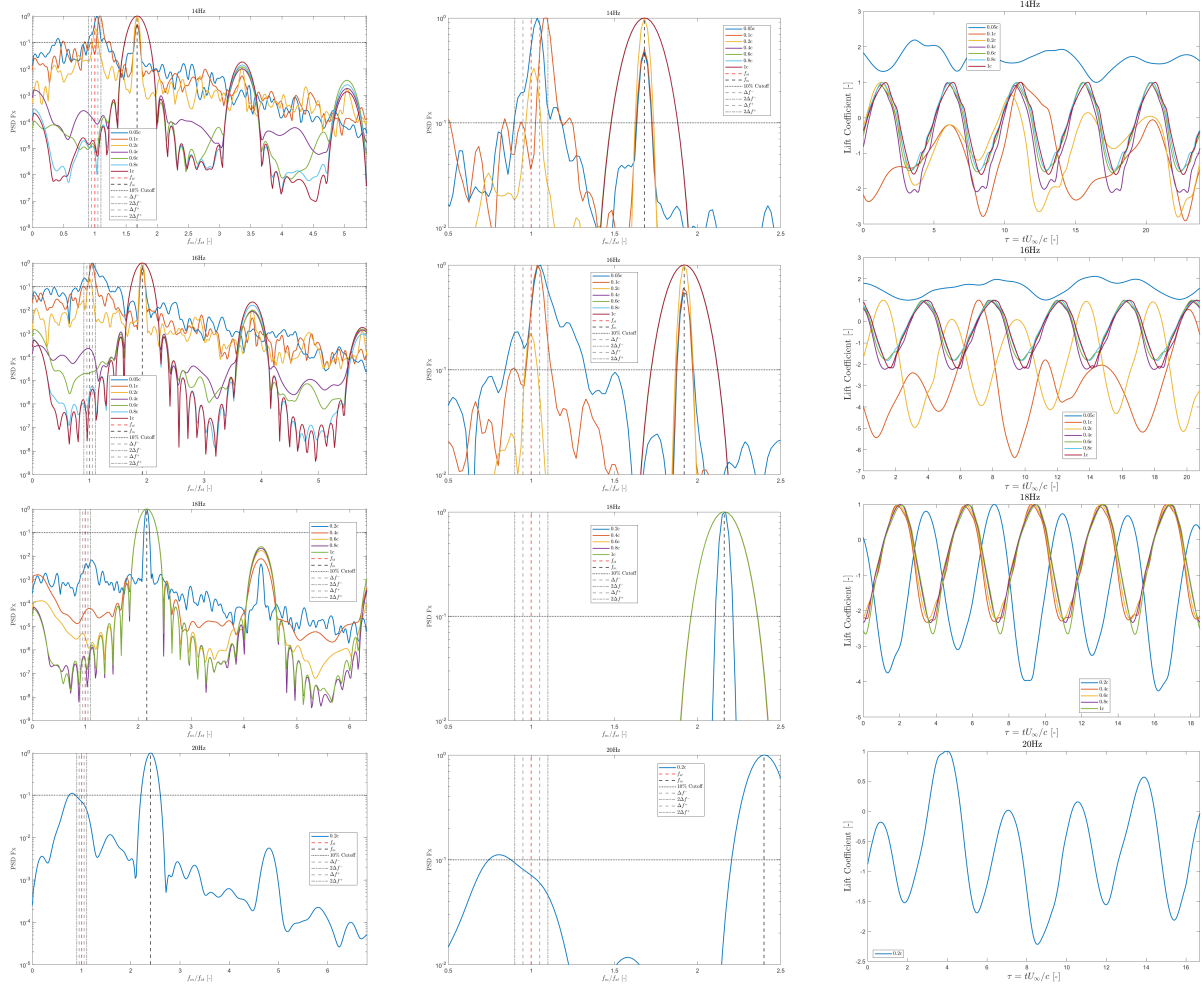


Figure P.2: CFD simulations for plunging cases at different frequencies: PSD (left), zoomed PSD (middle), and Time-Series (right).

APPENDIX Q

PSD and Time-Series for Surging Cases

Criteria to determine lock-in:

- Single peak at motion frequency f_m : Lock-in, marked with a circle
- Secondary peak at the Strouhal frequency f_{st} with a PSD energy within 10% of the largest peak: Unlocked, marked with an X
- Secondary peak at the Strouhal frequency f_{st} with a PSD energy less 10% but larger than 1% of the largest peak: Border, marked with a triangle

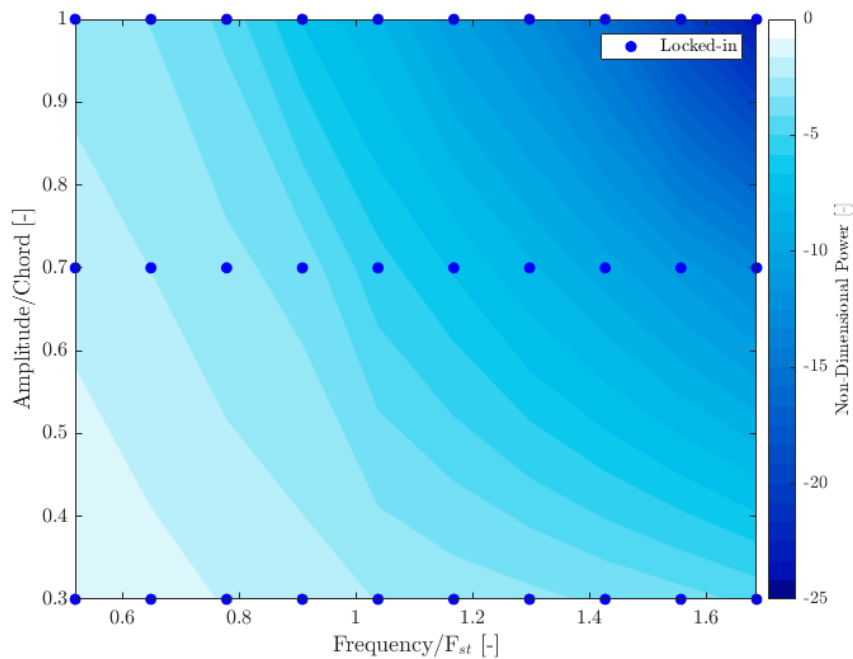
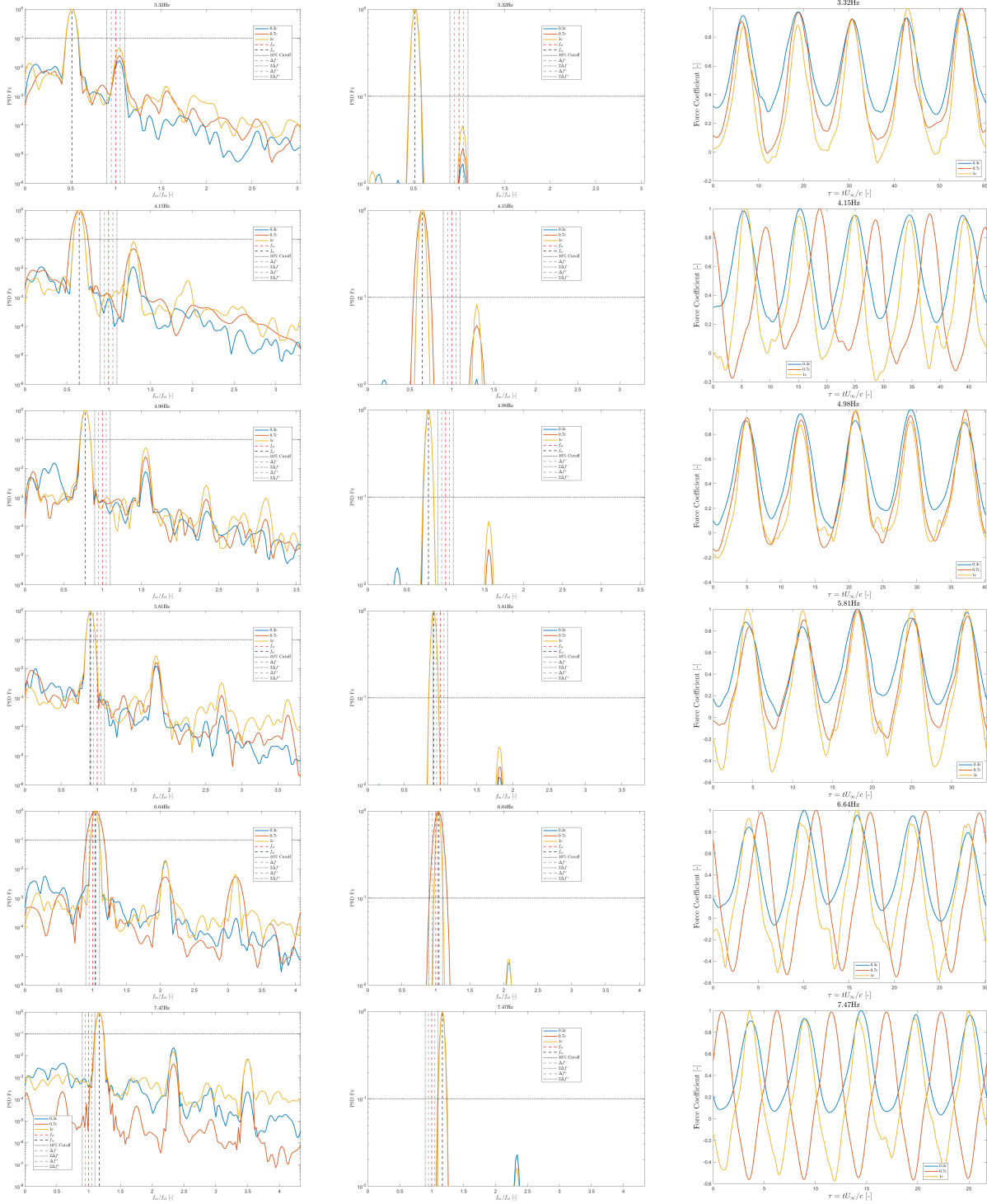


Figure Q.1: Lock-in diagram, with non-dimensional power plotted on the non-dimensional amplitude (a/c) against the non-dimensional frequency (f_m/f_{st})



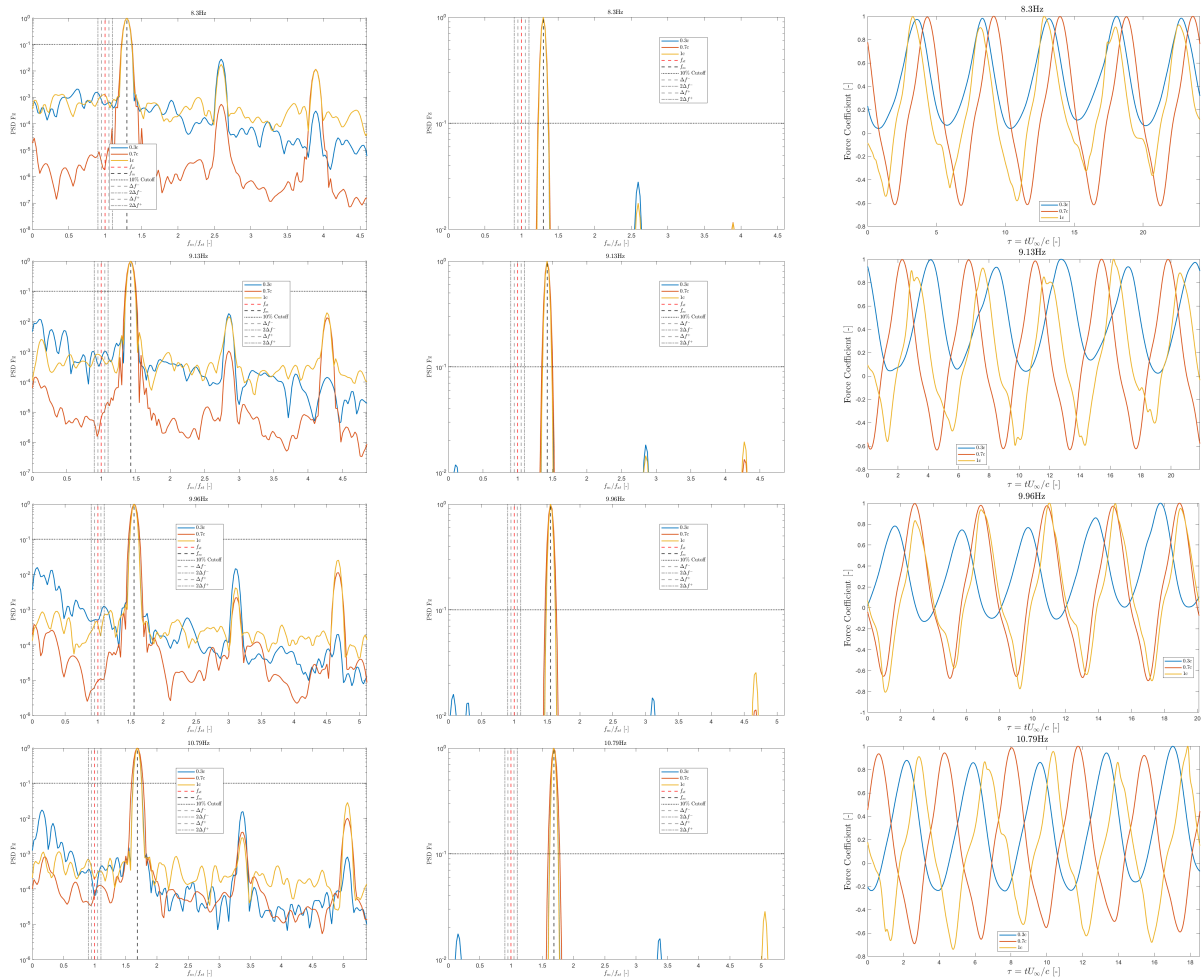


Figure Q.2: CFD simulations for surging cases at different frequencies: PSD (left), zoomed PSD (middle), and Time-Series (right).

